



UNIVERSIDADE FEDERAL DE SERGIPE
PRÓ-REITORIA DE PÓS-GRADUAÇÃO E PESQUISA
PROGRAMA DE PÓS-GRADUAÇÃO EM FÍSICA

Emergent Magnetism and Sublattice Interplay in $3d$ - $4f$ - $5d$ Double
and Quadruple Perovskites

John Matthias Attah-Baah

UFS
Ph.D. [Physics]
July 2025



Emergent Magnetism and Sublattice Interplay in $3d$ - $4f$ - $5d$ Double and Quadruple Perovskites

John Matthias Attah-Baah

A thesis submitted in partial fulfillment of the re
quirements for the degree of Doctor of Philosophy
in Physics (Condensed Matter Physics)

Supervisor: Prof. Dr. Nilson dos Santos Ferreira

Co-supervisor: Prof. Dr. Roger Douglas Johnson

UFS

Ph.D. [Physics]

July 2025

UNIVERSIDADE FEDERAL DE SERGIPE
Programa de Pós-Graduação em Física

**“Emergent Magnetism and Sublattice Interplay in 3d-4f-
5d Double and Quadruple Perovskites”**

por

John Matthias Attah-Baah

Tese de doutorado **APROVADA** em sessão pública no dia vinte e nove de julho do ano dois mil e vinte e cinco perante a banca examinadora constituída pelos seguintes professores:

Documento assinado digitalmente
gov.br NILSON DOS SANTOS FERREIRA
Data: 29/07/2025 18:06:49-0300
Verifique em <https://validar.itl.gov.br>

Prof. Dr. Nilson dos Santos Ferreira
(DFI-UFS)



Prof. Dr. Roger Douglas Johnson
(DofP-UCL)

Documento assinado digitalmente
gov.br NELSON ORLANDO MORENO SALAZAR
Data: 30/07/2025 11:03:47-0300
Verifique em <https://validar.itl.gov.br>

Prof. Dr. Nelson Orlando Moreno Salazar
(DFI-UFS)

Documento assinado digitalmente
gov.br GERSON CORTES DUARTE FILHO
Data: 29/07/2025 18:38:57-0300
Verifique em <https://validar.itl.gov.br>

Prof. Dr. Gerson Cortês Duarte Filho
(DFI-UFS)



Prof. Dr. George Amoako
(CMMP-UCC)

Documento assinado digitalmente
gov.br EDSON PASSAMANI CAETANO
Data: 30/07/2025 13:53:13-0300
Verifique em <https://validar.itl.gov.br>

Prof. Dr. Edson Passamani Caetano
(PPGFIS-UFES)


*"Materials do not think, yet they manifest the deepest truths
of the universe: emergence is the silent language of existence."*

J. M. Attah-Baah

Declaration

I, John Matthias Attah-Baah, confirm that the work presented in this thesis is my own. Where information has been derived from other sources, I confirm that this has been indicated in the thesis.

Signed

Documento assinado digitalmente
 **JOHN MATTHIAS ATTAH BAAH**
Data: 20/08/2025 21:12:22-0300
Verifique em <https://validar.it.gov.br>

Date 29/07/2025

Publications

1. R. S. Silva, F. Serrano-Sánchez, J. E. Rodrigues, C. Santos, **Attah-Baah, J. M.** R. D. dos Reis, J. L. Martínez, J. A. Alonso, and N. S. Ferreira, "Magnetostructural coupling, Kondo-like behavior, and magnetocaloric performance in Fe-doped $\text{Nd}_{0.5}(\text{Sr}_{0.4}\text{Ba}_{0.1})\text{CoO}_3$ perovskites," *Journal of Materials Chemistry C*, Royal Society of Chemistry, 2025.
2. **Attah-Baah, J.M.**, R. S. Silva Jr., C. Santos, M. H. Carvalho, and N. Ferreira, "Magnetocaloric Effect and Critical Behavior across the Second-Order Ferromagnetic–Paramagnetic Phase Transition of a NdSmNiMnO_6 Double Perovskite," *ACS Omega*, 2025.
DOI: [10.1021/acsomega.5c00940](https://doi.org/10.1021/acsomega.5c00940).
3. **Attah-Baah, J.M.**, D. D. Khalyavin, P. Manuel, N. S. Ferreira, A. A. Belik, and R. D. Johnson, "Spin reorientation and the interplay of magnetic sublattices in $\text{Er}_2\text{CuMnMn}_4\text{O}_{12}$," *Acta Crystallographica Section B*, 2024.
DOI: [10.1107/S2052520624008965](https://doi.org/10.1107/S2052520624008965).
4. **Attah-Baah, J.M.**, Santos, C., Silva Jr., R.S., et al. (2024). "Unveiling the impact of Fe-doping concentration on the local structure and morphological evolution of Cr_2O_3 nanoparticles". *Ceramics International*, DOI: [10.1016/j.ceramint.2024.06.389](https://doi.org/10.1016/j.ceramint.2024.06.389)
5. Santos, C., **Attah-Baah, J.M.**, Silva Junior, R.S., et al. (2023). "Insights into the Fe^{3+} doping effects on the structure and electron distribution of Cr_2O_3 nanoparticles". *Nanomaterials*, 13(6), 980. DOI: [10.3390/nano13060980](https://doi.org/10.3390/nano13060980)
6. Matos, R.S., **Attah-Baah, J.M.**, Monteiro, M.D.S., et al. (2023). "Effect of the amapá-latex chelating agent contents on the microstructure and photocatalytic properties of ZnO nanoparticles". *Journal of Materials Research and Technology*, DOI: [10.1016/j.jmrt.2022.12.119](https://doi.org/10.1016/j.jmrt.2022.12.119)

-
7. Moraes, C.G.P., Matos, R.S., Santos, C., **Attah-Baah, J.M.**, et al. (2022). "Investigating the correlation between the microstructure and electrical properties of FeSbO₄ ceramics". *Materials*, 15(19), 6555. DOI: [10.3390/ma15196555](https://doi.org/10.3390/ma15196555)
 8. Matos, R., **Attah-Baah, J.M.**, Monteiro, M., et al. (2022). "Evaluation of the photocatalytic activity of distinctive-shaped ZnO nanocrystals synthesized using latex of different plants native to the Amazon rainforest". *Nanomaterials*, 12(16), 2889. DOI: [10.3390/nano12162889](https://doi.org/10.3390/nano12162889)
 9. N. S. Ferreira, J. M. Sasaki, R. S. Silva Jr., **Attah-Baah, J. M.** and M. A. Macêdo, Visible-Light-Responsive Photocatalytic Activity Significantly Enhanced by Active [V_{Zn}⁺ + V_O⁺] Defects in Self-Assembled ZnO Nanoparticles, *Inorganic Chemistry*, **60** (7), 4475–4496, 2021. DOI: [10.1021/acs.inorgchem.0c03621](https://doi.org/10.1021/acs.inorgchem.0c03621).

Abstract

This thesis presents a systematic investigation of complex magnetic interactions in rare-earth containing perovskites, combining advanced neutron diffraction, magnetometry, and first-principles calculations to unravel the interplay between 3d-4f-5d exchange pathways, structural distortions, and functional properties. Through careful analysis of the double perovskite $\text{Nd}_2\text{NiMnO}_6$, we establish a monoclinic $\text{P2}_1/\text{n}$ structure with almost complete B-site ordering of Ni/Mn and reveal a rich magnetic phase diagram featuring: (i) ferromagnetic ordering of Ni^{2+} - Mn^{4+} sublattices at $T_N = 198$ K exhibiting mean-field critical behavior, (ii) a re-entrant spin-glass state below T_N , and (iii) non-collinear Nd^{3+} ordering below $T_{N1} = 22$ K driven by competing $f-d$ and $f-f$ exchange. The system demonstrates promising magnetocaloric performance ($\Delta S_M = 2.25 \text{ Jkg}^{-1}\text{K}^{-1}$ at 7 T) and significant spin-phonon coupling. The introduction of 5d Ir dopants in $\text{Nd}_2\text{NiMn}_{0.25}\text{Ir}_{0.75}\text{O}_6$ leads to three fundamental advances: (1) resolution of a unified Γ_1^+ magnetic structure eliminating previous phase coexistence models, (2) precise determination of reduced Mn/Ir moments ($0.38 \mu_B$) revealing strong spin-orbit frustration, and (3) discovery of coherent Nd^{3+} ordering with b -axis ferromagnetism and ac -plane canting. Remarkably, Ir mediates enhanced $3d-4f$ coupling despite suppressing B-site magnetization, demonstrating a novel route to engineer $3d-5d-4f$ interactions. Meanwhile, in NdSmNiMnO_6 , we identify a ferrimagnetic ground state ($\Delta E_{\text{FM-FiM}} \approx 0.02 \text{ eV}$) stabilized by $\text{P2}_1/\text{n}$ distortions ($\langle \text{Ni-O-Mn} \rangle \approx 146^\circ$), with pronounced magnetostriction effects and spin-phonon coupling evidenced by Raman mode hardening. The material shows excellent magnetocaloric properties ($\text{RCP} = 182 \text{ J/kg}$) and critical exponents revealing a mean-field to 3D Heisenberg crossover. First-principles calculations confirm the crucial role of orbital ordering and SOC-induced Sm^{3+} moment quenching. Finally, in the quadruple perovskite $\text{Er}_2\text{CuMnMn}_4\text{O}_{12}$, we uncover four distinct magnetic transitions featuring spin reorientations between $\pm b$ and $\pm c$ axes, culminating in a low-temperature phase ($T_{N4} = 7 \text{ K}$) with $k = (0, 0, \frac{1}{2})$ modulated Er_1 - Mn_3 coupling. The sequence of transitions highlights the complex interplay between transition metal and rare-earth sublattices in these frustrated systems. Collectively, this work establishes design principles for manipulating competing

exchange interactions in multifunctional perovskites, while demonstrating their potential for magnetic refrigeration and spintronic applications. The combination of structural tuning, $5d$ -orbital tuning, and sublattice-specific control presented here provides a roadmap for developing next-generation multifunctional materials with tailored magnetostructural properties.

keywords: double perovskite, columnar perovskites; ferrimagnetism; spin reorientation; magnetic frustration

Resumo

Esta tese apresenta uma investigação sistemática das interações magnéticas complexas em perovskitas contendo terras-raras, combinando técnicas avançadas de difração de nêutrons, magnetometria e cálculos de primeiros princípios para desvendar a interação entre vias de troca $3d-4f-5d$, distorções estruturais e propriedades funcionais. Através da análise detalhada da dupla perovskita $\text{Nd}_2\text{NiMnO}_6$, estabelecemos uma estrutura monoclinica $\text{P2}_1/\text{n}$ com ordenamento quase completo dos sítios B de Ni/Mn e revelamos um rico diagrama de fase magnética, caracterizado por: (i) ordenamento ferromagnético das sub-redes $\text{Ni}^{2+}\text{-Mn}^{4+}$ em $T_N = 198$ K, exibindo comportamento crítico de campo médio; (ii) um estado reentrante de vidro de spins abaixo de T_N ; e (iii) ordenamento não colinear de Nd^{3+} abaixo de $T_{N1} = 22$ K, impulsionado pela competição entre trocas $f-d$ e $f-f$. O sistema demonstra desempenho magnetocalórico promissor ($\Delta S_M = 2.25 \text{ Jkg}^{-1}\text{K}^{-1}$ a 7 T) e acoplamento spin-fônico significativo. A introdução de dopantes de Ir $5d$ em $\text{Nd}_2\text{NiMn}_{0.25}\text{Ir}_{0.75}\text{O}_6$ levou a três avanços fundamentais: (1) a resolução de uma estrutura magnética unificada Γ_1^+ , eliminando modelos anteriores de coexistência de fases; (2) a determinação precisa de momentos reduzidos de Mn/Ir ($0.38 \mu_B$), revelando forte frustração spin-órbita; e (3) a descoberta de um ordenamento coerente de Nd^{3+} com ferromagnetismo ao longo do eixo b e inclinação no plano ac . Notavelmente, o Ir media um acoplamento $3d-4f$ aprimorado, apesar de suprimir a magnetização no sítio B, demonstrando uma nova rota para projetar interações $3d-5d-4f$. Enquanto isso, em NdSmNiMnO_6 , identificamos um estado fundamental ferrimagnético ($\Delta E_{\text{FM-FiM}} \approx 0.02 \text{ eV}$) estabilizado por distorções $\text{P2}_1/\text{n}$ ($\langle \text{Ni-O-Mn} \rangle \approx 146^\circ$), com efeitos de magnetostrição pronunciados e acoplamento spin-fônico evidenciado pelo endurecimento de modos de Raman. O material exhibe excelentes propriedades magnetocalóricas ($\text{RCP} = 182 \text{ J/kg}$) e expoentes críticos que revelam uma transição entre comportamentos de campo médio e Heisenberg 3D. Cálculos de primeiros princípios confirmam o papel crucial do ordenamento orbital e do quenching do momento de Sm^{3+} induzido por SOC. Finalmente, na perovskita quádrupla $\text{Er}_2\text{CuMnMn}_4\text{O}_{12}$, descobrimos quatro transições magnéticas distintas, caracterizadas por reorientações de

spin entre os eixos $\pm b$ e $\pm c$, culminando em uma fase de baixa temperatura ($T_{N4} = 7$ K) com acoplamento modulado $\text{Er}_1\text{-Mn}_3$ em $k = (0, 0, \frac{1}{2})$. A sequência de transições destaca a interação complexa entre as sub-redes de metais de transição e terras-raras nesses sistemas frustrados. Coletivamente, este trabalho estabelece princípios de projeto para manipular interações de troca competitivas em perovskitas multifuncionais, demonstrando seu potencial para aplicações em refrigeração magnética e spintrônica. A combinação de ajuste estrutural, engenharia orbital $5d$ e controle específico de sub-redes apresentada aqui fornece um roteiro para o desenvolvimento de materiais multifuncionais de próxima geração com propriedades magnetoestruturais sob medida.

Palavras-chave: dupla perovskita, perovskitas colunares; ferrimagnetismo; re-orientação de spin; frustração magnética

Acknowledgements

To my parents, Mr. Williams Tonah and Wehelmina Effah - your prayers, sacrifices, and unconditional love made this journey possible. You gave me life, then gave that life wings. Likewise, to my siblings for believing in this journey. To my advisor, Prof. Dr. Nilson dos Santos Ferreira (UFS), my deepest gratitude for being both an academic compass and life mentor. Your razor-sharp intellect, unwavering integrity, and unexpected humor transformed research from a process into a passion. Thank you for teaching me that clarity is kindness in science, and for welcoming me into your family's warmth during our marathon thesis sessions. To Prof. Dr. Roger D. Johnson (UCL-UK)- your brilliant mind and exacting standards during my sandwich program didn't just improve this work; they redefined my scientific identity. Your ability to balance rigorous critique with zesty enthusiasm remains my gold standard for mentorship. To my wife, Ana Attah-Baah-warrior woman who single-handedly held our home together while I chased neutrons across continents. King Orion and I won this degree together with you. To Mrs. Adalhir Lima and all family members, your quiet sacrifices built these pages. To Prof. George Amoako, you were the one who threw the javelin of opportunity, and now its flight has become a triumph for humanity. To Prof. Nelson O. Salazar (UFS) - your early belief launched this journey. To Prof. Dr. Eduardo Granado (Unicamp)- your lab's doors and wisdom were gifts that shaped key findings. To Dr. Helena Maria Carvalho - your eleventh-hour heroism saved this thesis, and my sanity. For Prof. Dr. Ronaldo Silva: Your lab, a forge where my science took form-Open doors, open heart, weathering every storm. In glassware and data, your trust kept me warm; A debt etched in bonds no reaction could transform. For Prof. Dr. Marcus Vinicius: Direct or unseen, your support never ceased. My work bears your mark; its foundation increases. To Dr. R.S. Silva Jr., Dr. Diego Evaristo, Dr. Rai, and Dr. Cledson Santos - my troubleshooting dream team, I am deeply grateful. To Dr. Dylan Behr (UCL) - your transatlantic support proved academia has no borders. To Dr. Anderson, Emanuel Ph.D., Gilvan Ph.D., Leonardo Ph.D., Dr. Leo S.S. Oliveira, Klivan PhD, Jamil PhD, and Ericson PhD, our brotherhood turned grueling seminars into joyful discoveries. To Benjamin Sottie, Ph.D, Sir. Samuel Umama and

Katlego Ramogala, Ph.D- your home became my sanctuary, I bless you home. To Eugene Broni, Ph.D, a brother not by blood but by bond, my gratitude is as deep as kinship. To Eric Broni, for tirelessly safeguarding what matters overseas, your care leaves me forever grateful. To Uncle Bob(UK), you embraced me as both a son and brother, sheltering me through London's coldest days. While the world sees only glimpses of your kindness, I know the full measure of what you did, and my gratitude runs deeper than words can express. To Mr. Frank Prah(Mr Radiant) and the Fabrice team (UCL-UK): Without your internet and technical support, the LCN and UCL postgraduate program would be nothing. Thank you. To Dr. Lucas(UCL-UK)-thanks for the Inkscape-tutorship. To Shuan Boodram PhD (UCL-UK): I deeply appreciate your time driving us from Cambridge and those early morning conversations meant a lot. To Mallica Pandya PhD(UCL-UK): Thank you for your unwavering support and encouragement every time we crossed paths at LCN-those early morning conversations were truly uplifting. I'm deeply grateful. To all UCC Physics/Engineering/Materials/Chemistry Alumni: You built my inner core. I am forever grateful. To Mateos, PhD (Italy) - for pasta-fueled brainstorming. To Rev. Lands and Adwoa Amina - your prayers were my shield. To Okoh Agyemang, Mr. Lucas of Renatta Kaimbé and Stenio families, you became my Brazilian tribe. To Prof Heli, Kofi Nsiah(USA), I owe you deepest gratitude. To the Association of Foreigners at UFS, for making Brazil feel like home. To CAPES and CNPq - your investments made this research possible. To NPGFI/UFS faculty, your collective wisdom shaped my academic path. This dissertation stands on the shoulders of giants, some named here, many unnamed, all unforgettable.

Table of Contents

Chapter I Introduction

1.1 Cubic Perovskite Structure	35
1.2 The Goldschmidt Tolerance Factor	36
1.3 Related Perovskites Structure	37
1.3.1 Double Perovskites	38
1.3.2 Quadruple Perovskites	41
1.4 Structural Deviations	43
1.4.1 Octahedral Distortion: Jahn-Teller(J-T) Effect	44
1.4.2 Octahedral Rotation: Glazer Notation and Symmetry	45
1.4.3 A- or B-site Cation Displacement	48
1.5 State of the Art and Scope of the Thesis	49

Chapter II Theoretical Review

2.1 Crystal Symmetry	56
2.1.1 Point Group	57
2.1.2 Space Groups and Translational Symmetry	60
2.2 Magnetic Symmetry	61
2.3 Magnetism in Perovskite	70
2.3.1 Zener Double-Exchange Mechanism	71
2.3.2 Superexchange Interaction	73
2.3.3 Antisymmetric Exchange Interaction	76
2.3.4 Spin Glass	78

Chapter III Experimental

3.1 Synthesis	85
3.1.1 Doping of Perovskites	87
3.1.2 Sample Preparation	89
3.1.3 Characterization Techniques	90
3.1.3.1 X-Ray Scattering	90
3.1.3.2 Neutron Scattering	92
3.1.3.3 Scattering Specificities	94
a) Coherent Scattering:	98
b) Incoherent Scattering:	99

c) Coherent Part:	99
d) Incoherent Part:	99
3.1.4 Instruments, Data Acquisition and Analysis	107

Chapter IV Characterization of the magnetic phase transitions in double perovskite $\text{Nd}_2\text{NiMnO}_6$

4.1 Introduction	122
4.2 Experiment	124
4.3 Results and Discussion	125
4.3.1 Crystal Structure	125
4.3.2 DC magnetometry	129
4.3.3 AC magnetometry	132
4.3.4 Neutron powder diffraction	134
4.3.5 Magnetocaloric Effect	139
4.3.6 Critical Point Exponents	143
4.3.7 Phonon Dynamics	147
4.4 Conclusion	153

Chapter V Spin-Orbit Coupling and Exchange Interplay in $\text{Nd}_2\text{NiMn}_{0.25}\text{Ir}_{0.75}\text{O}_6$: A 3d-5d-4f Magnetism Paradigm

5.1 Introduction	156
5.2 Experiment	160
5.3 Results and Discussion	164
5.3.1 Crystal Structure	164
5.3.2 DC Magnetometry	165
5.3.3 AC magnetometry	168
5.3.4 Specific Heat	170
5.3.5 Raman Spectroscopy	173
5.3.6 Neutron powder diffraction	180
5.4 Conclusion	185

Chapter VI Magnetostructural Coupling: Analysis in NdSmNiMnO_6 Double Perovskite

6.1 Introduction	187
6.2 Experimental Procedures	190
6.2.1 Synthesis	190

6.2.2 Characterization191
6.2.3 DFT Calculations192
6.3 Results and Discussion194
6.3.1 Crystal Structure194
6.3.2 XANES198
6.3.3 Magnetic Properties200
6.3.4 Magnetoelastic Coupling204
6.3.5 DFT218
6.4 Conclusion223

Chapter VII MCE and Critical Behavior across the Second-Order FM-PM Phase Transition in the DP NdSmNiMnO₆

7.1 Introduction226
7.2 Experimental Procedures228
7.2.1 Synthesis228
7.2.2 Characterization229
7.3 Results and Discussion230
7.3.1 Structure Characterization230
7.3.2 Magnetocaloric Effect232
7.3.3 Critical Exponent Analysis238
7.4 Conclusion247

Chapter VIII Spin Reorientation and the Interplay of Magnetic Sub- lattices in ECMO

8.1 Introduction249
8.2 Experiment251
8.3 Results252
8.3.1 Magnetic susceptibility252
8.3.2 Specific heat253
8.3.3 Neutron powder diffraction255
8.3.4 Er ³⁺ crystal electric field262
8.4 Discussion264
8.5 Conclusions266

Chapter IX Conclusions

Chapter A Experimental

1.1 XRD Data of $\text{Nd}_2\text{NiMn}_{1-x}\text{Ir}_x\text{O}_6$.271
Chapter B $\text{Nd}_2\text{NiMnO}_6$	
2.1 Phonon Dynamics	.273
Chapter C $\text{Nd}_2\text{NiMn}_{0.25}\text{Ir}_{0.75}\text{O}_6$	
3.1 Crystal Structure	.274
3.2 AC Magnetometry	.274
3.3 Raman Spectroscopy	.277
3.4 Specific Heat	.278
Chapter D NdSmNiMnO_6	
4.0.1 Crystal Structure	.279
4.0.2 Magnetic Properties	.279
4.0.3 Magnetoelastic Coupling	.280
References	282

List of Figures

I.1	Schematic of the idealized cubic perovskite ABX_3 ($A = \text{Sr}$, $B = \text{Ti}$, $X = \text{O}$) $Pm\bar{3}m$ structure. The blue, green, and orange spheres are Sr^{2+} , Ti^{4+} and O^{2-} , showing corner-sharing TiO_6 octahedra geometry and the centrally located Sr-cation.	35
I.2	The crystal structure of $\text{Nd}_2\text{NiMnO}_6$ in the $P2_1/n$ space group is presented as a single unit cell. (a) The A -site with Nd atoms is depicted in orange. (b) The B -sites are shown, with Ni and Mn atoms represented in blue and royal. (c) The $(\text{NiMn})\text{O}_6$ octahedral tilt coordination is highlighted, with Ni and Mn octahedra shaded in blue and royal, respectively. The O^{2-} ions are represented by grey spheres.	40
I.3	(a) The $\text{AA}'_3\text{B}_4\text{O}_{12}$ structure; the squares represent square planar $\text{A}'\text{O}_4$ coordination polyhedra. (b) The distribution of the $\text{A}'\text{O}_4$ polyhedra within a unit cell. Adapted from [1].	42
I.4	The ideal cubic ABX_3 perovskite structure, along with its prevalent structural distortions, including octahedral tilting, cation displacement, and octahedral distortion—arising from ionic size mismatch [2].	44
I.5	Octahedral Rotation Modes and Tilt Patterns in Perovskite Transition Metal Oxides. (a) Octahedral rotations in perovskite transition metal oxides can be decomposed into components about three orthogonal axes intersecting at the central transition metal ion. (b) Examples of characteristic tilt systems include the $a^0a^0c^+$ and $a^0a^0c^-$ configurations, representing in-phase (c^+) and out-of-phase (c^-) rotations of adjacent octahedra about the z -axis, respectively. Additionally, the $a^+a^+c^0$ and $a^-a^-c^0$ patterns describe similar rotational behaviors in the xy -plane. The alternating rotation directions between neighboring octahedra in adjacent layers are especially evident in the $a^0a^0c^-$ configuration (far right), highlighting the layer-dependent nature of octahedral tilt systems [3].	47

I.6	Cation displacement (a) along a tetrad axis produces one long, one short, and four intermediate bonds. (b) along a triad axis results in three short and three long bonds. (c) along a diad axis gives two long and two short bonds in the plane, with two intermediate bonds perpendicular to the plane [1].	49
II.1	The double-exchange interaction: An electron preserves its spin orientation as it hops between adjacent localized ion cores, mediating ferromagnetic alignment. adapte from [4]	73
II.2	A representative superexchange interaction: Configuration (b) is energetically favored over configuration (a). Adapted from [4]	76
II.3	Two-dimensional random-site model illustrating the emergence of a ferromagnetic "cluster glass" component. In contrast, the SG phase transition corresponds to the cooperative freezing of individual spins without cluster formation. Representative systems include $\text{Cu}_{1-x}\text{Mn}_x$ and $\text{Eu}_x\text{Sr}_{1-x}\text{S}$ with $x < 0.1$ [5].	81
II.4	Square plaquettes with mixed Ising interactions: positive (ferromagnetic, F) and negative (antiferromagnetic, AF). (a) An unfrustrated plaquette, characterized by a four-bond product $\Phi = +1$; (b) a frustrated plaquette, where the four-bond product is $\Phi = -1$ [5]. . . .	83
II.5	Spatial oscillations of conduction electron polarization induced by a local magnetic moment placed at the origin. The coupling between the local moment (LM) and conduction electrons (CE) is negative and decays with distance following an approximate $\cos(2k_F r)/(2k_F r)^3$ dependence. The vertical axis, labeled 'j', may alternatively represent Friedel charge oscillations arising when an impurity with different valence is introduced into a metallic host. [5]	84
III.1	Schematic representation of a typical Bragg-Brentano XRD configuration used in powder diffraction. In this geometry, the X-ray source and detector are aligned symmetrically around the sample, with the incident angle θ equal to the diffraction angle θ	92

III.2	Engineering layout of the WISH diffractometer. The images show the instrument in the TS2 experimental hall (right) and the ^3He detector array inside the blockhouse (left). Neutrons are transported via a ballistic supermirror guide ($m = 2$), elliptical in both horizontal and vertical planes. The guide extends from 1.7 m downstream of the source to 0.5 m before the sample, with a total flight path of 40.0 m from the moderator face. The guide exit is a rectangular aperture measuring $20 \text{ mm} \times 40 \text{ mm}$109
III.3	Optical layout of the EMA beamline at Sirius synchrotron. The high-brilliance X-ray beam is generated by a cryogenic permanent magnet undulator (CPMU) and conditioned through a sequence of optical components including slits, a high-resolution double-crystal monochromator (HD-DCM), a quarter-wave plate (double phase retarder), harmonic rejection mirrors, and Kirkpatrick-Baez (KB) focusing mirrors. These elements are optimized for X-ray diffraction (XRD), X-ray absorption (XAS), and X-ray Raman spectroscopy (XRS) under extreme thermodynamic and magnetic conditions.111
III.4	Schematic diagram of a vibrating sample magnetometer (VSM) and a commercial VSM system.113
III.5	Schematic diagram of the Raman spectroscopy setup used in this study.117
IV.1	The cation ordered crystal structure of $\text{Nd}_2\text{NiMnO}_6$ (monoclinic $P2_1/n$) presented as a single unit cell. (a) The A -site with Nd atoms is depicted in red. (b) The B - and B' -sites are shown, with Ni and Mn atoms represented in blue and green, respectively. (c) and (d) Projections of the crystal structure along the a -axis illustrating the $(\text{Nd})\text{O}_8$ cuboctahedral coordinations and the $(\text{Ni}, \text{Mn})\text{O}_6$ tilted octahedral coordinations, respectively. The oxygen anions are represented by grey spheres.126

- IV.2 Neutron powder diffraction data measured in 3 magnetic phases; a) paramagnetic (230 K), b) first ordered (100 K) and c) ground state (1.5 K). Data are shown as red points, the fitted patterns as black lines, and the difference curve $I_{\text{obs}} - I_{\text{calc}}$ as blue lines at the bottom of the panes. The top and bottom row of green tick marks in each pane indicate the position of nuclear and magnetic Bragg peaks, respectively. 127
- IV.3 a) Temperature dependence of the DC magnetic susceptibility of $\text{Nd}_2\text{NiMnO}_6$ measured under ZFC and FCC conditions in an applied field of 1 kOe. The inset shows a comparison of M-T curves (ZFC/FCC) at different H_{dc} fields. (b) The inverse susceptibility ($\chi^{-1} = H/M$) as a function of temperature (T). The black line shows the paramagnetic region's best fit using the Curie-Weiss law. 130
- IV.4 Isothermal $M(H)$ curves conducted at different temperatures under applied fields up to ± 70 kOe. The inset shows the linear extrapolation of saturated magnetization at 100 K. 131
- IV.5 The real (a) and imaginary (b) parts of the AC magnetic susceptibility of $\text{Nd}_2\text{NiMnO}_6$, measured as a function of temperature at different frequencies under $H_{\text{dc}} = 2$ Oe. The inset shows an expanded view of T_{N2} 133
- IV.6 Refined magnetic structures of $\text{Nd}_2\text{NiMnO}_6$: (a) $m\Gamma_2^+$ Structure at 100 K, (b) $m\Gamma_1^+ + m\Gamma_2^+$ structure at 1.5 K, and (c) decomposition of F_\perp and A_\perp Nd moment components within the ac plane. Nd, Ni, and Mn atoms are represented in red, blue, and green, respectively, with the crystallographic unit cell outlined in grey. 137
- IV.7 (a) Isothermal 1st quadrant $M(H)$ curves conducted at $T = 2 - 300$ K with an interval of $\Delta T = 5$ K. (b) Thermal profile of field-induced magnetic entropy change, $-\Delta S_M$, estimated from isothermal magnetization curves from $T = 2 - 300$ K, under various applied magnetic fields. Inset shows the plot of normalized ($\frac{\Delta S_M}{\Delta S_M^{\text{max}}}$) versus reduced temperature θ 140
- IV.8 (a) Field dependence of maximum magnetic entropy change ($-\Delta S_M^{\text{max}}$) fit by a power law (solid red line). (b) Relative cooling power (RCP), with a power law fit (solid black line) 142

- IV.9 (a) Arrot plot of isotherms with $\delta = 3$. (b) Temperature dependence of the spontaneous magnetization $M_S(T)$ (left) and the inverse initial magnetic susceptibility $\chi_0^{-1}(T)$ (right), obtained from the field region of $H < 1.5$ T extrapolation of the Arrott plot with $\beta = 1/2$ and $\gamma = 1$ 145
- IV.10 (a) Kouvel-Fisher plots of $M_S/(dM_S/dT)^{-1}$ (left) and $\chi_0^{-1}/(d\chi_0^{-1}/dT)^{-1}$ (right) for $\text{Nd}_2\text{NiMnO}_6$, with solid lines representing linear fits. (b) Critical isotherm $M(H)$ measured at $T_C = 198$ K. Inset: log-log plot of the same data with the fitted slope corresponding to $1/\delta$. (c) Scaling plots of renormalized magnetization m versus renormalized field h below and above T_C , demonstrating data collapse onto two distinct branches. Inset: the same plots in log-log scale. (d) Plots of m^2 versus h/m for $\text{Nd}_2\text{NiMnO}_6$. Inset: rescaled $M(H)$ curves plotted as $MH^{-1/\delta}$ versus $\varepsilon H^{-1/(\beta\delta)}$, further confirming scaling behavior. 147
- IV.11 Raman mode analysis and temperature evolution in $\text{Nd}_2\text{NiMnO}_6$. (Top) Raman spectrum at 20 K fitted with Gaussian-Lorentzian (G-L) profiles, highlighting the decomposition into individual phonon modes: A_g^I , A_g^{II} , B_g^I , and A_g^{III} . Experimental data are shown in cyan, and the total fit is indicated by the blue curve. (Bottom) Temperature-dependent Raman intensity map (false-color contour plot) showing the evolution of phonon modes in the 400-750 cm^{-1} range, with mode sharpening and intensity enhancement upon cooling. 149
- IV.12 Temperature dependence of phonon frequencies (ω) and linewidths (Γ) for three A_g modes in $\text{Nd}_2\text{NiMnO}_6$. Panels (a-c) show ω_{A_g} fitted with Klemens and Balkanski models; deviations below $T_1 \approx 200$ K and $T_f \sim 50$ -100 K indicate spin-phonon coupling. Panels (d-f) show Γ_{A_g} , with anomalous broadening at magnetic transitions, confirming strong spin-lattice interactions. 151

IV.13	Temperature evolution of phonon frequency renormalization $\delta\omega(T) = \omega_{\text{obs}}(T) - \omega_{\text{anh}}(T)$ (green diamonds, left axis) and normalized square of magnetization $[M(T)/M_{\text{max}}]^2$ (black triangles, right axis) for three A_g Raman modes in $\text{Nd}_2\text{NiMnO}_6$. Panels (a)-(c) show A_g^{I} , A_g^{II} , and A_g^{III} modes, respectively. Good agreement is observed in the FM region ($T_1 < 200$ K), while deviation below 50 K signals competing AFM interactions and rare-earth sublattice effects.	153
V.1	The crystal structure of $\text{Nd}_2\text{NiMn}_{0.25}\text{Ir}_{0.75}\text{O}_6$ in the $P2_1/n$ space group is presented as a single unit cell. (a) The A -site with Nd atoms is depicted in brown. (b) The B -sites are shown, with Ni/Mn atoms represented in blue and red, and Ir in green. (c) A projection of the crystal structure along the a -axis illustrates the (Nd) O_8 cuboctahedral coordination. (d) The (NiMn) O_6 octahedral tilt coordination is highlighted, with Ni/Mn and Ir octahedra shaded in blue and green, respectively. The O^{2-} ions are represented by grey spheres.	160
V.2	Neutron powder diffraction data measured in 4 magnetic phases; a) paramagnetic (230 K), b) first ordered (100 K), c) ordering at 40 K, and d) ground state (1.5 K). Data are shown as red points, the fitted patterns as black lines, and the difference curve $I_{\text{obs}} - I_{\text{calc}}$ as blue lines at the bottom of the panes. The top and bottom row of green tick marks in each pane indicate the position of nuclear and magnetic Bragg peaks, respectively.	163
V.3	a) Temperature dependence of the DC magnetic susceptibility of $\text{Nd}_2\text{NiMn}_{0.25}\text{Ir}_{0.75}\text{O}_6$ measured under ZFC and FCC conditions in an applied field of 0.1 kOe. The inset shows a comparison of M-T curves (ZFC/FCC) at different H_{dc} fields(1-10 kOe). (b) The inverse susceptibility ($\chi^{-1} = H/M$) as a function of temperature (T), inset shown for 1-10 kOe fields. The black line shows the paramagnetic region's best fit using the Curie-Weiss law.	166
V.4	Isothermal $M(H)$ curves conducted at different temperatures under an applied field of ± 70 kOe. Inset shows the linear extrapolation of saturated magnetization.	168

- V.5 The real (a) and imaginary (b) parts of the AC magnetic susceptibility of $\text{Nd}_2\text{NiMn}_{0.25}\text{Ir}_{0.75}\text{O}_6$, measured as a function of temperature at different frequencies under $H_{dc} = 2$ Oe. The inset shows an expanded view of T_f 169
- V.6 Temperature dependence of C_p/T vs. T for $\text{Nd}_2\text{NiMn}_{0.25}\text{Ir}_{0.75}\text{O}_6$ measured under 0 T (black) and 4 T (red) magnetic fields. The inset displays expanded low-temperature (2-15 K) C_p/T data under various fields (up to 10 T), showing systematic suppression and broadening of the Schottky anomaly with increasing field. 171
- V.7 Raman spectrum of $\text{Nd}_2\text{NiMn}_{0.25}\text{Ir}_{0.75}\text{O}_6$ at 20 K, highlighting phonon mode decomposition. The experimental data (black asterisks) are fitted using a combination of Gaussian-Lorentzian (G-L) functions (solid red curve). Individual vibrational modes are labeled and shaded according to symmetry: $B_g^{\text{I-III}}$ (gray, blue, cyan), $A_g^{\text{I-IV}}$ (green, magenta, violet, orange). The multi-mode structure is consistent with the $P2_1/n$ symmetry of the monoclinic double perovskite phase. Strong and well-resolved features confirm B-site ordering and low-temperature lattice coherence. 174
- V.8 Temperature evolution of phonon frequencies $\omega(T)$ and full-width at half-maximum linewidths $\Gamma(T)$ for the A_g^{I} , B_g^{III} , and A_g^{III} Raman modes of $\text{Nd}_2\text{NiMn}_{0.25}\text{Ir}_{0.75}\text{O}_6$. Panels (a-c) show the frequency shifts, while panels (d-f) present the corresponding linewidth broadening as a function of temperature. Experimental data (blue diamonds) are fitted using Klemens-type anharmonic models (solid orange curves). In panel (a), a linear thermal model (dashed red line) is also shown for comparison. The shaded regions denote different magnetic regimes: white (paramagnetic), blue (spin-glass-like), and green (FM ordering), highlighting the spin-lattice coupling anomalies, particularly in B_g^{III} and A_g^{III} modes. 176

- V.9 Temperature dependence of phonon renormalization $\delta\omega(T) = \omega_{\text{obs}}(T) - \omega_{\text{anh}}(T)$ (left axis, blue diamonds) and normalized magnetization squared $[M(T)/M_{\text{max}}]^2$ (right axis, green triangles) for (a) A_g^I , (b) B_g^{III} , and (c) A_g^{III} Raman-active modes in $\text{Nd}_2\text{NiMn}_{0.25}\text{Ir}_{0.75}\text{O}_6$. The close correspondence between the two quantities near the ferromagnetic transition temperature ($T_C \approx 140$ K) indicates strong spin-phonon coupling. Deviations at lower temperatures are attributed to competing magnetic interactions and site disorder. 179
- V.10 Refined magnetic structure of $\text{Nd}_2\text{NiMn}_{0.25}\text{Ir}_{0.75}\text{O}_6$ at 1.5 K, corresponding to the $m\Gamma_1^+(F_{\parallel} + A_{\perp})$ irreducible representation. The left panel shows the three-dimensional view, while the right panel displays the projection along the a -axis. Magnetic moments are primarily aligned along the b -axis (F_{\parallel}) with an additional A -type antiferromagnetic component within the ac -plane (A_{\perp}) for the Nd sublattice. Nd, Ni, and Ir atoms are represented by maroon, blue, and green spheres, respectively. The crystallographic unit cell is outlined in black. Cartesian axes (a , b , c) are indicated for clarity. 183
- VI.1 Crystal structure of NdSmNiMnO_6 in the monoclinic $P2_1/n$ space group shown as a single unit cell. (a) The A-site cations Nd and Sm are represented in cyan and black, respectively. (b) The B-site transition metals Ni and Mn are shown in blue and royal. (c) Projection along the a -axis highlights the (Nd/Sm) O_8 cuboctahedral coordination. (d) The (NiMn) O_6 octahedral tilt system is emphasized, with NiO_6 and MnO_6 units shaded in royal and blue. Oxygen anions (O^{2-}) are shown as grey spheres. 195
- VI.2 Synchrotron X-ray diffraction data in selected phases: (a) paramagnetic phase (275 K), (b) ordered phase (175 K), and (c) 4 K. Experimental data are shown as red points, the fitted pattern as black lines, and the difference curve ($I_{\text{obs}} - I_{\text{calc}}$) as a blue line at the bottom of each panel. The top and bottom rows of green tick marks indicate the positions of nuclear and magnetic Bragg peaks, respectively. . 197

- VI.3 Temperature-dependent Ni and Mn K-edge XANES spectra of NdSmNiMnO₆ from 4-300 K. (a) Ni K-edge spectra show an absorption edge at ~ 8352 eV (Ni²⁺) and a pre-edge feature $P_{\text{E-Ni}}$ at ~ 8339 eV. The increased white-line intensity and peak broadening at lower temperatures indicate enhanced local distortion around Ni. (b) Mn K-edge spectra display a stable edge at ~ 6560 eV (Mn⁴⁺) with consistent pre-edge features P_{I} (~ 6544 eV) and P_{II} (~ 6549 - 6551 eV), suggesting a temperature-invariant MnO₆ octahedral environment and robust Mn-O hybridization. 199
- VI.4 (a) Temperature dependence of magnetization curves measured after zero-field cooling (ZFC) and field-cooled cooling (FCC) under an applied magnetic field of $H_{\text{dc}} = 100$ Oe for NdSmNiMnO₆. The inset shows a comparison of M - T curves (ZFC/FCC) at different H_{dc} fields. (b) Inverse susceptibility ($\chi^{-1} = H/M$) as a function of temperature measured at $H_{\text{dc}} = 1$ kOe. The black line represents the best fit to the Curie-Weiss (C-W) law in the paramagnetic region. The inset displays the derivative dM/dT^{-1} versus T , where the minimum is associated with the critical temperature T_{N} at various H_{dc} fields. 202
- VI.5 (a) Magnetic field dependence of magnetization (M - H) isotherms measured at $T = 2, 100, 200,$ and 300 K for NdSmNiMnO₆. The inset shows an expanded view of the low-field region of the isotherms. (b) Derivative dM/dH as a function of H at selected temperatures. The inset displays the Law of Approaching Saturation (LAS) fit to the high-field magnetization data. (c) Temperature dependence of the saturation magnetization (M_{S}) and coercivity (H_{C}), highlighting their evolution with temperature. 203
- VI.6 (a)-(c) Temperature variations of the unit-cell lattice parameters a , b , and c , deduced from temperature-dependent synchrotron X-ray diffraction (SXRD) pattern analysis. The solid red and blue lines represent the thermal expansion fits for the temperature regions $T < T_{\text{C}}$ and $T > T_{\text{C}}$, respectively. Notably, the thermal expansion behavior exhibits significant anomalies near T_{C} due to the magnetostriction effect, indicating strong coupling between the magnetic order and the lattice degrees of freedom. 206

- VI.7 Thermal variation of local structural parameters in NdSmNiMnO₆ extracted from temperature-dependent synchrotron X-ray diffraction (SXRD) analysis: (a-c) Ni-O bond lengths; (d-f) Mn-O bond lengths with inset showing Ni-Mn interatomic distances; (g-i) Ni-O-Mn bond angles. Anomalies near the magnetic transition temperature T_N are visible across all panels, signaling structural distortions in the NiO₆ and MnO₆ octahedra. 208
- VI.8 (a) Raman spectrum of NdSmNiMnO₆ measured at room temperature showing the dominant phonon modes. (b) Temperature-dependent Raman spectra collected between 10 and 300 K. The rightmost inset highlights the symmetric stretching mode (A_g) near 654 cm⁻¹, revealing subtle anomalies across the magnetic transition temperature. 209
- VI.9 (a-c) Temperature variation of selected phonon frequencies in NdSmNiMnO₆. (d-f) Temperature dependence of the FWHM of the respective phonon modes. The solid-wine, solid-red, and solid-black curves correspond to fits using the Klemens, Balkanski, and Grüneisen models (cubic-anharmonic fits) in regions of discontinuity, respectively. 215
- VI.10 (a) Temperature variation of $\delta\omega(T)$ and $\left\{\frac{M(T)}{M_{\text{Max}}}\right\}^2$ versus T for the A_g stretching mode. (b) Temperature variation of the unit-cell volume (V) as derived from temperature-dependent synchrotron X-ray diffraction (SXRD) pattern analysis. The solid-blue and red-dashed lines represent the thermal expansion fits of the curves in the regions $T > T_N$ and $T < T_N$, respectively. Due to the presence of a magnetostriction effect, the thermal expansion behavior of V shows a drastic change near T_N . The inset depicts the temperature variation of volume magnetostriction. 217
- VI.11 Monoclinic 20-atom crystal structures representing different magnetic configurations in a unit cell containing Nd, Sm, Ni, Mn, and O. The images illustrate the simulated spin orientations for ferrimagnetic (FiM1-FiM4) and ferromagnetic (FM1-FM4) arrangements. Configurations involving Nd/Sm positional interchange are omitted due to identical total energies. Spin directions along the c -axis are indicated by black (\uparrow) and red (\downarrow) arrows. 219

- VI.12 Total density of states (TDOS) and partial density of states (PDOS) calculated for ferrimagnetic (FiM) and ferromagnetic (FM) ground-state configurations. Panels (a) and (b) show results obtained using the GGA+U method, while panels (c) and (d) include spin-orbit coupling (SOC) within the GGA+U(SOC) framework. The vertical dashed line indicates the Fermi level. The shaded yellow regions represent Sm-4*f* contributions, while the shaded green regions highlight Nd-4*f* states. Band gap values for each configuration are indicated in the plots. 221
- VI.13 GGA+U(+SOC) partial density of spin states (PDOS) for Ni (top panel) and Mn (bottom panel) *d*-states, decomposed into t_{2g} (d_{xy} , d_{xz} , d_{yz}) and e_g ($d_{x^2-y^2}$, d_{z^2}) contributions. The dashed vertical line denotes the Fermi energy (E_F). Insets illustrate schematic electron occupation in crystal-field-split *d*-orbitals. 223
- VII.1 (a, b) Room-temperature XRD patterns and corresponding Rietveld refinements for the NdSmNiMnO₆ double perovskite. The red square symbols and black line represent the observed and calculated intensities, respectively. The short green vertical ticks mark the expected Bragg reflection positions for the monoclinic $P2_1/n$ (No. 14) and orthorhombic $Pbn2_1$ (No. 33) phases. The blue line at the bottom shows the difference between observed and calculated intensities. (c-f) Crystal structure representation of NdSmNiMnO₆. The light-gray lines outline a single unit cell, while shaded polyhedra highlight the cation–oxygen coordination environments. 232
- VII.2 (a) Isothermal magnetization curves measured at different temperatures in the range 2-156 K with $\Delta T = 8$ K and 156-196 K with $\Delta T = 1$ K for critical point analysis. (b) Temperature dependence of the field-induced magnetic entropy change ($-\Delta S_M$) estimated from isothermal $M(H)$ data between 2 and 292 K, under various applied magnetic fields. (c) Magnetic field dependence of the maximum entropy change ($-\Delta S_M^{\max}$). Inset: normalized entropy change ($\Delta S_M/\Delta S_M^{\max}$) as a function of reduced temperature θ . (d) Relative cooling power (RCP) as a function of applied magnetic field (H). 237

VII.3	(a) Isothermal magnetization curves measured at different temperatures between 156 and 188 K with $\Delta T = 1$ K. The isotherms are plotted as $M^{1/\beta}$ vs $(H/M)^{1/\gamma}$ using model parameters from: (b) Arrott-Noakes model, (c) Tricritical mean-field model, (d) Three-dimensional (3D) Heisenberg model, (e) 3D Ising model, and (f) 3D XY model.239
VII.4	Temperature dependence of the normalized slopes, $NS = S(T)/S(T_C)$, for the mean-field, tricritical mean-field, 3D Heisenberg, 3D Ising, and 3D XY models.241
VII.5	(a) Modified Arrott plot of isotherms with $\beta = 0.474$ and $\gamma = 0.954$. (b) Temperature dependence of the spontaneous magnetization M_S (left) and the inverse initial magnetic susceptibility $\chi_0^{-1}(T)$ (right), which are obtained from the high-field extrapolation of the modified Arrott plot. The T_C and exponent values are deduced by fitting Equations 215 and 216 (red curves). (c) Kouvel-Fisher plot for the temperature dependence of the spontaneous magnetization M_S (left) and the inverse initial magnetic susceptibility $\chi_0^{-1}(T)$ (right). The T_C and critical exponents are obtained from the linear fits (red lines).242
VII.6	(a) $M(H)$ curve at $T_C \sim 177$ K. Inset: the same plot in log-log scale with a solid fitting curve in the high-field region. (b) Scaling plots of renormalized magnetization $m = M \varepsilon ^{-\beta}$ versus renormalized field $h = H \varepsilon ^{-(\beta\delta)}$ below and above T_C for NdSmNiMnO ₆ . The inset shows the same scaling plots in the log-log scale. The collapse of the data onto two distinct universal branches (below and above T_C) confirms the validity of the obtained critical exponents and the reliability of the scaling hypothesis.243
VIII.1	The crystal structure of Er ₂ CuMnMn ₄ O ₁₂ . A single unit cell is shown by thin grey lines, and the cation oxygen coordinations are shaded in panes c-e.250
VIII.2	The real (a) and imaginary (b) parts of the AC magnetic susceptibility of Er ₂ CuMnMn ₄ O ₁₂ , measured as a function of temperature at different frequency 0.5 Oe excitation fields. The static DC field was zero. Four magnetic transitions are identified in (a), which bound phases CFI', FI, CFI ₁ , and CFI ₂ shaded blue, grey, green and purple, respectively.253

VIII.3 a) Temperature dependence of the DC magnetic susceptibility of $\text{Er}_2\text{CuMnMn}_4\text{O}_{12}$ measured under ZFC and FCC conditions in a 100 Oe applied field. The inset shows a Curie-Weiss fit (black dashed line) to the inverse susceptibility. b) Specific heat of $\text{Er}_2\text{CuMnMn}_4\text{O}_{12}$ measured as a function of temperature. The inset highlights the magnetic field dependence on the low temperature anomalies. Phases CFI', FI, CFI ₁ , and CFI ₂ are shaded blue, grey, green and purple, respectively.254
VIII.4 Neutron powder diffraction data measured in 5 phases; a) paramagnetic, b) CFI', c) FI, d) CFI ₁ , and e) CFI ₂ . Data are shown as red points, the fitted pattern as black lines, and the difference curve $I_{\text{obs}} - I_{\text{calc}}$ as a blue line at the bottom of the panes. The top and bottom row of green tick marks in each pane indicate the position of nuclear and magnetic Bragg peaks, respectively.257
VIII.5 Temperature dependence of the $\pm F_i$ magnetic moments on the a) Mn2, b) Mn3, and c) Mn4 sublattices, where the blue and red data correspond to Γ_4^+ (F_y) and Γ_2^+ (F_z) order, respectively. Pane d shows the antiferromagnetic components that lead to spin canting on the Mn3 sublattice.259
VIII.6 Temperature dependence of the Er1 and Er2 moments, whose respective magnetic modes transform a mZ_3^+ (antiferromagnetic, $m \mathbf{a}$), and $m\Gamma_4^+$ (ferromagnetic, $m \mathbf{b}$), respectively. Fits to a simple magnetisation model for a 2-level system are shown by red lines (see text for details).260
VIII.7 The magnetic structures of $\text{Er}_2\text{CuMnMn}_4\text{O}_{12}$ in each ordered phase. Er1, Er2, Cu1, Mn2, Mn3, and Mn4 sublattices are coloured red, green, black, purple, cyan and maroon, respectively (see Figure VIII.262)	.262
I.1 X-ray diffraction patterns of $\text{Nd}_2\text{NiMn}_{1-x}\text{Ir}_x\text{O}_6$ with $x = 0.00, 0.25, 0.50$, and 0.75 . The inset highlights a systematic shift to lower 2θ angles (black arrow) with increasing Ir doping, indicating lattice expansion. Progressive peak broadening and enhanced peak splitting reflect increasing lattice strain and symmetry lowering due to Ir incorporation.271

- I.2 Rietveld refinement of X-ray diffraction data for $\text{Nd}_2\text{NiMnO}_6$ at room temperature. The observed pattern (Y_{Obs}) is shown in red dots, the calculated pattern (Y_{Calc}) in black, and the difference ($Y_{\text{Obs}} - Y_{\text{Calc}}$) in blue. Vertical green ticks mark the Bragg reflection positions corresponding to the monoclinic $P2_1/n$ (space group 14) symmetry. The excellent agreement between the observed and calculated profiles confirms the phase purity and structural model. 272
- II.1 Temperature-dependent Raman spectra of $\text{Nd}_2\text{NiMnO}_6$ collected between 20 and 290 K. The measurements were performed with temperature steps of $\Delta T = 10$ K from 20 to 100 K, and $\Delta T = 5$ K from 100 to 290 K. The two prominent A_g phonon modes are labeled. Systematic shifts and linewidth changes with decreasing temperature reflect anharmonic effects and possible spin-phonon coupling. 273
- III.1 (a) Power-law fitting of τ vs T_f ; (b) Vogel-Fulcher (V-F) fitting shown in the inset. 276
- III.2 (Color online) Temperature-dependent Raman spectra of polycrystalline $\text{Nd}_2\text{NiMn}_{0.25}\text{Ir}_{0.75}\text{O}_6$ measured from 20 K to 290 K over the spectral range of 450-750 cm^{-1} . The measurements were conducted in backscattering geometry with a 532 nm excitation laser. Spectra are vertically offset for clarity. Prominent phonon modes exhibit temperature-driven softening and broadening, most notably in the high-frequency region ($\sim 650\text{-}700$ cm^{-1}), indicative of anharmonic effects and potential spin-phonon coupling. Color-coded arrows to the right denote the temperature scale with $\Delta T = 5$ K spacing up to 100 K and $\Delta T = 10$ K above. 277
- III.3 Temperature-dependent specific heat analysis of $\text{Nd}_2\text{NiMn}_{0.25}\text{Ir}_{0.75}\text{O}_6$ at $H = 0$ T: (a) Total specific heat $C_p(T)$ with fitted lattice contribution and extracted magnetic heat capacity $C_{\text{mag}}(T)$; (b) Low-temperature C_{mag} showing Schottky anomaly and corresponding fit with $\Delta = 14.60$ K; (c) Full model fit to $C_p(T)$ data below 50 K including phonon and Schottky contributions. 278

IV.1	Synchrotron X-ray diffraction (SXRD) patterns of NdSmNiMnO ₆ collected in the temperature range of 4-300 K. The patterns confirm phase stability across the full range with no evidence of structural transitions.279
IV.2	Inverse magnetic susceptibility ($\chi^{-1} = H/M$) of NdSmNiMnO ₆ as a function of temperature, measured under a DC field of $H_{\text{dc}} = 10$ kOe. The black line represents the best fit to the Curie–Weiss law in the paramagnetic region.280
IV.3	Thermal variation of octahedral bond angles in NdSmNiMnO ₆ obtained from temperature-dependent synchrotron X-ray diffraction (SXRD) analysis: (a-b) O-Ni-O bond angles; (c-d) O-Mn-O bond angles. Anomalies near T_N are evident in all panels, indicating the onset of structural distortion in the NiO ₆ and MnO ₆ octahedra.281

List of Tables

I.1	Some Important Oxide Materials	34
I.2	Atomistic positions in the ideal cubic perovskite structure of SrTiO ₃ (space group Pm$\bar{3}$m).	35
I.3	Octahedral tilting patterns in double perovskites	38
I.4	Double perovskite materials and applications	40
II.1	Crystallographic Point Groups Classified by Crystal System [6] . .	57
III.1	Experimental techniques and corresponding facilities used in this study	90
IV.1	Structural parameters of the Nd ₂ NiMnO ₆ sample obtained through Rietveld refinement from NPD data at 230 K. The lattice parameters were determined to be $a = 5.4078(1)$ Å, $b = 5.4767(1)$ Å, and $c = 7.6648(2)$ Å, with $\beta = 90.0277(4)^\circ$ and a unit cell volume of $V = 227.007(1)$ Å ³ . Bond valence sums (BVS) were calculated using the parameters, $R_0(\text{Nd}^{3+}) = 2.66$, $R_0(\text{Ni}^{2+}) = 2.17$, $R_0(\text{Mn}^{4+}) = 1.753$, and $B = 0.37$, where the bond valence, $\text{BV} = \exp((R_o - R)/B)$. N.B. For the BVS, the majority cation is used for mixed occupancy sites.	128
IV.2	Magnetic modes that span the four symmetry-equivalent <i>A</i> -site Nd (4 <i>e</i>) ions and the two symmetry-equivalent <i>B</i> -sites (2 <i>a</i> for Ni, 2 <i>b</i> for Mn) within a single $P2_1/n$ unit cell. We define four modes for the Γ -point propagation vector, $\mathbf{k} = (0, 0, 0)$: F_i, A_i, C_i , and G_i along with their components, which describe the relative alignment of magnetic moments across the symmetry-related atomic sites. The subscript <i>i</i> represents the directional component of the magnetic moment relative to the monoclinic <i>b</i> -axis.	135
IV.3	Magnetic structure parameters refined at 100 K and 1.5 K. The moment directions are defined in spherical coordinates [7, 8] $m_x = m \cos(\phi) \sin(\theta) \ \mathbf{a}$, and $m_y = m \sin(\phi) \sin(\theta) \ \mathbf{b}$ and $m_z = m \cos \theta \ \mathbf{c}^*$, such that $\phi = 0$ constrains moments to the <i>ac</i> -plane. In this case $\mathbf{m} = [m_x, 0, m_z]$ represents the polarization of magnetic modes F_\perp , and A_\perp	136

V.1	Structural parameters of $\text{Nd}_2\text{NiMn}_{0.25}\text{Ir}_{0.75}\text{O}_6$ obtained from Rietveld refinement of NPD data at 200 K. Lattice parameters are $a = 5.40481(3)$ Å, $b = 5.64717(3)$ Å, $c = 7.71597(3)$ Å, $\beta = 90.04178(2)^\circ$, and unit cell volume $V = 235.506(2)$ Å ³ . Bond valence sums (BVS) were calculated using $R_0(\text{Nd}^{3+}) = 2.12$, $R_0(\text{Ni}^{2+}) = 1.65$, $R_0(\text{Mn}^{4+}) = 1.91$, and $B = 0.37$. The bond valence is defined as $\text{BV} = \exp\left(\frac{R_0 - R}{B}\right)$. For mixed-occupancy sites, the majority cation is used in BVS calculations.162
VI.1	Structural parameters of NdSmNiMnO_6 in the $P2_1/n$ space group (#14), refined from NPD data. U_{iso} values are given in 10^{-3} Å ² units. Bond valence sums (BVS) are in $ e $. For mixed-occupancy sites, the majority cation is used in BVS calculations.193
VII.1	Structural parameters of NdSmNiMnO_6 in the $P2_1/n$ space group (No. 14), refined from XRD data at room temperature. U_{iso} values are given in 10^{-3} Å ² . Bond valence sums (BVS) are in $ e $. For mixed-occupancy sites, the majority cation is used in BVS calculations.229
VII.2	Comparative analysis of NdSmNiMnO_6 with well-known magnetocaloric materials. $-\Delta S_{\text{M}}^{\text{max}}$ is the maximum magnetic entropy change, and RCP is the relative cooling power.237
VIII.1	Crystal structure parameters of $\text{Er}_2\text{CuMnMn}_4\text{O}_{12}$ (space group $Pm\bar{m}n$) refined at 200 K. The lattice parameters were determined to be $a = 7.2640(1)$ Å, $b = 7.3187(1)$ Å, and $c = 7.7764(1)$ Å. Atomic Wyckoff positions are Er1,Er2: 2a $[1/4,1/4,z]$; Cu1,Mn2: 2b $[3/4,1/4,z]$; Mn3: 4c $[0,0,0]$; Mn4: 4d $[0,0,1/2]$; O1: 8g $[x,y,z]$; O2,O4: 4f $[x,1/4,z]$; and O3,O5: 4e $[1/4,y,z]$. Bond valence sums (BVS) were calculated using the parameters, $R_0(\text{Er}^{3+}) = 1.99$, $R_0(\text{Cu}^{2+}) = 1.68$, $R_0(\text{Mn}^{2+}) = 1.79$, $R_0(\text{Mn}^{3+}) = 1.76$, $R_0(\text{Mn}^{4+}) = 1.75$, and $B = 0.37$, where the bond valence, $\text{BV} = \exp((R_o - R)/B)$. N.B. For mixed occupancy sites we give the BVS of the majority cation.255

VIII.2	Magnetic structure parameters of $\text{Er}_2\text{CuMnMn}_4\text{O}_{12}$. The F and A labels denote ferromagnetic and Néel-type antiferromagnetic modes, respectively. The Y label denotes an Mn3/Mn4 mode of ferromagnetic stripes along \mathbf{a} , coupled antiferromagnetically along \mathbf{b} [9]. The subscripts indicate the polarisation of the modes. Freely refined and fixed values are given with and without standard uncertainties, respectively, and dashes indicate that the component is not allowed by the symmetry of the respective phase.258
VIII.3	Crystal electric field parameters for Er1 and Er2 in units μeV (3.s.264)	.264
III.1	Atomic coordinates, displacement parameters, and site information for the Fddd phase (D_{2h} , No. 70) at 200 K. U_{iso} in 10^{-2} \AA^2274
IV.1	Fitting parameters obtained from modeling the thermal expansion of the lattice parameters as a function of temperature.280

* CHAPTER I *

Introduction

Material science is poised to dominate the forefront of research and technological innovation, driven by its unparalleled multifunctional applicability across industries. Since the dawn of civilization, evidenced by epoch-defining eras such as the Stone, Bronze, and Iron Ages-human progress has been inextricably linked to material advancements. Today, we stand at the threshold of a new revolutionary epoch: the *Nano Age*, or what I term the ***Intelligent Materials Age (IMA)***. At this atomic and nanoscale frontier, materials are not merely components but transformative enablers, catalyzing breakthroughs in electronics, healthcare, energy, and beyond. Their influence transcends laboratories, reshaping global economies, redefining technological limits, and even molding cultural paradigms. As the backbone of modern innovation, material science has evolved from a supporting discipline to the very axis upon which the future pivots, an indispensable field that will dictate the trajectory of human advancement [10, 11]. Metal oxides, in particular, have emerged as crucial materials for various applications, including semiconductors [12], photocatalysis [13], and spintronics [14]. The rapid introduction of new consumer products that take advantage of these advanced materials underscores their growing importance. The extraordinary structural diversity of oxide materials enables the formation of a broad array of crystallographic frameworks, each of which exhibits distinct properties that cater to a wide range of technological applications. In particular, ABX₃-type compounds are well-known for their ability to crystallize in a multitude of structural motifs, including perovskite, corundum, ilmenite, LiNbO₃, several hexagonal BaMnO₃-type polytypes (such as 2H, 4H, 15R), hexagonal LuMnO₃-type, pyroxenes, rare-earth sesquioxide phases (A, B, and C-type or bixbyite), and others. These structures emerge as a function of the relative ionic radii of the cations at the A and B sites, as well as their electronic configurations and bonding characteristics[15–18].

Among these, perovskite structure, stands out as one of the most significant

and versatile frameworks in inorganic chemistry, both in terms of abundance and functional adaptability [19–21]. Perovskite (CaTiO_3), discovered in 1839 by the Prussian mineralogist Gustav Rose in the Ural Mountains, was named after the Russian mineralogist Count Lev Aleksevich von Petrovskii. This typically dark brown crystal, due to impurities, exhibits a hardness of 5.5–6, a density of 4000–4300 kg/m³, and a clear and highly refractive nature with an index of ≈ 2.38 [1]. The multiplicity of phases that pertain to the ternary perovskite family ABX_3 can be rationalized by assuming that perovskites are simple ionic compounds, where A is generally a divalent or trivalent alkaline-earth or lanthanoid ion, B is usually a transition-metal ion (i.e., $3d$, $4d$, or $5d$ metal ion), and X is an anion (e.g., $X = \text{O}, \text{F}$, etc.) [17, 22–25]. The B -cation is coordinated by six X -anions, forming BX_6 octahedra, which are connected by sharing corner X -anions (see Figure I.1). The cavity formed between the shared octahedra corners is occupied by the larger A -cation, which is coordinated to twelve X -anions, forming an AX_{12} coordination polyhedron. The ideal perovskite adopts a cubic configuration (space group $Pm\bar{3}m$) with a typical lattice constant of approximately $a_p \approx 3.8 \text{ \AA}$. However, this high-symmetry cubic form is rarely stabilized at room temperature due to inherent mismatches in the ionic sizes of A , B , and O atoms. Size mismatches among A , B , and oxygen atoms, quantified by the *Goldschmidt tolerance factor*-introduce structural distortions that give rise to various lower symmetry variants with rich and tunable physical properties and are often approximated as BX_6 octahedral tilts, described by the Glazer notation [15, 17, 26], allowing systematic investigation of competing magnetic interactions between multiple magnetic sublattices. Table I.1 provides an overview of some important oxide materials, their structures, and applications. In the subsequent chapter, the ideal ABO_3 perovskite structure is described along with some of the structural variations that occur that have significance in determining their chemical and physical properties.

Table I.1: Some Important Oxide Materials

Structure	Examples	Usage	Ref.
Perovskite	CaTiO_3 , BaTiO_3	Ferroelectric	[27]
Spinel	MgAl_2O_4 , Fe_3O_4	Ferrimagnetism	[28]
Ilmenite	FeTiO_3	Pigments	[29]
Pyrochlore	$\text{Y}_2\text{Ti}_2\text{O}_7$	Magnetic Materials	[30]
Rutile	TiO_2	Semiconductors	[31]
Corundum	Al_2O_3	Optical Components	[32]
Layered Oxides	LiCoO_2 , NaNiO_2	Battery Cathode	[33]
Garnet	$\text{Tb}_3\text{Fe}_5\text{O}_{12}$ / $\text{Y}_3\text{Fe}_5\text{O}_{12}$	Magnetic Memory	[34]

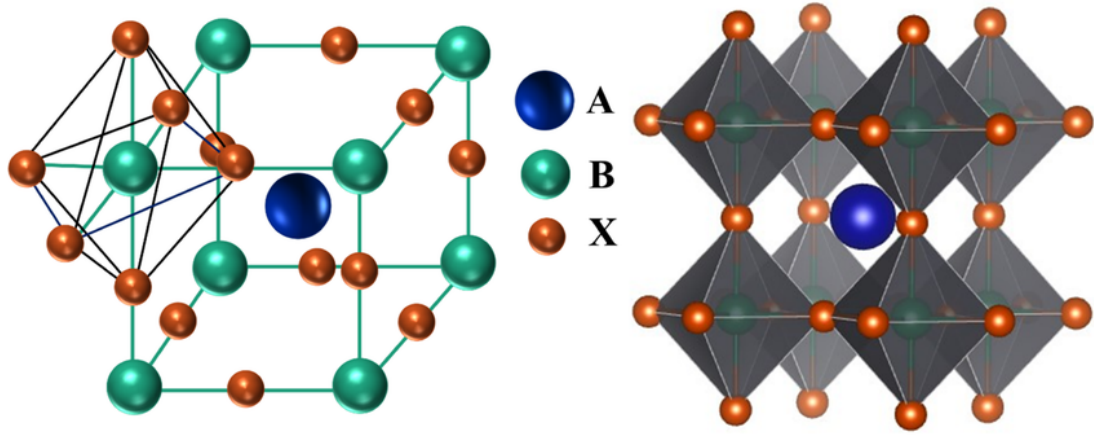


Figure I.1: Schematic of the idealized cubic perovskite ABX_3 ($A = \text{Sr}$, $B = \text{Ti}$, $X = \text{O}$) $Pm\bar{3}m$ structure. The blue, green, and orange spheres are Sr^{2+} , Ti^{4+} and O^{2-} , showing corner-sharing TiO_6 octahedra geometry and the centrally located Sr-cation.

1.1 Cubic Perovskite Structure

The *idealized*, or *aristotype*, perovskite structure represents the most symmetric form of the perovskite family and is essential for understanding both theoretical models and real-world deviations in structural behavior. A classic example of this archetype is strontium titanate (SrTiO_3), which adopts a cubic symmetry at room temperature, although it undergoes phase transitions and deviates from cubic form at lower temperatures. Structurally, the cubic unit cell of SrTiO_3 belongs to the space group $\mathbf{Pm}\bar{3}\mathbf{m}$ (No. 221), with a lattice parameter of $a = 0.3905 \text{ nm}$ and $Z = 1$, indicating one formula unit per unit cell. In crystallographic convention, the origin is typically set at the A-site cation, which is the Sr^{2+} ion. Under this convention, the atomic positions within the unit cell are defined as in Table I.2 [1, 24]:

Table I.2: Atomistic positions in the ideal cubic perovskite structure of SrTiO_3 (space group $\mathbf{Pm}\bar{3}\mathbf{m}$).

Site	Location	Coordinates
A (Sr^{2+} cation)	(2a)	(0, 0, 0)
B (Ti^{4+} cation)	(2b)	$\left(\frac{1}{2}, \frac{1}{2}, \frac{1}{2}\right)$
X (O^{2-} anion)	(6c)	$\left(\frac{1}{2}, \frac{1}{2}, 0\right)$ $\left(\frac{1}{2}, 0, \frac{1}{2}\right)$ $\left(0, \frac{1}{2}, \frac{1}{2}\right)$

Nevertheless, for crystallographic clarity, it is often advantageous to redefine

the origin of the unit cell to the position of the Ti^{4+} ion, which then lies at coordinates $(0,0,0)$. The Sr^{2+} ions translate to the center of the unit cell, at position $(\frac{1}{2}, \frac{1}{2}, \frac{1}{2})$, and the 12O^{2-} ions occupy the centered positions $(\frac{1}{2}, 0, 0)$, $(0, \frac{1}{2}, 0)$, and $(0, 0, \frac{1}{2})$ within the cubic cell [19]. Each Sr^{2+} ion is twelve-fold coordinated by O^{2-} ions, forming a cuboctahedral environment, which complements the corner-sharing network of TiO_6 octahedra extending throughout the structure (Figure I.1). Importantly, these octahedra are aligned parallel to each other, maintaining uniform $\text{Ti}^{4+}\text{-O}^{2-}$ bond lengths and strictly linear $\text{O}^{2-}\text{-Ti}^{4+}\text{-O}^{2-}$ linkages, reinforcing the structural regularity of the system [17].

1.2 The Goldschmidt Tolerance Factor

The ideal perovskite structure is crystallographically rigid due to the absence of adjustable atomic position parameters within its unit cell, necessitating that any compositional variation be accommodated solely through adjustments in the lattice parameter. Between 1924 and 1926, V.M. Goldschmidt, widely regarded as the pioneer of crystal chemistry, synthesized numerous perovskite compounds with diverse compositions-including BaTiO_3 [35], and introduced the empirical concept of the *tolerance factor*, t_G , as a predictor of structural feasibility and symmetry in perovskites [26, 35, 36].

$$t_G = \frac{r_A + r_O}{\sqrt{2}(r_B + r_O)} \quad (1)$$

Here, r_A and r_B represent the ionic radii of the cations of the A-site and the B-site, respectively, while r_O denotes the radius of the anion. It is crucial to apply ionic radii that correspond to the ions' specific coordination environments. The tolerance factor serves as a reliable metric for quantifying the degree of deviation from the ideal cubic structure, with $t_G \approx 1$ indicating minimal distortion. According to this relationship, t_G decreases with a reduction in r_A and/or an increase in r_B . Specifically, when $1.00 < t < 1.13$, the structure tends toward hexagonal symmetry; when $0.90 < t_G < 1.00$, it assumes a cubic form; and for $0.75 < t_G < 0.90$, an orthorhombic structure emerges. Notably, if $t_G < 0.75$, the perovskite transforms into a hexagonal ilmenite-type structure, as exemplified by FeTiO_3 [19, 36–38]. Generically, for a compound to crystallize in the perovskite structure, two fundamental requirements must be met: charge balance

and suitable ionic sizes. First, the structure must obey the electroneutrality condition, where the sum of the charges on the A- and B-site cations equals the charge of the three O-site anions. This criterion is commonly fulfilled in stoichiometries such as: $A^{1+}B^{5+}O^3$ (e.g., $KNbO_3$), $A^{2+}B^{4+}O^3$ (e.g., $SrTiO_3$), and $A^{3+}B^{3+}O^3$ (e.g., $LaAlO_3$) [19]. Second, the ionic radii must satisfy specific thresholds: $r_A > 0.090\text{nm}$ and $r_B > 0.051\text{nm}$. Furthermore, the Goldschmidt tolerance factor should lie within the range $0.8 < t_G < 1.0$ to ensure geometric compatibility of the ions within the perovskite structure [26, 39]. For perovskites with doped or mixed cation compositions, the conventional tolerance factor is extended using averaged ionic radii or mean bond lengths. In compounds doped at the A site with the general formula $A_{1-x}A'_xBO_3$, the tolerance factor becomes as follows:

$$t_G = \frac{(1-x)r_A + xr_{A'} + r_O}{\sqrt{2}(r_B + r_O)} \quad (2)$$

where $r_{A'}$ represents the ionic radius of the dopant [40]. In contrast, doping at the B site in compounds such as $AB_{1-x}B'_xO_3$ modifies the expression to:

$$t_G = \frac{r_A + r_O}{\sqrt{2}[(1-x)r_B + xr_{B'} + r_O]} \quad (3)$$

Additionally, for cases where accurate crystallographic data are available, the tolerance factor can be calculated on the basis of mean bond lengths:

$$t_g = \frac{\langle A-O \rangle}{\sqrt{2}\langle B-O \rangle} \quad (4)$$

where $\langle A-O \rangle$ and $\langle B-O \rangle$ are the average bond lengths between the respective cations and the anion [24, 36, 41]. These generalized forms provide greater accuracy in predicting structural stability in complex or doped perovskite systems.

1.3 Related Perovskites Structure

A brief discussion of ABO_3 related perovskite structures and factors affecting perovskite structures is presented.

1.3.1 Double Perovskites

In complex oxide perovskites where multiple cationic species coexist, significant disparities in charge or ionic radii frequently drive the system toward ordered cation arrangements. One of the most prominent structural outcomes of such ordering is the formation of rock-salt ordered double perovskites, NaCl with general formula $A_2BB'O_6$ [see Figure I.2], where B and B' are distinct transition metal cations occupying the octahedral sites alternately in a three-dimensional array [42]. These can be categorized into three principal structural variants: (i) A-site ordered, $AA'B_2X_6$; (ii) both A- and B-site ordered, $AA'BB'X_6$; and (iii) B-site ordered, $A_2BB'X_6$. This ordering minimizes lattice strain and electrostatic repulsion, stabilizing the structure [19]. To ensure charge neutrality, the charge-balance condition is governed by:

$$q_A + q_B + q_{B'} = -6 \quad (5)$$

Various common ionic combinations satisfy this criterion, such as A^{2+} : with B^{2+}/B'^{4+} : e.g., Ba_2FeMoO_6 [43], B^{3+}/B'^{3+} : e.g., Sr_2FeMoO_6 [44], or B^{2+}/B'^{4+} : e.g., La_2NiMnO_6 [45], and likewise for A^{3+} with suitable compensating B-site valences [23]. In the absence of octahedral tilting, the structure retains a cubic symmetry with space group $Fm\bar{3}m$ (No. 225), featuring a doubled unit cell compared to the parent perovskite. An illustrative example is Ba_2FeMoO_6 , which exhibits a cubic lattice with a parameter of $a = 0.81865$ nm [43]. However, smaller A-site cations induce tilting of the BO_6 and $B'O_6$ octahedra, leading to lower symmetry phases. For instance, the tilt system $a^0a^0c^-$ results in a tetragonal phase with space group $I4/m$ (No. 87), where the new lattice parameters relate to the pseudocubic cell by $a \approx b \approx \sqrt{2}a_p$ and $c \approx 2a_p$. A typical case is Sr_2FeMoO_6 , which adopts this distortion with $a = 0.55705$ nm and $c = 0.79253$ nm [44].

Table I.3: Octahedral tilting patterns in double perovskites

Tilt Pattern	Space Group	Unit Cell Parameters	Example
$a^0a^0a^0$	$Fm\bar{3}m$	$a = b = c = 2a_p$	Ba_2FeMoO_6
$a^0a^0c^-$	$I4/m$	$a = b \approx \sqrt{2}a_p, c \approx 2a_p$	Sr_2FeMoO_6
$a^-b^-a^-$	$Pnma$	$a \approx 2a_p, b \approx 2\sqrt{2}a_p$	Ca_2FeMoO_6

Further symmetry reduction to monoclinic ($P2_1/c$, No. 14) or alternative

tetragonal ($P4/mnc$, No. 128) phases is not uncommon as the tilt system evolves (e.g., $a^0a^0c^+$), with similar crystallographic axes orientation but altered connectivity and octahedral linkages [46]. The bond valence sum (BVS) method is frequently applied to evaluate local bonding environments and oxidation states. In $\text{Ca}_2\text{MgOsO}_6$, calculated BVS values of $\text{Ca}-\text{O} = 2.03$, $\text{Mg}-\text{O} = 2.15$, and $\text{Os}-\text{O} = 6.49$ indicate overbonding of Os, suggesting deviation from the formal Os^{6+} oxidation state [47]. A common structural defect is (i) *antisite disorder*, *ASD*, where B and B' cations randomly interchange positions, disrupting the ideal rock-salt ordering; and (ii) *antiphase boundary* (*APB*) disorder, where regions of perfectly ordered domains are separated by interfaces across which the B/B' ordering is reversed. Woodward [18] proposed a five-tier schema to systematically classify the extent and nature of cation disorder in double perovskites. This classification includes: (i) a fully disordered state, which may or may not exhibit short-range correlations; (ii) weakly ordered structures, with only marginal preference for B/B' site segregation; (iii) partially ordered systems, exhibiting moderate long-range order interrupted by disorder; (iv) highly ordered structures containing antiphase boundaries; and (v) perfectly ordered structures with uniform rock-salt B-site cation arrangement and no APBs. This disorder is known to be sensitive to synthesis conditions, temperature, and particle size, often leading to distinct surface and bulk orderings, especially in nanoscale systems [41]. These defects influence a range of functional properties including, magnetism and conductivity. Temperature-induced phase transitions are also prevalent where representative case is $\text{Ba}_2\text{BiIrO}_6$, which undergoes a transition from cubic ($Fm\bar{3}m$) at 500 K ($a = 0.85178$ nm) to a rhombohedral ($R\bar{3}c$, No. 167) phase at 300 K with hexagonal metrics $a = 0.60006$ nm, $c = 1.47497$ nm, then to Monoclinic ($C2/m$). Upon further cooling below 140 K, the structure transforms into a triclinic phase ($P\bar{1}$, No. 2) with nearly tetragonal geometry [48].

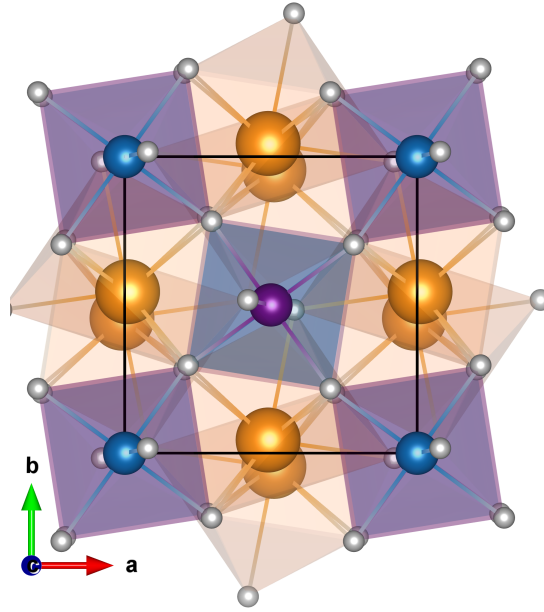


Figure I.2: The crystal structure of $\text{Nd}_2\text{NiMnO}_6$ in the $P2_1/n$ space group is presented as a single unit cell. (a) The A -site with Nd atoms is depicted in orange. (b) The B -sites are shown, with Ni and Mn atoms represented in blue and royal. (c) The $(\text{NiMn})\text{O}_6$ octahedral tilt coordination is highlighted, with Ni and Mn octahedra shaded in blue and royal, respectively. The O^{2-} ions are represented by grey spheres.

Table I.4: Double perovskite materials and applications

Compound	Ordering	Symm.	Property	Applic.
$\text{Sr}_2\text{FeMoO}_6$	Rock-salt	$I4/m$	Half-metallic ferrimagnet	Spintronics
$\text{La}_2\text{NiMnO}_6$	Rock-salt	$Pnma$	Ferromagnetic	Multiferroics
$\text{Cs}_2\text{AgBiBr}_6$	Rock-salt	$Fm\bar{3}m$	Direct bandgap	Photovoltaics

A critical determinant for the degree of B-site ordering is the difference in size and charge between the B and B' cations [42, 49]. This ordering influences key physical properties such as magnetism and conductivity. A rock-salt-ordered arrangement containing a single magnetic B-cation can form a face-centered cubic (FCC) magnetic sublattice, a geometry that fosters geometrical frustration and exotic magnetic ground states [50]. Minor changes in ordering or symmetry can significantly affect nearest-neighbor (NN) and next-nearest-neighbor (NNN) interactions, including $180^\circ \text{B} - \text{O} - \text{B}'$, $90^\circ \text{B}/\text{B}' - \text{O} - \text{O} - \text{B}/\text{B}'$, and $180^\circ \text{NNNB} - \text{O} - \text{B}'$ pathways, which collectively determine whether the magnetic ordering is long-ranged or frustrated [51]. The Goodenough-Kanamori-Anderson (GKA) rules generally govern the magnetic interactions. For instance, superexchange between two magnetic cations with half-filled orbitals via a $180^\circ \text{B} - \text{O} - \text{B}$ linkage typically results in antiferromagnetic ordering, such as the

$d^3 - O - d^3$) interaction. Conversely, ferromagnetic coupling occurs for mixed half-filled and empty or fully occupied orbitals (e.g., $(d^3 - O - d^5)$), especially when the $B - O - B$ angle is close to 90° [24, 37, 42, 52, 53]. Beyond the B-site, chemical substitution at the A-site also plays a pivotal role in modulating structural and functional properties. A-site doping introduces chemical pressure that alters the overlap of B-O orbitals, affects octahedral tilting, and may modify B-site oxidation states and superexchange pathways [23]. Notably, variations in the ionic radius of A-site dopants can indirectly affect B-O bond angles and lengths, thus tuning the electronic and magnetic behavior of the system [49].

1.3.2 Quadruple Perovskites

The emergence of A-site ordered perovskites, notably with formulas $AA'_3B_4O_{12}$ [see Figure. I.3a] and the more complex $A_2A'A''B_4O_{12}$, represents a major breakthrough in perovskite structural chemistry. In the canonical perovskite architecture (ABO_3), the A-site is typically occupied by large, electropositive ions in 12-fold coordination, while the B-site hosts smaller transition metal cations in octahedral coordination. However, in these quadruple perovskites, transition metals occupy A' -sites, which is chemically unusual due to their size and preferred coordination. The $AA'_3B_4O_{12}$ structure accommodates 3d transition metals such as Cu^{2+} and Mn^{3+} or other relevant cations, particularly, $Cu^{2+}, Co^{2+}, Pd^{2+}, Fe^{2+}$ [54–56] [see Figure I.3b for square-planar], etc., at the A' -site, where they are stabilized through strong Jahn-Teller distortions that favor square planar or elongated octahedral configurations. This is made possible by a cooperative $a^+a^+a^+$ tilt system of the BO_6 octahedra, which allows for sufficient lattice distortion to support these coordination geometries [1, 57].

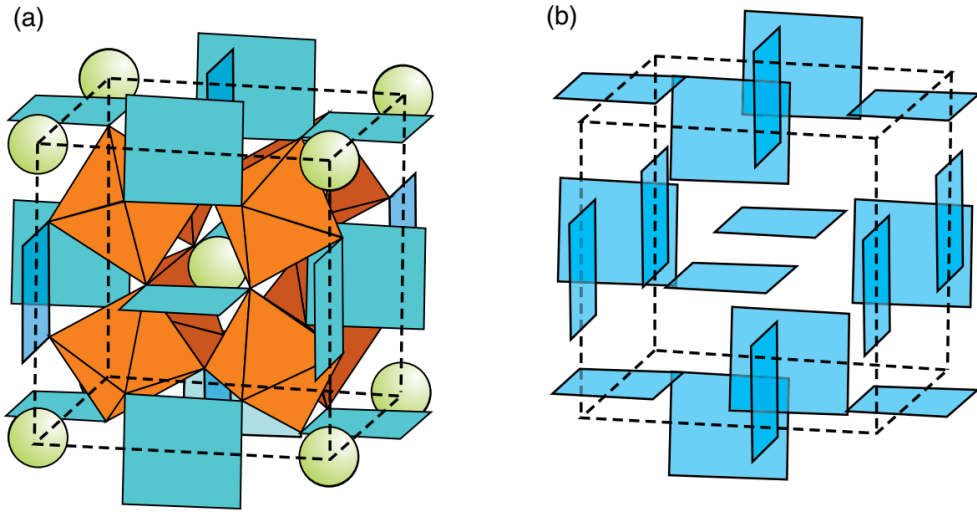


Figure I.3: (a) The $AA'_3B_4O_{12}$ structure; the squares represent square planar $A'O_4$ coordination polyhedra. (b) The distribution of the $A'O_4$ polyhedra within a unit cell. Adapted from [1].

These structural adaptations impart remarkable physical properties. For example, $\text{CaCu}_3\text{Ti}_4\text{O}_{12}$ is known for its exceptionally high dielectric constant, attributed to internal barrier layer capacitance enhanced by A-site ordering [58]. $\text{SrCu}_3\text{Fe}_4\text{O}_{12}$, on the other hand, exhibits negative thermal expansion, while $\text{LaCu}_3\text{Mn}_4\text{O}_{12}$ demonstrates colossal magnetoresistance, underscoring the potential for multifunctionality [1, 15]. Recent studies have also confirmed the presence of complex ferrimagnetic and relaxor ferroelectric behaviors in rare-earth substituted perovskites of the type $\text{R}_2\text{MnMn}(\text{MnTi}_3)\text{O}_{12}$ ($\text{R} = \text{Nd}, \text{Eu}, \text{Gd}$), further broadening their utility in magnetoelectronic devices [59]. The advancement to $\text{A}_2\text{A}'\text{A}''\text{B}_4\text{O}_{12}$ -type perovskites, pioneered by Belik and collaborators, introduces a new level of A-site ordering. Here, three chemically distinct cations are hosted at structurally unique sites: A in 10-fold coordination, A' in square planar, and A'' in a rare tetrahedral coordination - a novelty in oxygen-stable perovskites [15]. This columnar ordering along the c -axis emerges due to an $a^+a^+c^-$ octahedral tilt system, generating stacked polyhedral chains and enabling distinct site selectivity. These systems often require high-pressure synthesis to stabilize the unusual A'' site environment and have been successfully implemented in materials like $\text{NaRMn}_2\text{Ti}_4\text{O}_{12}$ ($\text{R} = \text{Sm}, \text{Eu}, \text{Gd}, \text{Dy}, \text{Ho}, \text{Y}$), showing uniform antiferromagnetic structures across compositions [60]. Despite these advances, synthesis challenges persist, particularly in achieving full cationic ordering at high pressures and maintaining structural purity. Deviations from ideal stoichiometry, such as Mn/Rh disorder or oxygen vacancies, have been shown to degrade dielectric performance and induce unexpected phase behavior [58]. Furthermore, understanding charge-

order phenomena and magneto-structural coupling in these systems remains an active area of research, as revealed in studies using neutron diffraction and synchrotron X-ray analyses [57, 61].

1.4 Structural Deviations

While the ionic size of constituent cations plays a fundamental role in determining the structural stability of perovskites and similar crystalline systems, it alone does not fully account for the observed deviations from the ideal cubic configuration. A comprehensive understanding of these deviations necessitates the consideration of additional intrinsic and extrinsic factors. Among these, the nature of bonding, the electronic configuration of the ions, external influences such as pressure and temperature, as well as the presence of vacancies or crystallographic defects, are all critical in shaping the final structure. These factors interact in complex ways, often giving rise to structural distortions that significantly influence the material's physical and chemical properties. Deviation from the ideal cubic structure is typically manifested through three primary mechanisms[see Figure I.4]: (i) co-operative tilting of the octahedra, (ii) distortion of the octahedra, and (iii) displacement of A-site or B-site cations from their ideal lattice positions. Among these, co-operative tilting of the octahedra emerges as the most prevalent and influential mode of structural distortion. However, to develop a holistic understanding of structural deviations, it is imperative to examine the role of the other contributing mechanisms and influencing factors. The following discussion delves into these additional parameters, highlighting their significance and interrelation in driving the system away from ideal symmetry.

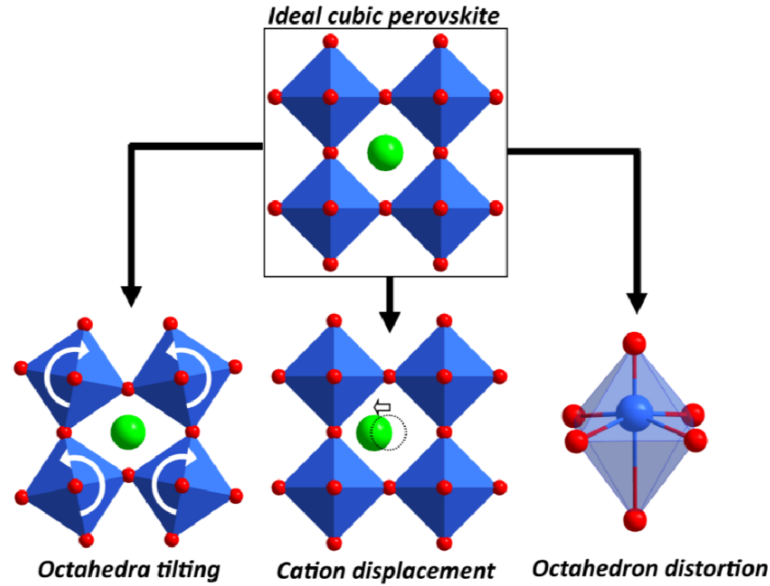


Figure I.4: The ideal cubic ABX_3 perovskite structure, along with its prevalent structural distortions, including octahedral tilting, cation displacement, and octahedral distortion—arising from ionic size mismatch [2].

1.4.1 Octahedral Distortion: Jahn-Teller(J-T) Effect

Among the most prominent and well-studied forms of octahedral distortion in perovskite structures is Jahn-Teller (J-T) distortion, which stems from the Jahn-Teller effect of first order. This fundamental principle of molecular symmetry asserts that any non-linear molecule with a degenerate electronic ground state is inherently unstable in a symmetric configuration and will undergo a geometric distortion to lift the degeneracy and lower its total energy [62–64]. The J-T effect is most pronounced in transition metal ions possessing certain electronic configurations, typically those with partially filled e_g orbitals. These so-called J-T active ions, such as Cr^{2+} , Mn^{3+} (d^4), Co^{2+} , Ni^{3+} (d^7), and Cu^{2+} (d^9), exhibit a degenerate ground state due to uneven filling of the e_g orbitals—specifically the $d_{x^2-y^2}$ and d_{z^2} orbitals [62, 65]. In an ideal octahedral field, these orbitals are degenerate, forming the level e_g , while the orbitals of lower energy t_{2g} (comprising d_{xy} , d_{yz} , and d_{xz}) remain unaffected in the first approximation. To remove this degeneracy, the octahedral environment undergoes distortion, commonly by elongation or compression along one of the crystallographic axes, resulting in either four short and two long B–O bonds or vice versa. The most frequently observed

outcome in perovskites is an elongation, often significant enough to resemble square planar or square pyramidal coordination geometries [66]. Although the impact on the t_{2g} orbitals is relatively minor, the splitting of the e_g level is energetically substantial and directly drives the distortion. Despite the modification of bond lengths, the A and B cations typically remain centrally located within their respective coordination polyhedra. However, the overall crystal symmetry is reduced, commonly transforming from cubic to tetragonal or orthorhombic. Importantly, Jahn-Teller distortions are highly sensitive to external conditions; increasing temperature or pressure can reverse the distortion, reinstating cubic symmetry in many perovskite systems [1]. The quantitative magnitude of octahedral distortion in perovskite structures can be expressed using the distortion parameter Δd , defined as:

$$\Delta d = \left(\frac{1}{6} \sum_{i=1}^6 \left(\frac{d_i - d_{av}}{d_{av}} \right)^2 \right)^{1/2} \quad (6)$$

where d_i represents each bond distance between the B-site cation and the O-site anions (B–O), and d_{av} is the average B–O bond distance [67–69]. An extensively studied example of such J-T distortion is KCuF_3 , which contains the J-T-active ion Cu^{2+} . The compound exhibits a pronounced elongation of the Cu–F bonds consistent with this distortion mechanism [67, 68].

1.4.2 Octahedral Rotation: Glazer Notation and Symmetry

Most real perovskite oxides deviate from the idealized cubic configuration [see Figure I.5a for the tilt deviation directions: (i)tetrad (z - γ), (ii)diad (y - β , and (iii) triad (x - α) axis] and instead crystallize in lower-symmetry phases such as rhombohedral, orthorhombic, or tetragonal structures due to factors like octahedral tilting or lattice strain [46], Figure I.5b. To systematically describe the patterns of octahedral rotation in these structures, Glazer [17] introduced a comprehensive classification system comprising 23 distinct tilt systems. In this scheme, the rotations of the $[\text{BO}_6]$ octahedra are expressed relative to the crystallographic axes, with the parameters a , b , and c representing the magnitudes of rotation around the $[100]$, $[010]$, and $[001]$ directions, respectively, conventionally ordered

as $a \leq b \leq c$. Identical letters denote equal tilt magnitudes, while differing letters reflect anisotropy in the rotations. For instance, the (abb) tilt system indicates equal rotations about the $[010]$ and $[001]$ axes, both larger than that about $[100]$, whereas the (abc) system describes unequal tilts along all three directions. Additionally, each tilt component is assigned a superscript of "+" (in-phase), "-" (out-of-phase), or "0" (no rotation). The "+" superscript signifies that adjacent octahedra rotate synchronously about a given axis, while "-" indicates alternating rotation directions, and "0" reflects the absence of rotation. The ideal cubic perovskite is therefore represented by the tilt system $(a^0a^0a^0)$, denoting no octahedral tilting [17]. To maintain the structural connectivity and coherence of the octahedral framework, two essential constraints must be satisfied: first, octahedra sharing a corner must rotate in opposite directions about the axis perpendicular to that face to preserve corner-sharing connectivity; second, adjacent octahedra may rotate either in-phase or out-of-phase about a given axis, provided the overall tilting pattern maintains structural continuity [70]. These geometric principles yield specific single-axis tilt systems such as $(a^+a^0a^0)$ and $(a^-a^0a^0)$, in which all octahedra exhibit either in-phase or out-of-phase rotations about the $[100]$ axis, with no tilting around the other directions. These configurations critically influence the electronic, magnetic, and ferroic behaviors of perovskite oxides and have been effectively visualized through symmetry-based structural models [71].

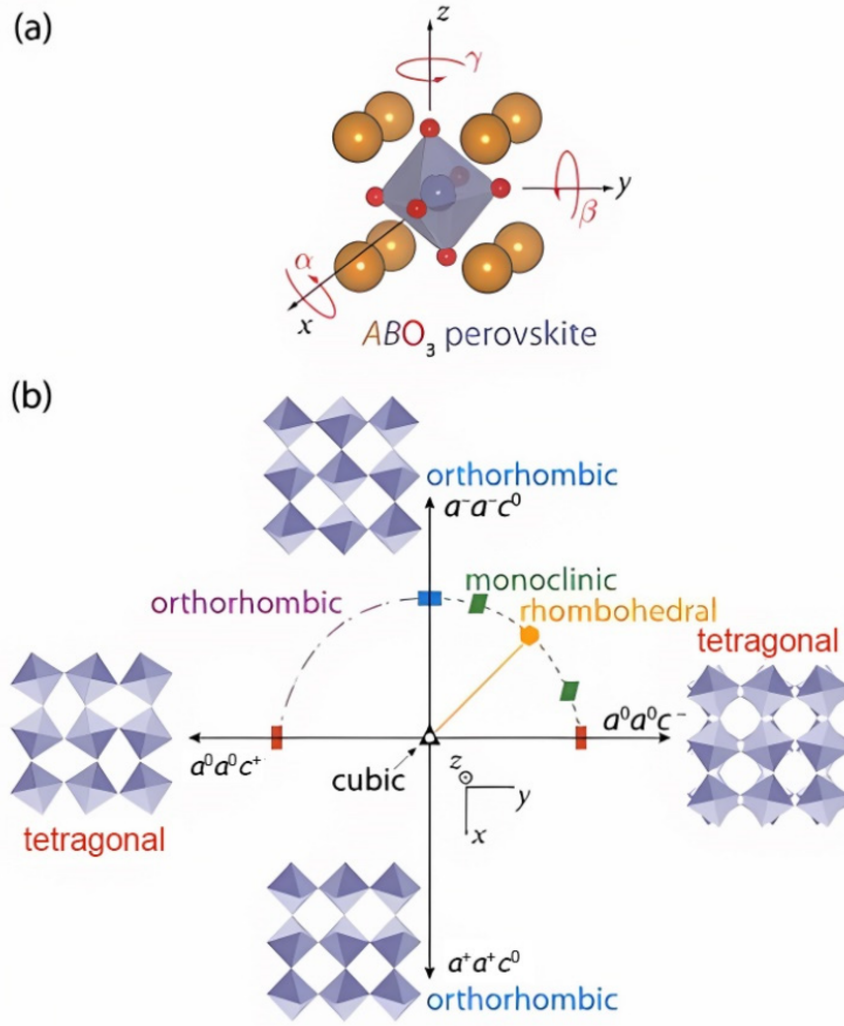


Figure I.5: Octahedral Rotation Modes and Tilt Patterns in Perovskite Transition Metal Oxides. (a) Octahedral rotations in perovskite transition metal oxides can be decomposed into components about three orthogonal axes intersecting at the central transition metal ion. (b) Examples of characteristic tilt systems include the $a^0a^0c^+$ and $a^0a^0c^-$ configurations, representing in-phase (c^+) and out-of-phase (c^-) rotations of adjacent octahedra about the z -axis, respectively. Additionally, the $a^+a^+c^0$ and $a^-a^-c^0$ patterns describe similar rotational behaviors in the xy -plane. The alternating rotation directions between neighboring octahedra in adjacent layers are especially evident in the $a^0a^0c^-$ configuration (far right), highlighting the layer-dependent nature of octahedral tilt systems [3].

Furthermore, a comprehensive group-theoretical analysis of octahedral tilt systems in perovskite oxides has revealed that, out of the 23 theoretically possible Glazer tilt systems, only 15 are experimentally realizable in real crystal structures, while the remaining eight are considered symmetry-allowed but physically unattainable, and thus redundant in practice [70]. The experimentally relevant tilt configurations include $a^0a^0a^0$ (23), $a^0a^0c^+$ (21), $a^0b^+b^+$ (16), $a^+a^+a^+$ (3), $a^+b^+c^+$ (1), $a^0a^0c^-$ (22), $a^0b^-b^-$ (20), $a^-a^-a^-$ (14), $a^0b^-c^-$ (19), $a^-b^-b^-$ (13), $a^-b^-c^-$ (12), $a^0b^+c^-$ (17), $a^+b^-b^-$ (10), $a^+b^-c^-$ (8), and $a^+a^+c^-$ (5). These tilt systems form a well-defined hierarchy of descent of the symmetry of the parent

cubic perovskite structure (space group $Pm\bar{3}m$) through successive reductions of symmetry to subgroups tetragonal, orthorhombic, monoclinic, and triclinic as shown in Figure I.5. This systematic lowering of symmetry governs the rich structural diversity and property tunability in perovskite materials. This hierarchical symmetry framework not only rationalizes the experimentally observed phases but also predicts possible pathways for phase transitions and coupled functional responses.

1.4.3 A- or B-site Cation Displacement

Finally, the off-centering of the B atom within the BO_6 octahedra—shifting toward one anion and away from the opposite O atom (Figure I.4), is a key structural distortion influencing material properties. This displacement creates a permanent dipole moment, driving ferroelectricity and multiferroicity [72, 73]. The mechanism is often linked to displacement instabilities, soft phonon modes, and order-disorder transitions. Transverse optical phonon softening at the Brillouin zone center precedes structural phase transitions, enabling cation displacements [72]. Such shifts are common in Pb^{2+} , Sn^{2+} , or Bi^{3+} systems, where stereochemically active lone pairs (ns^2 configuration) induce asymmetric electron density and off-centering [74]. For instance, in FeTiO_3 , Ti^{4+} displacement and Pb^{2+} lone-pair activity enhance ferroelectric polarization [75]. Cation displacements typically align with octahedral symmetry axes—tetrad, triad, or diad, reducing overall symmetry. Tetrad-axis displacement yields one long, one short, and four intermediate bonds (Figure I.6a); triad-axis displacement produces three short and three long bonds (Figure I.6b); diad-axis displacement results in two long, two short, and two intermediate bonds (Figure I.6c). The most stable configurations involve uniform B-site displacements, often coupled with smaller A-site shifts, octahedral tilting, and lattice deformations, enhancing polar and ferroic properties [1, 17, 70]. These displacements also modulate electronic band structures. In $\text{CH}_3\text{NH}_3\text{PbI}_3$, dynamic Pb^{2+} off-centering in PbI_6 octahedra modifies orbital overlap, tuning band gaps and improving charge transport [76]. In oxides, they influence dielectric, piezoelectric, and electro-optic responses, enabling applications in capacitors and memory devices. Multiferroics like BiFeO_3 exhibit Bi^{3+} (large lone-pair-driven shift) and Fe^{3+} displacements, yielding strong polar-

ization and antiferromagnetic coupling [77]. Displacements arise via displacive (phonon-driven) or order-disorder (Jahn-Teller) mechanisms [1], with the latter involving random off-centering at high temperatures and ordered displacement upon cooling [70, 78].

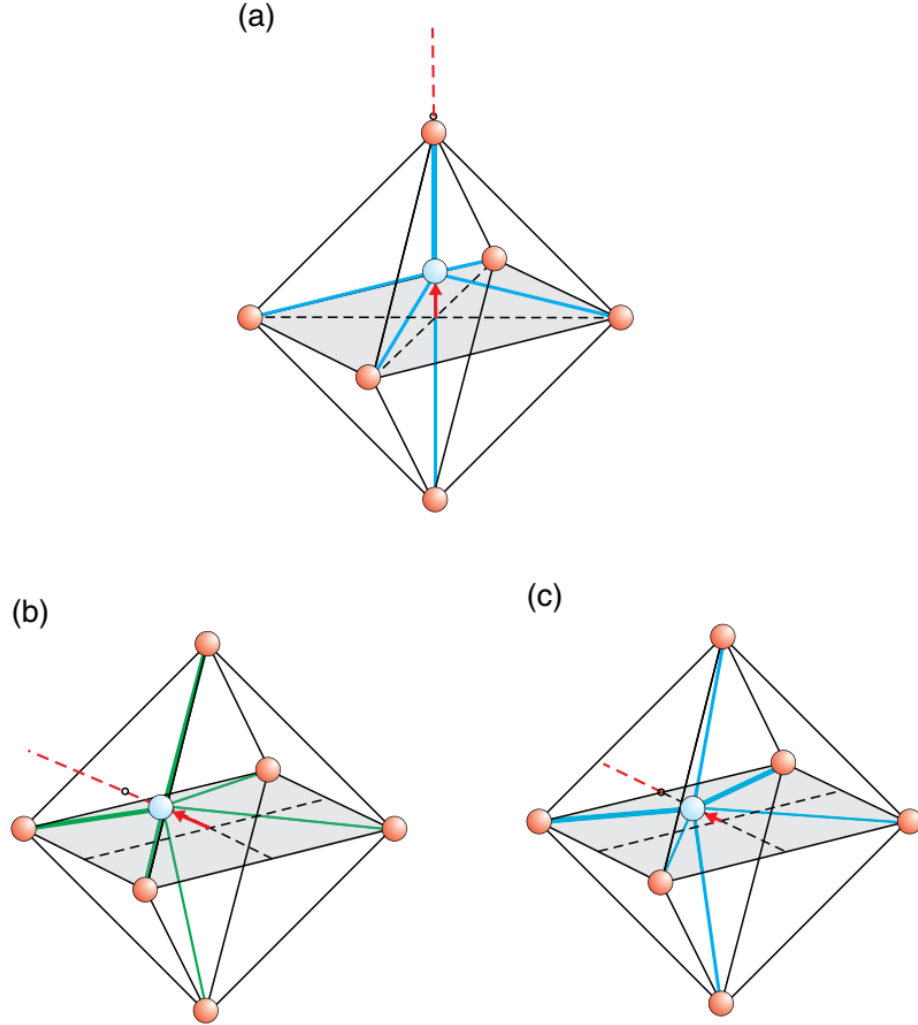


Figure I.6: Cation displacement (a) along a tetrad axis produces one long, one short, and four intermediate bonds. (b) along a triad axis results in three short and three long bonds. (c) along a diad axis gives two long and two short bonds in the plane, with two intermediate bonds perpendicular to the plane [1].

1.5 State of the Art and Scope of the Thesis

The pursuit of emergent phenomena in complex quantum materials is a central driver of condensed matter physics. Perovskite oxides represent a quintessential platform for this exploration, offering unparalleled structural flexibility that hosts a vast spectrum of electronic, magnetic, and orbital properties. A particularly

rich landscape emerges when multiple magnetic sublattices—specifically, transition metal ($3d$, $5d$) and rare-earth ($4f$) ion, are incorporated into the crystal lattice. The interplay between these subsystems, characterized by competing exchange interactions, strong spin-orbit coupling, and magneto-structural coupling, can lead to novel ground states such as non-collinear magnetism, spin frustration, and multiferroicity. These phenomena are not only of fundamental interest but are also paramount for next-generation technologies in spintronics, magnetic refrigeration, and quantum computing.

Despite progress, a comprehensive understanding of the tripartite interplay between $3d$, $4f$, and $5d$ cations remains a significant challenge. The complexity arises from the confluence of several factors: the strong SOC inherent to $4f$ and $5d$ ions, the diverse superexchange pathways mediated by oxygen, and the critical yet often overlooked role of structural distortions in modulating these interactions. Traditional studies have frequently examined these sublattices in isolation, thereby missing the essential physics that emerges from their synergy. Thus, this thesis addresses key unanswered questions in the field:

1. How does the strong SOC of $5d$ ions (e.g., Ir^{4+} , $J_{\text{eff}} = 1/2$) modify established $3d$ – $4f$ exchange pathways?
2. What is the precise nature of low-temperature magnetic ordering in rare-earth-based perovskites, particularly the role of the $4f$ sublattice and its potential for non-collinear order?
3. Can structural distortions be systematically exploited to control the competition between ferromagnetic (FM), ferrimagnetic (FiM), and antiferromagnetic (AFM) interactions?
4. How do coupled phenomena like spin–phonon coupling and magnetostriction govern functional properties such as the magnetocaloric effect in these multi-sublattice systems?

Methodological Approach

To bridge these gaps, this work employs a powerful synergy of advanced techniques. The foundation is the synthesis of high-purity polycrystalline samples of double and quadruple perovskites via optimized sol-gel routes. Their struc-

tural and magnetic properties are deciphered using a multi-pronged experimental approach: high-resolution neutron powder diffraction (NPD) and synchrotron X-ray diffraction (SXRD) for crystal and magnetic structure determination; dc and ac magnetometry to map magnetic phase transitions and dynamics; X-ray absorption spectroscopy (XANES) for element-specific electronic and coordination analysis; Raman spectroscopy to probe spin-phonon coupling; and specific heat measurements for thermodynamic analysis. Crucially, these experimental observations are validated and interpreted through first-principles density functional theory (DFT+ U +SOC) calculations, creating a closed loop between empirical evidence and fundamental theory.

Chapter I

Establishes the foundational context, detailing the crystal chemistry of perovskites, from the ideal cubic structure to the complex distortions and cation ordering schemes that define double ($A_2BB'O_6$) and quadruple ($AA'_3B_4O_{12}$) variants. It introduces key concepts like the Goldschmidt tolerance factor, Jahn-Teller distortions, and Glazer tilt systems.

Chapter II

Provides the theoretical underpinnings, reviewing crystal and magnetic symmetry, Landau theory of phase transitions, and the fundamental mechanisms of magnetism relevant to perovskites, including superexchange, double exchange, Dzyaloshinskii-Moriya interaction, and the physics of spin glasses.

Chapter III

Describes the comprehensive experimental methodology, covering sample synthesis via the sol-gel route, and the principles and operational details of all characterization techniques used, including neutron scattering theory, magnetometry, and Rietveld refinement methods.

Chapter IV: $\text{Nd}_2\text{NiMnO}_6$ (The $3d$ - $4f$ Prototype)

The double perovskite $\text{Nd}_2\text{NiMnO}_6$ served as the foundational system for this study, a material known to exhibit ferromagnetic order below approximately 200 K yet plagued by unresolved controversies regarding the precise nature of its low-temperature magnetic state. Prior literature contained conflicting interpretations, variously suggesting spin-glass behavior, cluster-glass formation, or an additional magnetic transition, often attributed to poorly understood valence fluctuations or antisite disorder (ASD). A principal gap involved the undefined magnetic structure, particularly the role and configuration of the Nd^{3+} moments and their relationship to the transition metal lattice. This work confirms the material crystallizes in the monoclinic $P2_1/n$ space group with a high degree of Ni/Mn B-site cationic ordering. The primary magnetic transition at $T_C = 198\text{ K}$ is unambiguously assigned to long-range ferromagnetic order within the Ni^{2+} ($S = 1$) and Mn^{4+} ($S = 3/2$) sublattices, mediated by the $\text{Ni}^{2+}\text{-O-Mn}^{4+}$ superexchange mechanism, and the system is confirmed to exhibit a significant magnetocaloric effect ($\Delta S_M = 2.25\text{ J kg}^{-1}\text{ K}^{-1}$ at 7 T). The novel findings of this chapter provide a resolution to the longstanding controversies: the identification of a re-entrant spin-glass state below T_C is attributed to magnetic frustration induced by a small but non-zero degree of ASD. Furthermore, the discovery of a second, distinct magnetic transition at $T_{N1} = 22\text{ K}$ signifies the onset of order within the Nd^{3+} sublattice. Neutron diffraction analysis at 1.5 K reveals this order takes the form of a complex, non-collinear magnetic structure, which is driven by a competition between ferromagnetic f - d exchange (Nd-Ni/Mn) and antiferromagnetic f - f exchange (Nd-Nd). Finally, critical exponent analysis conclusively demonstrates that the primary ferromagnetic transition belongs to the mean-field universality class, indicative of long-range interactions dominating near the critical temperature.

Chapter V: $\text{Nd}_2\text{NiMn}_{0.25}\text{Ir}_{0.75}\text{O}_6$ (Introducing the $5d$ Orbital)

This chapter investigates the consequences of introducing strong spin-orbit coupling by substituting the $3d$ Mn^{4+} ion with the $5d$ ion Ir^{4+} into the $4f$ -

containing double perovskite framework, an effect that was previously unexplored. The study confirms that Ir doping maintains the parent compound's monoclinic $P2_1/n$ structure while simultaneously inducing significant lattice expansion and strain, and it suppresses the ferromagnetic ordering temperature relative to the undoped compound. The novel findings, however, reveal a far more nuanced and profound impact. The magnetic structure is resolved as a unified model described by the Γ_1^+ irreducible representation, thereby eliminating previous speculative models that invoked phase coexistence. A quintessential signature of strong spin-orbit effects is observed in the form of severely reduced ordered moments on both the Mn and Ir sites ($\sim 0.38\mu_B$), providing direct evidence of intense spin-orbit frustration. A coherent magnetic order is also discovered for the Nd^{3+} sublattice, characterized by ferromagnetic alignment along the crystallographic b -axis and A-type antiferromagnetic canting within the ac -plane. The most striking and counterintuitive result is that the Ir^{4+} ion, despite suppressing the overall magnetization of the B-site, actively mediates a novel and enhanced coupling between the $3d$ and $4f$ magnetic sublattices, establishing a new paradigm for engineering interactions in multi-sublattice magnets.

Chapters VI & VII: NdSmNiMnO_6 (Rare-Earth Sublattice Engineering)

The investigation into NdSmNiMnO_6 explores the strategy of engineering the rare-earth sublattice itself by mixing two different magnetic ions, Nd^{3+} and Sm^{3+} , at the A-site. While this approach was recognized for tuning magnetic properties, its specific effects on the magnetic ground state, critical behavior, and magnetoelastic coupling remained unclear. The work confirms the structure remains monoclinic $P2_1/n$, and XANES spectroscopy verifies the stable presence of Ni^{2+} and Mn^{4+} valence states, ruling out stoichiometry-driven valence fluctuations. Chapter VI establishes that the ground state is ferrimagnetic, a finding directly linked to the specific structural distortion of a reduced Ni–O–Mn bond angle ($\sim 146^\circ$). This magneto-structural coupling is further evidenced by pronounced magnetostriction effects observed via high-resolution synchrotron XRD, which reveal clear anomalies in the lattice parameters and unit cell volume at the magnetic ordering temperature T_N . The intimate connection between spin and lat-

tice degrees of freedom is corroborated by the observation of strong spin-phonon coupling, manifested as anomalous hardening and broadening of specific Raman modes. Building on this foundation, Chapter VII quantifies the functional outcome of these interactions, demonstrating excellent magnetocaloric performance with a high Relative Cooling Power ($\text{RCP} = 182 \text{ J/kg}$). Critical exponent analysis of the phase transition reveals a crossover from mean-field to 3D Heisenberg behavior, signaling a change in the nature of magnetic fluctuations due to the specific rare-earth mixture. First-principles DFT+ U +SOC calculations provide the crucial microscopic origin of these phenomena, identifying orbital ordering and SOC-induced moment quenching on the Sm^{3+} ion as the key mechanisms stabilizing the ferrimagnetic ground state.

Chapter VIII: $\text{Er}_2\text{CuMnMn}_4\text{O}_{12}$ (The Quadruple Perovskite Challenge)

This chapter addresses the heightened complexity of the quadruple perovskite $\text{Er}_2\text{CuMnMn}_4\text{O}_{12}$, a system known for its rich magnetism where the sequence of magnetic transitions and the specific role of the Er^{3+} ion in driving spin reorientations were not fully resolved. The work confirms the compound crystallizes in the orthorhombic $Pmmn$ space group and that its bulk magnetic characterization shows multiple transitions in susceptibility and specific heat data. The novel findings unravel this complexity by identifying four distinct magnetic transitions (T_{N1} to T_{N4}) that define the material's phase diagram. A key discovery is the occurrence of spin reorientation events, where the magnetic moments collectively flip between the $\pm b$ and $\pm c$ axes, a process primarily driven by the evolving influence of the Er^{3+} sublattice with changing temperature. The study culminates in the determination of the low-temperature ground state ($T < 7 \text{ K}$), which is a modulated magnetic structure characterized by the propagation vector $\mathbf{k} = (0, 0, \frac{1}{2})$ and involves a specific coupling between the Er_1 and Mn_3 sublattices. These results provide clear evidence of the profoundly frustrated interplay between the multiple magnetic sublattices (Cu^{2+} , $\text{Mn}^{3+/4+}$, and Er^{3+}) that defines the physics of quadruple perovskites. Collectively, this thesis significantly advances the understanding of magnetism in complex perovskites by demonstrating that the macroscopic magnetic ground state and functional properties emerge

from a finely balanced and tunable competition between a network of exchange interactions, including $3d-3d$, $3d-5d$, $3d-4f$, $5d-4f$, and $4f-4f$ pathways. A central finding is that all these interactions are exquisitely sensitive to structural distortions, which can be harnessed as a design parameter. By providing precise magnetic structures, quantifying spin-orbit frustration, and establishing robust structure-property relationships across a series of strategic material systems, this work provides a comprehensive roadmap for the rational design of next-generation multifunctional magnetic materials.

* CHAPTER II *

Theoretical Review

Symmetry, in its broadest sense, is associated with pattern, order, and balance, invoking both aesthetic and structural harmony, from the bilateral structure of organisms to repeating motifs in crystals and the rhythmic structure of music. However, in science, symmetry takes on a deeper and more formal significance, thus, invariance of physical law under specific transformations [79–81]. In physics, a symmetry transformation is a mathematically defined operation, such as translation, rotation, reflection, or time reversal, applied uniformly to a system. If the fundamental Equations governing the system (e.g., Newton’s laws, Schrödinger’s equation) remain unchanged under such a transformation, the system is said to be symmetric to it [82]. Classically, a spatial translation moves every particle in a system by the same amount, and if the dynamics remain unchanged, the translational symmetry is preserved. Similarly, invariance under rotation implies rotational symmetry, and invariance under time reversal, particularly significant in magnetic systems, implies time-reversal symmetry [50]. These symmetries are not just abstract mathematical properties; they have concrete physical implications. According to Noether’s theorem, each continuous symmetry corresponds to a conserved quantity, momentum, angular momentum, or energy, providing a powerful link between symmetry and the conservation laws that govern physical behavior [83]. Understanding how symmetry constrains physical laws enables predictive modeling of material properties, phase transitions, and emergent phenomena in complex systems, an inquiry that forms the core focus of this chapter.

2.1 Crystal Symmetry

Crystal symmetry refers to the invariance of a crystal’s atomic arrangement under a set of well-defined spatial operations, including **rotations**, **reflections**, **translations**, and **inversions**. These symmetry operations do not alter intrinsic properties of the crystal, such as its energy, charge density distribution, or

structural phenomenon. Rather, they represent indistinguishable orientations or positions within the crystal lattice, enabling symmetry-based classifications that are fundamental to understanding the material's physical behavior [6, 84]. At the most fundamental level, a crystal lattice is an idealized, infinite array of points (representing atoms or molecules) arranged in a repeating pattern throughout three-dimensional space. This periodic structure can be mathematically described by the lattice translation vector:

$$\vec{R} = n_1\vec{a}_1 + n_2\vec{a}_2 + n_3\vec{a}_3 \quad (7)$$

where $n_1, n_2, n_3 \in \mathbb{Z}$ are integers, and $\vec{a}_1, \vec{a}_2, \vec{a}_3$ are the **primitive lattice vectors** that define the geometry of the unit cell [85]. This translational periodicity is the foundation of crystalline order, allowing a small representative volume (the unit cell) to characterize the entire structure. The symmetry resulting from this periodicity leads to the concept of **crystal systems**, including cubic, tetragonal, orthorhombic, monoclinic, triclinic, hexagonal, and trigonal, each defined by specific constraints on the lengths and angles of the unit cell [see Table II.1 for clarification]. In combination with additional symmetry operations such as rotational and mirror symmetries, these systems form the basis for classifying all crystal structures into **point and space groups**, which ultimately dictate the material's structural and physical properties.

Table II.1: Crystallographic Point Groups Classified by Crystal System [6]

Crystal System	Point Groups
Cubic	23, $m\bar{3}$, 432, $\bar{4}3m$, $m\bar{3}m$
Tetragonal	4, $\bar{4}$, 4/m, 422, 4mm, $\bar{4}2m$, 4/mmm
Orthorhombic	222, mm2, mmm
Hexagonal	6, $\bar{6}$, 6/m, 622, 6mm, $\bar{6}m2$, 6/mmm
Trigonal	3, $\bar{3}$, 32, 3m, $\bar{3}m$
Monoclinic	2, m, 2/m
Triclinic	1, $\bar{1}$

2.1.1 Point Group

Point groups consist of symmetry operations, **rotations**, **reflections**, **inversions**, and **rotoinversions**, that leave at least one point in a crystal unchanged. They describe **local symmetry** (fixed-point symmetry) independent of transla-

tion, influencing crystal morphology and material properties [6, 86, 87]. In 3D crystallography, **32 crystallographic point groups** (crystal classes) exist, constrained by lattice periodicity, which restricts rotational symmetry to 2-, 3-, 4-, and 6-fold axes [86, 88]. Unlike **translational symmetry** (periodic repetition via lattice vectors, defining crystalline order), point symmetry operates around fixed positions, typically atoms, molecular groups, or high-symmetry sites, while most general positions lack symmetry [84, 85, 87]. The four fundamental point symmetry operations generate equivalent atomic configurations, preserving the crystal's structural invariance.

Rotation

Rotational symmetry exists when a crystal appears unchanged after being rotated by a fixed angle about an axis. Mathematically, this angle is defined as:

$$\theta = \frac{2\pi}{n} \quad (8)$$

where n is an integer. Only specific values of n , namely 1, 2, 3, 4, and 6, are compatible with the translational periodicity of a crystal lattice. These are the only values that enable motifs to repeat without leaving gaps or overlaps in space [85]. For instance, a fourfold rotation axis (C_4) aligned along the z -axis will cyclically transform a point (x, y, z) into $(-y, x, z)$, then $(-x, -y, z)$, and finally $(y, -x, z)$, returning to the original position after a complete 360° rotation. The presence of a single 2-fold axis typically leads to monoclinic symmetry, a 4-fold axis defines tetragonal symmetry, a 3-fold axis results in trigonal or rhombohedral systems, and a 6-fold axis defines a hexagonal lattice. The cubic system is uniquely characterized by the presence of four 3-fold axes along the $\langle 111 \rangle$ directions [6, 86]. Rotation symmetries are typically denoted by the numbers 2, 3, 4, or 6, and in the Schoenflies notation, commonly used in chemistry and molecular symmetry, they are represented by C_n (e.g., C_2 , C_3 , C_4) [88].

Reflection (Mirror Planes)

A mirror or reflection operation flips a structure across a specific crystallographic plane such that every point and its image are equidistant from the plane but lie on opposite sides. A mirror plane perpendicular to the z -axis, for in-

stance, transforms a point (x, y, z) to $(x, y, -z)$. Mirror symmetry is fundamental in defining monoclinic and orthorhombic systems, depending on the number and orientation of the mirror planes. A single mirror plane normal to the \vec{b} lattice vector is commonly associated with monoclinic symmetry. The presence of two or three mutually perpendicular mirror planes increases symmetry to orthorhombic [6, 89]. Mirror planes are denoted by m in international notation. In Schoenflies notation, the symbol σ is used, with appropriate subscripts to denote orientation.

Inversion (Center of Symmetry)

Inversion symmetry involves a transformation through a center such that a point (x, y, z) is mapped to $(-x, -y, -z)$. A crystal that exhibits this symmetry is called centrosymmetric. The existence of a center of symmetry implies the absence of a permanent dipole moment, making such structures non-polar. Consequently, centrosymmetric crystals do not exhibit properties such as piezoelectricity or second-harmonic generation [84, 86]. This operation is denoted as $\bar{1}$ in international crystallographic notation and as i in Schoenflies notation. Inversion symmetry is critical for understanding centrosymmetric behavior in crystallographic and physical property contexts [90].

Rotoinversion

Rotoinversion is a compound symmetry operation combining rotation about an axis with inversion through a point. A threefold rotoinversion axis ($\bar{3}$), to illustrate, transforms a point (x, y, z) to $(-y, -z, -x)$. This operation combines cyclic permutation and inversion, resulting in more complex but highly structured symmetry behaviors. A fourfold rotoinversion axis ($\bar{4}$) aligned along the z -axis first rotates the point (x, y, z) to $(-y, x, z)$, and then inverts it through the origin to $(y, -x, -z)$. Interestingly, some rotoinversion operations are mathematically equivalent to mirror planes. For example, $\bar{2}$ symmetry is functionally identical to a mirror plane perpendicular to the axis of rotation [6]. In international notation, rotoinversion axes are represented as \bar{n} , while in the Schoenflies system, they are denoted as S_n [6, 86]. These operations are essential for classifying symmetries in hexagonal, trigonal, and cubic systems, especially where pure rotational or mirror operations alone are insufficient.

2.1.2 Space Groups and Translational Symmetry

Meanwhile, space groups provide a complete mathematical framework for describing the symmetry of a crystal structure, including both the point group symmetry and the periodicity of the lattice. They incorporate the effects of translational symmetry, extending the concept of symmetry across the entire infinite crystal lattice. Translational symmetry arises from the periodic repetition of a motif throughout space as already define. This basic symmetry of the crystal lattice ensures that an arrangement of atoms at one lattice point is identically reproduced at every other lattice point. Unlike inversion centers or mirror planes, which are associated with fixed spatial elements (a point, line, or plane), translational symmetry operates throughout the entire crystal and is central to defining the nature of crystalline solids [87, 91]. Nature often employs *non-symmorphic* symmetry operations, which combine point group elements with fractional translations, such as screw axes and glide planes substantially enriching the diversity of space groups. These groups arise from combining the 14 Bravais lattices with the 32 crystallographic point groups, incorporating non-symmorphic elements where relevant [87]. While the initial 61 *symmorphic* combinations (excluding screw and glide symmetries) yield a subset of space groups, the inclusion of non-symmorphic operations expands the total to 230, classified across the seven crystal systems and denoted using Hermann-Mauguin notation (e.g., $Fm\bar{3}m$ for a fully symmetric face-centered cubic lattice, with "F" indicating centering and the remaining symbols specifying symmetry elements) [6, 87]. In certain cases, specific symmetry combinations inherently generate others; for instance, a monoclinic C-centered lattice with a twofold axis naturally produces a 2_1 screw axis, reducing the number of truly distinct monoclinic C space groups from eight to five. This automatic implication of symmetries constrains the number of independent space groups, illustrating how the interplay of symmetry and periodicity culminates in the final count of 230 unique three-dimensional space groups [85, 86, 90].

Screw Axes

A screw axis combines a rotation about an axis with a translation parallel to that axis. Specifically, a 2_1 screw axis involves a 180° rotation (two-fold) followed by a translation of $\frac{1}{2}$ of the unit cell along the axis. This operation generates

symmetry-equivalent positions that are displaced both angularly and linearly. If the screw axis lies along the $[001]$ direction, then a point with coordinates (x, y, z) will be transformed to a new equivalent point at $(x, y, z + \frac{1}{2})$ under a 2_1 operation. Higher-order screw axes, such as 4_1 , 4_2 , and 4_3 , produce multiple equivalent positions in sequence. In the case of a 4_1 screw axis, the transformation sequence is as follows:

$$(x, y, z) \rightarrow (-y, x, z + \frac{1}{4}) \rightarrow (-x, -y, z + \frac{1}{2}) \rightarrow (y, -x, z + \frac{3}{4}) \quad (9)$$

These combined rotation-translation operations are fundamental elements of non-symmorphic space groups and significantly expand the range of symmetry operations available in crystallography [6, 86, 88, 91].

Glide Planes

A glide plane combines a mirror reflection in a plane with a translation parallel to that plane. In fact, a glide plane perpendicular to the c -axis—referred to as a c -glide, reflects a point across the plane and then translates it by half a unit cell along the c -direction. Thus, a point located at (x, y, z) would be transformed into $(x, y, -z + \frac{1}{2})$. Glide planes are classified according to the direction of the translation associated with the reflection. The most common types are a -, b -, and c -glides, which involve translations of $\frac{1}{2}$ along the a -, b -, and c -axes respectively. An n -glide involves a translation along the diagonal of a face, such as $\frac{1}{2}(a + b)$, while a d -glide corresponds to translation along the body diagonal of the unit cell and is commonly found in diamond-like structures. These symmetry operations are essential in non-symmorphic space groups and significantly expand the number of distinct symmetry configurations beyond those accounted for by pure point group operations [6, 89].

2.2 Magnetic Symmetry

Magnetic symmetry is a fundamental extension of crystallography, essential for describing magnetically ordered materials. While conventional crystallography relies on the 230 space groups to describe atomic arrangements, it fails to capture magnetic order. Magnetic symmetry addresses this by incorporat-

ing the **time-reversal operator** ($1'$), an **antiunitary** operation that reverses spins, magnetic moments, and time itself, with profound implications in quantum mechanics and condensed matter physics [87, 92]. The concept originated with A. V. Shubnikov, who introduced **antisymmetry** (later formalized as **Shubnikov groups**) by augmenting geometric symmetries with a binary degree of freedom (e.g., black-and-white coloring for magnetic order) [93]. I. Dzyaloshinskii expanded this model, applying group theory to antiferromagnets and ferromagnets and predicting novel magnetoelectric effects [94]. The field reached a breakthrough with Opechowski and Guccione's classification of **1,651 magnetic space groups (MSGs)**, derived from the interplay of spatial symmetry and time reversal [87, 95]. It is a fundamental constraint that governs quantum materials, dictating phenomena like magnetoelectric coupling in multiferroics. These cross-coupling effects require magnetic point groups that violate both time-reversal symmetry ($1'$) and inversion symmetry, unlocking otherwise forbidden interactions between magnetic and electric orders [96]. Similarly, in topological magnets, magnetic symmetry dictates the emergence of protected surface states, non-trivial Berry curvature, and the quantum anomalous Hall effect [97, 98]. Moreover, the fundamental distinction arises from how magnetic moments (axial vectors) transform under symmetry operations compared to atomic positions (polar vectors). This section provides a comprehensive overview of the mathematical foundations, classification schemes, and practical applications of magnetic symmetry in modern condensed matter physics [99]. Magnetic ordering emerges when atomic magnetic moments become correlated below a critical temperature T_c , transitioning from a disordered paramagnetic state (where $\langle m_R \rangle_t = 0$) to an ordered state ($\langle m_R \rangle_t \neq 0$). This ordering is primarily governed by exchange interactions between moments. The most common interaction is described by the isotropic Heisenberg Hamiltonian:

$$H_{\text{iso}} = - \sum_{il,jm} J_{ij}(\mathbf{R}_m - \mathbf{R}_l) \mathbf{m}_i \cdot \mathbf{m}_j = - \sum_{il,jm} J_{ij}(\mathbf{R}_m - \mathbf{R}_l) m_i m_j \cos \theta_{il,jm} \quad (10)$$

where J_{ij} represents the exchange integral between sites i and j , $\theta_{il,jm}$ is the angle between moments \mathbf{m}_i and \mathbf{m}_j , and $\mathbf{R}_m - \mathbf{R}_l$ is the interatomic distance vector [99]. In systems with significant spin-orbit coupling, additional anisotropic terms must be considered, including the Dzyaloshinskii-Moriya interaction [comprehensive de-

tails have been provided in 2.3.3]:

$$H_{\text{DMI}} = \sum_{i,j} \mathbf{D}_{ij} \cdot (\mathbf{m}_i \times \mathbf{m}_j) \quad (11)$$

and single-ion anisotropy:

$$H_{\text{aniso}} = - \sum_i K (\mathbf{m}_i \cdot \mathbf{n})^2 \quad (11)$$

where \mathbf{D}_{ij} is the DM vector and K is the anisotropy constant[99–101]. These interactions collectively determine the preferred orientation and spatial arrangement of magnetic moments in ordered phases. Notedly, the time-reversal operator $1'$ reverses magnetic moments i.e. $(1' \cdot \mathbf{m} = -\mathbf{m})$ while leaving atomic positions unchanged. When combined with conventional crystallographic operations, it generates new symmetry elements called primed operations (e.g., $m' = m \circ 1'$). The transformation properties of magnetic moments under a general symmetry operation (h, δ) are given by:

$$\mathbf{m}'_j = \det(h) \delta h \mathbf{m}_j \quad (12)$$

where h is the rotational part of the operation, $\delta = \pm 1$ for unprimed/primed operators respectively, and $\det(h)$ accounts for the axial vector nature of magnetic moments [95, 99], distinguishes magnetic symmetry from conventional crystallographic symmetry. Magnetic symmetry groups can be classified into three fundamental types. Colorless groups ($M_0 = G$) are identical to the 32 conventional crystallographic point groups, containing no time-reversal symmetry breaking. Grey groups ($P = G + G1'$) represent paramagnetic systems where every symmetry operation is paired with its time-reversed counterpart. Black-white groups ($M = H + (G - H)1'$), the most interesting for ordered magnetic systems, are formed when only an index-2 subgroup H retains unprimed symmetry while the remaining operations are combined with time reversal [92, 99]. For example, the point group $G = 4/m$ generates three distinct black-white magnetic groups: $4/m'$, $4'/m'$, and $4'/m$ [102].

Representation Theory

The representation theory approach provides a powerful method for determining all possible magnetic structures compatible with a given crystallographic space group and propagation vector \mathbf{k} . This formalism is particularly valuable for interpreting neutron diffraction data and predicting magnetic ground states. The magnetic representation Γ_{mag} is constructed as the tensor product of two fundamental representations:

$$\Gamma_{\text{mag}} = \Gamma_{\text{perm}} \otimes \Gamma_{\text{axial}} \quad (13)$$

The permutation representation Γ_{perm} describes how atomic sites transform under symmetry operations, including phase factors for \mathbf{k} -vector modulation:

$$\Gamma_{\text{perm}}(g)_{\alpha\beta} = \delta_{\alpha,g\beta} e^{-2\pi i \mathbf{k} \cdot (\mathbf{R}_g - \mathbf{R}_\beta)} \quad (14)$$

where g is a symmetry operation, \mathbf{R}_g is the transformed position, \mathbf{R}_β is original position of the atom, and $\delta_{\alpha,g\beta}$ ensures proper site permutation [99, 101]. The axial-vector representation

$$\Gamma_{\text{axial}}(g) = \det(h) \delta h \quad (15)$$

The magnetic representation is generally reducible and can be decomposed into irreducible representations (irreps) of the little group of \mathbf{k} :

$$\Gamma_{\text{mag}} = \sum_{\Gamma} n_{\Gamma} \Gamma \quad (16)$$

where n_{Γ} is the multiplicity of each irrep Γ . Basis vectors $\psi_n^{\Gamma}(j)$ for the irreps are obtained through projection operator techniques:

$$\psi_n^{\Gamma}(j) = \frac{d_{\Gamma}}{|G|} \sum_g \Gamma_n^{\Gamma}(g)^* O(g) e_j \quad (17)$$

Here, d_{Γ} is the dimension of irrep Γ , $O(g)$ is the symmetry operator acting on trial moment e_j , and the sum runs over all symmetry operations g in the little group [103]. The actual magnetic structure is described by Fourier coefficients $S_{\mathbf{k}j}$ that are linear combinations of these basis vectors:

$$S_{\mathbf{k}j} = \sum_{\Gamma, n} C_n^{\Gamma} S_n^{\Gamma}(j) \quad (18)$$

where C_n^{Γ} are mixing coefficients that act as order parameters. Structures described by a single irrep are maximally symmetric, while multi-irrep couplings typically lower the symmetry [101, 103]. A classic example is found in the neutron diffraction studies of perovskite manganites (La,Ca)MnO₃ by Wollan and Koehler[104], where the magnetic structure was determined to follow series of ferromagnetic and antiferromagnetic ordering. Today, magnetic symmetry underpins research on **skyrmions, chiral magnets, and correlated electron systems**, serving as both a theoretical blueprint and an experimental tool. It not only explains historical observations but also guides material design and refines experimental interpretations in neutron scattering, synchrotron studies, and magneto-optic measurements.

Landau Theory: Phase Transitions

Phase transitions are fundamental phenomena in condensed matter physics. They represent qualitative changes in the state of a physical system, often accompanied by symmetry breaking, as discussed above. A phase transition may be induced by varying temperature, pressure, magnetic field, or chemical composition. From a symmetry perspective, the high-temperature phase typically has a higher symmetry than the low-temperature ordered phase. Transitions can be classified as: (a) First-order: Discontinuous change, with latent heat, and (b) Second-order (Continuous): No latent heat, but discontinuity in first derivatives of free energy. The Landau theory, introduced by Lev Davidovich Landau [105], provides a powerful schema for analyzing continuous phase transitions based on the concept of an *order parameter* and symmetry considerations. The theory is phenomenological, which does not rely on microscopic interactions. Instead, it assumes the existence of an order parameter η , which is zero in the symmetric phase and non-zero in the symmetry-broken phase. The free energy F is analytic and invariant under the symmetry group of the high-temperature phase. The formalism is valid as long as the transition involves symmetry breaking, thus, near T_c , the free energy is expanded as [105–108]:

$$F(T, \eta) = F_0(T) + \Delta F(\eta^i) \quad (19)$$

where F_0 is order-parameter-independent (and thus irrelevant to the transition), while $\Delta F(\eta^i)$ is small near the critical point. Thus, the free energy contribution ΔF is invariant under all symmetry operations g of the parent group G_0 for arbitrary order parameter configurations. Furthermore, ΔF may exhibit additional invariance under fundamental spacetime symmetries, including parity (P) and time-reversal ($1'$)-provided any externally applied fields are simultaneously transformed according to their respective symmetry properties. Hence, considering that ΔF is small, we can impose the Taylor expansion of $\Delta F(\eta^i)$ in powers of η^i as:

$$\Delta F(\eta) = -\eta H + \frac{a}{2}\eta^2 + \frac{b}{4}\eta^4 + \mathcal{O}(\eta^6) \quad (20)$$

Here, H is a generalized external field conjugate to η . The linear coupling term $-\eta H$ requires η to be translationally invariant and to transform under rotations such that $-\eta H$ remains invariant. When these conditions are satisfied, the system exhibits a ferroic transition, as seen in classic examples like ferromagnetic, ferroelectric, and ferroelastic transitions. In such cases, the order parameter η directly corresponds to the generalized polarization ($P = -\frac{\partial F}{\partial H} = \eta$), representing physical quantities like magnetization, electric polarization, or strain. Also, the quadratic term $\sum_i \kappa_i \eta_i^2$ (where η_i have distinct symmetries, excluding cross terms $\eta_i \eta_j$) is always symmetry-allowed. Stability of the high-symmetry phase at $T > T_c$ requires $\kappa_i > 0$, ensuring positive curvature at $\eta = 0$. Landau transitions occur when one coefficient κ_i changes sign (e.g., as $a_0(T - T_c)\eta^2$), while others remain positive. Simultaneous sign changes for multiple coefficients are non-generic, explaining why transitions are typically driven by a **single symmetry mode**. Below T_c , only one order parameter (or symmetry-equivalent modes) becomes nonzero unless higher-order couplings exist. Thus, *Landau theory predicts that most phase transitions are governed by a single order parameter*. Furthermore, the cubic terms would render the free energy unbounded if truncated, but their presence **mandates first-order transitions**. Hence, for *Landau's continuity condition* a transition can be continuous *only* if all odd-order terms (notably cubic) are symmetry-excluded. To capture the transition behavior, one can write

the quadratic coefficient a as:

$$a = a'(T - T_c) \quad (21)$$

Ensuring that for $T > T_c$, the minimum of F occurs at $\eta = 0$ (disordered phase), and for $T < T_c$, a nonzero η emerges (ordered phase). To find equilibrium states, ΔF is minimize with respect to η :

$$\frac{d\Delta F}{d\eta} = -H + a\eta + b\eta^3 = 0 \quad (22)$$

This implies that, for the zero field Case: $H = 0$

$$a\eta + b\eta^3 = 0 \Rightarrow \eta(a + b\eta^2) = 0 \quad (23)$$

Hence,

$$\eta = 0 \quad \text{or} \quad \eta = \pm \sqrt{-\frac{a}{b}} = \pm \sqrt{\frac{a'}{b}(T_c - T)} \quad \text{for } T < T_c \quad (24)$$

Thus, the order parameter behaves as:

$$\eta(T) = \begin{cases} 0, & T > T_c \\ \pm \sqrt{\frac{a'}{b}(T_c - T)}, & T < T_c \end{cases} \quad (25)$$

This result gives the order parameter as a function of temperature and indicates a second-order phase transition with critical exponent $\beta = \frac{1}{2}$. We can define the generalized susceptibility as the response of the order parameter to the external field:

$$\chi = \frac{\partial \eta}{\partial H} \quad (26)$$

From:

$$\frac{d\Delta F}{d\eta} = -H + a\eta + b\eta^3 = 0 \quad (27)$$

finds,

$$-1 + (a + 3b\eta^2) \frac{d\eta}{dH} = 0 \Rightarrow \frac{d\eta}{dH} = \frac{1}{a + 3b\eta^2} \quad (28)$$

$$\boxed{\chi = (a + 3b\eta^2)^{-1}} \quad (29)$$

In Zero Field:

$$\chi^{-1}(T) = \begin{cases} a'(T - T_c), & T > T_c \\ 2a'(T_c - T), & T < T_c \end{cases} \quad (30)$$

This matches the Curie-Weiss law and implies a divergence at $T = T_c$, with critical exponent $\gamma = 1$. Now within Landau theory of phase transitions, the **zero-field entropy change** (ΔS) associated with the order parameter η is given by:

$$\Delta S = S - S_0 = - \left(\frac{\partial F}{\partial T} \right)_V \quad (31)$$

where S_0 is the background entropy not associated with the phase transition, applying the **chain rule** gives:

$$\Delta S = - \frac{\partial F}{\partial \eta} \cdot \frac{\partial \eta}{\partial T} \quad (32)$$

This relation holds below the critical temperature T_c , where $\eta \neq 0$. Hence, the free energy near the phase transition is expanded as:

$$F = F_0 + \frac{1}{2}a'(T - T_c)\eta^2 + \frac{1}{4}b\eta^4 \quad (33)$$

The derivative of F with respect to η gives the equilibrium condition as:

$$\frac{\partial F}{\partial \eta} = a'(T - T_c)\eta + b\eta^3 \quad (34)$$

Thus, at equilibrium, this derivative must vanish:

$$\frac{\partial F}{\partial \eta} = 0 \Rightarrow a'(T - T_c)\eta + b\eta^3 = 0 \quad (35)$$

Solving for η (for $T < T_c$) yields:

$$\eta = \left[\frac{a'(T_c - T)}{b} \right]^{1/2} \quad (36)$$

Compute $\frac{\partial \eta}{\partial T}$:

$$\frac{d\eta}{dT} = \frac{1}{2} \left[\frac{a'}{b} \right]^{1/2} (T_c - T)^{-1/2} (-1) \quad (37)$$

$$= -\frac{1}{2} \left[\frac{a'}{b} \right]^{1/2} (T_c - T)^{-1/2} \quad (38)$$

Plugging into the entropy change equation:

$$\Delta S = - \left(\frac{\partial F}{\partial \eta} \right) \left(\frac{d\eta}{dT} \right) \quad (39)$$

Since $\frac{\partial F}{\partial \eta} = 0$ at equilibrium, we use the total derivative of F with respect to T via the chain rule. Computing this yields:

$$\Delta S = - \frac{a'^2}{2b} (T_c - T) \quad (40)$$

To compute the specific heat change:

$$\Delta c_V = -T \frac{d^2 F}{dT^2} \quad (41)$$

Calculating second derivatives of F using $\eta(T)$ gives:

$$\Delta c_V|_{T < T_c} = \frac{a'^2}{2b} T \quad (42)$$

At $T = T_c$, this leads to a discontinuity:

$$\boxed{\Delta c_V(T_c) = \frac{a'^2}{2b} T_c} \quad (43)$$

If symmetry permits a cubic term:

$$\Delta F = \frac{a}{2} \eta^2 + \frac{c}{3} \eta^3 + \frac{b}{4} \eta^4 \quad (44)$$

Then the transition becomes first-order. A necessary condition for second-order transitions is that all odd-order terms must vanish by symmetry ($\eta \rightarrow -\eta$ invariance). Many structural phase transitions are displacive and involve the softening of a particular phonon mode:

$$\omega^2(T) \propto \chi^{-1}(T) \propto (T - T_0) \quad (45)$$

This is known as the Cochran relation [109], relating phonon softening to Landau susceptibility.

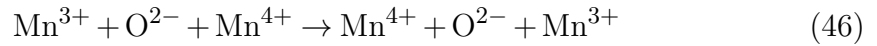
2.3 Magnetism in Perovskite

Magnetic materials can be examined through two principal theoretical frameworks: *the theory of the free electron band* and the *ionic model*. In certain perovskites, where metallic behavior dominates, free electron theory offers a suitable description. These materials show properties similar to elemental magnets, where interactions between electron spins, especially pronounced at lower temperatures, can produce ferromagnetic alignment. As temperature increases, these systems transition to *Pauli paramagnetic states*, where magnetic susceptibility becomes highly temperature independent [4, 28, 84]. However, many perovskites exhibit magnetic properties due to the presence of *paramagnetic cations* incorporated within their lattice. These cations, typically transition metals or lanthanides with partially filled *d* and *f* orbitals [comprehensive discussion has been provided in 1.3], carry intrinsic magnetic moments. The geometry of *local coordination* critically influences their magnetic behavior by modulating the energy splitting of these orbitals through *crystal-field or ligand-field interactions*. For 3d transition metal cations, the magnetic moment predominantly arises from the electron spin component, quantified by the *Russell-Saunders quantum number* (*S*), with possible configurations including high-spin (HS), intermediate-spin (IS), and low-spin (LS) states depending on the crystal field strength [53]. At elevated temperatures, random orientation of these magnetic moments results in paramagnetism, following the Curie or Curie-Weiss laws. As temperature decreases, exchange interactions can establish long-range magnetic ordering, producing either ferromagnetic/ferromagnetic or antiferromagnetic alignments, along with more complex configurations [110]. Superexchange is the dominant mechanism behind antiferromagnetic ordering in insulating perovskites. It mediates magnetic coupling between two cations via an intervening oxygen anion through virtual processes-without direct electron transfer. The interaction strength depends on the spatial overlap of cation and anion orbitals. Two key superexchange geometries govern magnetic behavior: 180° and 90° linkages. The GKA rules predict the resulting magnetic order based on cation *d*-orbital occupancy and crystal-field effects [28, 53]. In 180° superexchange (linear cation-anion-cation bonds), antiferromagnetic alignment dominates, while 90° coupling (near-right-angle bonds) favors weaker ferromagnetic interactions [28]. Also, superexchange is highly adaptable, sustaining magnetic order across diverse coordination envi-

ronments (octahedral, tetrahedral, square pyramidal) and even in distorted perovskites like *brownmillerites* [1]. Unlike direct exchange, which demands strict orbital overlap, superexchange is more robust against structural deviations. The balance between competing spin states is highly sensitive to composition and temperature. For example, in $\text{La}_{1-x}\text{Sr}_x\text{MnO}_3$, substituting La^{3+} with Sr^{2+} triggers a hole-doped transition from antiferromagnetic insulator to ferromagnetic metal [111, 112][see 2.3.1]. This underscores how electronic structure, lattice geometry, and external perturbations collectively dictate magnetic properties.

2.3.1 Zener Double-Exchange Mechanism

The magnetic and electronic properties of perovskite manganites, particularly $\text{La}_{1-x}\text{Sr}_x\text{MnO}_3$, exhibit a fascinating coexistence of ferromagnetism and metallic conductivity (itinerant electron behaviour). This behavior, puzzling within conventional magnetic and band theories, finds its most compelling theoretical explanation in the Zener double-exchange (DE) mechanism [113, 114]. The mechanism arises in mixed-valence systems containing both Mn^{3+} and Mn^{4+} ions, where hopping of conduction electrons is intimately linked with the alignment of localized magnetic moments. In these systems, the mixed-valence states of manganese ions, Mn^{3+} ($3d^4$, $t_{2g}^3 e_g^1$, $S = 2$) and Mn^{4+} ($3d^3$, t_{2g}^3 , $S = 3/2$) facilitate a unique hopping process mediated via an intervening oxygen ion. An electron hops from the e_g orbital of Mn^{3+} to the 2p orbital of the oxygen, and from there to the e_g orbital of a neighboring Mn^{4+} ion [115]. This simultaneous two-step transfer defines the double-exchange mechanism and can be summarized by:



Here, electron hopping is spin-dependent, with the intra-atomic Hund's coupling J_{ex} which aligns the spin of the itinerant e_g electron parallel to the localized t_{2g} core spin. When adjacent Mn ions possess parallel core spins, the kinetic energy gain due to electron delocalization is maximized, facilitating hopping of the e_g electron across the lattice, Figure II.1. However, if the core spins are antiparallel, Hund's rule imposes a significant energy penalty, effectively suppressing electron transfer. The mathematical manifestation of this dependence on spin orientation is captured in the angular modulation of the hopping amplitude: if the local

spin quantization axes of neighboring ions are misaligned by an angle θ , the overlap of spin eigenvectors leads to a transfer integral that scales as $\cos(\theta/2)$. Consequently, the effective hopping vanishes at $\theta = \pi$, reinforcing the notion that DE intrinsically favors ferromagnetic alignment of localized spins to preserve itinerant conductivity [4, 111, 116]. Herein, the energy integral for exchange is significant only when the spins of neighboring Mn ions are aligned, with the effective DE exchange energy proportional to:

$$E_{DE} \propto -t_{ij} \cos \frac{\theta_{ij}}{2} \quad (47)$$

where θ_{ij} is the angle between the localized t_{2g} spins on adjacent Mn sites, and t_{ij} is the transfer integral. Since the intra-atomic exchange J_{ex} is typically much larger than t_{ij} , the exchange energy between Mn sites can be approximated by:

$$U_{ex} = \frac{h\nu}{2} \quad (48)$$

where ν is the frequency of electron oscillation between Mn sites, and h is Planck's constant [113]. This exchange energy relates to the diffusion coefficient D for Mn^{4+} by:

$$D = \frac{\alpha^2 U_{ex}}{h} \quad (49)$$

where α is the lattice parameter. Incorporating the Einstein relation for electrical conductivity σ and the diffusion coefficient D [85]:

$$\sigma = \frac{ne^2 D}{kT} \quad (50)$$

where n is the number of Mn^{4+} ions per unit volume, e is the elementary charge, k is Boltzmann's constant, and T is the temperature. Substituting D into the Einstein relation gives:

$$\sigma = \frac{ne^2 \alpha^2 U_{ex}}{hkT} \quad (51)$$

Expressing n in terms of the fraction of Mn^{4+} ions x per unit volume as $n = \frac{x}{\alpha^3}$, the expression simplifies to:

$$\sigma = \frac{xe^2 U_{ex}}{\alpha h k T} \quad (52)$$

Assuming the ferromagnetic transition temperature T_C is directly proportional to U_{ex} [113, 117]:

$$U_{ex} \approx kT_C \quad (53)$$

Substituting into the conductivity expression leads to:

$$\sigma \approx \left(\frac{x e^2}{\alpha \hbar} \right) \left(\frac{T_C}{T} \right) \quad (54)$$

This equation reveals a direct relationship between electrical conductivity σ , ferromagnetic transition temperature T_C , and the fraction of Mn^{4+} ions x . It implies that the insulator-metal transition T_{IM} in manganites should occur around T_C , where electron mobility through double exchange becomes significant [111, 114]. The DE mechanism is highly sensitive to structural distortions, where the $\text{Mn} - \text{O} - \text{Mn}$ bond angle crucially affects the transfer integral t_{ij} , with maximal values achieved near 180° and reduced values for distorted geometries [114, 116]. Lattice distortions, tilts, and Jahn-Teller effects localize the e_g electrons, suppressing DE conductivity. Competing magnetic interactions must also be considered as noted by [116], superexchange interactions [2.3.2] between t_{2g} electrons can induce antiferromagnetic alignment, especially in systems where structural distortions weaken DE. The balance between DE ferromagnetism and superexchange antiferromagnetism is influenced by both lattice parameters and electron-lattice coupling [41, 111].



Figure II.1: The double-exchange interaction: An electron preserves its spin orientation as it hops between adjacent localized ion cores, mediating ferromagnetic alignment. adapte from [4]

2.3.2 Superexchange Interaction

The superexchange interaction (SE) constitutes a profound quantum mechanical phenomenon, whereby antiferromagnetic coupling emerges between localized spins residing on distinct cations, particularly in transition-metal oxides, where $3d - 3d$ are otherwise too spatially separated to permit direct exchange. This indirect interaction is mediated via a diamagnetic anion, most often oxygen, and is rooted in the quantum mechanical principle that electron pairs with

parallel spins occupying degenerate orbitals possess lower energy due to the intra-atomic exchange interaction of mixed wavefunctions of the form $\phi_{3d} = \alpha\psi_{3d} + \beta\psi_{2p}$, with $|\alpha|^2 + |\beta|^2 = 1$, quantified by the exchange energy J . Mathematically, the superexchange is modeled by the Heisenberg Hamiltonian:

$$\mathcal{H}_{SE} = -J_{ij} \mathbf{S}_i \cdot \mathbf{S}_j \quad (55)$$

where \mathbf{S}_i and \mathbf{S}_j denote the spin operators on neighboring cations, and J_{ij} is the superexchange integral, often negative for AFM coupling. Figure II.2 illustrates a representative superexchange pathway. For systems with singly occupied 3d orbitals or half-filled d shells, such as in Fe^{3+} or Mn^{2+} , the electronic configuration labeled as (b) is energetically more favorable than configuration (a). This preference arises because both electrons from the intervening oxygen 2p orbital can delocalize into the adjacent, unoccupied 3d orbitals, thereby lowering the total energy through enhanced orbital overlap and reduced electron repulsion.

Unlike *direct exchange*, which requires significant orbital overlap and therefore decays exponentially with the interatomic distance r as $J \propto e^{-\alpha r}$, superexchange operates mainly in insulating materials across larger cationic separations. The mechanism involves a second-order virtual hopping process, whereby two electrons are transferred simultaneously, leading to a transient $3d^{n+1}2p^5$ excited state. The resulting exchange interaction J is approximately of the order

$$J \approx -\frac{2t^2}{U}, \quad (56)$$

where t denotes the p–d hybridization integral. The magnitude and sign of the superexchange interaction J are highly sensitive to structural parameters, particularly the metal-oxygen-metal (M–O–M) bond angle, with the interaction strength varying as $\cos^2\theta$. Orbital occupancy and degeneracy of the 3d states are key factors influencing the nature of the superexchange, as elucidated in the paradigmatic model of Goodenough-Kanamori [53, 116]. Anderson later reformulated these principles in a simplified framework that omits explicit consideration of the oxygen orbitals [4, 110] as follows:

- (i) **Antiferromagnetic superexchange** ($J < 0$): Occurs when lobes of singly occupied 3d orbitals on adjacent cations point toward each other, resulting in significant orbital overlap and large hopping integrals. This configuration is typical for nearly linear **M – O – M** bond angles ($120 - 180^\circ$).

- (ii) **Weak ferromagnetic exchange:** Arises when symmetry constraints eliminate the overlap integral between singly occupied orbitals, as in $\sim 90^\circ$ $\text{M} - \text{O} - \text{M}$ bond geometries. Here, the exchange remains ferromagnetic but weak.
- (iii) **Also weak ferromagnetic exchange:** Occurs when there is orbital overlap between a singly occupied 3d orbital and either an empty or a doubly occupied 3d orbital of similar symmetry.

While ferromagnetic superexchange can occur under specific conditions, antiferromagnetic coupling is generally more prevalent due to the typically large overlap integrals between appropriately oriented orbitals. Also, delocalized and correlation superexchange are subtypes of this interaction, distinguished by the nature of electron transfer pathways: the former allows for cation-to-cation exchange via orbital delocalization, while the latter confines electron hopping strictly within the cation-anion-cation triad. The strength of the interaction correlates significantly with the bond character; σ -bond mediated paths dominate over π -bonded paths in strength, a principle observable in the variation of Néel temperatures T_N across 3d transition metal monoxides: $T_N(\text{MnO}) < T_N(\text{FeO}) < T_N(\text{CoO})$, directly reflecting the increasing overlap of σ -type bonds in the series [1]. Importantly, the efficacy of superexchange is not dependent on carrier mobility; it does not induce metallic conduction as does the DE mechanism. This was analytically contrasted in the seminal extension of Zener’s model by P.G. de Gennes (1960), who incorporated spin-lattice interactions and polaronic effects into the Hamiltonian to elucidate the distinct behaviors of DE and SE interactions in manganites of mixed valence [118]. Furthermore, the strength of superexchange increases with cationic valence, as higher valency enhances the overlap of virtual hopping states, thus, for identically configured cations, Fe^{3+} exhibits stronger coupling than Mn^{2+} due to its deeper lying unoccupied d orbitals [113]. Thus, superexchange is a foundational theory for magnetic ordering in insulating transition-metal oxides, guiding our understanding of spin-lattice coupling-central to this thesis

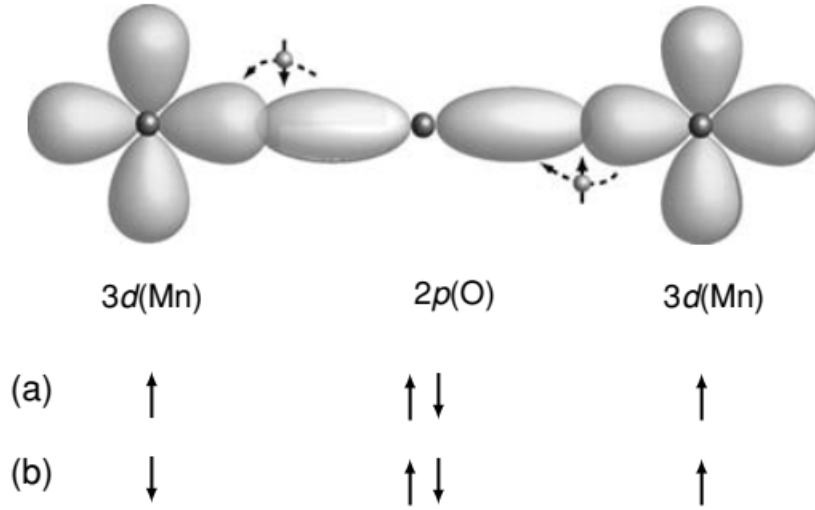


Figure II.2: A representative superexchange interaction: Configuration (b) is energetically favored over configuration (a). Adapted from [4]

2.3.3 Antisymmetric Exchange Interaction

In certain magnetic systems, particularly those lacking inversion symmetry at the midpoint between interacting magnetic ions, an antisymmetric exchange interaction, known as the Dzyaloshinskii-Moriya interaction (DMI), emerges as a relativistic correction to superexchange [119, 120]. This interaction contributes to canting of spins and underpins a variety of complex magnetic phenomena such as weak ferromagnetism, spin spirals, and magnetic skyrmions. The antisymmetric Hamiltonian describes the Dzyaloshinskii-Moriya interaction as seen in 2.2:

$$\mathcal{H}_{\text{DMI}} = - \sum_{\langle ij \rangle} \mathbf{D}_{ij} \cdot (\mathbf{S}_i \times \mathbf{S}_j), \quad (57)$$

where \mathbf{S}_i and \mathbf{S}_j are define in 2.3.2, and \mathbf{D}_{ij} is the Dzyaloshinskii-Moriya vector determined by the local symmetry of the crystal. The magnitude and direction of \mathbf{D}_{ij} are constrained by Moriya's symmetry rules [120], derived via group theoretical analysis of spin-orbit perturbed Hubbard-type Hamiltonians. Dzyaloshinskii first proposed, using Landau's theory of second-order phase transitions, that weak ferromagnetism in antiferromagnetic compounds like $\alpha\text{-Fe}_2\text{O}_3$, MnCO_3 , and CoCO_3 can be explained by relativistic corrections that preserve the crystal's magnetic symmetry [119]. Whence, a spontaneous magnetization \mathbf{m} arises only if it is invariant under all symmetry operations of the magnetic

point group. For $\alpha\text{-Fe}_2\text{O}_3$ in the high-temperature antiferromagnetic phase, such canting is symmetry-allowed and yields a net moment perpendicular to the basal spin plane. Mathematically, the free energy \mathcal{F} can be expanded in powers of the antiferromagnetic order parameter \mathbf{L} and net moment \mathbf{m} :

$$\mathcal{F} = \mathcal{F}_0 + A\mathbf{L}^2 + B\mathbf{m}^2 + C(\mathbf{L} \cdot \mathbf{m}) + \dots \quad (58)$$

The cross-term $C(\mathbf{L} \cdot \mathbf{m})$ vanishes by symmetry in centrosymmetric crystals but is allowed in non-centrosymmetric or magnetically non-equivalent environments. In $\alpha\text{-Fe}_2\text{O}_3$, this term results in a small but nonzero equilibrium value of \mathbf{m} perpendicular to \mathbf{L} , with $|\mathbf{m}/\mathbf{L}| \sim 10^{-2}$. Moriya's derivation introduces spin-orbit coupling into the second-order perturbation of the Hubbard Hamiltonian:

$$\mathcal{H} = \mathcal{H}_{\text{SE}} + \mathcal{H}_{\text{SOC}}, \quad \mathcal{H}_{\text{SOC}} = \lambda \mathbf{L} \cdot \mathbf{S}. \quad (59)$$

This leads to an effective antisymmetric term in the spin Hamiltonian when inversion symmetry is broken:

$$\mathbf{D}_{ij} \propto \frac{\lambda t_{ij}^2}{U^2} (\mathbf{r}_i - \mathbf{r}_j), \quad (60)$$

where t_{ij} is define previously define 2.3.1, U is the on-site Coulomb repulsion, and λ is the spin-orbit coupling constant. The vector $(\mathbf{r}_i - \mathbf{r}_j)$ encodes the lack of inversion symmetry. In real materials such as $\alpha\text{-Fe}_2\text{O}_3$, the DMI leads to canting of the Fe^{3+} moments away from the perfectly antiparallel configuration, producing a small net moment. The magnitude of this canting is approximately 1° , corresponding to a weak ferromagnetic moment of order 10^{-4} times the saturated moment [119]. Such effects are observed only when the antiferromagnetic order lies in a plane perpendicular to the crystallographic axis along which \mathbf{D} is aligned. DMI extends beyond weak ferromagnetism being essential in the stabilization of non-collinear magnetic structures and topological textures.

2.3.4 Spin Glass

"At the heart of spin-glass physics lies a profound question: As the system cools toward the freezing temperature T_f , does it merely slow into dynamical arrest, or does it cross a thermodynamic threshold, a Curie point for disorder? The spin-glass state, long shrouded in debate, now reveals its secret. Beyond kinetic freezing, beyond mere frustration, there emerges a critical transformation: ergodicity shatters, and the free energy landscape fractures into a labyrinth of metastable states. Here, in the absence of symmetry, a new order is born—not of atoms aligned, but of entangled spins, whispering their collective logic through the noise of disorder."[5, 121] [**emphasis mine**].

The answer, emerging from decades of theoretical and experimental work, is affirmative: Spin glasses undergo a thermodynamic phase transition at the freezing temperature T_f , marking the emergence of a new phase characterized by broken ergodicity and a novel order parameter [122, 123]. Unlike structural glasses, spin glasses provide well-defined statistical mechanical frameworks for studying spontaneous symmetry breaking in disordered systems [124]. The transition involves freezing into a disordered magnetic state with a rugged free-energy landscape containing numerous metastable states separated by substantial energy barriers. Theoretical models, particularly the Edwards-Anderson (EA) and Sherrington-Kirkpatrick (SK) models, describe this as a continuous phase transition and allow for rigorous mathematical treatment through replica symmetry breaking (RSB) solutions [122, 125]. Experimental evidence first emerged from AC susceptibility measurements in diluted magnetic alloys (e.g., CuMn, AuFe), showing sharp cusps at T_f that suggested a genuine phase transition [121]. While early DC measurements indicated gradual spin freezing similar to supercooled liquids [126], later theoretical work confirmed the existence of a true critical temperature T_f and time-reversal symmetry breaking [123]. The mid-1970s saw significant theoretical advances, including the introduction of the SK model Hamiltonian, which launched extensive research into understanding spin glass transitions [122, 125]. To capture the essential physics, they considered a model neglecting short-range spatial order and instead posited random interactions among nearest neighbors. The Hamiltonian is written as

$$\mathcal{H} = - \sum_{\langle i,j \rangle} J_{ij} \mathbf{S}_i \cdot \mathbf{S}_j - g\mu_B \sum_i \mathbf{H} \cdot \mathbf{S}_i, \quad (61)$$

where \mathbf{S}_i denotes an m -component spin (e.g., $m = 1$ for the Ising model, $m = 3$ for the Heisenberg model), g is the Landé factor, μ_B is the Bohr magneton, and \mathbf{H} is the external magnetic field. The interactions J_{ij} are quenched random variables drawn from a Gaussian probability distribution,

$$P(J_{ij}) = \frac{1}{\sqrt{2\pi J^2}} \exp\left(-\frac{J_{ij}^2}{2J^2}\right), \quad (62)$$

with $\langle J_{ij} \rangle = 0$ and $\langle J_{ij}^2 \rangle = J^2$, representing disorder with zero mean and variance J^2 . To analyze the system, one seeks to compute the free energy,

$$F = \langle F\{J_{ij}\} \rangle = -k_B T \langle \ln Z\{J_{ij}\} \rangle, \quad (63)$$

where $Z\{J_{ij}\}$ is the partition function for a given configuration of disorder, and the angular brackets $\langle \cdot \rangle$ denote disorder averaging over $P(J_{ij})$. Direct evaluation of $\langle \ln Z \rangle$ is challenging due to the nonlinearity of the logarithm. To circumvent this, Edwards and Anderson employed the *replica trick* [122], which relies on the identity

$$\langle \ln Z \rangle = \lim_{n \rightarrow 0} \frac{\langle Z^n \rangle - 1}{n}. \quad (64)$$

Here, one computes $\langle Z^n \rangle$ for integer n , treats n as a continuous variable, and analytically continues the result to $n \rightarrow 0$. For spins with m components, this leads to an effective system of n replicated spin configurations, with the replicated partition function:

$$\langle Z^n \rangle = \left\langle \text{Tr}_{\{S_i^\alpha\}} \exp\left(\frac{\beta}{2} \sum_{\langle i,j \rangle} J_{ij} \sum_{\alpha=1}^n \mathbf{S}_i^\alpha \cdot \mathbf{S}_j^\alpha\right) \right\rangle, \quad (65)$$

where $\alpha = 1, \dots, n$ indexes the replicas and the average is over the Gaussian disorder. After averaging the disorder, the effective theory becomes non-trivially coupled across replicas, leading to a complex mean-field analysis [122, 125, 127]. Several essential results emerge from this formulation: (i) Absence of Magnetic Long-Range Order: Within the replica-symmetric mean-field model, no ferromagnetic or antiferromagnetic long-range order is found in the spin-glass phase, consistent with experimental observations [122]. (ii) Magnetic Susceptibility and

the Edwards-Anderson Order Parameter q in the zero field is given by [128, 129]

$$\chi(T, H = 0) = \frac{NS(S+1)}{3k_B T} \left(\frac{g\mu_B}{2} \right)^2 (1 - q), \quad (66)$$

Here we have used the exact relations for spin correlations [122, 125]:

$$\chi(T, H = 0) = \frac{(g\mu_B)^2}{3k_B T} \sum_{i,j} (\langle S_i S_j \rangle - \langle S_i \rangle \langle S_j \rangle), \quad (67)$$

where the spin-glass order parameter $q = \langle \langle S_i \rangle^2 \rangle$ captures the degree of spin freezing. In the spin-glass state, $\langle S_i \rangle = 0$ but $q > 0$, reflecting the random, frozen nature of local moments. The temperature dependence of the susceptibility χ exhibits a cusp at the freezing temperature T_f , above which Curie-like behavior is recovered. The temperature derivative of susceptibility satisfies

$$\left. \frac{\partial \chi}{\partial T} \right|_{T=T_f} = 0 \quad (68)$$

in both the Ising ($m = 1$) and classical Heisenberg ($m = 3$, $S \rightarrow \infty$) cases. However, quantum Heisenberg models ($S = 1/2$) and Bethe lattice approximations yield finite slopes at T_f , in better agreement with experiments [127]. An applied magnetic field H typically rounds the susceptibility cusp, as predicted by replica-symmetric mean-field theory (MFA) [125], though the required field strength is often an order of magnitude larger than observed experimentally, highlighting theoretical limitations. Similarly, MFA predicts a sharp cusp in specific heat at T_f [122, 125, 127], which is generally more pronounced than experimental measurements suggest. The microstructure of spin-glass systems is well described by random-site models (Figure II.3), where magnetic impurities are randomly distributed in a non-magnetic metallic host, as seen in canonical spin glasses like AuFe and CuMn alloys. At low temperatures, the spins freeze cooperatively into a disordered yet correlated state, typically belonging to the Heisenberg universality class due to isotropic spin orientations. Higher impurity concentrations lead to locally aligned spin clusters, resulting in "cluster glass" behavior, whereas low concentrations favor collective freezing via long-range interactions, characteristic of the canonical spin-glass transition. Ising-like spin glasses, by contrast, exhibit discrete symmetry breaking with spins freezing into binary up-down configurations.

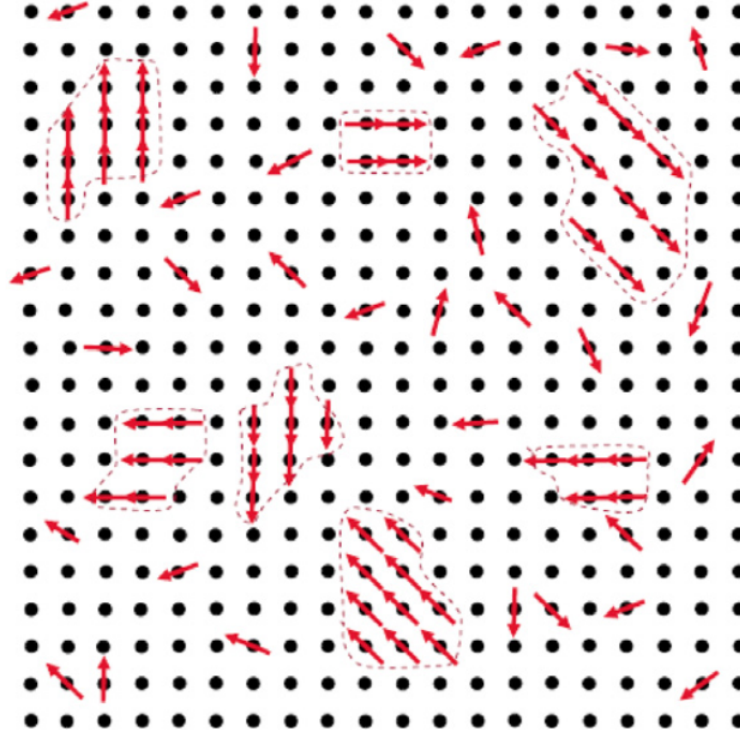


Figure II.3: Two-dimensional random-site model illustrating the emergence of a ferromagnetic "cluster glass" component. In contrast, the SG phase transition corresponds to the cooperative freezing of individual spins without cluster formation. Representative systems include $\text{Cu}_{1-x}\text{Mn}_x$ and $\text{Eu}_x\text{Sr}_{1-x}\text{S}$ with $x < 0.1$ [5].

Unlike conventional magnets, where the free energy landscape is dominated by deep minima corresponding to global order (e.g., net magnetization M in ferromagnets or staggered magnetization M_s in antiferromagnets), spin glasses exhibit a rugged, multivalley energy landscape due to frustration and competing interactions. Below T_f , the system becomes trapped in metastable states, with thermal fluctuations, aging, and external fields inducing slow, history-dependent transitions between valleys. This nonergodic behavior is central to the spin-glass phase. The transition itself arises from three key ingredients: (i) randomness: spatial disorder in interactions or magnetic moments, (ii) frustration: incompatibility among local interactions preventing global energy minimization, and (iii) competing interactions: coexistence of ferromagnetic and antiferromagnetic couplings. Systems fulfilling these criteria and exhibiting theoretical scaling behavior are considered "ideal" spin glasses, though such materials are rare and crucial for testing theoretical models [5]. Canonical spin glasses further display four experimental signatures: a sharp AC susceptibility cusp, irreversibility between field-cooled and zero-field-cooled magnetization, aging effects, and scaling behavior near $T_f(\omega)$. However, many real materials deviate from these criteria,

complicating the distinction between true spin glasses, long-range ordered magnets, and superparamagnetic blocking [5]. Figure II.4 introduces the concept of frustration within the context of a square plaquette of Ising spins. Although a simple square lattice without bond disorder is unfrustrated, random assignment of bond signs (ferromagnetic or antiferromagnetic) leads to local conflict, preventing global energy minimization. Geometric frustration naturally arises in more complex lattices, such as the kagome or triangular lattices, where the lattice geometry itself enforces unavoidable conflict among spin interactions. The underlying mechanism for the competing interactions is the celebrated Ruderman-Kittel-Kasuya-Yosida (RKKY) [130–132] interaction, depicted schematically in Figure II.5. The RKKY exchange coupling $J(r)$ between localized magnetic moments mediated by conduction electrons oscillates between ferromagnetic and antiferromagnetic character as a function of interatomic distance r , given by:

$$J(r) \propto \frac{\cos(2k_F r)}{r^3}, \quad (69)$$

where k_F is the Fermi wavevector. This oscillatory behavior naturally seeds randomness and frustration across a metallic host, thus generating the essential ingredients for spin glass behavior [5]. It is noteworthy that deviations from the ideal conditions can profoundly alter the ground state. Systems exhibiting purely antiferromagnetic interactions but possessing significant randomness and frustration may still exhibit a spin glass phase; however, modeling becomes more challenging. Conversely, if randomness is absent, frustration and competing interactions alone may yield a complex yet long-range ordered magnetic phase. A particularly interesting case arises in geometrically frustrated lattices such as the pyrochlore oxides. Here, strong antiferromagnetic interactions and intrinsic lattice frustration typically stabilize exotic disordered ground states, such as spin liquids. However, even a minute degree of disorder, such as slight variations in exchange interactions, can tip the balance, inducing a spin glass state. This mechanism has been elaborated by Andreanov *et al.* [133], who demonstrated that tiny amounts of defect-induced randomness are sufficient to stabilize a spin glass phase in otherwise clean, frustrated materials.

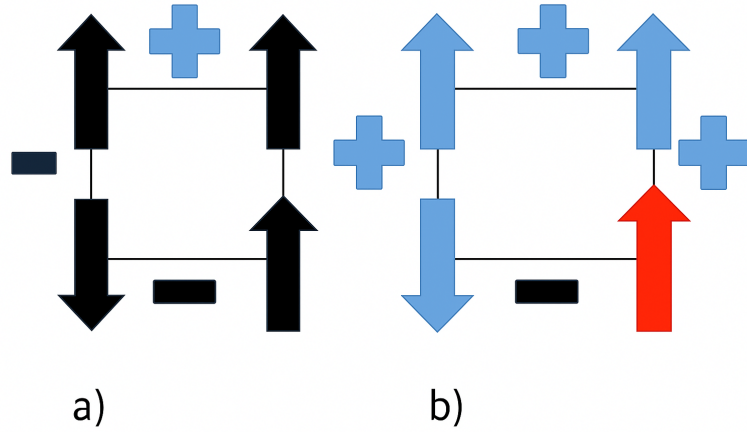


Figure II.4: Square plaquettes with mixed Ising interactions: positive (ferromagnetic, F) and negative (antiferromagnetic, AF). (a) An unfrustrated plaquette, characterized by a four-bond product $\Phi = +1$; (b) a frustrated plaquette, where the four-bond product is $\Phi = -1$ [5].

Critical Dynamics of the Freezing Transition

The onset of freezing is intricately linked to dynamic critical phenomena, where the out-of-phase susceptibility χ'' coincides with the inflection point of the rise in the real part of the susceptibility χ' . This peak defines a freezing temperature $T_f(\omega)$, which depends on the measurement frequency $\omega/2\pi$. Higher frequencies correspond to higher observed freezing temperatures, analogous to how a faster camera shutter captures quicker events in motion. The glass transition temperature T_g is considered the zero-frequency limit of $T_f(\omega)$. Investigating the frequency dependence of $T_f(\omega)$ is critical to discern whether the freezing process represents a simple dynamical slowing (as in independent superparamagnetic particles) or a genuine collective thermodynamic phase transition [134]. If freezing is a collective phenomenon, a divergence of the correlation length ξ near T_g is expected, characterized by:

$$\xi = \xi_0 \left(\frac{T_f(\omega) - T_g}{T_g} \right)^{-\nu} \quad (70)$$

where ν is the critical exponent associated with the correlation length. According to the dynamic scaling hypothesis, the response time τ scales with ξ as:

$$\tau \propto \xi^z \quad (71)$$

where z is the dynamic critical exponent. This yields the scaling form:

$$\tau = \tau_0 \left(\frac{T_f(\omega) - T_g}{T_g} \right)^{-z\nu} \quad (72)$$

as described by Binder and Young [135]. Empirical studies observe that response times diverge as $\omega \rightarrow 0$, confirming the critical nature of the freezing process at T_g [136–138]. This behavior contrasts with non-interacting superparamagnetic nanoparticles, where freezing follows a simple Arrhenius law:

$$\tau = \tau_0 \exp\left(\frac{U}{k_B T}\right) \quad (73)$$

where U is the anisotropy barrier. In dense systems with significant interactions, a superspin glass forms [139, 140].

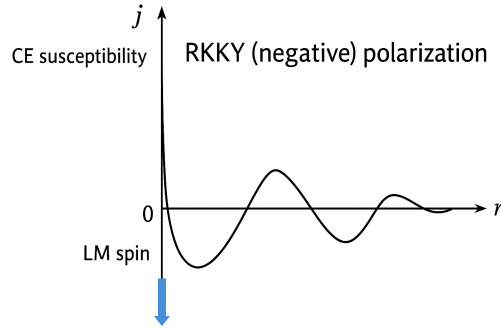


Figure II.5: Spatial oscillations of conduction electron polarization induced by a local magnetic moment placed at the origin. The coupling between the local moment (LM) and conduction electrons (CE) is negative and decays with distance following an approximate $\cos(2k_F r)/(2k_F r)^3$ dependence. The vertical axis, labeled 'j', may alternatively represent Friedel charge oscillations arising when an impurity with different valence is introduced into a metallic host. [5]

* CHAPTER III *

Experimental

This chapter describes the synthesis and characterization techniques employed in this study. Given that most methods are well-established, only essential details are provided. The samples were primarily synthesized using the sol-gel method, selected for its excellent stoichiometric control and chemical homogeneity, particularly advantageous for complex compositions and precise doping. Initial phase purity verification was performed using laboratory powder X-ray diffraction (XRD); representative patterns and refinement of Nd_2NiMO_6 are shown in Appendix A Figures I.1 and I.2, respectively. For comprehensive structural analysis, Rietveld refinement of both XRD and powder neutron diffraction (NPD) data was conducted using the FULLPROF suite. High-resolution synchrotron XRD measurements were additionally employed to resolve subtle structural distortions in select systems. Local structural and electronic properties were investigated through X-ray absorption spectroscopy, including XANES and EXAFS measurements. Raman spectroscopy complemented these studies by probing lattice vibrations and local disorder. The magnetic properties were characterized via dc and ac magnetization measurements, with selected samples further examined by neutron diffraction to determine magnetic structures. Additional insights into thermodynamic behavior were obtained from specific heat capacity measurements.

3.1 Synthesis

As emphasized in a recent report on future directions in solid-state chemistry, "synthesis is the essence of material science because it provides the objects of any further studies" [14]. Without synthesis, there are no materials to investigate experimentally, and the development of novel compounds with enhanced or entirely new properties potentially applicable in unforeseen domains becomes impossible [24]. Material synthesis can follow either exploratory (serendipitous) or directed strategies. However, producing a pure solid alone is often insufficient, many ap-

plications require precise control over morphology, particle size, and crystallinity, whether as amorphous solids, microcrystalline powders, or single crystals. The term *preparation* is more appropriate when these criteria (composition, purity, phase, morphology, and particle size) are met, whereas *synthesis* broadly refers to the production of pure compounds. Advances in preparation methods have optimized energy and time efficiency, with growing emphasis on greener and more sustainable approaches. Scalability also influences synthesis design, as challenges like toxic by-products or expensive reagents may be manageable at laboratory scale but prohibitive for industrial production. Metal oxide preparation is typically classified by the physical state of reactants: solid, liquid (melts or solutions), or gas/vapor. Specialized techniques exist for single crystals, thin films, and nanoparticles, spanning high-temperature, energy-intensive processes to milder low-temperature alternatives [24]. Among these materials, perovskite oxides have attracted significant attention due to their technological relevance. Innovations in their physical forms, such as thin films, porous structures, or nanoscale powders, have enabled tailored functionalities [14, 66]. Engineering specific structural features, like one-dimensional chains, has further enhanced direction-dependent properties, driving efforts to design novel compositions [66]. The ceramic (solid-state reaction) method, widely used since the 1940s, remains a cornerstone for perovskite synthesis. It involves grinding stoichiometric mixtures of oxides or carbonates, followed by repeated heat treatments ($>1000^{\circ}\text{C}$ for 24-72 h) to achieve phase purity [35, 37]. While accessible and effective under ambient conditions, this method has drawbacks: repeated grinding increases energy and time costs, and high temperatures can volatilize elements like Pb^{2+} (e.g., in PbTiO_3), altering stoichiometry [35]. An alternative, the solid-state metathesis (SSM) method, is particularly effective for non-oxide perovskites. SSM relies on highly exothermic ionic exchange reactions, often yielding thermodynamically stable phases at high adiabatic temperatures [141, 142]. Typical precursors include alkaline, chalcogenide, or boride compounds mixed with metal halides, enabling efficient perovskite formation [24]. To address energy and environmental concerns, soft-chemistry methods have gained prominence for perovskite synthesis. These techniques, such as sol-gel and coprecipitation, operate under milder conditions than solid-state routes while offering superior homogeneity, purity, and compositional flexibility [143–145]. They also facilitate diverse morphologies (e.g., thin films, fibers) that are challenging to achieve via conventional methods [14]. Aqueous

sol-gel synthesis, for example, enables low-temperature crystallization by forming stable colloidal sols through hydrolysis of metal salts (e.g., ZrCl_4 , TiCl_4), with particle sizes ranging from 1 nm to 1 μm . These sols are dehydrated into gels and calcined at reduced temperatures to form crystalline perovskite phases [35, 146]. Over the past decades, substantial effort has focused on further reducing processing temperatures and improving stoichiometric control. Notably, niobate-based perovskites such as KNbO_3 and NaNbO_3 have been synthesized at temperatures as low as 500–700 °C through hydroxide precursor reactions, a significant improvement over traditional methods [146].

3.1.1 Doping of Perovskites

The remarkable versatility of perovskite oxides, encompassing both conventional ABO_3 and double perovskite $\text{A}_2\text{BB}'\text{O}_6$ structures, stems from their exceptional tolerance to chemical modifications through cationic substitutions and variations in the variations in synthesis parameters. These complex materials exhibit tunable physicochemical properties that are critically dependent on several key factors: (i) the synthesis methodology employed, (ii) precise control of calcination conditions (including temperature profile, atmospheric composition and dwell time), and (iii) strategic doping at the A-site (rare earth) or B-site (transition metal) positions [147, 148]. Such modifications induce profound changes in the materials' oxidation state configurations, oxygen stoichiometry, and lattice dynamics, which collectively govern their catalytic performance, electronic transport characteristics, and magnetic behaviour. Central to the functional properties of perovskite systems is the B-site cation, whose strong covalent interaction with oxygen anions determines the fundamental electronic structure. The partial substitution of B-site cations in $\text{AB}_{1-y}\text{M}_x\text{O}_3$ compounds creates a synergistic system where the intrinsic properties of the host matrix interact with those of the dopant species [149, 150]. This doping/substitution strategy enables precise tuning of the material's characteristics while maintaining structural integrity, provided that the Goldschmidt tolerance factor remains within the optimal range of 0.8–1.0 and overall charge neutrality is preserved [section 1.2]. The A-site cations play a complementary role by stabilising unusual oxidation states through controlled lattice distortion and vacancy formation [149], making these materials exception-

ally adaptable for advanced applications in heterogeneous catalysis, spintronic devices, and energy storage systems [151, 152].

Double perovskite oxides of the general formula $\text{RE}_2\text{BB}'\text{O}_6$ exhibit enhanced structural complexity due to the rock-salt ordering of B-site cations. Their magnetic and electronic properties are primarily mediated by superexchange interactions between transition metal ions [see section 2.3], which can be systematically modified through the incorporation of 4d or 5d elements such as ruthenium or iridium. These heavier transition metals introduce strong spin-orbit coupling (SOC) effects, potentially leading to exotic quantum states including the $J_{\text{eff}} = 1/2$ ground state observed in iridium-based compounds Ln_2MIrO_6 ($\text{Ln} = \text{Sr, La, Nd, Pr}$, and $\text{M} = \text{Ni, Mn}$) [153–155] $\text{Sr}_2\text{FeOsO}_6$ [156]. Representative examples of the diverse functionalities observed in double perovskites include the ferromagnetic ordering in $\text{Nd}_2\text{NiMnO}_6$, which exhibits a Curie temperature of approximately $T_C \approx 200$ K; the multiferroic behaviour reported in $\text{Sm}_2\text{NiMnO}_6$; and the giant magnetocaloric effects demonstrated by both $\text{Gd}_2\text{NiMnO}_6$ and $\text{Gd}_2\text{CoMnO}_6$. In addition, $\text{Ln}_2\text{NiIrO}_6$ compounds are known for their strong spin-orbit coupling (SOC) interactions, while Ru-doped variants of similar systems show enhanced magnetic ordering temperatures, further broadening the application potential of these materials [155, 157–161]. Despite these significant advances, a notable gap remains in understanding the cooperative effects arising from simultaneous rare-earth (Nd, Sm) and transition-metal (Ir, Ru) doping within a single double perovskite matrix. This gap presents an important opportunity to explore new materials with potentially enhanced magnetostructural coupling, superior magnetocaloric performance, or multifunctional properties not yet observed. The substitution of manganese by iridium in $\text{RE}_2\text{NiMn}_{1-x}\text{T}_x\text{O}_6$ is supported by compelling fundamental and applied arguments. Iridium exhibits flexible oxidation states, typically $\text{Ir}^{3+}/\text{Ir}^{4+}/\text{Ir}^{5+}$, enabling enhanced redox activity and oxygen vacancy formation [151, 162]. These mechanisms facilitate charge compensation via: $\text{Ni}^{2+} \rightarrow \text{Ni}^{3+}$ and/or $\text{O}^{2-} \rightarrow V_{\text{O}}^{\bullet\bullet}$ both of which enhance electronic conductivity and maintain lattice integrity [163]. Stratically, the ionic radii of Ir^{4+} (0.625 Å) and Mn^{4+} (0.67 Å) are well matched, minimizing lattice distortion [151]. Moreover, $\text{Ir}-\text{O}$ bonds possess stronger covalency compared to $\text{Mn}-\text{O}$, improving structural stability under oxidative environments. Magnetically, doping modifies the superexchange pathways from $\text{Ni}^{2+}-\text{O}-\text{Mn}^{4+}$ to $\text{Ni}^{2+}-\text{O}-\text{Ir}^{4+}$, which can significantly influence the magnetic ordering temper-

ature (T_C), and may induce spin-glass states[5, 123]. This investigation focuses on the system $\text{RE}_2\text{NiMn}_{1-x}\text{T}_x\text{O}_6$, with three primary objectives: (1) to correlate the crystal structure with the observed magnetic and electronic properties; (2) to elucidate the role of spin-orbit coupling and crystal field effects in determining the system's electronic and magnetic behavior; and (3) to assess the application potential of these materials in magnetocaloric and related multifunctional domains, and also present on other dual-site doping combining Nd/Sm rare-earth and/or Ir/Ru transition metals.

3.1.2 Sample Preparation

The double perovskite systems studied in this work, namely $\text{RE}_2\text{NiMn}_{1-x}\text{T}_x\text{O}_{6-\delta}$, (where RE = Nd, Sm, T = Ir, and $x = \text{Ir}$; $0.0 \leq x \leq 0.75$), were synthesized using a modified sol-gel auto-combustion method. This technique was selected for its ability to promote cation homogeneity and low-temperature reactivity, both essential for achieving phase-pure double perovskite structures. The synthesis was carried out at the **MultLab Laboratory**, Department of Physics, Federal University of Sergipe (UFS). The high-purity precursors used include:

- $\text{Nd}(\text{NO}_3)_3 \cdot 6\text{H}_2\text{O}$ (99.9%),
- $\text{Ni}(\text{NO}_3)_2 \cdot 6\text{H}_2\text{O}$ (99.99%),
- $(\text{CH}_3\text{COO})_2\text{Mn} \cdot 4\text{H}_2\text{O}$ (99.97%),
- $\text{Sm}(\text{NO}_3)_3 \cdot 6\text{H}_2\text{O}$, and $\text{IrCl}_3 \cdot x\text{H}_2\text{O}$ for co-substitution.

To form a chelating complex, 2 g of glycine was added to a 2 M nitrate solution prepared in a molar ratio of: $\text{Nd} : \text{Ni} : \text{Mn} = 2 : 1 : 1$ and $\text{Nd} : \text{Sm} : \text{Ni} : \text{Mn} = 1 : 1 : 1 : 1$. The sol was heated at 200° for 24 hours to induce evaporation and xerogel formation. The xerogels were then ground and precalcined at 1000° for 12 hours to remove organic residues. Subsequently, the powders were pulverized, pressed under 80 MPa, and calcined again at 1200° for 48 hours in ambient air to achieve phase formation. Preliminary structural analysis was performed using X-ray diffraction with a Rigaku diffractometer equipped with a Cu $K\alpha_1$ radiation source ($\lambda = 1.540598 \text{ \AA}$). The scan range was $5^\circ \leq 2\theta \leq 90^\circ$, with a step size 0.02° and a step time of 20 s. The instrument operated at 40 kV and 40 mA,

using a $1/4^\circ$ fixed slit, $1/2^\circ$ anti-scattering slit, and a 10 mm mask. To further resolve cation ordering and magnetic sublattices, high-resolution neutron powder diffraction was employed at the ISIS Neutron and Muon Source, Rutherford Appleton Laboratory, UK. This allowed for precise identification of atomic positions and magnetic structure, particularly for iridium-substituted samples. Moreover, a comprehensive suite of techniques were used to evaluate the physical properties of the synthesized compounds. The following table summarizes the experimental facilities and associated measurements:

Table III.1: Experimental techniques and corresponding facilities used in this study

Technique	Measurement Type	Facility
XRD (Cu $K\alpha$)	Structural phase identification	MultLab, UFS (Brazil)
Neutron Powder Diffraction	Magnetic and cation ordering	ISIS Neutron Facility, Oxfordshire, UK
DC Magnetization	Magnetic phase transitions	IFGW, UNICAMP, Brazil
AC Susceptibility	Frequency-dependent magnetism	ISIS Neutron Facility, UK
Raman Spectroscopy	Lattice dynamics	IFGW, UNICAMP, Brazil
Specific Heat (Cp)	Thermodynamic behavior	IFGW, UNICAMP, Brazil
XANES/EXAFS	Local atomic structure, oxidation states	EMA Beamline, LNLS, Brazil

3.1.3 Characterization Techniques

The following section provides a concise overview of the characterization methods, along with a discussion of the Rietveld refinement procedures applied to the diffraction data for precise structural analysis.

3.1.3.1 X-Ray Scattering

X-ray diffractometry is a powerful, non-destructive analytical technique employed to investigate the physico-chemical properties of solid-state materials. It plays a central role in crystallography, materials science, industrial quality assurance, and medical diagnostics. XRD leverages the interaction of X-rays with the electron clouds of atoms in a periodic lattice, generating diffraction patterns that encode critical structural information such as phase identity, crystal symmetry, lattice constants, crystallinity, microstrain, grain size, and defect distributions [164]. The fundamental principle underlying XRD is **Bragg's Law** [165], which describes the condition for constructive interference of X-rays scattered by crystallographic planes:

$$n\lambda = 2d \sin \theta \quad (74)$$

where d is the interplanar spacing, n is the diffraction order (an integer), λ is the X-ray wavelength, and θ is the incident angle. Diffraction occurs only when the path difference between scattered X-ray beams from adjacent lattice planes is an integer multiple of the wavelength. In powder XRD, polycrystalline specimens are scanned over a wide 2θ angular range to capture all valid diffraction events, using geometries such as Bragg-Brentano[see Figure III.1 for schematic representation]. The resulting peaks can be indexed to specific d -spacings, which are characteristic of the crystal structure. The unit cell represents the smallest repeating unit in a crystal. The relationship between interplanar spacing and lattice constants depends on the crystal system. For cubic systems:

$$d_{hkl} = \frac{a}{\sqrt{h^2 + k^2 + l^2}} \quad (75)$$

where a is the lattice parameter, and (hkl) are Miller indices. X-ray wavelengths suitable for diffraction studies range from 0.1-10 Å, comparable to interatomic distances. Laboratory instruments typically use Cu K α radiation ($\lambda = 1.5406$ Å) due to its optimal scattering characteristics. High-brilliance synchrotron sources offer tunable energies, polarization control, and enhanced signal-to-noise ratios for advanced structural investigations. The intensity I_{hkl} of a diffracted beam is governed by the square of the structure factor F_{hkl} :

$$I_{hkl} \propto |F_{hkl}|^2 \quad (76)$$

where the structure factor is:

$$F_{hkl} = \sum_j f_j e^{2\pi i(hx_j + ky_j + lz_j)} e^{-B\left(\frac{\sin\theta}{\lambda}\right)^2} \quad (77)$$

with f_j : atomic scattering factor of the j^{th} atom, (x_j, y_j, z_j) : fractional coordinates of atom j within the unit cell, and $B = 8\pi^2\langle u^2 \rangle$: Debye-Waller factor accounting for thermal motion. The exponential Debye-Waller term represents attenuation due to atomic vibrations. As temperature increases, greater vibrational amplitudes lead to decreased diffraction intensity, particularly at high angles. XRD data interpretation typically includes:(a) Peak indexing and Miller index assignment,(b) Lattice parameter refinement,(c) Phase identification using crystallographic databases (e.g., ICDD PDF-4/5+)[166], (d) Quantitative analysis using the Scherrer equation:

$$D = \frac{K\lambda}{\beta \cos \theta} \quad (78)$$

where D is the crystallite size, K is the shape factor, and β is peak broadening (FWHM in radians).

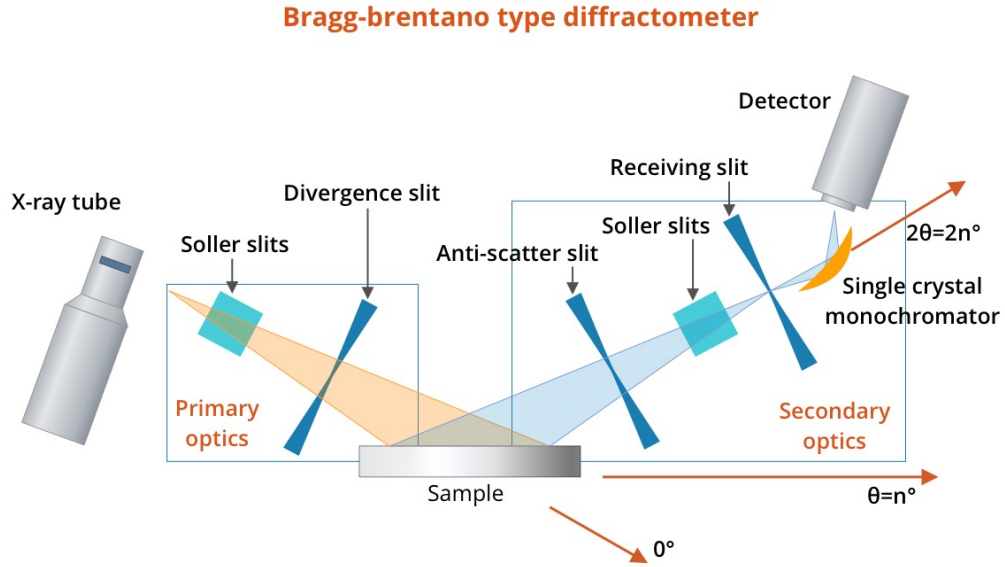


Figure III.1: Schematic representation of a typical Bragg-Brentano XRD configuration used in powder diffraction. In this geometry, the X-ray source and detector are aligned symmetrically around the sample, with the incident angle θ equal to the diffraction angle θ .

3.1.3.2 Neutron Scattering

Neutrons are massive, uncharged particles with a mass of $m_n = 1.675 \times 10^{-27}$ kg, an intrinsic spin- $\frac{1}{2}$, and a magnetic moment of $\mu_n = -1.913 \mu_N$, where μ_N is the nuclear magneton. They possess no electric charge, and their electric dipole moment lies below the current experimental detection limit of $3 \times 10^{-24} e \cdot \text{cm}$ [167]. The properties of neutrons—momentum p , velocity $v_n = p/m_n$, wave vector k , wavelength λ , and kinetic energy E , are interconnected through the de Broglie relation $p = \hbar k$, with \hbar denoting the reduced Planck constant. Thermal neutrons, which are in thermal equilibrium with a room-temperature moderator, are particularly suitable for scattering experiments. Their de Broglie wavelengths, typically in the range of 1 to 3 Å, closely match the interatomic distances in the solids, facilitating the coherent interference used to probe nuclear and magnetic structures. Their kinetic energies (10-80 meV) also align well with typical excitation energies in condensed matter systems.

With their electrical neutrality, neutrons exhibit a strong penetration power, enabling the investigation of bulk material properties. This allows their use in conjunction with complex experimental apparatus such as cryostats, dilution refrigerators, high-field magnets, and pressure cells. Furthermore, the neutron's magnetic moment interacts via dipole-dipole coupling with unpaired electrons in magnetic materials, making neutron scattering a precise tool for microscopic magnetic structure analysis.

Scattering Fundamentals

Neutron scattering is a quantum mechanical process in which a neutron interacts with a target and transitions from an initial quantum state to a final one. This process provides crucial information about both the atomic and magnetic structure of materials. The scattering process is fundamentally characterized by a transition between the quantum states of the scattering particles and the scatterers, driven by their mutual interaction. Initially, the combined system is in the state $|\psi_i\rangle$, which evolves into the final state $|\psi_f\rangle$ after the scattering event. Here, the scattering particle's energy and momentum are represented by ω and \mathbf{k} , respectively, while the scatterer's energy is denoted by E . When the scattering interaction H' is sufficiently weak, the Born approximation becomes applicable. In this regime, the wavefunctions of the scatterers and scattering particles can be treated as separable product states. Specifically, the initial and final states take the form $|\psi_i\rangle = |E_i; \omega_i, \vec{k}_i\rangle$ and $|\psi_f\rangle = |E_f; \omega_f, \vec{k}_f\rangle$, respectively. This approximation simplifies the analysis by decoupling the states of the interacting systems, allowing for a more tractable description of the scattering dynamics. The transition rate between these states is calculated using Fermi's Golden Rule:

$$W = \frac{2\pi}{\hbar} \left| \langle \psi_f | \hat{H}' | \psi_i \rangle \right|^2 \rho(\omega_f) \delta(\omega_i - \omega_f - E_i + E_f), \quad (79)$$

where \hat{H}' is the interaction Hamiltonian, $\rho(\omega_f)$ is the density of final neutron states, and the delta function ensures conservation of total energy in the scattering event. To compute $\rho(\omega_f)$, consider a volume element in reciprocal space with radius k_f , thickness dk_f , and solid angle $\Delta\Omega$. The number of neutron states within this volume is

$$\rho(\omega_f)d\omega_f = \frac{V}{(2\pi)^3} k_f^2 dk_f \Delta\Omega, \quad (80)$$

and since the energy of a neutron is $\omega_f = \frac{\hbar^2 k_f^2}{2m_n}$, its differential is

$$d\omega_f = \frac{\hbar^2 k_f}{m_n} dk_f \Rightarrow dk_f = \frac{m_n}{\hbar^2 k_f} d\omega_f. \quad (81)$$

Substituting back gives the final expression for the density of states:

$$\rho(\omega_f) = \frac{V m_n k_f}{8\pi^3 \hbar^2} \Delta\Omega. \quad (82)$$

The **incident flux** of neutrons I_0 , defined as the number of particles per unit area per unit time, is given by the group velocity over the sample volume:

$$I_0 = \frac{\hbar k_i}{m_n V}. \quad (83)$$

Combining all these expressions into the definition of the inelastic scattering cross-section,

$$\frac{d^2\sigma}{d\Omega d\omega} = \frac{W}{I_0 \Delta\Omega}, \quad (84)$$

Thus, the expression known as the **Master Formula** for neutron scattering [168] is obtained, with full generality preserved by not specifying the interaction Hamiltonian:

$$\frac{d^2\sigma}{d\Omega d\omega} = \frac{k_f}{k_i} \cdot \frac{m_n^2}{(2\pi\hbar)^3} \left| \langle \psi_f | \hat{H}' | \psi_i \rangle \right|^2 \delta(\omega_i - \omega_f - E_i + E_f) \quad (85)$$

3.1.3.3 Scattering Specificities

Recall that the double differential scattering cross section for a probe particle scattering off a quantum system (the "target") is given by Equations 85: where \hat{H}' is the Hamiltonian interaction between the probe and the target system, $|\psi_i\rangle, |\psi_f\rangle$ are defined previously, i.e., $|\vec{k}_i\rangle \otimes |\psi_i^{\text{target}}\rangle$, $\omega = \omega_i - \omega_f$ is the energy transferred from the probe to the target and k_i, k_f are the magnitudes of the initial and final wave vectors of the probe. In the first Born approximation, the probe-target interaction is written as:

$$\hat{H}' = \sum_j b_j e^{i\vec{Q} \cdot \hat{\vec{R}}_j} \quad (86)$$

Here, b_j is the scattering length for the j -th atom, \vec{Q} is the scattering amplitude operator, and $\hat{\vec{R}}_j$ is the position operator of the j -th atom in the target. The total initial and final states are:

$$|\psi_i\rangle = |\vec{k}_i\rangle \otimes |\psi_i^{\text{target}}\rangle = |\vec{k}_i \psi_i^{\text{target}}\rangle, \quad |\psi_f\rangle = |\vec{k}_f\rangle \otimes |\psi_f^{\text{target}}\rangle = |\vec{k}_f \psi_f^{\text{target}}\rangle \quad (87)$$

The transition matrix element becomes

$$\langle \psi_f | \hat{H}' | \psi_i \rangle = \sum_j b_j \langle \psi_f^{\text{target}} | e^{i\vec{Q} \cdot \hat{\vec{R}}_j} | \psi_i^{\text{target}} \rangle \quad (88)$$

Squaring this:

$$\left| \langle \psi_f | \hat{H}' | \psi_i \rangle \right|^2 = \sum_{j,j'} b_j b_{j'}^* \langle \psi_f | e^{i\vec{Q} \cdot \hat{\vec{R}}_j} | \psi_i \rangle \langle \psi_i | e^{-i\vec{Q} \cdot \hat{\vec{R}}_{j'}} | \psi_f \rangle \quad (89)$$

In thermal equilibrium, the system is described by the density operator:

$$\hat{\rho} = \frac{e^{-\beta \hat{H}}}{Z}, \quad Z = \text{Tr} \left(e^{-\beta \hat{H}} \right), \quad \beta = \frac{1}{k_B T} \quad (90)$$

The thermal average of any operator A is:

$$\langle A \rangle = \text{Tr}(\hat{\rho} A) = \sum_{\psi} p_{\psi} \langle \psi | A | \psi \rangle, \quad p_{\psi} = \frac{e^{-\beta E_{\psi}}}{Z} \quad (91)$$

Thus, the differential cross section becomes:

$$\begin{aligned} \frac{d^2 \sigma}{d\Omega dE_f} &= \frac{k_f}{k_i} \sum_{\psi_i, \psi_f} p_{\psi_i} \sum_{j,j'} b_j b_{j'}^* \langle \psi_f | e^{i\vec{Q} \cdot \hat{\vec{R}}_j} | \psi_i \rangle \langle \psi_i | e^{-i\vec{Q} \cdot \hat{\vec{R}}_{j'}} | \psi_f \rangle \\ &\quad \times \delta(E_{\psi_i} - E_{\psi_f} - \hbar\omega) \end{aligned}$$

Thus, resolving the final-state sum via the Fourier representation using:

$$\delta(E_{\psi_i} - E_{\psi_f} - \hbar\omega) = \frac{1}{2\pi\hbar} \int_{-\infty}^{\infty} dt e^{i(E_{\psi_i} - E_{\psi_f} - \hbar\omega)t/\hbar} \quad (92)$$

Substituting this into the matrix element:

$$\langle \psi_f | e^{i\vec{Q} \cdot \hat{R}_j} | \psi_i \rangle \langle \psi_i | e^{-i\vec{Q} \cdot \hat{R}_{j'}} | \psi_f \rangle \delta(E_{\psi_i} - E_{\psi_f} - \hbar\omega) = \frac{1}{2\pi\hbar} \int_{-\infty}^{\infty} dt e^{-i\omega t} \langle \psi_f | e^{i\hat{H}t/\hbar} e^{i\vec{Q} \cdot \hat{R}_j} e^{-i\hat{H}t/\hbar} | \psi_i \rangle \langle \psi_i | e^{-i\vec{Q} \cdot \hat{R}_{j'}} | \psi_f \rangle$$

Using closure over ψ_f :

$$\sum_{\psi_f} \langle \psi_i | e^{-i\vec{Q} \cdot \hat{R}_{j'}(0)} | \psi_f \rangle \langle \psi_f | e^{i\vec{Q} \cdot \hat{R}_j(t)} | \psi_i \rangle = \langle \psi_i | e^{-i\vec{Q} \cdot \hat{R}_{j'}(0)} e^{i\vec{Q} \cdot \hat{R}_j(t)} | \psi_i \rangle \quad (93)$$

Then the cross section becomes:

$$\frac{d^2\sigma}{d\Omega dE_f} = \frac{k_f}{k_i} \sum_{\psi_i} p_{\psi_i} \sum_{j,j'} b_j b_{j'}^* \frac{1}{2\pi\hbar} \int_{-\infty}^{\infty} dt e^{-i\omega t} \langle \psi_i | e^{-i\vec{Q} \cdot \hat{R}_{j'}(0)} e^{i\vec{Q} \cdot \hat{R}_j(t)} | \psi_i \rangle \quad (94)$$

Considering the time evolution of operators, we seek to employ the Heisenberg picture:

$$\hat{R}_j(t) = e^{i\hat{H}t/\hbar} \hat{R}_j(0) e^{-i\hat{H}t/\hbar} \Rightarrow e^{i\vec{Q} \cdot \hat{R}_j(t)} = e^{i\hat{H}t/\hbar} e^{i\vec{Q} \cdot \hat{R}_j(0)} e^{-i\hat{H}t/\hbar} \quad (95)$$

So the correlation function becomes:

$$\langle \psi_i | e^{-i\vec{Q} \cdot \hat{R}_{j'}(0)} e^{i\vec{Q} \cdot \hat{R}_j(t)} | \psi_i \rangle \quad (96)$$

Define the **scattering function** $S(\vec{Q}, \omega)$ (dynamic structure factor):

$$S(\vec{Q}, \omega) = \frac{1}{2\pi\hbar} \sum_{\psi_i} p_{\psi_i} \sum_{j,j'} b_j b_{j'}^* \int_{-\infty}^{\infty} dt e^{-i\omega t} \langle \psi_i | e^{-i\vec{Q} \cdot \hat{R}_{j'}(0)} e^{i\vec{Q} \cdot \hat{R}_j(t)} | \psi_i \rangle \quad (97)$$

Thus, the final expression is as follows.

$$\boxed{\frac{d^2\sigma}{d\Omega dE_f} = \frac{k_f}{k_i} \cdot S(\vec{Q}, \omega)} \quad (98)$$

where $S(\vec{Q}, \omega)$ is a Fourier transform of the position-position correlation functions that encode spatial and temporal correlations in the sample. It is an observable quantity measured in neutron or X-ray scattering. With spinful probes, spin degrees of freedom can be included. If spin is included and the final spin state is

unobserved:

$$S(\vec{Q}, \omega) = \frac{1}{2\pi\hbar} \sum_{\psi_i, \sigma_i, \sigma_f} p(\psi_i) p(\sigma_i) \sum_{j, j'} b_j b_{j'}^* \int dt e^{-i\omega t} \langle \psi_i; \sigma_i | e^{-i\vec{Q} \cdot \hat{\vec{R}}_{j'}(0)} e^{i\vec{Q} \cdot \hat{\vec{R}}_j(t)} | \psi_i; \sigma_f \rangle \quad (99)$$

The formalism developed so far applies broadly to probe-target interactions within the Born approximation. However, neutron scattering exhibits unique characteristics because neutrons interact directly with atomic nuclei. This interaction is governed not by charge (as in X-ray scattering), but by nuclear forces, which are short-ranged, complex, and strongly dependent on nuclear isotopes and spin states. These peculiarities introduce statistical variability in the length of the scattering b_j at each site, even in chemically pure materials. This variability is not captured by the dynamical structure function $S_{j,j'}(\vec{Q}, \omega)$, which depends only on the spatial and temporal correlations of the nuclei, but appears in the scattering length factors that weight these correlations. The full scattering function is given by:

$$S(\vec{Q}, \omega) = \sum_{j, j'} b_j b_{j'}^* S_{j,j'}(\vec{Q}, \omega) \quad (100)$$

with:

$$S_{j,j'}(\vec{Q}, \omega) = \frac{1}{2\pi\hbar} \sum_{\psi_i} p(\psi_i) \int_{-\infty}^{\infty} dt \langle \psi_i | e^{-i\vec{Q} \cdot \hat{\vec{R}}_{j'}(0)} e^{i\vec{Q} \cdot \hat{\vec{R}}_j(t)} | \psi_i \rangle e^{-i\omega t} \quad (101)$$

Here, $S_{j,j'}(\vec{Q}, \omega)$ quantifies time-dependent correlations between nuclei at sites j and j' , b_j is the (possibly random) nuclear scattering length at site j , and $p(\psi_i)$ is the thermal population of the initial quantum state $|\psi_i\rangle$. Notably, unlike in X-ray scattering (which couples to electron clouds), neutron-nucleus scattering lengths b_j vary due to: (i) isotopic differences and (ii) nuclear spin states, distributed thermally or according to spin multiplicity. These variations do not affect $S_{j,j'}$, which are pure quantum-mechanical correlation functions, but they do modify the prefactors $b_j b_{j'}^*$, leading us to separate the total scattering into coherent and incoherent parts. Suppose a system has two isotopes, with scattering lengths c_1 and c_2 , appearing with equal probability. Where the Cross terms ($j \neq j'$) is:

$$\langle b_j b_{j'} \rangle = \frac{1}{4} (c_1^2 + 2c_1 c_2 + c_2^2) = \bar{c}^2, \quad \text{where } \bar{c} = \frac{1}{2} (c_1 + c_2) \quad (101)$$

and the Diagonal terms ($j = j'$) is given as:

$$\langle b_j^2 \rangle = \frac{1}{2}(c_1^2 + c_2^2) = \bar{c}^2 \quad (102)$$

Thus, cross terms reflect the square of the mean \rightarrow coherent scattering, while the diagonal terms reflect the mean of the squares \rightarrow incoherent scattering. The difference gives the statistical variance:

$$\text{Var}(b) = \bar{b}^2 - \bar{b}^2 \quad (103)$$

In macroscopic systems, scattering length randomness arises from a statistical distribution of isotopes or spin states. For each site j :

- $p_j^{(i)}$: probability of configuration i ,
- $b_j^{(i)}$: scattering length in configuration i ,

then:

$$\bar{b}_j = \sum_i p_j^{(i)} b_j^{(i)} \quad (104)$$

$$\bar{b}_j^2 = \sum_i p_j^{(i)} (b_j^{(i)})^2 \quad (105)$$

The scattering function becomes:

$$S(\vec{Q}, \omega) = \sum_{j \neq j'} \bar{b}_j \bar{b}_{j'}^* S_{j,j'}(\vec{Q}, \omega) + \sum_j (\bar{b}_j^2 - |\bar{b}_j|^2) S_{j,j}(\vec{Q}, \omega) \quad (106)$$

The total cross section is as follows:

$$\frac{d^2 \sigma}{d\Omega dE_f} = \left(\frac{d^2 \sigma}{d\Omega dE_f} \right)_{\text{coh}} + \left(\frac{d^2 \sigma}{d\Omega dE_f} \right)_{\text{inc}} \quad (107)$$

a) Coherent Scattering:

$$\left(\frac{d^2 \sigma}{d\Omega dE_f} \right)_{\text{coh}} = \frac{k_f}{k_i} \cdot \frac{1}{2\pi\hbar} \sum_{\psi_i} p(\psi_i) \sum_{j \neq j'} \bar{b}_j \bar{b}_{j'}^* \int dt \langle \psi_i | e^{-i\vec{Q} \cdot \hat{R}_{j'}(0)} e^{i\vec{Q} \cdot \hat{R}_j(t)} | \psi_i \rangle e^{-i\omega t} \quad (108)$$

b) Incoherent Scattering:

$$\left(\frac{d^2\sigma}{d\Omega dE_f} \right)_{\text{inc}} = \frac{k_f}{k_i} \cdot \frac{1}{2\pi\hbar} \sum_{\psi_i} p(\psi_i) \sum_j (\bar{b}_j^2 - |\bar{b}_j|^2) \int dt \langle \psi_i | e^{-i\vec{Q} \cdot \hat{R}_j(0)} e^{i\vec{Q} \cdot \hat{R}_j(t)} | \psi_i \rangle e^{-i\omega t} \quad (109)$$

For systems with identical or monatomic systems:

$$\sigma_{\text{coh}} = 4\pi \bar{b}^2 \quad (110)$$

$$\sigma_{\text{inc}} = 4\pi (\bar{b}^2 - \bar{b}^2) \quad (111)$$

Then:

c) Coherent Part:

$$\left(\frac{d^2\sigma}{d\Omega dE_f} \right)_{\text{coh}} = \frac{\sigma_{\text{coh}}}{4\pi} \cdot \frac{k_f}{k_i} \cdot \frac{1}{2\pi\hbar} \sum_{\psi_i} p(\psi_i) \sum_{j,j'} \int dt \langle \psi_i | e^{-i\vec{Q} \cdot \hat{R}_{j'}(0)} e^{i\vec{Q} \cdot \hat{R}_j(t)} | \psi_i \rangle e^{-i\omega t} \quad (112)$$

d) Incoherent Part:

$$\left(\frac{d^2\sigma}{d\Omega dE_f} \right)_{\text{inc}} = \frac{\sigma_{\text{inc}}}{4\pi} \cdot \frac{k_f}{k_i} \cdot \frac{1}{2\pi\hbar} \sum_{\psi_i} p(\psi_i) \sum_j \int dt \langle \psi_i | e^{-i\vec{Q} \cdot \hat{R}_j(0)} e^{i\vec{Q} \cdot \hat{R}_j(t)} | \psi_i \rangle e^{-i\omega t} \quad (113)$$

Thus, the decomposition of the neutron scattering cross section into coherent and incoherent components provides a powerful interpretative framework. Coherent scattering arises from interference between waves scattered by different nuclei and is sensitive to spatial correlations in the material. It reveals collective dynamics, including lattice vibrations (phonons), structural correlations, and long-range order-features typically observed in crystalline solids. Contrastingly, incoherent scattering originates from randomness in scattering lengths, due to variations in nuclear spin and isotopic composition. It reflects the self-correlations of individual atoms and is particularly useful for studying local dynamics such as diffusion, vibrational relaxation, and atomic disorder making it essential for prob-

ing disordered systems, glasses, and liquids. Unlike X-rays, which scatter from electron density, neutron scattering directly couples to the nucleus. This makes it uniquely sensitive to nuclear-level randomness, allowing the incoherent component to emerge naturally from isotopic or spin-based fluctuations. This thesis seeks to utilize neutron elastic scattering as a primary tool to investigate and understand the structural and dynamical properties of the system under study.

Magnetic Scattering Amplitude

Physically, the neutron possesses a magnetic dipole moment due to its spin σ , even though it is electrically neutral. When a neutron moves in the vicinity of magnetic atoms, specifically, near unpaired electrons, it interacts with the magnetic field $\mathbf{H}(\mathbf{r})$ that these electrons produce. This field comprises two main components: a classical dipolar field originating from the electron's spin and a field arising from its orbital motion, which can be treated in terms of magnetostatics and quantum electrodynamics. Mathematically, the interaction energy of a neutron at position \mathbf{r} in the presence of a magnetic field is expressed as [168, 169]:

$$V_M(\mathbf{r}) = -\boldsymbol{\mu}_n \cdot \mathbf{H}(\mathbf{r}) \quad (114)$$

Here, $\boldsymbol{\mu}_n = \gamma_n \mu_N \boldsymbol{\sigma}$ is the neutron magnetic moment operator, γ_n is the gyromagnetic ratio of the neutron (negative), and μ_N is the nuclear magneton. If the magnetic field arises from N unpaired electrons at positions \mathbf{R}_i , the total magnetic field experienced by the neutron can be written in terms of the classical expressions for the magnetic field due to a dipole and moving charge, yielding the full interaction potential:

$$V_M(\mathbf{r}) = -\boldsymbol{\mu}_n \cdot \sum_{i=1}^N \left[\nabla \times \left(\frac{\boldsymbol{\mu}_i \times (\mathbf{r} - \mathbf{R}_i)}{|\mathbf{r} - \mathbf{R}_i|^3} \right) - \frac{2\mu_B}{\hbar} \frac{\mathbf{p}_i \times (\mathbf{r} - \mathbf{R}_i)}{|\mathbf{r} - \mathbf{R}_i|^3} \right] \quad (115)$$

The two terms represent the magnetic field from the electron spin magnetic moment (via the curl of a vector potential) and the contribution from the orbital motion of electrons treated via their linear momentum \mathbf{p}_i . The spin term is directly tied to the intrinsic angular momentum of the electron, \mathbf{s}_i , through $\boldsymbol{\mu}_i = -2\mu_B \mathbf{s}_i$, while the orbital term reflects the effective current loops generated by moving charges in orbitals. To analyze the scattering process, we ones more employ the first Born approximation, which considers the potential as a weak perturbation

to the neutron's wavefunction. Whence, the scattering amplitude operator $a(\mathbf{Q})$ is defined via the matrix element of the potential in momentum space:

$$\left(\frac{m}{2\pi\hbar^2}\right) \langle \mathbf{k}_f, \sigma_f | V(\mathbf{r}) | \mathbf{k}_i, \sigma_i \rangle = \langle \sigma_f | a(\mathbf{Q}) | \sigma_i \rangle \quad (116)$$

The wave vector transfer in the scattering process is $\mathbf{Q} = \mathbf{k}_i - \mathbf{k}_f$, and the final expression for the magnetic scattering amplitude, obtained by Fourier transforming the magnetic field and integrating over space is:

$$a_M(\mathbf{Q}) = p \boldsymbol{\sigma} \cdot [\hat{\mathbf{Q}} \times \mathbf{M}(\mathbf{Q}) \times \hat{\mathbf{Q}}] \quad (117)$$

Here, $\mathbf{M}(\mathbf{Q})$ is the Fourier transform of the total magnetization density $\mathbf{M}(\mathbf{r})$, and $\hat{\mathbf{Q}} = \mathbf{Q}/|\mathbf{Q}|$ is the unit vector in the direction of the scattering vector. The constant $p = \left(\frac{m}{2\pi\hbar^2}\right) 4\pi\gamma\mu_N\mu_B$ encapsulates physical constants and sets the scale of the magnetic scattering strength; its numerical value is approximately $0.2696 \times 10^{-12} \text{cm}$, corresponding to the scattering amplitude of a moment of $1\mu_B$ at zero momentum transfer. The magnetization density itself is composed of both spin and orbital components, reflecting the two physical origins of the magnetic moment:

$$\mathbf{M}(\mathbf{r}) = \mathbf{M}_S(\mathbf{r}) + \mathbf{M}_L(\mathbf{r}) \quad (118)$$

Each term is a spatial distribution representing either the spin or orbital contributions of electrons to the local magnetization. In the context of crystals, this density is typically localized around atoms and can be modeled using atomic or ionic wavefunctions. The appearance of the double vector product in the amplitude formula reflects a fundamental symmetry: only the components of the magnetization perpendicular to the scattering vector contribute to magnetic scattering. This projection,

$$\mathbf{M}_\perp(\mathbf{Q}) = \hat{\mathbf{Q}} \times \mathbf{M}(\mathbf{Q}) \times \hat{\mathbf{Q}} \quad (119)$$

ensures that longitudinal components (parallel to \mathbf{Q}) do not affect the neutron's spin and therefore do not lead to scattering. This transverse nature of the magnetic scattering operator allows determination of both the direction and magnitude of magnetic moments, a distinct advantage over nuclear scattering. Practical calculations, especially in crystalline materials, one often simplifies the treatment by using a single-ion approximation. In this case, the total magnetization is

modeled as a sum over discrete atomic sites, each carrying a localized magnetic moment $\boldsymbol{\mu}_j$, modulated by a spatial density function $\rho_j(\mathbf{r} - \mathbf{R}_j)$. The Fourier transform of this distribution yields:

$$\mathbf{M}(\mathbf{Q}) = \sum_j \boldsymbol{\mu}_j f_j(\mathbf{Q}) e^{i\mathbf{Q} \cdot \mathbf{R}_j} \quad (120)$$

where $f_j(\mathbf{Q})$ is the magnetic form factor, which accounts for the spatial extent of the magnetization density. It represents the reduction in scattering amplitude at higher Q , due to the wave nature of the neutron failing to fully resolve small-scale features of the electron cloud. At $Q = 0$, the form factor is normalized such that $f(0) = 1$. Taking into account the projection of the local moment perpendicular to \mathbf{Q} , the scattering amplitude for a single ion becomes:

$$a_M(\mathbf{Q}) = p f(\mathbf{Q}) \boldsymbol{\sigma} \cdot \boldsymbol{\mu}_\perp \quad (121)$$

with

$$\boldsymbol{\mu}_\perp = \boldsymbol{\mu} - (\boldsymbol{\mu} \cdot \hat{\mathbf{Q}}) \hat{\mathbf{Q}} \quad (122)$$

The measurable quantity in an experiment is the differential cross section. For unpolarized neutrons and randomly oriented magnetic moments, the spin average yields:

$$\left(\frac{d\sigma_M}{d\Omega} \right) = p^2 f(\mathbf{Q})^2 |\boldsymbol{\mu}_\perp|^2 \quad (123)$$

This relation emphasizes the key role played by the magnetic form factor and the transverse component of the magnetic moment in determining the intensity of magnetic scattering. Notably, because the cross section is proportional to the square of $\boldsymbol{\mu}_\perp$, magnetic reflections may vanish entirely if the magnetic moment is aligned along \mathbf{Q} , a fact that is critical for interpreting experimental data and for designing polarized neutron experiments. The noncentral and long-range nature of magnetic scattering, contrasted with the central, short-range nuclear scattering, makes its theoretical treatment more intricate but also more informative. The angular dependence of the cross section, through the $\hat{\mathbf{Q}}$ -dependent projection, encodes rich information about the spatial orientation of magnetic moments. For crystalline materials, further elaboration is required to account for the periodic lattice, unit cell structure, and long-range magnetic order, which is the subject of the following section.

Crystal Scattering

To describe neutron scattering from a periodic system, one must account for interference effects arising from the coherent scattering of neutrons off multiple atoms and unit cells. This gives rise to Bragg diffraction[see section 3.1.3.1], governed by the reciprocal lattice structure, and introduces the concept of structure factors, nuclear and magnetic, that encode the relative phases and amplitudes of scattering from different atoms. Let us consider a three-dimensional crystal composed of a large number of unit cells. Each unit cell contains several atoms, indexed by ν , located at positions \mathbf{r}_ν within the unit cell. The position of atom ν in the unit cell labeled by n is denoted:

$$\mathbf{R}_{n\nu} = \mathbf{R}_n + \mathbf{r}_\nu \quad (124)$$

Here, \mathbf{R}_n is the Bravais lattice vector of cell n , which can be expressed as:

$$\mathbf{R}_n = n_a \mathbf{a} + n_b \mathbf{b} + n_c \mathbf{c} \quad (125)$$

with $(n_a, n_b, n_c) \in \mathbb{Z}^3$, and $\mathbf{a}, \mathbf{b}, \mathbf{c}$ are the direct lattice vectors defining the unit cell. The corresponding **reciprocal lattice** vectors are defined via:

$$\mathbf{a}^* = \frac{2\pi}{V} (\mathbf{b} \times \mathbf{c}) \quad (126)$$

$$\mathbf{b}^* = \frac{2\pi}{V} (\mathbf{c} \times \mathbf{a}) \quad (127)$$

$$\mathbf{c}^* = \frac{2\pi}{V} (\mathbf{a} \times \mathbf{b}) \quad (128)$$

where $V = \mathbf{a} \cdot (\mathbf{b} \times \mathbf{c})$ is the volume of the unit cell. Any **reciprocal lattice vector** can be written as:

$$\mathbf{H} = h\mathbf{a}^* + k\mathbf{b}^* + l\mathbf{c}^* \quad (129)$$

with $h, k, l \in \mathbb{Z}$. Before extending to the magnetic case, it is useful to recall the nuclear scattering result. The nuclear interaction potential, assuming the neutron interacts via Fermi pseudo-potential with nuclei at $\mathbf{R}_{n\nu}$, is:

$$V_N(\mathbf{r}) = \frac{2\pi\hbar^2}{m} \sum_{n,\nu} b_\nu \delta(\mathbf{r} - \mathbf{R}_{n\nu}) \quad (130)$$

where b_ν is the (isotope-dependent) nuclear scattering length of atom ν . The scattering amplitude becomes:

$$a_N(\mathbf{Q}) = \sum_{n,\nu} b_\nu e^{i\mathbf{Q}\cdot\mathbf{R}_{n\nu}} = \sum_n e^{i\mathbf{Q}\cdot\mathbf{R}_n} \sum_\nu b_\nu e^{i\mathbf{Q}\cdot\mathbf{r}_\nu} \quad (131)$$

The sum over unit cells yields:

$$\sum_n e^{i\mathbf{Q}\cdot\mathbf{R}_n} = N\delta_{\mathbf{Q},\mathbf{H}} \quad (132)$$

by virtue of the discrete translational symmetry of the lattice. Thus, elastic nuclear scattering occurs only at reciprocal lattice vectors $\mathbf{Q} = \mathbf{H}$, satisfying the Bragg condition. The nuclear differential cross section becomes:

$$\frac{d\sigma_N}{d\Omega} = (2\pi)^3 \frac{N}{V} \sum_{\mathbf{H}} |F_N(\mathbf{Q})|^2 \delta(\mathbf{Q} - \mathbf{H}) \quad (133)$$

with the nuclear structure factor:

$$F_N(\mathbf{Q}) = \sum_\nu b_\nu e^{i\mathbf{Q}\cdot\mathbf{r}_\nu} \quad (134)$$

This expression is central to the theory of diffraction from periodic solids.

Magnetic Scattering

We now turn to the case of **magnetic scattering** from a crystalline system where atoms at positions $\mathbf{R}_{n\nu}$ carry magnetic moments. Unlike nuclear scattering, magnetic scattering is a vector process that depends on the orientation of magnetic moments relative to the scattering vector. Assume that atom ν in unit cell n carries a magnetic moment $\boldsymbol{\mu}_{n\nu}$. In the ordered (e.g., magnetically ordered) phase, this distribution is periodic and can be expressed as a Fourier series over propagation vectors \mathbf{k} :

$$\boldsymbol{\mu}_{n\nu} = \sum_{\mathbf{k}} \mathbf{m}_{\nu,\mathbf{k}} e^{-i\mathbf{k}\cdot\mathbf{R}_n} \quad (135)$$

Here, $\mathbf{m}_{\nu,\mathbf{k}}$ is the Fourier component (complex vector) of the magnetic moment associated with propagation vector \mathbf{k} . The sum over \mathbf{k} is restricted to a **star** of symmetry-allowed wave vectors (propagation vectors), typically confined to the **first Brillouin zone**. The total magnetization density in the crystal can then

be written:

$$\mathbf{M}(\mathbf{r}) = \sum_{n,\nu} \boldsymbol{\mu}_{n\nu} \rho_\nu(\mathbf{r} - \mathbf{R}_{n\nu}) \quad (136)$$

Taking the Fourier transform:

$$\mathbf{M}(\mathbf{Q}) = \sum_{n,\nu} \boldsymbol{\mu}_{n\nu} f_\nu(\mathbf{Q}) e^{i\mathbf{Q} \cdot \mathbf{R}_{n\nu}} \quad (137)$$

Substituting the expansion of $\boldsymbol{\mu}_{n\nu}$, and defining $\mathbf{Q} = \mathbf{H} + \mathbf{k}$, we obtain:

$$\mathbf{M}(\mathbf{Q}) = \sum_{\nu} f_\nu(\mathbf{Q}) \mathbf{m}_{\nu,\mathbf{k}} e^{i\mathbf{Q} \cdot \mathbf{r}_\nu} \sum_n e^{i(\mathbf{Q}-\mathbf{k}) \cdot \mathbf{R}_n} \quad (138)$$

Using the identity $\sum_n e^{i\mathbf{H} \cdot \mathbf{R}_n} = N \delta_{\mathbf{Q}-\mathbf{k},\mathbf{H}}$, we arrive at:

$$\mathbf{M}(\mathbf{Q}) = N \sum_{\nu} f_\nu(\mathbf{Q}) \mathbf{m}_{\nu,\mathbf{k}} e^{i\mathbf{Q} \cdot \mathbf{r}_\nu} \quad (139)$$

This defines the **magnetic structure factor**:

$$\mathbf{F}_M(\mathbf{Q}) = p \sum_{\nu} f_\nu(\mathbf{Q}) \mathbf{m}_{\nu,\mathbf{k}} e^{i\mathbf{Q} \cdot \mathbf{r}_\nu} \quad (140)$$

Finally, since only the transverse component of $\mathbf{F}_M(\mathbf{Q})$ contributes to the scattering, we define:

$$\mathbf{F}_{M,\perp}(\mathbf{Q}) = \hat{\mathbf{Q}} \times \mathbf{F}_M(\mathbf{Q}) \times \hat{\mathbf{Q}} \quad (141)$$

The differential magnetic scattering cross section in the elastic regime becomes:

$$\frac{d\sigma_M}{d\Omega} = (2\pi)^3 \frac{N}{V} \sum_{\mathbf{H}} \sum_{\mathbf{k}} \left| \mathbf{F}_{M,\perp}(\mathbf{Q}) \right|^2 \delta(\mathbf{Q} - \mathbf{H} - \mathbf{k}) \quad (142)$$

This expression shows that: (i) Magnetic scattering occurs at positions $\mathbf{Q} = \mathbf{H} + \mathbf{k}$, i.e., at *satellite peaks* displaced from the nuclear Bragg peaks by the propagation vector \mathbf{k} . (ii) For *commensurate magnetic structures*, \mathbf{k} is a rational multiple of the reciprocal lattice vectors, and peaks appear periodically. (iii) For *incommensurate* \mathbf{k} , peaks are quasi-periodic and do not coincide with nuclear reflections. The intensity of each magnetic peak is given by the squared modulus of the transverse magnetic structure factor, which depends on the orientation and magnitude of magnetic moments, their arrangement in the unit cell, and the magnetic form factor.

Propagation Vector

Although it is often intuitive to think of magnetic structures in terms of ferromagnetic, antiferromagnetic, or ferrimagnetic arrangements within the unit cell, such representations can become inadequate or ambiguous, especially in complex materials. To overcome these limitations, neutron scattering theory employs a more general and rigorous approach based on the propagation vector formalism, which provides a powerful method to describe magnetic structures in both real and reciprocal space. Let recall that the full position of atom (n, ν) is given by equation 124 and assume that in the magnetically ordered state, each atom (n, ν) carries a magnetic moment $\boldsymbol{\mu}_{n\nu}$. The distribution of magnetic moments in the crystal must obey the translational symmetry of the lattice, albeit possibly modulated by a larger periodicity or an incommensurate modulation. This spatial periodicity of the magnetic structure allows us to write the magnetic moment as a Fourier series:

$$\boldsymbol{\mu}_{n\nu} = \sum_{\mathbf{k}} \mathbf{m}_{\nu, \mathbf{k}} e^{-i\mathbf{k} \cdot \mathbf{R}_n} \quad (143)$$

Here, \mathbf{k} is the *magnetic propagation vector*, and $\mathbf{m}_{\nu, \mathbf{k}}$ is the corresponding complex-valued Fourier component, each encoding the amplitude and phase of the magnetic moment on sublattice ν for modulation vector \mathbf{k} . This expression reflects the essential periodicity of the magnetic structure with respect to the underlying crystal lattice. The vectors \mathbf{k} can take values in the first Brillouin zone, and due to the real-valued nature of physical magnetic moments, each component must satisfy the reality condition:

$$\mathbf{m}_{\nu, -\mathbf{k}} = \mathbf{m}_{\nu, \mathbf{k}}^* \quad (144)$$

This ensures that the inverse Fourier transform yields a real moment at each site. If \mathbf{k} lies on a special point or surface of the Brillouin zone such that $\mathbf{k} = -\mathbf{k}$ (modulo a reciprocal lattice vector), then $\mathbf{m}_{\nu, \mathbf{k}}$ must be real.

3.1.4 Instruments, Data Acquisition and Analysis

This section provides an overview of the experimental instrumentation and analytical techniques employed throughout the present thesis. It includes a description of the major characterization tools used to probe the structural, magnetic, and electronic properties of the synthesized materials. Emphasis is placed on both the principles of operation of each instrument and the rationale for their selection based on the specific requirements of the study. The methodologies presented here form the foundation of the data acquisition and analysis workflows and are critical to interpreting the experimental results discussed in subsequent chapters.

WISH

Neutron diffraction experiments presented in this thesis were conducted using the **WISH diffractometer** at the ISIS Neutron and Muon Source, situated on the second target station (TS-II), which is optimized for high brilliance at long neutron wavelengths. WISH is a time-of-flight (TOF) diffractometer that exploits the pulsed nature of the neutron source to obtain high-resolution diffraction data over a wide momentum transfer Q range [170, 171]. The instrument utilizes a beam of **cold neutrons**, characterized by their long wavelengths and low energies, making it exceptionally powerful for determining complex magnetic structures, such as those investigated in this thesis. The instrument is particularly suitable for studies of magnetic structures in both powder and single-crystal samples. Neutrons are generated by bombarding a tantalum target with high-energy protons and are moderated via a 40 K solid methane moderator, producing a peak flux at approximately 2.8 Å. A ballistic supermirror guide ($m = 2$), elliptical in cross-section, transports the beam over a 40 m primary flight path to the sample. This long flight path ensures high resolution across the Q -range.

The WISH detector array consists of ^3He position-sensitive tubes arranged cylindrically to cover a scattering angle of $2\theta = 10^\circ$ to 170° . These detectors collect data simultaneously over a large Q -range and currently span one side of the array (760 tubes), with plans for full completion underway. A significant upgrade to the instrument is the installation of a Gd_2O_3 -coated oscillating ra-

dial collimator and plans for an argon-filled secondary containment tank. These enhancements are designed to drastically reduce background noise originating from the sample environment equipment (e.g., cryostats), which is essential for resolving the weak magnetic scattering signals from complex, multi-sublattice perovskites. The instrument supports three resolution modes via piezoelectric slits: (a) High-resolution mode: $\Delta\frac{Q}{Q} \approx 0.3\%$, (b) Medium-resolution mode and (c) High-flux mode. Neutron wavelength λ is computed from the time-of-flight t and path length L using:

$$\lambda = \frac{h}{m_n v} = \frac{ht}{m_n L} \quad (145)$$

where h is Planck's constant. The chopper system includes two counter-rotating double-disk choppers and a single-disk chopper operating at 10-20 Hz to define the neutron bandwidth (up to 9.4 Å) and eliminate frame overlap. Powder samples (1 – 2 g) are loaded into cylindrical vanadium or aluminium cans and mounted in cryostats. Aluminium provides low neutron absorption with higher coherent scattering, while vanadium is nearly transparent. The sample space is viewed through a 0.8 mm thick aluminium window. Several corrections are applied before data analysis: (i) flux normalization: compensates for fluctuations in incident neutron flux, (ii) absorption correction: accounts for exponential attenuation per the Beer-Lambert law, and (iii) multiple scattering: neglected for powder samples due to minimal effect. For randomly oriented crystallites in powder samples, scattering occurs in Debye-Scherrer cones. The integrated intensity is extracted around the corresponding rings. A geometrical Lorentz correction is applied to ensure accurate reflection intensity measurement:

$$L = d^4 \sin(\theta) \quad (146)$$

This correction is specific to TOF experiments where diffraction intensities vary with detection angle. WISH data is acquired in histogram format (with a transition to event-mode planned) and reduced using the **Mantid** software, developed jointly by ISIS and the Spallation Neutron Source (SNS) at Oak Ridge National Laboratory [see layout Adapted from [170]].

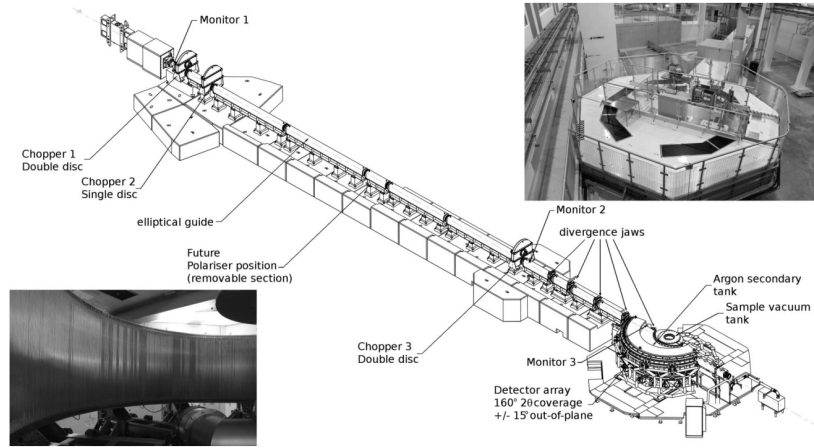


Figure III.2: Engineering layout of the WISH diffractometer. The images show the instrument in the TS2 experimental hall (right) and the ^3He detector array inside the blockhouse (left). Neutrons are transported via a ballistic supermirror guide ($m = 2$), elliptical in both horizontal and vertical planes. The guide extends from 1.7 m downstream of the source to 0.5 m before the sample, with a total flight path of 40.0 m from the moderator face. The guide exit is a rectangular aperture measuring 20 mm \times 40 mm.

EMA Beamline

High-resolution synchrotron X-ray diffraction (SXRD) and X-ray absorption near-edge structure (XANES) measurements were performed at the **EMA beamline** (Extreme Methods of Analysis) at the Brazilian Synchrotron Light Laboratory (LNLS) [172], located at the Sirius 4th-generation synchrotron source. The EMA beamline provides an ultra-bright, microfocused X-ray beam suited for structural and spectroscopic analysis under a variety of sample environments.

SXRD Experiments

SXRD data were acquired using a high-flux monochromatic beam with an incident wavelength of $\lambda = 0.4959\text{\AA}$, selected for optimal resolution and minimized sample absorption. Polycrystalline samples of NdSmNiMnO_6 were sealed in quartz-glass capillaries with a diameter of 0.5 mm which effectively suppressed absorption effects and reduced preferential orientation. The capillary diameter was specifically chosen to ensure an effective beam spot interaction of less than $0.1 \times 0.1 \mu\text{m}^2$, maximizing signal homogeneity across the sample. Diffraction data were collected over a 2θ range of 1° to 30° in continuous scanning mode, providing high-resolution structural profiles across the selected angular domain. Measurements were conducted over a broad temperature range from

4 K to 275 K, controlled via a helium flow cryostat. A thermal stabilization interval of 15 to 20 minutes was maintained at each temperature point to ensure equilibrium and enhance data reliability.

XANES Measurements

XANES spectra were collected at EMA beamline station 52, exploiting the high-brilliance source generated by a 22 mm period Kyma undulator, see Figure III.3. The source delivers photon energies from 5.7 keV (3rd harmonic) to 35 keV (15th harmonic), covering the K-edges of both Ni and Mn. A high-resolution LN₂-cooled double-crystal monochromator (DCM), employing silicon (111) crystals [173], was used to monochromatize the beam. The final focusing was achieved through an achromatic Kirkpatrick-Baez (K-B) mirror system, producing a beam spot of $10 \times 10 \mu\text{m}^2$ at the sample. XANES measurements at the Ni and Mn K-edges were performed in transmission mode. The intensity of the incident beam (I_0) and transmitted beam (I_t) were recorded using ionization chambers filled with optimized gas mixtures to ensure linear response within the target energy range. Absorption coefficients were calculated using the Beer-Lambert law: $\text{ABS} = \mu t = \ln\left(\frac{I_0}{I_t}\right)$, where μ is the linear absorption coefficient and t is the sample thickness. For each composition, three spectra were collected and individually normalized to the absorption edge jump. Final spectra were obtained by averaging the normalized datasets to improve signal-to-noise ratio and reproducibility. This procedure ensures that small spectral features, indicative of valence state changes or local coordination distortions, were robustly captured and compared across temperatures.

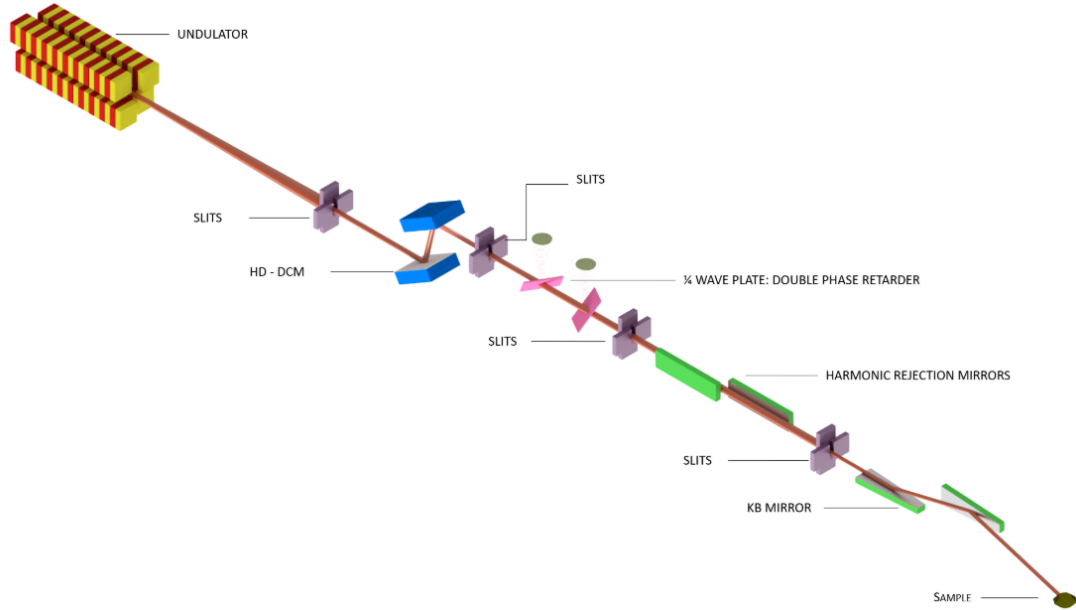


Figure III.3: Optical layout of the EMA beamline at Sirius synchrotron. The high-brilliance X-ray beam is generated by a cryogenic permanent magnet undulator (CPMU) and conditioned through a sequence of optical components including slits, a high-resolution double-crystal monochromator (HD-DCM), a quarter-wave plate (double phase retarder), harmonic rejection mirrors, and Kirkpatrick-Baez (KB) focusing mirrors. These elements are optimized for X-ray diffraction (XRD), X-ray absorption (XAS), and X-ray Raman spectroscopy (XRS) under extreme thermodynamic and magnetic conditions.

Magnetometer

DC magnetization measurements are pivotal in understanding magnetic phase transitions, magnetic ordering, and related phenomena in various materials, especially in complex oxides, spin glasses, and superconductors. The magnetization (M) of a sample is commonly studied as a function of temperature ($M(T)$) under a constant magnetic field or as a function of magnetic field ($M(H)$) at a fixed temperature. These protocols are crucial in elucidating intrinsic magnetic behaviors such as superparamagnetism, spin-glass transitions, exchange bias, and ferromagnetic or superconducting orderings. Particularly, in zero-field-cooled (ZFC) measurements, the sample is first cooled in the absence of an external magnetic field to the lowest measurement temperature. A constant magnetic field is then applied, and magnetization data is collected during warming. In Field-Cooled (FC) measurements, the sample is cooled in the presence of a magnetic field. FC measurements can be conducted in two ways: during cooling (field-cooled cooling - FCC) or during warming (field-cooled warming - FCW). These contrasting protocols help identify metastable magnetic states and thermal hysteresis, offering

insights into first-order phase transitions (e.g., martensitic transformations) and second-order transitions (e.g., paramagnetic to ferromagnetic transitions).

VSM

The Vibrating Sample Magnetometer (VSM) is a widely used technique for measuring the magnetic properties of materials with high sensitivity and rapid response [174]. Its working principle is grounded in Faraday's law of electromagnetic induction, which states that an electromotive force (emf) is induced in a coil when there is a time-dependent change in the magnetic flux passing through it. In a VSM setup [Figure III.4], the sample magnetized under an applied external magnetic field, is mounted on a non-magnetic rod and made to oscillate sinusoidally in the vertical direction between a set of symmetrically arranged pickup coils. As the magnetized sample vibrates, it produces a periodic change in magnetic flux through the coils, thereby inducing an alternating emf. If the pickup coil has N turns and cross-sectional area A , and the magnetic flux density is B , the induced voltage V is given by:

$$V = -N \frac{d(BA)}{dt} \quad (147)$$

For a magnetic sample in an applied field H , the magnetic flux density is defined as $B = \mu_0(H + M)$, where μ_0 is the permeability of free space and M is the magnetization. When the sample oscillates with displacement varying as $\sin(\omega t)$, the magnetization also varies sinusoidally, i.e., $M = M_0 \sin(\omega t)$. The resulting emf is therefore directly proportional to the sample's magnetic moment and the frequency of vibration. To accurately extract the signal corresponding to the sample's magnetization, the induced emf is processed using a lock-in amplifier synchronized with the vibration frequency. This selective amplification filters out noise and ensures that only the signal component matching the sample vibration is measured. Consequently, the output voltage is a direct measure of the sample's magnetic moment.

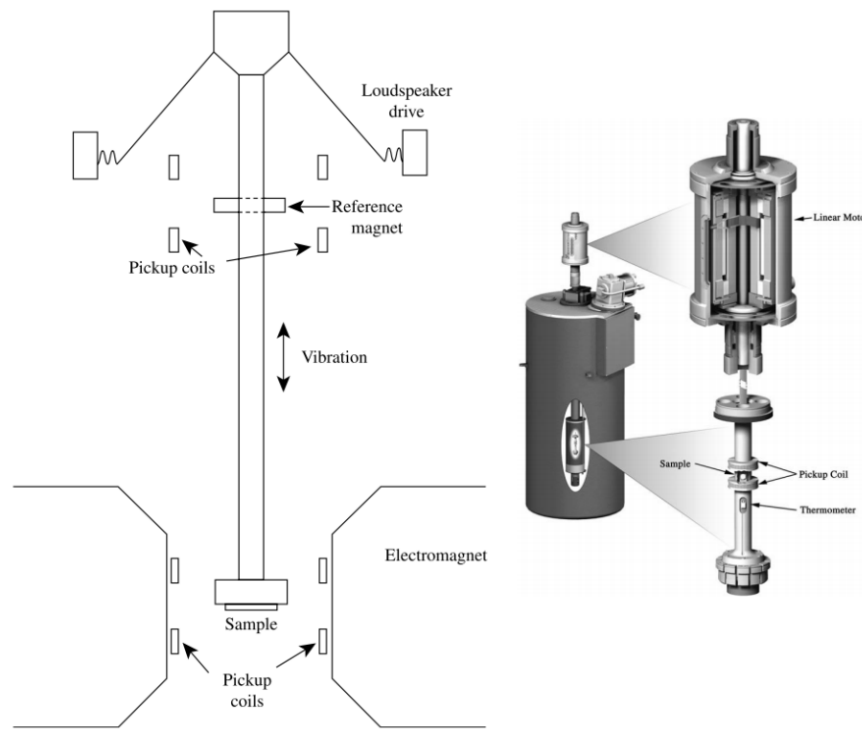


Figure III.4: Schematic diagram of a vibrating sample magnetometer (VSM) and a commercial VSM system.

SQUID

A Superconducting Quantum Interference Device (SQUID) magnetometer operates based on quantum mechanical principles, utilizing a superconducting ring interrupted by one or more Josephson junctions, thin insulating barriers between superconducting segments, to detect magnetic flux with exceptional sensitivity [174]. The core principle lies in the device's ability to measure discrete magnetic flux quanta, making it one of the most sensitive tools available for detecting extremely small magnetic signals. The SQUID system determines the total magnetic moment of a sample in absolute units by directly measuring the change in magnetic flux as the sample is moved through a set of superconducting pickup coils. These coils are part of a flux transformer circuit that includes a transducer coil coupled to the SQUID sensor. As the sample traverses the center of the coil assembly, its magnetic moment induces a current in the pickup coils. This current is converted to a voltage signal by the SQUID probe, which is then amplified and processed by the magnetometer's electronic system. The system detects magnetization changes below 10^{-6} emu at 1 Hz and is operated via MultiVu software for automation and control. Due to its unparalleled sensitivity, the SQUID magnetometer is uniquely suited for high-precision DC magnetization measurements.

In the present study, ZFC (Zero-Field-Cooled) and FC (Field-Cooled) magnetization measurements were performed using a SQUID magnetometer system (Quantum Design) to investigate magnetic behavior across varying temperatures and magnetic field conditions. In contrast, specific heat (C_p) and resistivity measurements were carried out using the standard Quantum Design configuration within the PPMS-14T system. A dense pellet of the powdered sample were prepared by pressing the material into a compact form and sintering it at 1200 °C for 24 hours. This high-temperature sintering process was essential to enhance grain connectivity and reduce porosity, thereby ensuring reliable and reproducible electrical transport measurements. The resulting pellet provided the mechanical and electrical integrity required for an accurate resistivity characterization.

Sample Preparation and Experimental Protocol

Powdered samples (6-12 mg) were carefully loaded into clean, dry capsules and secured in a custom-designed vibrating sample magnetometer (VSM) holder. Precise alignment was achieved using a centering station to ensure optimal positioning relative to the VSM gradiometer pickup coils. The sample was then affixed to an oscillating rod, with its motion centered vertically within the detection coil assembly. Before measurements, the sample chamber was thoroughly purged and sealed to minimize environmental interference. Temperature-dependent magnetization ($M(T)$) measurements were conducted from 5 K to 300 K under a constant applied magnetic field. Hysteresis loops ($M(H)$) were recorded by sweeping the field between ± 7 kOe. The raw magnetic moment data were normalized to both sample mass and molar mass, with molar magnetic susceptibility subsequently derived from these values. This standardized approach ensured consistent and reproducible quantification of the magnetic properties.

$$\chi_{\text{mol}} = \frac{M_{\text{mol}}}{H} \quad (148)$$

AC Magnetic Susceptibility Measurements

AC magnetic susceptibility measurements involve superimposing a small alternating magnetic field onto a static direct current magnetic field. This AC drive field induces a time-dependent magnetic moment in the sample, which generates

a corresponding magnetic flux. This changing flux induces a voltage in the detection coils by Faraday's law, enabling the measurement of the magnetic response of the sample without requiring physical movement of the sample. The detection circuitry is optimized to operate within a narrow frequency bandwidth, typically centered at the fundamental frequency of the applied AC drive field, thereby enhancing signal sensitivity and noise rejection. At sufficiently low frequencies, the magnetic response of the sample closely mirrors the behavior observed in conventional DC magnetometry. In this quasi-static limit, the induced AC magnetic moment M_{AC} is directly proportional to the slope of the magnetization curve $M(H)$, expressed as:

$$M_{AC} = \left(\frac{dM}{dH} \right) H_{AC} \sin(\omega t) \quad (149)$$

where H_{AC} is the amplitude of the AC drive field, ω is the angular frequency, and $\chi = \frac{dM}{dH}$ is the differential magnetic susceptibility. This susceptibility reflects the sensitivity of the magnetization of the sample to variations in the applied magnetic field and is the principal quantity measured in AC magnetometry. A key advantage of AC susceptibility measurements lies in their ability to sensitively detect small changes in the magnetic response, even when the absolute magnetization is large. This is because the technique probes the local slope of the $M(H)$ curve rather than the absolute value of the magnetization. As the frequency of the AC drive increases, dynamic processes within the material begin to dominate. Under these conditions, the sample's magnetization cannot fully follow the oscillating magnetic field due to energy dissipation and relaxation phenomena. Consequently, the magnetization lags behind the drive field, introducing a measurable phase shift φ between the excitation and the response. This dynamic behavior leads to the definition of AC susceptibility as a complex quantity:

$$\chi = \chi' - i\chi'' \quad (150)$$

where: (i) $\chi' = \chi \cos \varphi$ is the in-phase (real) component, associated with the reversible, elastic response of the magnetic system and (ii) $\chi'' = \chi \sin \varphi$ is the out-of-phase (imaginary) component, which captures energy loss mechanisms such as magnetic relaxation, eddy currents, and domain wall damping. The phase angle φ is related to the ratio of the imaginary and real components via:

$$\varphi = \arctan \left(\frac{\chi''}{\chi'} \right) \quad (151)$$

and the total susceptibility magnitude is given by:

$$\chi = \sqrt{\chi'^2 + \chi''^2} \quad (152)$$

In ferromagnetic materials, a nonzero χ'' can be attributed to irreversible domain wall motion or magnetic hysteresis-related energy absorption. Both χ' and χ'' are highly sensitive to thermodynamic phase transitions, making AC susceptibility a powerful tool for detecting critical phenomena such as magnetic ordering, superconducting transitions, and spin-glass freezing. In this study, AC magnetic susceptibility measurements were performed using a SQUID-VSM system (Quantum Design) over the temperature range of 2-300 K. The measurements were conducted under zero DC field conditions during cooling from 300 K to 2 K, with AC excitation field amplitudes of 0.5, 1, and 2 Oe. The susceptibility was recorded at four different excitation frequencies: 11, 110, 320, and 540 Hz, to investigate the frequency-dependent magnetic response of the sample.

Raman Spectroscopy

Raman spectroscopy has evolved significantly since its discovery by Sir Chandrasekhara Venkata Raman in 1928, when he first observed the phenomenon of inelastic light scattering [175]. Advances in optical components, such as excitation sources, controlled sample environments, high-resolution monochromators with holographic gratings, and sensitive detection systems, have transformed Raman spectroscopy into a powerful high-resolution analytical technique. Modern instrumentation allows for precise measurements of low-energy excitations, which is why we represent the experimental setup used in this study in Figure III.5. A quasi-backscattering geometry was employed for both incident and scattered light. The excitation source consisted of a diode-pumped laser (DPL) operating at a single continuous wavelength of 532 nm. To enhance spectral stability and minimize noise, the laser was coupled to a Volume Bragg Grating (VBG), ensuring a narrow linewidth. The beam was then guided and focused onto the sample using a series of mirrors (M) and a lens (L). The scattered light was collected through another lens and passed through notch filters (NF) to suppress elastic

(Rayleigh) scattering before entering the spectrometer. A high-resolution triple-grating T64000 Jobin-Yvon Raman spectrometer was used for spectral analysis, equipped with 1800 mm^{-1} gratings and a liquid-nitrogen-cooled charge-coupled device (CCD) detector. To prepare the samples for measurement, the synthesized powders were compacted into pellets and sintered at 1200°C for 24 hours. Small pieces (approximately 1 mm) of the sintered samples were mounted on a copper holder attached to a cold finger inside a closed-cycle helium cryostat, which maintained a base temperature of 20 K. Temperature calibration and control were achieved using a pre-calibrated CERNOX CX-1050-CU-1.4L sensor connected to a Lakeshore C340 temperature controller. For temperature-dependent Raman measurements, a silicon reference sample was used to correct for minor mechanical backlash in the spectrometer wave number readings. The spectrometer was centered at 470 cm^{-1} to capture Stokes scattering signals, ensuring accurate and reproducible spectral data. This setup enabled a detailed investigation of the vibrational and electronic excitations in the studied materials.

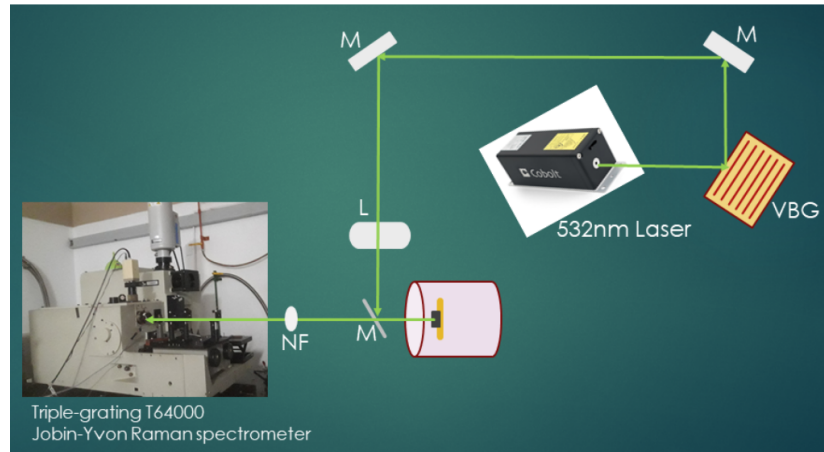


Figure III.5: Schematic diagram of the Raman spectroscopy setup used in this study.

Rietveld Refinement

Developed by Hugo Rietveld in 1969 [176], the Rietveld method revolutionized powder diffraction analysis by shifting from traditional single-peak intensity extraction to a full-profile fitting approach. Unlike conventional methods that rely on extracting integrated intensities from isolated Bragg peaks, the Rietveld approach operates directly on the full profile intensities obtained from step-scanning measurements in reciprocal space (Q-space). This holistic treatment significantly enhances the accuracy and reliability of structural determination, particularly

in systems with complex or overlapping diffraction patterns. A central advantage of this method is its capacity to resolve the pervasive issue of peak overlap, which is inherent in powder diffraction. Rather than treating each peak independently, Rietveld refinement fits a calculated diffraction profile to the entire observed dataset across the full Q -range. This profile is constructed as the sum of mathematically defined peak-shaped functions, each corresponding to a Bragg reflection characterized by its position, intensity, and width. The refinement employs a least-squares minimization algorithm that iteratively adjusts structural parameters, including lattice constants, atomic positions, site occupancies, and thermal vibration parameters (atomic displacement parameters), to reduce the residual between the observed and calculated diffraction patterns. This simultaneous fitting approach not only handles peak overlap but also allows for the incorporation of microstructural effects such as strain, crystallite size broadening, and preferred orientation. As a result, it often achieves a level of precision comparable to, or exceeding, that of single-crystal diffraction, particularly when dealing with polycrystalline or multiphase materials.

In neutron diffraction, the Rietveld method extends beyond nuclear structures to encompass magnetic structures. Its capability to refine both nuclear and magnetic contributions makes it particularly powerful for characterizing magnetic materials. Furthermore, it is highly effective even when working with incomplete, low-quality, or constrained datasets, making it an invaluable tool in challenging experimental conditions. When applied to time-of-flight (TOF) neutron diffraction data, Rietveld refinement integrates sophisticated models to account for peak broadening mechanisms unique to TOF instrumentation. These include: (i) Neutron wavelength uncertainties, intrinsic to TOF experiments; (ii) Resolution effects related to detector pixelation, which influence Q -space precision; and (iii) Asymmetric peak profiles, which stem from the time structure of the neutron pulse. Asymmetric peak shapes in TOF data are accurately modeled using convolutions of back-to-back exponential functions with intrinsic peak profiles. Meanwhile, broader instrumental and sample-related effects are captured using the pseudo-Voigt profile, a composite function combining Gaussian (associated with instrument resolution and strain) and Lorentzian (linked to crystallite size and defects) contributions. This flexible modeling framework is universally applied across X-ray, neutron, and synchrotron scattering experiments.

The core objective of the Rietveld refinement is to minimize the residual func-

tion [177, 178]:

$$S = \sum_i w_i (y_i^{\text{obs}} - y_i^{\text{calc}})^2 \quad (153)$$

where y_i^{obs} is the observed intensity at step i , y_i^{calc} is the calculated intensity at step i , and w_i is the statistical weighting factor, typically $1/\sigma_i^2$.

The calculated intensity is given by:

$$y_i^{\text{calc}} = s \sum_k L_k |F_k|^2 \phi(2\theta_i - 2\theta_k) P_k A + y_i^{\text{bkg}} \quad (154)$$

where s is the scale factor, L_k is the Lorentz-polarization factor, F_k is the structure factor for the k -th reflection, ϕ is the peak profile function, P_k is the preferred orientation factor, A_k is the absorption correction, and y_i^{bkg} is the background intensity. The refinement quality is assessed using multiple statistical indicators:

Profile Residual (R_p):

$$R_p = 100 \times \frac{\sum_i |y_i^{\text{obs}} - y_i^{\text{calc}}|}{\sum_i y_i^{\text{obs}}} \quad (155)$$

Weighted Profile Residual (R_{wp}):

$$R_{wp} = 100 \times \sqrt{\frac{\sum_i w_i (y_i^{\text{obs}} - y_i^{\text{calc}})^2}{\sum_i w_i (y_i^{\text{obs}})^2}} \quad (156)$$

Bragg Residual (R_B):

$$R_B = 100 \times \frac{\sum_k |I_k^{\text{obs}} - I_k^{\text{calc}}|}{\sum_k I_k^{\text{obs}}} \quad (157)$$

Crystallographic Residual (R_F):

$$R_F = 100 \times \frac{\sum_k |F_k^{\text{obs}} - F_k^{\text{calc}}|}{\sum_k F_k^{\text{obs}}} \quad (158)$$

Goodness of Fit (Reduced Chi-squared, χ^2):

$$\chi^2 = \left(\frac{R_{wp}}{R_{exp}} \right)^2 \quad (159)$$

The expected residual R_{exp} is calculated as:

$$R_{\text{exp}} = 100 \times \sqrt{\frac{n-p}{\sum_i w_i (y_i^{\text{obs}})^2}} \quad (160)$$

where n is the number of observations and p is the number of refined parameters. These statistical indicators serve as critical metrics for evaluating both the convergence and the quality of the refinement. Lower values of R_p , R_{wp} , R_B , R_F , and χ^2 indicate a better fit between the model and the experimental data. An ideal refinement aims for χ^2 close to 1. Values significantly above 1 suggest poor model quality or insufficient parameterization, while values significantly below 1 may indicate overfitting. All Rietveld refinements in this study were performed using the **FULLPROF** [177, 178] software package.

* CHAPTER IV *

Characterization of the magnetic phase transitions in double perovskite $\text{Nd}_2\text{NiMnO}_6$

Through detailed analysis of neutron powder diffraction data we confirm that the double perovskite $\text{Nd}_2\text{NiMnO}_6$ adopts a monoclinic $P2_1/n$ structure with nearly complete B-site ordering of Ni^{2+} and Mn^{4+} cations. Below $T_C = 198\text{ K}$, magnetic susceptibility measurements and further analysis of neutron diffraction data reveal that the Ni^{2+} and Mn^{4+} sublattices undergo ferromagnetic ordering, as expected of strong 3d – 3d exchange interactions. Upon cooling through $T_N = 22\text{ K}$, a secondary magnetic transition is observed, below which we have discovered an additional non-collinear symmetry-breaking order of Nd^{3+} moments. We argue that the canting of the rare-earth moments naturally arises through the competition of f-d and f-f Heisenberg exchange interactions, which may be finely balanced in the double perovskite framework. Furthermore, the symmetry of the ground state magnetic structure implies significant Nd^{3+} easy plane anisotropy, and an effective decoupling of the antiferromagnetic spin canting from the transition metal sublattice. Between T_C and T_N , $\text{Nd}_2\text{NiMnO}_6$ shows anomalous behaviour in the frequency dependent AC magnetic susceptibility that is characteristic of reentrant spin-glass-like properties attributed to antisite disorder and competing interactions. Finally, analysis of isothermal magnetization yielded magnetic entropy changes that suggest $\text{Nd}_2\text{NiMnO}_6$ and related compounds have potential for magnetic refrigeration, showing a peak in the magnetic entropy change of $2.25\text{ J kg}^{-1}\text{ K}^{-1}$ at T_C under a 7 T field. The scaling behaviour of the magnetic entropy, paired with analysis of other critical exponents, showed that the ferromagnetic transition at T_C is consistent with a mean-field second-order phase transition. Taken together, our results have provided crucial details on the magnetic properties of $\text{Nd}_2\text{NiMnO}_6$, and further consolidate the expectation that double perovskites may serve as model systems for investigating competing magnetic interactions, magnetocaloric effects, and re-entrant spin-glass behavior.

Acknowledgements: The research presented in this chapter will be published as John M. Attah-Baah *et al.* (submitted). I synthesized the polycrystalline $\text{Nd}_2\text{NiMnO}_6$ sample under the supervision of Prof. Nilson Ferreira. NPD measurements were performed with Dr. Roger Johnson (co-supervisor), Dr. Dmitry Khalyavin, and Dr. Pascal Manuel, with data analysis conducted under Dr. Johnson’s guidance. Magnetic characterization was carried out with support from Romualdo Jr. and Maria Carvalho, supervised by Prof. Ferreira. Raman spectroscopy measurements were performed with the assistance of Diego Evaristo using Dr. Grando’s laboratory facilities. I sincerely appreciate their valuable contributions and expertise. This work was supported by CNPq (309184/2022-3, 141485/2021-0), CAPES (Finance Code 001; PDSE 88881.846711/2023-01), and FAPESP (EMU 18/08040-5). I acknowledge University College London for hosting and IFGW/UNICAMP for magnetometry access.

4.1 Introduction

The ABO_3 perovskite oxides are one of the most versatile families of crystal structures, and have been duly explored throughout the study of complex magnetic materials [179]. The versatility emerges primarily due to patterns of BO_6 octahedral tilts and rotations [18], typically described using Glazer notation [17, 26, 179], that can accommodate size mismatches among A and B cations and oxygen anions as quantified by the Goldschmidt tolerance factor. A vast range of perovskite materials have hence been synthesized with magnetic cations at both the A and B site. Derived from this structural framework are the rare-earth (RE) double perovskites (DPs), with general chemical formula $RE_2BB'\text{O}_6$. Here, three distinct crystallographic sites are now capable of accommodating different magnetic ion species, where the B and B' sites are usually occupied by transition metal ions [22, 24, 25].

In the presence of typical $a^-a^-c^+$ octahedral tilting, disorder among, say, B^{3+} and B'^{3+} cations maintains orthorhombic $Pnma$ symmetry. However, rock-salt ordering of, say, B^{2+} and B'^{4+} cations driven by electrostatic forces lowers the crystal symmetry to monoclinic $P2_1/n$. Notably, many such ordered DP compounds exhibit ferromagnetism (FM), which arises due to exchange interactions between the B^{2+} and B'^{4+} ions [180]. This scenario is distinct from the ternary

ABO_3 parent compounds which are typically antiferromagnetic (AFM) due to exchange. In some DPs, antisite disorder (ASD) of B and B' cations can introduce vastly more complex magnetic states [181, 182]. For example, in the nominally ordered DP $\text{La}_2\text{NiMnO}_6$, both FM and AFM orders coexist. The FM coupling is attributed to $\text{Ni}^{2+}(\text{t}_{2g}^6\text{e}_g^2) - \text{O}^2 - \text{Mn}^{4+}(\text{t}_{2g}^3\text{e}_g^0)$ exchange, while AFM coupling is associated with the $\text{Ni}^{2+/3+} - \text{O} - \text{Ni}^{2+/3+}$ and $\text{Mn}^{3+/4+} - \text{O} - \text{Mn}^{3+/4+}$ exchange induced by the ASD, which together lead to a spin- or cluster-glass state below 70 K [183]. Unveiling the complex interplay between these exchange interactions, and how they couple to local structural distortions leading to phenomena such as magnetocrystalline anisotropy and multiferroicity [184], is quintessential for designing multifunctional materials.

It was recently shown that replacing La^{3+} with magnetic RE^{3+} ions such as Nd^{3+} , *i.e.* $\text{Nd}_2\text{NiMnO}_6$, can dramatically modify the magneto-structural phase diagram. $\text{Nd}_2\text{NiMnO}_6$ crystallizes in a nominally B^{2+} and B'^{4+} cation ordered monoclinic $P2_1/n$ crystal structure. We note that both computational and experimental evidence have confirmed the presence of Ni^{2+} and Mn^{4+} ions, and refuted the possibility of mixed valence states providing clarity on the compound's magnetic dynamics [157, 185]. Introducing Nd^{3+} into the structure results in a reduced $\text{Ni} - \text{O} - \text{Mn}$ bond angle, weakening the ferromagnetic exchange and lowering T_C to ~ 200 K [186, 187]. A long-range ordered ferromagnetic structure has been proposed below $T < T_C$ [188]. A second magnetic transition near ~ 100 K was reported, and assigned to valence state fluctuations (*e.g.* $\text{Ni}^{3+}/\text{Mn}^{3+}$) [188] that may be attributed to ASD-induced frustration resulting in cluster-glass behavior [159]. Furthermore, interactions between the Nd^{3+} and transition metal sublattices are expected to become significant at temperatures below 50 K [187]. Indeed, this magnetic interplay has been highlighted by the low temperature ordering of the Nd moments relative to the $\text{Ni} - \text{Mn}$ magnetic structure, as indicated by neutron diffraction studies [189].

In this system, we report a detailed study of the structural and magnetic properties of $\text{Nd}_2\text{NiMnO}_6$ using DC and AC magnetometry combined with neutron powder diffraction. Our findings confirm the presence of Ni^{2+} and Mn^{4+} cations, with no evidence of Ni^{3+} or Mn^{3+} . We show that magnetic ordering develops below $T_C \sim 198$ K, with neutron diffraction confirming FM Ni-Mn exchange coupling [157]. Just below 100 K, anomalies in the AC magnetization suggest reentrant spin-glass behavior, which may be attributed to frustration be-

tween sublattice interactions in the presence of ASD, as evidenced by our mixed occupancy structural refinements. We have discovered a subtle kink in the AC susceptibility near $T_N = 22\text{ K}$ consistent with a second magnetic phase transition, which occurs concomitantly with the previously reported downturn in DC magnetization at low temperature [159, 187, 188]. Analysis of neutron diffraction data measured at 1.5 K demonstrates the onset of complex, non-collinear magnetic order of Nd^{3+} ions that contrasts previous studies [157]. Here, we find that the non-collinear order naturally arises from a competition between FM coupling of Nd^{3+} and transition metal ions (f - d exchange), and AFM coupling of Nd^{3+} ions (f - f exchange). Further, we note that spin-orbit coupling within the Nd $4f$ manifold and weak Dzyaloshinskii-Moriya interactions may contribute additional complexity in the presence of non-collinear spin arrangements. Finally, critical behavior analysis and magnetocaloric studies underscore the multifunctionality of $\text{Nd}_2\text{NiMnO}_6$, reinforcing its potential in magnetic applications.

4.2 Experiment

A polycrystalline sample of $\text{Nd}_2\text{NiMnO}_6$ was synthesized by a modified sol-gel route, using glycine ($\text{C}_2\text{H}_5\text{NO}_2$) as a chelating agent. In a sequential process, 2 g of $\text{C}_2\text{H}_5\text{NO}_2$ was slowly added to a 2 M starting solution containing a stoichiometric amount of $\text{Nd}(\text{NO}_3)_3 \cdot 6\text{H}_2\text{O}$, $\text{Ni}(\text{NO}_3)_2 \cdot 6\text{H}_2\text{O}$, and $\text{Mn}(\text{CH}_2\text{CO}_2)_2 \cdot 4\text{H}_2\text{O}$, with high purity (Aldrich, 99.97%) in a proportion of 2:1:1(Nd:Ni:Mn). The prepared sample solutions were kept at 200°C for 24 h on a hot plate for evaporation and xerogel formation. Subsequently, all the swollen xerogels were ground and pre-calcined at 1000°C for 12 hours to remove all organic solvent substrates. The resulting powder was successively pulverized and pressed at 80 MPa to form a dense pellet. The final calcination was carried out at 1200°C for 24 hours to help obtain the pure DP phase. The sample's formation and phase purity were initially analyzed at room temperature (RT) by x-ray diffraction (XRD) using a Rigaku DMAX Ultima+ diffractometer with monochromatic $\text{Cu-K}\alpha$ radiation, operating at 40 kV and 40 mA. Data were collected over a 2θ range of 5° to 90° with a step size of 0.02° in 2θ and a counting time of 20 s per step. The instrument was configured with a fixed divergence slit of $1/4^\circ$, an anti-scattering slit of $1/2^\circ$, and a sample mask of 10 mm. DC magnetometry measurements were

conducted using a superconducting quantum interference device (SQUID) magnetometer (MPMS-3, Quantum Design) within the temperature range of 2-300 K, with a maximum applied magnetic field (H) of ± 70 kOe. Demagnetization protocols were employed to ensure minimal bias from any trapped flux within the superconducting magnet. AC magnetometry measurements were performed using a Quantum Design Physical Properties Measurement System (PPMS) at ISIS Neutron and Muon Source, UK, with excitation fields of 0.5, 1, and 2 Oe, on cooling in zero DC field from 300 to 2 K. The measurement was repeated for 11, 110, 320, and 540 Hz excitation frequencies.

Neutron powder diffraction (NPD) measurements were conducted using the WISH diffractometer [190] at ISIS Neutron and Muon Source, UK. A 1.5485 g sample was loaded into a 6 mm diameter vanadium can, and mounted within a ^4He cryostat. High-counting-statistics measurements, each lasting 60 minutes, were conducted in the paramagnetic phase at 230 K and in the magnetic phases at 100 K (high temperature) and 1.5 K (low temperature). Subsequent crystal and magnetic structure refinements were performed using the FULLPROF suite [191]. Symmetry analysis were performed using the ISOTROPY software suite [102], including the ISODISTORT tool [192].

4.3 Results and Discussion

4.3.1 Crystal Structure

The cation ordered monoclinic ($P2_1/n$) DP crystal structure is shown in Figure IV.1, where Nd atoms occupy general positions (4e), while Ni and Mn are distributed across two symmetry inequivalent sublattices (2a and 2b, respectively). Three symmetry inequivalent oxygen sublattices (O1, O2, and O3) are located on general positions (4e). This structural model was refined against NPD data measured within the paramagnetic phase (at 230 K). Excellent agreement between the model and data were achieved (see Figure IV.2a), and the refined structural parameters are summarised in Table IV.1, which include lattice parameters, atomic positions, isotropic thermal factors, bond valence sum (BVS), selected bond distances and bond angles, and refinement reliability factors. We note that the absence of discernible impurity peaks up to the limits of instrumental sensitivity

confirmed that our $\text{Nd}_2\text{NiMnO}_6$ sample was phase-pure.

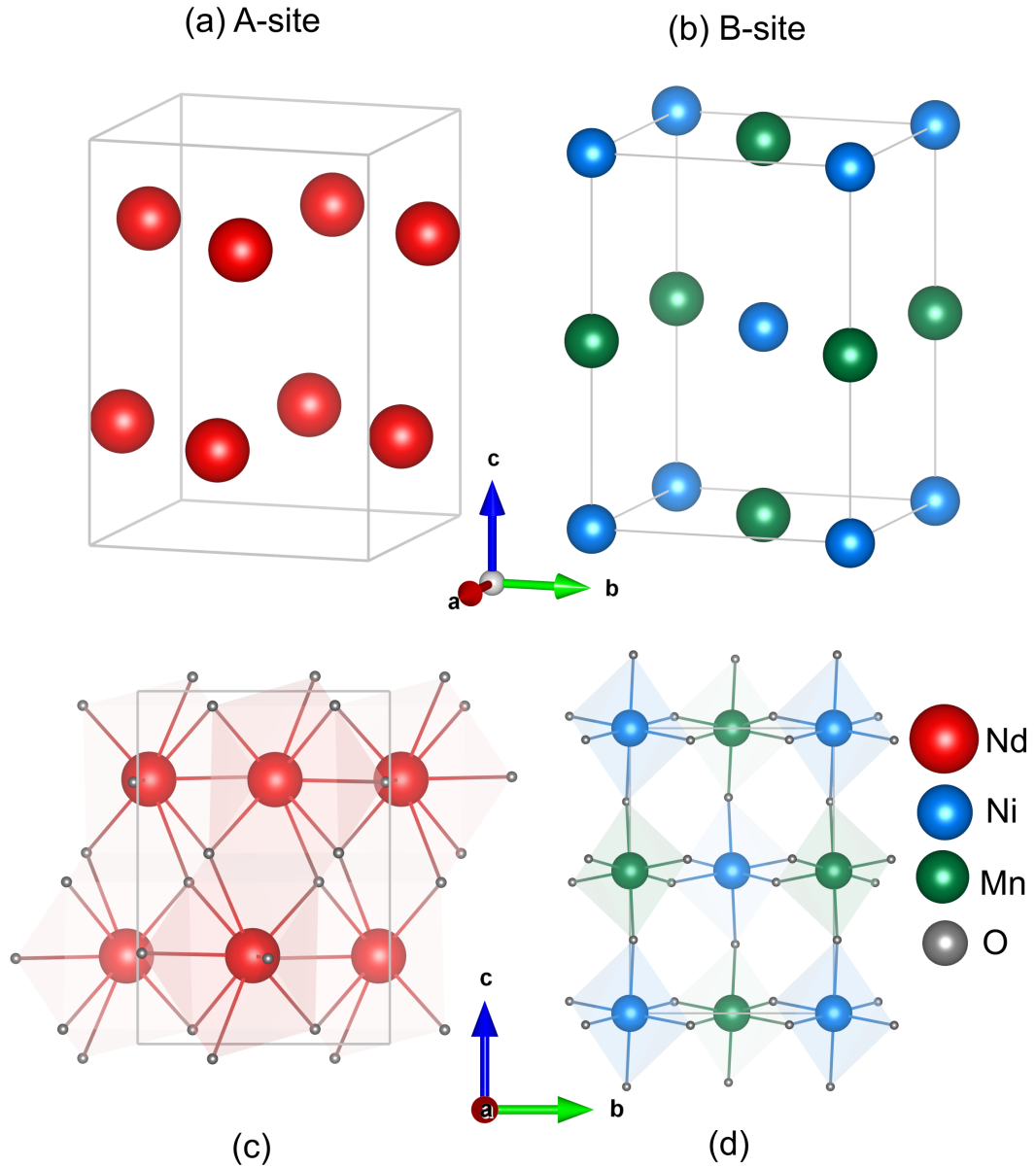


Figure IV.1: The cation ordered crystal structure of $\text{Nd}_2\text{NiMnO}_6$ (monoclinic $P2_1/n$) presented as a single unit cell. (a) The A -site with Nd atoms is depicted in red. (b) The B - and B' -sites are shown, with Ni and Mn atoms represented in blue and green, respectively. (c) and (d) Projections of the crystal structure along the a -axis illustrating the $(\text{Nd})\text{O}_8$ cuboctahedral coordinations and the $(\text{Ni,Mn})\text{O}_6$ tilted octahedral coordinations, respectively. The oxygen anions are represented by grey spheres.

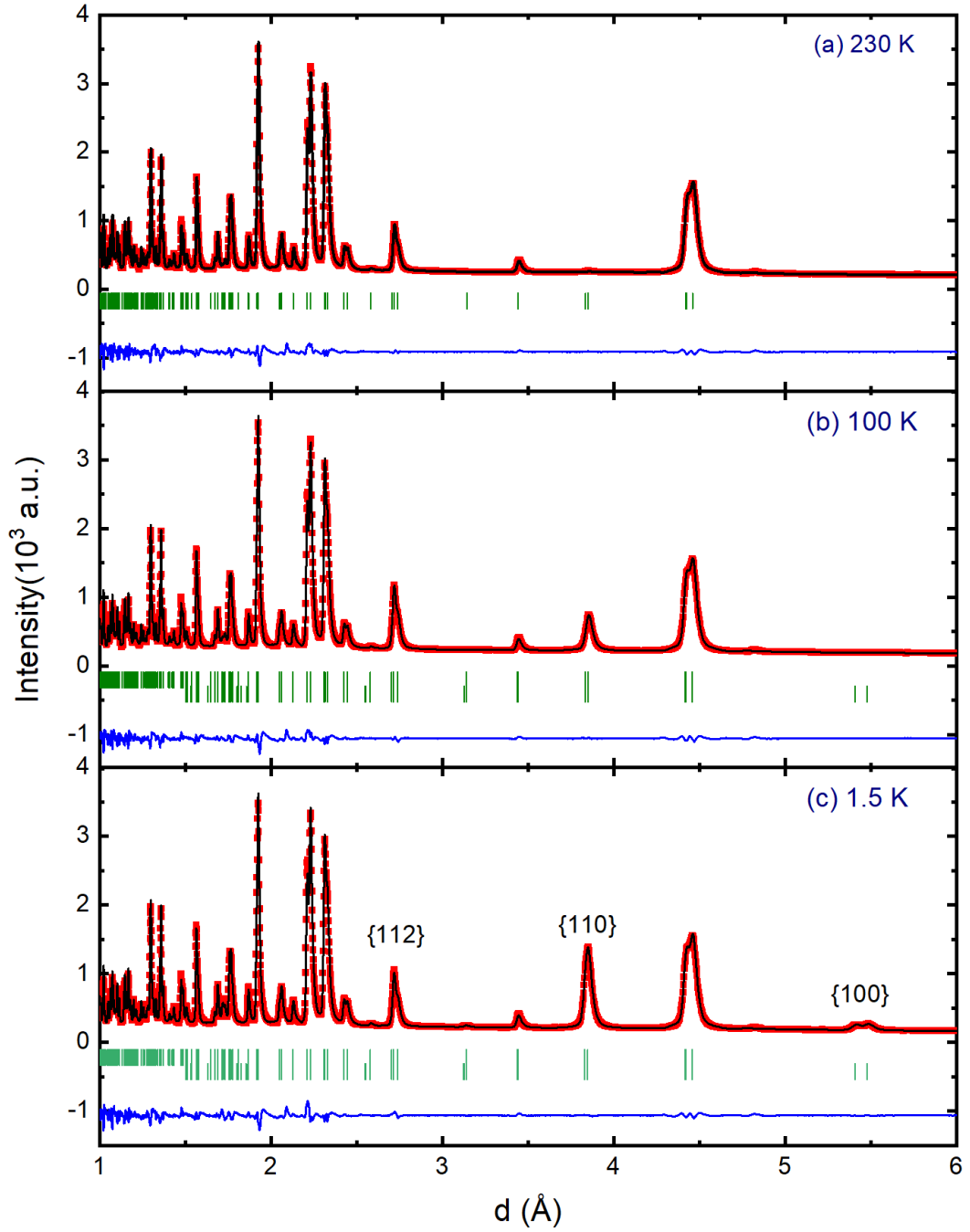


Figure IV.2: Neutron powder diffraction data measured in 3 magnetic phases; a) paramagnetic (230 K), b) first ordered (100 K) and c) ground state (1.5 K). Data are shown as red points, the fitted patterns as black lines, and the difference curve $I_{\text{obs}} - I_{\text{calc}}$ as blue lines at the bottom of the panes. The top and bottom row of green tick marks in each pane indicate the position of nuclear and magnetic Bragg peaks, respectively.

Table IV.1: Structural parameters of the Nd₂NiMnO₆ sample obtained through Rietveld refinement from NPD data at 230 K. The lattice parameters were determined to be $a = 5.4078(1)$ Å, $b = 5.4767(1)$ Å, and $c = 7.6648(2)$ Å, with $\beta = 90.0277(4)^\circ$ and a unit cell volume of $V = 227.007(1)$ Å³. Bond valence sums (BVS) were calculated using the parameters, $R_0(\text{Nd}^{3+}) = 2.66$, $R_0(\text{Ni}^{2+}) = 2.17$, $R_0(\text{Mn}^{4+}) = 1.753$, and $B = 0.37$, where the bond valence, $\text{BV} = \exp((R_o - R)/B)$. N.B. For the BVS, the majority cation is used for mixed occupancy sites.

Structural parameters				
Atom	Frac. Coord.	$U_{\text{iso}} (\times 10^{-2} \text{\AA}^2)$	BVS ($ e $)	Occ.
Nd	$x = 0.0097(6)$ $y = 0.5445(3)$ $z = 0.7495(4)$	0.98(1)	+3.27	Nd
Ni	$x = y = z = 0$	1.06(1)	+1.94	91%Ni 9% Mn
Mn	$z = 0.5$	1.06(1)	+3.59	91%Mn 9% Ni
O1	$x = 0.0787(5)$ $y = 0.0167(4)$ $z = 0.2575(6)$	1.26(7)	-	O
O2	$x = 0.2165(5)$ $y = 0.2967(6)$ $z = -0.0420(9)$	0.42(1)	-	O
O3	$x = 0.2030(6)$ $y = 0.2823(6)$ $z = 0.5404(10)$	1.42(2)	- -	O
Bond angles				
$\langle \text{O1-Ni-O1} \rangle$		180.0(0)		
$\langle \text{O1-Ni-O2} \rangle$		89.9(3), 90.1(3)		
$\langle \text{O1-Ni-O3} \rangle$		89.5(3), 90.5(3)		
$\langle \text{O1-Mn-O1} \rangle$		180.0(0)		
$\langle \text{O1-Mn-O2} \rangle$		89.3(3), 90.7(3)		
$\langle \text{O1-Mn-O3} \rangle$		89.5(3), 90.5(3)		
$\langle \text{Ni-O1-Mn} \rangle$		154.38(2)		
$\langle \text{Ni-O2-Mn} \rangle$		153.9(4)		
$\langle \text{Ni-O3-Mn} \rangle$		154.5(4)		
Bond lengths				
Ni-O1		2.021(5)		
Ni-O2		2.029(4)		
Ni-O3		2.024(4)		
Mn-O1		1.909(5)		
Mn-O2		1.922(4)		
Mn-O3		1.921(4)		
Reliability factors				
χ^2		11		
$R_{\text{P}}(\%)$		4.55		
$w_{\text{P}}(\%)$		3.04		
R_{Bragg}		3.82		

The degree of long-range cation ordering between Ni and Mn sites was refined

against the NPD data, revealing 9% ASD (Table IV.1). The refined lattice parameters; $a = 5.40779(1) \text{ \AA}$, $b = 5.47668(1) \text{ \AA}$, $c = 7.66482(2) \text{ \AA}$, with $\beta = 90.02769(4)^\circ$ and a unit cell volume of $V = 227.007(1) \text{ \AA}^3$ corroborates those previously published [157, 182, 183, 189]. The bond valence sum (BVS) analysis is consistent with the expected valences of Nd^{3+} , Ni^{2+} , and Mn^{4+} . Local crystal structure analysis reveals significant bond length and angle variations, indicating a highly distorted crystalline structure within the ordered $\text{Nd}_2\text{NiMnO}_6$ system. The Ni-O bond lengths are significantly longer than the Mn-O bond lengths, consistent with well-established cation order (and the calculated BVS), and the Ni-O-Mn bond angles indicate a significant departure from 180° due to octahedral tilting, resulting in complex magnetic exchange pathways [159, 193]. Using refined lattice parameters, the octahedral rotation angles: θ (octahedra tilt about the pseudocubic $(110)_p$ axis), ϕ (octahedral rotation about the pseudocubic $(001)_p$ axis), Φ (combine tilt about the three-fold $(111)_p$ axes), and Θ (octahedra distortion from average bonds) were calculated to quantify deviations from the ideal cubic perovskite configuration [194]. The angles were estimated as follows: $\theta = \cos^{-1}(a/b) \approx 9.10^\circ$, $\phi = \cos^{-1}(\sqrt{2}a/c) \approx 3.82^\circ$, $\Phi = \cos^{-1}(\sqrt{2}a^2/bc) = \cos^{-1}(\cos\gamma\cos\phi) \approx 9.86^\circ$, and $\Theta = [180 - \langle \text{Ni} - \text{O} - \text{Mn} \rangle]/2 \approx 12.87^\circ$.

4.3.2 DC magnetometry

The DC magnetic susceptibility χ , measured as a function of temperature, is presented in Figure IV.3a. Both field-cooled-cooling (FCC) and zero-field-cooled (ZFC) data exhibit a sharp increase in susceptibility on cooling below ≈ 200 K, likely signaling the onset of ferromagnetic or ferrimagnetic (FiM) long-range magnetic order. On further cooling, a downturn in the susceptibility can be seen below ≈ 50 K. These observations are consistent with previous reports [182, 183, 187, 193]. Below ≈ 200 K, the FCC and ZFC curves bifurcate, indicating a small degree of irreversibility due to spin freezing or blocking associated with magnetic anisotropy. The inset to Figure IV.3a shows $\chi(T)$ measured at higher fields ($H = 5$ and 10 kOe), where broadening of the transition and suppression of bifurcation are evident.

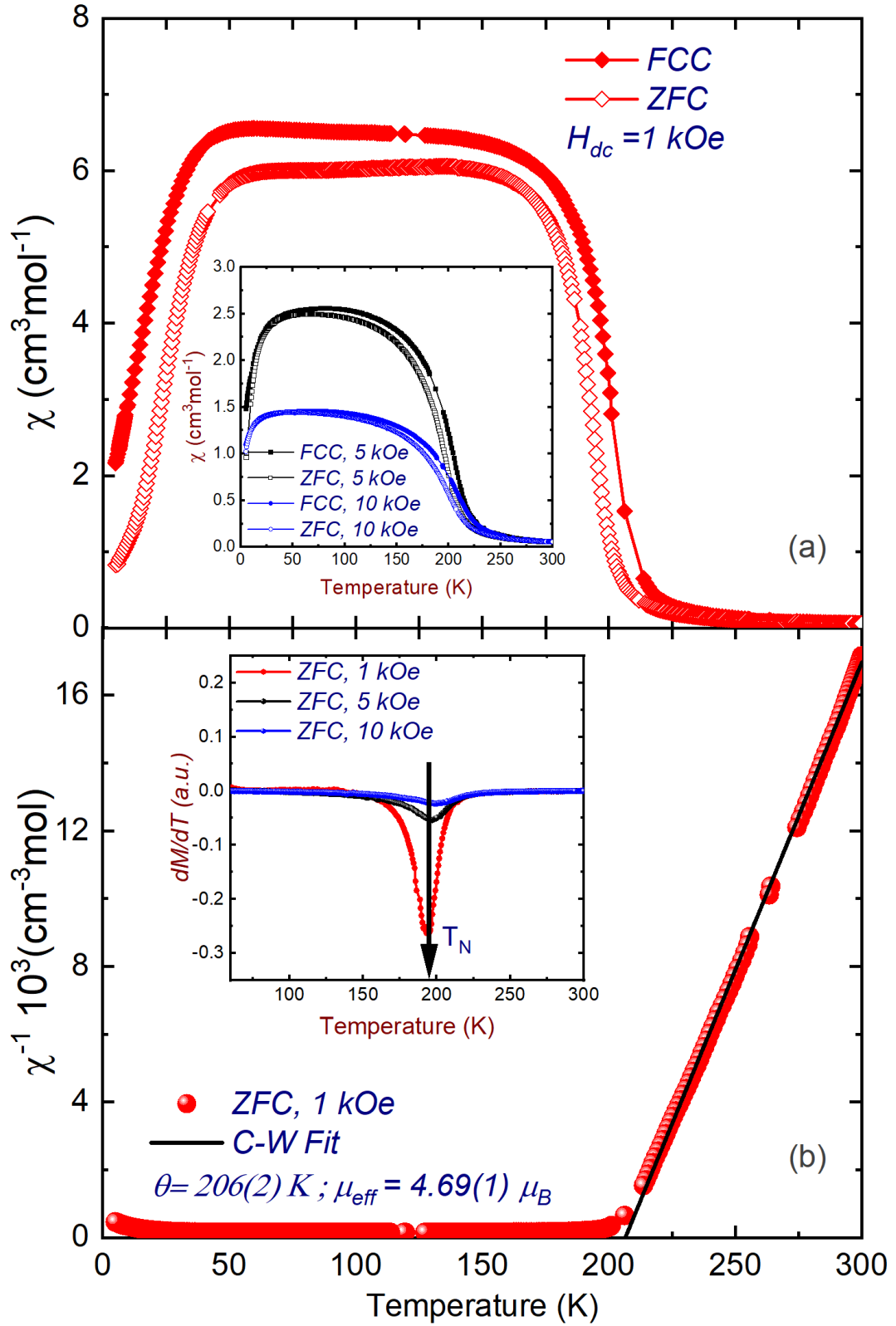


Figure IV.3: a) Temperature dependence of the DC magnetic susceptibility of $\text{Nd}_2\text{NiMnO}_6$ measured under ZFC and FCC conditions in an applied field of 1 kOe. The inset shows a comparison of M-T curves (ZFC/FCC) at different H_{dc} fields. (b) The inverse susceptibility ($\chi^{-1} = H/M$) as a function of temperature (T). The black line shows the paramagnetic region's best fit using the Curie-Weiss law.

Figure IV.3b shows the linear region of the inverse susceptibility χ^{-1} vs T

(above T_C in the region of 215 – 300 K), suggesting paramagnetic behavior well-described by the Curie-Weiss law:

$$\chi^{-1} = \frac{T - \theta_{\text{CW}}}{C}, \quad (161)$$

where C is the Curie-Weiss constant. Fitting to this linear region gave a positive Curie-Weiss temperature of $\theta_{\text{CW}} \approx 206(2) \text{ K}$, consistent with unfrustrated and dominant FM interactions. The calculated effective magnetic moment (μ_{eff}) was found to be $4.69(1) \mu_{\text{B}}/\text{f.u.}$ which is in excellent agreement with the theoretical value of $\mu = 4.80 \mu_{\text{B}}/\text{f.u.}$ (considering spin only moments, where $g_L = 2$, $S = 1$ and $S = \frac{3}{2}$ for Ni^{2+} and Mn^{4+} , respectively), hence confirming the oxidation states obtained by BVS analysis, above. The inset derivative dM/dT highlights the first transition, where a pronounced dip is observed at $T_C \approx 198 \text{ K}$, marking the onset of FM/FiM ordering. Furthermore, the field dependence in peak position ($H = 5$ and 10 kOe) is noticeable, where the position of T_C shifts to a higher temperature with increasing field.

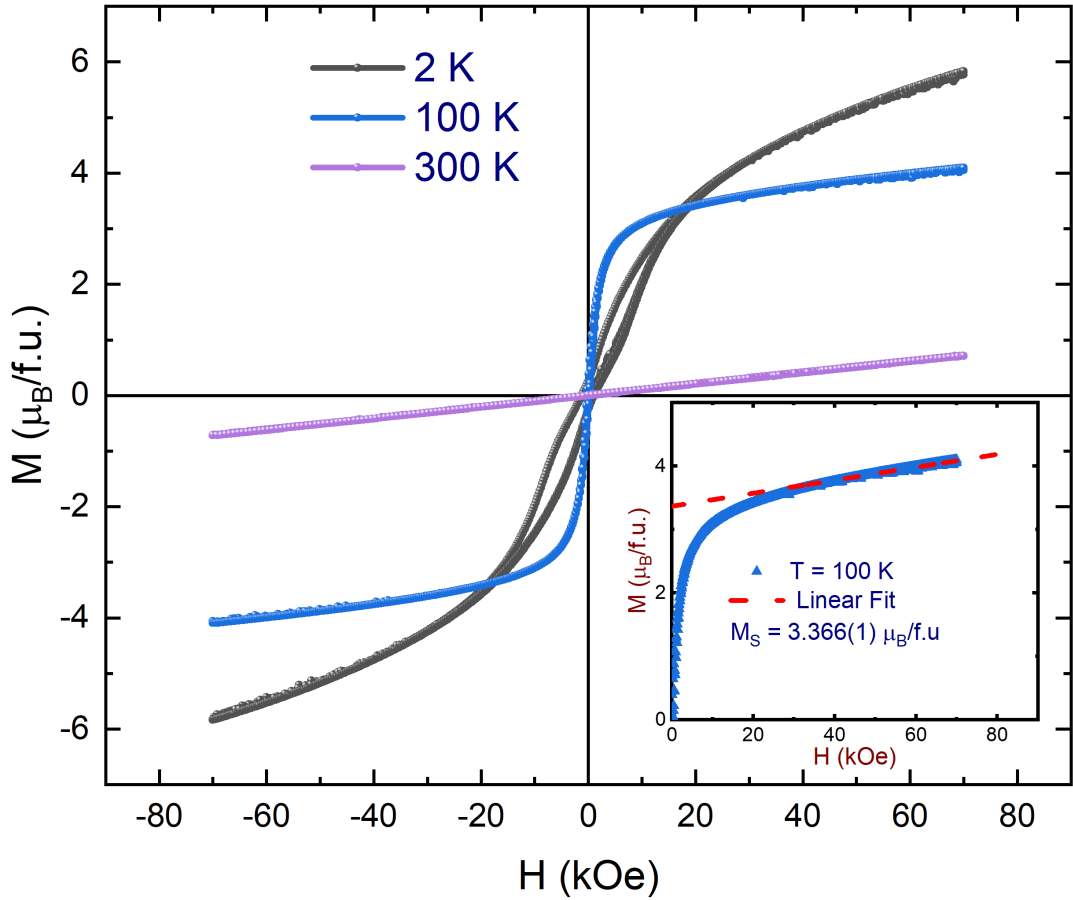


Figure IV.4: Isothermal $M(H)$ curves conducted at different temperatures under applied fields up to $\pm 70 \text{ kOe}$. The inset shows the linear extrapolation of saturated magnetization at 100 K.

Figure IV.4 shows isothermal $M(H)$ measurements performed at various temperatures. At $T = 300\text{ K}$, the field dependent magnetization is linear, as expected for the paramagnetic (PM) state. Upon cooling below the FM transition at T_C , the magnetization increased with an ' S' '-like shape without any sign of hysteresis (see, *e.g.* data measured at $T = 100\text{ K}$), but with remarkably rapid switching typically characteristic of a FiM or weak FM. The linear fit of the high-field region at $T = 100\text{ K}$ (see inset of Figure IV.4) yielded $M_S = 3.366(1)\mu_B/f.u.$, which is lower than the theoretically calculated value likely due to thermal fluctuations. Upon cooling to 2 K , the isothermal magnetization adopts a subtle double hysteresis loop, which may be indicative of frustrated interactions arising from the interplay of rare-earth and transition metal sublattices [195, 196]. A complete set of isothermal magnetization measurements are given in 4.3.6, which are used to show that the critical exponents that characterise phase transition at T_C are consistent with mean-field behaviour.

4.3.3 AC magnetometry

The temperature-dependence of the real, $\chi'(T)$, and imaginary, $\chi''(T)$, components of the ac magnetic susceptibility is shown in Figure IV.5. Both components show a sharp maximum at $T_C \approx 200\text{ K}$, which does not shift in temperature upon changing the excitation frequency; characteristic of a phase transition to long-range magnetic order [159, 197, 198]. The real component is frequency independent at all temperatures, and shows a drop in susceptibility below 50 K resembling the features observed in the FCC-ZFC DC magnetization (Figure IV.3). To the contrary, below T_C , $\chi''(T)$ shows a strong frequency dependence, with a broad maxima in the temperature range of $50 - 100\text{ K}$ shifting to higher temperatures as the frequency is increased. The magnitude of these shifts is consistent with re-entrant glassy behavior of spin clusters reported in other materials [199–201]. True reentrance occurs when FM long-range order vanishes at lower temperatures, and is replaced by a spin-glass state stabilized by disorder and competing interactions. However, our neutron powder diffraction results discussed below clearly show a large degree of long-range order is maintained down to the lowest measured temperatures. This discrepancy can be reconciled by the suggestion that at re-entrance, a randomly canted ferromagnetic state may be realized at

low temperature, rather than a pure spin-glass phase [201]. At low temperature, $\chi''(T)$ shows a sharp, frequency-independent anomaly at $T_N \approx 22$ K (see inset to Figure IV.5b), consistent with a second, low temperature magnetic phase transition. We note that $\chi'(T)$ was independent of the amplitude of the excitation field, while $\chi''(T)$ showed a small uniform increase between T_C and T_N on increasing the excitation from 0.5 to 2 Oe.

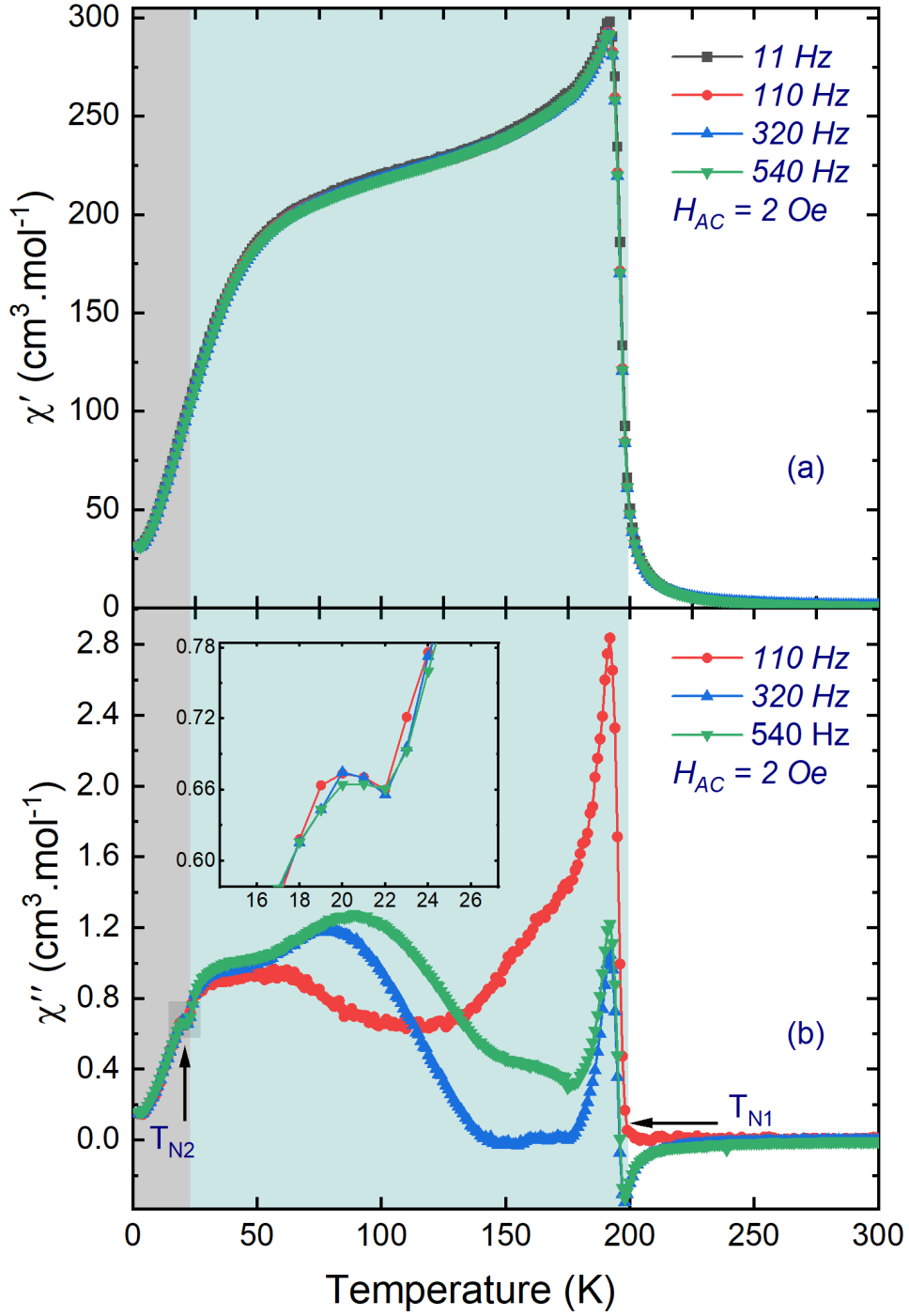


Figure IV.5: The real (a) and imaginary (b) parts of the AC magnetic susceptibility of $\text{Nd}_2\text{NiMnO}_6$, measured as a function of temperature at different frequencies under $H_{dc} = 2$ Oe. The inset shows an expanded view of T_{N2} .

4.3.4 Neutron powder diffraction

Notable changes in the NPD data were observed as the sample temperature decreased, consistent with the magnetic susceptibility anomalies described above. Below $T_C = 198$ K, magnetic peaks emerged that could be indexed as $\{112\}$, $\{110\}$, and $\{100\}$ relative to the $P2_1/n$ crystal structure (see Figure IV.2b). The magnetic peak widths were comparable to those of the nuclear reflections, indicating the onset of well-established long-range magnetic order. Furthermore, as the magnetic peaks coincided with the nuclear Bragg positions, the respective magnetic structure must have a Γ -point propagation vector, $\mathbf{k} = (0, 0, 0)$.

Magnetic symmetry analysis was performed using ISODISTORT. Table IV.2 defines symmetry-adapted modes for each magnetic sublattice, labeled F_i , A_i , C_i , and G_i , in terms of relative signs of the magnetic moment components at each site. Linear combinations of these modes that transform by single irreducible representations are shown towards the bottom of Table IV.2, where the polarisation (spin direction) of the mode is noted in subscript relative to the monoclinic b -axis. Only two irreducible representations (Γ_1^+ and Γ_2^+) enter into the decomposition of the magnetic representation for Ni and Mn sites, while four irreps (Γ_1^\pm and Γ_2^\pm) appear in the decomposition for Nd. We focus first on Γ_1^+ and Γ_2^+ magnetic structure solutions under the robust assumption that the magnetic transition metal ions play a central role in the stability of long-range magnetic order. Symmetry adapted modes of the former symmetry (Γ_1^+) involve a FM F mode aligned parallel to the monoclinic b -axis, supplemented by an AFM A -type mode perpendicular to b . Modes of the latter symmetry (Γ_2^+) are similar, but with the F mode perpendicular to the monoclinic b -axis and an A -type mode parallel to b . These magnetic structures correspond to the magnetic space groups $P2_1/n.1(14.75)$ and $P2_1'/n'(14.79)$, respectively.

Table IV.2: Magnetic modes that span the four symmetry-equivalent A -site Nd ($4e$) ions and the two symmetry-equivalent B -sites ($2a$ for Ni, $2b$ for Mn) within a single $P2_1/n$ unit cell. We define four modes for the Γ -point propagation vector, $\mathbf{k} = (0,0,0)$: F_i, A_i, C_i , and G_i along with their components, which describe the relative alignment of magnetic moments across the symmetry-related atomic sites. The subscript i represents the directional component of the magnetic moment relative to the monoclinic b -axis.

	Frac. coords.			Mag. modes			
<i>A</i> Site	<i>x</i>	<i>y</i>	<i>z</i>	<i>F_i</i>	<i>A_i</i>	<i>C_i</i>	<i>G_i</i>
Nd1	0	$\frac{1}{2}$	$\frac{3}{4}$	+	+	+	+
Nd2	$\frac{1}{2}$	0	$\frac{3}{4}$	+	−	−	+
Nd3	0	$\frac{1}{2}$	$\frac{1}{4}$	+	+	−	−
Nd4	$\frac{1}{2}$	0	$\frac{1}{4}$	+	−	+	−
<i>B</i> site							
Ni1	0	0	0	+	+		
Ni2	$\frac{1}{2}$	$\frac{1}{2}$	$\frac{1}{2}$	+	−		
Mn1	0	0	$\frac{1}{2}$	+	+		
Mn2	$\frac{1}{2}$	$\frac{1}{2}$	0	+	−		
Irrep.	Nd		Ni		Mn		
Γ_1^+	F_{\parallel}, A_{\perp}		F_{\parallel}, A_{\perp}		F_{\parallel}, A_{\perp}		
Γ_2^+	A_{\parallel}, F_{\perp}		A_{\parallel}, F_{\perp}		A_{\parallel}, F_{\perp}		
Γ_1^-	G_{\parallel}, C_{\perp}						
Γ_2^-	C_{\parallel}, G_{\perp}						

Two magnetic structure models that included magnetic moments on the A , B and B' sites, and transforming by Γ_1^+ and Γ_2^+ respectively, were tested against the NPD data measured at $T = 100\text{ K}$. Rietveld refinements achieved a reasonably good fit for both models, however, detailed examination conclusively identified that the $m\Gamma_2^+$ magnetic structure model (space group $P2_1'/n'$ (No. 14.79, basis = $[1,0,0], [0,1,0], [0,0,1]$, origin = $[0,0,0]$) was found to reproduce the observed magnetic intensities precisely. The initial, fully general model included nine free mode amplitudes, but we could readily exclude Nd moments from the $T = 100\text{ K}$ which refined to values close to zero within their standard uncertainty. The absence of Nd magnetic moments at this temperature is consistent with the typical behavior of A -site rare-earth ions in perovskite manganites, which are known to order at lower temperatures due to weak $f-d$ interactions [202]. Subsequent refinements also excluded the B and B' site A -type mode amplitude, as the fit to the data was insensitive to this subtle staggered magnetization along the b -axis, hence the F modes were constrained to be collinear within the ac plane.

The final refinement yielded excellent agreement factors ($R = 4.56\%$, $wR = 3.98\%$, $R_{\text{mag}} = 1.47\%$) with just three free parameters, confirming the reliability of the model. Magnetic moments for $1.75(1) \mu_B/\text{Ni}^{2+}$ and $2.18(1) \mu_B/\text{Mn}^{4+}$, with a polar angle $\theta = 143.56(2)^\circ$ were found (as detailed in IV.3). The refinement result is shown in Figure IV.6b, and the magnetic structure is depicted in Figure IV.6a, which is fully consistent with dominant d - d exchange interactions between Ni^{2+} and Mn^{4+} ions.

Table IV.3: Magnetic structure parameters refined at 100 K and 1.5 K. The moment directions are defined in spherical coordinates [7, 8] $m_x = m \cos(\phi) \sin(\theta) \|\mathbf{a}$, and $m_y = m \sin(\phi) \sin(\theta) \|\mathbf{b}$ and $m_z = m \cos \theta \|\mathbf{c}^*$, such that $\phi = 0$ constrains moments to the ac -plane. In this case $\mathbf{m} = [m_x, 0, m_z]$ represents the polarization of magnetic modes F_\perp , and A_\perp .

	100 K	1.5 K	
	$m\Gamma_2^+ (F_\perp)$	$m\Gamma_1^+ (A_\perp)$	$m\Gamma_2^+ (F_\perp)$
Ni			
$m (\mu_B)$	1.75(1)	—	1.89(1)
$\theta (^\circ)$	143.56(2)	—	103.08(2)
Mn			
$m (\mu_B)$	2.18(1)	—	2.45(1)
$\theta (^\circ)$	143.56(2)	—	103.08(2)
Nd			
$m (\mu_B)$	—	$\pm 0.68(4)$	$-0.91(2)$
$\theta (^\circ)$	—	193.08(2)	103.08(2)
$R (\%)$	4.56	4.87	
$wR (\%)$	3.98	4.42	
$R_{\text{Mag}} (\%)$	1.47	2.29	

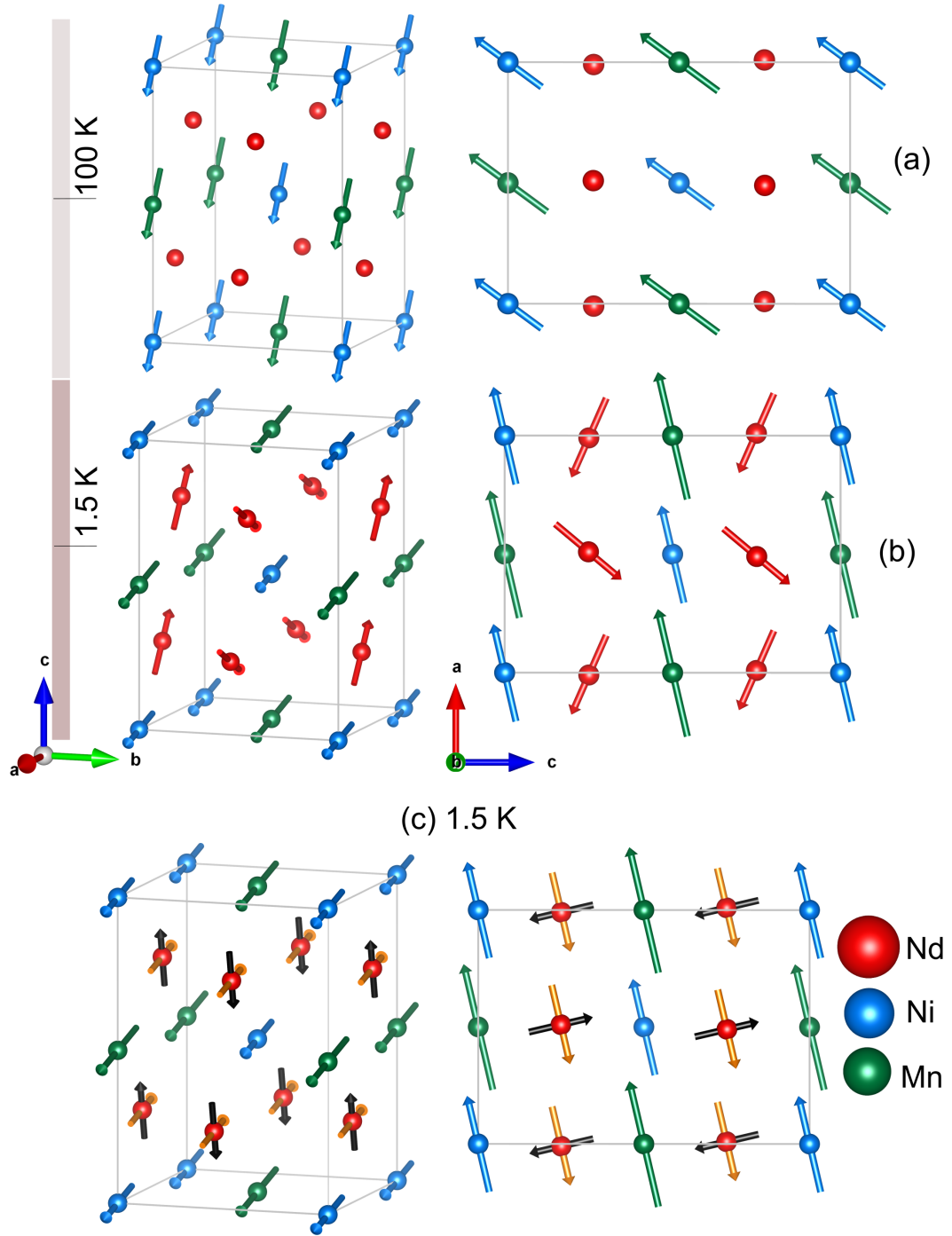


Figure IV.6: Refined magnetic structures of $\text{Nd}_2\text{NiMnO}_6$: (a) $m\Gamma_2^+$ Structure at 100 K, (b) $m\Gamma_1^+ + m\Gamma_2^+$ structure at 1.5 K, and (c) decomposition of F_\perp and A_\perp Nd moment components within the ac plane. Nd, Ni, and Mn atoms are represented in red, blue, and green, respectively, with the crystallographic unit cell outlined in grey.

At 1.5 K additional magnetic reflections ($\{100\}$ and $\{010\}$) appeared in the neutron diffraction data, concomitant with a redistribution of intensity in the magnetic peaks discussed above. These observations are consistent with a low temperature transition at $T_N = 22$ K (see Fig IV.5) to a ground state magnetic structure that is distinct from that refined at 100 K. The magnetic structure

maintains the Γ -point propagation vector ($\mathbf{k} = (0,0,0)$) in the ground state, and returning to our general Γ_2^+ magnetic structure model, we found that the observed changes in the NPD data could be partly accounted for by a rotation of the Ni and Mn FM moments within the ac plane, plus an additional F_\perp mode located on the Nd sublattice (Γ_2^+), but with moments aligned antiparallel relative to the Ni and Mn sublattices, clearly indicating that AFM f - d exchange interactions become significant at low temperature.

A complete description of the 1.5 K NPD data required an additional Nd A_\perp mode that transforms under Γ_1^+ , resulting in a non-collinear magnetic structure with moments constrained to the ac -plane. The admixture of Γ_1^+ and Γ_2^+ modes lowers the symmetry of this structure to $P\bar{1}.1$ (No. 2.4), with a basis defined by $[1,0,0]$, $[0,1,0]$, $[0,0,1]$, and origin at $[0,0,0]$. The final refinement yielded excellent agreement between observed and calculated profiles with factors ($R = 4.87\%$, $wR = 4.42\%$, $R_{mag} = 2.29\%$), confirming the reliability of the model. For the F_\perp modes, magnetic moments of $1.89(1) \mu_B/\text{Ni}^{2+}$, $2.45(1) \mu_B/\text{Mn}^{4+}$ and $-0.91(2) \mu_B/\text{Nd}^{3+}$, with a polar angle $\theta = 103.08(2)^\circ$, were found. The additional A_\perp mode is associated with an Nd magnetic moment component of $0.68(4) \mu_B$ with a polar spin angle of $\theta = 193.03(2)^\circ$ in the ac plane (perpendicular to the FM Nd moments). The refinement result is shown in Figure IV.2c, and the magnetic structure is depicted in Figures IV.6b and IV.6c. These findings contradict the previously reported ground state magnetic structure [189]. However, the above non-collinear ordering of Nd moments can be naturally understood in terms of competing antiferromagnetic f - d and f - f exchange interactions. The former introduces antiparallel alignment of the Nd F mode (yellow arrows in figure IV.6c) with respect to the transition metal moments, while the latter introduces an orthogonal, superposed Nd A mode (black arrows in figure IV.6c). At the mean-field level, the canting angle will then depend on the relative strength of the f - d and f - f exchange. We note that the Nd A mode must break symmetry to lie within the ac plane, as opposed to alignment along the b -axis allowed within the Γ_2^+ magnetic symmetry. This symmetry breaking may be driven by significant easy-plane anisotropy of the Nd^{3+} ions, and interestingly, effectively decouples the Nd A mode from the transition metal ferromagnetic structure.

4.3.5 Magnetocaloric Effect

The net change in magnetic entropy ($-\Delta S_M$) can be quantitatively estimated using isothermal magnetization $M(H)$ data, providing insight into the magnetocaloric effect (MCE) and associated magnetic transitions. As shown in Figure IV.7a, the $M(H)$ curves measured over the field range of 0–7 T at temperatures from 2–300 K demonstrate a sharp increase at low fields, followed by a linear rise without approaching saturation at high fields. The finite change in total magnetic entropy of a system due to a change in temperature (ΔT) and magnetic field (ΔH) is expressed as

$$\begin{aligned}\Delta S_{MT} &= S_M(H + \Delta H, T + \Delta T) - S_M(H, T) \\ &= \int_H^{H+\Delta H} \left[\frac{\partial M(H, T + \Delta T)}{\partial T} \right]_H dH \\ &\quad + \int_T^{T+\Delta T} \frac{C'_H(H, T)}{T} dT,\end{aligned}\tag{162}$$

To aid analysis of discrete magnetization data the above equation can be approximated as [203, 204]

$$\Delta S_M(T) = \frac{(M(T) - M(T + \Delta T))}{\Delta T} H,\tag{163}$$

where $M(T)$ and $M(T + \Delta T)$ represent values of the isothermal magnetization measured at temperatures T and $T + \Delta T$, at an applied field of H . Note that in this case we have taken the change in field ΔH to be relative to zero [205]). Figure IV.7b shows the temperature dependence of $-\Delta S_M$ for different fields. ΔS_M exhibits a broad peak centered at T_C decreasing symmetrically on both sides as expected for a second-order FM-PM phase transition, and below $T < 50$ K anomalous behavior occurs likely due to the ordering of Nd³⁺ rare-earth ions [180].

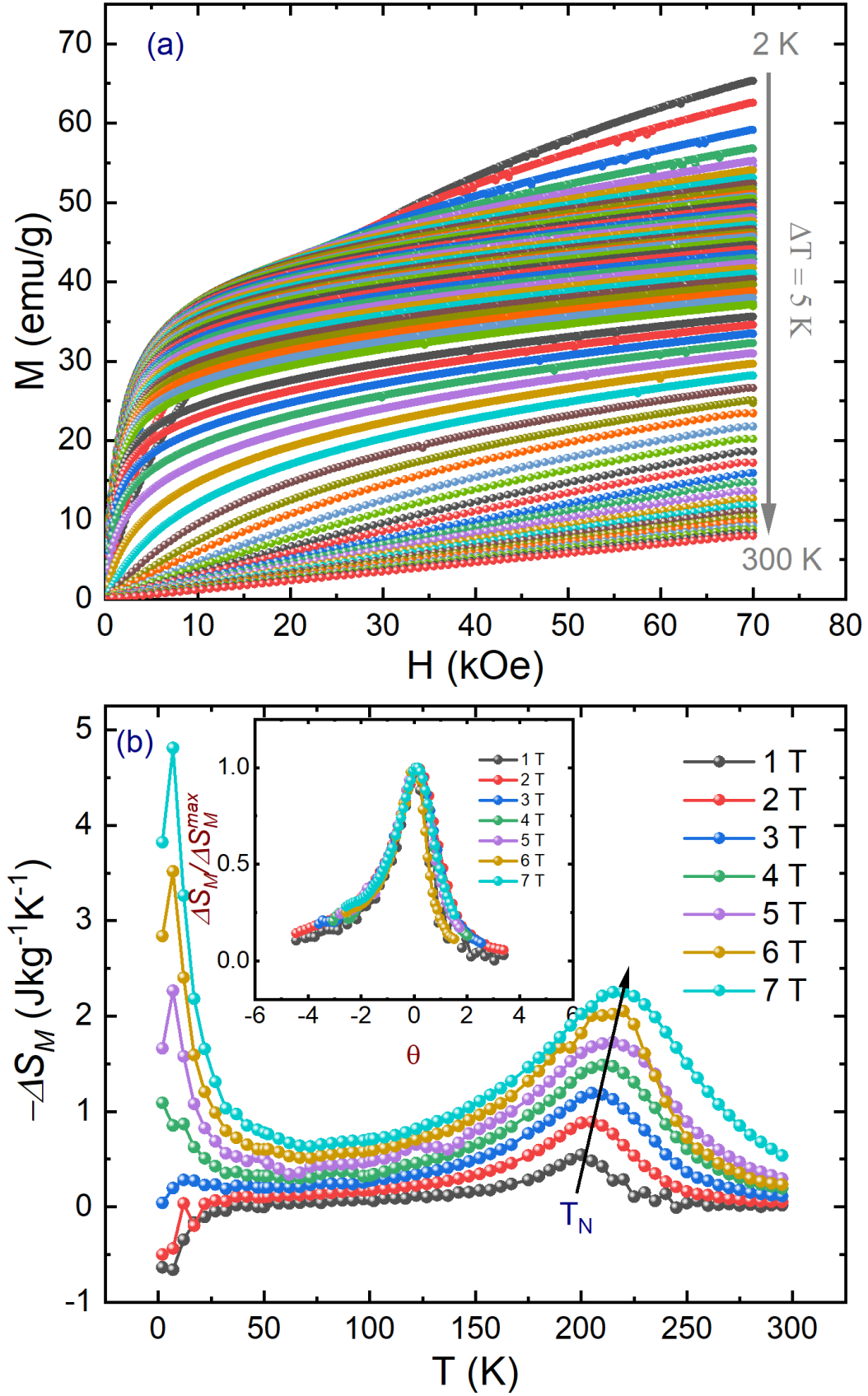


Figure IV.7: (a) Isothermal 1st quadrant $M(H)$ curves conducted at $T = 2 - 300$ K with an interval of $\Delta T = 5$ K. (b) Thermal profile of field-induced magnetic entropy change, $-\Delta S_M$, estimated from isothermal magnetization curves from $T = 2 - 300$ K, under various applied magnetic fields. Inset shows the plot of normalized ($\frac{\Delta S_M}{\Delta S_M^{\max}}$) versus reduced temperature θ .

The peak in $-\Delta S_M(T)$ at T_C increases with increasing field, and shifts to higher temperatures. At $H = 7$ T, a maximum entropy change of $-\Delta S_M^{max} = 2.25 \text{ J kg}^{-1} \text{ K}^{-1}$ is observed, which is smaller than some values reported for Ni/Mn-based double perovskites [185, 206] but somewhat larger than previous measurements on the Nd system [180]. We note that $-\Delta S_M^{max}$ follows a power law dependence on field, $-\Delta S_M^{max} \propto H^n$, with $n = 0.667(1)$ as shown in Figure IV.8a. This value agrees strongly with the mean-field ferromagnetic value of $n = 2/3$ [207–209].

The MCE at T_C was further examined using a normalizing universal scaling law. First, values of $-\Delta S_M(T)$ for a given applied field were scaled by a factor $\Delta S_M / \Delta S_M^{max}$, and second, the temperatures were scaled to a reduced temperature θ_{\pm} defined as follows [208]:

$$\theta_- = \frac{T_{max} - T}{T_{Cold} - T_{max}}, \quad T < T_{max}, \quad (164)$$

$$\theta_+ = \frac{T - T_{max}}{T_{Hot} - T_{max}}, \quad T > T_{max}, \quad (165)$$

where T_{max} denotes the temperature at $-\Delta S_M^{max}$, and T_{Cold} and T_{Hot} are the temperatures of two reference points (below and above T_C) at full-width-half-maximum of the peak in $-\Delta S_M$. As highlighted in the inset of Figure IV.7b, the rescaled curves collapse onto a single unified curve; behaviour typical of a second-order FM phase transition.

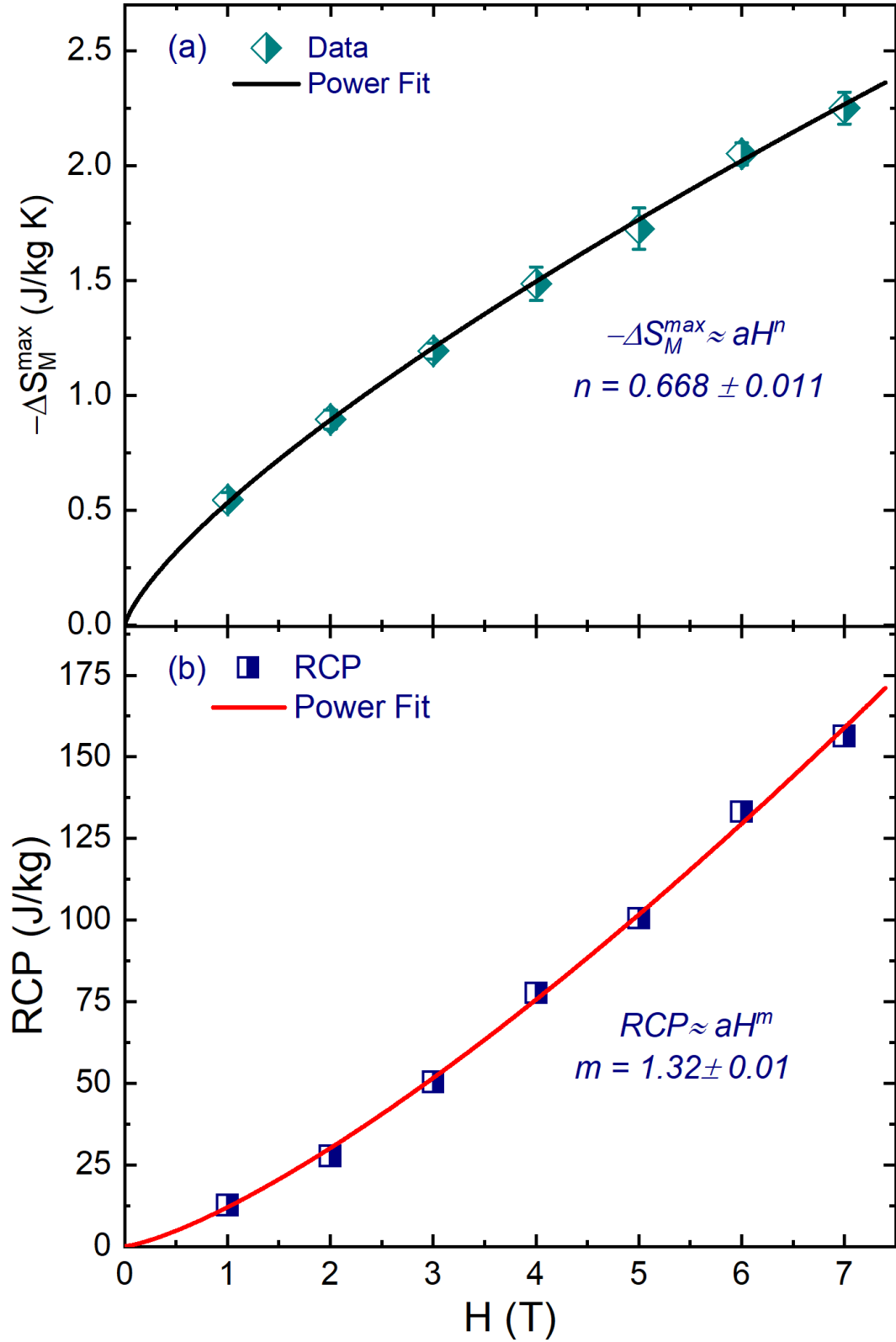


Figure IV.8: (a) Field dependence of maximum magnetic entropy change ($-\Delta S_M^{\max}$) fit by a power law (solid red line). (b) Relative cooling power (RCP), with a power law fit (solid black line)

The relative cooling power (RCP) parameter is typically used to evaluate the cooling efficiency of candidate MCE materials. The RCP can be determined from

the $-\Delta S_M(T)$ curves using the equation [210, 211]

$$RCP = |\Delta S_M^{max}| \cdot \Delta T_{FWHM}, \quad (166)$$

where $\Delta T_{FWHM} = T_{Hot} - T_{Cold}$. The RCP value as a function of the magnetic field H is displayed in Figure IV.8b, which shows a monotonic increase with ΔH from $\sim 13 \text{ Jkg}^{-1}\text{K}^{-1}$ at 1 T to $\sim 157 \text{ Jkg}^{-1}\text{K}^{-1}$ at 7 T. The field dependence could be well fit by the power law $RCP \approx H^m$, with $m = 1.12(3)$. These values of RCP are comparable to or exceed those of other oxide-based magnetocaloric materials but remain below the benchmarks for room-temperature refrigeration (typically $> 300 \text{ Jkg}^{-1}\text{K}^{-1} \leq 5\text{T}$) [212, 213]. However, the strong field dependence suggests that $\text{Nd}_2\text{NiMnO}_6$ and related compounds could be promising for cryogenic cooling application, where moderate RCP values ($\sim 50 - 200 \text{ Jkg}^{-1}\text{K}^{-1} \leq 5\text{T}$) are sufficient [204, 207, 214]. Further optimization, such as chemical substitution and/or nano-structuring may enhance their performance towards practical refrigerants.

4.3.6 Critical Point Exponents

The critical behavior of magnetic systems near a second-order phase transition is characterized by a set of interrelated critical exponents: β, γ , and δ , which are defined as follows:

$$M(T) \propto (T_C - T)^\beta, \quad T < T_C, \quad (167)$$

$$\chi_0^{-1} \propto (T - T_C)^\gamma, \quad T > T_C \quad (168)$$

$$M \propto H^{\frac{1}{\delta}}, \quad T = T_C \quad (169)$$

Mean-field theories predict critical exponents of $\beta = 1/2$, $\gamma = 1$, and $\delta = 3$. In this case, Arrott plots (M^2 vs H/M), which measure the critical exponent δ , are expected to consist of a set of parallel straight line isotherms close to T_C . The Arrott plot for $\text{Nd}_2\text{NiMnO}_6$ within the temperature range of 184 – 212 K is shown in Figure IV.9a, and clearly adheres to the mean-field value of $\delta = 3$. We note that the low-field regions have been excluded, where strong curvature and deviations from linearity arise due to demagnetization effects and higher-order contributions. The value of $T_C = 197(7)$ K was determined by identifying

the isotherm that intersects the origin. Figure IV.9b shows the temperature dependence of the spontaneous magnetization, $M(T)$, and the inverse magnetic susceptibility, $\chi^{-1}(T)$, obtained by extrapolating the isotherms discussed above. Fitting Equations 167 and 168 to the $T < T_C$ and $T > T_C$ regions yield T_C values of 196.88(1) K and 198.03(1) K, respectively, and provide excellent agreement with the data for mean-field values of the critical exponents.

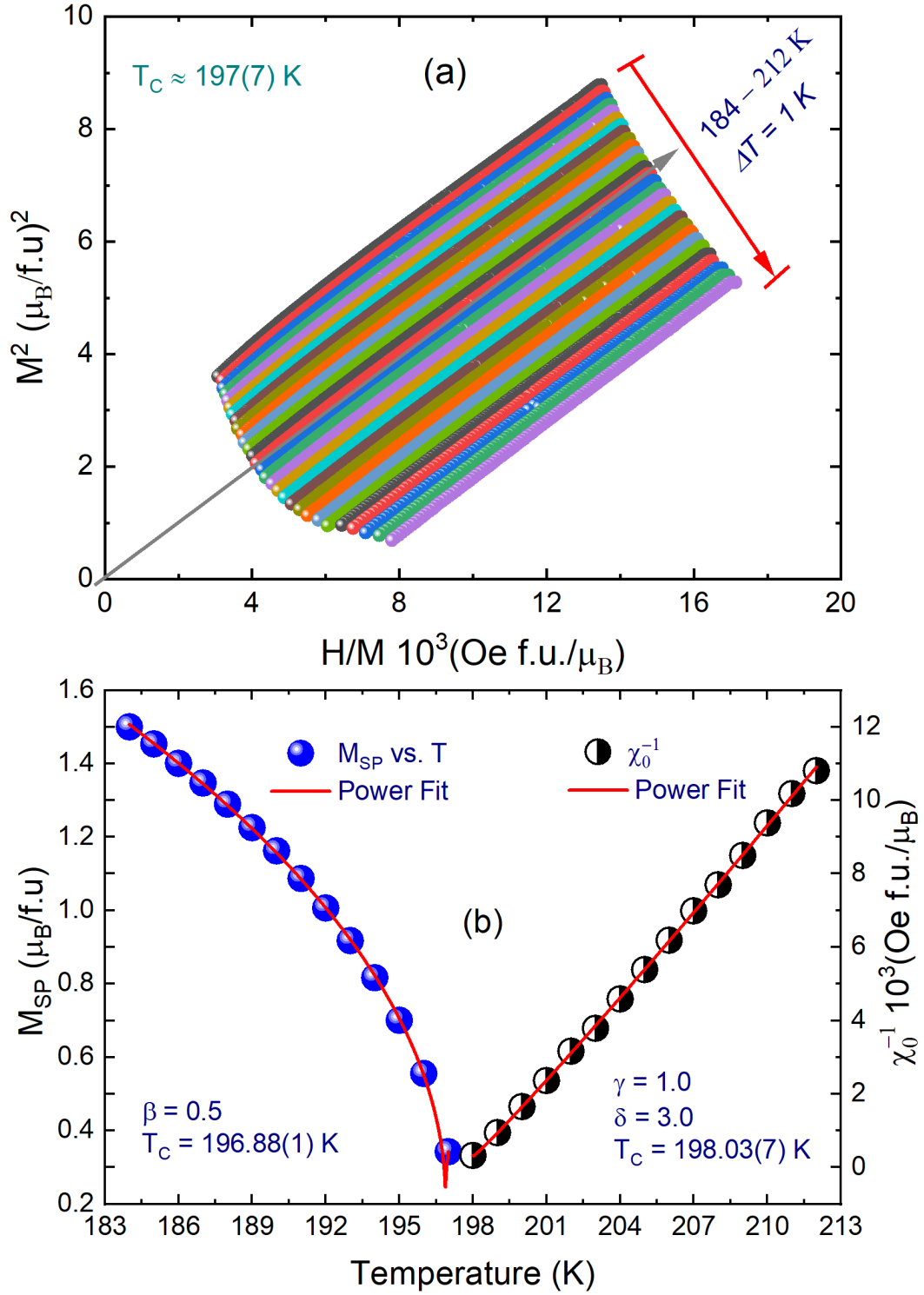


Figure IV.9: (a) Arrot plot of isotherms with $\delta = 3$. (b) Temperature dependence of the spontaneous magnetization $M_S(T)$ (left) and the inverse initial magnetic susceptibility $\chi_0^{-1}(T)$ (right), obtained from the field region of $H < 1.5 \text{ T}$ extrapolation of the Arrott plot with $\beta = 1/2$ and $\gamma = 1$.

Furthermore, the critical behavior of $\text{Nd}_2\text{NiMnO}_6$ was examined using Kouvel-Fisher (KF) analysis [215] with mean-field critical exponents ($\beta = 0.5$, $\gamma = 1.0$, $\delta = 3.0$). The KF relations for spontaneous magnetization $M_S(T)$ and inverse

susceptibility $\chi_0^{-1}(T)$ are given by:

$$\frac{M_S(T)}{dM_S/dT} = \frac{T - T_C}{\beta} \quad (170)$$

$$\frac{\chi_0^{-1}(T)}{d\chi_0^{-1}/dT} = \frac{T - T_C}{\gamma} \quad (171)$$

Figure IV.10a shows linear fits from Kouvel-Fisher analysis yielding consistent Curie temperatures ($T_C = 196.88(1)$ K from magnetization, $T_C = 198.06(6)$ K from susceptibility), with less than 2% discrepancy confirming mean-field behavior. The critical isotherm analysis in Figure IV.10b at $T_C = 198$ K demonstrates mean-field scaling through [216–218]: (i) the obtained slope 0.333(3) matching $1/\delta$ for $\delta = 3.0$, and (ii) excellent data collapse ($R^2 > 0.99$). Together with Widom scaling ($\delta = 1 + \gamma/\beta$ for $\beta = 0.5$, $\gamma = 1.0$), these results establish Nd₂NiMnO₆ as a model mean-field system with dominant long-range interactions, contrasting with defect-affected perovskites [211, 214, 219]. To verify the reliability of the critical exponents and T_C , we employ the scaling theory of magnetic phase transitions. Near the critical region, the magnetization follows the scaling relation [216, 218]:

$$M(H, \varepsilon) = \varepsilon^\beta f_\pm \left(\frac{H}{\varepsilon^{\beta\gamma}} \right) \quad (172)$$

where $\varepsilon = |T - T_C|/T_C$, and f_+ ($T > T_C$) and f_- ($T < T_C$) are regular analytic functions. Defining the renormalized magnetization $m = M|\varepsilon|^{-\beta}$ and field $h = H|\varepsilon|^{-(\beta\gamma)}$, Equation (172) reduces to:

$$m = f_\pm(h) \quad (173)$$

Figure IV.10c presents the scaled magnetization $m \equiv M|\varepsilon|^{-\beta}$ versus scaled field $h \equiv H|\varepsilon|^{-\beta\gamma}$, showing complete data collapse onto distinct branches for $T < T_C$ (ordered phase) and $T > T_C$ (disordered phase) [219] in both linear and logarithmic (inset) representations. This scaling behavior is further confirmed through two independent tests: (i) the m^2 versus h/m plot in Figure IV.10d main panel, and (ii) the universal scaling plot of $MH^{-1/\delta}$ versus $\varepsilon H^{-1/(\beta\delta)}$ in Figure IV.10 inset. The perfect data collapse in all representations, with T_C ($\varepsilon = 0$) precisely located at the origin of the scaled coordinates, provides rigorous validation of both the critical exponents with a transition temperature $T_C = 198.06(6)$ K.

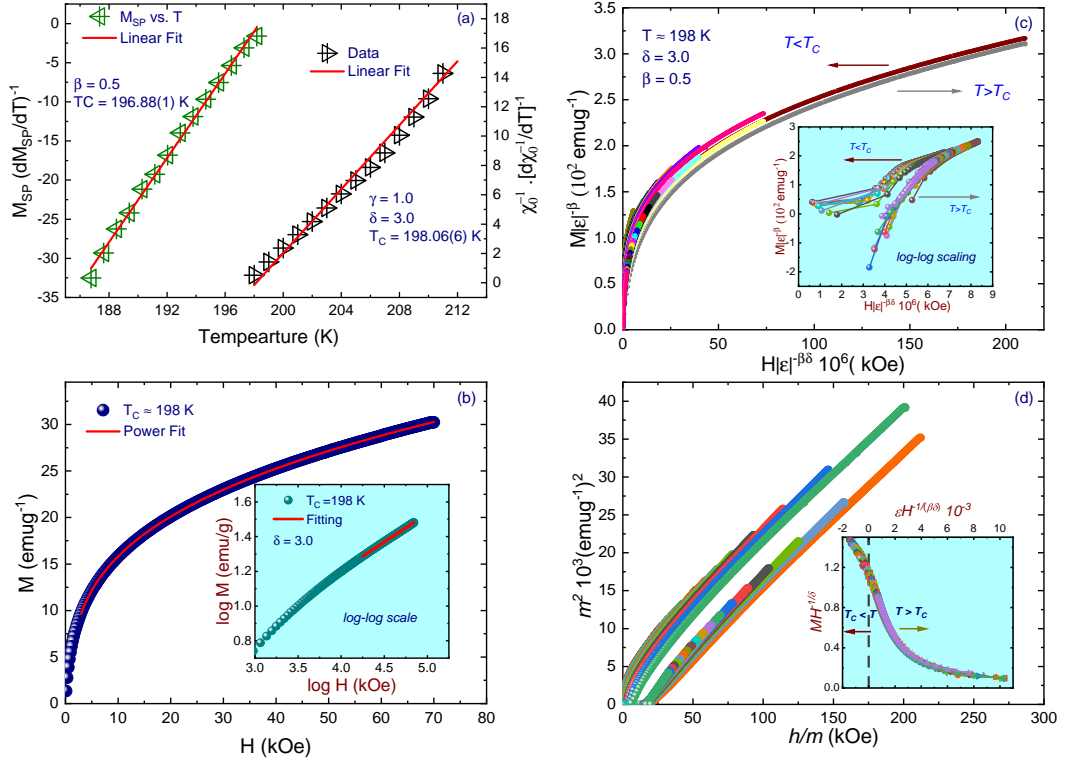


Figure IV.10: (a) Kouvel-Fisher plots of $M_S/(dM_S/dT)^{-1}$ (left) and $\chi_0^{-1}/(d\chi_0^{-1}/dT)^{-1}$ (right) for $\text{Nd}_2\text{NiMnO}_6$, with solid lines representing linear fits. (b) Critical isotherm $M(H)$ measured at $T_C = 198 \text{ K}$. Inset: log-log plot of the same data with the fitted slope corresponding to $1/\delta$. (c) Scaling plots of renormalized magnetization m versus renormalized field h below and above T_C , demonstrating data collapse onto two distinct branches. Inset: the same plots in log-log scale. (d) Plots of m^2 versus h/m for $\text{Nd}_2\text{NiMnO}_6$. Inset: rescaled $M(H)$ curves plotted as $MH^{-1/\delta}$ versus $\epsilon H^{-1/(\beta\delta)}$, further confirming scaling behavior.

4.3.7 Phonon Dynamics

The low-temperature (20 K) Raman spectrum of $\text{Nd}_2\text{NiMnO}_6$, shown in Figure IV.11, exhibits four well-resolved phonon modes at $A_g^I = 497.61(38) \text{ cm}^{-1}$, $A_g^{II} = 514.19(13) \text{ cm}^{-1}$, $B_g = 635.35(58) \text{ cm}^{-1}$, and $A_g^{III} = 655.53(9) \text{ cm}^{-1}$, as determined by Gaussian-Lorentzian (G-L) deconvolution. The absence of spectral weight near 377 cm^{-1} , a characteristic of rare-earth oxide (e.g., Nd_2O_3) impurities [220, 221], confirms phase purity. The 2D Raman intensity map (Figure IV.11, below) demonstrates the persistence of these modes across 20-300 K, with no abrupt shifts or splitting, unequivocally ruling out structural phase transitions. This thermal stability is further corroborated by the full temperature-dependent dataset provided in the Appendix 2.1, mirroring the behavior of isostructural $\text{La}_2\text{CoMnO}_6$ [222] and $\text{La}_2\text{NiMnO}_6$ [222, 223]. The A_g modes ($497\text{-}655 \text{ cm}^{-1}$) are assigned to symmetric stretching vibrations of the (Ni/Mn) O_6 octahedra,

while the B_g mode (635 cm^{-1}) arises from antisymmetric bending motions of oxygen atoms [223–225]. The narrow linewidth of A_g^{III} ($\Delta\omega \approx 0.9\text{ cm}^{-1}$) suggests minimal anharmonicity, whereas the broader B_g mode ($\Delta\omega \approx 5.8\text{ cm}^{-1}$) may reflect coupling to spin fluctuations or local disorder[226]. These assignments align with group-theoretical predictions for $P2_1/n$, which anticipate 24 Raman-active modes ($12A_g + 12B_g$) from translational/librational (T/L) modes ($< 400\text{ cm}^{-1}$) and octahedral distortions (ν_1, ν_2, ν_5) [17, 18, 220, 224, 227]. The reduced mode count in NNMO compared to theory likely stems from overlapping peaks or selective resonance enhancement [228], contrasting with Gd-substituted YCMO, where smaller A-site cations (Y^{3+} , Gd^{3+}) amplify octahedral tilting and activate additional modes [221].

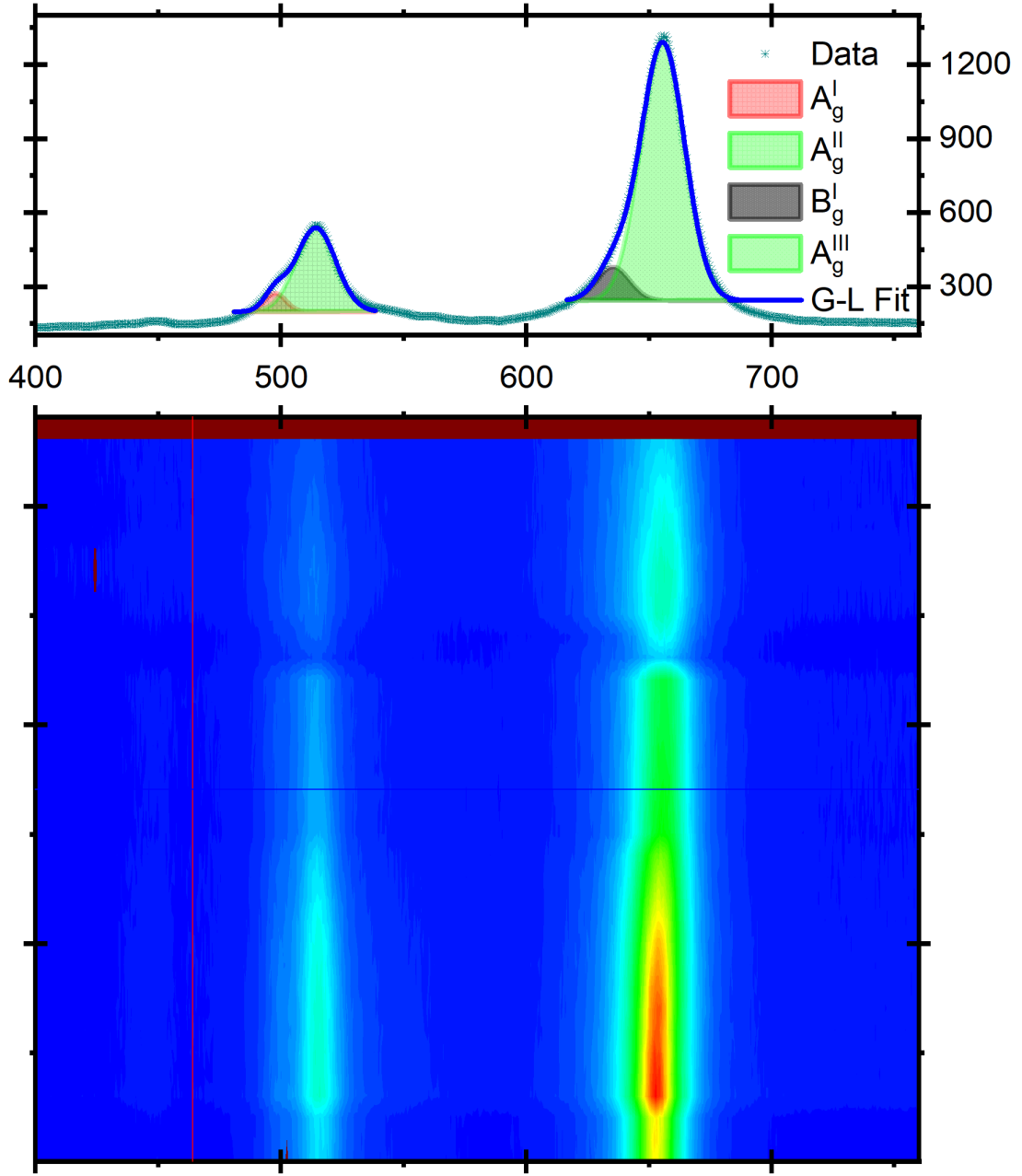


Figure IV.11: Raman mode analysis and temperature evolution in $\text{Nd}_2\text{NiMnO}_6$. (Top) Raman spectrum at 20 K fitted with Gaussian-Lorentzian (G-L) profiles, highlighting the decomposition into individual phonon modes: A_g^I , A_g^{II} , B_g^I , and A_g^{III} . Experimental data are shown in cyan, and the total fit is indicated by the blue curve. (Bottom) Temperature-dependent Raman intensity map (false-color contour plot) showing the evolution of phonon modes in the 400-750 cm^{-1} range, with mode sharpening and intensity enhancement upon cooling.

To quantify spin-phonon coupling effects, we first establish the intrinsic lattice contribution through anharmonic phonon renormalization described by the Balkanski model[229, 230]:

$$\omega_{\text{anh}}(T) = \omega(0) - A \left[1 + \frac{2}{e^{\hbar\omega(0)/2k_B T} - 1} \right] \quad (174)$$

where $\omega(0)$ represents the zero-temperature frequency and A the anharmonic cou-

pling constant. Systematic deviations from this behavior below magnetic transitions reveal significant spin-phonon coupling. Interestingly, $\text{Nd}_2\text{NiMnO}_6$ reveals three distinct regimes of spin-lattice interaction (Figure III.5). The A_g^{I} mode ($\omega(0) = 504.09 \pm 0.05 \text{ cm}^{-1}$) shows anomalous hardening ($\delta\omega = +2.08 \text{ cm}^{-1}$) below the ferromagnetic transition in $T_1 \approx 200 \text{ K}$, which persists until the glass cluster freezes in $T_f \approx 80 \text{ K}$. This reverses below 30 K with a sharp jump at the Nd^{3+} ordering temperature (20 K). The A_g^{II} mode exhibits even stronger coupling ($\delta\omega = 3.62(48) \text{ cm}^{-1}$), requiring a modified Balkanski model ($\omega_0 = 524.38 \pm 0.48 \text{ cm}^{-1}$, $C = 2.55 \pm 0.49$) to capture the magnetic effects. These effects are 20-30% stronger than in $\text{La}_2\text{NiMnO}_6$ [222, 224, 231], consistent with enhanced magnetoelastic coupling from the smaller Nd^{3+} ionic radius (1.27 \AA vs 1.36 \AA) [232]. In contrast, the A_g^{III} mode shows subtler behavior, with a gradual softening ($\omega_0 = 656.88 \pm 0.07 \text{ cm}^{-1}$) below approximately 180 K . Phonon lifetime analysis reveals complementary evidence of spin-phonon coupling through linewidth modifications:

$$\Gamma_{\text{anh}}(T) = \Gamma(0) + B \left[1 + \frac{2}{e^{\hbar\omega(0)/2k_B T} - 1} \right] \quad (175)$$

The A_g^{I} mode shows a striking 2.32 cm^{-1} linewidth increase below T_1 , exceeding predictions from both linear and anharmonic models. The A_g^{II} mode displays a characteristic V-shaped $\Gamma(T)$ profile with 3.94 cm^{-1} deviation, while A_g^{III} exhibits a 2.97 cm^{-1} broadening below 160 K with distinct temperature dependence. These observations demonstrate mode-specific coupling: (i) A_g^{I} primarily responds to Ni/Mn ferromagnetism, (ii) A_g^{II} sensitively probes cluster-glass dynamics, and (iii) A_g^{III} shows selective decoupling from Nd^{3+} ordering. The quantitative agreement with first-principles predictions for similar systems [233, 234] validates the proposed coupling mechanisms, establishing $\text{Nd}_2\text{NiMnO}_6$ as an ideal platform for studying hierarchical spin-lattice interactions.

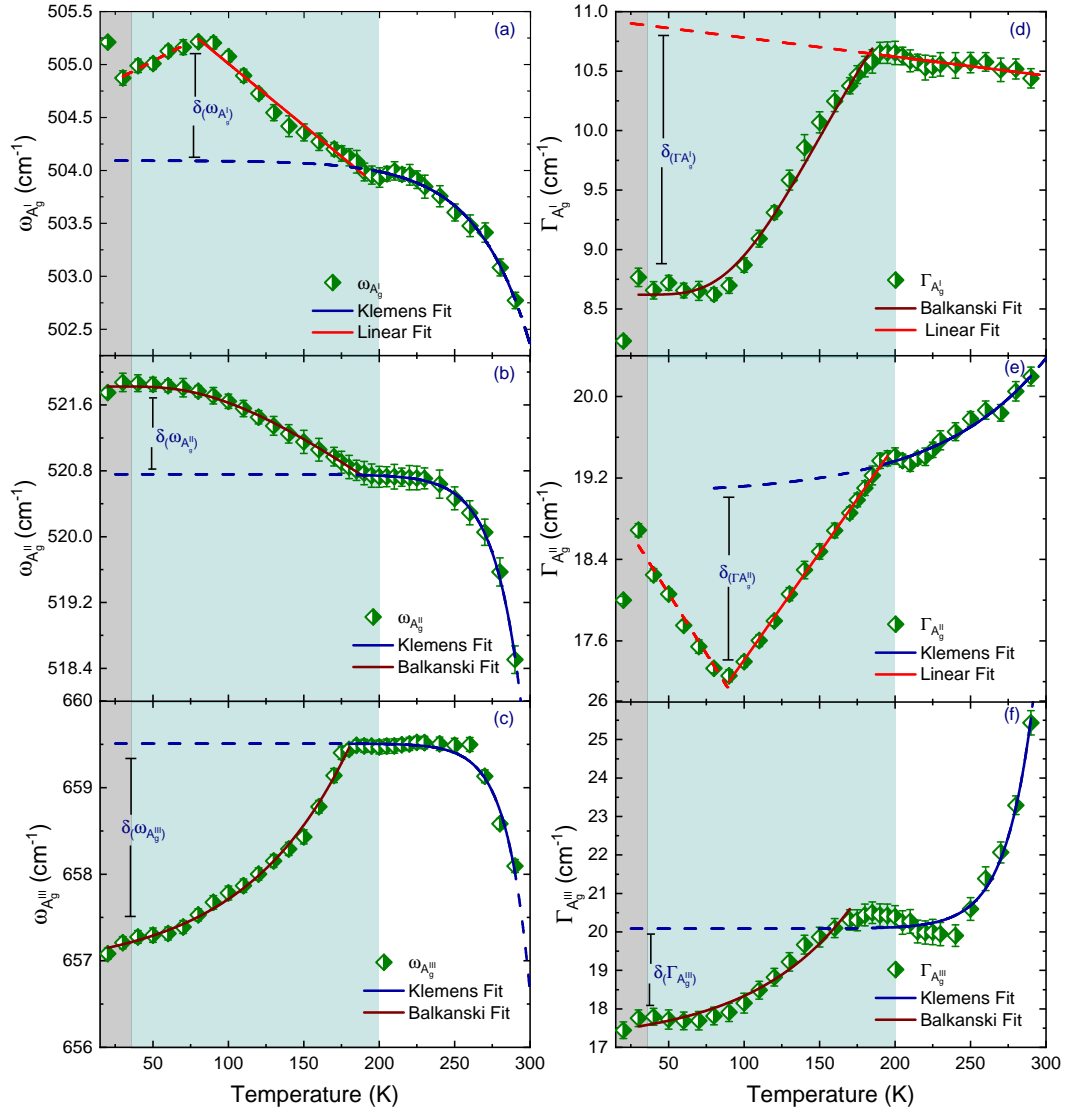


Figure IV.12: Temperature dependence of phonon frequencies (ω) and linewidths (Γ) for three A_g modes in $\text{Nd}_2\text{NiMnO}_6$. Panels (a-c) show ω_{A_g} fitted with Klemens and Balkanski models; deviations below $T_1 \approx 200$ K and $T_f \sim 50$ -100 K indicate spin-phonon coupling. Panels (d-f) show Γ_{A_g} , with anomalous broadening at magnetic transitions, confirming strong spin-lattice interactions.

The temperature evolution of phonon renormalization in NNMO reveals a complex hierarchy of spin-phonon interactions that conventional mean-field theories cannot fully describe. The observed frequency shifts $\delta\omega_{A_g}(T) = \omega_{\text{obs}}(T) - \omega_{\text{anh}}(T)$ for the three Raman-active modes follow the fundamental spin-phonon coupling relation [235]:

$$\Delta\omega(T) = \lambda \langle S_i \cdot S_j \rangle \approx \lambda \left[\frac{M(T)}{M_{\text{max}}} \right]^2, \quad (176)$$

where λ represents the mode-specific coupling strength. Below the ferromagnetic transition at $T_1 = 200$ K, the A_g^I mode ($\lambda = 1.12 \text{ cm}^{-1}$) shows an immediate

deviation from the $[M(T)]^2$ scaling, indicating its acute sensitivity to local spin disorder and antisite defects. In contrast, the A_g^{II} mode ($\lambda = 0.99 \text{ cm}^{-1}$) maintains nearly perfect overlap with $[M(T)]^2$ down to 50 K, representing one of the clearest experimental demonstrations of mean-field spin-phonon coupling in double perovskites. The A_g^{III} stretching mode exhibits the most dramatic behavior, with both the strongest coupling ($\lambda = -2.43 \text{ cm}^{-1}$) and the most pronounced deviation from mean-field scaling. Its immediate non-overlap below 200 K reveals dominant coupling to Ni-Mn spin fluctuations rather than long-range order, while the large negative λ suggests a significant phonon softening mechanism likely involving magnetostrictive effects in the Ni-O-Mn bonds [231, 232, 236].. In the reentrant cluster-glass regime (100-22 K), the modes show fundamentally different responses to magnetic frustration. While A_g^{I} and A_g^{III} unexpectedly reconverge with $[M(T)]^2$ below 100 K, suggesting a temperature-dependent recovery of spin-lattice coherence, A_g^{II} maintains its scaling until abruptly diverging at 50 K. Below the Nd^{3+} ordering temperature of 22 K, all modes show universal anomalies but with important distinctions: the strongly negative λ of A_g^{III} leads to strong softening, while the positive λ modes (A_g^{I} and A_g^{II}) harden conventionally. These observations demonstrate that different phonon modes in NNMO probe distinct aspects of the spin correlation function $\langle S_i \cdot S_j \rangle$ across various length scales. The A_g^{II} mode's persistent mean-field scaling implies it responds primarily to long-range order, while A_g^{I} and A_g^{III} are sensitive to short-range correlations and defect-induced frustration. This complex behavior establishes NNMO as a model system for studying competing spin-phonon coupling mechanisms, with important implications for understanding magnetoelectric effects in related multiferroic materials.

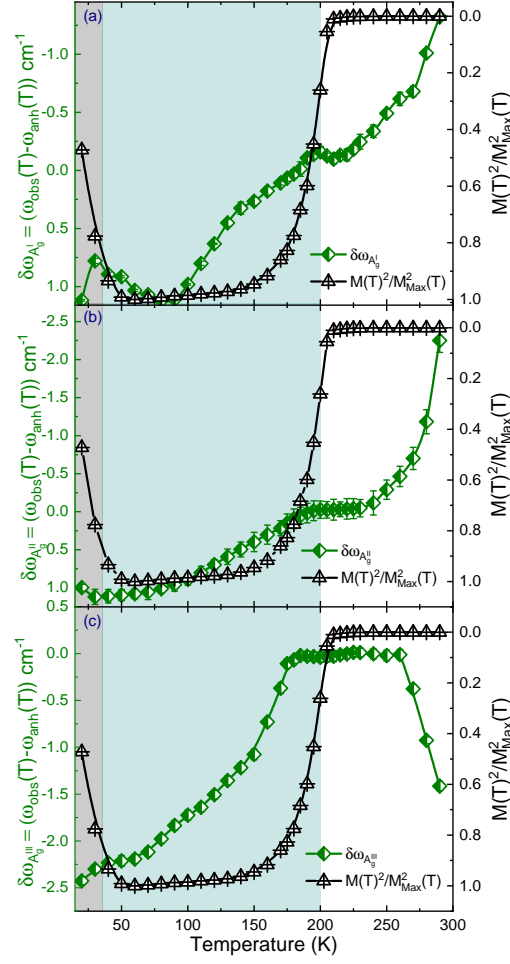


Figure IV.13: Temperature evolution of phonon frequency renormalization $\delta\omega(T) = \omega_{\text{obs}}(T) - \omega_{\text{anh}}(T)$ (green diamonds, left axis) and normalized square of magnetization $[M(T)/M_{\text{max}}]^2$ (black triangles, right axis) for three A_g Raman modes in $\text{Nd}_2\text{NiMnO}_6$. Panels (a)-(c) show A_g^{I} , A_g^{II} , and A_g^{III} modes, respectively. Good agreement is observed in the FM region ($T_1 < 200$ K), while deviation below 50 K signals competing AFM interactions and rare-earth sublattice effects.

4.4 Conclusion

In summary, we have shown that our polycrystalline sample of the double perovskite $\text{Nd}_2\text{NiMnO}_6$ adopts a monoclinic crystal structure (space group $P2_1/n$), which hosts nearly complete B -site ordering of Ni^{2+} and Mn^{4+} cations (antisite disorder was found to be 9%). This cation ordering was established directly by neutron powder diffraction, and confirmed through bond valence sum analysis and consideration of local distortions of the perovskite structure. Magnetometry and neutron powder diffraction measurements revealed two magnetic phase transitions. The first at $T_C = 198\text{K}$ corresponded to ferromagnetic ordering of the Ni^{2+} and Mn^{4+} sublattices, which was consistent with dominant ferromag-

netic d - d exchange confirmed by Curie-Weiss analysis of the paramagnetic susceptibility that yielded a positive Curie-Weiss constant ($\theta_{\text{CW}} \approx 206 \text{ K}$). Scaling analysis revealed that the critical phenomena at T_{C} adhered to mean-field behaviour characteristic of a second-order phase transition. Yet, below T_{C} AC susceptibility measurements revealed frequency-dependent behaviour consistent with a re-entrant spin-glass-like state. The second transition occurred on further cooling below $T_{\text{N}} = 22 \text{ K}$, and was characterised by the additional non-collinear ordering of Nd^{3+} moments driven by antiferromagnetic f - d exchange, and frustrated by competing antiferromagnetic f - f exchange. Symmetry analysis of this ground state magnetic structure points towards significant easy plane anisotropy of the Nd^{3+} ions. The magneto-caloric effect was characterized by determining a significant magnetic entropy change ($-\Delta S_M$) at T_{C} , where the maximum change was found to be $2.25 \text{ J kg}^{-1} \text{ K}^{-1}$ under an applied field of 7 T. The respective relative cooling power was found to increase linearly with the field, stressing the potential for double perovskites such as $\text{Nd}_2\text{NiMnO}_6$ to be used in magnetic refrigeration applications. Also, $\text{Nd}_2\text{NiMnO}_6$ reveals distinct, mode-dependent spin-phonon coupling across its magnetic transitions, demonstrating hierarchical magneto-structural interactions. Overall, these results underpin $\text{Nd}_2\text{NiMnO}_6$ as a model system for investigating the effects of multiple competing magnetic sublattices, significant magneto-caloric effects, and possible reentrant spin-glass behavior in complex oxides.

* CHAPTER V *

Spin-Orbit Coupling and Exchange Interplay in $\text{Nd}_2\text{NiMn}_{0.25}\text{Ir}_{0.75}\text{O}_6$: A 3d-5d-4f Magnetism Paradigm

Through combined neutron diffraction, magnetometry, and Raman spectroscopy, we demonstrate that Ir substitution transforms the double perovskite $\text{Nd}_2\text{NiMnO}_6$ into a spin-orbit-driven cluster-glass system, $\text{Nd}_2\text{NiMn}_{0.25}\text{Ir}_{0.75}\text{O}_6$. The compound adopts a monoclinic $P2_1/n$ structure, exhibiting significant antisite disorder between Ni/Nd and Ni/Mn sites. Below $T_N = 140$ K, long-range ferromagnetic order sets in via 3d – 5d [Ni^{2+} -($\text{Mn}^{4+}/\text{Ir}^{4+}$)] exchange interactions, though this transition is suppressed by nearly 58 K relative to the parent phase due to the influence of 5d spin-orbit coupling and B-site disorder. Temperature-resolved neutron diffraction reveals a progressive evolution of the magnetic structure. At 100 K, Ni^{2+} moments align collinearly along the b-axis with a magnitude of $1.31(11) \mu_B$, while the Mn/Ir sublattice remains only partially ordered $0.69 \mu_B$. Further cooling to 40 K leads to enhanced Ni^{2+} moments reaching $1.572(9) \mu_B$, concurrently with a notable decrease in Mn/Ir moment to $0.43 \mu_B$, evidencing increasing frustration within the mixed 3d-5d sublattice. At 1.5 K, neutron refinements resolve a coherent magnetic ground state that contrasts with phase-separated behavior seen in analogues such as $\text{Nd}_2\text{NiIrO}_6$. The data show b-axis ferromagnetism arising from Ni^{2+} and Nd^{3+} alignment, while Nd^{3+} moments additionally exhibit antiferromagnetic canting in the ac-plane. This state simultaneously reconciles previously reported inconsistencies in the effective moment size of Ir^{4+} ions and reveals a pronounced collapse of the Mn/Ir sublattice moment compared to $\text{Nd}_2\text{NiMnO}_6$. The magnetic structure of Nd^{3+} below $T_{\text{Nd}} = 23$ K is consistent with a non-collinear configuration, distinct from those found in related systems, and arises from competing anisotropies: Ir^{4+} -induced strong single-ion anisotropy that pins collinearity of Ni^{2+} spins along b, while Nd^{3+} balances f-f exchange with f-d coupling. The resulting compromise gives rise to a magnetically frustrated state that retains frequency-dependent susceptibility and reduced rare-

earth moment values ($1.18 \mu_B$), indicative of reentrant-cluster-glassy dynamics. In addition to the magnetic complexity, Raman spectroscopy reveals a substantial spin-phonon coupling strength and broad anomalies in the heat capacity, further underscoring the correlated nature of disorder in this system. These combined observations establish that Ir substitution simultaneously enhances 3d-4f coupling through parallel Ni/Nd alignment and suppresses overall B-site magnetization through spin-orbit-driven frustration, highlighting a compelling strategy for tuning emergent quantum states in 3d-5d-4f oxides and providing direct insight into the microscopic origin of exotic magnetic behavior in spin-orbit coupled double perovskites.

Acknowledgements: The research presented in this chapter will be published as John M. Attah-Baah *et al.* (in preparation). I thank my collaborators for their essential contributions: Romualdo Silva Jr. for experimental support (sample synthesis and magnetometry) under Prof. Nilson S. Ferreira’s supervision; Dr. Maria H. Carvalho for specific heat measurements; and Dr. Diego Evaristo for Raman spectroscopy (instrumentation by Dr. Eduardo Granado). Neutron diffraction was performed with Dr. Roger Johnson, Dmitry Khalyavin, and Pascal Manuel, with data and symmetry analysis conducted by me under Dr. Johnson’s guidance. This work was supported by CNPq (309184/2022-3, 141485/2021-0), CAPES (Finance Code 001; PDSE 88881.846711/2023-01), and FAPESP (EMU 18/08040-5). I acknowledge University College London for hosting and IFGW/UNICAMP for magnetometry access.

5.1 Introduction

The A₂BB’O₆ double perovskite family has emerged as a rich platform for exploring complex magnetic phenomena due to its inherent structural flexibility and the interplay between charge, spin, and lattice degrees of freedom [237, 238]. These materials exhibit a wide range of properties, including ferromagnetism (FM), antiferromagnetism (AFM), ferrimagnetism (FiM), magnetocaloric effects (MCE), and multiferroicity, making them ideal for fundamental studies and potential technological applications [186, 239, 240]. The magnetic behavior in double perovskites is primarily governed by the nature of superexchange

(B – O – B') and super-superexchange (B – O – B' – O – B) interactions, which are highly sensitive to the choice of cations occupying the A , B , and B' sites [53, 116]. While most studies have focused on systems with one or two magnetic ions, recent interest has shifted toward hetero-tri-spin systems (3d – 5d – 4f), where the coexistence of multiple magnetic sublattices introduces additional complexity due to competing exchange pathways [49, 154, 241]. The incorporation of Ir⁴⁺ (5d⁵) cations in double perovskites has emerged as a rich platform for investigating competing quantum interactions in correlated electron systems. Three key energy scales govern the electronic and magnetic behavior: the large spin-orbit coupling ($\lambda \approx 0.4\text{--}0.5$ eV), which splits the t_{2g} manifold into $J_{\text{eff}} = 1/2$ and $J_{\text{eff}} = 3/2$ states; the cubic crystal field splitting ($\Delta_{\text{CF}} \approx 3\text{--}4$ eV); and the intermediate on-site Coulomb repulsion ($U \approx 2\text{--}3$ eV) [242, 243]. The delicate balance among these three energy scales leads to several remarkable phenomena that are unique to 5d-based systems. One of the most prominent consequences is the formation of a $J_{\text{eff}} = 1/2$ ground state, initially proposed for Sr₂IrO₄ [242], which gives rise to a pseudospin-1/2 moment capable of supporting exotic quantum phases. However, in double perovskite architectures, this picture becomes significantly more complex due to multiple competing effects. Structural distortions tend to mix J_{eff} states and break the ideal octahedral symmetry. Simultaneously, strong hybridization between Ir 5d orbitals and neighboring 3d cations alters the electronic structure, while the presence of both B-O-B' and B-O-B'-O-B exchange paths introduces competition between magnetic interactions. A representative example is La₂CoIrO₆, where XMCD and neutron diffraction studies have shown a canted ferrimagnetic state below $T_C \approx 95$ K [244]. In this system, high-spin Co²⁺ ($S = 3/2$) couples antiferromagnetically to Ir⁴⁺ through 180° superexchange. Despite the expected 1 μ_B moment for a pure $J_{\text{eff}} = 1/2$ state, the observed Ir⁴⁺ magnetic moment is only about 0.3 μ_B , reflecting strong covalency and hybridization effects. Moreover, below $T \approx 30$ K, the system exhibits reentrant spin-glass behavior, attributed to the frustration of the Co/Ir magnetic sublattice and the impact of antisite disorder [245]. Similarly, Nd₂NiMnO₆ exhibits FM ordering between Ni²⁺ and Mn⁴⁺ at 200 K, followed by AFM coupling with Nd³⁺ at 50 K, highlighting the role of 3d – 4f couplings [157, 246, 247]. Despite these advances, 3d-5d-4f double perovskites remain underexplored, particularly those with Ni²⁺ and Ir⁴⁺ on the B/B' sites and a magnetic rare-earth ion (e.g., Nd³⁺) on the A-site. The magnetic properties of Ln₂NiIrO₆ double perovskites have been exten-

sively characterized through neutron diffraction studies, revealing complex behavior that varies significantly with the rare-earth ion [154, 248, 249]. For La₂NiIrO₆, which contains only 3d (Ni²⁺) and 5d (Ir⁴⁺) magnetic ions, both Ferreira *et al.* [154] and Ritter *et al.* [248] identified a magnetic propagation vector $\mathbf{k} = (\frac{1}{2}, \frac{1}{2}, 0)$ below $T_N \approx 80$ K. However, their refined models differ significantly in moment sizes, with Ritter's high-resolution study reporting notably reduced values (Ni²⁺: 1.53(5) μ_B ; Ir⁴⁺: 0.17(3) μ_B). This discrepancy underscores the experimental difficulty in resolving the small Ir moment, particularly in the presence of Ir's strong neutron absorption. In Pr₂NiIrO₆, even more pronounced differences between proposed magnetic models emerge [154, 249], while Nd₂NiIrO₆ displays the most complex magnetic behavior in the series. High-statistics neutron diffraction measurements have revealed three magnetic transitions and a coexistence of both $\mathbf{k} = 0$ and $\mathbf{k} = (\frac{1}{2}, \frac{1}{2}, 0)$ phases below 15K [248]. We explore Nd₂NiMn_{0.25}Ir_{0.75}O₆, where partial substitution of Mn⁴⁺ for Ir⁴⁺ creates a unique bridge between 3d-3d superexchange and 3d-5d spin-orbit-coupled interactions. This strategic doping introduces competing magnetic mechanisms through: (i) the replacement of strong Ni-Mn ferromagnetic superexchange with SOC-mediated Ni-Ir pathways, (ii) structural distortions including *b*-axis elongation and octahedral tilting, and (iii) modification of Ni/Mn-O-Ir bond angles into the 148°-150° range, beyond which the Goodenough-Kanamori rules lose predictive power [53, 116]. Despite this complexity, the Nd³⁺ sublattice remains magnetically active, and the structural evolution observed here is consistent with trends seen in fully Ir-substituted analogs IV. Neutron diffraction confirms a $\mathbf{k} = (0, 0, 0)$ ground state comprising ferromagnetic ordering within the Ni/Mn/Ir sublattice, accompanied by antiferromagnetically aligned Nd³⁺ moments. However, a deeper comparison with Nd₂NiMnO₆ reveals critical modifications driven by Ir substitution. The Ni²⁺ moments remain strictly aligned along the *b*-axis ($F \parallel$), indicating that Ir induces significant single-ion anisotropy (SIA) that overcomes the easy-plane tendency observed in the parent compound. Concurrently, the ordered moment of the Mn/Ir sublattice is sharply reduced ($2.18\mu_B \rightarrow 0.38\mu_B$), signaling increased magnetic frustration from Ir's spin-orbit entangled 5d electrons. The Nd³⁺ sublattice develops a well-defined Γ_1^+ magnetic mode, characterized by *b*-axis ferromagnetism and *ac*-plane canting ($A \perp$), in contrast to the symmetry-broken noncollinear order observed in Nd₂NiMnO₆. AC susceptibility measurements conducted below $T_{Nd} \approx 23$ K further corroborate this complexity, revealing persistent frequency-

dependent broadening that implies incomplete Nd ordering. This disorder likely stems from competing interactions among Nd's single-ion *b*-axis anisotropy, *f-f* exchange favoring antiparallel canting in the *ac*-plane, and random local fields from the frustrated Mn/Ir network. The refined Nd³⁺ moment of $1.18\mu_B$ at 1.5 K, well below its free-ion value, supports this interpretation. Unlike prior studies that relied primarily on neutron diffraction [154, 248, 249], we adopt a multimodal approach integrating DC/AC magnetometry, Raman spectroscopy, and specific heat measurements [250]. Raman data reveals strong spin-phonon coupling, as evidenced by phonon renormalization below the magnetic transition, which complements the magnetic symmetry resolved via diffraction. AC susceptibility exposes reentrant-spin-cluster-like dynamics superimposed on long-range ferromagnetic order, a hallmark of disorder and frustration due to mixed B-site occupancy (Ni/Mn/Ir). Heat capacity anomalies further verify the presence of a magnetic phase transition, Shocktly anomalies from the Nd³⁺, supporting the overall picture of a highly tunable, competing-interaction-driven magnetic landscape.

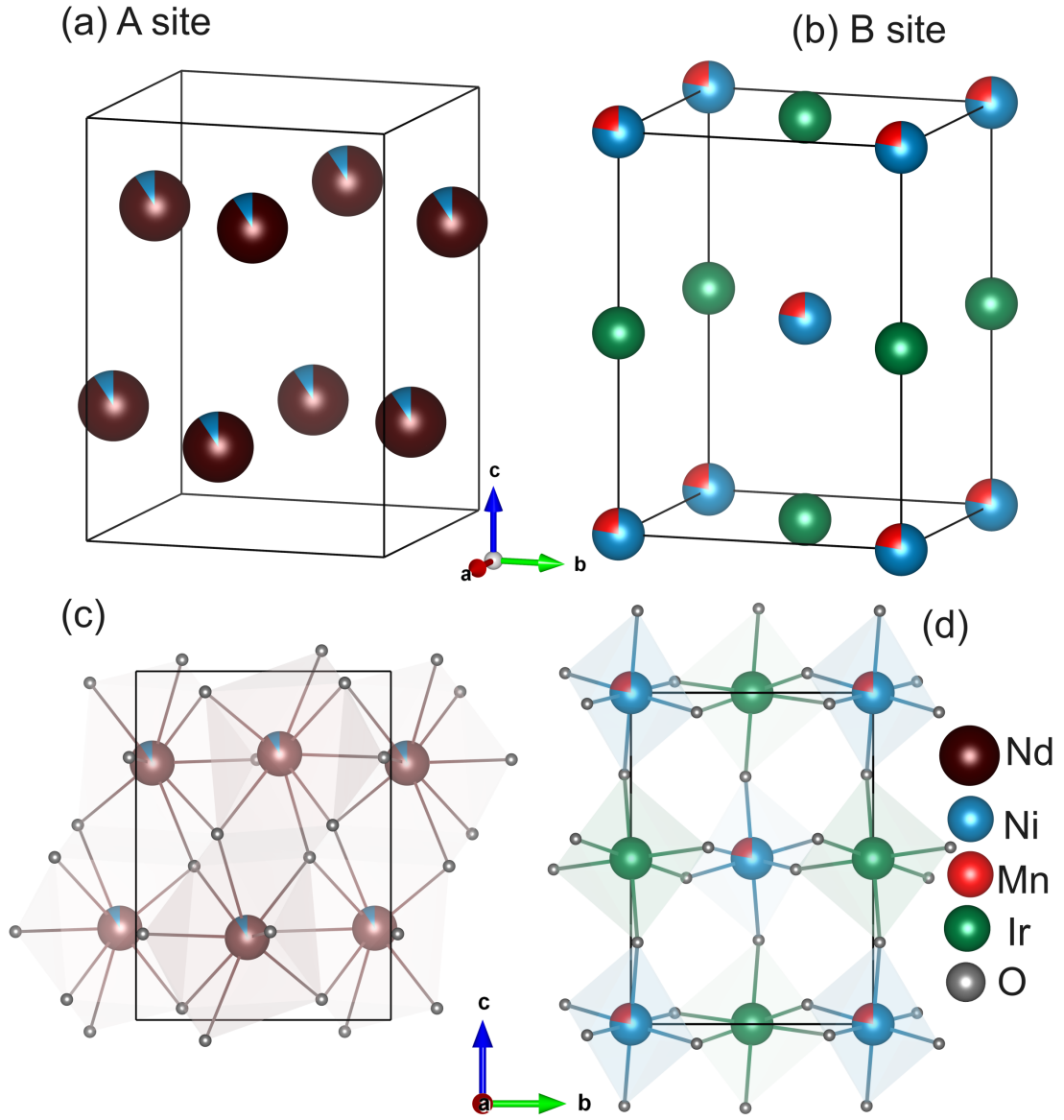


Figure V.1: The crystal structure of $\text{Nd}_2\text{NiMn}_{0.25}\text{Ir}_{0.75}\text{O}_6$ in the $P2_1/n$ space group is presented as a single unit cell. (a) The A -site with Nd atoms is depicted in brown. (b) The B -sites are shown, with Ni/Mn atoms represented in blue and red, and Ir in green. (c) A projection of the crystal structure along the a -axis illustrates the $(\text{Nd})\text{O}_8$ cuboctahedral coordination. (d) The $(\text{NiMn})\text{O}_6$ octahedral tilt coordination is highlighted, with Ni/Mn and Ir octahedra shaded in blue and green, respectively. The O^{2-} ions are represented by grey spheres.

5.2 Experiment

A target polycrystalline $\text{Nd}_2\text{NiMn}_{0.25}\text{Ir}_{0.75}\text{O}_6$ (NNMIO) was synthesized via a modified sol-gel method employing glycerin as a chelating aid. A stoichiometric mixture of high-purity precursors $\text{Nd}(\text{NO}_3)_3 \cdot 6\text{H}_2\text{O}$, $\text{Ni}(\text{NO}_3)_2 \cdot 6\text{H}_2\text{O}$, $\text{Mn}(\text{CH}_3\text{CO}_2)_2 \cdot 4\text{H}_2\text{O}$ and IrCl_3 (Sigma-Aldrich, 99.97%) in a molar ratio of 2:1:0.25:0.75 (Nd:Ni:Mn:Ir) was dissolved in a 2 M aqueous solution. Glycerin

(2 g) was added dropwise to homogenize the solution, which was then evaporated at 200 °C for 24 h to form a xerogel. The dried gel was ground and pre-calcined at 1000 °C for 12 h (ramp rate: 5 °C/min) to remove organic residues. The powder was pelletized under a uniaxial pressure of 80 MPa and sintered at 1200 °C for 48 h to yield phase-pure double-perovskite crystals. Phase purity was verified by powder X-ray diffraction using a Rigaku diffractometer with Cu K α radiation ($\lambda = 1.5406$ Å) at room temperature. Data were collected over a 2θ range of $5^\circ \leq 2\theta \leq 90^\circ$ with a step size of 0.02° and a counting time of 20 s per step. The instrument was configured with fixed slits (divergence slit: $1/4^\circ$; anti-scatter slit: $1/2^\circ$) and a 10 mm mask. Temperature- and field-dependent magnetization were measured using a SQUID magnetometer (MPMS-3, Quantum Design) in the temperature range of 2-300 K under magnetic fields up to ± 70 kOe. To mitigate artifacts caused by trapped magnetic flux, the superconducting magnet was demagnetized by oscillating the field during coil quenching, followed by thermal cycling to 300 K (above the critical temperature of the superconducting coil) prior to each measurement. Frequency-dependent AC susceptibility was measured using a PPMS (Quantum Design) at the ISIS Neutron and Muon Source. Measurements were conducted on cooling from 300 K to 2 K under zero applied DC field, with an AC field amplitude of 0.5-2 Oe and frequencies between 11 and 540 Hz. Raman spectra were acquired in quasi-backscattering geometry using a 532 nm diode-pumped laser stabilized by a volume Bragg grating (VBG). The beam was focused onto the sample using mirror-lens optics, with scattered light collected through notch filters and analyzed by a triple-grating T64000 spectrometer (1800 mm^{-1} gratings, LN₂-cooled CCD). Sample pellets (sintered at 1200°C for 24 hr) were mounted on a cold finger in a closed-cycle cryostat (20 K base temperature), with temperature controlled via a CERNOX sensor (Lakeshore C340). Spectra were calibrated using a silicon reference, with the spectrometer centered at 470 cm^{-1} for Stokes signal detection. High-resolution neutron powder diffraction data were collected using the WISH diffractometer [190] at the ISIS Neutron and Muon Source. A 1.7 g powder sample was loaded into a 6 mm diameter cylindrical vanadium can and cooled using a ⁴He closed-cycle refrigerator. In the paramagnetic (PM) state, data were recorded at 200 K for approximately 2 h to establish the nuclear structure baseline. To capture magnetic ordering, high-statistics datasets were collected at 100, 40, and 1.5 K, each with a counting time of approximately 3 h. Rietveld refinements of

both crystal and magnetic structures were performed using the FULLPROF suite [191]. Symmetry analysis to determine allowed magnetic modes was conducted using the ISOTROPY software suite [102] and ISODISTORT [192].

Table V.1: Structural parameters of Nd₂NiMn_{0.25}Ir_{0.75}O₆ obtained from Rietveld refinement of NPD data at 200 K. Lattice parameters are $a = 5.40481(3)$ Å, $b = 5.64717(3)$ Å, $c = 7.71597(3)$ Å, $\beta = 90.04178(2)^\circ$, and unit cell volume $V = 235.506(2)$ Å³. Bond valence sums (BVS) were calculated using $R_0(\text{Nd}^{3+}) = 2.12$, $R_0(\text{Ni}^{2+}) = 1.65$, $R_0(\text{Mn}^{4+}) = 1.91$, and $B = 0.37$. The bond valence is defined as $\text{BV} = \exp\left(\frac{R_0 - R}{B}\right)$. For mixed-occupancy sites, the majority cation is used in BVS calculations.

Atom	Frac. Coord.	$U_{\text{iso}}(\times 10^{-2} \text{ \AA}^2)$	BVS($ e $)	Occupation
Nd	$x = 0.0187(9)$ $y = 0.5635(4)$ $z = 0.7633(7)$	1.124(6)	+3.27	91%Nd, 9%Ni
Ni/Mn	$x = y = z = 0$	0.528(4)	+2.84	78% Ni, %22 Mn
Ir	$z = 0.5$	0.528(4)	+3.62	Ir
O1	$x = 0.0904(6)$ $y = 0.0272(7)$ $z = 0.2468(2)$	7.439(5)	-	O
O2	$x = 0.1922(14)$ $y = 0.2716(13)$ $z = -0.0589(9)$	7.439(5)	-	O
O3	$x = 0.2039(14)$ $y = 0.3191(10)$ $z = 0.5334(10)$	7.439(5)	-	O

Bond	Length (Å)	Bond Angles (°)	
Ni/Mn – O1	1.972(14)	$\langle \text{O1} - \text{Ni/Mn} - \text{O1} \rangle$	180.00(0)
Ni/Mn – O2	1.908(8)	$\langle \text{O1} - \text{Ni/Mn} - \text{O2} \rangle$	88.1(3), 91.9(3)
Ni/Mn – O3	1.916(8)	$\langle \text{O1} - \text{Ni/Mn} - \text{O3} \rangle$	88.0(3), 92.0(3)
Ir – O1	2.020(14)	$\langle \text{O1} - \text{Ir} - \text{O1} \rangle$	180.00(0)
Ir – O2	2.153(8)	$\langle \text{O1} - \text{Ir} - \text{O2} \rangle$	86.4(3), 93.6(3)
Ir – O3	2.128(7)	$\langle \text{O1} - \text{Ir} - \text{O3} \rangle$	85.8(3), 94.2(3)
		$\langle \text{Ir} - \text{O1} - \text{Ni/Mn} \rangle$	150.26(2)
		$\langle \text{Ir} - \text{O2} - \text{Ni/Mn} \rangle$	148.4(4)
		$\langle \text{Ir} - \text{O3} - \text{Ni/Mn} \rangle$	150.2(4)

Refinement Parameters			
χ^2	12.5	R_{P} (%)	3.85
wR_{P} (%)	2.89	R_{Bragg} (%)	5.58
Frac. (%)	96.93(2)		

$$t_g = \frac{r_{\text{Nd}^{3+}} + r_{\text{O}^{2-}}}{\sqrt{2} \left(\frac{r_{\text{Ni}^{2+}} + r_{\text{Mn}^{4+}}}{2} + r_{\text{Ir}^{4+}} + r_{\text{O}^{2-}} \right)} \quad (177)$$

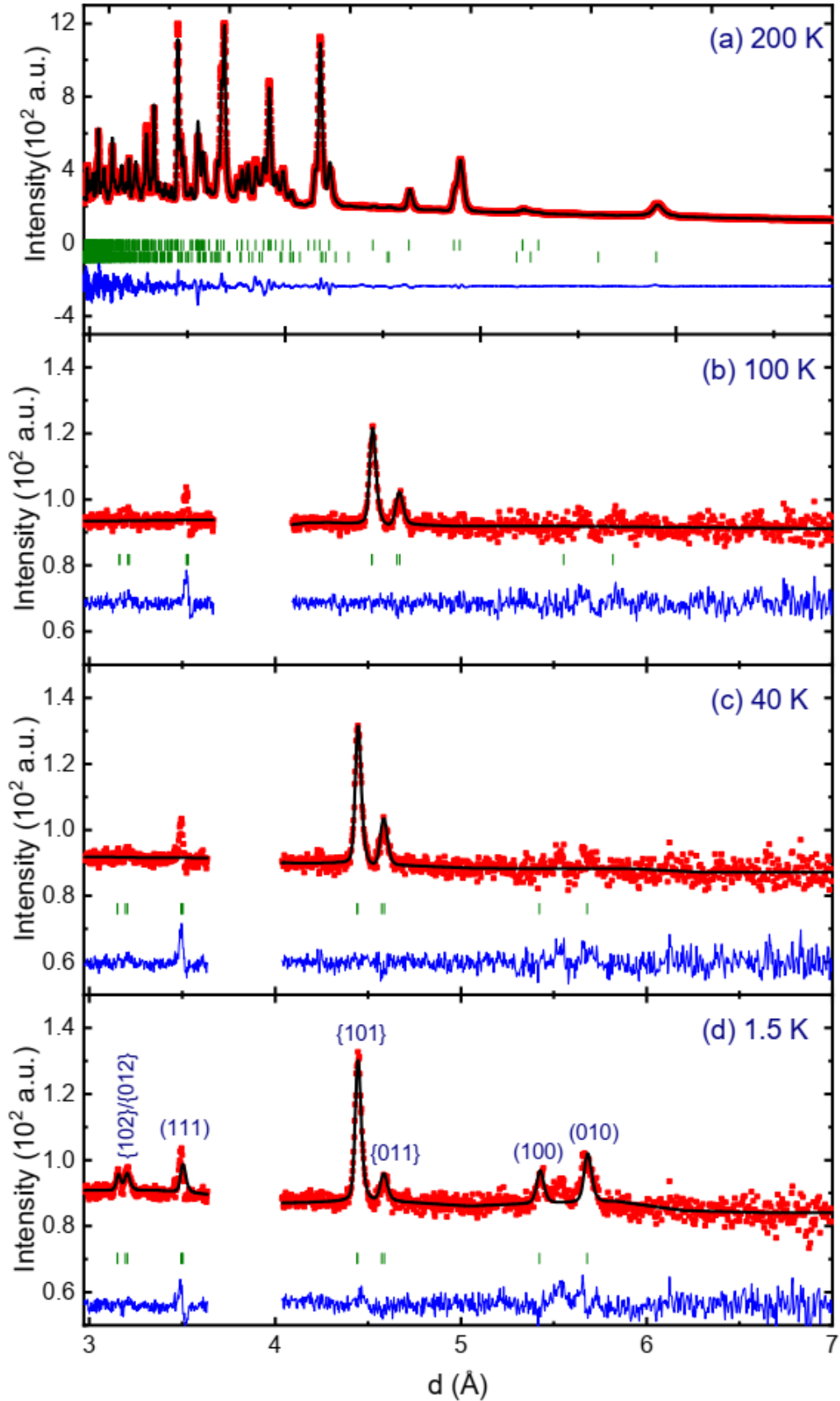


Figure V.2: Neutron powder diffraction data measured in 4 magnetic phases; a) paramagnetic (230 K), b) first ordered (100 K), c) ordering at 40 K, and d) ground state (1.5 K). Data are shown as red points, the fitted patterns as black lines, and the difference curve $I_{\text{obs}} - I_{\text{calc}}$ as blue lines at the bottom of the panes. The top and bottom row of green tick marks in each pane indicate the position of nuclear and magnetic Bragg peaks, respectively.

5.3 Results and Discussion

5.3.1 Crystal Structure

The polycrystalline Nd₂NiMn_{0.25}Ir_{0.75}O₆ crystallizes in the monoclinic $P2_1/n$ space group (No. 14), as confirmed by NPD data. This structural model remains stable across the entire measured temperature range (1.5 - 300 K), with no evidence of phase transitions. High-resolution NPD data collected at 100, 40, and 1.5 K confirm the persistence of the monoclinic symmetry into the magnetically ordered regime. The crystal structure features Nd³⁺ ions occupying the *A*-site 4e Wyckoff positions, forming distorted cuboctahedral (Nd)O₈ coordination polyhedra [Figure V.1(a,c)]. The B-site exhibits a partially ordered arrangement of transition metals, with Ni²⁺/Mn⁴⁺ (78:22 ratio) predominantly occupying the 2a (0,0,0) position and Ir⁴⁺ residing at the 2b (0,0, $\frac{1}{2}$) site. Notably, approximately 9% antisite disorder occurs, where Ni substitutes at Nd positions (Table V.1). Three distinct oxygen sites (O1 - O3) occupy general 4e positions, completing the corner-sharing (Ni/Mn)O₆ and IrO₆ octahedral system characteristic of double perovskites [Figure V.1(b,d)]. The Ir-O bonds display significant anisotropy (2.020 - 2.153 Å), reflecting strong octahedral distortion, while Ni/Mn-O bonds are more symmetric (1.908 - 1.972 Å), and octahedral tilting (Ir-O-Ni/Mn angles \approx 148°-150°). The calculated Goldschmidt tolerance factor ($t_g = 0.93$) confirms the monoclinic distortion, in line with observed bond-length asymmetries. Bond valence sums: +3.27 (Nd), +3.62 (Ir), and +2.84 (Ni/Mn), support the expected oxidation states and indicate partial charge delocalization [49]. The refined lattice parameters at 200 K ($a = 5.40481(3)$ Å, $b = 5.64717(3)$ Å, $c = 7.71597(3)$ Å, $\beta = 90.04178(2)^\circ$) reveal three significant structural modifications compared to the parent Nd₂NiMnO₆ compound ($a = 5.4078(1)$ Å, $b = 5.4767(1)$ Å, $c = 7.6648(2)$ Å, $\beta = 90.0277(4)^\circ$). First, the *a*-axis shows a slight contraction ($\Delta a = -0.06\%$), while the *c*-axis expands more substantially ($\Delta c = +0.67\%$), reflecting the competing effects of Ir⁴⁺ substitution, its larger ionic radius (0.625 Å for Ir⁴⁺ vs. 0.530 Å for Mn⁴⁺ in octahedral coordination) would normally promote expansion, but this is partially counterbalanced by enhanced metal-oxygen covalency, comparable to trends in Nd₂NiIrO₆ [248]. Most strikingly, the *b*-axis undergoes a pronounced 3.11% expansion, significantly altering the axial ratio from $b/a = 1.0127$ in the parent compound to 1.0448 in the Ir-doped system. The

monoclinic angle β increases slightly by 0.014° , indicating subtle but measurable changes in the octahedral tilting pattern. These modifications closely resemble those observed in the Ln₂NiIrO₆ series (Ln = La, Nd, Eu, Gd) [49, 251, 252], confirming that partial Ir substitution drives the system toward the structural characteristics of the full iridate analogs. The anisotropic response highlights how selective orbital hybridization, particularly the enhanced π -bonding between Ir 5d and O 2p orbitals, can preferentially affect specific crystallographic directions in these complex oxides. A minor polymorph β -IrCl₃ impurity phase ($\sim 3\%$) was identified in the NPD data and included in the refinement [see Appendix 3.1 for structural parameters]. The β -IrCl₃ impurity ($\sim 3\%$) persists due to kinetic stabilization during high-temperature calcination (800-1200°C), where rapid perovskite formation traps metastable orthorhombic(*Fddd*) β -IrCl₃ (versus the thermodynamically favored α -IrCl₃ below 500°C). This is exacerbated by chlorine entrapment at grain boundaries and oxygen-deficient conditions [253, 254]. The excellent agreement factors ($R_P = 3.85\%$, $wP = 2.89\%$, $R_{\text{Bragg}} = 5.58\%$) confirm the reliability of the structural model (Table V.1). No other impurities were detected, indicating high phase purity(97%) aside from this trace contamination, Figure V.2a.

5.3.2 DC Magnetometry

The magnetic behavior of Nd₂NiMn_{0.25}Ir_{0.75}O₆ reveals a complex interplay of competing interactions, as evidenced by temperature-dependent susceptibility measurements (Figure V.3a). Under 100 Oe, the FC/ZFC bifurcation at 176 K signals spin freezing, characteristic of systems with significant magnetic anisotropy [5]. The susceptibility exhibits multiple anomalies: a sharp rise near 150 K followed by dips at 115 K and 45 K, culminating in a final rise below 25 K. This structured behavior suggests a rich magnetic phase diagram, with the 150-115 K region likely marking long-range order establishment. Field-dependent studies (inset) demonstrate how higher fields (1-10 kOe) suppress these features, revealing the delicate balance between ferromagnetic alignment and competing interactions [255].

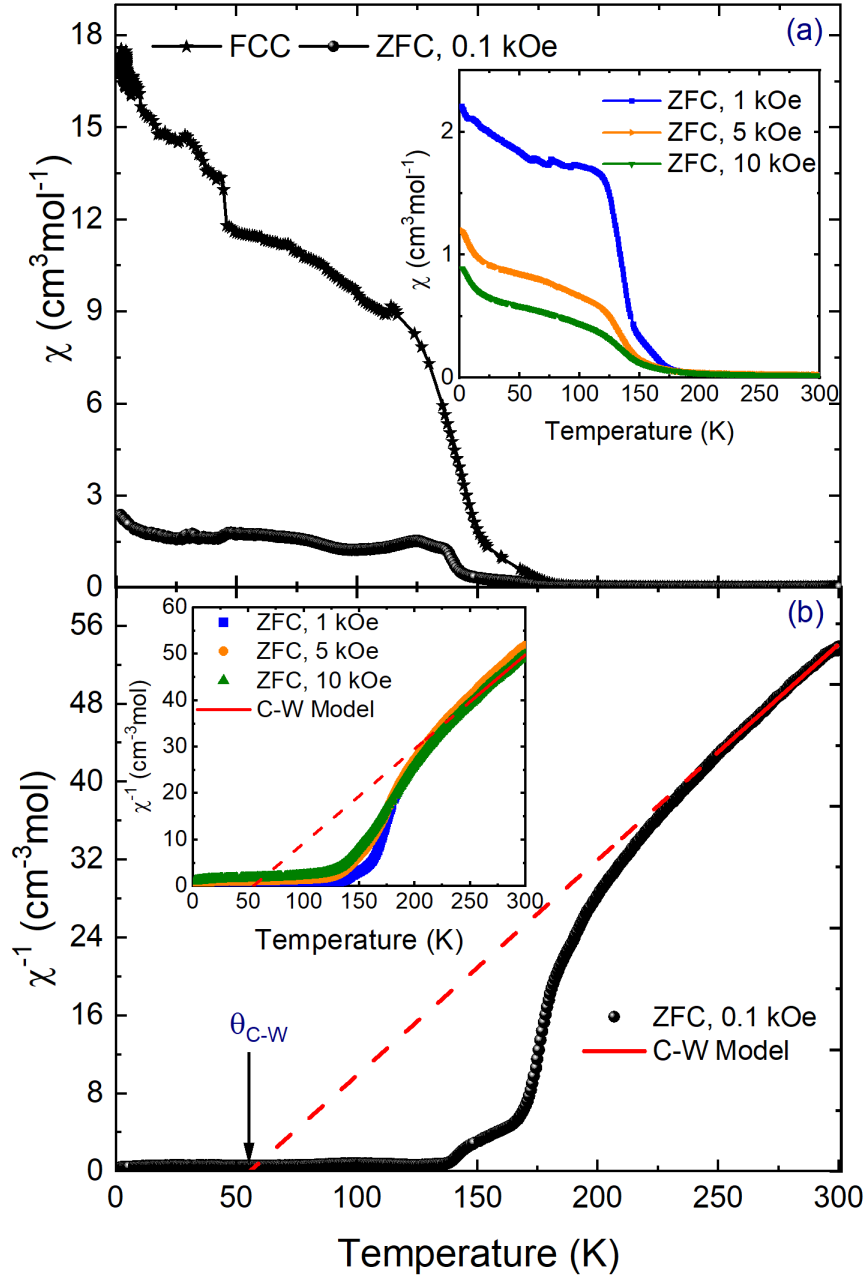


Figure V.3: a) Temperature dependence of the DC magnetic susceptibility of Nd₂NiMn_{0.25}Ir_{0.75}O₆ measured under ZFC and FCC conditions in an applied field of 0.1 kOe. The inset shows a comparison of M-T curves (ZFC/FCC) at different H_{dc} fields (1-10 kOe). (b) The inverse susceptibility ($\chi^{-1} = H/M$) as a function of temperature (T), inset shown for 1-10 kOe fields. The black line shows the paramagnetic region's best fit using the Curie-Weiss law.

The transition temperature ($T_N \approx 140$ K at 100 Oe) decreases systematically with applied field (135 K at 1 kOe, 128 K at 5 kOe, and 125 K at 10 kOe), demonstrating field-induced suppression of magnetic order [256]. The persistence of a 25 K anomaly across all fields suggests a strong ordering, likely involving the Nd³⁺ sublattice coupling. Curie-Weiss analysis yields $\theta_{CW} \approx +56(1)$ K (Figure V.3b), confirming dominant ferromagnetic interactions, with higher-field measurements

showing consistent θ_{CW} values (+54 to +55 K). The effective moments (6.01–6.28 μ_{B}) agree well with the theoretical estimate of 6.34 μ_{B} , calculated from individual contributions of Nd³⁺ (3.62 μ_{B}), Ni²⁺ (2.83 μ_{B}), Mn⁴⁺ (3.87 μ_{B}), and Ir⁴⁺ (1.73 μ_{B}). The transition-metal-only contribution (3.75 μ_{B}) highlights the significant role of Nd³⁺ in the total moment. These results align with other Ir-based double perovskites like R₂NiIrO₆ (R = La, Pr, Nd) (3.30–6.10 μ_{B}) [257] and Nd₂NiIrO₆ (6.2 μ_{B}) [248]. The reduced Ir⁴⁺ moment reflects strong spin-orbit coupling effects, potentially inducing $J_{\text{eff}} = 1/2$ behavior as observed in other iridates [258, 259].

The field dependence magnetization data $M(H)$ [Figure V.4] at 2 K, 100 K, and 300 K reveal a progressive evolution of magnetic behavior that aligns with the insights from the inverse susceptibility (χ^{-1}) analysis. At 2 K, the M-H curve shows a maximum magnetization of 3.01 μ_{B} /f.u. at 70 kOe, though it is unsaturated even at high fields. The linear high-field fit [inset] gives an effective saturation moment $M_{\text{s}} \approx 2.01 \mu_{\text{B}}$ /f.u., much lower than both the Curie-Weiss effective moment ($\mu_{\text{eff}} \approx 6.01\text{--}6.28 \mu_{\text{B}}$) and the theoretical spin-only calculated moment ($\mu_{\text{eff}}^{\text{calc}} \approx 6.34 \mu_{\text{B}}$). This stark contrast underscores the impact of antisite disorder evidenced in our mixed-occupation refinements Table V.1, which introduces magnetic frustration, spin canting, and noncollinear spin arrangements, limiting the net field-aligned moment despite the presence of strong ferromagnetic exchange (evident from $\theta_{\text{CW}} \approx +56$ K). At 100 K, the M-H moment decreases to 1.19 μ_{B} /f.u. at 70 kOe, consistent with the reduced long-range order approaching the Curie temperature ($\sim 140\text{--}150$ K from M-T analysis). The system displays lower coercivity (0.16 kOe) and remanent magnetization (0.58 μ_{B} /f.u.), indicating weakened but still present ferromagnetic interactions. At 300 K, the magnetization is negligible, consistent with the fully paramagnetic phase as predicted by Curie-Weiss behavior.

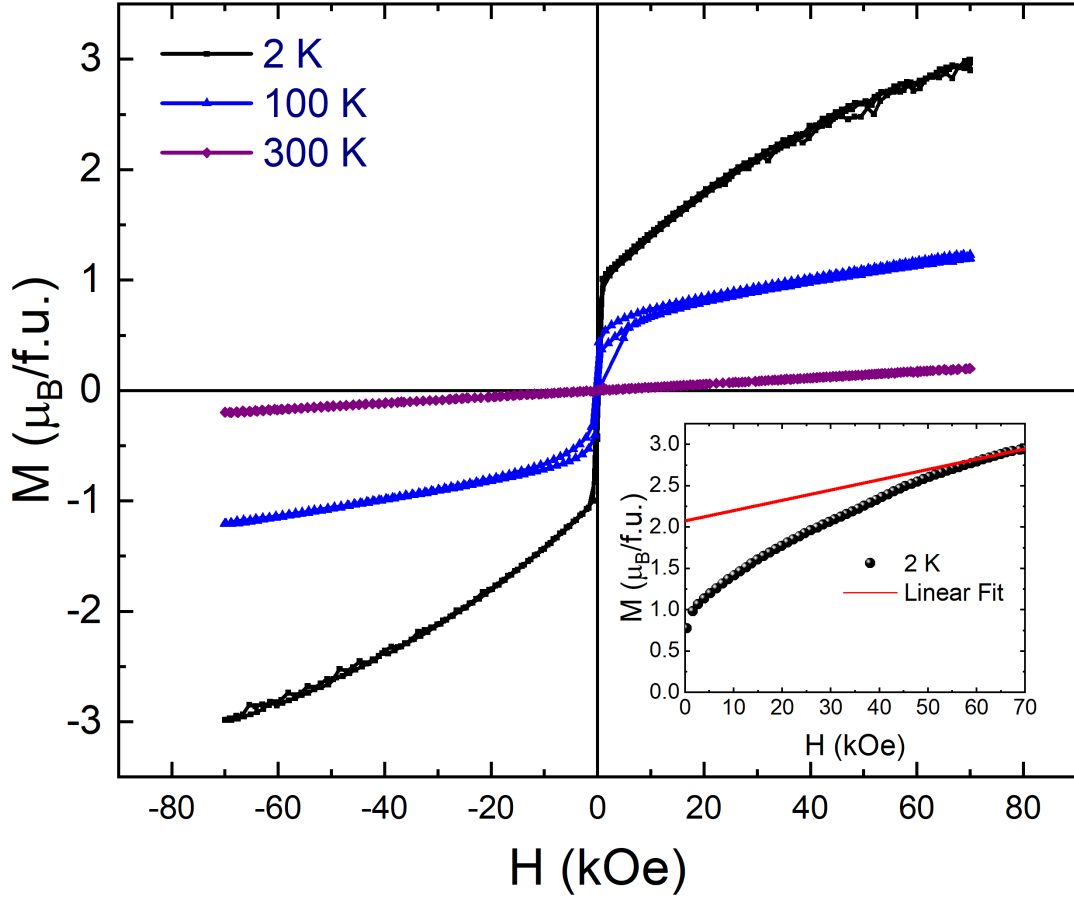


Figure V.4: Isothermal $M(H)$ curves conducted at different temperatures under an applied field of ± 70 kOe. Inset shows the linear extrapolation of saturated magnetization.

5.3.3 AC magnetometry

AC susceptibility measurements (Figure V.5) expose the complex magnetic hierarchy in Nd₂NiMn_{0.25}Ir_{0.75}O₆, where B-site disorder orchestrates competing interactions across distinct temperature regimes. The high-temperature anomaly at 168 K, appearing as frequency-independent shoulders in both χ' and χ'' , signals the formation of short-range magnetic correlations or ferromagnetic clusters above the ordering temperature, a direct consequence of B-site disorder that creates spatially inhomogeneous exchange pathways [112, 260]. The sharp, dispersionless peak at $T_N = 140$ K confirms long-range ferromagnetic order within the transition-metal sublattice, with the frequency independence ruling out glassy behavior at this stage and instead reflecting strong Ni²⁺-(Mn⁴⁺/Ir⁴⁺) exchange [257]. Below this ordering temperature, the system enters a reentrant spin-glass phase characterized by broad, frequency-dependent peaks in χ'' centered at $T_f \approx 80$ -

85 K[zoom-in inset V.5].

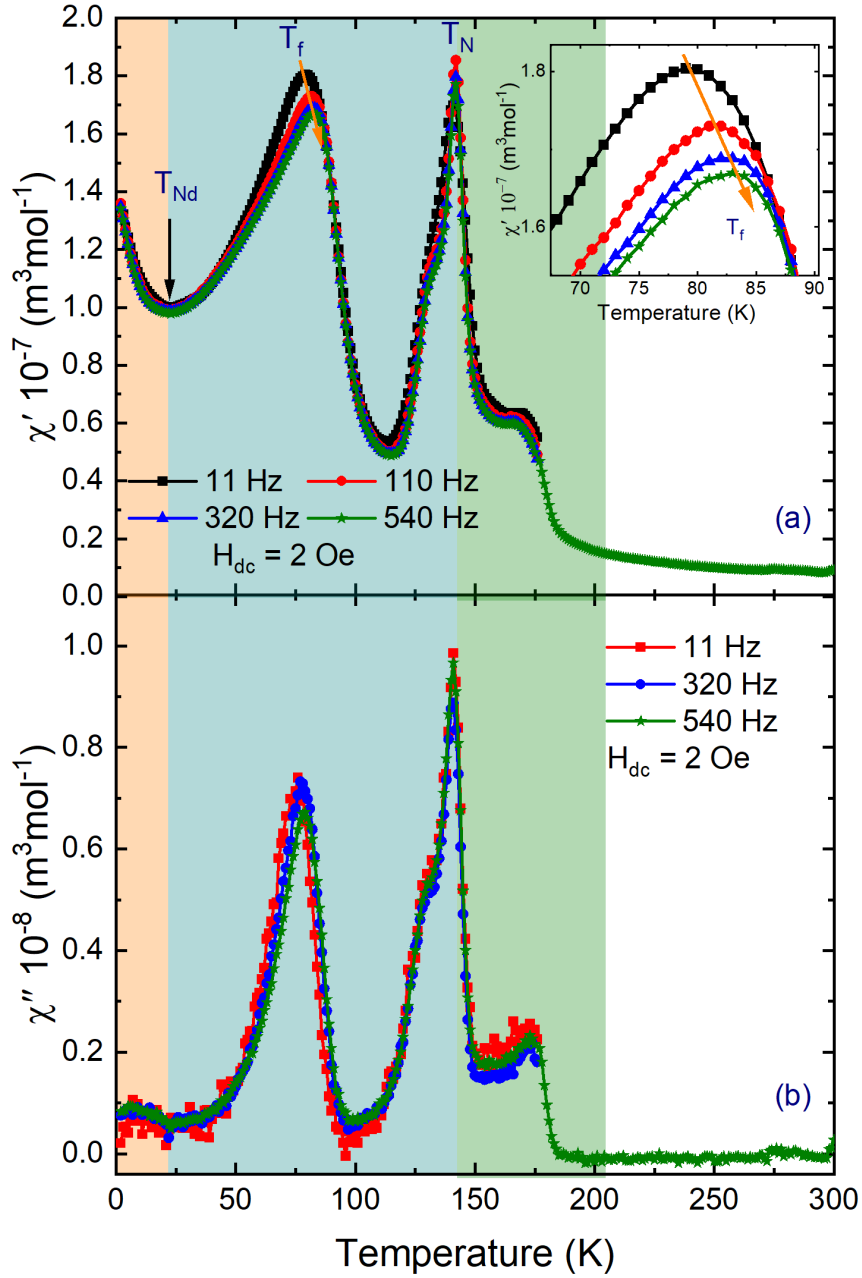


Figure V.5: The real (a) and imaginary (b) parts of the AC magnetic susceptibility of $\text{Nd}_2\text{NiMn}_{0.25}\text{Ir}_{0.75}\text{O}_6$, measured as a function of temperature at different frequencies under $H_{dc} = 2$ Oe. The inset shows an expanded view of T_f .

Quantitative analysis yields a Mydosh parameter $m = 0.0205$ from the T_f shift between 1 Hz and 1 kHz, firmly establishing cluster-glass behavior ($0.005 < m < 0.08$) [5]. This glassy regime emerges from the competition between ferromagnetic $\text{Ni}^{2+}\text{-Mn}^{4+}/\text{Ir}^{4+}$ exchange and antiferromagnetic interactions induced by antisite disorder, creating frozen magnetic clusters within the ferromagnetic matrix [261]. The low-temperature transition at $T_{Nd} = 23$ K, marked by sharp enhancements in both susceptibility components, reflects the ordering of Nd^{3+}

moments through f - d coupling to the transition-metal network [248]. The coexistence of long-range order and glassy dynamics finds theoretical grounding in the Sherrington-Kirkpatrick [262] and Gabay-Toulouse [127] models, which describe such frustrated systems where disorder prevents conventional magnetic ground states [see Appendix 3.2 for a complementary analysis].

5.3.4 Specific Heat

Figure V.6 shows the temperature dependence of the specific heat divided by temperature (C/T) for Nd₂NiMn_{0.25}Ir_{0.75}O₆, measured at zero field (0 T) and under an applied field of 4 T in the temperature range of 2-300 K. The main features include a pronounced downturn approximately 15 K, characteristic of a Schottky-like anomaly, and a broad hump centered around ~ 135 K, indicative of an onset of ferromagnetic correlations within the Ni/Mn/Ir sublattices. At higher temperatures, the specific heat decays smoothly, dominated by the phononic (lattice) contribution. The broad hump is consistent with the formation of ferromagnetic clusters within the Griffiths phase (GP) region above the Curie temperature (T_N). The inset of Figure V.6 highlights the evolution of the low-temperature peak under varying magnetic fields from 0 to 10 T, revealing a clear field dependence of the Schottky anomaly. Also, a sharper upturn near ~ 5 K in the C_p/T vs. T curves for all fields indicates the onset of Nd³⁺ magnetic ordering at low temperatures. This behavior aligns with similar findings in other antisite disordered systems, such as Pr₂MnNiO₆, where magnetic inhomogeneities and cluster-glass behavior are reported to coexist below the magnetic ordering temperature [200].

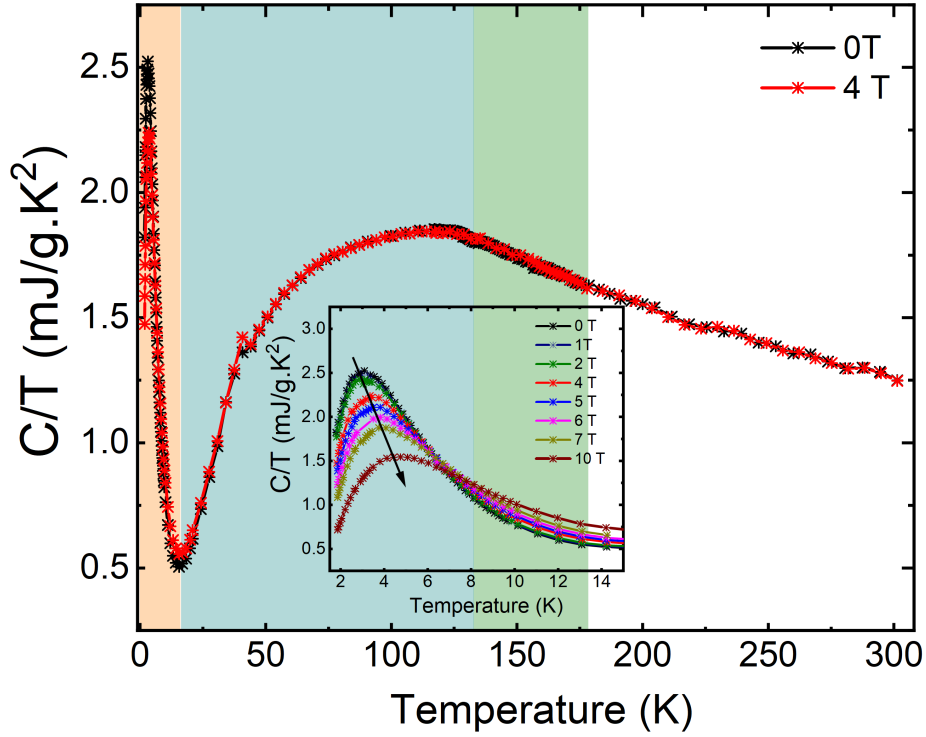


Figure V.6: Temperature dependence of C_p/T vs. T for $\text{Nd}_2\text{NiMn}_{0.25}\text{Ir}_{0.75}\text{O}_6$ measured under 0 T (black) and 4 T (red) magnetic fields. The inset displays expanded low-temperature (2–15 K) C_p/T data under various fields (up to 10 T), showing systematic suppression and broadening of the Schottky anomaly with increasing field.

For detailed analysis of the low-temperature thermodynamic behavior, we focused on the zero-field data ($H = 0$ T), which best captures the intrinsic lattice and crystal field effects without magnetic field perturbations. As a first step, the low-temperature specific heat is fitted using the standard polynomial expression:

$$C_p(T) = \gamma T + B_3 T^3 + B_5 T^5 \quad (178)$$

Figure III.3 (a)[Appendix 3.4] presents the total specific heat $C_p(T)$ of NNMIO measured in zero magnetic field up to 300 K. The black circles denote the experimental data, while the blue curve represents the fitted lattice contribution based on a Debye-type phonon model. A noticeable deviation between the total C_p and the lattice fit emerges below ~ 150 K, indicating the presence of additional magnetic contributions. This becomes more evident in the red curve, which shows the extracted magnetic specific heat $C_{\text{mag}}(T)$. Zooming in to the low-temperature regime (2–20 K), a detailed examination of the C_p/T versus T plots reveals a slope change around 15 K [Figure III.3(b), Appendix 3.4], characteristic of a Schottky anomaly, arising from the Zeeman splitting of the Nd^{3+} ion's $^4\text{I}_{9/2}$ ground state multiplet. Unlike the sharp anomalies commonly seen in structurally parents

perovskites such as NdMnO₃ [263] PrMnO₃ [264], the anomaly in this system is broader and more gradual, reflecting the impact of local site disorder and a distribution of Nd-O environments. As shown in Appendix 3.4 Figure III.3(b), the Schottky fit (dashed line) qualitatively reproduces the peak in $C_{\text{mag}}(T)$, although a slight underestimation of the entropy near the peak is evident, likely due to a spread in crystal field levels caused by local structural disorder. To quantitatively capture the thermal behavior below 50 K, the specific heat data at $H = 0$ T was modeled using a full expression incorporating both lattice and Schottky contributions [see Appendix 3.4, Figure III.3(c)] [200, 265]:

$$C_p(T) = \gamma T + B_3 T^3 + B_5 T^5 + C_{\text{Schottky}}(T) \quad (179)$$

The first term, γT , typically associated with electronic excitations in metals, is instead interpreted here as a signature of low-energy magnetic excitations due to spin disorder or glassy dynamics, corroborated by the large value $\gamma = 75.37 \text{ mJ/mol} \cdot \text{K}^2$, higher than [200, 266]. The $B_3 T^3$ term arises from the Debye model of lattice vibrations, with $B_3 = 6.86 \times 10^{-4} \text{ J/mol} \cdot \text{K}^4$. This yields a Debye temperature:

$$\theta_D = \left(\frac{12\pi^4 R}{5B_3} \right)^{1/3} \approx 141.5 \text{ K} \quad (180)$$

The low Debye temperature (Θ_D) suggests soft phonon modes, likely arising from lattice strain and bonding asymmetry induced by Ni/Mn/Ir substitution. Crucially, the model requires a $B_5 T^5$ term ($B_5 = -1.49 \times 10^{-7} \text{ J/mol} \cdot \text{K}^6$) to accurately capture deviations from ideal Debye behavior, accounting for anharmonic effects and optical phonon contributions above ~ 10 K. Omitting this term produces significant misfits, underscoring its essential role in describing the system's complex lattice dynamics. The Schottky contribution was modeled using:

$$C_p = \frac{1}{2} R \sum_{i=1}^n w_i \left(\frac{\Delta_i}{k_B} \right)^2 \frac{\exp\left(\frac{\Delta_i}{k_B}\right)}{\left[1 + \exp\left(\frac{\Delta_i}{k_B}\right)\right]^2} \quad (181)$$

where Δ represents the crystal field splitting and w is a degeneracy-weighted factor. Fitting yields $\Delta = 10.95 \pm 0.14 \text{ K}$ and $w = 5.33 \pm 0.11$, values consistent with a singlet-singlet transition. The excellent agreement between the full model and the experimental data in Figure III.3(c) confirms that both lattice and crystal field effects significantly contribute to the low-temperature specific heat of

NNMIO. This interpretation is consistent with previous studies in analogous Nd-based perovskites that exhibit broadened Schottky features due to exchange fields and local symmetry fluctuations[267]. To quantify the magnetic contribution, the total entropy change due to magnetic excitations was computed by integrating the magnetic heat capacity C_{mag} over temperature:

$$\Delta S_{\text{mag}} = \int \frac{C_{\text{mag}}}{T} dT = 77.37 \text{ J/mol} \cdot \text{K} \quad (182)$$

Such a substantial entropy release supports the activation of multiple CEF levels and reinforces the role of Nd³⁺-based excitations in the observed thermal anomalies.

5.3.5 Raman Spectroscopy

Temperature-dependent Raman spectra of Nd₂NiMn_{0.25}Ir_{0.75}O₆ (Figure III.2 Appendix 3.3), acquired from 20-290 K ($\Delta T = 5$ K for 20-100 K; $\Delta T = 10$ K above 100 K), reveal well-defined phonon modes (450-750 cm⁻¹) with systematic variations in intensity, linewidth, and frequency. Below 50 K, sharp peaks dominate the 600-720 cm⁻¹ region, corresponding to (Ni/Mn/Ir)O₆ octahedral stretching vibrations. The observed phonon behavior reflects the material's structural evolution from ideal Fm $\bar{3}$ m symmetry (with four Raman-active modes: $A_{1g} + E_g + 2F_{2g}$) to reduced P2₁/n symmetry due to significant B-site cation mismatch (Ni²⁺, Mn⁴⁺, Ir⁴⁺ vs. Nd³⁺) [225]. This symmetry reduction theoretically activates 24 Raman modes ($12A_g + 12B_g$), though only seven are experimentally resolved at 20 K through Gaussian-Lorentzian fitting (Figure V.7): B_g^{I} (466 cm⁻¹), A_g^{I} (505 cm⁻¹), B_g^{II} (581 cm⁻¹), A_g^{II} (604 cm⁻¹), B_g^{III} (646 cm⁻¹), A_g^{III} (687 cm⁻¹), and A_g^{IV} (740 cm⁻¹). DFT calculations and similar systems [225, 233, 268] confirm these assignments, with bending modes (below 600 cm⁻¹) showing minimal thermal variation and stretching modes (above 600 cm⁻¹) displaying strong temperature dependence. The Ir-induced distortion produces two distinct peaks (646 and 687 cm⁻¹) where comparable systems typically show one broad feature[231, 269]. The B_g^{III} mode (646 cm⁻¹) exhibits significant softening (6-8 cm⁻¹) and broadening, demonstrating strong spin-phonon coupling via Ni²⁺/Mn⁴⁺-O-Ir⁴⁺ exchange, while the A_g^{III} mode (687 cm⁻¹) shows anomalous hardening.

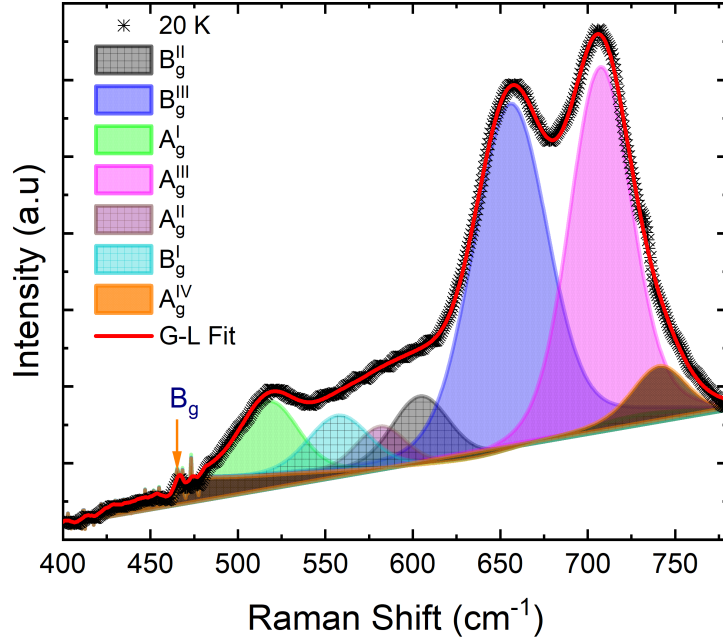


Figure V.7: Raman spectrum of $\text{Nd}_2\text{NiMn}_{0.25}\text{Ir}_{0.75}\text{O}_6$ at 20 K, highlighting phonon mode decomposition. The experimental data (black asterisks) are fitted using a combination of Gaussian-Lorentzian (G-L) functions (solid red curve). Individual vibrational modes are labeled and shaded according to symmetry: $B_g^{\text{I-III}}$ (gray, blue, cyan), $A_g^{\text{I-IV}}$ (green, magenta, violet, orange). The multi-mode structure is consistent with the $P2_1/n$ symmetry of the monoclinic double perovskite phase. Strong and well-resolved features confirm B-site ordering and low-temperature lattice coherence.

To probe the interplay between magnetic ordering and lattice dynamics, we focus on the A_g^{I} (505 cm^{-1}), B_g^{III} (646 cm^{-1}), and A_g^{III} (687 cm^{-1}) modes, which exhibit distinct responses to spin-lattice interactions. To quantitatively analyze the temperature-dependent phonon behavior, we modeled the Raman shifts and linewidths using anharmonic coupling theory, accounting for three-phonon interactions through both Klemens approaches [230]:

$$\omega_{\text{anh}}(T) = \omega_0 + C_1 \left[1 + \frac{2}{e^x - 1} \right] + C_2 \left[1 + \frac{3}{e^y - 1} + \frac{3}{(e^y - 1)^2} \right], \quad (183)$$

$$\Gamma_{\text{FWHM}}(T) = K_1 \left[1 + \frac{2}{e^x - 1} \right] + K_2 \left[1 + \frac{3}{e^y - 1} + \frac{3}{(e^y - 1)^2} \right], \quad (184)$$

where $x = \frac{\hbar\omega_0}{2k_B T}$ and $y = \frac{\hbar\omega_0}{3k_B T}$ represent the phonon occupation factors. C_1 , C_2 , K_1 , and K_2 are the anharmonic coupling constants for frequency and linewidth, respectively. For modes exhibiting linear trends, a simplified linear temperature dependence was adopted:

$$\omega(T) = \omega_0 + \alpha T, \quad (185)$$

where α is the thermal coefficient of frequency shift. Temperature-dependent

Raman measurements uncover striking evidence of strong spin-phonon coupling with all observed modes (A_g^I , B_g^{III} , and A_g^{III}) exhibiting pronounced deviations from conventional anharmonic behavior that correlate with magnetic transitions. The A_g^I mode (Figure V.8a) shows a remarkable 2.5 cm^{-1} hardening below 180 K, peaking near 140 K, coinciding with the onset of long-range magnetic order. This anomalous stiffening, well described by two distinct linear regimes ($\alpha = -0.041 \text{ cm}^{-1}/\text{K}$ above 130 K and $\alpha = +0.027 \text{ cm}^{-1}/\text{K}$ below), directly reflects exchange striction effects as the spin system orders [41, 270]. The B_g^{III} mode (Figure V.8b) reveals even more complex behavior, with anomalous softening between 170-230 K followed by stabilization and eventual stiffening below 130 K, indicating the evolution from ferromagnetic clusters to long-range order[271]. Most remarkably, the A_g^{III} mode (Figure V.8c) displays a saturation plateau below 130 K and subsequent softening below 50 K, indicating complete spin correlation and possible spin-driven phonon renormalization. These concurrent anomalies across all modes demonstrate a global lattice response to magnetic ordering, analogous to effects observed in La₂NiMnO₆ (exchange striction) [225] and Sr₂IrO₄ (spin-orbit-entangled magnetism) [272]. While similar phonon hardening has been reported in RCrO₃ systems [273], the precise mechanism-whether direct spin-phonon coupling or magnetostriction-mediated effects-requires further investigation.

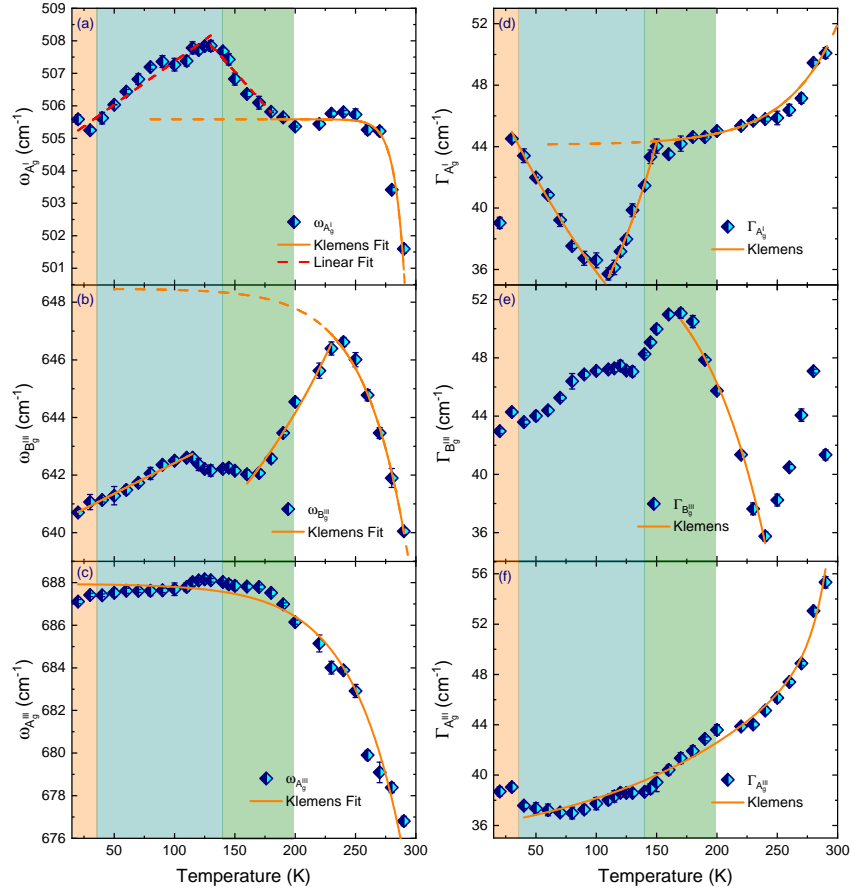


Figure V.8: Temperature evolution of phonon frequencies $\omega(T)$ and full-width at half-maximum linewidths $\Gamma(T)$ for the A_g^I , B_g^{III} , and A_g^{III} Raman modes of $\text{Nd}_2\text{NiMn}_{0.25}\text{Ir}_{0.75}\text{O}_6$. Panels (a-c) show the frequency shifts, while panels (d-f) present the corresponding linewidth broadening as a function of temperature. Experimental data (blue diamonds) are fitted using Klemens-type anharmonic models (solid orange curves). In panel (a), a linear thermal model (dashed red line) is also shown for comparison. The shaded regions denote different magnetic regimes: white (paramagnetic), blue (spin-glass-like), and green (FM ordering), highlighting the spin-lattice coupling anomalies, particularly in B_g^{III} and A_g^{III} modes.

The temperature evolution of phonon linewidths reveals distinct signatures of spin-lattice coupling across different vibrational modes. The A_g^I mode (Figure V.8d) displays a pronounced minimum in FWHM near 115 K, with the linewidth suppression below 140 K ($\omega_0 = 17.28 \pm 1.52 \text{ cm}^{-1}$, $K_1 = 32.87 \pm 1.88$) signaling enhanced phonon coherence due to long-range magnetic ordering of the $\text{Ni}^{2+}/\text{Mn}^{4+}/\text{Ir}^{4+}$ sublattices. This behavior contrasts sharply with the conventional anharmonic expectation ($\omega_0 = 44.12 \pm 0.31 \text{ cm}^{-1}$, $K_1 = 0.007 \pm 0.009$ at high T), mirroring effects observed in $\text{La}_2\text{NiMnO}_6$, $\text{La}_2\text{CoMnO}_6$ and Y_2CoMnO_6 , where magnetic ordering induces phonon lifetime renormalization [221, 225, 274, 275]. The subsequent linewidth broadening above 140 K reflects increased scattering from spin fluctuations and spin-orbit-coupled states of Ir^{4+} ($5d^4$), analogous to phenomena reported in Sr_2IrO_4 and Ba_2YIrO_6 [268, 272, 276]. The B_g^{III} mode

(Figure V.8e) shows markedly different behavior, with monotonic broadening up to 170 K (deviating from Klemens model predictions with $\omega_0 = 56.77 \pm 4.59 \text{ cm}^{-1}$, $K_1 = -0.29 \pm 0.52$) that stems from three factors: (1) static disorder from B-site cation mixing, (2) magnetostrictive strain effects, and (3) spin-orbit-enhanced electron-phonon coupling. The peak near 170 K coincides with the development of short-range magnetic correlations, while the high- T decrease indicates weakening spin-lattice interactions in the paramagnetic regime. In contrast, the A_g^{III} mode (Figure V.8f) follows ideal anharmonic behavior ($\omega_0 = 33.61 \pm 2.24 \text{ cm}^{-1}$, $K_1 = (0.75 \pm 0.12) \times 10^{-9}$, $K_2 = 12.70 \pm 0.36$) across the entire temperature range, demonstrating its decoupling from magnetic degrees of freedom. The minor deviations near magnetic transitions may arise from weak magnetostrictive effects or/and potentially thermally activated electron-phonon coupling [234, 277]. In magnetic oxides, phonons are sensitive probes of underlying spin correlations. Sushkov *et al.* [278] showed in ZnCr₂O₄ that phonon frequency shifts above and below the spin-Peierls transition closely track the nearest-neighbor spin correlation function $\langle \mathbf{S}_i \cdot \mathbf{S}_j \rangle$ measured independently via magnetic specific heat, demonstrating a direct link between lattice vibrations and magnetism. Adapting their approach, one can express the coupled phonon frequency as:

$$\omega(T) = \omega_0 + \lambda \langle \mathbf{S}_i \cdot \mathbf{S}_j \rangle, \quad (186)$$

where ω_0 is the baseline phonon frequency in the absence of spin-lattice interaction, and λ quantifies the spin-phonon coupling strength. The spin-phonon coupling constant (λ) was calculated using the Sushkov formalism [278], which relates λ to the exchange coupling (J) and phonon frequency (ω_0) via

$$\lambda = \frac{k^2 a^2 J}{\hbar m \omega_0}, \quad \text{where} \quad k = \sqrt{\frac{2z}{3}} a_B^{-1}, \quad a = \frac{2z}{3a_B}, \quad J = \frac{3k_B \Theta_{\text{CW}}}{z S_{\text{eff}}(S_{\text{eff}} + 1)}. \quad (187)$$

Here, $z = 6$ is the coordination number, $a_B = 0.529 \text{ \AA}$ is the Bohr radius, and $S_{\text{eff}} = 0.866$ represents the effective spin from Ni²⁺-Mn⁴⁺/Ir⁴⁺ mixing. Using $\Theta_{\text{CW}} = 55.5 \text{ K}$ (from Curie-Weiss analysis) and the A_g^{I} phonon mode ($\omega_0 = 505.6 \text{ cm}^{-1}$), we obtain $J = +0.46 \text{ meV}$ and $\lambda = 2.1 \text{ cm}^{-1}$. Similar calculations for the B_g^{III} ($\omega_0 = 648.5 \text{ cm}^{-1}$) and A_g^{III} ($\omega_0 = 687.9 \text{ cm}^{-1}$) modes yield $\lambda = 1.6 \text{ cm}^{-1}$ and $\lambda = 1.5 \text{ cm}^{-1}$, respectively. These results are consistent with prior studies on other geometrically frustrated systems and 3d-5d perovskite systems, such as ZnCr₂O₄ ($\lambda \approx 3\text{-}6 \text{ cm}^{-1}$) [278], Sr₂CoO₄ [279], NaOsO₃ [280], and Eu₂ZnIrO₆

[268], but show systematically weaker coupling due to Ir⁴⁺ dilution, emphasizing the impact of spin-orbit interaction in moderating spin-lattice coupling. To investigate spin-lattice interactions in NNMIO, we analyzed the temperature dependence of phonon frequency shifts, $\delta\omega(T) = \omega_{\text{obs}}(T) - \omega_{\text{anh}}(T)$, where $\omega_{\text{obs}}(T)$ is the measured phonon frequency and $\omega_{\text{anh}}(T)$ is the anharmonic baseline. According to the model proposed by Granado *et al.* [235], this shift is proportional to the spin-spin correlation function, which under mean-field approximation scales with the square of the normalized magnetization:

$$\delta\omega(T) = \lambda \left[\frac{M(T)}{M_{\text{max}}} \right]^2, \quad (188)$$

where λ is the spin-phonon coupling constant, $M(T)$ is the magnetization at temperature T , and M_{max} is the saturation magnetization in the ordered state. Figure V.9 compares $\delta\omega(T)$ (blue diamonds, left axis) with $[M(T)/M_{\text{max}}]^2$ (green triangles, right axis) for three Raman-active modes: (a) A_g^I , (b) B_g^{III} , and (c) A_g^{III} . In all modes, a strong temperature dependence of $\delta\omega(T)$ is evident near the magnetic transition at $T_C \approx 140$ K. In panels (a) and (b), the phonon frequency shifts closely track the evolution of the magnetization, indicating a strong spin-phonon coupling. The A_g^I mode exhibits a smooth increase in $\delta\omega(T)$ below T_C , saturating in tandem with $[M(T)/M_{\text{max}}]^2$. The B_g^{III} mode shows a sharper anomaly, with $\delta\omega(T)$ peaking between 100-120 K. In contrast, the A_g^{III} mode [panel (c)] shows delayed and nonlinear behavior, with $\delta\omega(T)$ becoming strongly negative only below ~ 100 K. This divergence suggests that the high-frequency mode is influenced by additional structural or exchange effects. The partial mismatch between $\delta\omega(T)$ and $[M(T)/M_{\text{max}}]^2$ likely results from the coexistence of multiple magnetic phases, ferromagnetic, FM cluster observed in the GP-phase, and possible spin-glass regions, typical in B-site disordered perovskites. These competing interactions, varying in both sign and magnitude, renormalize phonon modes differently. Similar behavior has been reported in Y₂CoMnO₆, La₂CoMnO₆, Pr₂CoFeO₆, and Sr_{0.6}Ba_{0.4}MnO₃ [225, 233, 281].

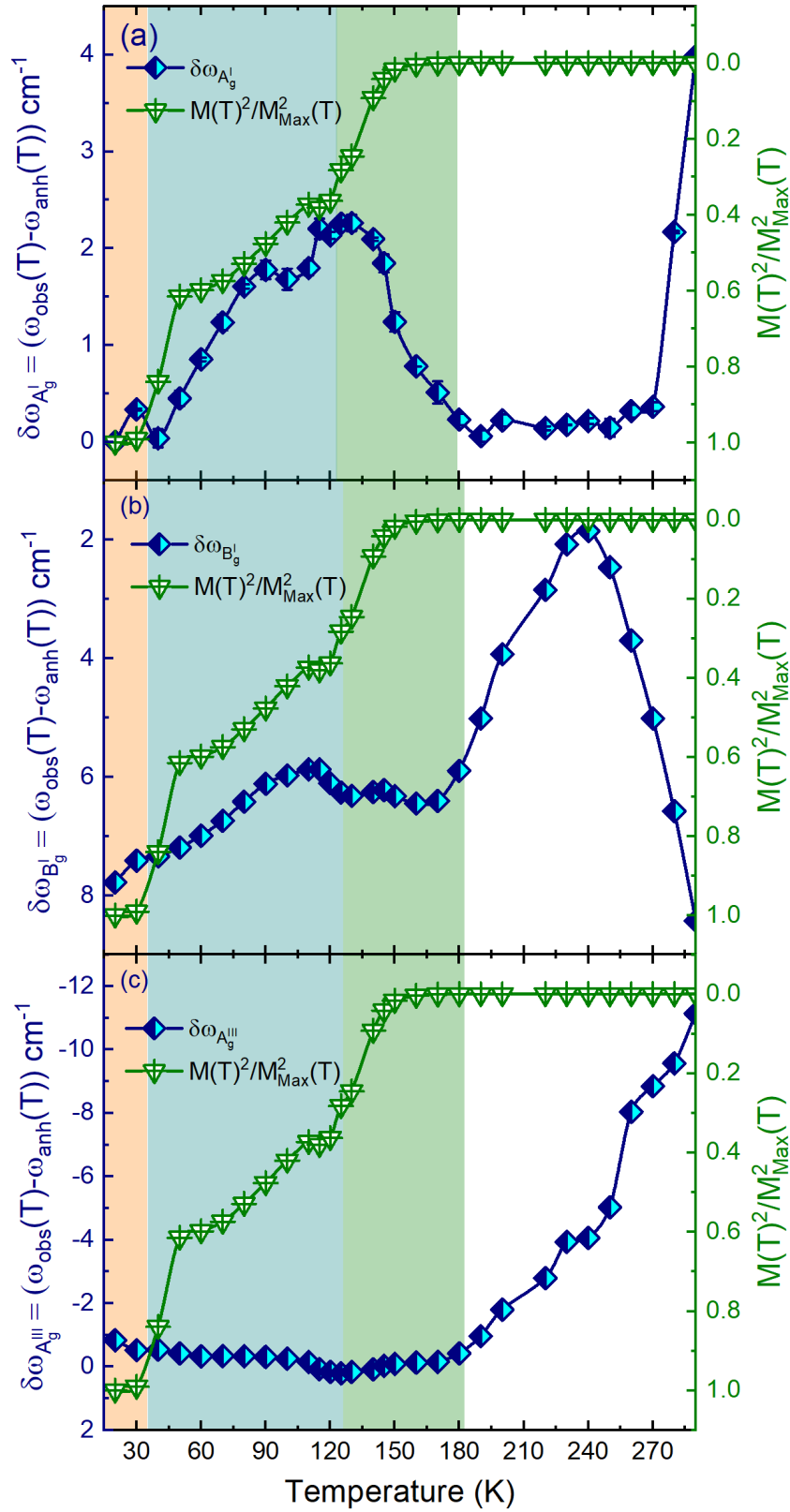


Figure V.9: Temperature dependence of phonon renormalization $\delta\omega(T) = \omega_{\text{obs}}(T) - \omega_{\text{anh}}(T)$ (left axis, blue diamonds) and normalized magnetization squared $[M(T)/M_{\text{max}}]^2$ (right axis, green triangles) for (a) A_g^I , (b) B_g^{III} , and (c) A_g^{III} Raman-active modes in $\text{Nd}_2\text{NiMn}_{0.25}\text{Ir}_{0.75}\text{O}_6$. The close correspondence between the two quantities near the ferromagnetic transition temperature ($T_C \approx 140 \text{ K}$) indicates strong spin-phonon coupling. Deviations at lower temperatures are attributed to competing magnetic interactions and site disorder.

5.3.6 Neutron powder diffraction

Concomitant with changes in the magnetometry data, pronounced evolution in the neutron powder diffraction patterns was observed upon cooling. Below the onset of magnetic ordering ($T_N \approx 140$ K), additional magnetic reflections appeared, which could be indexed relative to the monoclinic parent space group $P2_1/n$, specifically on the (100), (010), and (111) families of reflections. This behavior is fully consistent with the development of long-range magnetic order at the Γ -point ($\mathbf{k} = (0,0,0)$), indicative of a commensurate magnetic ground state. To rigorously isolate the magnetic scattering, refinements were performed on difference patterns obtained by subtracting the paramagnetic phase at 200 K from the datasets collected at 100 K, 40 K, and 1.5 K. This subtraction procedure effectively removes nuclear Bragg contributions and incoherent backgrounds, allowing direct modeling of the magnetic scattering. However, as is common with difference refinements, data in the d -spacing regions between 3.7 Å and 4.0 Å, as well as above 6.7 Å, were excluded due to residual instrumental artifacts, parasitic backgrounds, and deteriorated signal-to-noise ratios. Excluding these regions was critical to stabilizing the refinement. Magnetic symmetry analysis, performed using ISODISTORT, combined with structure factor calculations for the three cation sublattices (Ni, Mn/Ir, and Nd), revealed characteristic magnetic reflection conditions of the monoclinic system: specifically, $h0l$ reflections where $h + l = 2n$, and $0k0$ reflections where $k = 2$. These selection rules are fully consistent with the parent compound Nd₂NiMnO₆, whose magnetic symmetry was previously analyzed and presented in [IV.2](#).

At $T = 100$ K, we tested two magnetic structure models against neutron NPD data, both incorporating magnetic moments on the A , B , and B' sites and transforming according to the irreducible representations Γ_1^+ and Γ_2^+ . After detailed analysis, the Γ_1^+ magnetic structure in the $P2_1/n.1(14.75)$ space group was unambiguously identified as the model that best reproduces the observed magnetic intensities. The basis vectors for this model were defined as $[1,0,0]$, $[0,1,0]$, and $[0,0,1]$, with the origin at $[0,0,0]$ and compatible with FM F mode aligned parallel to the monoclinic b -axis, augmented by an AFM A -type mode perpendicular to b . The refinement results indicate a second-order magnetic transition at T_N , with the Ni²⁺ sublattice ordering ferromagnetically along the b -axis and no detectable canting into the ac -plane. This configuration transforms according to

the irreducible representation $m\Gamma_1^+$, which is fully consistent with the symmetry constraints of the monoclinic $P2_1/n$ structure. Magnetic structure factor calculations further validate this model, showing non-vanishing intensity exclusively at reflections satisfying the condition $h0l$ with $h+l=2n$. In contrast, reflections such as (010), (100), and (111) remain systematically weak or absent due to symmetry-induced cancellations. To enhance refinement stability and minimize correlations with the nuclear structure, the Ni1 and Ni2 magnetic sublattices were constrained to have identical moment magnitudes. The refinement converged to a magnetic moment of $1.31(11)\mu_B$ per Ni ion, with strict alignment along $\theta = 90^\circ$ and $\varphi = 90^\circ$ (parallel to the b -axis). While the Mn/Ir sublattice contribution was not explicitly refined, its effects were evaluated post hoc using representative reflections such as (101), ($\bar{1}01$), and (011), whose intensity is sensitive to the interference between Ni and Mn/Ir sublattices. The analysis assumed a simplified model with magnetic structure factors:

$$\begin{aligned} F_{(101)} &\propto -(m_1 + m_2) + (m_3 + m_4), \\ F_{(011)} &\propto -(m_1 + m_2) + (m_3 + m_4), \end{aligned} \quad (189)$$

$$\begin{aligned} I_{(101)} &\propto m_1^2 + m_3^2 - 2m_1m_3, \\ I_{(011)} &\propto m_1^2 + m_3^2 - 2m_1m_3. \end{aligned} \quad (190)$$

under the assumptions $|m_1| = |m_2| = |m_{\text{Ni}}|$ and $|m_3| = |m_4| = |m_{\text{Mn}}|$, with an antialigned configuration defined as $m_1 = m_{\text{Ni}} - m_{\text{Mn}}$. Using the refined Ni moment $m_{\text{Ni}} = 1.31\mu_B$ and assuming the fully saturated value $m_{\text{Ni}} = 2\mu_B$, the analysis yields an effective Mn/Ir moment of approximately $0.69\mu_B$ with a total free-ion moment of $m_T = 1.32\mu_B$. This partial compensation explains the suppression of (011) and enhancement of (010) intensities, with the residual Mn/Ir moment indicating incomplete ordering due to frustration in the mixed Mn⁴⁺/Ir⁴⁺ sublattice. Despite this suppression, the final refinement achieved excellent statistical agreement ($R_p = 1.45\%$, $R_{wp} = 1.80\%$, $R_{exp} = 1.72\%$, $R_{mag} = 1.10\%$, with model shown in Figure V.2b, consistent with dominant d - d exchange interactions. Upon cooling to 40 K, the diffraction pattern reveals subtle but significant changes in the magnetic scattering. While the intensities of the (010) and (101) reflections remain nearly constant, the (011) reflection exhibits a marked increase, signaling an evolution in the magnetic ground state. Symmetry analysis confirms that the propagation vector $\mathbf{k} = 0$ is retained, with the magnetic structure still

transforming under the $m\Gamma_1^+$ representation. Refinement of the magnetic signal (40 K – 200 K) shows that the Ni²⁺ sublattice maintains its collinear ferromagnetic alignment along the b -axis, with the ordered moment increasing to $1.572(9)\mu_B$ ($\theta = 90^\circ$, $\varphi = 90^\circ$). Structure factor analysis, following the same interference model as at 100 K, yields a Mn/Ir moment of approximately $0.43\mu_B$, a reduction from $0.69\mu_B$ at 100 K with a total free-ion moment of $m_T = 1.63\mu_B$. Residual discrepancies persist in low index reflections (100), (010), and (111), which are attributable to microstructural disorder arising from the large ionic radius and mass contrast between Mn⁴⁺ and Ir⁴⁺. These effects introduce diffuse scattering and peak broadening not fully captured by the magnetic model. The refinement achieves excellent agreement ($R_p = 1.92\%$, $R_{wp} = 2.39\%$, $R_{exp} = 2.01\%$, $R_{mag} = 2.39\%$) [model shown Figure V.2c], supporting the $m\Gamma_1^+$ -type ferromagnetic order dominated by Ni²⁺, with a diminishing yet non-negligible Mn/Ir contribution, consistent with dominant d - d exchange interactions

At 1.5 K, Nd₂NiMn_{0.25}Ir_{0.75}O₆ achieves its fully ordered ground state described by the Γ_1^+ ($F \parallel$, $A \perp$) representation with propagation vector $\mathbf{k} = (0,0,0)$. The magnetic structure features three interacting sublattices: (i) Ni²⁺ ions exhibit perfect collinear ferromagnetism along the b -axis with $m = -1.616(96)\mu_B$; (ii) the Mn/Ir sublattice shows alignment yielding a net moment of $-0.384(8)\mu_B$ through the relation $m = m_{Ni} - m_{Mn/Ir}$; and (iii) Nd³⁺ ions order coherently with $m = 1.182(26)\mu_B$ per site, displaying simultaneous ferromagnetic b -axis alignment [$-1.052(26)\mu_B$] and A -type antiferromagnetic canting in the ac -plane [$\pm 0.373(9)\mu_B$ (along a) and $\pm 0.393(9)\mu_B$ (along c)]. This configuration produces a total magnetic moment of $1.66\mu_B$ per formula unit while maintaining $\mathbf{k} = (0,0,0)$ periodicity. The competing $F \parallel$ (b -axis) and $A \perp$ (ac -plane) interactions explain the characteristic reflection modulation, notably the suppression of (011) through Nd interference effects and enhancement of (102)/(012) via interplane correlations. High-quality refinements ($R_p = 1.53\%$, $R_{wp} = 1.82\%$, $R_{mag} = 3.90\%$) validate this model, where the residual intensity in (100) and (111) arises from the Mn / Ir disorder within the symmetry. The refinement results are presented in Figure V.2d, and the corresponding magnetic structure is illustrated in Figure V.10. The systematic moment reduction in the Mn/Ir sublattice ($m_{Mn/Ir} = 0.69\mu_B$ at 100 K \rightarrow $0.43\mu_B$ at 40 K \rightarrow $0.38\mu_B$ at 1.5 K) reveals progressive relief of 5d-electron frustration with cooling. This behavior contrasts sharply with related iridates that require multiple \mathbf{k} -vectors for mag-

netic structure description, whereas our system maintains both Γ_1^+ symmetry and a propagation vector $\mathbf{k} = (0,0,0)$ across all temperatures. The conserved order parameter indicates a unified magnetic ground state distinct from the phase-separated scenarios reported in analogous compounds, the observed non-collinear arrangement emerges from competing anisotropies: Ir⁴⁺-mediated effects: Strong single-ion anisotropy enforces strict collinearity of Ni²⁺ spins along the *b*-axis. Nd³⁺ contributions: Balanced *f-f* exchange and *f-d* coupling induce canting in the *ac*-plane. This dual-anisotropy mechanism explains both the robust *b*-axis alignment of the transition-metal moments and the temperature-dependent moment reduction in the 5d sublattice.

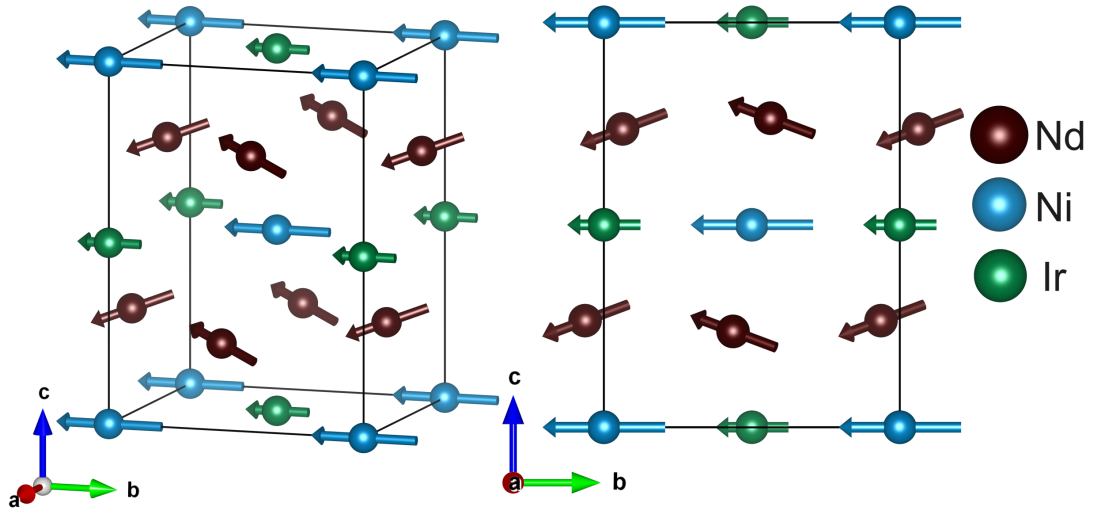


Figure V.10: Refined magnetic structure of Nd₂NiMn_{0.25}Ir_{0.75}O₆ at 1.5K, corresponding to the $m\Gamma_1^+(F_{\parallel} + A_{\perp})$ irreducible representation. The left panel shows the three-dimensional view, while the right panel displays the projection along the *a*-axis. Magnetic moments are primarily aligned along the *b*-axis (F_{\parallel}) with an additional *A*-type antiferromagnetic component within the *ac*-plane (A_{\perp}) for the Nd sublattice. Nd, Ni, and Ir atoms are represented by maroon, blue, and green spheres, respectively. The crystallographic unit cell is outlined in black. Cartesian axes (*a*, *b*, *c*) are indicated for clarity.

Our study of Nd₂NiMn_{0.25}Ir_{0.75}O₆ represents a significant improvement over previous investigations of Ir-based double perovskites, particularly Nd₂NiIrO₆ [154, 248]. While earlier works either lacked complete sublattice resolution or required coexisting magnetic phases ($\mathbf{k} = (0,0,0)$ and $\mathbf{k} = (\frac{1}{2}, \frac{1}{2}, 0)$) to explain low-temperature behavior, our system achieves three key breakthroughs. First, we resolve the full magnetic structure within a single Γ_1^+ (F_{\parallel} , A_{\perp}) model across all temperatures, eliminating the need for phase coexistence as proposed for Nd₂NiIrO₆ [248]. This unified approach provides a more consistent description of the magnetic ordering. Second, our work significantly improves upon pre-

vious moment refinements. While Ref.[154] could only determine Ni ($1.71\mu_B$) and Ir ($0.32\mu_B$) moments at 40 K ($R_{\text{mag}} = 25.7$), we simultaneously refine Ni ($-1.616\mu_B$), Mn/Ir ($-0.38\mu_B$), and Nd ($-1.18\mu_B$) moments at 1.5 K with superior agreement ($R_{\text{mag}} = 3.9$). Third, we identify previously unresolved features of the magnetic structure. Unlike the *b*-axis-confined moments proposed in Ref. [154], we observe Nd³⁺ canting in the *ac*-plane ($\pm 0.38\mu_B$) coexisting with *b*-axis ferromagnetism. Our Mn/Ir substitution also clarifies the debate about Ir⁴⁺ moments, demonstrating intermediate values (0.38 - $0.69\mu_B$) that reconcile earlier conflicting reports of $0.32\mu_B$ [154] and $1.02\mu_B$ [248]. These advances gain particular importance when compared to isostructural Nd₂ZnIrO₆ [257], highlighting the unique role 3d-5d-4f interactions. Meanwhile, the magnetic structures of Nd₂NiMn_{0.25}Ir_{0.75}O₆ and Nd₂NiMnO₆ reveal fundamental differences in their 3d-5d-4f interactions. Both systems order with $\mathbf{k} = (0, 0, 0)$, but the Ir-doped compound exhibits three key modifications. The Ni²⁺ moments maintain strict *b*-axis alignment (F_{\parallel}) rather than canting into the *ac*-plane, suggesting Ir-induced single-ion anisotropy (SIA) competes with the native Ni/Mn easy-plane anisotropy. The Mn/Ir sublattice moment reduces dramatically ($2.18\mu_B \rightarrow 0.38\mu_B$), indicating strong frustration from Ir's spin-orbit-coupled 5d states. Furthermore, Nd³⁺ ordering develops a coherent Γ_1^+ mode with *b*-axis ferromagnetism plus *ac*-plane canting (A_{\perp}), contrasting with Nd₂NiMnO₆'s symmetry-breaking non-collinear structure. The DC and AC susceptibility data below $T_{\text{Nd}} \approx 23$ K exhibit persistent frequency-dependent broadening, indicating that partial Nd disorder survives even in the magnetically ordered state. This behavior likely arises from competing interactions: (1) Nd's single-ion easy-axis anisotropy, which favors *b*-axis alignment; (2) *f*-*f* exchange (*A*-mode) that stabilizes antiparallel *ac*-plane canting; and (3) disordered local fields originating from the frustrated Mn/Ir sublattice. The refined Nd moments ($1.18\mu_B$ at 1.5 K) remain significantly reduced compared to free-ion values, further corroborating this picture of incomplete ordering. Notably, Ir substitution introduces a dual effect: while it suppresses magnetization on the B-site (Mn/Ir), it simultaneously enhances 3d-4f coupling, as evidenced by the strong *b*-axis alignment of both Ni and Nd moments. This suggests that Ir mediates longer-range Nd-Ni exchange interactions, which partially mitigate the local disorder effects. The resulting ground state stabilizes the Γ_1^+ symmetry despite competing anisotropies, demonstrating a novel pathway to engineer coherent 3d-5d-4f magnetism in frustrated systems.

5.4 Conclusion

Through a multimodal experimental approach, we establish that Ir substitution in Nd₂NiMn_{0.25}Ir_{0.75}O₆ creates a spin-orbit-driven cluster-glass system with emergent quantum behaviors. The compound's monoclinic $P2_1/n$ structure, featuring significant antisite disorder, hosts a complex magnetic landscape where long-range ferromagnetic order ($T_N = 140$ K) mediated by 3d-5d exchange coexists with pronounced frustration. Neutron diffraction reveals a temperature-dependent hierarchy of interactions: collinear Ni²⁺ ordering ($1.31(11)\mu_B$ along b) dominates at 100 K, while the Mn/Ir sublattice remains only partially ordered ($0.69\mu_B$). By 1.5 K, the system evolves into a coherent yet frustrated ground state—Ni²⁺ and Nd³⁺ align ferromagnetically along b , while Nd³⁺ simultaneously exhibits ac -plane canting ($1.18\mu_B$), a direct consequence of competing anisotropies: Ir⁴⁺ spin-orbit-coupling-driven collinearity versus Nd³⁺ f - d exchange. This non-collinear configuration resolves longstanding discrepancies in Ir⁴⁺ moment sizes and demonstrates a 58 K suppression of T_N relative to the parent compound, underscoring the destabilizing role of 5d spin-orbit coupling and disorder. Crucially, the system avoids the phase separation observed in analogues like Nd₂NiIrO₆, instead forming a reentrant cluster-glass state evidenced by frequency-dependent susceptibility and reduced moments. Complementary Raman and heat capacity measurements confirm strong spin-phonon coupling and correlated disorder effects. Our work delineates a materials design paradigm where 5d substitution simultaneously enhances 3d-4f coupling via parallel Ni/Nd alignment and introduces SOC-driven frustration. This dual mechanism offers a pathway to engineer exotic complex 3d-5d-4f perovskites and reveals microscopic interplay between competing interactions in spin-orbit coupled oxides, with broad implications for manipulating emergent phenomena in complex materials.

* CHAPTER VI *

Magnetostructural Coupling: Analysis in NdSmNiMnO₆ Double Perovskite

We present a comprehensive investigation of the double perovskite NdSmNiMnO₆, combining high-resolution synchrotron X-ray diffraction, magnetometry, XANES, Raman spectroscopy, and DFT calculations to elucidate its structure-property relationships. Rietveld refinement of synchrotron data reveals a well-ordered monoclinic ($P2_1/n$) structure with rock-salt arrangement of Ni^{2+} and Mn^{4+} cations, characterized by significant octahedral distortions ($\langle Ni-O-Mn \rangle \approx 146^\circ$). Magnetic measurements identify two distinct transitions: (i) a dominant ferromagnetic ordering at $T_1 = 175$ K driven by Ni^{2+} -O- Mn^{4+} superexchange, and (ii) a low-temperature ferrimagnetic state ($T_{Nd/Sm} = 4$ K) arising from competing interactions between rare-earth moments (Nd^{3+}/Sm^{3+}) and the transition metal network. XANES spectra provide definitive evidence for the Ni^{2+} ($t_{2g}^6 e_g^2$) and Mn^{4+} ($t_{2g}^3 e_g^0$) oxidation states, with edge positions and pre-peak intensities matching reference compounds. The material exhibits strong magnetoelastic coupling, manifested through: (1) anomalous phonon hardening in Raman spectra below T_N , (2) distinct lattice parameter anomalies at magnetic transitions, and (3) DFT-predicted magnetostriction effects. First-principles calculations reveal a ferrimagnetic ground state with local moments of $1.6 \mu_B$ (Ni) and $3.0 \mu_B$ (Mn), stabilized by cooperative Jahn-Teller distortions. Notably, spin-orbit coupling quenches the Sm^{3+} moment by 94% ($4.93 \mu_B \rightarrow 0.3 \mu_B$), while preserving an insulating gap of 1.6-1.7 eV through Ni/Mn 3d-O 2p hybridization. These results establish NdSmNiMnO₆ as a model for understanding how A-site disorder (Nd/Sm), B-site ordering (Ni/Mn), and spin-lattice interactions collectively tune emergent properties in double perovskites. The observed interplay between electronic correlations, orbital physics, and magnetostructural coupling provides a blueprint for designing multifunctional oxides with tailored magnetic and electronic responses.

Acknowledgements: The results presented in this chapter will be published as John M. Attah-Baah *et al.* (in preparation). I gratefully acknowledge my

collaborators for their essential contributions: Dr. Romualdo Silva Jr. (under Prof. Nilson S. Ferreira's supervision) for sample synthesis and magnetometry, Dr. Rai for Raman spectroscopy, and Dr. Cledson Santos for DFT calculations. All data analysis was performed by the author. This work was supported by CNPq (309184/2022-3, 141485/2021-0) and IFGW/UNICAMP for magnetometry access.

6.1 Introduction

The novel properties of perovskites have been known for a while, particularly the paramagnetic (PM) to ferromagnetic (FM) transition at Curie temperature (T_C) and the attributed insulator-metal transition (T_{IM}) in the case of cobalt and manganite [37]. Rare-earth based double perovskite (DP) oxides, denoted by $\text{RE}_2\text{BB}'\text{O}_6$, where B and B' span 3d, 4d, 5d, and 4f elements, and X represents O, F, etc., manifest in three ordered variants: $\text{AA}'\text{B}_2\text{O}_6$, $\text{AA}'\text{BB}'\text{O}_6$, or $\text{AA}'\text{BB}'\text{O}_6$ [24, 25, 282]. Among these, $\text{AA}'\text{BB}'\text{O}_6$ stands out for its ability to incorporate diverse elements in both the AA'- and BB'-sites, offering a broad spectrum of intriguing properties. These materials possess versatile characteristics that include catalytic activity, electronic and ionic conductivity, chemical stability, and magnetic properties, promising applications in spintronics and magnetocalorics, among others [206, 283–288]. The $\text{RE}_2\text{BB}'\text{O}_6$ compounds have been observed to adopt two distinct crystal structures: monoclinic $P2_1/n$ space group and orthorhombic $Pbnm$ structure, and are synthesis dependent. In the monoclinic structure, layers of B^{2+} and B'^{4+} ions alternate periodically, whereas in the orthorhombic structure, B^{3+} and B'^{3+} ions are randomly distributed throughout the lattice. Notably, most ordered double perovskite compounds exhibit ferromagnetism, which arises from the super-exchange (SE) interactions between the ordered B^{2+} and B'^{4+} ions. However, even in the ordered state, a certain fraction of B and B' cations exchange their positions within the crystal lattice, a phenomenon referred to as antisite disorder (ASD) in these materials [182]. Particularly, $\text{La}_2\text{BB}'\text{O}_6$ (B = Co, Ni, and B' = Mn) are the most studied ordered DPs, which illustrate FM semiconducting properties with a T_C close to room temperature ($T_C \sim 220$ K for $\text{La}_2\text{CoMnO}_6$ and $T_C \sim 280$ K for $\text{La}_2\text{NiMnO}_6$). AFM and FM ordering generally coexist in these oxides, where the AFM coupling is

associated with the negative $\text{Co}^{2+}\text{-O-Co}^{2+}$, $\text{Ni}^{2+/3+}\text{-O-Ni}^{2+/3+}$ and $\text{Mn}^{4+/3+}\text{-O-Mn}^{4+/3+}$ SE interaction induced by the ASD, while the FM coupling is attributed to the positive long-range $\text{Co}^{2+}/\text{Ni}^{2+} (t_{2g}^6 e_g^2)\text{-O}^{2-}\text{Mn}^{4+} (t_{2g}^3 e_g^0)$ SE interaction [289–291].

Arguably, there has been a great controversy in recent literature about the origin of FM in Ni/Mn based DPs. Initially, Goodenough et al. [292] reported FM transition with a T_C around 280 K, attributing it to $\text{Ni}^{3+}\text{-O}^{2-}\text{-Mn}^{3+}$ exchange interactions. Subsequently, Blasse [293] proposed that the FM ordering in LNMO arises from $\text{Ni}^{2+}\text{-O}^{2-}\text{-Mn}^{4+}$ SE interactions. Das et al. [186] in their theoretical investigations, employed first-principle calculations to further support the notion of $\text{Ni}^{2+}\text{-O}^{2-}\text{-Mn}^{4+}$ SE-mediated FM in LNMO. The valency of Ni/Mn cations and the magnetization (M) of LNMO have been extensively discussed in the literature. However, a recent study employing X-ray absorption spectroscopy (XAS) by Choudhary et al. [234] elucidated the valence states of Ni/Mn ions in LNMO. They identified Ni^{2+} and Mn^{4+} valence states in a specific LNMO sample, with a predominant FM interaction below 270 K attributed to $\text{Ni}^{2+}\text{-O}^{2-}\text{-Mn}^{4+}$ SE coupling. Additionally, the ASD mechanism contributes to $\text{Ni}^{2+}\text{-O}^{2-}\text{-Ni}^{2+}$ and $\text{Mn}^{4+}\text{-O}^{2-}\text{-Mn}^{4+}$ AFM couplings alongside the dominant FM interaction due to $\text{Ni}^{2+}\text{-O}^{2-}\text{-Mn}^{4+}$ coupling. Following these findings, numerous reports on Ni/Mn-based DPs have favored either one of these interactions [158, 293–299]. Also, anomalous phonon softening at magnetic transition temperatures is attributed to phonon renormalization due to magnetic spin ordering, suggesting a direct spin-phonon coupling (SPC) effect. Particularly, Sharma et al. [300] reported a magnetically-driven ferroelectric transition in Y_2CoMnO_6 . This rare-earth double perovskite exhibits a ferromagnetic ordering at $T_N \approx 80$ K, subsequently leading to the emergence of ferroelectricity. This phenomenon is attributed to spin-phonon coupling, a mechanism that has been extensively investigated in RE DPs ($\text{RE}_2\text{BB}'\text{O}_6$): $\text{La}_2\text{NiMnO}_6$ [300], $\text{Tb}_2\text{NiMnO}_6$ [301], $\text{Pr}_2\text{NiMnO}_6$ [275], Y_2NiMnO_6 [301], $\text{La}_{1-x}\text{Mn}_{1-x}\text{O}_3$ [235], RFeO_3 ($R = \text{Nd, Tb, Eu and Gd}$)[302] etc., due to its role in governing the magnetodielectric response. Additionally, Y_2CoMnO_6 has demonstrated intriguing phenomena such as disorder-induced exchange bias and multicaloric effects [303, 304], further highlighting its multifunctional nature. However, magnetostriction may also influence phonon behavior indirectly by coupling spins and phonons. Y_2CoMnO_6 [305] is the sole identified DP system potentially exhibiting magnetostriction, which could me-

diate observed SPC effects, yet direct evidence is lacking. A key experimental approach for probing such coupling, particularly in systems where the interaction strength is weak, is Raman spectroscopy [225, 273, 306, 307]. This technique directly identifies the underlying mechanism of spin-phonon interactions, distinguishing whether they arise intrinsically from the spin-lattice interactions or are mediated via magnetostriction effects.

Hence, investigating thermal variations of lattice parameters and Raman frequencies near magnetic transitions can elucidate the role of magnetostriction in driving SPC in DP systems. The investigation of La₂NiMnO₆ in both bulk and thin-film configurations has been extensively documented; however, the study of other rare-earth-based double perovskites (RE₂NiMnO₆) remains relatively unexplored, particularly in the context of AA'BB'O₆-type structures. To date, no reported work has focused on the NdSmNiMnO₆ system. Interestingly, the substitution of Sm³⁺ for Nd³⁺, and vice versa, is driven by crystal stability, electronic band modifications, and magnetoelectric coupling [116, 308]. The A-site cations (Nd³⁺, Sm³⁺) strongly influence the B-site (Ni/Mn) sublattice, affecting magnetic and transport behavior [309]. Structural stability is governed by the Goldschmidt tolerance factor t_G , where ionic radius differences between Nd³⁺ (1.109 Å) and Sm³⁺ (1.079 Å) modify Ni-O-Mn bond angles, orbital hybridization, and superexchange interactions [26, 310]. Sm doping induces chemical pressure, enhancing octahedral tilting and lattice distortions, which modulate electronic bandwidth and charge transport. Magnetism arises from competing ferromagnetic 180° (Ni²⁺-O-Mn⁴⁺) and antiferromagnetic (Ni³⁺-O-Mn³⁺) superexchange, governed by the Goodenough-Kanamori-Anderson (GKA) rules [42, 53, 116, 311]. Furthermore, Sm substitution introduces A-site disorder, leading to charge fluctuations, altered Ni/Mn valence states, and double-exchange modifications. This disorder can induce spin frustration and phase competition, potentially resulting in glassy magnetic states, as observed in related perovskites [41, 312].

We present a comprehensive investigation of the novel rare-earth double perovskite NdSmNiMnO₆, driven by the intricate magnetic phenomena and unresolved controversies characteristic of this class of materials. By integrating state-of-the-art experimental techniques with first-principles theoretical modeling, we establish fundamental structure-property correlations that dictate its emergent physical behavior. High-resolution synchrotron X-ray diffraction,

combined with Rietveld refinement, precisely determines the crystallographic structure and cationic ordering, while X-ray Absorption Near Edge Structure (XANES) spectroscopy provides critical insights into the local electronic structure and valence states of the transition metal ions. Additionally, DC magnetometry measurements unveil complex magnetic interactions, and Raman spectroscopy probes spin-phonon coupling mechanisms, elucidating the role of lattice dynamics in the observed magnetism. These experimental findings are further corroborated by rigorous density functional theory (DFT) calculations, which unravel the microscopic origins of electronic structure, magnetic exchange interactions, and stable ground-state configurations. Our holistic approach uncovers the intricate interplay between A-site disorder (Nd³⁺/Sm³⁺) and B-site cation ordering (Ni²⁺/Mn⁴⁺), revealing their profound influence on the correlated electronic and magnetic properties of this unexplored double perovskite system. This study not only advances our understanding of rare-earth perovskites but also paves the way for the rational design of novel multifunctional materials with tunable quantum properties.

6.2 Experimental Procedures

6.2.1 Synthesis

The polycrystalline double perovskite NdSmNiMnO₆ was prepared by a modified sol-gel method, using glycine as chelating agent. In a sequential synthesis process, 2 g of glycine was slowly added to a 2 M starting solution containing Nd(NO₃)₃·6H₂O, Sm(NO₃)₃·6H₂O, Ni(NO₃)₂·6H₂O, and (CH₃COO)₂Mn·4H₂O, all with high purity (Aldrich, 99.97%) in a ratio of 1:1:1:1 (Nd:Sm:Ni:Mn). The prepared sample solutions were kept at 200°C for 24 h on a hot plate for evaporation and xerogel formation. Finally, all the swollen xerogels were ground and pre-calcined at 1000°C for 12 h to remove all organic solvent residues. Furthermore, these samples were subjected to successive pulverization and pressed at a pressure of 80 MPa. The final calcination was carried out in an oven with ambient atmosphere at 1200°C for 48 h to form the pure double perovskite phase.

6.2.2 Characterization

Synchrotron X-ray diffraction (SXRD) data were collected at the EMA beam-line of the Brazilian Synchrotron Light Laboratory (LNLS) using a high-flux monochromatic X-ray beam with an incident wavelength of $\lambda = 0.4959$ Å optimized for high-resolution structural analysis. The NdSmNiMnO₆ samples were encapsulated in 0.5 mm diameter quartz-glass capillaries and measured continuously to mitigate preferential orientation effects. This capillary size was selected to minimize absorption effects, ensuring a total μm^2 below $0.1 \times 0.1 \mu\text{m}^2$. High-resolution powder diffraction patterns were recorded over a 2θ range of 1-30° in continuous scanning mode, covering a broad temperature range from 4 K to 275 K. A stabilization period of 15-20 minutes was maintained at each temperature step to ensure thermal equilibrium before data acquisition, thereby enhancing the reliability of the collected diffraction profiles. Phase identification was performed by comparing the experimental SXRD patterns to standards from the International Centre for Diffraction Data (ICDD) database using the X'Pert Highscore software (PANalytical). Rietveld refinement [176] of the entire patterns was carried out using the FullProf software [313], based on the space group and unit cell parameters found during indexing. The pseudo-Voigt function modified by Thompson-Cox-Hastings [314] was used to fit parameters such as a scale factor, zero shift, fourth-order polynomial background, lattice parameters, peak shapes and widths, thermal factors, asymmetry parameters, and site occupancies. All parameters were refined by interactive least squares [315] to minimize the difference between the experimental and calculated profiles. Magnetic measurements were performed using a superconducting quantum interference device (SQUID) magnetometer (MPMS-3, Quantum Design) within the temperature range of 2-300 K, with a maximum applied magnetic field of ± 70 kOe. To ensure minimal bias from trapped flux within the superconducting magnet, demagnetization protocols were employed, oscillating the magnetic field during the decrease process. The chamber temperature was routinely brought to 300 K, exceeding the superconducting coils' critical temperature, before starting new experiments. Helium was used to cool the coils before performing temperature-dependent magnetization (M-T) and isothermal magnetization (M-H) measurements. Raman spectroscopy measurements were performed using a Jobin Yvon Horiba T64000 triple spectrometer equipped with an N₂-cooled charge-coupled device (CCD) detection system. The

spectrometer was coupled to an Olympus microscope with a 20 \times magnification lens, a focal length of 20.5 mm, and a numerical aperture (NA) of 0.35. Excitation was provided by a laser source with a wavelength of 514 nm and a power of approximately 2.3 mW. Raman spectra were recorded in the 200-1600 cm⁻¹ range, with a spectral resolution of 2 cm⁻¹. Low-temperature measurements were conducted using a Janis CCS-150 closed-loop helium cryostat controlled by a Lakeshore 335 temperature controller, with an accuracy of approximately 0.1 K. XANES measurements were performed at the Extreme Methods of Analysis (EMA) beamline [316] of the Sirius synchrotron. The X-ray source is a 22 mm period Kyma undulator, delivering photons in the 5.7 keV (3rd harmonic) to 35 keV (15th harmonic) energy range. The X-ray beam was monochromatized using an LN₂-cooled high-resolution double-crystal monochromator (DCM) with silicon (111) crystals [173]. An achromatic set of Kirkpatrick-Baez (K-B) mirrors focused the beam to a spot size of 10 \times 10 μm^2 at the sample. The Ni K-edge and Mn K-edge spectra were collected at the 3rd harmonic using the DCM [111] setting in transmission mode. The incident (I_0) and transmitted (I_t) beam intensities were measured using ion chambers with appropriate gases for this energy range. The absorption spectra were calculated using the Beer-Lambert law, $\text{ABS} = \mu t = \ln\left(\frac{I_0}{I_t}\right)$, where μ is the absorption coefficient and t is the sample thickness. Three spectra were collected for each sample, normalized to the absorption edge jump, and then averaged to produce the final results.

6.2.3 DFT Calculations

First-principles DFT calculations [317, 318] were performed to investigate the electronic structure and magnetic properties of NdSmNiMnO₆. Calculations were carried out using the Full-Potential Linearized Augmented Plane Wave (FP-LAPW) method [319] implemented in the WIEN2k code [320]. Exchange-correlation effects were treated with the PBEsol functional, including an on-site Hubbard U correction ($U_{\text{eff}} = U - J$) following Anisimov et al. [321]. The effective U_{eff} values were set to 4.0 eV for Ni and Mn d -electrons, 3.0 eV for Nd, and 6.2 eV for Sm ions. Spin-orbit coupling (SOC) was included within the GGA+ U +SOC approximation [322]. Brillouin zone integration was performed using a 6 \times 6 \times 6 Monkhorst-Pack k-point grid. Atomic sphere radii (RMT) were set to 2.15 a.u.

for Nd/Sm, 1.80 a.u. for Ni, 1.90 a.u. for Mn, and 1.55 a.u. for O. Inside the atomic spheres, wave functions were expanded up to $l_{\max} = 10$. The plane-wave cutoff parameter was set as $k_{\max} = 6.0/R_{\text{MT}}(\text{O})$. The Fourier expansion cutoff for the charge density was $G_{\max} = 16$. The valence electron configurations considered were Nd ($4f^4 6s^2$), Sm ($4f^6 6s^2$), Ni ($3d^8 4s^2$), Mn ($3d^5 4s^2$), and O ($2s^2 2p^4$). Self-consistent iterations were continued until the total energy convergence reached less than 10^{-5} Ry, charge density differences were below 10^{-5} e/bohr³, and atomic forces were minimized to within 2 mRy/bohr.

Table VI.1: Structural parameters of NdSmNiMnO₆ in the $P2_1/n$ space group (#14), refined from NPD data. U_{iso} values are given in 10^{-3} \AA^2 units. Bond valence sums (BVS) are in $|e|$. For mixed-occupancy sites, the majority cation is used in BVS calculations.

Atom	Frac. Coord.	U_{iso} ($\times 10^{-3} \text{ \AA}^2$)	BVS ($ e $)	Occupation
Nd/Sm	$x = 0.0074(3)$ $y = 0.5495(7)$ $z = 0.7554(8)$	3.53(2)	+2.95 / +3.37	Nd/Sm
Mn	$x = y = z = 0$	1.19(5)	+3.94	74% Mn, 26% Ni
Ni	$x = 0.5$	1.19(5)	+2.05	74% Ni, 26% Mn
O1	$x = 0.0933(7)$ $y = 0.0160(6)$ $z = 0.2513(2)$	1.27(2)	–	O
O2	$x = 0.1664(10)$ $y = 0.3123(10)$ $z = -0.0509(12)$	0.43(1)	–	O
O3	$x = 0.2747(14)$ $y = 0.27475(15)$ $z = 0.5708(11)$	1.42(2)	–	O

Bond	Length (\AA)	Bond Angles ($^\circ$)
Mn – O1	1.97(2)	$\langle \text{O1-Mn-O1} \rangle$ 180(0)
Mn – O2	1.97(7)	$\langle \text{O1-Mn-O2} \rangle$ 89(3), 91(3)
Mn – O3	1.81(8)	$\langle \text{O1-Mn-O3} \rangle$ 82(10), 98(3)
$\langle \text{Mn-O} \rangle$	1.92(6)	$\langle \text{O1-Ni-O1} \rangle$ 180(0)
Ni – O1	1.97(2)	$\langle \text{O1-Ni-O2} \rangle$ 88(3), 92(8)
Ni – O2	2.11(7)	$\langle \text{O1-Ni-O3} \rangle$ 87(3), 93(3)
Ni – O3	2.18(8)	$\langle \text{Ni-O1-Mn} \rangle$ 149(3)
$\langle \text{Ni-O} \rangle$	2.09(5)	$\langle \text{Ni-O2-Mn} \rangle$ 142(4)
		$\langle \text{Ni-O3-Mn} \rangle$ 147(5)

Parameter	4 K	175 K	275 K
R_p (%)	1.91	2.48	2.21
wR_p (%)	2.96	3.87	3.46
R_{exp} (%)	8.27	8.66	8.84
R_{Bragg} (%)	3.32	3.96	3.24
χ^2	0.13	0.20	0.16

6.3 Results and Discussion

6.3.1 Crystal Structure

The temperature-dependent SXRD measurements conducted in the 4-300 K range [as shown in Appendix 4.0.1 Figure IV.1] confirm that the SXRD data refine well with the $P2_1/n$ symmetry model, indicating no global structural transition down to 4 K [see Figure VI.2(a-c)]. The goodness of fit, expressed by R_p , wR_p , R_{exp} , R_{Bragg} , and χ^2 , confirms a good agreement between the refined and experimental SXRD patterns. The obtained Rietveld parameters and corresponding Wyckoff positions are summarized in Table VI.1, with lattice parameters: $a = 5.3746(6)$ Å, $b = 5.4858(6)$ Å, $c = 7.6292(9)$ Å, $\beta = 90.01699(4)^\circ$, $V = 224.936(4)$ Å³. Double perovskites typically exhibit octahedral cation ordering and an $a^-a^-b^+$ octahedral tilting pattern, analogous to the GdFeO₃-type structure (Pnma, $a^-b^+a^-$), which is the most prevalent tilt system in both ordered and conventional ABO₃ perovskites [17, 23]. In this structure, octahedral cations occupy fixed Wyckoff positions: B [Ni (2a) (0, 1/2, 0)] and B' [Mn (2b) (1/2, 0, 0)], while the A-site (Nd/Sm) cations and three distinct oxygen anions reside at general 4e (x, y, z) positions [see Figure VI.1(a-b)]. Notably, interchanging the Wyckoff positions of Ni and Mn renders the system invariant. This configuration results from the interplay of the Goldschmidt tolerance factor and cooperative octahedral tilting, collectively stabilizing the $P2_1/n$ symmetry by optimizing ionic packing and minimizing lattice energy [17, 323]. Figures VI.1(c-d) illustrate the Nd/Sm coordination with eight oxygen atoms forming a cuboctahedral geometry, while Ni/Mn are coordinated with six oxygen atoms forming octahedral units. This structural model was generated using **VESTA** software [324] at 275 K. The Goldschmidt tolerance factor (t_G) for NdSmNiMnO₆ (NSNMO) is calculated using:

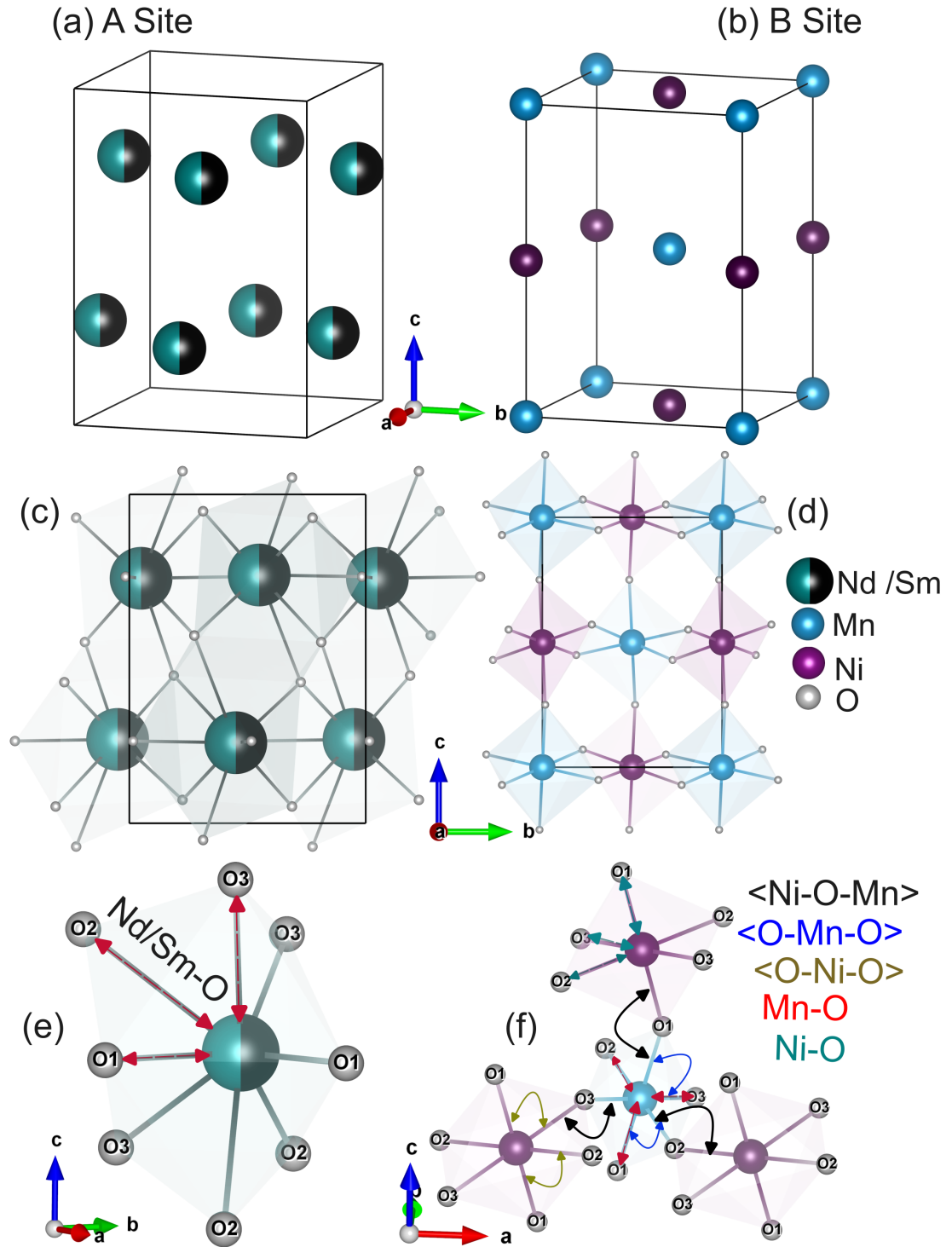


Figure VI.1: Crystal structure of NdSmNiMnO₆ in the monoclinic $P2_1/n$ space group shown as a single unit cell. (a) The A-site cations Nd and Sm are represented in cyan and black, respectively. (b) The B-site transition metals Ni and Mn are shown in blue and royal. (c) Projection along the a -axis highlights the (Nd/Sm)O₈ cuboctahedral coordination. (d) The (NiMn)O₆ octahedral tilt system is emphasized, with NiO₆ and MnO₆ units shaded in royal and blue. Oxygen anions (O²⁻) are shown as grey spheres.

where ionic radii are taken from Shannon's tables [39]. Considering Ni^{2+/3+} and Mn^{3+/4+} in VI coordination, the calculated t_G values of 0.834 (low spin) and 0.862 (high spin) fall within the expected range, supporting a monoclinic (P2₁/n) or orthorhombic (Pnma) symmetry due to octahedral tilting and cation size mismatch. Local crystal structure analysis reveals non-equivalent bond lengths and bond angles with Mn-O1 = Mn-O2 ≠ Mn-O3, Ni-O1 ≠ Ni-O2 ≠ Ni-O3, and Ni-O-Mn bond angles ≠ 180°, indicating a distorted crystalline structure within the ordered NSNMO system. Structural refinement yields average bond lengths of Ni-O = 2.09(5) Å and Mn-O = 1.92(6) Å, with an average bond angle of Ni-O-Mn = 146(5)°. These values align with those reported for other double perovskites [158, 159, 193, 198]. Assessing distortion in perovskite structures involves calculating octahedral tilt angles (γ , φ , Φ) relative to an ideal cubic structure. These are defined as: $\gamma = \cos^{-1}\left(\frac{a}{b}\right)$, $\varphi = \cos^{-1}\left(\frac{\sqrt{2}a}{c}\right)$, $\Phi = \cos^{-1}\left(\frac{\sqrt{2}a^2}{bc}\right) = \cos^{-1}(\cos\gamma\cos\varphi)$. Applying these equations to the refined lattice parameters yields: $\gamma = 11.56^\circ$, $\varphi = 4.94^\circ$, $\Phi = 12.45^\circ$. These angles quantify the extent of octahedral tilting in NSNMO. Furthermore, the octahedral distortion is characterized by: $\Theta = \frac{180 - \langle \text{Ni-O-Mn} \rangle}{2}$ yielding $\Theta = 17.00^\circ$, indicating significant distortion from the ideal cubic framework, consistent with other reported double perovskites [195]. Such structural distortions are often correlated with emerging magnetic competition and frustration effects in these materials, suggesting similar phenomena in the NSNMO system. The valence state analysis was performed using the bond valence sum (BVS) method:

$$\text{BV} = \exp\left(\frac{R_0 - R_i}{B}\right) \quad (192)$$

where $R_0(\text{Nd}^{3+}) = 2.02$, $R_0(\text{Sm}^{3+}) = 2.07$, $R_0(\text{Ni}^{2+}) = 1.654$, $R_0(\text{Mn}^{4+}) = 1.753$, and $B = 0.37$. R_i represents the experimentally obtained bond lengths for Nd/Sm-O, Ni-O, and Mn-O. The BVS analysis yields valence states of $\text{Nd}^{3+} = 2.95$, $\text{Sm}^{3+} = 3.31$, $\text{Ni}^{2+} = 2.05$, and $\text{Mn}^{4+} = 3.94$, confirming their expected oxidation states and the structural stability of the NSNMO crystal.

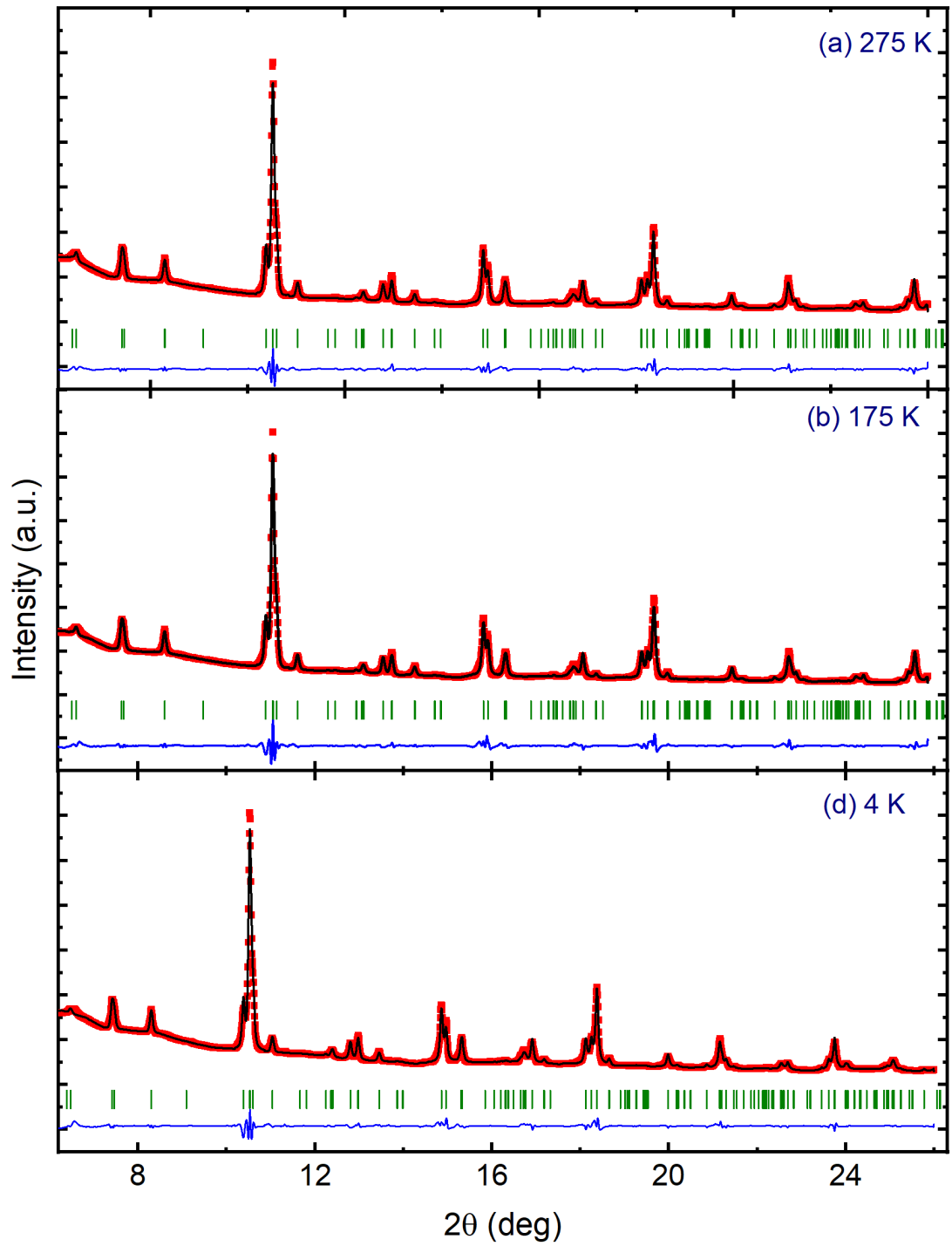


Figure VI.2: Synchrotron X-ray diffraction data in selected phases: (a) paramagnetic phase (275 K), (b) ordered phase (175 K), and (c) 4 K. Experimental data are shown as red points, the fitted pattern as black lines, and the difference curve ($I_{\text{obs}} - I_{\text{calc}}$) as a blue line at the bottom of each panel. The top and bottom rows of green tick marks indicate the positions of nuclear and magnetic Bragg peaks, respectively.

6.3.2 XANES

The temperature-dependent Ni and Mn K-edge XANES spectra of NdSmNiMnO₆ reveal fundamental differences in the electronic and structural responses of the two transition metal sites. The Ni K-edge spectra (Figure VI.3a) exhibit an absorption edge at 8352 eV, confirming the Ni²⁺ oxidation state, consistent with reports across the RNiMnO₆ series [325, 326]. The pre-edge feature at 8339 eV ($P_{\text{E-Ni}}$) gains intensity at lower temperatures, suggesting enhanced $1s \rightarrow 3d$ transitions through increased $3d$ - $4p$ orbital mixing due to progressive octahedral distortion. This is accompanied by broadening of the white-line feature (8355-8365 eV), indicative of growing static disorder and modified Ni-O hybridization at reduced temperatures, phenomena previously observed in related systems like La₂NiMnO₆ [157, 327, 328]. In striking contrast, the Mn K-edge spectra (Figure VI.3b) demonstrate exceptional thermal stability, with the main edge fixed at 6560 eV (characteristic of Mn⁴⁺) and pre-edge features at 6544 eV (P_{I}) and 6549-6551 eV (P_{II}) maintaining constant intensity across the entire temperature range [329]. This temperature invariance confirms the structural rigidity of MnO₆ octahedra and robust Mn-O hybridization, in agreement with studies showing that Mn⁴⁺ serves as a structural anchor in RNMO systems [297]. The absence of spectral evolution contrasts sharply with the temperature-sensitive Ni site, highlighting the distinct roles of these cations in the perovskite framework. The complementary behaviors of Ni and Mn sites provide crucial insights into the material's functional properties. While the Mn⁴⁺ sublattice maintains structural integrity, the Ni²⁺ site exhibits a thermal response through modified local symmetry and electronic structure. This differential response may underlie the compound's magnetoelectric coupling, as the flexible NiO₆ octahedra could mediate interactions between the rigid Mn sublattice and rare-earth ions [330, 331]. These findings reinforce the picture of RNMO systems as materials where structural and electronic functionality emerges from the interplay between stable (Mn⁴⁺) and responsive (Ni²⁺) sublattices, consistent with BVS calculations.

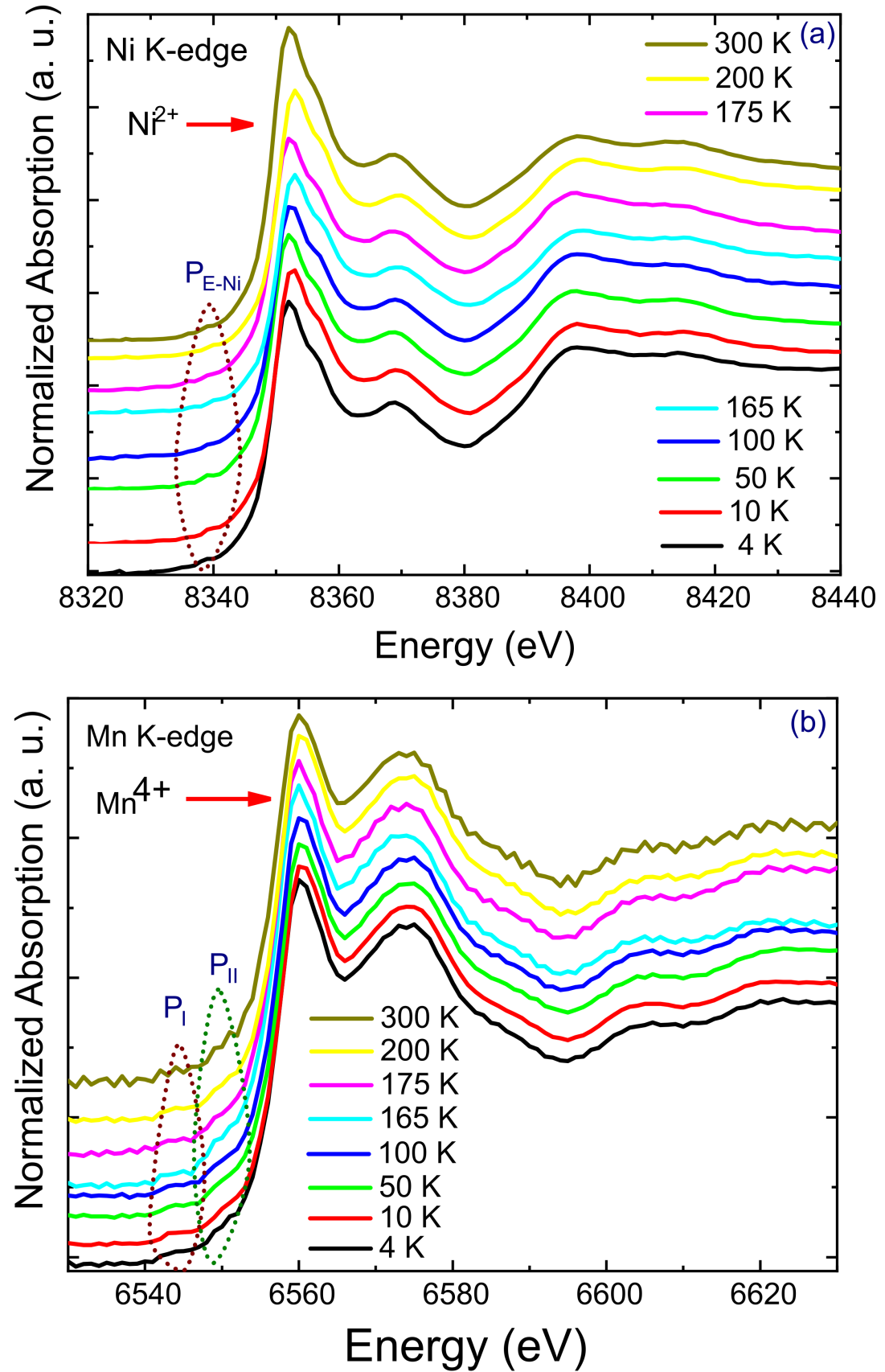


Figure VI.3: Temperature-dependent Ni and Mn K-edge XANES spectra of NdSmNiMnO₆ from 4-300 K. (a) Ni K-edge spectra show an absorption edge at ~ 8352 eV (Ni²⁺) and a pre-edge feature P_{E-Ni} at ~ 8339 eV. The increased white-line intensity and peak broadening at lower temperatures indicate enhanced local distortion around Ni. (b) Mn K-edge spectra display a stable edge at ~ 6560 eV (Mn⁴⁺) with consistent pre-edge features P_I (~ 6544 eV) and P_{II} (~ 6549 - 6551 eV), suggesting a temperature-invariant MnO₆ octahedral environment and robust Mn-O hybridization.

6.3.3 Magnetic Properties

The DC temperature-dependent magnetization (M - T) of the NdSmNiMnO₆ sample under Zero-Field Cooling (ZFC) and Field-Cooled Cooling (FCC) conditions was measured with an applied field of $H_{dc} = 100$ Oe, as shown in Figure VI.4(a). Upon cooling, a sharp increase in magnetization appears around $T \sim 180$ K in both ZFC and FCC curves, indicating a ferromagnetic/ferrimagnetic to paramagnetic (FM/FiM-PM) transition. Below this, the FCC curve shows near-saturation behavior followed by a downturn anomaly near $T \sim 50$ K, suggesting dynamic domain effects originating from coexisting FM and AFM regions. This behavior is likely driven by anti-site disorder (ASD) and/or rare-earth (RE) moment ordering [195, 286, 288]. The bifurcation in the ZFC curve at low temperatures points to an inhomogeneous or magnetocrystalline anisotropic state, consistent with similar behaviors in related materials [332, 333]. The inset of Figure VI.4(a) compares M - T curves at different H_{dc} fields, showing that the irreversibility temperature T_{irr} -defined by the deviation between M_{FCC} and M_{ZFC} -reduces with increasing field and vanishes at 10 kOe. This confirms the presence of magnetic heterogeneity. During FCC, the external field aligns FM spins, while ZFC allows random orientation due to local anisotropy fields. The lower magnetization in ZFC arises from insufficient field strength (≤ 10 kOe) to overcome these local anisotropy barriers. As the field increases, this anisotropy is overcome, leading to the alignment of FM clusters and elimination of ZFC-FCC separation, consistent with behavior observed in other double perovskites [195, 332, 334]. These magnetic features arise from the coexistence of various exchange pathways, such as, Ni^{2+}/Mn^{4+} -O- Ni^{2+}/Mn^{4+} , Ni^{3+}/Mn^{3+} -O- Ni^{3+}/Mn^{3+} , Ni^{2+}/Mn^{4+} -O- Nd^{3+}/Sm^{3+} , and Nd^{3+}/Sm^{3+} -O- Nd^{3+}/Sm^{3+} . The inverse susceptibility ($1/\chi$) vs. T curve shown in Figure 3(b) displays Curie-Weiss-like behavior in the high-temperature paramagnetic region. Fitting the data from 190–245 K using the Curie-Weiss law, $\chi = \frac{C}{T - \theta_{CW}}$, yields a Weiss temperature $\theta_{CW} = 168.90(2)$ K and Curie constant $C = 0.00641(3)$. The corresponding effective magnetic moments are $\mu_{obs} = 5.52(1) \mu_B/\text{f.u.}$ (1 kOe) and $1.59(2) \mu_B/\text{f.u.}$ (10 kOe)[see Appendix 4.0.3, Figure IV.2]. The suppression in μ_{obs} may be attributed to spin fluctuations, disorder, or low-to-high spin transitions in $Ni^{2+/3+}$ -O- $Mn^{3+/4+}$ linkages. Additionally, canted or AFM alignment of Nd^{3+}/Sm^{3+} moments may lead to a field-dependent evolution toward a collinear state, effectively reducing the mea-

sured moment [335, 336]. The positive Weiss temperatures ($\theta_{\text{CW}} = 168\text{--}171.92\text{ K}$) up to 10 kOe indicate robust ferromagnetic interactions within the Ni-O-Mn sublattice [182]. The expected theoretical effective moment assuming a spin-only configuration is given by: $\mu_{\text{cal}}^2 = [\mu_{\text{Nd}^{3+}/\text{Sm}^{3+}}^2 + \mu_{\text{Ni}^{2+}/\text{Mn}^{4+}}^2]$ where $\mu_{\text{Nd}^{3+}/\text{Sm}^{3+}} = g_J \sqrt{J(J+1)}$ and $\mu_{\text{Ni}^{2+}}, \mu_{\text{Mn}^{4+}} = g_L \sqrt{S(S+1)}$. Using this expression, we estimate $\mu_{\text{cal}} \approx 6.07\ \mu_{\text{B}}$ and $4.83\ \mu_{\text{B}}$, respectively. The transition temperature was confirmed via the first derivative of $M_{\text{ZFC}}(T)$ [dM/dT , inset of Figure VI.4(b)], which shows a magnetic ordering temperature $T_{\text{N}} \approx 170\text{ K}$ —lower than that reported for Nd₂NiMnO₆ [158, 185]. To further investigate the magnetic state, isothermal magnetization $M(H)$ curves were recorded at various temperatures [Figure VI.5(a)]. At $T = 300\text{ K}$, $M(H)$ is linear, indicating paramagnetic behavior. Below T_{N} , the magnetization rapidly increases, showing weak coercivity. However, even under high fields, $M(H)$ does not fully saturate and retains a linear high-field component, implying the presence of unsaturated spins or competing AFM contributions. These results, combined with the downturn in $M(T)$ at low temperatures, support a ferrimagnetic ground state wherein Ni²⁺/Mn⁴⁺ ions (spin-only moment $\sim 4.83\ \mu_{\text{B}}$) order ferromagnetically, while Nd³⁺/Sm³⁺ moments align antiferromagnetically or remain partially canted [183]. The saturation magnetization (M_{S}) extracted from the $M(H)$ isotherm at 2 K [inset Figure VI.5(a)] was found to be $M_{\text{S}} = 5.01(3)\ \mu_{\text{B}}$, slightly lower than the theoretically estimated spin-orbit value ($\mu_{\text{cal}} = 6.07\ \mu_{\text{B}}$). This agreement with experimentally observed values confirms that the dominant contribution to the FM sublattice originates from super-exchange interactions between Ni²⁺-O²⁻-Mn⁴⁺ even at the ground state. The linearly increasing component of the $M(H)$ curves is attributed in part to magnetic anisotropy within the polycrystalline matrix, where some grains align with their hard axis along the direction of the applied field [195]. Figure VI.5(b) presents the temperature dependence of M_{S} and coercivity (H_{C}). Both parameters decrease markedly with increasing temperature, consistent with thermal agitation that disrupts the polarization alignment [337]. However, H_{C} exhibits a discontinuity above $T > 200\text{ K}$, likely due to domain wall pinning caused by AFM defects and/or magnetocrystalline anisotropy within the sublattices [183, 338].

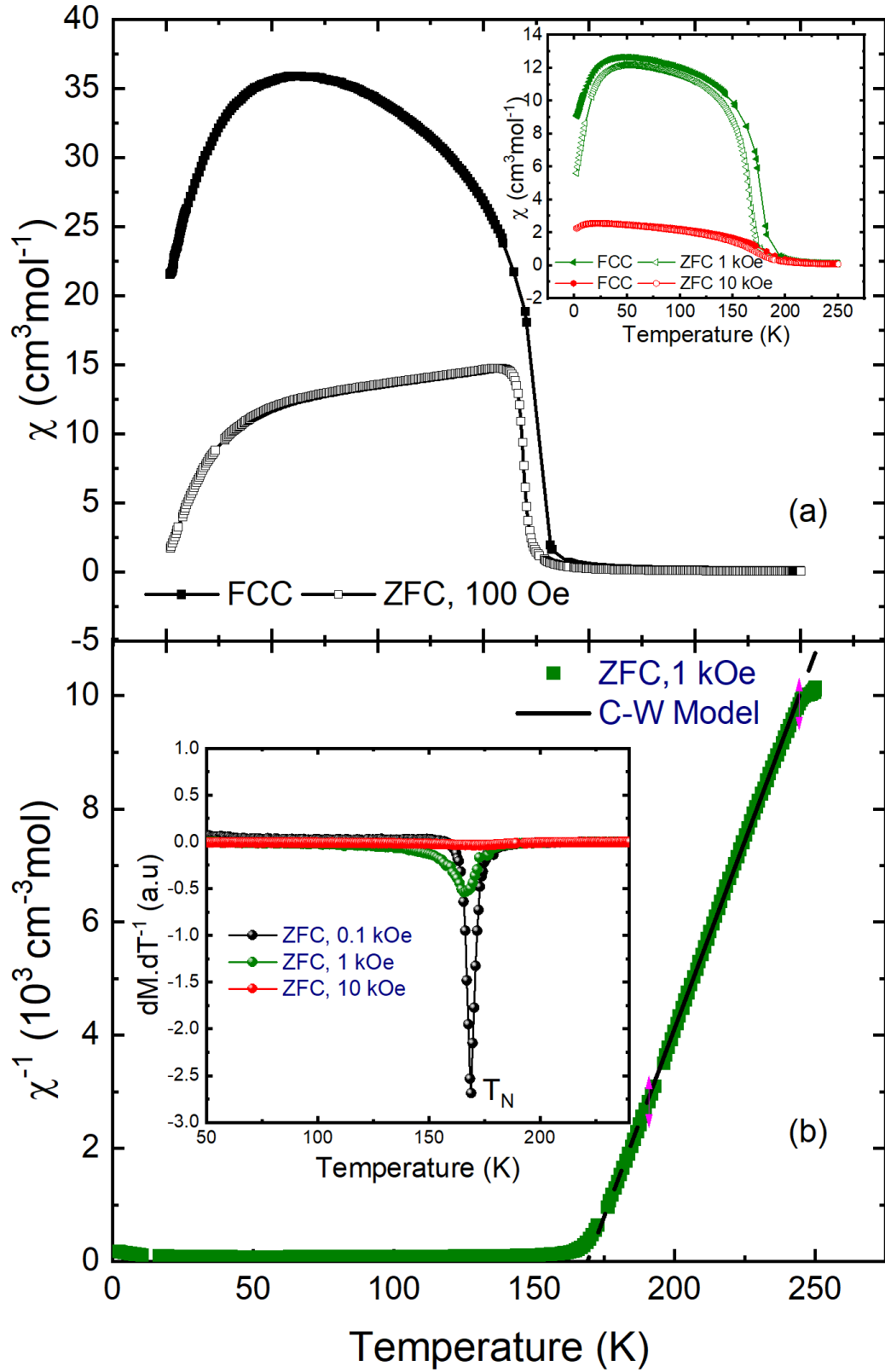


Figure VI.4: (a) Temperature dependence of magnetization curves measured after zero-field cooling (ZFC) and field-cooled cooling (FCC) under an applied magnetic field of $H_{dc} = 100$ Oe for NdSmNiMnO₆. The inset shows a comparison of M - T curves (ZFC/FCC) at different H_{dc} fields. (b) Inverse susceptibility ($\chi^{-1} = H/M$) as a function of temperature measured at $H_{dc} = 1$ kOe. The black line represents the best fit to the Curie-Weiss (C-W) law in the paramagnetic region. The inset displays the derivative dM/dT^{-1} versus T , where the minimum is associated with the critical temperature T_N at various H_{dc} fields.

In general, the observed FM ordering in NSNMO arises from super-exchange interactions between Ni²⁺ and Mn⁴⁺ via oxygen anions, as predicted by the Goodenough-Kanamori rules [53, 116]. The presence of octahedral distortions leads to deviations in the $\angle\text{Ni-O-Mn}$ bond angles from the ideal 180°, which introduces antisymmetric Dzyaloshinskii–Moriya (DM) interactions [120, 339]. As a result, the system adopts a canted antiferromagnetic (CAFM) ground state below T_N . In octahedral coordination, Ni²⁺ ($3d^8$: $t_{2g}^6e_g^2$) has a half-filled e_g orbital, while Mn⁴⁺ ($3d^3$: $t_{2g}^3e_g^0$) has half-filled t_{2g} and empty e_g states. Superexchange occurs via virtual hopping of electrons: (i) from Ni- e_g to Mn- e_g orbitals (promoting FM alignment), (ii) and from Ni- e_g to Mn- t_{2g} orbitals (favoring AFM coupling). When the $\angle\text{Ni-O-Mn}$ bond angle is near 180°, strong overlap between Ni- e_g and Mn- e_g orbitals facilitates FM interactions. As the bond angle approaches 90°, hopping between Ni- e_g and Mn- t_{2g} orbitals becomes dominant, favoring antiparallel spin alignment. Consequently, the degree of spin polarization between Ni- e_g and Mn- t_{2g} orbitals increases as the bond angle decreases, while the Ni- e_g to Mn- e_g overlap weakens [332, 340]. This complex interplay explains the observed suppression of the Curie temperature (T_C) in NSNMO, as seen in the shift to lower temperatures in $M(T)$ curves [inset Figure VI.4(b)], and correlates with the reduction in $\angle\text{Ni-O-Mn}$ bond angles observed in the SXRD structural analysis (Table VI.1).

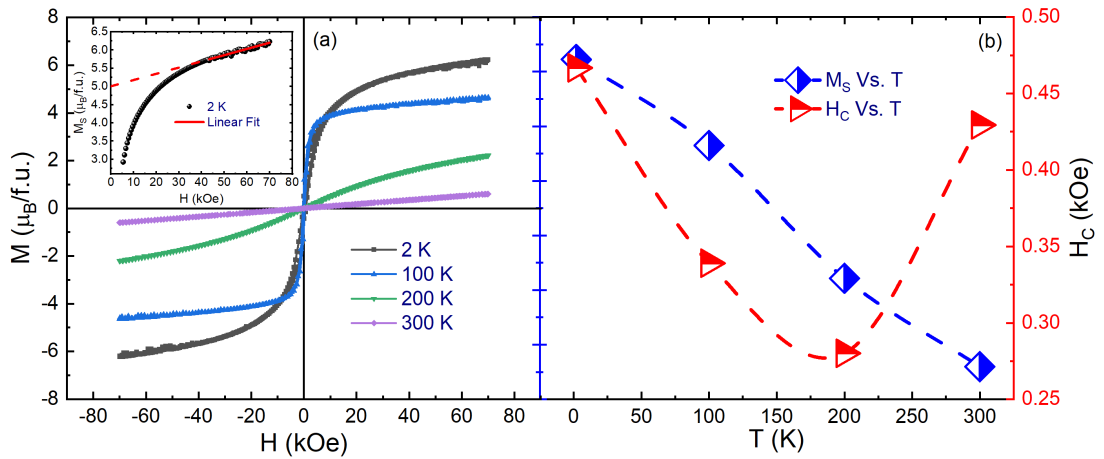


Figure VI.5: (a) Magnetic field dependence of magnetization (M – H) isotherms measured at $T = 2, 100, 200$, and 300 K for NdSmNiMnO₆. The inset shows an expanded view of the low-field region of the isotherms. (b) Derivative dM/dH as a function of H at selected temperatures. The inset displays the Law of Approaching Saturation (LAS) fit to the high-field magnetization data. (c) Temperature dependence of the saturation magnetization (M_S) and coercivity (H_C), highlighting their evolution with temperature.

6.3.4 Magnetoelastic Coupling

To explore the evolution of the crystal structure of NdSmNiMnO₆ with temperature, particularly in the proximity of its critical temperature T_N , we analyzed the thermal variations of the refined lattice parameters a , b , and c , which are governed purely by elastic degrees of freedom, as depicted in Figure VI.6(a-c). Remarkably, all lattice parameters display conspicuous anomalies, exhibiting abrupt features in the vicinity of $T_N \approx 165\text{--}175$ K and $T_{\text{Nd/Sm}} \approx 50$ K (transition ascribed to rare-earth metals) [180, 207]. Between 4 and 50 K, the lattice parameters show a slight increase, followed by a decrease, then a pronounced increase until a displaced peak maximum near $T_N \approx 175$ K. This provides definitive evidence of magnetoelastic coupling, also known as the magnetostriction effect, in the system. This is corroborated by the discontinuity observed in the thermal expansion plots of the SXRD data, which are fitted using the following thermal expansion equations [84, 341]:

$$a(T) = a_0 \left\{ 1 + \frac{Be^{(d/T)}}{[e^{(d/T)} - 1]} \right\}, \quad (193)$$

$$b(T) = b_0 \left\{ 1 + \frac{Ce^{(e/T)}}{[e^{(e/T)} - 1]} \right\}, \quad (194)$$

$$c(T) = c_0 \left\{ 1 + \frac{De^{(f/T)}}{[e^{(f/T)} - 1]} \right\}, \quad (195)$$

where B , C , D , d , e , and f are adjustable fitting parameters. The fitted values are summarized in Table IV.1. A single curve was insufficient to fit the lattice parameters across the entire temperature range; however, satisfactory fits were achieved by applying separate curves for the regions above and below T_N , as shown in Figure VI.6. Throughout the entire temperature range studied, neither peak splitting nor additional Bragg peaks were observed in the SXRD patterns, confirming the absence of any global symmetry-breaking structural transition. Nevertheless, spontaneous lattice distortions associated with magnetic ordering, while preserving the global crystal symmetry, were evident. This spontaneous magnetostriction effect can be quantitatively evaluated from SXRD data, offering considerable advantages over conventional strain-gauge or capacitive methods [341]. The calculated unit cell parameter variations are $\Delta a/a = +0.127\%$,

$\Delta b/b = +0.128\%$, and $\Delta c/c = +0.18\%$, revealing significant anisotropy in the system. Above 180 K, all lattice parameters increase appreciably up to 300 K. These anomalous thermal variations near T_N are attributed to structural distortions induced by the magnetostriction effect [288], which arises from the coupling between spin ordering and lattice dynamics. At 275 K, the Ni-O1 bond length remains at 1.97 Å, while Ni-O2 and Ni-O3 extend to 2.11 Å and 2.18 Å, respectively. The bond angles $\langle \text{Ni-O1-Mn} \rangle$, $\langle \text{Ni-O2-Mn} \rangle$, and $\langle \text{Ni-O3-Mn} \rangle$ exhibit substantial variations of 149, 142, and 147°, respectively. Similarly, for Mn, the Mn-O1 and Mn-O2 bond lengths are both approximately 1.97 Å, while Mn-O3 is slightly shorter at 1.81 Å. The corresponding bond angles include $\langle \text{O1-Mn-O1} \rangle = 180^\circ$ (linear), and distorted angles of $\langle \text{O1-Mn-O2} \rangle$ and $\langle \text{O1-Mn-O3} \rangle$, confirming anisotropic exchange interactions. These structural features are detailed in Figures VI.7(a-i), IV.3(a-d). The average bond lengths $\langle \text{Ni-O} \rangle = 2.09(5)$ Å and $\langle \text{Mn-O} \rangle = 1.92(6)$ Å suggest a distortion-driven charge redistribution mechanism, consistent with observations in other double perovskites where structural anomalies are strongly correlated with spin reorientation phenomena [41].

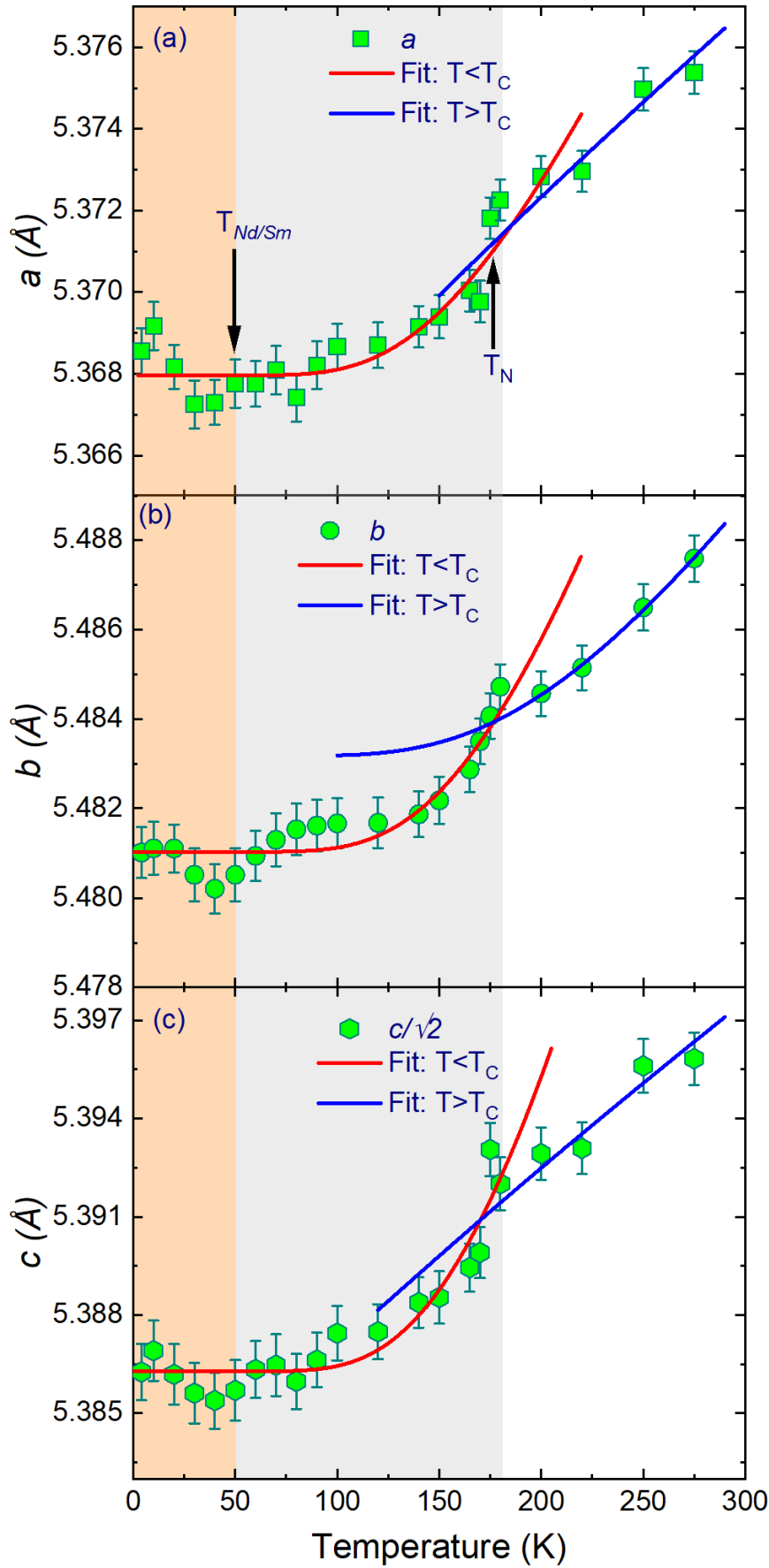


Figure VI.6: (a)-(c) Temperature variations of the unit-cell lattice parameters a , b , and c , deduced from temperature-dependent synchrotron X-ray diffraction (SXRD) pattern analysis. The solid red and blue lines represent the thermal expansion fits for the temperature regions $T < T_C$ and $T > T_C$, respectively. Notably, the thermal expansion behavior exhibits significant anomalies near T_C due to the magnetostriction effect, indicating strong coupling between the magnetic order and the lattice degrees of freedom.

The thermal evolution of these bond parameters traced down to 4 K reveals significant distortions in the NiO₆ and MnO₆ octahedra near the magnetic transition temperature, T_N , indicating a strong magnetostructural coupling driven by spin-lattice interactions. The anomalies observed in the Mn-O and Ni-O bond lengths, along with their associated angles near T_N , suggest a spontaneous lattice distortion driven by the onset of magnetic order, as seen in the a , b , and c lattice parameters. The interplane interactions, particularly the Ni-O1-Mn (149(3)°), Ni-O2-Mn (142(4)°), and Ni-O3-Mn (147(5)°) pathways, play a crucial role in three-dimensional magnetic connectivity, implying a significant role in mediating inter-sublattice magnetic interactions. The observed anomalies in Ni-O and Mn-O bond lengths near T_N further suggest charge delocalization-driven structural modifications akin to polaronic effects in doped manganites [342]. Thus, the evolution of structural distortions in NdSmNiMnO₆ is intricately linked to its magnetic ordering via magnetostructural coupling, with the Ni-O-Mn bond angles and bond lengths serving as critical indicators of this phenomenon. The Different magnetic states, PM, FM and coexisting FM + AFM, are delineated in Figures VI.7(a-i), IV.3(a-d). Considering single-ion crystal field contributions to the magnetoelastic response, two primary interactions are defined [41]: the crystal electric field, which links the anisotropic electron charge density to the lattice, and the spin-orbit interaction, which couples spin and orbital magnetic moments, as evidenced in the $T_{Nd/Sm}$ phase. Beyond these fundamental contributions, more intricate mechanisms can also induce significant magnetostriction, including exchange-driven magnetostriction, where spin interactions modify the lattice, and forced magnetostriction, resulting from external magnetic constraints near T_N .

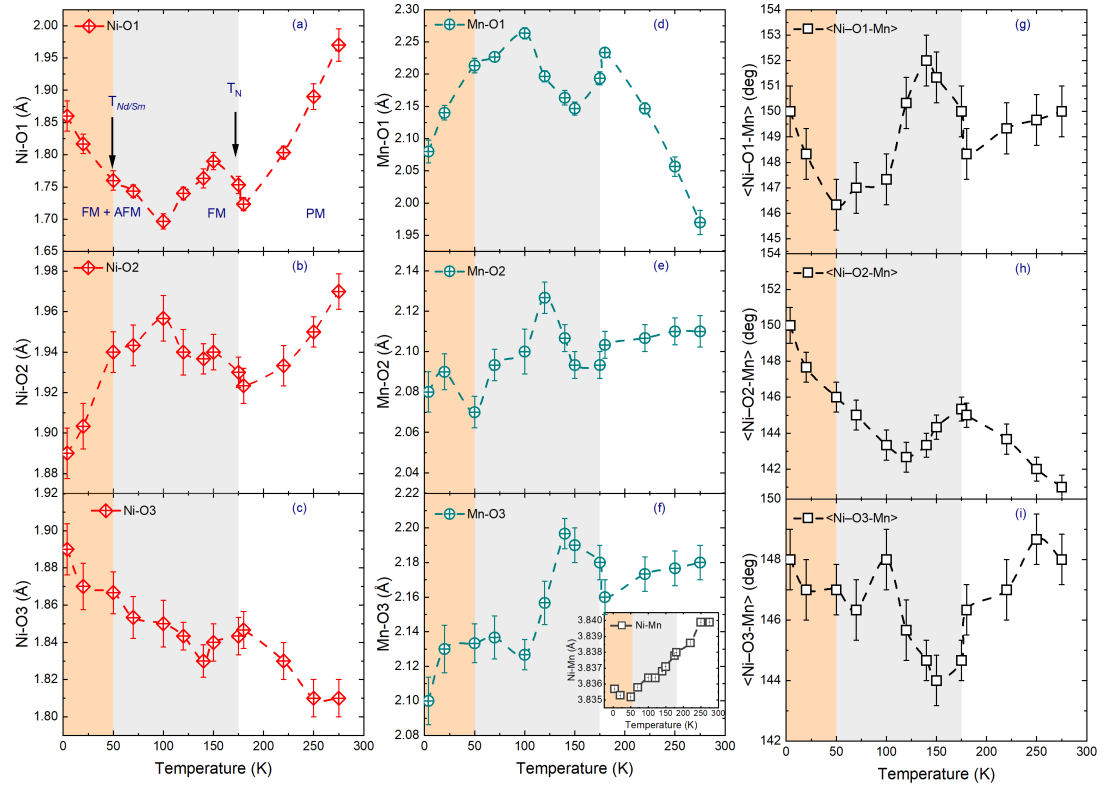


Figure VI.7: Thermal variation of local structural parameters in NdSmNiMnO₆ extracted from temperature-dependent synchrotron X-ray diffraction (SXRD) analysis: (a-c) Ni-O bond lengths; (d-f) Mn-O bond lengths with inset showing Ni-Mn interatomic distances; (g-i) Ni-O-Mn bond angles. Anomalies near the magnetic transition temperature T_N are visible across all panels, signaling structural distortions in the NiO₆ and MnO₆ octahedra.

The Raman spectra recorded at room temperature reveal a prominent mode at 654 cm⁻¹, with a broad peak situated at 508 cm⁻¹, as shown in Figure VI.8. A schematic interpretation assigns modes below 200 cm⁻¹ to the displacement of rare-earth ions, while those above 300 cm⁻¹ are attributed solely to the motion of light oxygen ions. Phonon modes in the intermediate frequency range are associated with both ion types. The primary modes at approximately 654 and 508 cm⁻¹ are identified as the symmetry/breathing (A_g) and asymmetry/bending (A_g/B_g) vibrations of the (Ni/Mn)O₆ octahedra, respectively, and are consistent with findings in prior studies on Ni/Mn-based double perovskite systems [274, 301, 343, 344]. The 654 cm⁻¹ symmetric mode encompasses both in-plane and out-of-plane vibrations of the Ni/Mn-O bond, whereas in the 508 cm⁻¹ asymmetric stretching mode, O²⁻ ions oscillate perpendicularly to the Ni/Mn-O bond. The broadening and asymmetry of the first-order strong A_g and B_g modes, particularly at 508 cm⁻¹, arise from cation disorder, electronic correlations, and structural distortions. Ni/Mn site disorder disrupts lattice periodicity, while nearly identical Ni/Mn-O vibrational frequencies cause spectral overlap. Bond-

length variations within (Ni/Mn)O₆ octahedra, influenced by local strain, further shape the spectral envelope, as evidenced by the structural analysis. Additionally, nanoscale domains with varying degrees of ordering and oxidation state fluctuations of Ni and Mn contribute to the complexity of the Ni/Mn–O stretching bands [274, 328, 345]. Several additional broad bands spanning the range of 840–1300 cm⁻¹ are evident. This high-frequency broadband can be deconstructed into two distinct, relatively weak, and broad modes denoted at 840-1183 and 1300 cm⁻¹, akin to observations in [328]. The modes spanning 840-1183 cm⁻¹ correspond to overtones of the fundamental stretching modes (B_g and A_g) or multiple-phonon processes, as shown in Figure VI.8(a). The other prominent peak manifesting near ~ 1300 cm⁻¹ arises from multi-phonon and/or two-phonon + magnon (Ph-Mag) scattering processes [346–348]. In this summation process, significant contributions primarily come from phonons and magnons with a maximal density of states, specifically those with wave vectors approaching the Brillouin zone boundary.

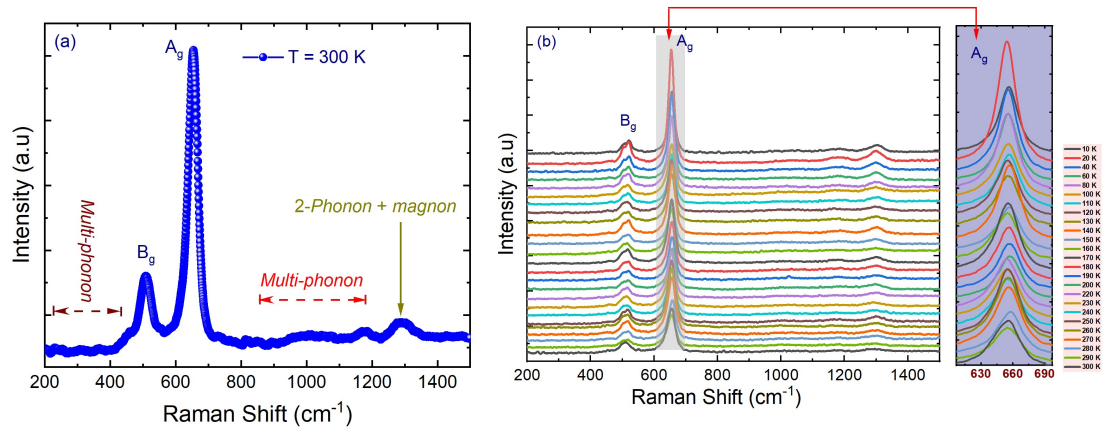


Figure VI.8: (a) Raman spectrum of NdSmNiMnO₆ measured at room temperature showing the dominant phonon modes. (b) Temperature-dependent Raman spectra collected between 10 and 300 K. The rightmost inset highlights the symmetric stretching mode (A_g) near 654 cm⁻¹, revealing subtle anomalies across the magnetic transition temperature.

To provide deeper insights into the impact of magnetic ordering arising from phenomena such as spin-phonon coupling, electron-phonon coupling, and/or magnetostriction contributions, a series of Raman spectra was recorded over the temperature range of 10-300 K, as illustrated with their enlarged spectral section in Figure VI.8(b). The temperature-dependence of Raman-active A_g , B_g , and Ph-Mag modes were chosen for analysis, whilst modes in the ranges of 200-400 and 840-1183 cm⁻¹ were too weak to be monitored due to resolution limitations. Meanwhile, the prominent factors influencing the progressive temperature-

dependent shifts and linewidths in Raman frequencies include vibrational frequencies associated with volumetric changes or thermal expansion, along with the influence of anharmonic coupling on phonon branches. The determination of the Raman shift is contingent upon the real part of the phonon self-energy as [349, 350]:

$$\omega(T) = \omega_0 + \Delta_1 T + \Delta_2 T, \quad (196)$$

where ω_0 is the harmonic frequency of the optical mode, $\omega_0 + \Delta_2(0)$ is the Raman shift as $T \rightarrow 0$ K, and $\Delta_1 T$ is the thermal-expansion contribution to the shift, written as:

$$\Delta_1 T = \omega_0 \exp\left(-3\gamma_0 \int_0^T \alpha(T') dT'\right) - \omega_0, \quad (197)$$

where γ_0 is the Grüneisen parameter for the optical Raman mode and $\alpha(T)$ is the temperature-dependent linear thermal expansion coefficient. However, the anharmonic phonon coupling term $\Delta_2 T$ is due to third-, fourth-, and higher-order anharmonic terms in the Hamiltonian, and is modeled as:

$$\Delta_2 T = C_1 \sum_{i=1}^2 \frac{1}{\exp(x_i) - 1} + C_2 \sum_{j=1}^3 \frac{1}{\exp(y_j) - 1} + \frac{1}{2} \sum_{j=1}^3 \frac{1}{\exp(y_j) - 1}, \quad (198)$$

where C_1 and C_2 are adjustable fitting parameters, and $x_1 + x_2 = y_1 + y_2 + y_3 = \frac{\hbar\omega_0}{k_B T}$, in which the first and second terms couple the optical phonon to two phonons (three-phonon process) and higher-order phonons (four-phonon process), respectively. Correspondingly, the temperature-dependent Raman linewidth can be modeled as [229, 349, 350]:

$$\Gamma(T) = K_1 \left[1 + \sum_{i=1}^2 \frac{1}{\exp(x_i) - 1} \right] + K_2 \left[1 + \sum_{j=1}^3 \left(\frac{1}{\exp(y_j) - 1} + \frac{1}{(\exp(y_j) - 1)^2} \right) \right], \quad (199)$$

where the linewidth, $\Gamma(T)$, represents the imaginary component of the self-energy and characterizes the phonon damping rate. In this context, $x_i = y_j = \hbar\omega_0/(k_B T)$, while K_1 and K_2 are fitting parameters. The first term in the $\Gamma(T)$ equation corresponds to three-phonon processes (decay into two phonons). Conversely, the second term is associated with four-phonon processes, representing phenomena

where three phonons contribute to the decay. Notably, Balkanski et al. [351] included decay into a four-phonon process, while Klemens [352] focused on a pure three-phonon process, wherein the optical phonon decayed into two acoustic phonons of the same frequency, disregarding the thermal-expansion term. In contrast, Tang et al. [349] incorporated all these modes in their experimental fitting. In our fitting, we used both the Klemens and Balkanski models, setting $x = x_1 = \hbar\omega_0/(2k_B T)$ and $y = y_1 = y_2 = y_3 = \hbar\omega_0/(3k_B T)$ in the absence of significant structural changes. This approach accounts for three-phonon interactions, where \hbar and k_B denote the reduced Planck's constant and the Boltzmann constant, respectively. The temperature dependence of the anharmonicity-induced wavenumber shift $\omega_{\text{anh}}(T)$ and the full width at half maximum $\Gamma_{\text{FWHM}}(T)$ are given by Equations. (219), (220), and (221), and can be expressed as:

$$\omega_{\text{anh}}(T) = \omega_0 + C_1 \left[1 + \frac{2}{\exp(x) - 1} \right] + C_2 \left[1 + \frac{3}{\exp(y) - 1} + \frac{3}{(\exp(y) - 1)^2} \right], \quad (200)$$

$$\Gamma_{\text{FWHM}}(T) = K_1 \left[1 + \frac{2}{\exp(x) - 1} \right] + K_2 \left[1 + \frac{3}{\exp(y) - 1} + \frac{3}{(\exp(y) - 1)^2} \right], \quad (201)$$

$$\omega(T) = \omega_0 + \alpha T, \quad (202)$$

$$\omega(T) = \omega_1 + \alpha_1 T, \quad (203)$$

where C_1 , C_2 , K_1 , and K_2 are defined above, and $\alpha = \frac{d\omega}{dT}$ [353] is the temperature coefficient of the Raman shift.

Figure 8(a-c) presents the temperature-dependent Raman excitation frequencies for the A_g, B_g, and Ph-Mag modes, respectively. Remarkably, all phonon modes exhibit anharmonic behavior as the dominant factor influencing their trends. The A_g and B_g phonon modes follow standard cubic-anharmonicity behavior, showing significant hardening consistent with the typical anharmonic law. However, they deviate from the expected theoretical anharmonic curve near the PM-to-FM phase transition ($T_N \sim 180$ K), as shown in Figure VI.9(a,b). This anomalous behavior suggests the presence of short-range ordering (SRO) above T_N , as also observed in magnetometry and SXRD analyses, identifying a PM-to-

FM transition at $T_N \sim 175$ K. Such anomalies point toward strong spin-phonon coupling in the ferromagnetic sublattice, leading to notable phonon deviations at lower temperatures [354]. For $T < T_N$, both modes show noticeable hardening and softening down to about 150 K and 130 K, respectively. In our analysis, we employed both the Klemens model and the Grüneisen linear model. Fitting with only the Klemens three-phonon process yields the dashed wine-colored curve in Figure VI.9(a,b), with $\omega_0 = 654.22 \text{ cm}^{-1}$ and $C \approx -1.5 \times 10^{-5} \text{ cm}^{-1}$ for A_g , and $\omega_0 = 514.81 \text{ cm}^{-1}$ and $C \approx -2.5 \times 10^{-5} \text{ cm}^{-1}$ for B_g . While this curve fits reasonably well up to $T_N \sim 175$ K, it becomes inadequate below T_N . We therefore used the Grüneisen linear model (solid black line in Figure VI.9(a,b)) with adjustable parameters $\omega_0 \approx 654.51 \text{ cm}^{-1}$, $\alpha \approx 0.0015 \text{ cm}^{-1}/\text{K}$, $\omega_1 \approx 517.18 \text{ cm}^{-1}$, and $\alpha_1 \approx 0.026 \text{ cm}^{-1}/\text{K}$. Notably, the deduced coupling constants were comparable to other reported experimental and theoretical values [229, 338, 350]. These observations suggest that factors beyond simple anharmonicity may influence the wavenumber shift of the A_g and B_g modes in this DP system—potentially a new relaxation phenomenon caused by spin-phonon coupling [355]. Bhadram et al. [273], studying spin-phonon coupling in RCrO₃ compounds, reported phonon-mode hardening below T_N . They attributed this to (i) direct spin-phonon coupling and/or (ii) magnetostriction-induced coupling. Therefore, the observed wavenumber shifts in the A_g and B_g modes here could arise from both direct spin-phonon coupling and magnetostriction, in addition to anharmonicity. Meanwhile, the Ph-Mag mode shows a deviation from anharmonic behavior below the magnetic ordering temperature T_N , plateauing at low temperature (Figure VI.9c). We fit this experimental data with both Klemens and Balkanski (solid red line) models, yielding $\omega_0 \approx 1299.55 \text{ cm}^{-1}$, $C_1 \approx -8.39 \times 10^{-4} \text{ cm}^{-1}$, and $C_2 \approx -1.83 \times 10^{-3} \text{ cm}^{-1}$. We also observed a GP phase between the FM and PM states, with a noticeable change around $T_{Nd/Sm} \sim 50$ K, attributed to ordering arising from antisite disorder (ASD). Raman modes, being highly sensitive to lattice adjustments or disorder, capture these phenomena even when $M(T)$ curves do not show clear ASD-driven transitions. Iliev et al. [274] observed an additional spin-phonon coupling emerging around 133 K, attributed to short-range AFM ordering from ASD, distinct from the long-range ferromagnetic ordering at 230 K. Thus, below 180 K, the anomalies observed in our system are likely associated with ASD between Ni-Ni and Mn-Mn, which polarizes the Nd/Sm sublattice.

It is crucial to elaborate on the uncertainty regarding whether the spin-phonon

coupling (SPC) in the system represents a direct interaction or is mediated by magnetostriction. To clarify this, we conducted a dedicated analysis by plotting the full width at half maximum (FWHM) of selected phonon modes, as illustrated in Figure VI.9(d-f). Traditionally, the FWHM of a relevant phonon mode remains unaffected by subtle changes in lattice or volumetric parameters induced by the magnetostriction effect. However, the FWHM is associated with the occupation probability of phonons (i.e., the Bose factor) and can therefore be influenced by spin-phonon coupling, often exhibiting anomalies across magnetic transitions [307, 356, 357]. The observed behavior in NdSmNiMnO₆ [Figure VI.9(d, f)] reveals a distinct and abrupt increase in the FWHM near its magnetic transition temperature, unequivocally ruling out any association with magnetostriction. Conversely, the broadening of the FWHM in the Ph-Mag mode indicates a decrease in phonon lifetime below T_N . This implies that the stability of phonon-quantized vibrational modes of the lattice diminishes as the magnetic transition occurs. Therefore, we can assert with confidence that the anomaly observed across the magnetic transition temperature in the FWHM shape parameters of the A_g and Ph-Mag phonon modes is solely induced by spin-phonon coupling. Any time the phonon mode interacts with real electron states, the linewidth increases as described by $\Gamma_{\text{FWHM}}(T)$, consistent with prior reports [358]. For the quantitative analysis, we considered the Klemens, Grüneisen, and Balkanski models for fitting, yielding the following extrapolated parameters: (i) For A_g mode: $\omega_0 \approx 29.88 \text{ cm}^{-1}$, $C_1 \approx 0.013 \text{ cm}^{-1}$ and (ii) For Ph-Mag mode: $\omega_0 \approx 19.45 \text{ cm}^{-1}$, $\alpha \approx 0.037 \text{ cm}^{-1}$; $\omega_0 \approx 51.92 \text{ cm}^{-1}$, $C_1 \approx 1.05 \text{ cm}^{-1}$, and $C_2 \approx 0.065 \text{ cm}^{-1}$. Notwithstanding, the asymmetric mode B_g displayed a non-monotonous linewidth decrease with temperature, as indicated by the Klemens (dashed wine-colored line) and Grüneisen (solid black line) fits in their respective regions of discontinuity [Figure VI.9(e)]. The anomalous fluctuations in $\Gamma_{\text{FWHM}}(T)$ for B_g at T_N , around $T \approx 100 \text{ K}$, and at $T_{\text{Nd/Sm}}$ arise from competing spin, charge, and lattice interactions. At T_N , the transition to the FM state modifies spin-phonon coupling, inducing phonon hardening due to reduced spin disorder [235]. The intermediate disorder-induced softening near 100 K is attributed to antisite disorder (ASD) [69, 304]. Similarly, at $T_{\text{Nd/Sm}}$, rare-earth ($\text{Nd}^{3+}/\text{Sm}^{3+}$) exchange interactions alter crystal field effects, further shifting phonon frequencies. Additionally, $\text{Ni}^{2+}/\text{Mn}^{4+}$ site misplacements create fluctuating AFM/FM clusters that enhance phonon scattering and charge localization [359]. Concurrently, magnetoelastic coupling amplifies

lattice distortions near these transitions, leading to intermittent phonon softening and hardening as the structure stabilizes. These observed features lead us to conclude that the SPC in the B_g asymmetric mode is triggered or mediated by the magnetostriction effect in this double perovskite system. This represents the first observation of such behavior in NdSmNiMnO₆, aside from what has been reported by Nanoto et al. [307] in CaMn₇O₁₂.

Recently, Granado et al. [306] formulated that, within the mean-field approximation, any magnetic material exhibiting long-range ordering promotes a renormalization of the phonon frequency, thereby enhancing the coupling between spins and phonons. This is expressed as [341, 357, 359, 360]:

$$\Delta\omega_{s-ph}(T) = \omega(T) - \omega_{anh}(T) = \lambda_{s-ph} \langle S_i \cdot S_j \rangle \approx \lambda_{s-ph} S^2 \emptyset(T) = \lambda_{s-ph} S^2 \left\{ \frac{M(T)}{M_{\text{Max}}} \right\}^2, \quad (204)$$

where, for nearest-neighbor spins localized at the i th and j th sites, the renormalized phonon mode is directly proportional to the spin-spin correlation function $\langle S_i \cdot S_j \rangle$ (considering four neighboring B/B'-site cations in NSNMO). The constant λ_{s-ph} measures the spin-phonon coupling strength. The order parameter is given as $\emptyset(T) = 1 - \left(\frac{T}{T_N}\right)^\gamma$, which is proportional to the normalized magnetic moment $\left\{ \frac{M(T)}{M_{\text{Max}}} \right\}^2$, where M_{Max} denotes the maximum magnetization value obtained from $M(T)$. Finally, $\Delta\omega_{s-ph}(T)$ represents the phonon frequency difference between the value predicted by the anharmonic model and the experimentally observed phonon mode. Figure VI.10(a) displays a clear deviation between the variation of the phonon mode and the normalized magnetic moment. The two curves exhibit essentially similar trends, overlapping up to the vicinity of T_N and obeying the mean-field approximation, but begin to diverge just below T_N . This further elucidates the presence of strong interaction between the lattice dynamics and magnetic excitations via spin-phonon coupling in the system. The unconventional behavior displayed by NdSmNiMnO₆ below T_N is similar to that observed in other double perovskites [355, 357, 361, 362], and can be attributed to competition between FM and AFM magnetic states arising from its frustrated spin pattern (discussed earlier), due to competing magnetic exchange interactions such as Ni³⁺-O-Ni³⁺, Mn³⁺-O-Mn³⁺, Mn⁴⁺-O-Mn⁴⁺ (AFM), and Ni²⁺-O-Mn⁴⁺ (FM), as highlighted in VI.10(a).

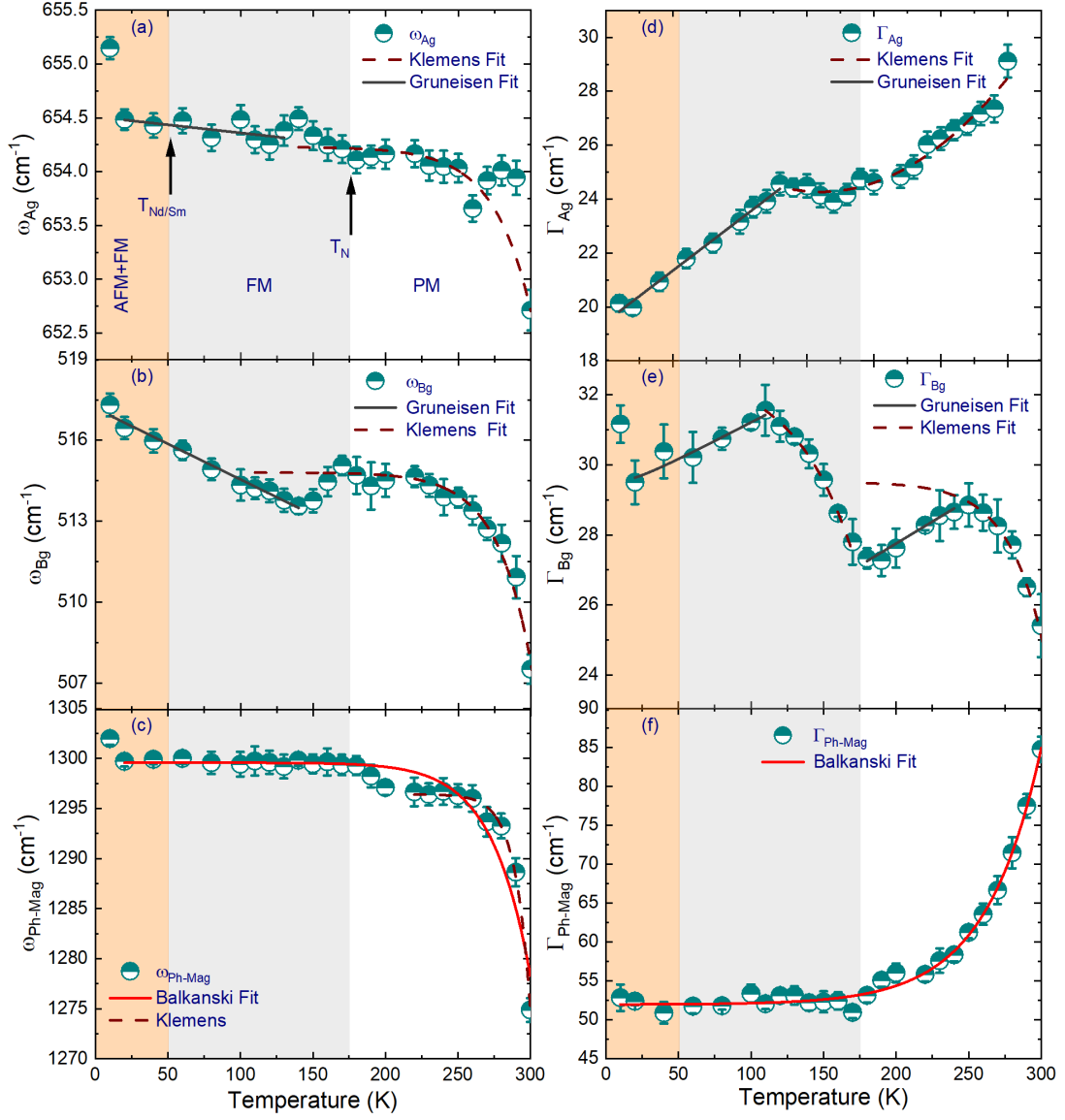


Figure VI.9: (a-c) Temperature variation of selected phonon frequencies in NdSmNiMnO₆. (d-f) Temperature dependence of the FWHM of the respective phonon modes. The solid-wine, solid-red, and solid-black curves correspond to fits using the Klemens, Balkanski, and Grüneisen models (cubic-anharmonic fits) in regions of discontinuity, respectively.

Finally, we analyzed the magnetostriction behavior induced by volumetric expansion. Here, we treated the unit cell volume using the thermal expansion formalism, as seen in Figure VI.10(b). Typically, the thermal variation of a system's unit-cell volume or lattice parameters associated with thermal expansion follows the Grüneisen approximation [41, 359]:

$$V(T) = V_0 + \frac{9\gamma N K_B}{B_0} \left(\frac{T}{\theta_D} \right)^3 \int_0^{\frac{\theta_D}{T}} \frac{x^3}{e^x - 1} dx = V_0 \left\{ 1 + \frac{A}{\left[e^{\frac{\theta_D}{T}} - 1 \right]} \right\}. \quad (205)$$

Here, V_0 is the volume constant at $T = 0$ K, A is an adjustable fitting parameter, N the number of atoms in the unit cell, B_0 the isothermal bulk modulus, γ the Grüneisen parameter, and θ_D the Debye temperature. It is evident from Figure VI.10(b) that over the entire temperature range (0-300 K), the unit cell volume V could not be adequately fitted with the above equation using a single curve, similar to the behavior seen in the other lattice parameters. Instead, a reasonable fit was achieved by fitting two distinct temperature regions separately, *i.e.*, above and below T_C , as demonstrated in Figure VI.10(b). The fitting yielded: $V_0 = 224.114 \pm 0.019 \text{ \AA}^3$, $A = 0.088 \pm 0.094 \text{ Pa}^{-1}$, $\theta_D = 665.399 \text{ K}$ which are higher than the results reported by Pal et al. [341]. Similarly, the overall volume variation was estimated as $\Delta V/V = +0.43\%$ as the temperature increased from 4 to 300 K. The spontaneous volume magnetostriction, $\lambda_{ms}^V(T)$, at a given temperature T , quantifies the magnetically induced lattice deformation by comparing the system's volume in magnetically ordered states (such as ferromagnetic, FM, and antiferromagnetic, AFM) with that in a hypothetical paramagnetic (PM) state at the same temperature. This is expressed as:

$$\lambda_{ms}^V(T) = \frac{V_{FM}(T) - V_{PM}(T)}{V_{PM}(T)}, \quad (206)$$

where $V_{FM}(T)$ represents the actual volume in the FM state at temperature T , while $V_{PM}(T)$ corresponds to the volume of the system in the hypothetical PM state at the same T . The temperature dependence of $\lambda_{ms}^V(T)$, as derived from the $V(T)$ versus T curve [see inset in Figure VI.10(b)], reveals a sharp drop near T_N . This behavior closely follows the magnetization $M(T)$ curve [see Figure VI.10(a)], demonstrating a strong correlation between the magnetic and lattice degrees of freedom. Such correlation aligns with spin-lattice coupling dynamics, where exchange interactions responsible for long-range magnetic ordering induce lattice distortions via magnetoelastic effects. At $T = 4$ K, the estimated $\lambda_{ms}^V(T) \approx 43 \times 10^{-4}$, while at $T = 275$ K, $\lambda_{ms}^V(T) \approx 4.25 \times 10^{-4}$. These values are comparable to those reported by Pal et al.[354], Poojitha et al.[363], and Kusz et al.[359]. These observations suggest that the magnetostriction effect leads to altered thermal expansion behavior of the lattice parameters below T_N (due to the rise of various exchange interactions as strong magnetic correlations develop) and concurrently results in substantial structural distortion of the lattice, as discussed in earlier chapters.

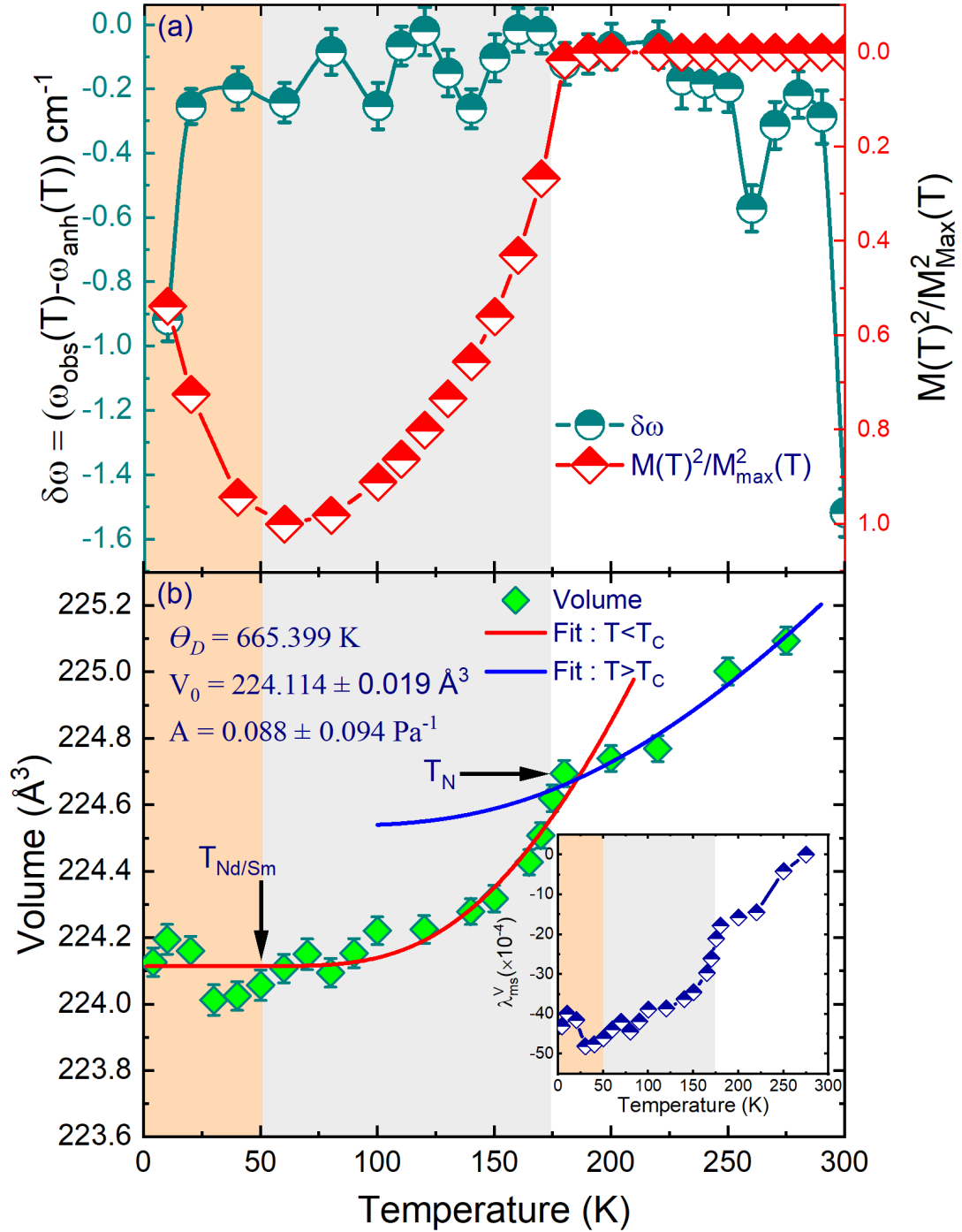


Figure VI.10: (a) Temperature variation of $\delta\omega(T)$ and $\left\{ \frac{M(T)}{M_{\text{Max}}} \right\}^2$ versus T for the Ag stretching mode. (b) Temperature variation of the unit-cell volume (V) as derived from temperature-dependent synchrotron X-ray diffraction (SXRD) pattern analysis. The solid-blue and red-dashed lines represent the thermal expansion fits of the curves in the regions $T > T_N$ and $T < T_N$, respectively. Due to the presence of a magnetostriction effect, the thermal expansion behavior of V shows a drastic change near T_N . The inset depicts the temperature variation of volume magnetostriction.

6.3.5 DFT

First-principles spin-polarized density functional theory (DFT) calculations were performed to investigate the magnetic and electronic ground-state properties of the NdSmNiMnO₆ double perovskite. To assess the stability of different spin configurations, multiple magnetic orderings were systematically evaluated, explicitly accounting for cationic site ordering and the occupancy preferences of Nd/Sm (A-site) and Ni/Mn (B-site) ions (see Figure VI.1). Monoclinic 20-atom unit cells were modeled using experimentally derived lattice parameters and atomic positions determined in this study. Among the tested configurations, the rock-salt-type ferrimagnetic (FiM2) and ferromagnetic (FM2) orderings (Figure VI.11) yielded the lowest total energies, consistent with the crystallographic structure resolved via Rietveld refinement. This refinement confirmed predominant occupation of Ni and Mn ions at distinct B and B' sublattice sites (Figure VI.1), reinforcing the structural basis for the computed magnetic states. Structural optimization was performed within the GGA(PBEsol)+*U* framework, with Hubbard *U* corrections applied to Ni and Mn *d*-orbitals, as well as to Nd and Sm *f*-states, to account for strong electron correlations. The calculations revealed that the lattice parameters $b = 5.486 \text{ \AA}$ and $c = 7.629 \text{ \AA}$ remained consistent with experimental values, while the *a*-axis ($a = 5.266 \text{ \AA}$) contracted slightly. This resulted in equivalent unit-cell volumes (220.438 \AA^3) for both FiM2 and FM2 configurations, suggesting comparable structural stability. For simplicity, the most stable FiM2 and FM2 cells will hereafter be referred to as FiM and FM, respectively. GGA+*U* electronic band-structure calculations reveal a narrow energy difference ($\sim 0.02 \text{ eV}$) between the ferrimagnetic (FiM) and ferromagnetic (FM) ground states, indicating a low-energy pathway for interconversion between these magnetic phases. The relative stability of each phase is governed by the exchange interaction between Nd spins and the Ni-O-Mn ferromagnetic sublattice. In the FiM configuration, Nd moments align parallel to each other but antiparallel to the Ni and Mn spins, stabilizing a compensated magnetic structure. Conversely, the FM phase arises from a spin-flip reorientation of Nd ions, which instead couple ferromagnetically with the Ni and Mn sublattices. The FiM-to-FM transition is mediated by local superexchange pathways within the Ni-O-Nd-O-Mn linkages, where competing exchange interactions dictate the energetics of spin alignment. The small energy barrier between the FiM and FM states underlines the material's

magnetic tunability, with modest fluctuations in temperature or external fields likely enabling phase switching. This behavior aligns with the experimentally observed interplay between A-site rare-earth magnetism and B-site transition-metal ordering in NdSmNiMnO₆ double perovskites, highlighting the critical role of cationic coordination geometry in stabilizing competing magnetic orders. Figure VI.12(a,b) display the spin-polarized total density of states (TDOS) and partial density of states (PDOS) computed using the GGA+*U* method for ferrimagnetic (FiM) and ferromagnetic (FM) ground-state configurations. To elucidate the role of Ni/Mn 3*d* and Nd/Sm 4*f* electronic states, spin-orbit coupling (SOC) was explicitly included in the calculations (denoted as GGA+*U*+SOC). The electronic structure and magnetic properties of Ni, Mn, and Nd exhibit negligible sensitivity to SOC. In contrast, the Sm 4*f* bands undergo subtle modifications in energy and occupation upon SOC inclusion, as shown in Figure VI.12(c,d).

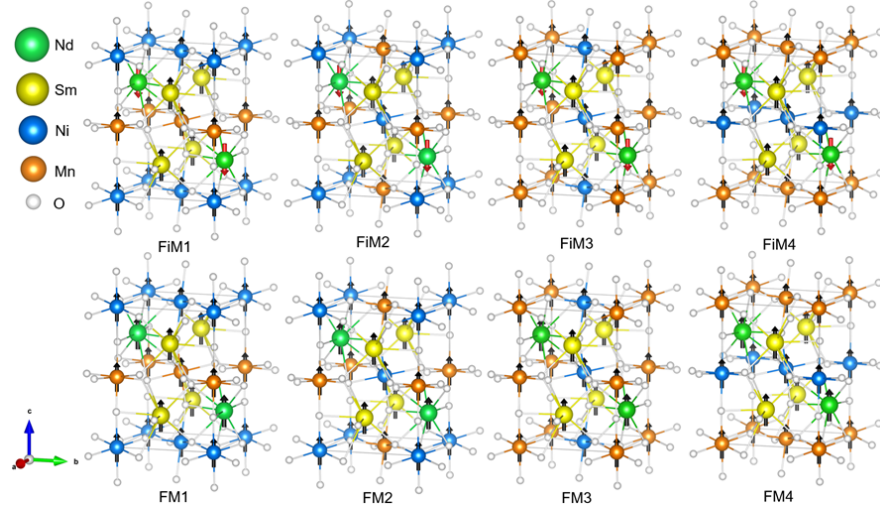


Figure VI.11: Monoclinic 20-atom crystal structures representing different magnetic configurations in a unit cell containing Nd, Sm, Ni, Mn, and O. The images illustrate the simulated spin orientations for ferrimagnetic (FiM1-FiM4) and ferromagnetic (FM1-FM4) arrangements. Configurations involving Nd/Sm positional interchange are omitted due to identical total energies. Spin directions along the *c*-axis are indicated by black (↑) and red (↓) arrows.

The local magnetic moments of Nd ($\sim 2.93 \mu_B$), Ni ($\sim 1.6 \mu_B$), and Mn ($\sim 3.0 \mu_B$) remained nearly identical across both FiM and FM configurations. Strikingly, the Sm moment decreased substantially from $\sim 4.93 \mu_B$ (without SOC) to $\sim 0.3 \mu_B$ (with SOC), leading to significant reductions in the total cell magnetic moments—from $26.0 \mu_B$ to $15.9 \mu_B$ (FM) and from $14.0 \mu_B$ to $4.7 \mu_B$ (FiM). The difference in spin moment intensities at the Ni and Mn octahedral sites gives rise to both short- and long-range magnetic interactions within NdSmNiMnO₆. The higher magnetic moment observed at the Mn

site is attributed to its dominant longer-range interactions compared to Ni. However, both experimental (Table VII.1) and computed $\langle\text{Ni-O}\rangle$ and $\langle\text{Mn-O}\rangle$ bond lengths (2.02 Å and 1.90 Å, respectively) suggest the opposite trend. This can be rationalized through electronic structure analysis: Ni^{2+} ($3d^8$) exhibits closed-shell-like behavior, enhancing intra-atomic Coulomb repulsion and suppressing Ni $3d$ -O $2p$ hybridization. In contrast, Mn^{4+} ($3d^3$) facilitates stronger Mn $3d$ -O $2p$ orbital mixing due to its reduced electron density, favoring shorter bonds despite its higher magnetic moment. Furthermore, the calculated density of states (DOS) for both FiM and FM profiles (Figure VI.12) indicates that spin-orbit coupling (SOC) significantly impacts the Sm $4f$ electronic states. When SOC is included, a distinct energy band splitting of the Sm $4f$ manifold is observed (Figure VI.12c,d). This splitting results in a more balanced occupation of spin-up and spin-down channels within the energy range of -2.0 eV to -6.0 eV, thereby quenching the Sm moment to $\sim 0.3 \mu_B$. In contrast, without SOC, Sm exhibits intense spin-up polarization with limited dispersion (Figure VI.12c,d), yielding a nearly atomic moment of $\sim 4.94 \mu_B$. The calculated bandgap energies of approximately 1.7 eV (FiM) and 1.6 eV (FM) confirm the insulating nature of NdSmNiMnO₆. The bandgap exhibits negligible sensitivity to SOC, retaining values of ~ 1.65 eV (FiM) and ~ 1.55 eV (FM) while preserving the insulating behavior. Despite this, SOC induces partial alignment of spin-up and spin-down bands near the Fermi level (Figure VI.12). Notably, the FiM and FM band structures share nearly identical shapes, orbital characters, and energy positions. The partial density of states (PDOS) at the valence band maximum reveals contributions from hybridized O $2p$, Ni $3d$, and a prominent Nd $4f$ peak. Polarized Mn $3d$ bands predominantly occupy the spin-up valence manifold within the -1.0 to -6.0 eV range. Exchange splitting between spin-unbalanced Ni $3d$ bands, observed at -4.0 eV (spin-up) and -1.0 eV (spin-down), accounts for their net magnetic moment. The conduction band minimum primarily consists of Mn $3d$ states weakly hybridized with O $2p$. Upon SOC inclusion, Sm $4f$ states shift to lower energies and hybridize with Mn $3d$, slightly reducing the bandgap. Empty Nd $4f$ states appear as sharp spin-down (FiM) and spin-up (FM) peaks near -3.0 eV, along with two prominent bands at -5.0 eV in their respective spin channels. Additionally, two nearly overlapping spin-down bands of Ni- and Mn- $3d$ orbitals are located around 3 eV.

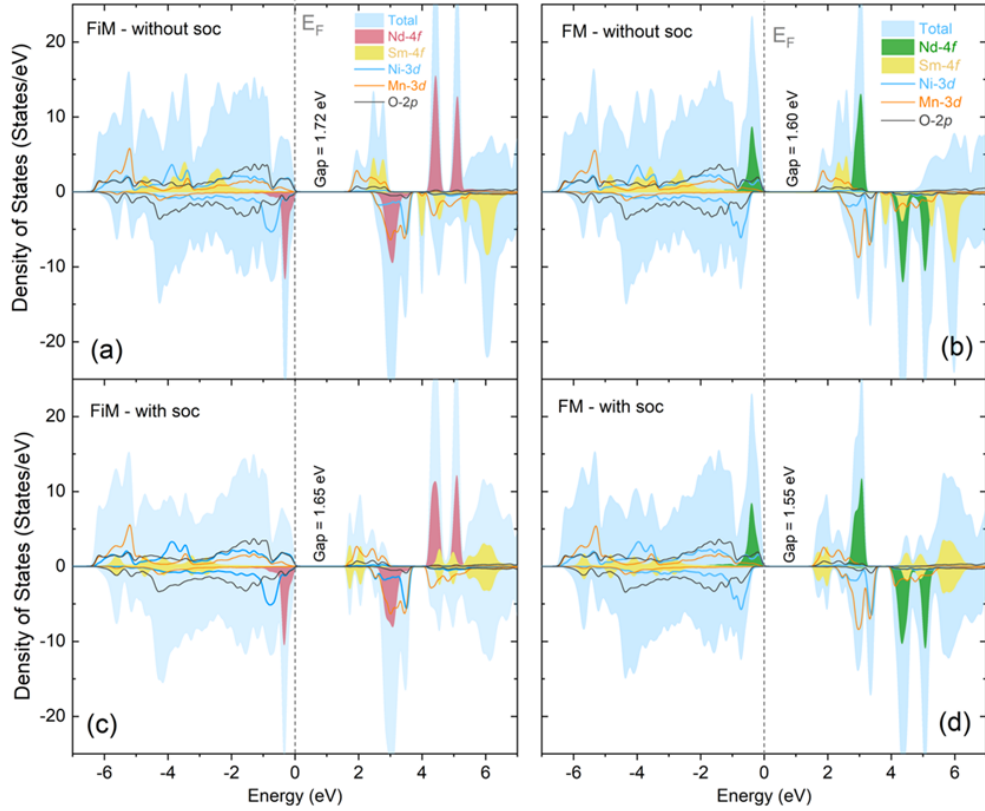


Figure VI.12: Total density of states (TDOS) and partial density of states (PDOS) calculated for ferrimagnetic (FiM) and ferromagnetic (FM) ground-state configurations. Panels (a) and (b) show results obtained using the GGA+U method, while panels (c) and (d) include spin-orbit coupling (SOC) within the GGA+U(SOC) framework. The vertical dashed line indicates the Fermi level. The shaded yellow regions represent Sm-4*f* contributions, while the shaded green regions highlight Nd-4*f* states. Band gap values for each configuration are indicated in the plots.

In an octahedral coordination complex, the electron distribution between the t_{2g} and e_g orbitals is governed by the interplay of crystal-field splitting and electron pairing energy. To clarify these effects in the presence of Jahn–Teller distortion, we analyze the electronic band populations of the Ni and Mn 3*d* orbitals for the GGA+U(+SOC) FiM ground state. Figures VI.13a,b present the computed PDOS for Ni and Mn t_{2g} and e_g orbital contributions. The Ni²⁺ ion adopts an intermediate-spin (IS) configuration ($S = 1$), characterized by a $t_{2g}^5 e_g^3$ electronic configuration. In contrast, the Mn⁴⁺ ion ($3d^3$) exhibits a half-filled t_{2g} manifold ($t_{2g}^3 e_g^0$, $S = 3/2$) that is nominally Jahn–Teller inactive in an ideal octahedral field. However, lattice distortions and interactions with neighboring ions (such as Ni and O) can promote partial e_g -orbital participation. Our calculations reveal evidence of orbital ordering in which the Ni and Mn e_g manifold favors the $d_{x^2-y^2}$ orbital over the d_{xy} t_{2g} component in the Ni²⁺–O–Mn⁴⁺ ferromagnetic interaction. This is evidenced by the fully occupied Ni $d_{x^2-y^2}$ e_g spin-down band near -1.0 eV and the half-filled Ni d_{xy} t_{2g} spin-down state near 3.0 eV (high-

lighted in Figure VI.13a). The lower panel (Figure VI.13 b) shows a corresponding preference in the Mn d -orbital manifold: the singly occupied $d_{x^2-y^2}$ e_g orbital hybridizes with the d_{xz} and d_{yz} t_{2g} states in the spin-up valence band, while the d_{xy} orbital remains unoccupied, appearing at approximately 3.0 eV (spin-up) and 5.0 eV (spin-down) in the conduction band. Insets in Figure VI.13 illustrate the computed electron distributions for Ni and Mn sites. This orbital ordering is accompanied by a significant Jahn–Teller distortion. The reduced Ni–O–Mn bond angle of approximately 152° decreases the crystal-field splitting energy and influences the Ni/Mn e_g orbital population. The Ni²⁺–O–Mn⁴⁺ exchange pathway is mediated via O $2p$ orbitals, enabling a double-exchange mechanism. The deviation from the ideal 180° bond angle is a hallmark of cooperative Jahn–Teller distortions and orbital ordering, which together optimize orbital overlap and stabilize the ferromagnetic sublattice formed by Ni²⁺ and Mn⁴⁺. This bond-angle reduction to 152° reflects the structural compromise that lowers electronic energy while enhancing magnetic exchange efficiency. Such behavior has also been reported in the related double perovskite La₂NiMnO₆ [186, 364], where ferromagnetic coupling between Mn⁴⁺ and Ni²⁺ is known to be oxygen-mediated. Our DFT results agree closely with experimental expectations, with computed local moments of $\sim 3.0 \mu_B$ (Mn⁴⁺) and $\sim 1.6 \mu_B$ (Ni²⁺) matching well with reported values [186, 364]. Moreover, the extra e_g electron introduced in the Mn⁴⁺ state activates new exchange pathways consistent with a double-exchange-like mechanism. This arises because the e_g – e_g overlap is present in the Ni²⁺ ($t_{2g}^5 e_g^3$) \leftrightarrow Mn⁴⁺ ($t_{2g}^2 e_g^1$) interaction but absent in the ideal $t_{2g}^3 e_g^0$ scenario. This overlap stabilizes the ferromagnetic Ni²⁺–O–Mn⁴⁺ interaction in agreement with experimental observations. According to the classic Goodenough–Kanamori rules, a 180° Ni²⁺ (IS) and Mn⁴⁺ (LS) superexchange would normally favor antiferromagnetism. However, the observed bond-angle deviation and strong e_g hybridization instead promote ferromagnetic coupling via the double-exchange mechanism. Notably, Mn⁴⁺ in the $t_{2g}^2 e_g^1$ configuration is susceptible to Jahn–Teller distortions, which modify orbital overlaps, reduce crystal-field splitting, and further stabilize the ferromagnetic Ni/Mn sublattice through cooperative e_g – e_g double-exchange interactions driven by both orbital ordering and structural distortions.

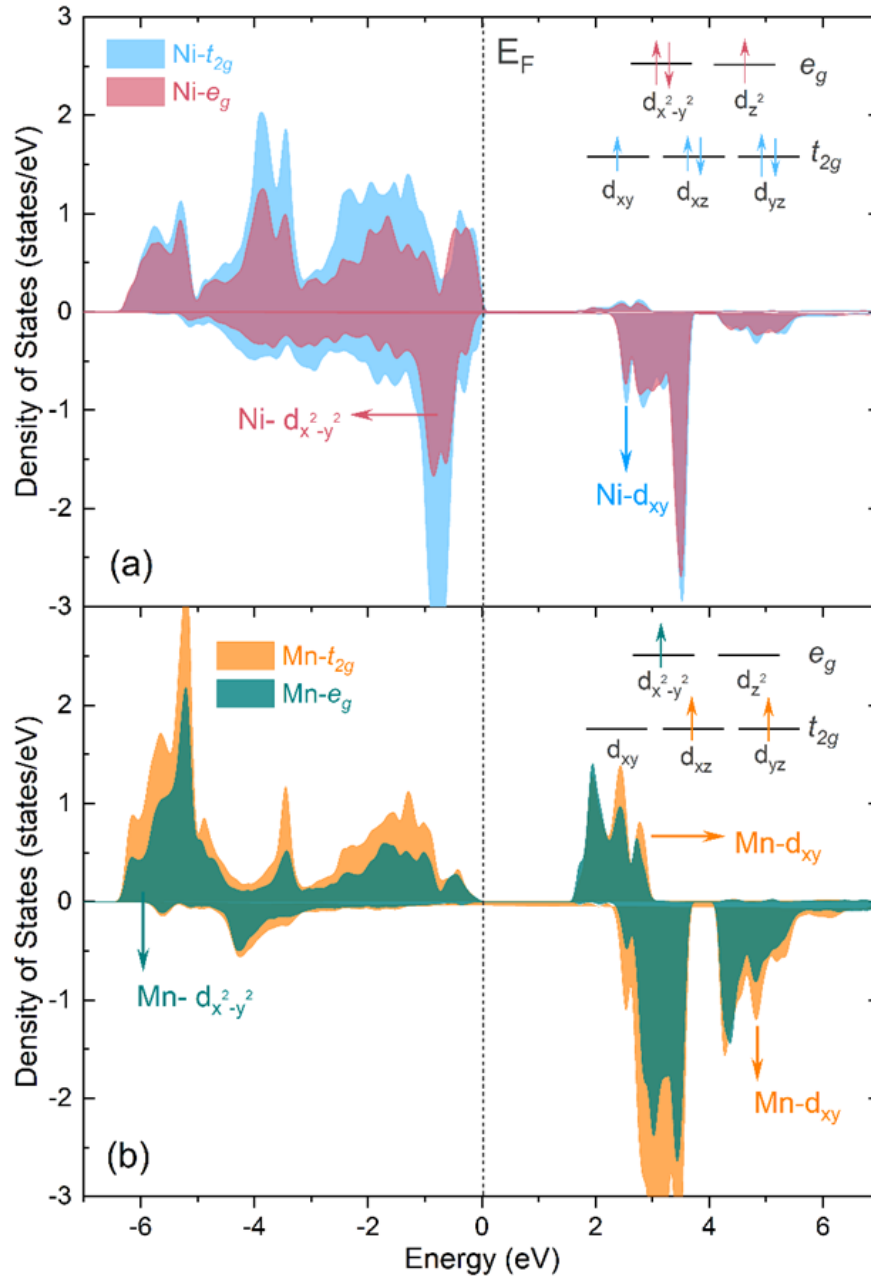


Figure VI.13: GGA+U(+SOC) partial density of spin states (PDOS) for Ni (top panel) and Mn (bottom panel) d -states, decomposed into t_{2g} (d_{xy} , d_{xz} , d_{yz}) and e_g ($d_{x^2-y^2}$, d_{z^2}) contributions. The dashed vertical line denotes the Fermi energy (E_F). Insets illustrate schematic electron occupation in crystal-field-split d -orbitals.

6.4 Conclusion

In conclusion, we have identified the ferrimagnetic (FiM) state as the most stable ground-state configuration of NdSmNiMnO₆, thereby resolving key questions about its magnetic and structural properties. The FiM ordering originates from the antiparallel alignment of Nd³⁺ spins with the ferromagnetically coupled

Ni²⁺-Mn⁴⁺ sublattice, driven primarily by superexchange interactions. The small calculated energy difference (~ 0.02 eV) between the FiM and ferromagnetic (FM) states suggests a highly tunable system, in which external perturbations such as temperature or applied magnetic fields could readily induce magnetic phase transitions. This magnetic flexibility, combined with the insulating nature of the material, highlights its potential for spintronic and magnetocaloric applications. Structurally, the monoclinic $P2_1/n$ symmetry with its characteristic octahedral distortions ($\langle Ni-O-Mn \rangle \approx 146^\circ$) plays a crucial role in stabilizing the FiM state. Magnetostriction effects are evident through pronounced anomalies in lattice parameters near $T_C \approx 175$ K, indicating strong coupling between spin and lattice degrees of freedom. Complementary Raman spectroscopy measurements confirm this spin-lattice coupling, revealing anomalous phonon mode hardening below T_C due to spin-phonon interactions. These experimental observations are supported by our DFT calculations, which not only confirm the FiM ground state but also provide detailed insight into the electronic structure. In particular, they reveal the quenching of the Sm³⁺ moment under spin-orbit coupling (SOC), as well as the important role of orbital ordering and octahedra distortions within the Ni²⁺-Mn⁴⁺ sublattice in stabilizing the FM interactions. Additionally, the presence of antisite disorder is predicted to introduce magnetic frustration effects. The material's insulating band gap (approximately 1.6-1.7 eV) remains robust under SOC, with the valence band primarily composed of hybridized Ni/Mn 3d and O 2p states. Overall, the interplay of A-site disorder, B-site ordering, spin-orbit coupling, and spin-lattice interactions in NdSmNiMnO₆ offers a comprehensive insight for understanding related double perovskites and guides the design of multifunctional materials with tunable magnetic and electronic properties.

* CHAPTER VII *

MCE and Critical Behavior across the Second-Order FM-PM Phase Transition in the DP NdSmNiMnO₆

A key challenge remains to improve or discover magnetic solids with optimal magnetocaloric effect (MCE) performance, providing a promising and environmentally friendly cooling technology. Herein, we report the crystal structure, magnetocaloric effect, and critical behavior of the double perovskite NdSmNiMnO₆ synthesized by a modified sol-gel process. X-ray diffraction structural investigation reveals that NdSmNiMnO₆ crystallizes in the monoclinic $P2_1/n$ (14) space group. Magnetocaloric analysis unveils a maximum magnetic entropy change of $-\Delta S_M^{\max} = 2.38 \text{ J kg}^{-1} \text{ K}^{-1}$ (at 0.7 T) near the ferromagnetic to paramagnetic second-order phase transition at 180 K. Furthermore, the estimated relative cooling power value increases from ~ 25 to $\sim 182 \text{ J kg}^{-1} \text{ K}^{-1}$ as the applied field changes up to 0.7 T, suggesting a promising magnetic refrigerant material. The critical behavior, investigated using techniques such as the modified Arrott plot, the Kouvel-Fisher method, and critical isotherm analysis, reliably yields critical exponents $\beta = 0.469$, $\gamma = 0.978$, and $\delta = 3.09$, in agreement with the scaling hypothesis. Lastly, renormalization group theory analysis revealed a magnetic interaction distance decaying as $J(r) \propto r^{-4.63}$, which lies between the three-dimensional (3D) Heisenberg and mean-field models, suggesting that the critical behavior of NdSmNiMnO₆ can be attributed to the competition between long- and short-range magnetic interactions.

Acknowledgements: The research presented in this chapter has been published as John M. Attah-Baah *et al.*, *ACS Omega* **2025**, 10 (18), 18973–18985. I gratefully acknowledge my collaborators for their essential contributions. Sample synthesis and magnetometry measurements were performed by Romualdo Silva Jr. under the supervision of Prof. Nilson S. Ferreira. All data processing and analysis were conducted independently by me. This work was supported

by CAPES (Finance Code 001), CNPq (grants 309184/2022-3 and 141485/2021-0), and FAPESP (grants 2017/10581-1 and 2020/10580-8). I sincerely thank all collaborators for their valuable support throughout this research.

7.1 Introduction

The rare-earth (RE)-based double-perovskite oxides with general formula RE₂BB'O₆, where B and B' are transition metal ions, are derived from the canonical perovskite oxide ABO₃ [24, 25, 282]. The aristo-type or idealized perovskite structure has a cubic symmetry with a Pm $\bar{3}$ m representative space group, where the octahedral cation sublattice adopts a NaCl-like topology, which is the most prevalent form of B-cation ordering in perovskites. This 1:1 rock-salt ordering of B-site cations doubles the unit cell of the undistorted ABO₃ perovskite, transitioning its space group symmetry from Pm $\bar{3}$ m to Fm $\bar{3}$ m [365, 366]. These systems typically adopt either an orthorhombic or a monoclinic crystal structure. Both maintain patterns of octahedral tilts to satisfy constraints imposed by the tolerance factor. The orthorhombic structure contains chemical and charge disorder at the B sites, while in the monoclinic case, B-site cations are ordered by both chemical species and charge (e.g., B²⁺ and B'⁴⁺) [182]. Its Glazer tilt system is typically described as $a^-a^-b^+$, where the adjacent octahedra show antiphase tilting along the a^- and b^+ axes (a^-) and in-phase tilting along the c -axis (b^+) [17, 287, 366, 367]. This tilt configuration reduces symmetry, leading to monoclinic distortions caused by antiphase tilts along the a^- and b^+ axes. In contrast, the in-phase tilts along the c -axis maintain partial coherence, contributing to the monoclinic symmetry observed in this case. These combined distortions affect bond angles and lengths, influencing the material's magnetic, electronic, and structural properties [23]. Most ordered double perovskites exhibit ferromagnetism (FM), which arises from superexchange (SE) interactions between the ordered B²⁺ and B'⁴⁺ ions; however, antisite disorder (ASD) of the B-site cations can profoundly impact the magnetic state [182]. In the case of nominally cation-ordered La₂NiMnO₆, antiferromagnetic (AFM) Ni^{2+/3+}-O-Ni^{2+/3+} and Mn^{4+/3+}-O-Mn^{4+/3+} SE interactions induced by ASD coexist and compete with FM coupling attributed to Ni²⁺-O²⁻-Mn⁴⁺ interactions [289–291]. Moreover, magnetic refrigeration

(MR) harnesses magnetocaloric effects (MCEs) in magnetic materials, presenting a promising, eco-friendly cooling technology. A key challenge remains the enhancement or discovery of magnetic solids with optimal MCE performances to bridge the gap between research discovery and practical implementation. For example, Gd₂ZnMnO₆ exhibits outstanding MCE performance with a magnetic entropy change of $-\Delta S_M^{\max} \approx 25.2 \text{ J kg}^{-1} \text{ K}^{-1}$ around 6.4 K under $\Delta H = 0\text{--}7 \text{ T}$ [368]. Zhang *et al.* [210] also observed a remarkable reversible cryogenic MCE in Gd₂TiMgO₆, with $-\Delta S_M^{\max} = 46.21 \text{ J kg}^{-1} \text{ K}^{-1}$ and refrigerant capacity (RC) of 300.27 J kg^{-1} at $\sim 3.3 \text{ K}$ under a magnetic field range of $0\text{--}7 \text{ T}$. These values notably surpass those of many renowned cryogenic MC materials and even outperform the commercial magnetic refrigerant gadolinium gallium garnet (GGG). Although magnetic materials with first-order phase transitions typically exhibit large ΔS_M , this effect is confined to a narrow temperature range near the phase transition and is often accompanied by hysteresis, resulting in low cooling power. To address these limitations, materials with second-order phase transitions are preferred as magnetocaloric candidates. These materials lack thermal hysteresis and exhibit smaller peak entropy changes (ΔS_M^{\max}), but their significant entropy variation over a broader temperature range provides higher net cooling power [183, 369].

While bulk and thin film configurations of La₂NiMnO₆ have been extensively studied, exploration into other rare-earth double perovskites (RE₂NiMnO₆) remains relatively limited, particularly AA'BB'O₆. To the best of our knowledge, no work has been performed on NdSmNiMnO₆. The substitution of Sm³⁺ for Nd³⁺ in this compound is motivated by fundamental considerations such as crystal stability, modifications to the electronic band structure, and enhanced magnetoelectric coupling [116, 308]. The A-site cation (Nd³⁺, Sm³⁺) significantly influences the B-site (Ni/Mn) sublattice, directly impacting magnetic and transport properties [309]. Structural stability quantified by the Goldschmidt tolerance factor, t_G (Equation 207), defined as where r_A (Nd, Sm), r_B (Ni, Mn), and r_O are the ionic radii of A-site cations, B-site cations, and oxygen, respectively [26]. The slight ionic radius difference between Nd³⁺ (1.109 Å) and Sm³⁺ (1.079 Å) alters Ni-O-Mn bond angles, bond lengths, orbital hybridization, and superexchange interactions [310]. Sm doping induces chemical pressure, enhancing octahedral tilting and lattice distortions, which modify the electronic bandwidth and charge transport. Also, magnetic interactions arise from competing FM and AFM SE,

governed by the Goodenough–Kanamori–Anderson (GKA) rules [42, 53, 116]. The primary exchange pathways are FM 180° (Ni²⁺–O–Mn⁴⁺) and AFM (Ni³⁺–O–Mn³⁺) [181]. Furthermore, Sm substitution induces A-site disorder, leading to local charge fluctuations and modified Ni/Mn valence states, which impact double-exchange mechanisms [41]. This disorder can introduce spin frustration and phase competition, potentially resulting in glassy magnetic states, as observed in related perovskites [312]. Additionally, the magnetocaloric effect (MCE) in double perovskites depends on magnetic entropy changes (ΔS_M), optimized by tuning the Curie temperature (T_C) via Sm-induced lattice distortions, enhancing entropy-driven magnetic phase transitions through Ni²⁺–Mn⁴⁺ interactions, and introducing anisotropic exchange interactions for improved refrigerant capacity [208, 370, 371]. Finally, the mixed valence states (Ni^{2+/3+} and Mn^{3+/4+}) enhance spin polarization, making NdSmNiMnO₆ a promising candidate. Hereafter, we present a robust investigation of the crystal structure, magnetocaloric effects (MCEs), and critical behavior of the ordered double perovskite NdSmNiMnO₆.

7.2 Experimental Procedures

7.2.1 Synthesis

The polycrystalline double perovskite NdSmNiMnO₆ was prepared by a modified sol–gel method, using glycine to accelerate intrinsic combustion. In a sequential synthesis process, 2 g of glycine was slowly added to a 2 M starting solution containing Nd(NO₃)₃·6H₂O, Sm(NO₃)₃·6H₂O, Ni(NO₃)₂·6H₂O, and (CH₃COO)₂Mn·4H₂O, all of high purity (Aldrich, 99.97%), in a molar ratio of 1:1:1:1 (Nd/Sm/Ni/Mn). The prepared sample solutions were kept at 200°C for 24 hours on a hot plate for evaporation and xerogel formation. Finally, all of the swollen xerogels were ground and calcined at 1000°C for 12 hours to remove all organic substrates. Furthermore, these samples were subjected to successive pulverization and pressed at a pressure of 80 MPa. A final calcination step was performed in an oven under ambient atmosphere at 1200°C for 24 hours to promote phase formation and obtain the pure double perovskite phase.

7.2.2 Characterization

The structural characterization of NdSmNiMnO₆ was performed by X-ray diffraction (XRD) using a Rigaku diffractometer operating with a Cu tube ($K_{\alpha 1} = 1.540598 \text{ \AA}$). The following conditions were considered: scan range of $5\text{--}90^\circ$ (2θ), 40 kV, 40 mA, step size 0.02° in 2θ , and counting time of 20 seconds per step, with a fixed slit of $1/4^\circ$, antiscattering slit of $1/2^\circ$, and a mask of 10 mm. Rietveld refinement [176] of the entire diffraction pattern was performed using the FULLPROF software package [313], following the procedure outlined in reference [372]. Magnetic measurements were conducted using a superconducting quantum interference device (SQUID) magnetometer (MPMS-3, Quantum Design) over the temperature range of 2–300 K, with a maximum applied magnetic field of $\pm 70 \text{ kOe}$. To eliminate bias from any trapped flux in the superconducting magnet, demagnetization protocols were employed: the magnetic field was oscillated during ramp-down to ensure negligible residual flux. Additionally, the sample chamber was routinely brought to 300 K (above the superconducting coil's critical temperature) before starting a new measurement series. The SQUID magnetometer coils were cooled by helium infusion prior to performing temperature-dependent magnetization $M(T)$ and isothermal field-dependent magnetization $M(H)$ measurements.

Table VII.1: Structural parameters of NdSmNiMnO₆ in the $P2_1/n$ space group (No. 14), refined from XRD data at room temperature. U_{iso} values are given in 10^{-3} \AA^2 . Bond valence sums (BVS) are in $|e|$. For mixed-occupancy sites, the majority cation is used in BVS calculations.

Atom	Frac. Coord.	U_{iso} (10^{-3} \AA^2)	BVS ($ e $)	Occupation
Nd/Sm	$x = 0.0092(6)$ $y = 0.5491(2)$ $z = 0.75047(8)$	0.12(1)	+3.40 / +1.73	Nd/Sm
Mn	$x = y = z = 0$	0.31(2)	+3.98	76% Mn, 24% Ni
Ni	$x = 0.5$	0.31(2)	+2.88	76% Ni, 24% Mn
O1	$x = 0.0907(3)$ $y = 0.0202(2)$ $z = 0.2384(6)$	1.26(2)	—	O
O2	$x = 0.2029(5)$ $y = 0.2552(5)$ $z = -0.0477(3)$	0.42(1)	—	O
O3	$x = 0.2186(5)$ $y = 0.3341(5)$ $z = 0.55093(3)$	1.42(2)	—	O

Bond	Length (Å)	Bond Angles (°)
Ni–O1	1.89(5)	$\langle \text{O1–Ni–O1} \rangle = 180.0(0)$
Ni–O2	1.81(3)	$\langle \text{O1–Ni–O2} \rangle = 89.9(3), 90.1(3)$
Ni–O3	1.81(3)	$\langle \text{O1–Ni–O3} \rangle = 89.0(10), 91.0(10)$
Mn–O1	2.06(5)	$\langle \text{O1–Mn–O1} \rangle = 180.0(0)$
Mn–O2	2.12(3)	$\langle \text{O1–Mn–O2} \rangle = 88.6(8), 91.4(8)$
Mn–O3	2.21(3)	$\langle \text{O1–Mn–O3} \rangle = 89.9(8), 90.1(8)$
$\langle \text{Ni–O} \rangle$	1.84(4)	$\langle \text{Ni–O1–Mn} \rangle = 150.5(9)$
$\langle \text{Mn–O} \rangle$	2.13(4)	$\langle \text{Ni–O2–Mn} \rangle = 155.3(5)$
		$\langle \text{Ni–O3–Mn} \rangle = 145.6(5)$

7.3 Results and Discussion

7.3.1 Structure Characterization

The XRD pattern for the NdSmNiMnO₆ powder sample, as obtained experimentally and refined using the FULLPROF software, is presented in Figure VII.1a,b. In the refinement process, atomic positions and Debye–Waller factors were iteratively refined over multiple cycles using a pseudo-Voigt function modified by Thompson–Cox–Hastings [314], which accounted for axial divergence asymmetry. The refinement was conducted using various structural models: the conventional orthorhombic symmetry $Pbnm$ (No. 62) (not shown), $Pbn2_1$ (No. 33), and the monoclinic space group $P2_1/n$ (#14). The orthorhombic symmetries $Pbnm$ and $Pbn2_1$ correspond to configurations with randomly distributed B-site cations, whereas the monoclinic $P2_1/n$ structure reflects ordered B-site cations. A more accurate fitting was achieved using the $P2_1/n$ space group, indicating that NdSmNiMnO₆ crystallizes in monoclinic symmetry. The refined lattice parameters were determined as: $a = 5.3779(2)$ Å, $b = 5.4849(2)$ Å, $c = 7.63667(2)$ Å, $\beta = 89.8412(3)^\circ$, $V = 225.260(1)$ Å³. In this structure, Nd/Sm share the same crystallographic A-site and are coordinated by eight oxygen atoms, forming polyhedra (Figure VII.1c,d). The Ni/Mn cations are distinctly located at the B/B' sites, each coordinated by six oxygen atoms, forming NiO₆ and MnO₆ octahedra (Figure VII.1e,f). The absence of any discernible impurity peaks within the resolution limits of the instrument confirms the formation of a highly pure, single-phase NdSmNiMnO₆ compound. Furthermore, the goodness-of-fit parameters, R_p , R_{wp} , R_{exp} , and χ^2 , were determined, and the Rietveld refinement results, including Wyckoff site information, are summarized in Table VII.1, confirming excellent agreement between the refined and experimental XRD patterns.

Additionally, the stability and deformation of the perovskite crystal structure can be determined through the calculation of the Goldschmidt tolerance factor, t_G , using the modified formula:

$$t_G = \frac{\left(\frac{r_{\text{Nd}} + r_{\text{Sm}}}{2} + r_{\text{O}}\right)}{\sqrt{2} \left(\frac{r_{\text{Ni}} + r_{\text{Mn}}}{2} + r_{\text{O}}\right)} \quad (207)$$

where r_{Nd} , r_{Sm} , r_{Ni} , r_{Mn} , and r_{O} are the ionic radii of Nd, Sm, Ni, Mn, and O, respectively, taken from Shannon's ionic radii tables [39, 41]. The calculated t_G values for NdSmNiMnO₆ at room temperature, considering Ni^{2+/3+} and Mn^{3+/4+} in VI coordination under both low-spin (LS) and high-spin (HS) states, are 0.834 and 0.862, respectively. These values fall within the empirical range expected for monoclinic or orthorhombic symmetry in perovskite structures [41, 338]. Local crystal structural analysis reveals non-identical bond lengths and bond angles, namely: Ni–O₁ ≠ Ni–O₂ = Ni–O₃ ≠ Mn–O₁ ≠ Mn–O₂ ≠ Mn–O₃, and ⟨Ni–O₁–Mn⟩ ≠ ⟨Ni–O₂–Mn⟩ ≠ ⟨Ni–O₃–Mn⟩ ≠ 180°, as summarized in Table VII.1. This strongly indicates the presence of lattice distortions in NdSmNiMnO₆, characteristic of ordered double perovskites. Structural refinement yields average bond lengths of ⟨Ni–O⟩ = 1.84(4) Å and ⟨Mn–O⟩ = 2.13(4) Å, together with an average bond angle of ⟨Ni/Mn–O–Ni/Mn⟩ = 150.50(6)°, consistent with those reported in similar perovskite systems [158, 159, 193, 198]. Using the refined lattice parameters, the octahedral rotation angles (γ, φ, Φ) were estimated using the following relationships: $\gamma = \cos^{-1}\left(\frac{a}{b}\right) \approx 11.34^\circ$, $\varphi = \cos^{-1}\left(\frac{\sqrt{2}a}{c}\right) \approx 5.18^\circ$, $\Phi = \cos^{-1}\left(\frac{\sqrt{2}a^2}{bc}\right) = \cos^{-1}(\cos \gamma \cdot \cos \varphi) \approx 12.45^\circ$, $\Theta = \frac{180 - \langle \text{Ni}^\vee \text{O}^\vee \text{Mn} \rangle}{2} \approx 14.77^\circ$. These angles quantitatively describe the extent of octahedral rotations in the perovskite framework, providing valuable insight into its deviation from an ideal cubic geometry. Structural distortions such as these are typical signatures of magnetic competition and frustration, which are commonly observed in complex perovskite systems.

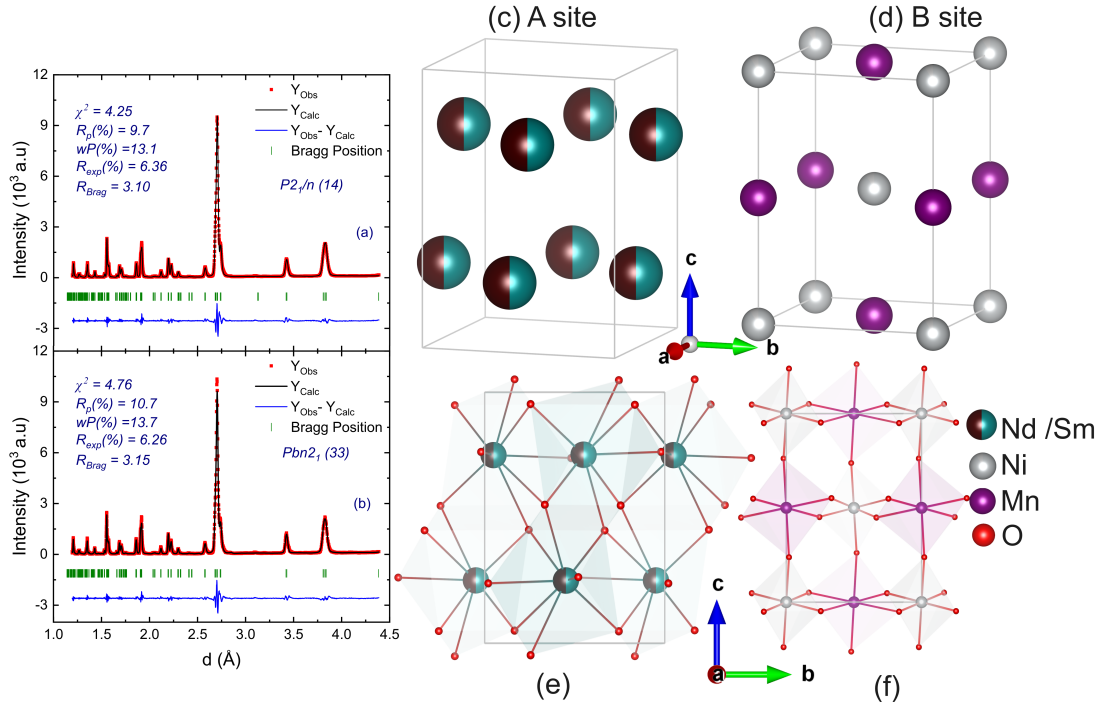


Figure VII.1: (a, b) Room-temperature XRD patterns and corresponding Rietveld refinements for the NdSmNiMnO₆ double perovskite. The red square symbols and black line represent the observed and calculated intensities, respectively. The short green vertical ticks mark the expected Bragg reflection positions for the monoclinic $P2_1/n$ (No. 14) and orthorhombic $Pbn2_1$ (No. 33) phases. The blue line at the bottom shows the difference between observed and calculated intensities. (c-f) Crystal structure representation of NdSmNiMnO₆. The light-gray lines outline a single unit cell, while shaded polyhedra highlight the cation-oxygen coordination environments.

7.3.2 Magnetocaloric Effect

The magnetocaloric effect (MCE) consists of the magnetization response to temperature variation under an applied magnetic field. Usually, the MCE is quantified by the magnetic entropy change (ΔS_M), estimated through the analysis of isotherms ($M-H$) at several temperatures. Figure VII.2a illustrates the $M-H$ curves collected with applied fields up to 7 T and various temperatures between 2 and 300 K. The curves show a typical saturation trend at low temperatures, with a transition to the paramagnetic (PM) state ($T > T_C$) as the temperature increases up to 300 K. The ΔS_M under a change in magnetic field can be evaluated from the Maxwell relation as follows:

$$\Delta S_M(T, H) = \int_0^{H_{\max}} \left(\frac{\partial M(H, T)}{\partial T} \right)_H dH = \Delta S(0, T) - \Delta S_M = -\Delta S_M(0, T) \quad (208)$$

Notwithstanding, due to the discrete interval of T and H in magnetic measurements, the above equation has been approximated as:

$$-\Delta S_M = - \sum_j \frac{(M_j - M_{j+1})}{(T_j - T_{j+1})} \Delta H_j \quad (209)$$

where M_j and M_{j+1} are the magnetization values measured in the applied field H_j at temperatures T_j and T_{j+1} , respectively [198, 203].

Figure VII.2b shows the temperature dependence of $-\Delta S_M$ for different magnetic fields. A broad peak centered at $T_C \approx 180$ K is observed, characteristic of the conventional MCE, confirming the FM-PM order transition. This peak presents a maximum entropy change of $-\Delta S_{M,\max} = 2.38 \text{ J kg}^{-1} \text{ K}^{-1}$ at 7 T, which is lower than in other Ni/Mn-based double perovskites [185, 206, 286], but higher than in SmCaCoMnO₆ [203] and La_{2-x}Sr_xCoMnO₆ [373]. Interestingly, at low temperatures ($T < 50$ K), a negative $-\Delta S_M$ behavior is observed under fields up to 2 T. As the field increases, it transitions to a positive MCE state in the range 3-7 T (see blue arrows in Figure VII.2). This abrupt rise in $-\Delta S_M$ for fields greater than 4 T is attributed to the ordering of rare-earth ions [180, 198]. This phenomenon is linked to the antiferromagnetic (AFM) ordering of (Nd³⁺, Sm³⁺) moments. Prior studies indicate that rare-earth sublattices containing Nd and Sm can undergo AFM coupling at low temperatures, significantly influencing magnetization in weak fields [41]. In this system, complex magnetic interactions emerge between the rare-earth (Nd/Sm) and transition-metal (Ni-Mn) sublattices. At low fields, Nd/Sm moments align antiferromagnetically with the Ni/Mn sublattice, leading to a negative ΔS_M . However, as field strength increases, these moments reorient ferromagnetically, resulting in a positive ΔS_M characteristic of a metamagnetic-like transition [338, 374]. This AFM interaction competes with the intrinsic FM component, reducing overall magnetization at low temperatures under weak fields. Its disappearance at higher temperatures supports the role of rare-earth ordering, as thermal fluctuations suppress AFM coupling. Similar field-dependent entropy effects have been reported in perovskite systems like Nd₂NiMnO₆ [185] and Y₂NiMnO₆ [204]. Furthermore, a small asymmetrical peak at $T \approx 214$ K appears for fields greater than 4 T, possibly due to disorder, magnetic frustration, or an emerging Griffiths phase [198, 375].

Notably, the observed $-\Delta S_M$ value remains below the theoretical limit ($-\Delta S_{M,\text{limit}}$), which is generally estimated from the contribution of uncoupled

rare-earth (RE) ions. The theoretical limit is expressed as:

$$-\Delta S_{\text{M,limit}} = R \cdot \ln(2J + 1) \quad (210)$$

where R is the universal gas constant and J accounts for the half-filled $4f$ orbital of Nd³⁺/Sm³⁺ ions, characterized by high-spin states of $J = 9/2$ and $5/2$, respectively [210, 376]. The calculated $-\Delta S_{\text{M,limit}}$ is 22.52 J kg⁻¹ K⁻¹ for NdSmNiMnO₆. This observed disparity is likely associated with additional internal entropy losses originating from phonon contributions, as well as constraints on the ΔH values during measurement [288, 290]. It is plausible that the division of the A-site by Nd and Sm caused a modification of the global bandwidth, deviating the Ni–O–Ni/Mn bond angle from 180° and altering Ni/Mn–O bond lengths, as observed in XRD analysis—unlike in Nd₂NiMnO₆ [158]. Consequently, electron-spin coupling in the system increases, enhancing the FM interactions in NdSmNiMnO₆ [207]. Generically, the exponent n characterizes the field dependence of the magnetic entropy change (ΔS_{M}) in magnetocaloric materials, following the relation: $\Delta S_{\text{M}} \propto H^n$. The value of n provides insights into the nature of the magnetic phase transition. According to Law et al. (2018) [377], a maximum n value exceeding 2 is indicative of a first-order phase transition (FOPT), while second-order phase transitions (SOPTs) typically yield lower values. In our analysis, we determined $n = 0.66(13)$ (see Figure VII.2c), closely aligning with the mean-field prediction of $n = 2/3$ [207, 288]. This suggests that our material undergoes a second-order phase transition (SOPT), consistent with other perovskite systems. For instance, in La_{0.6}Ca_{0.3}Sr_{0.1}MnO₃, the exponent n was approximately 0.58 [378], and in Ag-doped manganites, $n \approx 0.669$ [379], both confirming the SOPT nature. These consistent findings underline the reliability of using the exponent n as a diagnostic criterion for magnetic phase transitions. The proximity of our n value to $2/3$ supports the classification of the transition as second-order.

To further clarify the characteristics of the FM phase transition, we examine the MCE via a normalizing universal scaling law [208]. All curves were constructed phenomenologically by scaling all $-\Delta S_{\text{M}}$ curves against their respective maximum values ($-\Delta S_{\text{M,max}}$), expressed as $(\Delta S_{\text{M}}/\Delta S_{\text{M,max}})$. For this, the reduced temperature θ^{\pm} is defined as:

$$\theta^- = \frac{T_{\max} - T}{T_a - T_{\max}}, \quad T < T_{\max} \quad (211)$$

$$\theta^+ = \frac{T - T_{\max}}{T_b - T_{\max}}, \quad T > T_{\max} \quad (212)$$

where T_{\max} denotes the temperature at $-\Delta S_{M,\max}$, and T_a and T_b are two reference temperatures (below and above T_C), defined by: $\Delta S_M(T_a, T_b) = \frac{1}{2}\Delta S_{M,\max}$. As highlighted in the inset of Figure VII.2c, all rescaled $\Delta S_M/\Delta S_{M,\max}(\theta)$ curves collapse into a single curve. The observed unification at $\theta > 0$ confirms the characteristic behavior of materials undergoing typical FM second-order phase transitions (FM-SOPT). However, the non-collapsing character at $\theta < 0$ is attributed to normalizing uncertainties or the possible presence of a first-order phase transition (FOPT) due to antisite disorder (ASD).

Normally, the relative cooling power (RCP) parameter is used to evaluate the cooling efficiency of magnetocaloric materials. RCP can be determined from $-\Delta S_M(T)$ curves [210, 211] using the relation:

$$\text{RCP} = |\Delta S_{M,\max}| \times \delta T_{\text{FWHM}} \quad (213)$$

where $\delta T_{\text{FWHM}} = T_{\text{Hot}} - T_{\text{Cold}}$ is the full width at half-maximum of the magnetic entropy change. The RCP value as a function of magnetic field H is displayed in Figure VII.2d for NdSmNiMnO₆. Significantly, RCP shows an increasing trend with increasing ΔH , following a power law of the form $\text{RCP} \approx H^m$, where m is a scaling exponent. For the NdSmNiMnO₆ sample, the estimated RCP increases from approximately 25 Jkg⁻¹K⁻¹ to 182 Jkg⁻¹K⁻¹ as the applied field increases from 1 to 7 T. The landmark discovery of MCE properties in pure Gd by Brown [212] has set the benchmark for ideal MCE materials. According to Phan and Yu [239], optimal magnetocaloric materials should exhibit large magnetic entropy change ($-\Delta S_M$), high adiabatic temperature change (ΔT_{ad}), a Curie temperature near room temperature (~ 300 K), broad operating temperature range (e.g., 10-80 K), minimal magnetic and thermal hysteresis, small lattice entropy, high thermal conductivity, and excellent chemical stability. Recent studies emphasize that perovskite manganites offer advantages such as tunable Curie temperatures, high chemical stability, and low hysteresis, making them attractive for magnetic cooling technologies [380]. Table VII.2 provides a comparative evaluation of NdSmNiMnO₆ against well-established mag-

netocaloric materials, illustrating that its performance exceeds some reported values. Compared to high-performance systems, the maximum magnetic entropy change of NdSmNiMnO₆ ($-\Delta S_{M,\max} = 2.38 \text{ J kg}^{-1} \text{ K}^{-1}$ at 7 T) is significantly lower than in Gd [213], Gd₅SiGe₂ [239], Ln_{0.5}Ca_{0.5}MnO₃ (Ln = Dy, Gd) [381], and MnFeP-based alloys [374]. For instance, Tb₂FeCrO₆ achieves $-\Delta S_M = 12.9 \text{ J kg}^{-1} \text{ K}^{-1}$ under similar field conditions [382], and Mn-substituted SmFeO₃ perovskites exhibit broader operational temperature spans and higher entropy changes [383]. Likewise, La(Fe_{0.98}Co_{0.02})_{11.7}Al_{1.3} demonstrates $-\Delta S_M \sim 10.6 \text{ J kg}^{-1} \text{ K}^{-1}$ at 0-5 T [384], outperforming NdSmNiMnO₆ in absolute values. Nevertheless, the RCP remains a crucial performance metric for evaluating refrigeration efficiency. NdSmNiMnO₆ demonstrates a notable RCP increase from ~ 25 to $\sim 182 \text{ J kg}^{-1} \text{ K}^{-1}$ over the field range 0-1 T to 0-7 T, likely due to the extended temperature span of the MCE. Table 2 compares the RCP and $-\Delta S_M$ values of NdSmNiMnO₆ with other systems. This RCP surpasses values reported for La_{0.5}Nd_{0.2}Ca_{0.3}MnO₃ and La_{0.7}Ca_{0.3}MnO₃ [385], reinforcing its suitability for practical applications. Although NdSmNiMnO₆ underperforms in terms of absolute entropy change, its superior RCP and promising thermal response highlight its potential. With further optimization of composition and microstructure, NdSmNiMnO₆ may evolve into a viable candidate for future magnetic refrigeration technologies [204, 207, 210, 211].

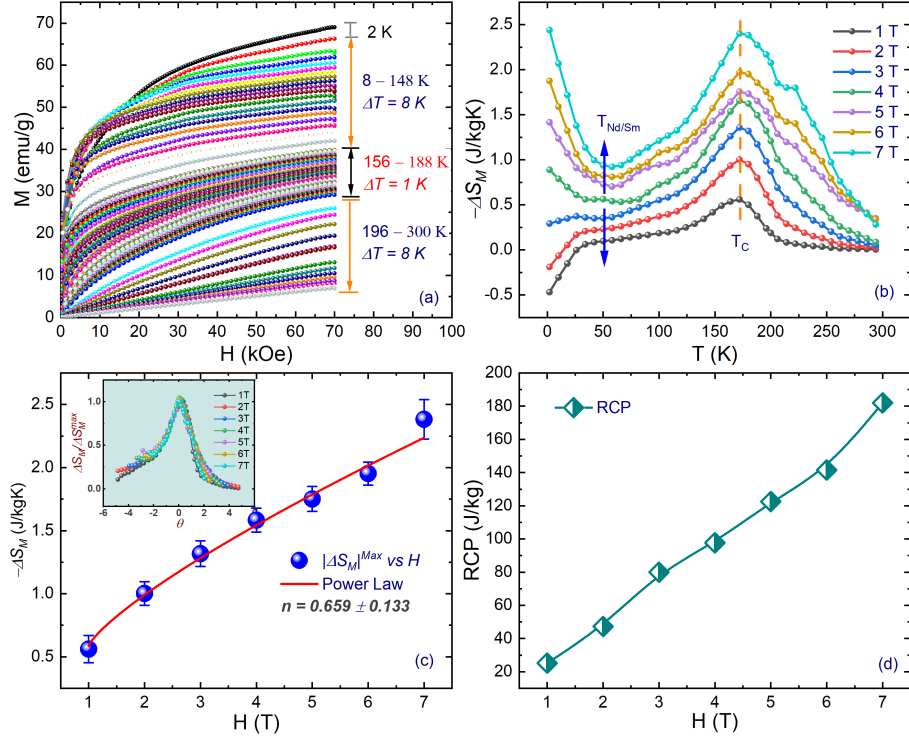


Figure VII.2: (a) Isothermal magnetization curves measured at different temperatures in the range 2–156 K with $\Delta T = 8$ K and 156–196 K with $\Delta T = 1$ K for critical point analysis. (b) Temperature dependence of the field-induced magnetic entropy change ($-\Delta S_M$) estimated from isothermal $M(H)$ data between 2 and 292 K, under various applied magnetic fields. (c) Magnetic field dependence of the maximum entropy change ($-\Delta S_M^{\max}$). Inset: normalized entropy change ($\Delta S_M / \Delta S_M^{\max}$) as a function of reduced temperature θ . (d) Relative cooling power (RCP) as a function of applied magnetic field (H).

Table VII.2: Comparative analysis of NdSmNiMnO₆ with well-known magnetocaloric materials. $-\Delta S_M^{\max}$ is the maximum magnetic entropy change, and RCP is the relative cooling power.

Material	$-\Delta S_M^{\max}$ (J kg ⁻¹ K ⁻¹)	RCP (J kg ⁻¹)	Reference
Gd	10.2	~410	Tegus [213]
La _{0.87} Sr _{0.13} MnO ₃	5.80	~232	Phan & Yu [239]
Gd ₅ SiGe ₂	18.4	~535	Pecharsky <i>et al.</i> [386]
Pr _{0.63} Sr _{0.37} MnO ₃	2.57–8.52	~511	Phan <i>et al.</i> [387]
MnFeP _{0.45} As _{0.55}	18.6	~500	Tegus <i>et al.</i> [213]
Fe ₂ P-based alloy	7.8	~390	Fujita <i>et al.</i> [374]
La _{0.7} Ca _{0.3} MnO ₃	1.38	~41	Wang <i>et al.</i> [385]
Ln _{0.5} Ca _{0.5} MnO ₃ (Ln = Dy, Gd)	8.5–22.8	–	Das <i>et al.</i> [388]
(R _{0.2} Gd _{0.2} Eu _{0.2} Dy _{0.2} Tb _{0.2})CrO ₃	2.8–13.6	143.71–159.03	Zheng <i>et al.</i> [381]
(R = Pr, Nd, Sm)			
La _{0.5} Nd _{0.2} Ca _{0.3} MnO ₃	2.31	~60	Wang <i>et al.</i> [385]
La _{0.6} Ca _{0.4} MnO ₃	5.00	~135	Phan & Yu [389]
NdSmNiMnO₆	2.38	~182	This study

7.3.3 Critical Exponent Analysis

To elucidate the nature of magnetic interactions near the magnetic phase transition temperature $T_C = 177$ K, we conducted a comprehensive analysis of the critical exponents for NdSmNiMnO₆. According to the scaling hypothesis, a second-order phase transition (SOFT) is characterized by interconnected critical exponents [390]. In the vicinity of a SOFT, the correlation length diverges as $\xi = \xi_0 \left| \frac{T-T_C}{T_C} \right|^{-\nu}$ and universal scaling laws govern the spontaneous magnetization M_S and the inverse initial magnetic susceptibility χ_0^{-1} . The critical exponents β , γ , and δ characterize M_S below T_C , χ_0^{-1} above T_C , and $M(H)$ at T_C , respectively [391]:

$$M_S(T) = M_0(-\varepsilon)^\beta, \quad \varepsilon < 0, \quad T < T_C \quad (214)$$

$$\chi_0^{-1} = \lim_{H \rightarrow 0} \left(\frac{H}{M} \right) = (h_0 m_0) \varepsilon^\gamma, \quad \varepsilon > 0, \quad T > T_C \quad (215)$$

$$M = D H^{1/\delta}, \quad \varepsilon = 0, \quad T = T_C \quad (216)$$

where $\varepsilon = (T - T_C)/T_C$ is the reduced temperature, and h_0/m_0 , D , and M_0 are amplitude constants [216, 219]. The magnetic equation of state, connecting $M(H, \varepsilon)$, H , and T , is expressed as:

$$M(H, T) = |\varepsilon|^\beta f_\pm \left(\frac{H}{|\varepsilon|^{\beta+\gamma}} \right) \quad (217)$$

where f_+ and f_- are regular functions for $T > T_C$ and $T < T_C$, respectively. We define the renormalized variables as:

$$m \equiv |\varepsilon|^{-\beta} M(H, \varepsilon), \quad h \equiv |\varepsilon|^{-(\beta+\gamma)} H \quad (218)$$

This relation is validated when a plot of $|\varepsilon|^{-\beta} M(H, \varepsilon)$ versus $|\varepsilon|^{-(\beta+\gamma)} H$ collapses the data into two universal curves—one for $T < T_C$ and the other for $T > T_C$ [219, 333, 392].

Figure VII.3a shows the isotherms collected near T_C between 156 and 188 K at $\Delta T = 1$ K. The Arrott-Noakes plot (M^2 vs H/M) using mean-field exponents $\beta = 0.5$ and $\gamma = 1.0$ [217] is presented in Figure VII.3b. For an accurate model, the isotherm at $T = T_C$ should pass through the origin, with $\chi_0^{-1}(T)$ and $M_S(T)$

given by the intercepts on the H/M and M^2 axes, respectively. However, unlike the Landau mean-field hypothesis, the Arrott-Noakes plots for NdSmNiMnO₆ exhibit nonlinear downward curvature, indicating the inadequacy of the mean-field model. Nonetheless, the order of the magnetic transition can still be assessed using Banerjee's criterion [393], where the slope of M^2 vs H/M determines the nature of the transition. A negative slope indicates a first-order phase transition, while a positive slope confirms a second-order phase transition. Thus, the observed positive slope in the Arrott-Noakes plot confirms that NdSmNiMnO₆ undergoes a second-order phase transition.

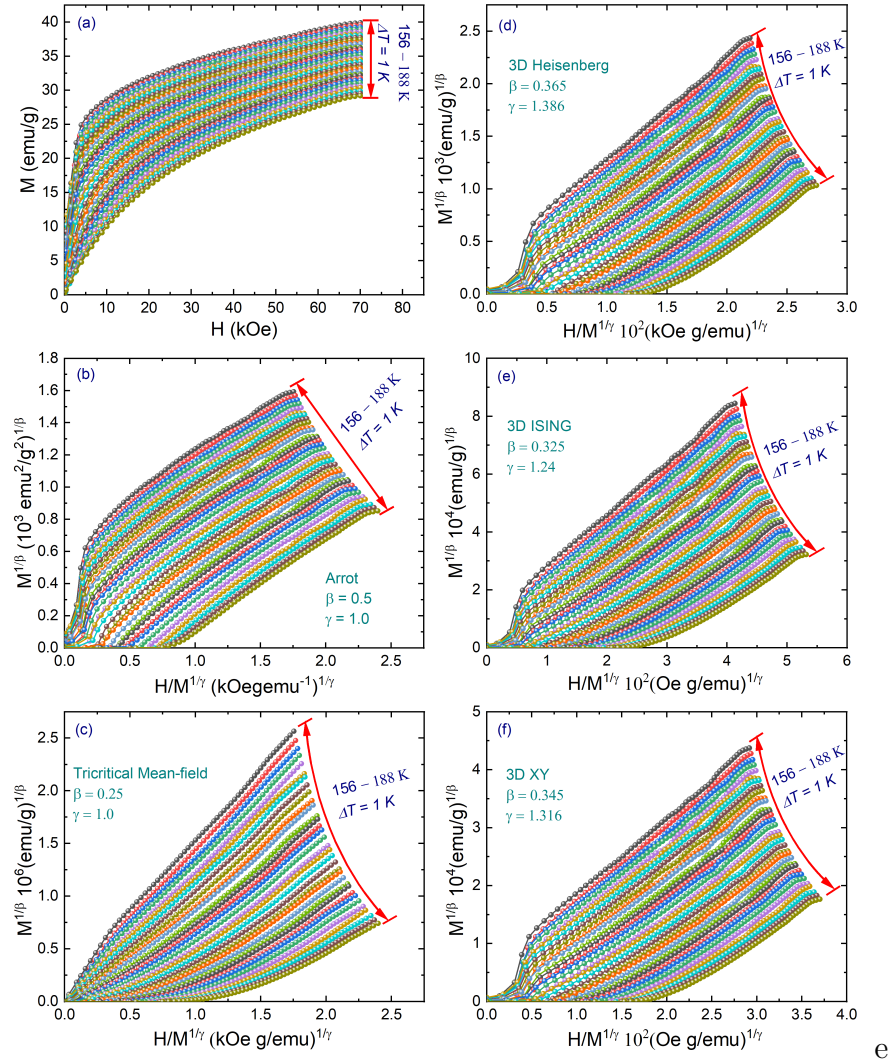


Figure VII.3: (a) Isothermal magnetization curves measured at different temperatures between 156 and 188 K with $\Delta T = 1$ K. The isotherms are plotted as $M^{1/\beta}$ vs $(H/M)^{1/\gamma}$ using model parameters from: (b) Arrott-Noakes model, (c) Tricritical mean-field model, (d) Three-dimensional (3D) Heisenberg model, (e) 3D Ising model, and (f) 3D XY model.

Mostly, the modified Arrott-Noakes plot (MAP) was utilized to probe the critical behavior based on different models [217], described as

$$\left(\frac{H}{M}\right)^{1/\gamma} = a\varepsilon + bM^{1/\beta}, \quad (219)$$

where ε has been defined earlier, and a and b are constants. Figure VII.3(c-f) depicts the MAP for the models: tricritical mean-field ($\beta = 0.25$, $\gamma = 1.0$), 3D Heisenberg ($\beta = 0.365$, $\gamma = 1.386$), 3D Ising ($\beta = 0.325$, $\gamma = 1.24$), and 3D XY ($\beta = 0.345$, $\gamma = 1.316$), respectively. All replotted MAPs display a slight curvature in the low-field region, indicative of the average effect across domains magnetized in diverse directions. Conversely, within the high-field region, all constructions manifest quasi-linear profiles, implying potential 3D magnetic behavior within the material. To identify the optimal model, we introduce the normalized slopes (NS) defined as $NS = \frac{S(T)}{S(T_C)}$, where $S(T)$ represents the slope of the MAP curves. The $NS(T)$ curves are presented in Figure VII.4. In an ideal scenario, the MAP is expected to yield a set of parallel straight lines, resulting in all NS values being equal to 1.0. However, our observations indicate that the critical behavior of NdSmNiMnO₆ deviates slightly from adherence to these universality classes. We noted that the NS approaches the mean-field model below $T < T_C$, aligned with the nearly isotropic magnetic nature evident at low temperatures. In contrast, the NS for the 3D Heisenberg model exhibits optimal agreement above $T > T_C$, signifying that the critical behavior of the NdSmNiMnO₆ system may not conform to a singular universality class, which is in contrast to other double perovskite compounds [193, 204, 394].

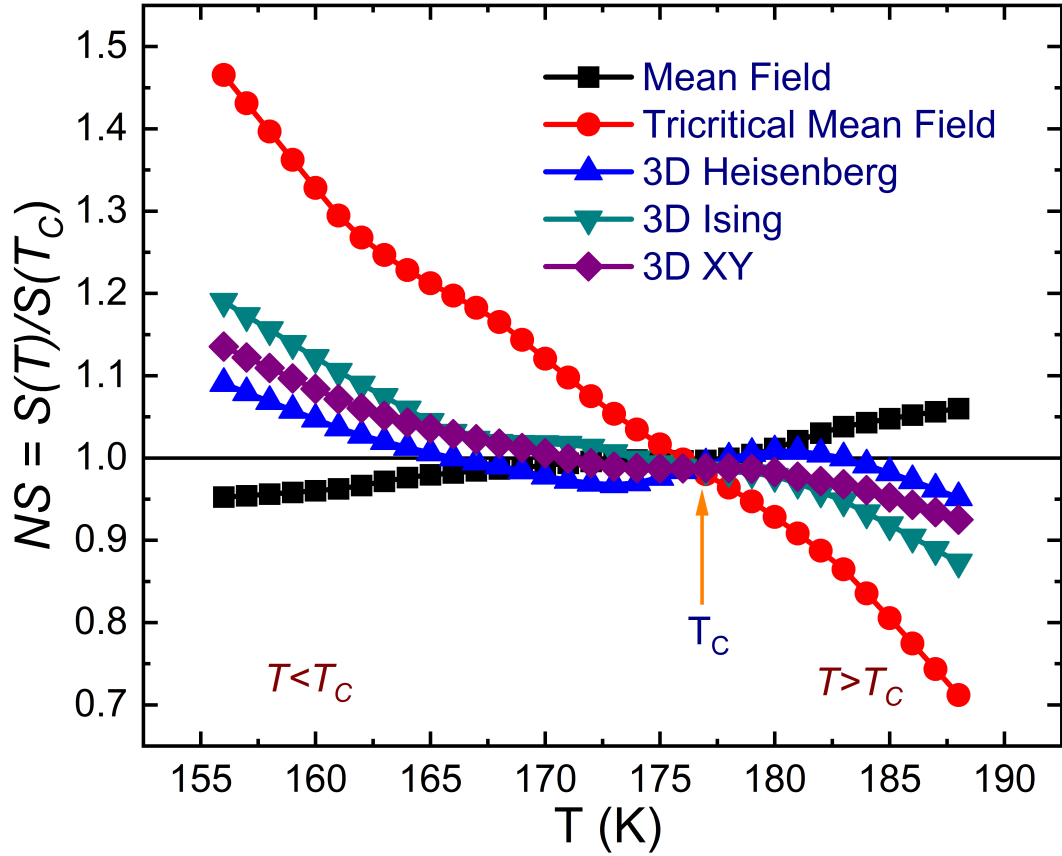


Figure VII.4: Temperature dependence of the normalized slopes, $NS = S(T)/S(T_C)$, for the mean-field, tricritical mean-field, 3D Heisenberg, 3D Ising, and 3D XY models.

Hence, we employ an iterative approach to precisely determine the critical exponents β and γ [198, 392]. By linear extrapolation from the high-field region to the intercepts with the axes $M^{1/\beta}$ and $(H/M)^{1/\gamma}$, reliable values of $M_S(T)$ and $\chi_0^{-1}(T)$ are obtained. Subsequently, fitting the data using Equations 215 and 216 yields a set of β and γ . These values are then employed to reconstruct the MAP, leading to the generation of new $M_S(T)$ and $\chi_0^{-1}(T)$. The process is repeated iteratively, refining the values of β and γ until convergence is achieved. As depicted in Figure VII.5(a), a series of parallel straight lines in the high-field regime is attained through the converged β and γ values. Figure VII.6(b) displays the final temperature dependence of $M_S(T)$ (left) and $\chi_0^{-1}(T)$ (right), which are obtained from the high-field MAP curve extrapolation. The fitting yields critical exponents $\beta = 0.474$ with $T_C = 177$ K and $\gamma = 0.954$ with $T_C = 178$ K.

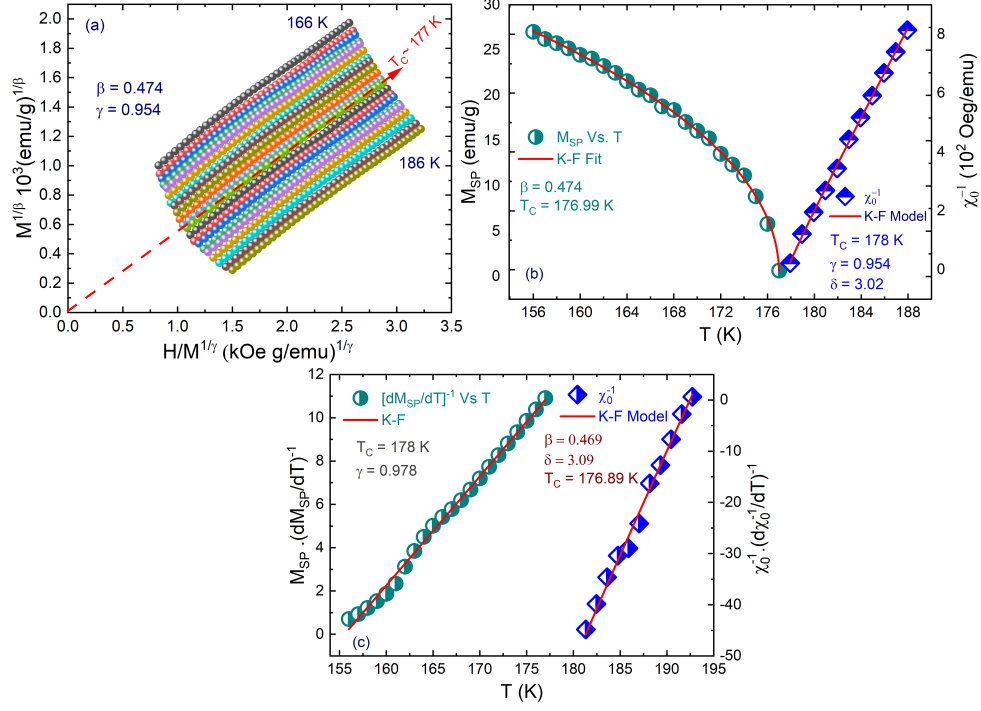


Figure VII.5: (a) Modified Arrott plot of isotherms with $\beta = 0.474$ and $\gamma = 0.954$. (b) Temperature dependence of the spontaneous magnetization M_S (left) and the inverse initial magnetic susceptibility $\chi_0^{-1}(T)$ (right), which are obtained from the high-field extrapolation of the modified Arrott plot. The T_C and exponent values are deduced by fitting Equations 215 and 216 (red curves). (c) Kouvel-Fisher plot for the temperature dependence of the spontaneous magnetization M_S (left) and the inverse initial magnetic susceptibility $\chi_0^{-1}(T)$ (right). The T_C and critical exponents are obtained from the linear fits (red lines).

Alternatively, for a more precise determination of the critical exponents and T_C , we have examined the $M_{\text{SP}}(T)$ and $\chi_0^{-1}(T)$ data using the Kouvel–Fisher (K–F) plot analysis [215]:

$$\frac{M_{\text{SP}}(T)}{\frac{dM_{\text{SP}}}{dT}} = \frac{T - T_C}{\beta} \quad (220)$$

$$\frac{\chi_0^{-1}(T)}{\frac{d\chi_0^{-1}(T)}{dT}} = \frac{T - T_C}{\gamma} \quad (221)$$

where $\frac{M_{\text{SP}}(T)}{\frac{dM_{\text{SP}}}{dT}}$ and $\frac{\chi_0^{-1}(T)}{\frac{d\chi_0^{-1}(T)}{dT}}$ are linear in temperature with slopes $1/\beta$ and $1/\gamma$, and the intercepts signify $-T_C/\beta$ and $-T_C/\gamma$, respectively. The critical exponents and T_C determined through the K-F method are found to be $\beta = 0.469$ with $T_C = 176.89 \text{ K}$ and $\gamma = 0.978$ with $T_C = 178 \text{ K}$ (see Figure VII.5c). Remarkably, these critical exponent values and T_C closely agree with those computed using the mean-field model and the 3D Heisenberg model. This congruence suggests that the derived values of the critical exponents are self-consistent and unequivocal.

The critical exponent δ , related to the magnetization isotherm at T_C through eq. (10), with D representing the critical amplitudes, can be ascertained by fitting the high-field slope of $\log_{10}(M)$ vs. $\log_{10}(H)$ at T_C . Figure VII.6a illustrates the $M(H)$ curve at $T_C \sim 177$ K, with the inset depicting the same plot in log-log scale. Fitting the $M(H)$ curve at $H > 5$ kOe yields $\delta = 3.26$ and $\delta = 3.01$ for the log-log fits, respectively. Additionally, the critical exponents obtained through scaling analysis adhere to the Widom scaling relation [395], given as $\delta = 1 + \frac{\gamma}{\beta}$. Utilizing the determined values of β and γ from the MAP and the K-F method yielded δ values of 3.02 and 3.09, respectively, which are proximate to the aforementioned δ value. This underscores the reliability of the critical exponents derived from the magnetization data and their agreement with the scaling hypothesis.

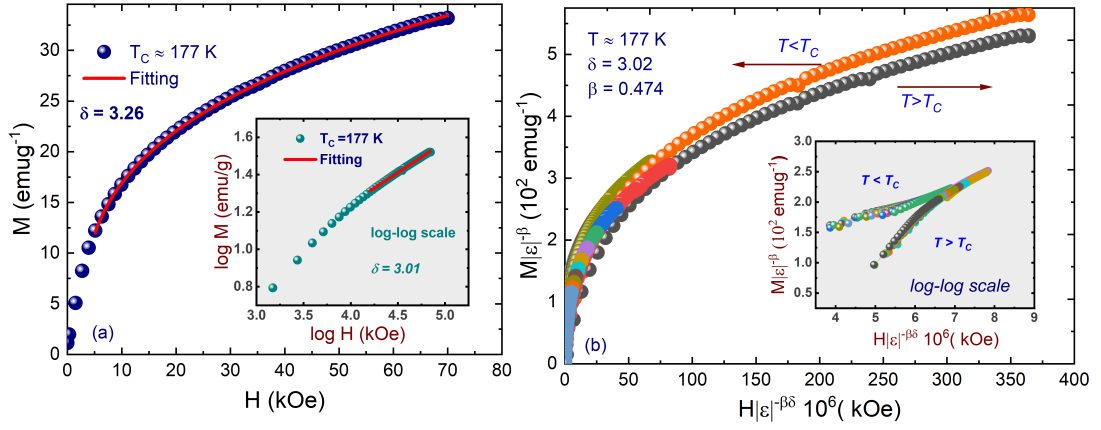


Figure VII.6: (a) $M(H)$ curve at $T_C \sim 177$ K. Inset: the same plot in log-log scale with a solid fitting curve in the high-field region. (b) Scaling plots of renormalized magnetization $m = M|\varepsilon|^{-\beta}$ versus renormalized field $h = H|\varepsilon|^{-(\beta\delta)}$ below and above T_C for NdSmNiMnO₆. The inset shows the same scaling plots in the log-log scale. The collapse of the data onto two distinct universal branches (below and above T_C) confirms the validity of the obtained critical exponents and the reliability of the scaling hypothesis.

Based on the scaling hypothesis, the credibility of the acquired critical exponents was affirmed through the magnetic equation of state in the asymptotic critical region, as clarified earlier in Equation 219. To affirm this, we constructed a plot of $|\varepsilon|^{-\beta} M(H, \varepsilon)$ vs. $|\varepsilon|^{-\beta\delta} H$ with the β , δ , and T_C values derived through the K-F technique. Figure VII.6b displays the $M|\varepsilon|^{-\beta}$ vs. $H|\varepsilon|^{-\beta\delta}$ curves in the scaled data at $T < T_C$ and $T > T_C$, and the inset presents the same data in log-log coordinates for clarity. All magnetization curves collapse into two distinct branches ($T < T_C$ and $T > T_C$), implying the accuracy and consistency of the critical exponents and T_C values for NdSmNiMnO₆ following the scaling hypothesis. The typically subtle departure from the scaling curves noted in the low-magnetic-field region is attributed to the reconfiguration of the magnetic do-

main. In this regime, magnetic moments exhibit an incomplete alignment with the applied magnetic field.

Finally, as is well-established, the universality class governing the magnetic transition in homogeneous magnets is dependent upon the exchange interaction $J(r)$. Analysis using renormalization group theory suggests that the decay of interaction with distance r can be described as

$$J(r) \propto r^{-(d+\sigma)} \quad (222)$$

where d represents spatial dimensionality and σ denotes the range of interaction, assuming a positive value. In the context of 3D isotropic materials ($d = 3$), this relationship translates to $J(r) \propto r^{-(3+\sigma)}$. If $\sigma > 2$, it indicates a more rapid decrease than r^{-5} ; hence, the applicability of the 3D Heisenberg model ($\beta = 0.365$, $\gamma = 1.336$, and $d = 4.8$) emerges. For $\sigma = \frac{3}{2}$, corresponding to the mean-field model ($\beta = 0.5$, $\gamma = 1.0$, and $d = 3$), this signifies that $J(r)$ decreases more gradually than $r^{-4.5}$. Within the intermediate range, i.e., $J(r) \propto r^{-(3+\sigma)}$ with $3/2 \leq \sigma \leq 2$, the exponent aligns with a distinct universality class reliant on the specific value of σ . In this range, both the tricritical mean-field theory and the 3D Ising model are plausible. Fischer et al. [396] propose a relationship between the exponent γ and the interaction range σ as

$$\gamma = 1 + \frac{4d(n+2)}{(n+8)}\Delta\sigma + \frac{8(n+2)(n-4)}{d^2(n+8)^2} \left[1 + \frac{2G(d/2)(7n+20)(n-4)}{(n+8)} \right] \Delta\sigma^2 \quad (223)$$

where $\Delta\sigma = (\sigma - d/2)$, $G(d/2) = \frac{3}{14}(d/2)^2$, and n is the magnetic spin dimensionality given as $n = 1 + \left(\beta - \frac{1}{\beta} + \gamma\right)$ [198]. From the β and γ values obtained from the scaling analysis, we deduced a self-consistent critical exponent $n = 0.632$, which agrees with the previously mentioned mean-field experimental value, as depicted in Figure 5c. Therefore, using eq. (223) and the obtained value $\gamma = 0.954$ in this study, we calculated $\sigma = 1.629$, indicating that the magnetic interaction distance decays with $J(r) \propto r^{-4.629}$, which is close to other ferromagnetic perovskite systems [204, 219]. Indeed, $J(r)$ lies between the characteristics of the 3D Heisenberg model and the mean-field model, suggesting that the critical behavior of NdSmNiMnO₆ can be attributed to the competition between long- and short-range magnetic interactions rather than purely long-range interaction regimes [397]. Nonetheless, its closer resemblance to the mean-field model sug-

gests that the dominant spin interactions are of a long-range magnetic nature. Furthermore, we note that our values of β and γ obtained from the modified Arrott plot align closely with the mean-field predictions but deviate significantly from the Heisenberg model, which suggests that the system does not exhibit a purely short-range 3D Heisenberg-like transition. Similar deviations have been observed by Pramanik et al., such as in Pr_{0.5}Ca_{0.5}MnO₃ [392], where long-range interactions play a significant role in determining the critical behavior. Hence, the exchange distance $J(r)$ analysis suggested that the long-range magnetic interaction coupling between ordered Ni-Mn ions at B-B' sites dominates near T_N , which is responsible for the magnetic nature of the NdSmNiMnO₆ double perovskite. Furthermore, under the correlation length critical exponent relation, $\vartheta = \gamma/\sigma$ (i.e., $\vartheta = 0.584$), the critical exponents $\alpha = (2 - \vartheta d)$, $\beta = (2 - \alpha - \gamma)/2$, and $\delta = (1 + \gamma/\beta)$ are determined, yielding values of approximately 0.243, 0.401, and 3.38, respectively. Notably, these calculated values closely align with the experimentally observed values in our study.

The critical exponents obtained for NdSmNiMnO₆ ($\beta = 0.469$, $\gamma = 0.978$, $\delta = 3.09$) suggest a behavior intermediate between the 3D Heisenberg model ($\beta \approx 0.365$, $\gamma \approx 1.386$, $\delta \approx 4.8$) and the mean-field model ($\beta \approx 0.5$, $\gamma \approx 1.0$, $\delta \approx 3.0$) [396, 398]. Such deviations are commonly observed in complex magnetic oxides, where multiple competing interactions influence the critical exponents. A key factor contributing to this behavior is the competition between nearest-neighbor (NN) and next-nearest-neighbor (NNN) interactions, a phenomenon reported in perovskite-based oxides. In NdSmNiMnO₆, the coexistence of ferromagnetic (FM) and antiferromagnetic (AFM) interactions arising from double-exchange (DE) and superexchange (SE) mechanisms alters the effective correlation length [399]. For instance, La_{0.67}Ca_{0.33}MnO₃ and Nd_{0.5}Sr_{0.5}MnO₃ exhibit competing interactions that produce deviations from conventional universality classes [239]. Moreover, the presence of a Griffiths-like phase, characterized by the persistence of local magnetic clusters above the transition temperature due to disorder and inhomogeneity, could induce this behavior [400]. In the case of NdSmNiMnO₆, the slightly elevated β value (0.469) suggests an inhomogeneous ordering process, consistent with the study by Bray et al. [401] for perovskite oxides, where structural disorder and phase separation broaden the critical region. The presence of such magnetic clusters results in modified scaling behavior, contributing to the deviation from classical universality classes. Further, the

universality class of a phase transition is determined by the effective interaction range, as proposed by the renormalization theory [402]. Particularly, the crossover interaction is influenced by bond-angle distortions, spin-orbit coupling, and the cooperative Jahn-Teller effect, modifying the interaction range. In our case, the observed bond-angle deviations and octahedral tilting in NdSmNiMnO₆ suggest that the magnetic SE pathways between Ni and Mn ions are significantly affected, influencing DE and SE interactions [116, 258]. In aristotype cubic perovskites, magnetic superexchange follows the GKA rule, with 180° Ni-O-Mn bonds favoring strong FM coupling and AFM double exchange occurring for partially delocalized electrons. However, the observed Ni-O-Mn bond angles ($\sim 150.5^\circ$) deviate from 180°, weakening direct AFM superexchange while allowing for competing FM-DE interactions, a feature of magnetically frustrated systems [403]. The estimated octahedral rotation angles (γ , φ , Φ , and Θ) further support this magnetic competition hypothesis, i.e., the significant tilting of NiO₆ and MnO₆ octahedra modifies orbital overlap, altering the Ni²⁺-O-Mn⁴⁺ SE-like interactions, which can lead to the emergence of magnetic phase coexistence [197]. Several studies have reported that octahedral perovskite distortions result in noncollinear magnetic ordering, magnetic phase separation, and spin-glass-like behavior due to competing interactions [404–406]. In NdSmNiMnO₆, the combination of bond length/bond-angle variations, octahedral tilting, and local lattice distortions likely contributes to frustrated magnetic behavior observed below $T < T_N$ in the MCE analysis, explaining the observed complex critical exponents and intermediate universality class. Also, our critical exponents, tested using the Widom scaling equation [$\delta = 1 + \gamma/\beta = 3.09$], the Arrott plots, and Kouvel-Fisher analysis, demonstrate that the exponents are self-consistent. On the other hand, magnetocrystalline anisotropy and spin fluctuations play a critical role in determining the critical behavior of NdSmNiMnO₆. In systems with strong anisotropic interactions, critical exponents often deviate from classical models due to anisotropic spin fluctuations and spin-orbital coupling effects [401]. This is evident in our MCE analysis: the Nd/Sm sublattice flipped from negative to positive entropy change in the temperature range below ~ 50 K as the field increases from 0-3 to 0-7 T. The interplays between spin, charge, and orbital degrees of freedom likely influence the scaling behavior, where the presence of unquenched orbital moments and anisotropic exchange interactions can lead to modified critical behavior [374]. Hence, NdSmNiMnO₆ and the observed exponents suggest

a scenario where short-range spin interactions dominate at lower temperatures, but longer-range interactions contribute near the Curie temperature, leading to deviations from standard universality classes.

7.4 Conclusion

In summary, we have successfully synthesized the NdSmNiMnO₆ double perovskite and systematically studied its crystal structure, magnetocaloric effect, and critical behavior. The monoclinic structure of NdSmNiMnO₆ identified from the XRD pattern and refined by Rietveld demonstrated that Nd/Sm shared the same crystallographic A-site, whereas Ni/Mn cations are distinctly distributed at the octahedron B-B' sites. The $-\Delta S_{\text{M}}^{\text{max}}$ and RCP at the applied field of 0–7 T are found to be 2.38 and 182 J/kg · K, respectively, suggesting that NdSmNiMnO₆ can be considered a promising magnetic refrigerant. The critical exponents β , γ , and δ obtained by different methods indicate a proximity to the conventional universality class of the mean-field model in the limit of $T < T_{\text{C}}$ and a 3D Heisenberg-like phenomenon at $T > T_{\text{C}}$. Finally, the exchange distance $J(r)$ analysis suggested that in NdSmNiMnO₆, the observed exponents suggest a scenario where short-range spin interactions dominate at lower temperatures, but longer-range interactions contribute near the Curie temperature, leading to deviations from standard universality classes.

* CHAPTER VIII *

Spin Reorientation and the Interplay of Magnetic Sublattices in ECMO

Through a combination of magnetic susceptibility, specific heat, and neutron powder diffraction measurements we have revealed a sequence of 4 magnetic phase transitions in the columnar quadruple perovskite $\text{Er}_2\text{CuMnMn}_4\text{O}_{12}$. A key feature of the quadruple perovskite structural framework is the complex interplay of multiple magnetic sublattices via frustrated exchange topologies and competing magnetic anisotropies. We show that in $\text{Er}_2\text{CuMnMn}_4\text{O}_{12}$, this phenomenology gives rise to multiple spin-reorientation transitions driven by the competition of easy-axis single ion anisotropy and the Dzyaloshinskii-Moriya interaction; both within the manganese B-site sublattice. At low temperature one Er sublattice orders due to a finite f-d exchange field aligned parallel to its Ising axis, while the other Er sublattice remains non-magnetic until a final, symmetry-breaking phase transition into the ground state. This non-trivial low-temperature interplay of transition metal and rare-earth sublattices, as well as an observed $\mathbf{k} = (0,0,1/2)$ periodicity in both manganese spin canting and Er ordering, raises future challenges to develop a complete understanding of the $R_2\text{CuMnMn}_4\text{O}_{12}$ family.

Acknowledgements: The work presented in this chapter has been published as John M. Attah-Baah *et al.*, *Acta Cryst. B* **80**, 656–664 (2024). Sample synthesis and bulk characterization (magnetometry and calorimetry) were performed by **Alexei Belik**. Neutron powder diffraction (NPD) experiments were conducted by **Roger Johnson**, **Pascal Manuel**, and **Dmitry Khalyavin**, with data analysis carried out by me. Symmetry analyses were performed collaboratively by myself and **Roger Johnson**, who also developed the analytical model presented in Section [8.3.4](#).

8.1 Introduction

Spin-reorientation transitions are characterised by the spontaneous rotation of ordered magnetic moments [407], and have been found to occur in antiferromagnets [408–411], canted antiferromagnetics (weak ferromagnets) [412, 413], ferromagnets [414] and ferrimagnets [9, 415]. This phenomenon is of keen interest, not only from a fundamental perspective, but also because deterministic magnetization switching may be utilised in nanoscale functional spintronic components [416]. In this regard, spin-reorientation transitions in ferrimagnets are arguably the most appealing, as ferrimagnets carry a net magnetization while switching in the ultra-fast regime [417]. Spin-reorientation typically occurs due to competition between different magnetic sublattices with different magnetic anisotropies; a typical example is that of the rare-earth orthoferrites, in which spin-reorientation is driven by magnetic f - d exchange interactions between rare-earth and transition metal sublattices [412].

In quadruple perovskites, multiple magnetic sublattices may be introduced into the structure, allowing for complex frustrated exchange topologies and competing magnetic anisotropies. Indeed, many non-trivial magnetic phases have been observed in this structural family with properties including multiferroicity [418–420], low-field magnetoresistance [421], incommensurate magneto-structural coupling [422], and spin-reorientation transitions [9, 415]. The columnar quadruple perovskite $R_2\text{CuMnMn}_4\text{O}_{12}$ ($R=\text{Dy, Y}$) undergoes 3 magnetic phase transitions, two of which are spin-reorientation transitions involving the rotation of a ferrimagnetic magnetization by 90 degrees [9]. Remarkably, these transitions could not be explained by the conventional f - d exchange model, and it was proposed that these phenomena originated in the competition between single-ion anisotropy and anisotropy due to the Dzyaloshinskii-Moriya interaction, tuned by spin canting induced by frustrated Heisenberg exchange [9].

In this paper, we extend previous work on $R_2\text{CuMnMn}_4\text{O}_{12}$, and report the experimental characterization of the magnetic phases exhibited by $\text{Er}_2\text{CuMnMn}_4\text{O}_{12}$. The crystal structure of $\text{Er}_2\text{CuMnMn}_4\text{O}_{12}$ is shown in Figure VIII.1. As is typical of perovskite-derived structures, the B site manganese ions are octahedrally coordinated forming a pseudo-cubic corner-sharing framework (Figure VIII.1b and VIII.1e). In the columnar perovskite aristotype (space group $P\frac{4_2}{n}mc$) [423, 424], the MnO_6 octahedra are severely tilted in an $a^+a^+c^-$

pattern (Glazer notation [425]). These octahedral tilts split the A sites into 3 symmetry inequivalent sublattices that are typically labelled A , A' , and A'' (Figure VIII.1a). The A sites are occupied by erbium, and sit within a distorted 10-fold oxygen coordination (Figure VIII.1c). The A' sites are nominally occupied by copper (labelled Cu1) within a square-planar oxygen coordination, and the A'' sites are nominally occupied by manganese (labelled Mn2) within a tetrahedral oxygen coordination (Figure VIII.1d).

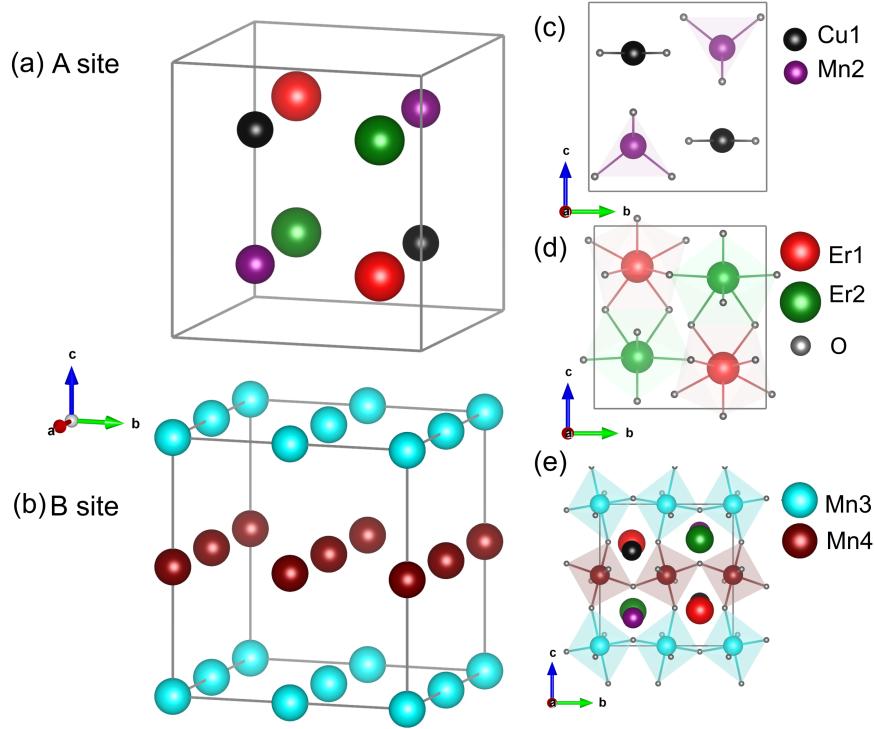


Figure VIII.1: The crystal structure of $\text{Er}_2\text{CuMnMn}_4\text{O}_{12}$. A single unit cell is shown by thin grey lines, and the cation oxygen coordinations are shaded in panes c-e.

The $R_2\text{CuMnMn}_4\text{O}_{12}$ family also support layered charge and ferro-orbital ordering [426] that breaks the symmetry between nearest neighbor MnO_6 layers stacked along \mathbf{c} , which we label Mn3 and Mn4, respectively. Mn3 ions carry a nominally 3+ oxidation state, and the cooperative Jahn-Teller distortions align $d_{3z^2-r^2}$ orbitals approximately parallel to \mathbf{c} . The Mn4 ions are nominally 4+ and their octahedral coordination is undistorted to good approximation. A secondary consequence of the charge and orbital ordering is the splitting of the A sites into two sublattices, now related by a *pseudo*- 4_2 screw, which we label Er1 and Er2. The space group of this distorted phase is $Pm\bar{m}n$.

In this paper, we show that the complex interplay of the numerous magnetic sublattices described above leads to 4 magnetic phase transitions in

$\text{Er}_2\text{CuMnMn}_4\text{O}_{12}$, characterized by the onset of ferrimagnetic order, spin-reorientation, spin-canting, and the polarisation of Er ions. The mechanism for spin-reorientation is likely the same as that proposed for other $R_2\text{CuMnMn}_4\text{O}_{12}$ compounds ($R = \text{Dy}, \text{Y}$), which show a similar sequence of phase transitions [9]. However, the nature of the observed low temperature coupling between rare-earth and transition metal sublattices in $\text{Er}_2\text{CuMnMn}_4\text{O}_{12}$, as well as the emergence of $\mathbf{k} = (0, 0, 1/2)$ modulations found at low temperature for $R = \text{Er}, \text{Dy}$, and Y , pose interesting questions for future studies.

The paper is organized as follows. In Section 8.2, we describe the experimental methods, and in Sections 8.3.1, 8.3.2, and 8.3.3 we present the results of magnetic susceptibility, specific heat, and neutron powder diffraction measurements, respectively. In Section 8.3.4, we find an approximate form for the Er crystal electric field using a simple point charge model, from which we successfully explain the empirical behavior of the Er ions at low temperature. Our results are discussed in Section 8.4, and finally, we draw conclusions in Section 8.5.

8.2 Experiment

A sample with the target chemical composition of $\text{Er}_{2.1}\text{Cu}_{0.95}\text{Mn}_{0.95}\text{Mn}_4\text{O}_{12}$ was prepared from a stoichiometric mixture of Er_2O_3 , CuO , Mn_2O_3 and $\text{MnO}_{1.839}$ by a high-pressure, high-temperature method at 6 GPa and about 1650 K for 90 min in Pt capsules. The target chemical composition was slightly shifted from $\text{Er}_2\text{CuMnMn}_4\text{O}_{12}$ to reduce the amount of a $\text{ErCu}_{3-x}\text{Mn}_{4+x}\text{O}_{12}$ -type impurity. We note that neutron diffraction cannot distinguish between Er and Cu, and refinement of synchrotron X-ray diffraction data not shown here indicated that the tetrahedral Mn2 site accommodates the excess Er. For simplicity, we will use the chemical formula $\text{Er}_2\text{CuMnMn}_4\text{O}_{12}$ throughout the paper. AC magnetometry measurements were performed using a Quantum Design MPMS-1T with an excitation field of 0.5 Oe, on cooling in zero DC field from 225 to 2 K. The measurement was repeated for excitation frequencies of 2, 7, 110, 300, and 500 Hz. DC magnetometry measurements were performed using a Quantum Design MPMS-XL, having cooled the sample in zero magnetic field and measured on warming (ZFC), and measured in field on cooling (FCC), between 300 and 2 K in 100 Oe and between 400 and 2 K in 10 kOe fields. Specific heat data were

collected using a Quantum Design PPMS on cooling in zero applied field, and in applied fields of 1, 2, 5, 10, 30, 50, and 70 kOe. Neutron powder diffraction measurements were performed using the WISH diffractometer [190] at ISIS, the UK Neutron and Muon Source. A 1.8 g sample was loaded into a 6 mm diameter vanadium can, and mounted within a ^4He cryostat. Data with high counting statistics were collected in each magnetic phase including paramagnetic for reference (1.5, 9, 30, 140, and 200 K), and with lower counting statistics on warming through the phases in finer temperature steps (3–10 K intervals). Crystal and magnetic structure refinements were performed using the FULLPROF suite [427] against data collected in detector banks at average 2θ positions of 58.3° and 152.8° .

8.3 Results

8.3.1 Magnetic susceptibility

The temperature dependence of the real (χ') and imaginary (χ'') parts of the AC magnetic susceptibility are plotted in Figures VIII.2a and VIII.2b, respectively. Sharp anomalies in χ' indicate the presence of 4 magnetic phase transitions at $T_{N1} \simeq 172$ K, $T_{N2} \simeq 115$ K, $T_{N3} \simeq 17$ K, and $T_{N4} \simeq 7$ K. We label the respective phases as CFI' ($T_{N2} \leq T \leq T_{N1}$), FI ($T_{N3} \leq T \leq T_{N2}$), CFI₁ ($T_{N4} \leq T \leq T_{N3}$), and CFI₂ ($T \leq T_{N4}$), which is consistent with the labeling scheme adopted in Reference [9]. Anomalous behaviour at these temperatures is also seen in χ'' , which shows a strong frequency dependence in the CFI' phase, indicative of non-trivial magnetic fluctuations.

The DC magnetic susceptibility is shown in Figure VIII.3a. Anomalies corroborate the phase transitions observed in the AC susceptibility data, described above. Furthermore, the sharp onset of magnetisation below T_C shows that the CFI' phase is characterised by a significant ferromagnetic or ferrimagnetic moment, which is greatly reduced on cooling into the CFI₁ and CFI₂ phases. The broad anomaly at T_N was also observed in $\text{Dy}_2\text{CuMnMn}_4\text{O}_{12}$ and $\text{Y}_2\text{CuMnMn}_4\text{O}_{12}$, where it was assigned to a softening of magnetic correlations in the proximity of a spin reorientation transition [9]. The inset to Figure VIII.3a shows the inverse susceptibility against temperature. Fitting the Curie-Weiss

model to the paramagnetic regime gave $\mu_{\text{eff}} = 15.4\mu_{\text{B}}/\text{f.u.}$ and $\theta_{\text{CW}} = 83.0$ K. The positive value for θ_{CW} indicates dominant ferromagnetic interactions, and the effective moment is close to the theoretical value of $\mu = 17.3\mu_{\text{B}}/\text{f.u.}$ (assuming $g = 2$ for transition metals).

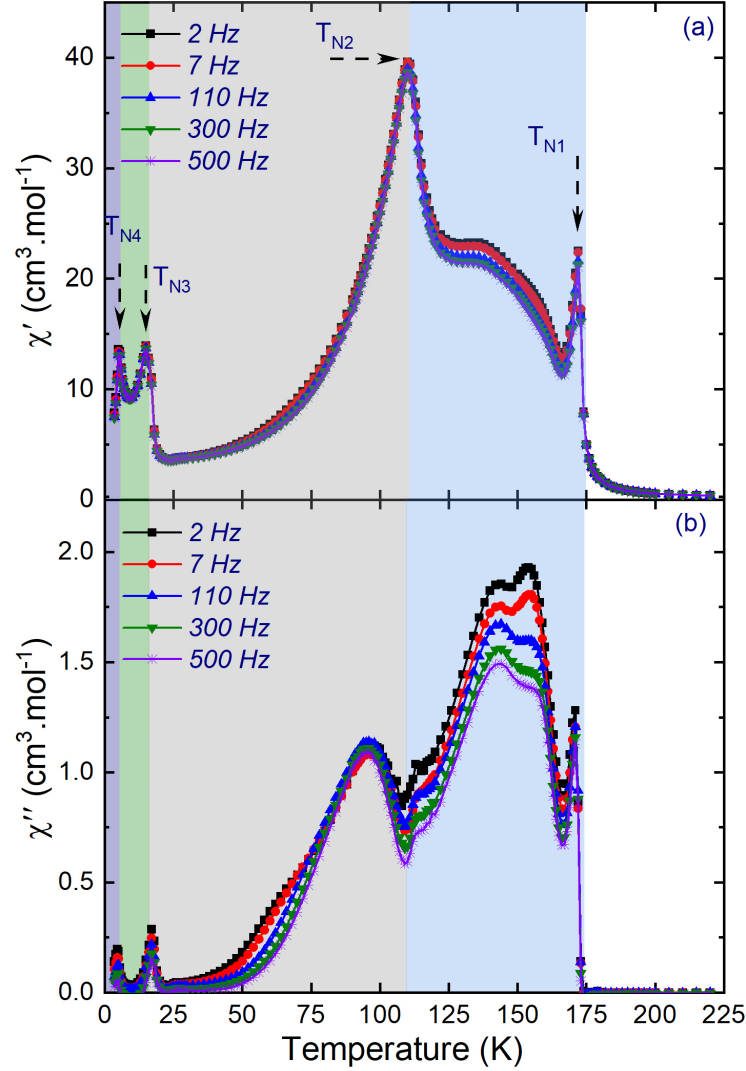


Figure VIII.2: The real (a) and imaginary (b) parts of the AC magnetic susceptibility of $\text{Er}_2\text{CuMnMn}_4\text{O}_{12}$, measured as a function of temperature at different frequency 0.5 Oe excitation fields. The static DC field was zero. Four magnetic transitions are identified in (a), which bound phases CFI' , FI, CFI_1 , and CFI_2 shaded blue, grey, green and purple, respectively.

8.3.2 Specific heat

The temperature dependence of the specific heat is shown in Figure VIII.3b. Clear anomalies are observed at each phase transition, with sharp peaks seen at T_{N1} and T_{N2} . We will later show that these transitions are associated with the

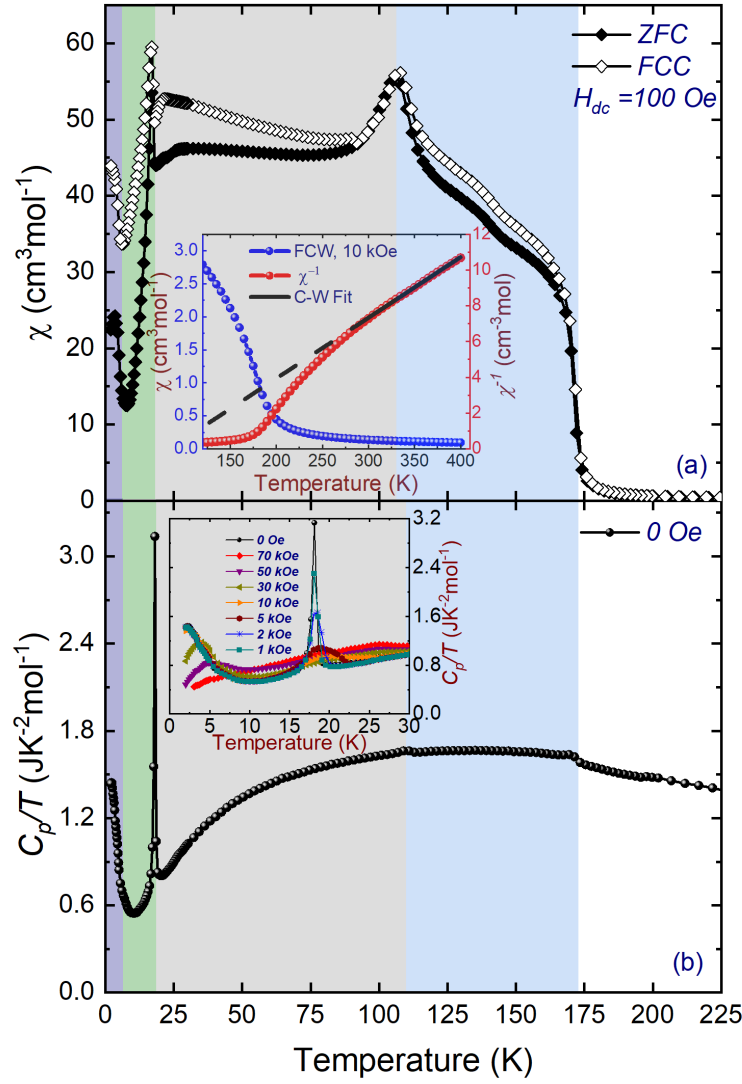


Figure VIII.3: a) Temperature dependence of the DC magnetic susceptibility of $\text{Er}_2\text{CuMnMn}_4\text{O}_{12}$ measured under ZFC and FCC conditions in a 100 Oe applied field. The inset shows a Curie-Weiss fit (black dashed line) to the inverse susceptibility. b) Specific heat of $\text{Er}_2\text{CuMnMn}_4\text{O}_{12}$ measured as a function of temperature. The inset highlights the magnetic field dependence on the low temperature anomalies. Phases CFI' , FI, CFI_1 , and CFI_2 are shaded blue, grey, green and purple, respectively.

ordering of Er^{3+} moments. Hence, these low temperature peaks in specific heat likely originate in the sequential splitting of Er^{3+} ground state doublets. Unfortunately, quantitative analysis of the entropy was not possible due to poor thermal conductivity from the pressed polycrystalline sample. However, the field dependent behaviour shown in the inset to Figure VIII.3b is consistent with a gradual, powder averaged field-induced splitting of the Er^{3+} ground state resulting in a ‘smearing’ of the peak in specific heat.

8.3.3 Neutron powder diffraction

The crystal structure of $\text{Er}_2\text{CuMnMn}_4\text{O}_{12}$ was refined against neutron powder diffraction data measured in the paramagnetic phase at 200 K. The structure of $\text{Y}_2\text{CuMnMn}_4\text{O}_{12}$ [9], with Y replaced by Er, was taken as a starting model. The crystal structure parameters are given in Table VIII.1, and the fit to the data is shown in Figure VIII.4a. Excellent agreement between model and data was achieved ($R = 4.58\%$, $wR = 3.28\%$, and $R_{\text{Bragg}} = 6.0\%$).

Table VIII.1: Crystal structure parameters of $\text{Er}_2\text{CuMnMn}_4\text{O}_{12}$ (space group $Pmmn$) refined at 200 K. The lattice parameters were determined to be $a = 7.2640(1)$ Å, $b = 7.3187(1)$ Å, and $c = 7.7764(1)$ Å. Atomic Wyckoff positions are Er1,Er2: 2a $[1/4, 1/4, z]$; Cu1,Mn2: 2b $[3/4, 1/4, z]$; Mn3: 4c $[0, 0, 0]$; Mn4: 4d $[0, 0, 1/2]$; O1: 8g $[x, y, z]$; O2,O4: 4f $[x, 1/4, z]$; and O3,O5: 4e $[1/4, y, z]$. Bond valence sums (BVS) were calculated using the parameters, $R_0(\text{Er}^{3+}) = 1.99$, $R_0(\text{Cu}^{2+}) = 1.68$, $R_0(\text{Mn}^{2+}) = 1.79$, $R_0(\text{Mn}^{3+}) = 1.76$, $R_0(\text{Mn}^{4+}) = 1.75$, and $B = 0.37$, where the bond valence, $\text{BV} = \exp((R_o - R)/B)$. N.B. For mixed occupancy sites we give the BVS of the majority cation.

Atom	Frac. coord.	$U_{\text{iso}} (\times 10^{-2} \text{Å}^2)$	BVS ($ e $)	Occupation
Er1	$z = 0.7785(6)$	1.21(11)	+2.86	Er
Er2	$z = 0.2834(6)$	0.74(10)	+2.90	Er
Cu1	$z = 0.7308(9)$	0.98(2)	+1.98	76%Cu, 24% Mn
Mn2	$z = 0.2410(6)$	1.5(8)	+1.93	76%Mn, 24% Cu
Mn3	-	0.72(2)	+3.27	Mn
Mn4	-	0.45(2)	+3.74	Mn
O1	$x = 0.4388(2)$ $y = -0.0624(3)$ $z = 0.2669(3)$	0.90(7)	-	O
O2	$x = 0.0587(4)$ $z = 0.0413(3)$	0.97(10)	-	O
O3	$y = 0.5335(4)$ $z = 0.9218(4)$	0.59(9)	-	O
O4	$x = 0.5343(4)$ $z = 0.4188(4)$	0.74(10)	-	O
O5	$y = 0.4353(4)$ $z = 0.5414(4)$	0.82(9)	-	O

On cooling through T_{N1} , new Bragg intensities appear in the neutron powder diffraction data (see Figure VIII.4b). Given the coincidence with the magnetic susceptibility anomaly we can reasonably assume these new intensities originate

in magnetic order. The magnetic peaks have a similar width to the nuclear peaks, indicating long-range magnetic correlations. The magnetic intensities appear in the same positions as nuclear intensities, and therefore index by the Γ -point propagation vector, $\mathbf{k} = (0, 0, 0)$. A complete symmetry analysis of Γ -point magnetic structures in the $Pmmn$ $R_2\text{CuMnMn}_4\text{O}_{12}$ columnar perovskites ($R = \text{Dy}$ and Y) was reported in the Supplemental Material of Reference [9]. The magnetic representation decomposes into 8 irreducible representations, of which only 4 allow for a net ferromagnetic moment observed in the DC magnetic susceptibility data; they are $m\Gamma_1^+$, $m\Gamma_2^+$, $m\Gamma_3^+$, and $m\Gamma_4^+$. Magnetic structure models constrained to each symmetry were systematically refined against neutron powder diffraction data measured at 140 K, representative of phase CFI'. The only model compatible with the diffraction data was that transforming as $m\Gamma_4^+$. Within this symmetry, all magnetic sublattices (Er1, Er2, Cu1, Mn2, Mn3, and Mn4) can adopt ferromagnetic order polarised along $\pm\mathbf{b}$, with the addition of Mn3 and Mn4 antiferromagnetic A- and Y-type modes polarised along \mathbf{a} and \mathbf{c} , respectively [9]. The linear combination of ferromagnetic and antiferromagnetic modes leads to spin canting.

Our starting model had 10 free parameters (mode amplitudes), but after initial refinement the Er1, Er2, and Cu1 mode amplitudes could be set to zero. It is not surprising that the Er1 and Er2 moments are zero at this temperature, as A-site rare-earth ions in perovskite manganites typically order below low temperature phase transitions due to relatively weak f - d interactions. The absence of a moment at the Cu1 site can be understood as being due to a mixed cation occupation refined against the paramagnetic data (see Table VIII.1). If we assume the random distribution of 76% Cu and 24% Mn ions carry magnetic moments of 1 and 3 μ_B , respectively, and are aligned in opposite directions with respect to the nearest neighbour sublattices due to opposite sign interactions, then the average moment at that site is approximately zero.

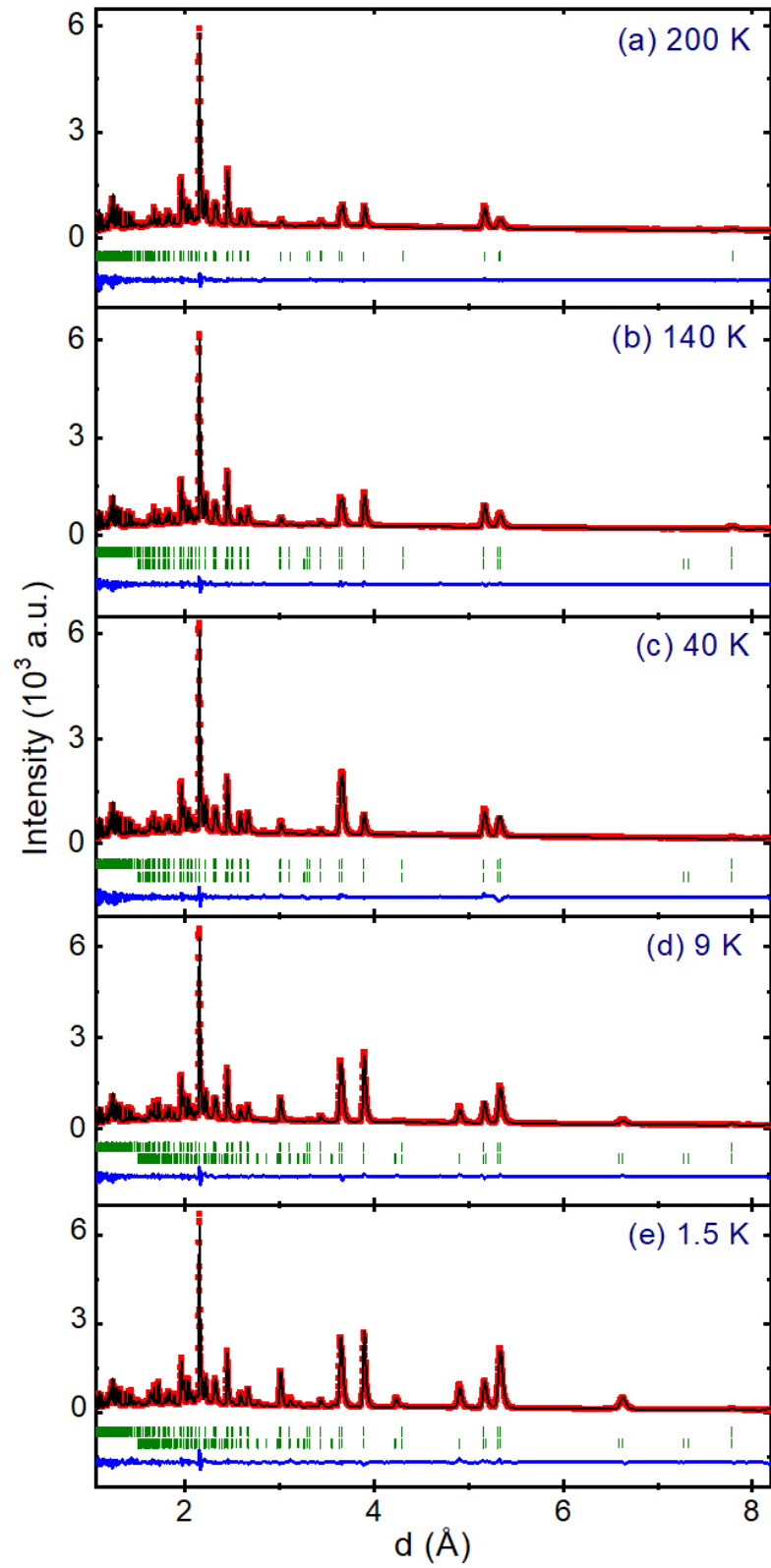


Figure VIII.4: Neutron powder diffraction data measured in 5 phases; a) paramagnetic, b) CFI', c) FI, d) CFI₁, and e) CFI₂. Data are shown as red points, the fitted pattern as black lines, and the difference curve $I_{\text{obs}} - I_{\text{calc}}$ as a blue line at the bottom of the panes. The top and bottom row of green tick marks in each pane indicate the position of nuclear and magnetic Bragg peaks, respectively.

Table VIII.2: Magnetic structure parameters of $\text{Er}_2\text{CuMnMn}_4\text{O}_{12}$. The F and A labels denote ferromagnetic and Néel-type antiferromagnetic modes, respectively. The Y label denotes an Mn3/Mn4 mode of ferromagnetic stripes along \mathbf{a} , coupled antiferromagnetically along \mathbf{b} [9]. The subscripts indicate the polarisation of the modes. Freely refined and fixed values are given with and without standard uncertainties, respectively, and dashes indicate that the component is not allowed by the symmetry of the respective phase.

	$m\Gamma_2^+$	$m\Gamma_4^+$		mZ_4^+		mZ_3^+
Atom	$F_z (\mu_B)$	$F_y (\mu_B)$	$A_x (\mu_B)$	$A_x (\mu_B)$	$Y_z (\mu_B)$	$A_x (\mu_B)$
CFI' phase at 140 K						
Er1	-	0	-	-	-	-
Er2	-	0	-	-	-	-
Cu1	-	0	-	-	-	-
Mn2	-	-2.15(4)	-	-	-	-
Mn3	-	2.28(3)	0.19(2)	-	-	-
Mn4	-	1.31(3)	0	-	-	-
FI phase at 40 K						
Er1	0	-	-	-	-	-
Er2	0	-	-	-	-	-
Cu1	0	-	-	-	-	-
Mn2	-3.14(4)	-	-	-	-	-
Mn3	3.22(4)	-	-	-	-	-
Mn4	2.27(3)	-	-	-	-	-
CFI₁ phase at 9 K						
Er1	-	0	-	-	-	-
Er2	-	-5.02(4)	-	-	-	-
Cu1	-	0	-	-	-	-
Mn2	-	-3.23(6)	-	-	-	-
Mn3	-	1.91(3)	0	2.28(2)	0.93(3)	-
Mn4	-	2.70(3)	0	-	-	-
CFI₂ phase at 1.5 K						
Er1	-	0	-	0	-	-3.96(4)
Er2	-	-7.35(4)	-	0	-	0
Cu1	-	0	-	0	-	0
Mn2	-	-3.23	-	0	-	0
Mn3	-	1.91	0	2.28	0.93	-
Mn4	-	2.70	0	-	-	-

Further refinement indicated that the Y-type mode amplitudes should also be set to zero, while an additional A-type mode was required to properly account for the diffraction intensities. We note, however, that it was not possible to determine whether this mode resided on the Mn3 or Mn4 sublattice. Here, we propose a model in which spin canting occurs on the Mn3 sites - consistent with the low temperature structure. The final refinement of just 4 free parameters (given in Table VIII.2) gave excellent agreement with the data

($R_{\text{mag}} = 2.00\%$). The refinement is shown in Figure VIII.4b, and the evolution of the magnetic moment components as a function of temperature is shown in Figure VIII.5. The magnetic space group for phase CFI' is $Pmm'n'$ (#59.410, basis= $\{[0, 1, 0], [-1, 0, 0], [0, 0, 1]\}$, origin= $[1/2, 1/2, 0]$, see supplementary mcif for full description).

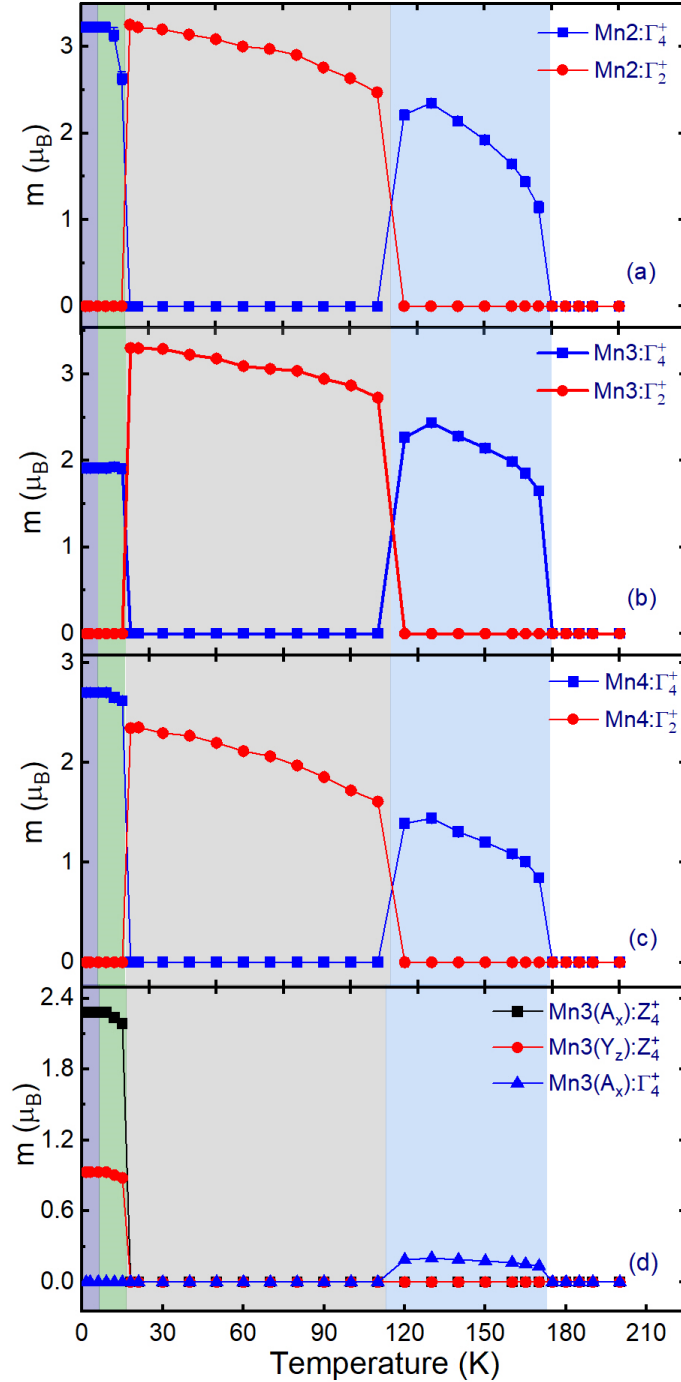


Figure VIII.5: Temperature dependence of the $\pm F_i$ magnetic moments on the a) Mn2, b) Mn3, and c) Mn4 sublattices, where the blue and red data correspond to Γ_4^+ (F_y) and Γ_2^+ (F_z) order, respectively. Pane d shows the antiferromagnetic components that lead to spin canting on the Mn3 sublattice.

Cooling through T_{N2} gave rise to a redistribution of intensity amongst the Γ -point magnetic Bragg peaks consistent with a reorientation of the ferromagnetic modes from parallel to $\pm\mathbf{b}$, to parallel to $\pm\mathbf{c}$. Hence, the transition at T_{N2} is identified as a spin reorientation transition, from a structure transforming as $m\Gamma_4^+$ to one transforming as $m\Gamma_2^+$. The reoriented magnetic structure (maintaining zero moment on the Er1, Er2, and Cu1 sublattices) was refined against data measured at 40 K (see Figure VIII.4c), an excellent fit was achieved ($R_{\text{mag}} = 1.98\%$), and the mode amplitudes are given in Table VIII.2. We note that an A-type canting mode is not allowed within $m\Gamma_2^+$ symmetry, and other symmetry-allowed Mn3 and Mn4 canting modes were found to be zero. The magnetic space group for phase FI is $Pm'm'n$ (#59.409, basis= $\{[1,0,0],[0,1,0],[0,0,1]\}$, origin= $[1/2,1/2,0]$, see supplementary mcif for full description).

Below T_{N3} the Γ -point magnetic intensities change once more. Modelling of the diffraction pattern showed that the Mn2, Mn3, and Mn4 Γ -point magnetic structure returned to being polarised parallel to $\pm\mathbf{b}$. Furthermore, an additional ferromagnetic mode on the Er2 sublattice, also polarised parallel to $\pm\mathbf{b}$, was required to fully account for the Γ -point intensities (see Figure VIII.6). This Er2 mode transformed by the same $m\Gamma_4^+$ irrep as the transition metal sublattices. Systematic tests against the data showed that no additional Γ -point modes appeared on any other sublattice, including Er1. The temperature dependence of the transition metal moments (Figure VIII.5) showed that all moments approached saturation at the Γ -point, with the exception of the Mn3 sublattice, which showed a large drop in the Γ -point component through T_{N3} .

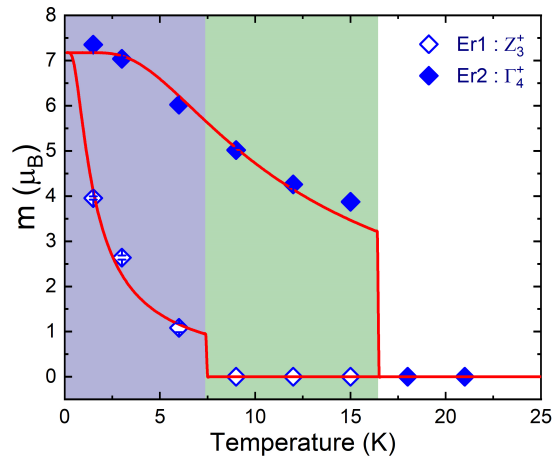


Figure VIII.6: Temperature dependence of the Er1 and Er2 moments, whose respective magnetic modes transform a mZ_3^+ (antiferromagnetic, $m||\mathbf{a}$), and $m\Gamma_4^+$ (ferromagnetic, $m||\mathbf{b}$), respectively. Fits to a simple magnetisation model for a 2-level system are shown by red lines (see text for details).

In addition to the above changes, new diffraction peaks appeared below T_{N3} , which could be indexed with the Z-point propagation vector $\mathbf{k} = (0, 0, 1/2)$. Symmetry analysis reported in the Supplemental Material of reference [9] identified 8 possible Z-point symmetries. All were tested against the diffraction data, and it was found that the new Z-point intensities could be uniquely accounted for by A- and Y-type antiferromagnetic modes on the Mn3 sublattice, polarised along $\pm\mathbf{a}$ and $\pm\mathbf{c}$, respectively. These modes transform by the mZ_4^+ irrep, and correspond to a canting of the Mn3 moment, which, in any given layer, is similar to that found in phase CFI' albeit with a small additional Y mode. The main difference is that in the low temperature CFI₁ phase the relative sign of the canting alternates from one unit cell to the next along $\pm\mathbf{c}$ in accordance with the Z-point propagation vector. We note that this additional antiferromagnetic mode is consistent with the observed reduction in the Mn3 moment at the Γ -point. A final refinement of the combined Γ -point and Z-point structures gave excellent agreement with the data ($R_{\text{mag}} = 3.13\%$) as shown in Figure VIII.4d, and the refined sublattice moments are given in Table VIII.2. The magnetic space group for phase CFI₁ is $Pmm'n'$ (#59.410, basis= $\{[0, 1, 0], [-1, 0, 0], [0, 0, 2]\}$, origin= $[1/2, 1/2, 0]$, see supplementary mcif for full description).

Finally, below T_{N4} additional intensity appears at the Z-point Bragg peaks. Systematic tests of magnetic structures constrained by the CFI₁ phase magnetic symmetry (mZ_4^+) failed to account for this additional intensity, implying a symmetry breaking admixture of another Z-point irrep — consistent with the observation of a sharp phase transition. Expanding the magnetic structure tests to models transforming by all Z-point irreps, we identified an antiferromagnetic mode on the Er1 sublattice polarised parallel to $\pm\mathbf{a}$ (perpendicular to Er2 moments), transforming as mZ_3^+ , that uniquely accounted for the changes in neutron powder diffraction observed below T_{N2} (see Figure VIII.6 for the temperature dependence of the Er moment). Unfortunately, peak overlap now led to excessive correlation between freely refining parameters, so it was necessary to fix the CFI₁ magnetic structure in refinements within the lower temperature CFI₂ phase. Still, excellent agreement with the data was achieved ($R_{\text{mag}} = 3.82\%$, Figure VIII.4e), and the parameters are summarised in Table VIII.2. The magnetic space group for phase CFI₂ is $P2'/c'$ (#13.69, basis= $\{[-1, 0, 0], [0, 0, 2], [1, 1, 0]\}$, origin= $[1/2, 1/2, 0]$, see supplementary mcif for full description).

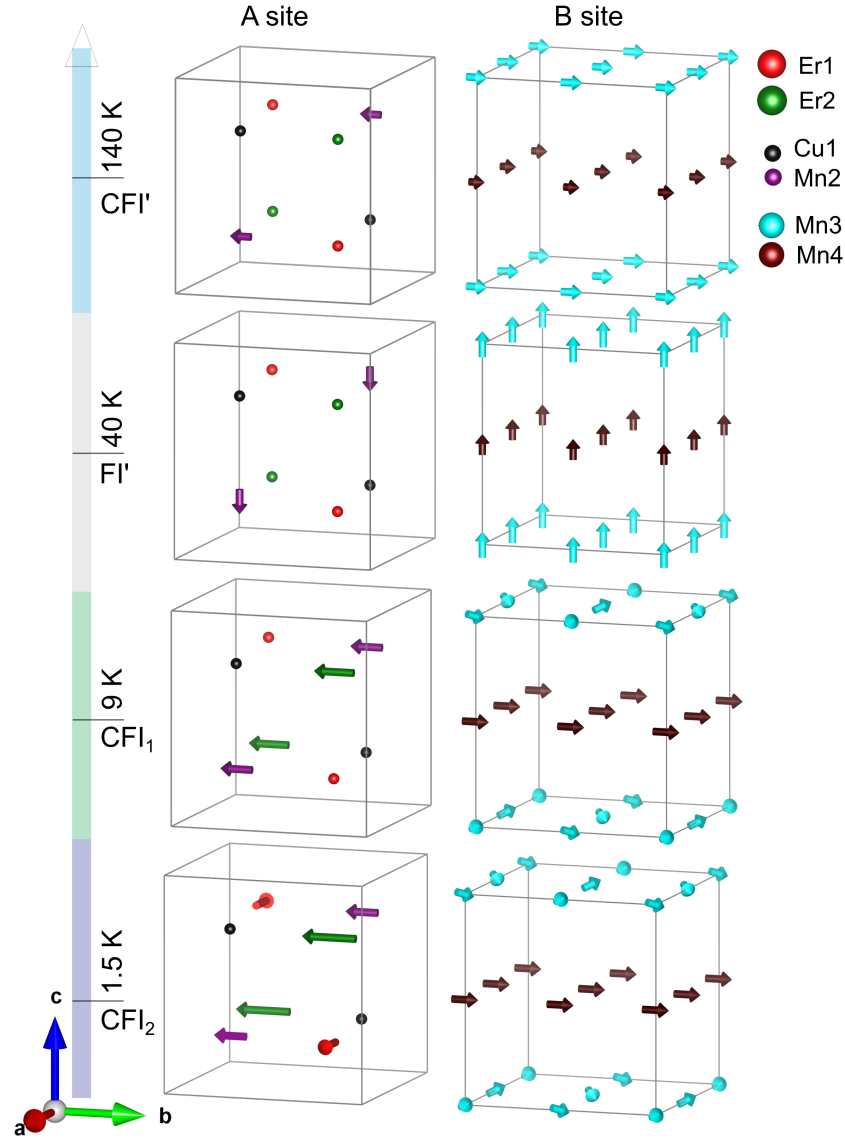


Figure VIII.7: The magnetic structures of $\text{Er}_2\text{CuMnMn}_4\text{O}_{12}$ in each ordered phase. Er1, Er2, Cu1, Mn2, Mn3, and Mn4 sublattices are coloured red, green, black, purple, cyan and maroon, respectively (see Figure VIII.1).

8.3.4 Er^{3+} crystal electric field

The site point symmetry of both Er ions is $mm2$, with pairs of Er1 and Er2 ions related by a $\text{pseudo-}4_2$ screw parallel to \mathbf{c} (as present in the $P4/nmc$ columnar perovskite aristotype [424]). Hund's rules give $J = 15/2$ and $g_J = 6/5$ for the free Er^{3+} ion. In an orthorhombic $mm2$ crystal electric field (CEF), the degeneracy of states $|J, m_J\rangle$ will be lifted to 8 Kramers doublets. Assuming the energy gap between the ground state doublet and all others is $\gg k_B T$, the magnetisation of a given Er ion in an effective f - d exchange field, B_{eff} , will then be described by

that of a two level system;

$$m = \mu \cdot \tanh\left(\frac{\mu B_{\text{eff}}}{k_B T}\right) \quad (224)$$

where μ is the available Er moment dependent on the ground state wavefunctions. The red lines in Figure VIII.6 show fits of Equation 224 to the temperature dependence of the Er moments. The value of μ was constrained to be the same for both Er1 and Er2, and reasonable agreement is found for refined parameters $\mu = 7.2(1)\mu_B$, $B_{\text{eff}}^{\text{Er1}} = 0.20(2)$ T, and $B_{\text{eff}}^{\text{Er2}} = 1.6(1)$ T.

The ground state wavefunctions for Er1 and Er2 were estimated using a point charge model for the CEF. The Hamiltonian for a given Er ion is written

$$\mathcal{H} = \sum_n \sum_{m=-n}^n B_n^m O_n^m + g_J \mu_B \mathbf{J} \cdot \mathbf{B}_{\text{eff}}, \quad (225)$$

The second term is the Zeeman energy, and the first term is the CEF energy, where O_n^m are Stevens operator equivalents [428] and the CEF parameters

$$B_n^m = A_n^m \langle r^n \rangle \Theta_n. \quad (226)$$

Here, Θ_n are the Stevens factors [428], $\langle r^n \rangle$ are radial expectation values for Er^{3+} [429], and in the point charge approximation

$$A_n^m = \frac{-|e|^2}{(2n+1)\epsilon_0} C_n^m \sum_i \frac{q_i}{r_i^{n+1}} Z_n^m(\theta_i, \phi_i). \quad (227)$$

The summation is taken over i nearest neighbour atoms of charge q_i and position (r_i, θ_i, ϕ_i) . Z_n^m is a tesseral harmonic with numerical factor C_n^m , and ϵ_0 is the permittivity of free space. For each Er site, twelve oxygen ions were taken as nearest neighbours, with positions refined against the paramagnetic neutron powder diffraction data (described above). The calculated values of symmetry allowed B_n^m are given in Table VIII.3.

Table VIII.3: Crystal electric field parameters for Er1 and Er2 in units μeV (3.s.f.).

Atom	Crystal field parameters				
	B_2^0	B_2^2	B_4^0	B_4^2	B_4^4
Er1	340	-259	-0.138	-1.34	0.490
Er2	260	255	-0.0973	1.08	0.635
	B_6^0	B_6^2	B_6^4	B_6^6	
Er1	-0.00145	0.00703	0.0238	-0.0207	
Er2	-0.00148	-0.0111	0.0240	0.0226	

The CEF parameter magnitudes are similar for Er1 and Er2 with a sign change for B_2^2 , B_4^2 , B_6^2 , and B_6^6 , which is expected if they are related by *pseudo-4₂* screw. The Hamiltonian was diagonalized for both Er ions, with small magnetic fields systematically applied parallel to **a**, **b**, and **c** to lift the doublet degeneracy. Evaluating the expectation value of the total angular momentum operators for the ground state wavefunctions showed that Er1 has a strong Ising-like single ion anisotropy parallel to **a**, and Er2 has a strong Ising-like single ion anisotropy parallel to **b**, in accordance with the empirical moment directions refined at low temperature.

8.4 Discussion

A similar sequence of phase transitions was observed in $R_2\text{CuMnMn}_4\text{O}_{12}$ ($R = \text{Y}$ and Dy), where it was understood that frustrated Heisenberg exchange stabilised large spin canting (specifically the admixture of F and A modes) on the Mn3 sublattice in the CFI' and CFI phases. This spin canting introduced magnetic anisotropy via the Dzyaloshinskii-Moriya (DM) interaction, which could then compete with Mn3 single-ion-anisotropy (SIA). In $\text{Y}_2\text{CuMnMn}_4\text{O}_{12}$, this scenario provided a mechanism for both high and low temperature spin-reorientation transitions at $T_{\text{N}2}$ and $T_{\text{N}3}$, even in the absence of f - d exchange. In $\text{Dy}_2\text{CuMnMn}_4\text{O}_{12}$, both phase transitions similarly occurred, but at $T_{\text{N}3}$ the spin canting was not accompanied by spin-reorientation on account of the dominant Dy SIA parallel to **c** introduced via f - d exchange. In both $R = \text{Dy}$ and Y compounds the low temperature spin canting was associated with a Z-point antiferromagnetic mode, as observed in the present study, and the origin of this

doubled periodicity along \mathbf{c} had not been explained [9].

The spin-reorientation transitions observed in $\text{Er}_2\text{CuMnMn}_4\text{O}_{12}$ at $T_{\text{N}2}$ and $T_{\text{N}3}$ can be explained by the same mechanism proposed for $\text{Y}_2\text{CuMnMn}_4\text{O}_{12}$. In addition, the Er2 moment becomes polarised below $T_{\text{N}3}$ due to a finite f - d exchange field parallel to its Ising axis after spin-reorientation. To the contrary, the Er1 ions do not develop a moment at this temperature due to their Ising axis being perpendicular to the magnetization of the transition metal sublattice. Further, the Er1 Z-point symmetry-adapted mode for irrep mZ_4^+ is polarised along \mathbf{b} [9], hence coupling to the mZ_4^+ Mn3 A mode is also prevented by the Er1 Ising anisotropy. Instead, the Er1 ions remain unpolarised, introducing a low temperature instability that leads to the symmetry breaking phase transition at $T_{\text{N}4}$. We find that below $T_{\text{N}4}$, the Er1 moments develop a finite polarisation parallel to their Ising axis, with their long-range order transforming by the mZ_3^+ irrep. This irrep is different to that of the Mn3 canting (mZ_4^+), which is consistent with the symmetry breaking transition but leads to questions regarding the nature of the coupling between Er1 and transition metal spins. We propose two possible scenarios. Firstly, that the transition at $T_{\text{N}4}$ is magnetostructural (akin to a spin-Jahn-Teller transition [430]) whereby a spontaneous symmetry-breaking structural distortion facilitates coupling between the mZ_3^+ A mode at the Er1 sublattice and the mZ_4^+ A mode at the Mn3 sublattice. Secondly, the Mn3 canting may adopt an additional mZ_3^+ mode, which then couples directly to the Er1 sublattice. In the former case the primary energy cost associated with the transition is elastic, while in the latter case the primary energy cost is in magnetic exchange.

Finally, we note that the above behaviour is consistent with the refined parameters of our two level system fitted to the Er1 and Er2 moment temperature dependencies. Both Er1 and Er2 can develop the same size moment in the ground state (below the base temperature of the neutron powder diffraction experiment), but the Er1 moment reduces rapidly on warming due to the weaker f - d exchange field while the Er2 moment is sustained to higher temperatures by a larger field. This is consistent with the sequence of phase transitions, and exactly what one would expect if the Er1 moment is coupled to an antiferromagnetic mode of the single Mn3 sublattice while the Er2 moment is coupled to multiple ferromagnetic sublattices.

8.5 Conclusions

In summary, we have shown that $\text{Er}_2\text{CuMnMn}_4\text{O}_{12}$ undergoes 4 magnetic phase transitions. Below $T_{\text{N}1} \simeq 172$ K, the system adopts ferrimagnetic order of transition metal ions polarized along $\pm\mathbf{b}$, with antiferromagnetic canting on the Mn3 B site sublattice. A spin-reorientation transition occurs at $T_{\text{N}2} \simeq 115$ K, where the ferrimagnetic order rotates to be polarized along $\pm\mathbf{c}$. The antiferromagnetic canting vanishes in this phase in accordance with magnetic symmetry. A second spin-reorientation transition occurs at $T_{\text{N}3} \simeq 17$ K, where the ferrimagnetic order returns to $\pm\mathbf{b}$. Mn3 sublattice antiferromagnetic canting also reappears at $T_{\text{N}3}$, but now with a doubled periodicity along \mathbf{c} ($\mathbf{k} = (0,0,1/2)$). Furthermore, the transition metal ferrimagnetic order is now accompanied by a moment at the Er2 sublattice, which has an Ising axis parallel to the ferrimagnetic magnetization. To the contrary, the Er1 sublattice remains non-magnetic in this phase as its Ising axis is perpendicular to the ferrimagnetic magnetization. As a result, a fourth and final symmetry-breaking phase transition occurs at $T_{\text{N}4} \simeq 7$ K characterized by the $\mathbf{k} = (0,0,1/2)$ ordering of the Er1 moments that couple to the pre-existing antiferromagnetic spin canting of the Mn3 sublattice. The mechanism for spin-reorientation is likely the same as that proposed for other $R_2\text{CuMnMn}_4\text{O}_{12}$ compounds, which show a similar sequence of phase transitions [9]. However, the nature of the low temperature coupling between Er1 and Mn3 sublattices is not clear from our elastic diffraction data or symmetry analysis. We have proposed two scenarios based on elastic and magnetic energies, and it would be interesting to differentiate these two mechanisms in future studies. Furthermore, the origin of the $\mathbf{k} = (0,0,1/2)$ modulation in $\text{Er}_2\text{CuMnMn}_4\text{O}_{12}$, and other $R_2\text{CuMnMn}_4\text{O}_{12}$ compounds ($R = \text{Y}, \text{Dy}$), is currently unknown, presumably originating in subtleties of the exchange topology in this complex, multi-sublattice system.

* CHAPTER IX *

Conclusions

This thesis presents a systematic investigation of complex magnetic oxides, focusing on double perovskites and quadruple perovskites with competing spin interactions. Through a combination of neutron diffraction, magnetometry, calorimetry, and theoretical modeling, we have uncovered rich magnetic phase diagrams, spin-lattice coupling effects, and potential applications in magnetocaloric and spintronic technologies.

In **Nd₂NiMnO₆** (Chapter IV), we established a monoclinic $P2_1/n$ structure with nearly B-site ordering of Ni/Mn cations and two distinct magnetic transitions: a ferromagnetic (FM) ordering of Ni²⁺-Mn⁴⁺ at $T_N = 198$ K, followed by a non-collinear Nd³⁺ ordering below $T_{N1} = 22$ K due to competing f - d and f - f exchange. The system exhibits a significant magnetocaloric effect (MCE) with a maximum entropy change of $2.25 \text{ J kg}^{-1} \text{ K}^{-1}$ at 7 T, alongside evidence of spin-phonon coupling and re-entrant spin-glass behavior. These findings highlight the material's potential for magnetic refrigeration and its role as a model system for studying competing magnetic sublattices.

The introduction of **Ir substitution (Nd₂NiMn_{0.25}Ir_{0.75}O₆**, Chapter V) revealed striking modifications in magnetic interactions. Unlike Nd₂NiMnO₆, the Ir-doped system stabilizes a single Γ_1^+ magnetic structure with reduced Mn/Ir moments ($0.38 \mu_B$) and enhanced Ni²⁺-Nd³⁺ coupling. The persistence of frequency-dependent susceptibility below $T_{Nd} \approx 23$ K indicates residual spin disorder, suggesting that Ir's spin-orbit coupling introduces competing anisotropies while mediating longer-range $3d$ - $5d$ - $4f$ exchange. This work resolves longstanding debates on Ir⁴⁺ magnetism and demonstrates how $5d$ incorporation can engineer coherent magnetic states in frustrated systems.

Moving to **NdSmNiMnO₆** (Chapters VI & VII), we identified a ferrimagnetic (FiM) ground state stabilized by $P2_1/n$ distortions and strong magnetostructural coupling. The FiM state, with Nd³⁺ antiparallel to the Ni-Mn sublattice, exhibits a narrow energy gap (~ 0.02 eV) to the FM state, implying high tunabil-

ity. The material's insulating bandgap (~ 1.6 eV) and pronounced spin-phonon coupling, evidenced by Raman mode hardening below $T_N \approx 175$ K, underscore its potential for spintronics. Additionally, its competitive MCE performance ($-\Delta S_{\text{max}} = 2.38 \text{ J kg}^{-1} \text{ K}^{-1}$, $\text{RCP} = 182 \text{ J kg}^{-1}$) and critical exponents near mean-field/3D Heisenberg crossover regimes suggest a complex interplay of short- and long-range spin interactions.

Finally, in **Er₂CuMnMn₄O₁₂** (Chapter VIII), we uncovered four magnetic transitions driven by spin reorientations and rare-earth coupling. Below $T_N \approx 172$ K, ferrimagnetic order emerges, followed by spin reorientations at $T_{N1} \approx 115$ K and $T_{N3} \approx 17$ K, where Er^{3+} moments order with a $k = (0, 0, \frac{1}{2})$ modulation. The low-temperature phase reveals an unusual coupling between Er_1 and Mn_3 sublattices, whose mechanism remains unresolved but likely involves exchange topology or magnetic frustration.

Implications

Collectively, these studies provide significant advances in understanding the intricate balance between competing exchange interactions, spin-lattice coupling, and anisotropy engineering in complex oxide systems. The work has particularly elucidated the roles of $3d-4f$, $5d-4f$, and $f-f$ exchange pathways in governing the magnetic behavior of these materials. Among the key outcomes, the magnetocaloric potential of $\text{Nd}_2\text{NiMnO}_6$ and NdSmNiMnO_6 stands out, with their competitive magnetic entropy changes and relative cooling power suggesting promising applications in low-temperature refrigeration technologies. The incorporation of Ir dopants has revealed new possibilities for spin-orbit control, demonstrating how $5d$ ions can be strategically used to tailor magnetic order and anisotropy, thereby enabling the design of coherent multi-sublattice states with engineered properties. Furthermore, the studies have shed light on the complex effects of structural disorder, showing how A-site (Nd/Sm) and B-site (Ni/Mn/Ir) disorder can be leveraged to tune magnetic responses across a spectrum from spin-glass dynamics to ferrimagnetic/ferromagnetic phase competition. Importantly, detailed analyses of critical exponents have uncovered crossover regimes between mean-field and three-dimensional (3D) Heisenberg behavior, providing valuable insights into the interplay between localized and itinerant magnetism in

these systems. These findings not only deepen our fundamental understanding of complex magnetic perovskites but also establish a model for the rational design of next-generation materials with tailored functionalities for both scientific and technological applications.

Future Prospects

This thesis has established a strong phenomenon for understanding complex magnetic interactions in double perovskites, yet several critical questions demand further exploration through advanced characterization techniques and theoretical modeling. If all other factors are equal, a primary focus will be elucidating the microscopic origins of spin reorientation in $\text{Er}_2\text{CuMnMn}_4\text{O}_{12}$, where competing anisotropies between the Er^{3+} and transition-metal sublattices likely drive the observed multi-stage transitions. Inelastic neutron scattering (INS) will be indispensable for mapping low-energy spin-wave excitations to distinguish between single-ion anisotropy and exchange-mediated reorientation mechanisms, as demonstrated in analogous kagome magnets. Complementary muon spin spectroscopy (μSR) could quantify the role of antisite disorder in promoting spin-glass behavior by probing local spin dynamics, where antisite defects modify exchange bias effects. High-pressure diffraction studies may further decouple lattice-driven versus electronic contributions to spin reorientation, building on models of $4f$ - $3d$ coupling in rare-earth perovskites. For the $\text{Nd}_2\text{NiMnO}_6$ (NNMO) and $\text{Nd}_2\text{NiMn}_{0.25}\text{Ir}_{0.75}\text{O}_6$ (NNMIO) systems, our already-collected resonant inelastic X-ray scattering (RIXS) data will reveal spin-orbital entanglement at Ni/Mn edges, clarifying how Ir doping modifies d - d exchange hierarchies. Synchrotron XANES/EXAFS measurements will resolve oxidation states and local distortions, particularly the antisite disorder in NNMO and Ir-induced bond-length modifications in NNMIO, with temperature-dependent EXAFS tracking dynamic octahedral distortion effects across transitions. These experimental efforts will be synergized with DFT+ U +SOC calculations to model the interfacial charge transfer and spin-orbit coupling effects of Ir $5d$ states in mediating $3d$ - $4f$ exchange. Thin-film engineering presents transformative opportunities: epitaxial strain in NNMO/NNMIO heterostructures could enhance magnetoresistance by tuning spin-phonon coupling, while topological insulator interfaces may induce

chiral spin textures for orbitronic devices. The magnetocaloric performance of these materials could be optimized by leveraging Ir's spin-orbit tuning to boost the relative cooling power, as suggested by the large entropy changes already observed. Ultimately, integrating these approaches will enable the rational design of next-generation spintronic and refrigeration materials, bridging fundamental insights from RIXS, SXRD, and XANES with applied thin-film technologies to harness competing $3d$ - $5d$ - $4f$ interactions.

* APPENDIX A *

Experimental

1.1 XRD Data of $\text{Nd}_2\text{NiMn}_{1-x}\text{Ir}_x\text{O}_6$

X-ray diffraction patterns of $\text{Nd}_2\text{NiMn}_{1-x}\text{Ir}_x\text{O}_6$ with $x = 0.00, 0.25, 0.50$, and 0.75 . and Rietveld refinement of X-ray diffraction data for $\text{Nd}_2\text{NiMnO}_6$

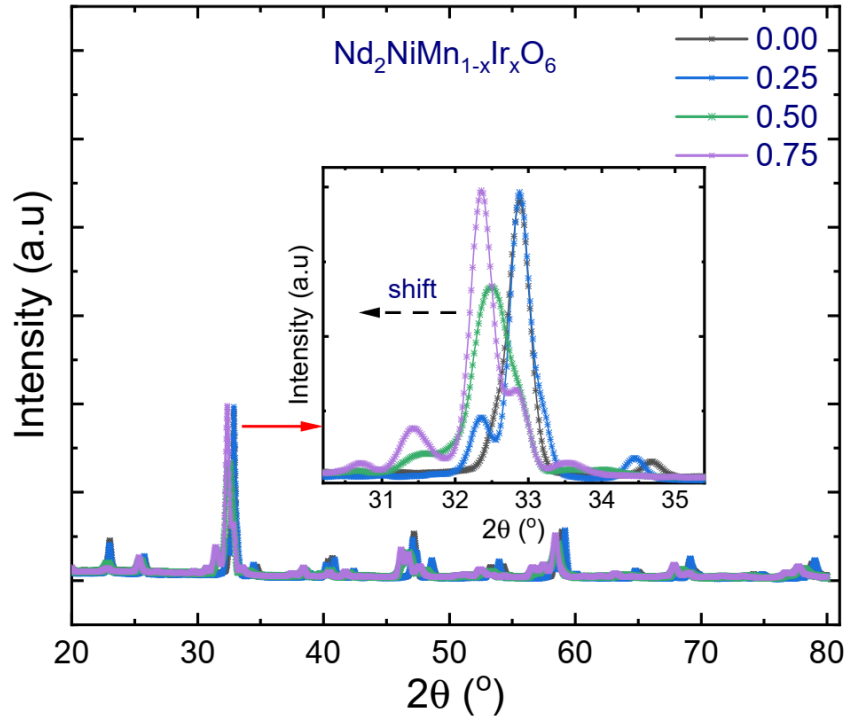


Figure I.1: X-ray diffraction patterns of $\text{Nd}_2\text{NiMn}_{1-x}\text{Ir}_x\text{O}_6$ with $x = 0.00, 0.25, 0.50$, and 0.75 . The inset highlights a systematic shift to lower 2θ angles (black arrow) with increasing Ir doping, indicating lattice expansion. Progressive peak broadening and enhanced peak splitting reflect increasing lattice strain and symmetry lowering due to Ir incorporation.

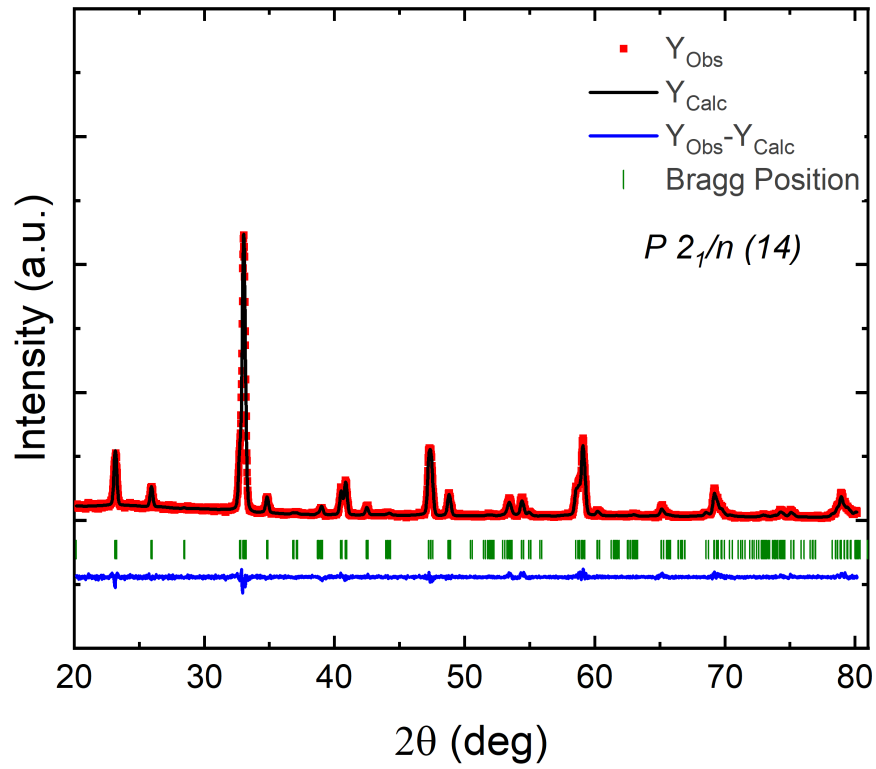


Figure I.2: Rietveld refinement of X-ray diffraction data for $\text{Nd}_2\text{NiMnO}_6$ at room temperature. The observed pattern (Y_{Obs}) is shown in red dots, the calculated pattern (Y_{Calc}) in black, and the difference ($Y_{\text{Obs}} - Y_{\text{Calc}}$) in blue. Vertical green ticks mark the Bragg reflection positions corresponding to the monoclinic $P2_1/n$ (space group 14) symmetry. The excellent agreement between the observed and calculated profiles confirms the phase purity and structural model.

* APPENDIX B *

$\text{Nd}_2\text{NiMnO}_6$

2.1 Phonon Dynamics

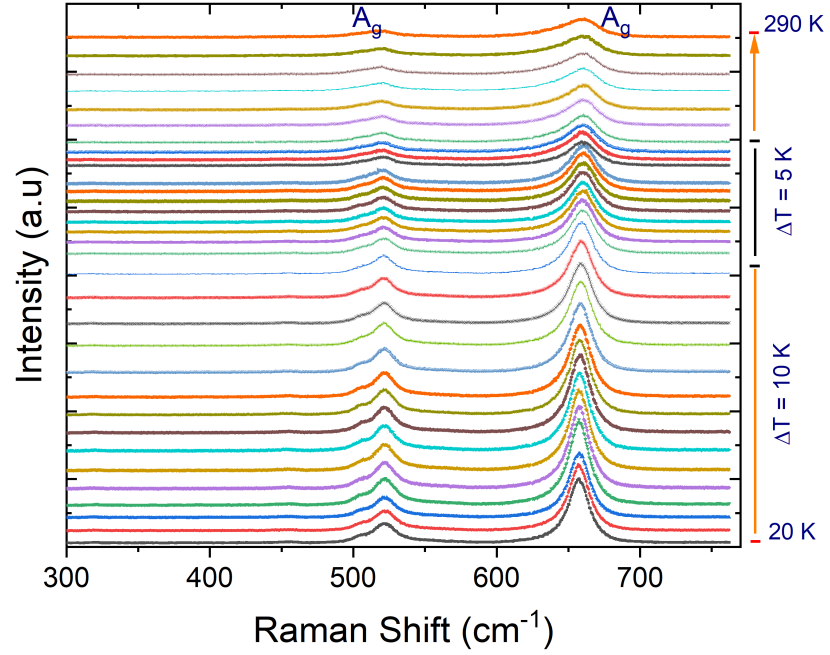


Figure II.1: Temperature-dependent Raman spectra of $\text{Nd}_2\text{NiMnO}_6$ collected between 20 and 290 K. The measurements were performed with temperature steps of $\Delta T = 10 \text{ K}$ from 20 to 100 K, and $\Delta T = 5 \text{ K}$ from 100 to 290 K. The two prominent A_g phonon modes are labeled. Systematic shifts and linewidth changes with decreasing temperature reflect anharmonic effects and possible spin-phonon coupling.

* APPENDIX C *

Nd₂NiMn_{0.25}Ir_{0.75}O₆

3.1 Crystal Structure

Table III.1: Atomic coordinates, displacement parameters, and site information for the Fddd phase (D_{2h} , No. 70) at 200 K. U_{iso} in 10^{-2} \AA^2 .

Atom	x	y	z	U_{iso} ($\times 10^{-2} \text{ \AA}^2$)	Occ.	Wyck.
Ir1	0.1250	0.1250	0.0485(2)	0.63	Ir	16f
	0.95549(4)	(y)	(z)			
Cl1	(x)	0.1250	0.1250	0.63	Cl	16f
Cl2	0.1219	0.3630	0.0373	0.63	Cl	32h

Bond Angle	Angle ($^\circ$)
$\langle \text{Ir} - \text{O3} - \text{Ni/Mn} \rangle$	150.2(4)

Lattice Parameter	Value	Unit
a	7.0255(3)	\AA
b	10.0294(6)	\AA
c	20.2097(2)	\AA
$\alpha = \beta = \gamma$	90.00	$^\circ$
V	1424.006(2)	\AA^3
R_{Bragg} (%)	5.49	—
Phase fraction (%)	3.07(1)	—

3.2 AC Magnetometry

The Néel-Arrhenius (N-A) model was applied to analyze the frequency-dependent freezing temperature, using the equation

$$\tau = \tau_0 \exp\left(\frac{E_a}{k_B T}\right) \quad (228)$$

where E_a is the anisotropy energy barrier, k_B is the Boltzmann constant, and τ_0 is the attempt time typical for superparamagnetic systems (10^{-10} to 10^{-13} s). Fitting the linearized form: $\ln(f) = \ln\left(\frac{1}{\tau_0}\right) - \frac{E_a}{k_B} \cdot \frac{1}{T}$, yields a strong correlation

($R^2 = 0.99452$)[Appendix 3.2]. The calculated energy barrier is $E_a \approx 5263.44 \times k_B$ indicating substantial anisotropy. However, the attempt time is $\tau_0 \approx 1.067 \times 10^{-30}$ s which is far below the physically acceptable range. This unrealistic value clearly indicates that the Néel-Arrhenius model fails to capture the relaxation dynamics, suggesting significant interparticle interactions, such as dipole-dipole or exchange coupling. Therefore, interaction-sensitive models such as the Vogel-Fulcher(V-F) law or dynamic power-law scaling are more suitable to describe the magnetic behavior of the system accurately. The temperature-dependent relaxation dynamics are first analyzed using the Vogel-Fulcher (V-F) law, which is typically employed to describe interacting spin systems with collective dynamics. The V-F relation is expressed as:

$$\tau = \tau_0 \exp \left(\frac{E_a}{k_B(T_f - T_0)} \right) \quad (229)$$

where T_f is the freezing temperature at a given frequency, and T_0 is the Vogel-Fulcher temperature, representing the ideal glass transition point where the system would freeze in the absence of thermal fluctuations. The V-F model fitting, shown in the inset of Figure III.1(b), yields the parameters: $T_0 = 74.50 \pm 1.03$ K, $a = \frac{E_a}{k_B} = 70.65 \pm 0.98$, and $\ln(\tau_0) = -0.203$, corresponding to $\tau_0 \approx 0.816$ s. The proximity of T_0 to T_f indicates significant inter-cluster magnetic interactions, a key characteristic of cluster-glass systems. Notably, the extracted τ_0 is considerably larger than values typical for canonical spin-glass (SG) systems, which generally lie in the range of 10^{-10} to 10^{-13} s. Instead, it aligns with cluster-glass (CG) systems, where τ_0 typically ranges from 10^{-6} to 10^{-10} seconds. For comparison, superparamagnetic (SPM) systems exhibit τ_0 between 10^{-9} and 10^{-11} s. This elevated τ_0 strongly indicates the dominance of slow, collective spin dynamics characteristic of cluster-glass behavior. To further confirm this behavior, the frequency-dependent shift in T_f is analyzed using the power law dynamic scaling model, presented in Figure III.1(b). The power law describes the divergence of relaxation time near the spin-glass transition temperature T_{SG} according to:

$$\tau = \tau_0 \left(\frac{T_f}{T_{SG}} - 1 \right)^{-z\nu} \quad (230)$$

where T_{SG} is the zero-frequency spin-glass transition temperature, $z\nu$ is the dynamic scaling exponent related to the growth of the correlation length (ξ), and τ_0 is the characteristic relaxation time. The power law fitting yields $T_{SG} =$

83.93 ± 4.02 K, $z\nu = 4.78 \pm 0.21$, and $\tau_0 = 7.11 \times 10^{-7}$ s. The value of $z\nu$ is consistent with the expected range of 4-13 for spin-glass systems, supporting the applicability of dynamic scaling. However, the relatively large τ_0 reinforces the conclusion from the V-F analysis that the magnetic dynamics are governed by the freezing of spin clusters rather than isolated atomic spins, supporting the ASD presence as evidenced from the mixed-occupation refinement.

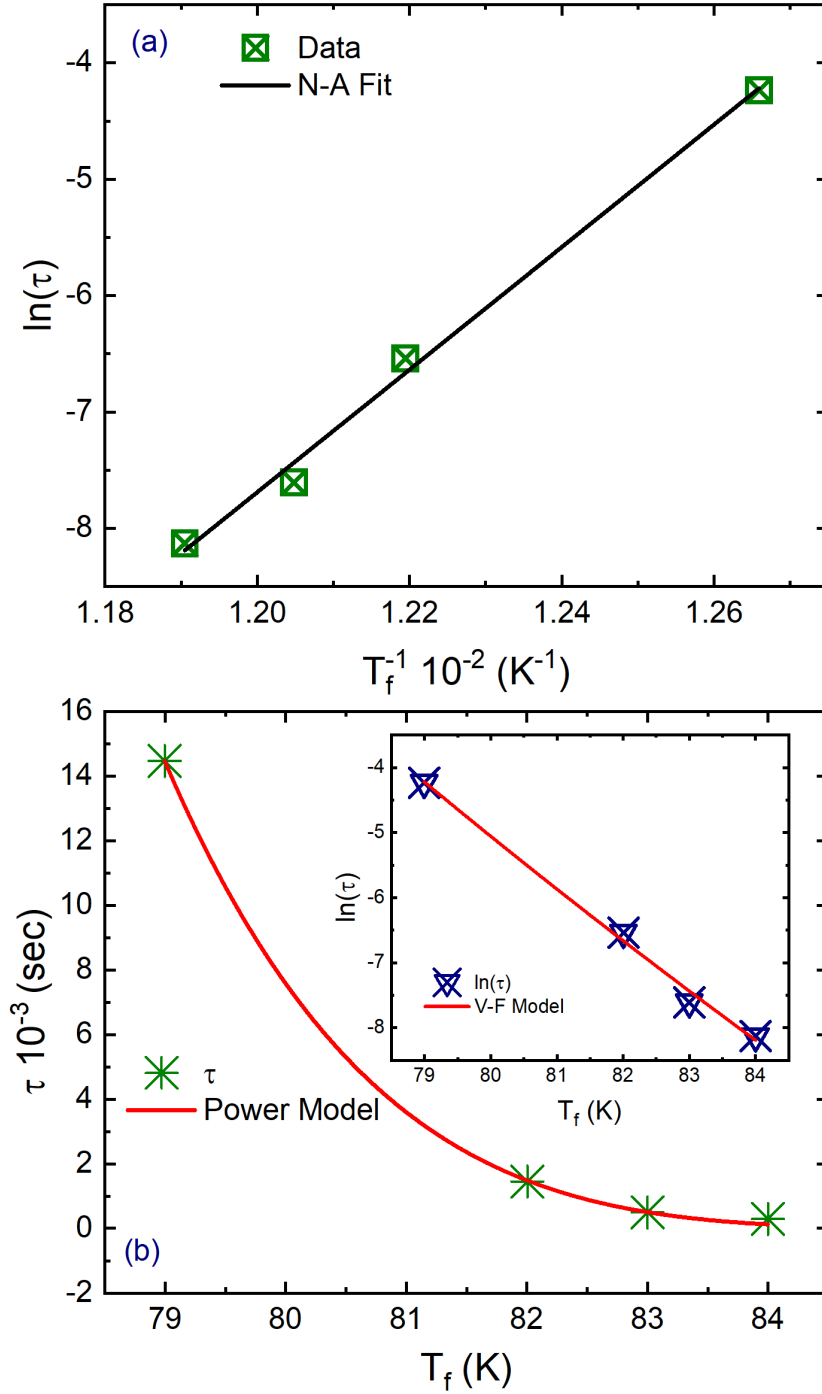


Figure III.1: (a) Power-law fitting of τ vs T_f ; (b) Vogel-Fulcher (V-F) fitting shown in the inset.

3.3 Raman Spectroscopy

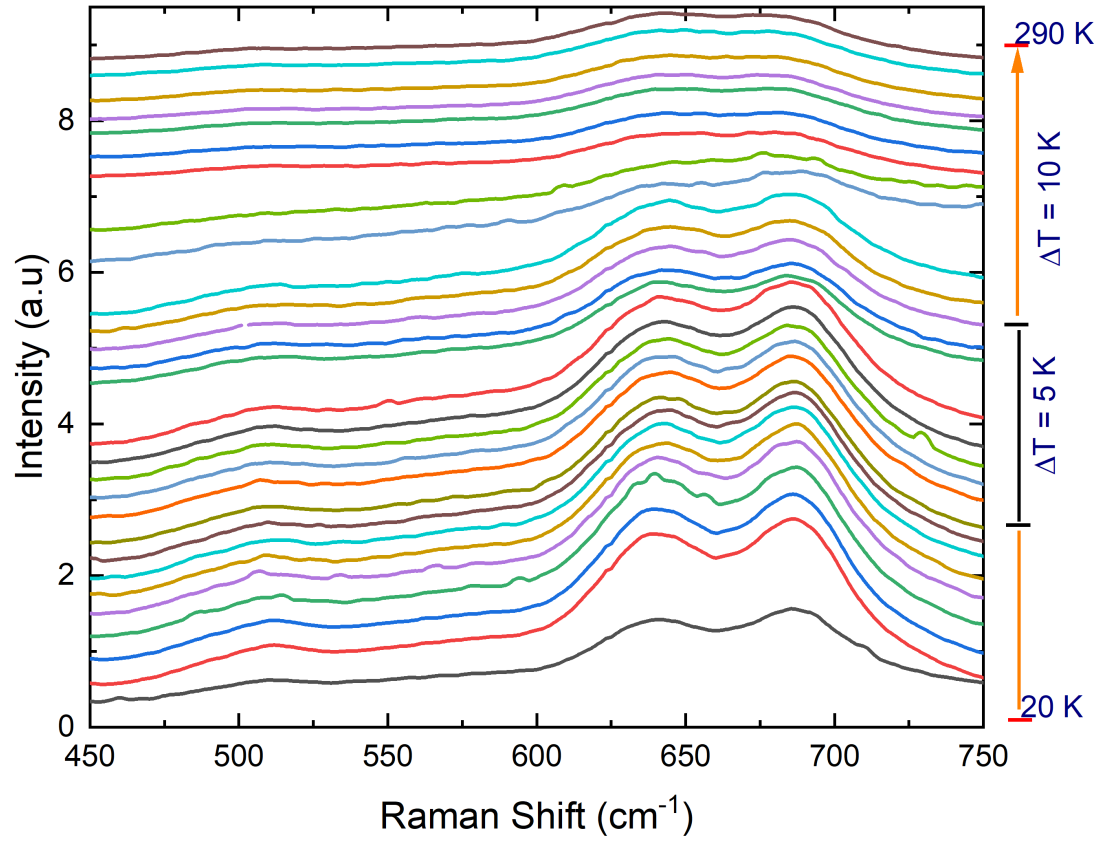


Figure III.2: (Color online) Temperature-dependent Raman spectra of polycrystalline $\text{Nd}_2\text{NiMn}_{0.25}\text{Ir}_{0.75}\text{O}_6$ measured from 20 K to 290 K over the spectral range of 450-750 cm^{-1} . The measurements were conducted in backscattering geometry with a 532 nm excitation laser. Spectra are vertically offset for clarity. Prominent phonon modes exhibit temperature-driven softening and broadening, most notably in the high-frequency region ($\sim 650\text{-}700 \text{ cm}^{-1}$), indicative of anharmonic effects and potential spin-phonon coupling. Color-coded arrows to the right denote the temperature scale with $\Delta T = 5 \text{ K}$ spacing up to 100 K and $\Delta T = 10 \text{ K}$ above.

3.4 Specific Heat

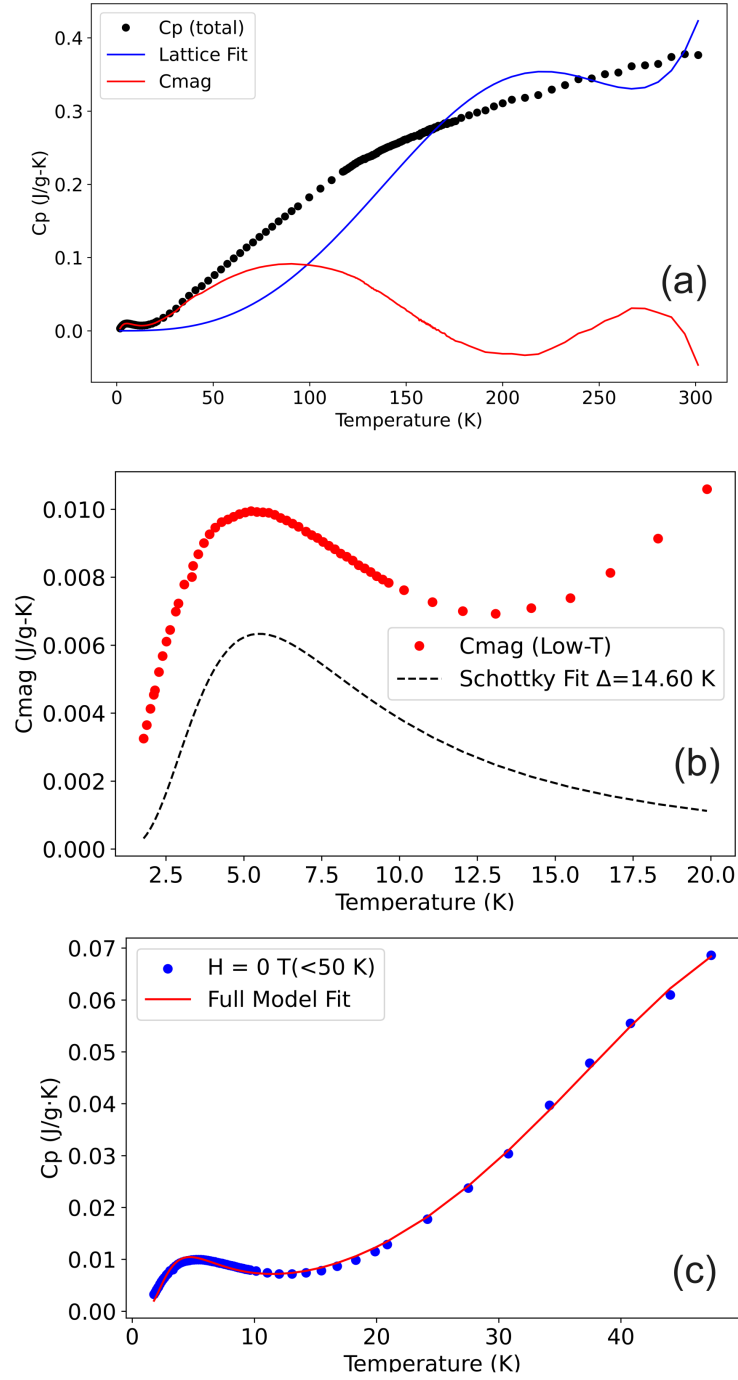


Figure III.3: Temperature-dependent specific heat analysis of $\text{Nd}_2\text{NiMn}_{0.25}\text{Ir}_{0.75}\text{O}_6$ at $H = 0$ T: (a) Total specific heat $C_p(T)$ with fitted lattice contribution and extracted magnetic heat capacity $C_{\text{mag}}(T)$; (b) Low-temperature C_{mag} showing Schottky anomaly and corresponding fit with $\Delta = 14.60$ K; (c) Full model fit to $C_p(T)$ data below 50 K including phonon and Schottky contributions.

* APPENDIX D *

NdSmNiMnO₆

4.0.1 Crystal Structure

structure characterization of SXRD data

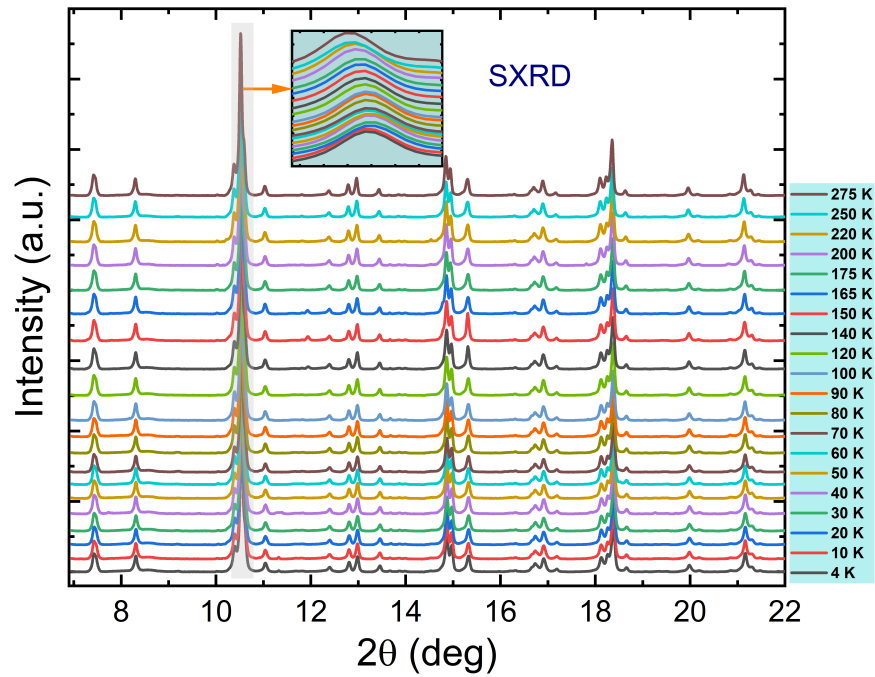


Figure IV.1: Synchrotron X-ray diffraction (SXRD) patterns of NdSmNiMnO₆ collected in the temperature range of 4-300 K. The patterns confirm phase stability across the full range with no evidence of structural transitions.

4.0.2 Magnetic Properties

Applied field at 10 kOe

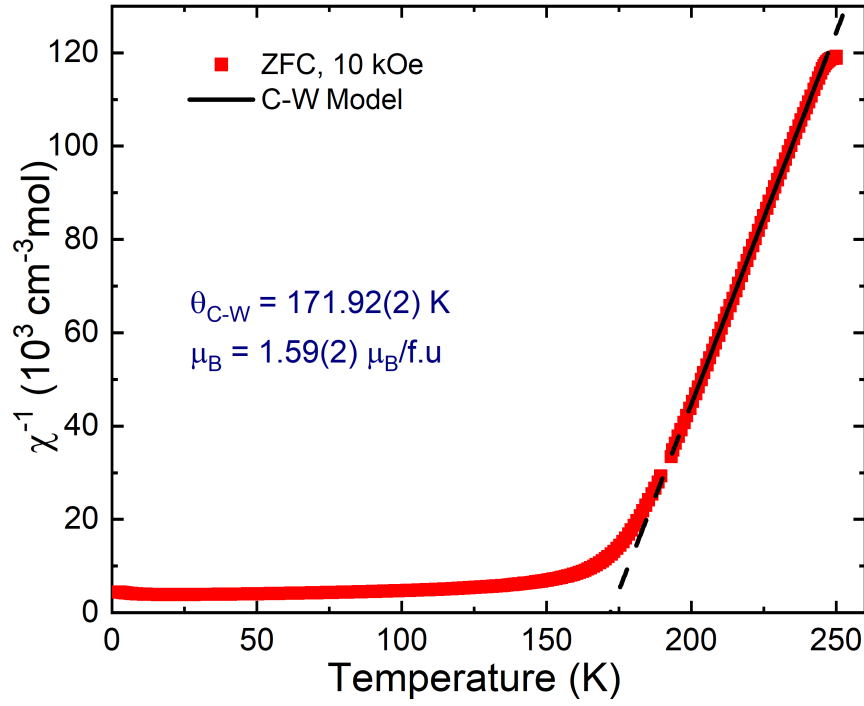


Figure IV.2: Inverse magnetic susceptibility ($\chi^{-1} = H/M$) of NdSmNiMnO₆ as a function of temperature, measured under a DC field of $H_{dc} = 10$ kOe. The black line represents the best fit to the Curie–Weiss law in the paramagnetic region.

4.0.3 Magnetoelastic Coupling

Table IV.1: Fitting parameters obtained from modeling the thermal expansion of the lattice parameters as a function of temperature.

Parameter	Temp. Range (K)	Fitting Parameters
a	4–175	$a_0 = 5.36796$, $B = 11.1915$, $d = 834.949$
	175–275	$a_0 = 5.36538$, $B = 0.69946$, $d = 299.795$
b	4–175	$b_0 = 5.48103$, $C = 17.198$, $e = 923.606$
	175–275	$b_0 = 5.48317$, $C = 10.543$, $e = 1072.606$
c	4–165	$c_0 = 5.38628$, $D = 34.948$, $f = 933.880$
	165–275	$c_0 = 5.38472$, $D = 0.76435$, $f = 297.387$

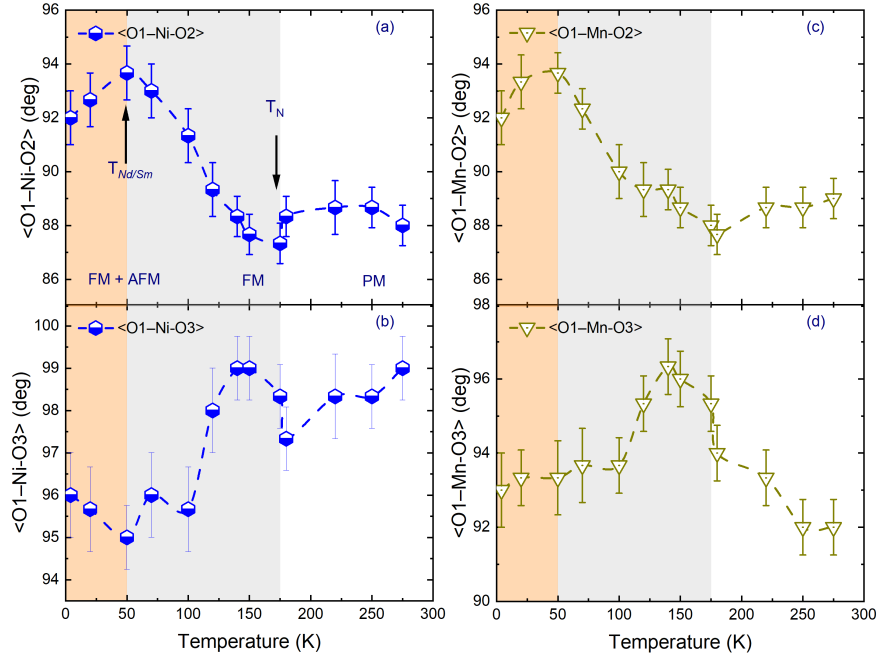


Figure IV.3: Thermal variation of octahedral bond angles in NdSmNiMnO₆ obtained from temperature-dependent synchrotron X-ray diffraction (SXRD) analysis: (a-b) O-Ni-O bond angles; (c-d) O-Mn-O bond angles. Anomalies near T_N are evident in all panels, indicating the onset of structural distortion in the NiO₆ and MnO₆ octahedra.

Bibliography

- [1] Richard JD Tilley. *Perovskites: structure-property relationships*. John Wiley & Sons, 2016.
- [2] Alberto Garcia, Emilio José Juárez-Pérez, Socorro Castro-García, Manuel Sánchez-Andújar, and Maria Antonia Senaris-Rodriguez. Hybrid organic-inorganic perovskites: A spin-off of oxidic perovskites. *OAJ Materials and Devices*, 5(1), 2020.
- [3] James M Rondinelli and Nicola A Spaldin. Structure and properties of functional oxide thin films: insights from electronic-structure calculations. *Advanced materials*, 23(30):3363–3381, 2011.
- [4] John MD Coey. *Magnetism and magnetic materials*. Cambridge university press, 2010.
- [5] John A Mydosh. *Spin glasses: an experimental introduction*. CRC press, 1993.
- [6] Theo Hahn, editor. *International Tables for Crystallography, Volume A: Space-Group Symmetry*. Springer, 2002.
- [7] Dylan Behr, Ran Liu, Kazunari Yamaura, Alexei A Belik, Dmitry D Khalyavin, and Roger D Johnson. Magnetic structures of $\text{prmn}_7\text{o}_{12}$: Intersublattice magnetoelastic coupling and incommensurate spin canting. *Physical Review B*, 110(13):134426, 2024.
- [8] Mustakim R Zhumaev, Mirzo Z Sharipov, and Mirzokhid N Rizoqulov. Unusual spin dynamics. In *Journal of Physics: Conference Series*, volume 2388, page 012005. IOP Publishing, 2022.
- [9] A. M. Vibhakar, D. D. Khalyavin, P. Manuel, J. Liu, A. A. Belik, and R. D. Johnson. Spontaneous rotation of ferrimagnetism driven by antiferromagnetic spin canting. *Phys. Rev. Lett.*, 124:127201, 2020. doi: 10.1103/PhysRevLett.124.127201. URL <https://link.aps.org/doi/10.1103/PhysRevLett.124.127201>.

- [10] William D Callister Jr and David G Rethwisch. *Materials science and engineering: an introduction*. John wiley & sons, 2020.
- [11] B Viswanathan, V Suryakumar, B Venugopal, SH Roshna, and N Hariprasad. Perovskite materials an introduction. *National Centre For Catalysis Research, Department of Chemistry Indian Institute of Technology, Madras*, 2019.
- [12] Angus Rockett. *The materials science of semiconductors*. Springer Science & Business Media, 2007.
- [13] Robert S Matos, John M Attah-Baah, Michael DS Monteiro, Benilde FO Costa, Marcelo A Mâcedo, Simone PA Da Paz, Rômulo S Angélica, Tiago M de Souza, Ștefan Țălu, Rosane MPB Oliveira, et al. Evaluation of the photocatalytic activity of distinctive-shaped zno nanocrystals synthesized using latex of different plants native to the amazon rainforest. *Nanomaterials*, 12(16):2889, 2022.
- [14] Chintamani Nagesa Ramachandra Rao and Jagannatha Gopalakrishnan. *New directions in solid state chemistry*. Cambridge University Press, 1997.
- [15] Alexei A Belik. Rise of a-site columnar-ordered $a_2a'a''b_4o_{12}$ quadruple perovskites with intrinsic triple order. *Dalton Transactions*, 47(10):3209–3217, 2018.
- [16] Daniel M Giaquinta and Hans-Conrad Zur Loye. Structural predictions in the abo_3 phase diagram. *Chemistry of materials*, 6(4):365–372, 1994.
- [17] Anthony M Glazer. The classification of tilted octahedra in perovskites. *Acta Crystallographica Section B: Structural Crystallography and Crystal Chemistry*, 28(11):3384–3392, 1972.
- [18] Patrick M Woodward. Octahedral tilting in perovskites. ii. structure stabilizing forces. *Acta Crystallographica Section B: Structural Science*, 53(1):44–66, 1997.
- [19] Roger H Mitchell. Perovskites: modern and ancient. (*Almaz Press*), 2002.
- [20] Graham King and Patrick M Woodward. Cation ordering in perovskites. *Journal of Materials Chemistry*, 20(28):5785–5796, 2010.

- [21] Jan Reedijk and Kenneth R Poeppelmeier. Comprehensive inorganic chemistry ii: from elements to applications. *Comprehensive Journal*, 2:20–30, 2013.
- [22] RD Johnson, DD Khalyavin, P Manuel, L Zhang, K Yamaura, and AA Belik. Emergence of a magnetostructural dipolar glass in the quadruple perovskite $\text{dy}_{1-\delta}\text{mn}_{7+\delta}\text{o}_{12}$. *Physical Review Letters*, 125(9):097601, 2020.
- [23] Patrick M Woodward. Octahedral tilting in perovskites. i. geometrical considerations. *Structural Science*, 53(1):32–43, 1997.
- [24] Pascal Granger, Vasile I Parvulescu, Serge Kaliaguine, and Wilfrid Prellier. Perovskites and related mixed oxides: concepts and applications. *Wiley-VCH Verlag GmbH & Co. KGaA, Boschstr. 12, 69469 Weinheim, Germany*, 2015.
- [25] Mark R Levy. Chapter 3: perovskite perfect lattice. *Cryst. Struct. Defect Prop. Predict. Ceram. Mater*, pages 79–114, 2005.
- [26] VM Goldschmidt. Geochemischeverteilungsgesetze, vii: Die gesetze der krystallochemie (nach untersuchungen gemeinsam mit t. barth, g. lunde, w. zachariasen); skripter nersk. *Vid. Akademie, Oslo, Mat. Nat. Kl*, 14(2), 1926.
- [27] Henry J Snaith. Perovskites: the emergence of a new era for low-cost, high-efficiency solar cells. *The journal of physical chemistry letters*, 4(21):3623–3630, 2013.
- [28] John B Goodenough. Magnetism and the chemical bond. (*No Title*), 1963.
- [29] Asu Ram Jha. *Rare earth materials: properties and applications*. CRC Press, 2014.
- [30] MA Subramanian, BH Toby, AP Ramirez, WJ Marshall, AW Sleight, and GH Kwei. Colossal magnetoresistance without $\text{mn}^{3+}/\text{mn}^{4+}$ double exchange in the stoichiometric pyrochlore $\text{tl}_2\text{mn}_2\text{o}_7$. *Science*, 273(5271):81–84, 1996.
- [31] Akira Fujishima and Kenichi Honda. Electrochemical photolysis of water at a semiconductor electrode. *nature*, 238(5358):37–38, 1972.

- [32] Guillaume Salek, Alexis Devoti, Emilie Lataste, Alain Demourgues, Alain Garcia, Veronique Jubera, and Manuel Gaudon. Optical properties versus temperature of cr-doped γ - and α - Al_2O_3 : Irreversible thermal sensors application. *Journal of Luminescence*, 179:189–196, 2016. doi: 10.1016/j.jlumin.2016.06.031.
- [33] Ralf Riedel. Handbook of ceramic hard materials. (*No Title*), 2000.
- [34] Jing Ming Liang, Xu Wen Zhao, Xin Yuan, Yu Kuai Liu, Sheung Mei Ng, Hon Fai Wong, Pei Gen Li, Yan Zhou, Fu Xiang Zhang, Chee Leung Mak, et al. Interlayer antiferromagnetic coupling in $\text{tb}_3\text{fe}_5\text{o}_{12}/\text{y}_3\text{fe}_5\text{o}_{12}$ bilayers. *Applied physics letters*, 123(9), 2023.
- [35] A SI Bhalla, Ruyan Guo, and Rustum Roy. The perovskite structure—a review of its role in ceramic science and technology. *Materials research innovations*, 4(1):3–26, 2000.
- [36] Marwa Sebai, Ghada Bousselmi, Jean-Louis Lazzari, and Mounir Kanzari. Preparation and characterization of $\text{Cu}_2\text{Zn}_x\text{Fe}_{1-x}\text{S}_4$ thin films deposited on intrinsic silicon substrates. *Materials Today Communications*, 35:105558, 2023.
- [37] Asish K Kundu. Magnetic perovskites. *Eng. Mater*, 2016.
- [38] Harumi Yokokawa, Natsuko Sakai, Tatsuya Kawada, and Masayuki Dokiya. Thermodynamic stabilities of perovskite oxides for electrodes and other electrochemical materials. *Solid State Ionics*, 52(1-3):43–56, 1992.
- [39] Robert D Shannon. Revised effective ionic radii and systematic studies of interatomic distances in halides and chalcogenides. *Foundations of Crystallography*, 32(5):751–767, 1976.
- [40] Olaf Muller and Rustum Roy. The major ternary structural families. (*No Title*), 1974.
- [41] D Serrate, JM De Teresa, and MR Ibarra. Double perovskites with ferromagnetism above room temperature. *Journal of Physics: Condensed Matter*, 19(2):023201, 2006.

- [42] Mark T Anderson, Kevin B Greenwood, Gregg A Taylor, and Kenneth R Poeppelmeier. B-cation arrangements in double perovskites. *Progress in solid state chemistry*, 22(3):197–233, 1993.
- [43] K-I Kobayashi, T Kimura, H Sawada, K Terakura, and Y Tokura. Room-temperature magnetoresistance in an oxide material with an ordered double-perovskite structure. *Nature*, 395(6703):677–680, 1998.
- [44] Yasuhide Tomioka, Tetsuji Okuda, Youichi Okimoto, Reiji Kumai, K-I Kobayashi, and Yoshinori Tokura. Magnetic and electronic properties of a single crystal of ordered double perovskite $\text{Sr}_2\text{FeMoO}_6$. *Physical Review B*, 61(1):422, 2000.
- [45] Nyrisa S Rogado, Jun Li, Arthur W Sleight, and Mas A Subramanian. Magnetocapacitance and magnetoresistance near room temperature in a ferromagnetic semiconductor: $\text{La}_2\text{NiMnO}_6$. *Advanced Materials*, 17(18):2225–2227, 2005.
- [46] Patrick M Woodward. Octahedral tilting in perovskites. ii. structure stabilizing forces. *Acta Crystallographica Section B: Structural Science*, 53(1):44–66, 1997.
- [47] Sergey V Eremeev, Tatiana V Menshchikova, Igor V Silkin, Maia G Vergniory, Pedro M Echenique, and Eugene V Chulkov. Sublattice effect on topological surface states in complex (snt) $n > 1$ (bi 2 te 3) $m = 1$ compounds. *Physical Review B*, 91(24):245145, 2015.
- [48] Chris D Ling, Brendan J Kennedy, Qingdi Zhou, Jarrah R Spencer, and Maxim Avdeev. Synthesis, structures, and phase transitions of barium bismuth iridium oxide perovskites $\text{Ba}_2\text{BiIrO}_6$ and $\text{Ba}_3\text{BiIr}_2\text{O}_9$. *Journal of solid state chemistry*, 183(3):727–735, 2010.
- [49] Sami Vasala and Maarit Karppinen. $\text{A}_2\text{B}'\text{B}''\text{O}_6$ perovskites: a review. *Progress in solid state chemistry*, 43(1-2):1–36, 2015.
- [50] Stephen Blundell. *Magnetism in condensed matter*. OUP Oxford, 2001.
- [51] H Falcón, JA Barbero, G Araujo, MT Casais, MJ Martinez-Lope, JA Alonso, and JLG Fierro. Double perovskite oxides $\text{A}_2\text{FeMoO}_6 - \delta$ ($a =$

- ca, sr and ba) as catalysts for methane combustion. *Applied Catalysis B: Environmental*, 53(1):37–45, 2004.
- [52] John B Goodenough. An interpretation of the magnetic properties of the perovskite-type mixed crystals $\text{La}_{1-x}\text{Sr}_x\text{CoO}_3$. *Journal of Physics and Chemistry of Solids*, 6(2-3):287–297, 1958.
- [53] Junjiro Kanamori. Superexchange interaction and symmetry properties of electron orbitals. *Journal of Physics and Chemistry of Solids*, 10(2-3):87–98, 1959.
- [54] Kentaro Shiro, Ikuya Yamada, Naoya Ikeda, Kenya Ohgushi, Masaichiro Mizumaki, Ryoji Takahashi, Norimasa Nishiyama, Toru Inoue, and Tetsuo Irifune. Pd^{2+} -incorporated perovskite $\text{CaPd}_{3-b}\text{Ti}_b\text{O}_{12}$ ($b = \text{Ti, V}$). *Inorganic Chemistry*, 52(3):1604–1609, 2013.
- [55] Sergey V Ovsyannikov, Yury G Zainulin, Nadezda I Kadyrova, Alexander P Tyutyunnik, Anna S Semenova, Deepa Kasinathan, Alexander A Tsirlin, Nobuyoshi Miyajima, and Alexander E Karkin. New antiferromagnetic perovskite $\text{CaCo}_3\text{V}_4\text{O}_{12}$ prepared at high-pressure and high-temperature conditions. *Inorganic Chemistry*, 52(20):11703–11710, 2013.
- [56] K Leinenweber, J Linton, A Navrotsky, Y Fei, and JB Parise. High-pressure perovskites on the join CaTiO_3 - FeTiO_3 . *Physics and Chemistry of Minerals*, 22(4):251–258, 1995.
- [57] Wellington Castro Ferreira. Optical and structural properties of perovskite-related structures under extreme conditions of pressure and temperature. *Optical Journal*, 1:1–10, 2020.
- [58] Corey Elizabeth Frank. *Design and Synthesis of Perovskites and Corundum Derivatives with Unusual Magnetic, Electronic, and Structural Coupling*. PhD thesis, Rutgers The State University of New Jersey, School of Graduate Studies, 2021.
- [59] Ran Liu, Masahiko Tanaka, Hiromu Mori, Yoshiyuki Inaguma, Kazunari Yamaura, and Alexei A Belik. Ferrimagnetic and relaxor ferroelectric properties of $\text{R}_2\text{MnMn}(\text{MnTi}_3)\text{O}_{12}$ perovskites with $\text{R} = \text{Nd, Eu, and Gd}$. *Journal of Materials Chemistry C*, 9(3):947–956, 2021.

- [60] Ran Liu, Rebecca Scatena, Dmitry D Khalyavin, Roger D Johnson, Yoshiyuki Inaguma, Masahiko Tanaka, Yoshitaka Matsushita, Kazunari Yamaura, and Alexei A Belik. High-pressure synthesis, crystal structures, and properties of a-site columnar-ordered quadruple perovskites $\text{R}_{1-x}\text{Mn}_2\text{Ti}_4\text{O}_{12}$ with $\text{R} = \text{Sm, Eu, Gd, Dy, Ho, Y}$. *Inorganic Chemistry*, 59(13): 9065–9076, 2020.
- [61] AA Belik. New subfamily of perovskites with triple ordering. *XXXI* .—, 2022, pages 12–13, 2022.
- [62] H Jahn and Edward Teller. Stability of degenerate electronic states in polyatomic molecules. *Phys. Rev*, 49:874, 1936.
- [63] Hermann Arthur Jahn and Edward Teller. Stability of polyatomic molecules in degenerate electronic states—orbital degeneracy. *Proceedings of the Royal Society of London. Series A-Mathematical and Physical Sciences*, 161 (905):220–235, 1937.
- [64] Isaac B Bersuker. *The Jahn-teller effect*. Cambridge Cambridge University Press, 2006.
- [65] John B Goodenough. Electronic and ionic transport properties and other physical aspects of perovskites. *Reports on Progress in Physics*, 67(11): 1915, 2004.
- [66] J Rodriguez-Carvajal, M Hennion, F Moussa, AH Moudden, L Pinsard, and AJPRB Revcolevschi. Neutron-diffraction study of the jahn-teller transition in stoichiometric LaMnO_3 . *Physical Review B*, 57(6):R3189, 1998.
- [67] Junjiro Kanamori. Crystal distortion in magnetic compounds. *Journal of Applied Physics*, 31(5):S14–S23, 1960.
- [68] JD Axe and G Shirane. Study of the α - β quartz phase transformation by inelastic neutron scattering. *Physical Review B*, 1(1):342, 1970.
- [69] JA Alonso, MJ Martínez-Lope, MT Casais, JL García-Muñoz, MT Fernández-Díaz, and MAG Aranda. High-temperature structural evolution of R_2NiO_3 ($\text{R} = \text{Ho, Y, Er, Lu}$) perovskites: Charge disproportionation and electronic localization. *Physical Review B*, 64(9):094102, 2001.

- [70] Christopher J Howard and Harold T Stokes. Group-theoretical analysis of octahedral tilting in perovskites. *Structural Science*, 54(6):782–789, 1998.
- [71] Caixia Yue, Wenying Zhang, Min Wang, Jia Liu, Jiamei Zhang, and Denglu Hou. Crystal structure and octahedral deformation of orthorhombic perovskite abo_3 : Case study of SrRuO_3 . *Journal of Solid State Chemistry*, 309: 122998, 2022.
- [72] Malcolm E Lines and Alastair M Glass. *Principles and applications of ferroelectrics and related materials*. Oxford university press, 2001.
- [73] Rohan Mishra. *First Principles Study of Double Perovskites and Group III-V Compounds*. The Ohio State University, 2012.
- [74] Ram Seshadri and Nicola A Hill. Visualizing the role of bi 6s “lone pairs” in the off-center distortion in ferromagnetic BiMnO_3 . *Chemistry of materials*, 13(9):2892–2899, 2001.
- [75] Nicole A Benedek and Craig J Fennie. Why are there so few perovskite ferroelectrics? *The Journal of Physical Chemistry C*, 117(26):13339–13349, 2013.
- [76] Jacky Even, Laurent Pedesseau, and Claudine Katan. Analysis of multivaleley and multibandgap absorption and enhancement of free carriers related to exciton screening in hybrid perovskites. *The Journal of Physical Chemistry C*, 118(22):11566–11572, 2014.
- [77] Manfred Fiebig, Thomas Lottermoser, Dennis Meier, and Morgan Trassin. The evolution of multiferroics. *Nature Reviews Materials*, 1(8):1–14, 2016.
- [78] HP Rooksby. Compounds of the structural type of calcium titanate. *Nature*, 155(3938):484–484, 1945.
- [79] Daniel L Stein and Charles M Newman. *Spin glasses and complexity*. Princeton University Press, 2013.
- [80] Hermann Weyl. *Symmetry*. Princeton University Press, 2015.
- [81] David J Gross. The role of symmetry in fundamental physics. *Proceedings of the National Academy of Sciences*, 93(25):14256–14259, 1996.

- [82] LD Landau and EM Lifshitz. Mechanics (course of theoretical physics, volume 1). *New York*, 1976.
- [83] E Noether. Invariante variationsprobleme. nachr. d. könig. gesellsch. d. wiss. zu göttingen, math-phys. klasse, 235–257. english translation by tavel ma (1971). *Transport Theory and Statistical Physics*, 1(3):183–207, 1918.
- [84] C Kittel. Int. to solid state physics, 8th edn., maruzen, 2005.
- [85] Neil W Ashcroft and ND Mermin. Solid state. *Physics (New York: Holt, Rinehart and Winston) Appendix C*, 1, 1976.
- [86] Martin T Dove. *Structure and dynamics: an atomic view of materials*, volume 1. Oxford University Press, 2003.
- [87] Christopher Bradley and Arthur Cracknell. *The mathematical theory of symmetry in solids: representation theory for point groups and space groups*. Oxford University Press, 2009.
- [88] F Albert Cotton. *Chemical applications of group theory*. John Wiley & Sons, 1991.
- [89] John Frederick Nye. *Physical properties of crystals: their representation by tensors and matrices*. Oxford university press, 1985.
- [90] Pierre Toledano and Jean-claude Toledano. *Landau Theory Of Phase Transitions, The: Application To Structural, Incommensurate, Magnetic And Liquid Crystal Systems*, volume 3. World Scientific Publishing Company, 1987.
- [91] Norman FM Henry and Kathleen Lonsdale. *International Tables for X-Ray Crystallography Volume I Symmetry Groups*. Kynoch Press, 1969.
- [92] Daniel B Litvin. Magnetic group tables. *International Union of Crystallography*, 10:9780955360220001, 2013.
- [93] AV Shubnikov. Symmetry and antisymmetry of finite figures, moscow: Ussr acad, 1951.
- [94] IE Dzyaloshinskii et al. Thermodynamic theory of weak ferromagnetism in antiferromagnetic substances. *Sov. Phys. JETP*, 5(6):1259–1272, 1957.

- [95] W Opechowski and R Guccione. Magnetism, gt rado and h. shul, eds, 1965.
- [96] Nicola A Spaldin and Manfred Fiebig. The renaissance of magnetoelectric multiferroics. *Science*, 309(5733):391–392, 2005.
- [97] Yoshinori Tokura, Kenji Yasuda, and Atsushi Tsukazaki. Magnetic topological insulators. *Nature Reviews Physics*, 1(2):126–143, 2019.
- [98] Rahul M Nandkishore and Michael Hermele. Fractons. *Annual Review of Condensed Matter Physics*, 10(1):295–313, 2019.
- [99] J Rodríguez-Carvajal and F Bourée. Symmetry and magnetic structures. In *EPJ Web of Conferences*, volume 22, page 00010. EDP Sciences, 2012.
- [100] I Dzyaloshinskii. I. dzyaloshinskii phys. chem. solids, 4 (1960). *Sov. Phys.—JETP*, 6:1130, 1958.
- [101] EF Bertaut. Representation analysis of magnetic structures. *Foundations of Crystallography*, 24(1):217–231, 1968.
- [102] H. T. Stokes, D. M. Hatch, and B. J. Campbell. Isotropy software suite, 2005. <https://stokes.byu.edu/>.
- [103] Yurii A Izyumov. *Magnetic neutron diffraction*. Springer Science & Business Media, 2012.
- [104] EO Wollan and WC Koehler. Neutron diffraction study of the magnetic properties of the series of perovskite-type compounds $[(1-x)\text{La}, x\text{Ca}]\text{MnO}_3$. *Physical Review*, 100(2):545, 1955.
- [105] LD Landau and EM Lifshitz. Chapter i—the fundamental principles of statistical physics. *Course of Theoretical Physics*, 1980:1–33, 1980.
- [106] Lev Landau. The theory of phase transitions. *Nature*, 138(3498):840–841, 1936.
- [107] Nigel Goldenfeld. *Lectures on phase transitions and the renormalization group*. CRC Press, 2018.
- [108] Paul M Chaikin, Tom C Lubensky, and Thomas A Witten. *Principles of condensed matter physics*, volume 10. Cambridge university press Cambridge, 1995.

- [109] W Cochran. Crystal stability and the theory of ferroelectricity. *Advances in Physics*, 9(36):387–423, 1960.
- [110] Philip W Anderson. Antiferromagnetism. theory of superexchange interaction. *Physical Review*, 79(2):350, 1950.
- [111] Andrew J Millis, Peter B Littlewood, and Boris I Shraiman. Double exchange alone does not explain the resistivity of $\text{La}_{1-x}\text{Sr}_x\text{MnO}_3$. *Physical review letters*, 74(25):5144, 1995.
- [112] Elbio Dagotto. Complexity in strongly correlated electronic systems. *Science*, 309(5732):257–262, 2005.
- [113] Clarence Zener. Interaction between the d-shells in the transition metals. ii. ferromagnetic compounds of manganese with perovskite structure. *Physical Review*, 82(3):403, 1951.
- [114] Yoshinori Tokura. *Colossal magnetoresistive oxides*. CRC Press, 2000.
- [115] K KUNDU ASISH. Magnetic perovskites: Synthesis, structure and physical properties, 2017.
- [116] John B Goodenough. Theory of the role of covalence in the perovskite-type manganites $[\text{La}, \text{M}(\text{II})]\text{MnO}_3$. *Physical Review*, 100(2):564, 1955.
- [117] Elbio Dagotto. *Nanoscale phase separation and colossal magnetoresistance: the physics of manganites and related compounds*. Springer Science & Business Media, 2003.
- [118] P-G De Gennes. Effects of double exchange in magnetic crystals. *Physical Review*, 118(1):141, 1960.
- [119] I Dzyaloshinskii. I. dzyaloshinskii phys. chem. solids, 4 (1960). *Sov. Phys.—JETP*, 6:1130, 1958.
- [120] Tôru Moriya. Anisotropic superexchange interaction and weak ferromagnetism. *Physical review*, 120(1):91, 1960.
- [121] Vincent Cannella and John A Mydosh. Magnetic ordering in gold-iron alloys. *Physical Review B*, 6(11):4220, 1972.

- [122] Samuel Frederick Edwards and Phil W Anderson. Theory of spin glasses. *Journal of Physics F: Metal Physics*, 5(5):965, 1975.
- [123] Kurt Binder and A Peter Young. Spin glasses: Experimental facts, theoretical concepts, and open questions. *Reviews of Modern physics*, 58(4):801, 1986.
- [124] Konrad H. Fischer and John A. Hertz. *Spin Glasses*. Cambridge University Press, 1993.
- [125] David Sherrington and Scott Kirkpatrick. Solvable model of a spin-glass. *Physical review letters*, 35(26):1792, 1975.
- [126] OS Lutes and JL Schmit. Low-temperature magnetic transitions in dilute au-based alloys with cr, mn, and fe. *Physical Review*, 134(3A):A676, 1964.
- [127] Marc Gabay and Gérard Toulouse. Coexistence of spin-glass and ferromagnetic orderings. *Physical Review Letters*, 47(3):201, 1981.
- [128] JRL de Almeida and DJ Thouless. Stability of the sherrington-kirkpatrick solution of a spin glass model. *J. Phys. A: Math. Gen*, 11(5):983, 1978.
- [129] RG Palmer and DL Stein. Abrahams. e. and anderson, pw. *Phys. Rev. Lett*, 53:958, 1984.
- [130] Melvin A Ruderman and Charles Kittel. Indirect exchange coupling of nuclear magnetic moments by conduction electrons. *Physical Review*, 96(1):99, 1954.
- [131] Tadao Kasuya. A theory of metallic ferro-and antiferromagnetism on zener's model. *Progress of theoretical physics*, 16(1):45–57, 1956.
- [132] Kei Yosida. Magnetic properties of cu-mn alloys. *Physical Review*, 106(5):893, 1957.
- [133] Alexei Andreanov, John T Chalker, Timothy E Saunders, and David Sherrington. Spin-glass transition in geometrically frustrated antiferromagnets with weak disorder. *Physical Review B—Condensed Matter and Materials Physics*, 81(1):014406, 2010.
- [134] JL Tholence. Ac susceptibility of cu mn and ag mn spin-glasses. *Physica B+ C*, 108(1-3):1287–1288, 1981.

- [135] K Binder and AP Young. Logarithmic dynamic scaling in spin-glasses. *Physical Review B*, 29(5):2864, 1984.
- [136] N Bontemps, J Rajchenbach, RV Chamberlin, and R Orbach. Dynamic scaling in the eu 0.4 sr 0.6 s spin-glass. *Physical Review B*, 30(11):6514, 1984.
- [137] E Vincent, J Hammann, and M Alba. Dynamic critical behaviour of the cdcr 2×0.85 in 2×0.15 s 4 spin-glass. *Solid state communications*, 58(1):57–62, 1986.
- [138] H Kawamura and T Taniguchi. Spin glasses. In *Handbook of magnetic materials*, volume 24, pages 1–137. Elsevier, 2015.
- [139] JL Dormann, Franco D’Orazio, F Lucari, E Tronc, P Prené, JP Jolivet, D Fiorani, R Cherkaoui, and M Nogues. Thermal variation of the relaxation time of the magnetic moment of γ -fe 2 o 3 nanoparticles with interparticle interactions of various strengths. *Physical Review B*, 53(21):14291, 1996.
- [140] Sawako Nakamae, Caroline Crauste-Thibierge, Denis L’Hôte, Eric Vincent, Emmanuelle Dubois, Vincent Dupuis, and Regine Perzynski. Dynamic correlation length growth in superspin glass: Bridging experiments and simulations. *Applied Physics Letters*, 101(24), 2012.
- [141] IP Parkin. Solid state metathesis reaction for metal borides, silicides, pnictides and chalcogenides: ionic or elemental pathways. *Chemical Society Reviews*, 25(3):199–207, 1996.
- [142] Tapas Kumar Mandal and J Gopalakrishnan. From rocksalt to perovskite: a metathesis route for the synthesis of perovskite oxides of current interest. *Journal of Materials Chemistry*, 14(8):1273–1280, 2004.
- [143] M Stanley Whittingham. Hydrothermal synthesis of transition metal oxides under mild conditions. *Current Opinion in Solid State and Materials Science*, 1(2):227–232, 1996.
- [144] Thierry Delahaye, Ali Al-Zein, Marie-Hélène Berger, Xavier Bril, and Jean-François Hocheplé. Hydrothermal synthesis of ferroelectric mixed potassium niobate–lead titanate nanoparticles. *Journal of the American Ceramic Society*, 97(5):1456–1464, 2014.

- [145] Stefan G Ebbinghaus, Hans-Peter Abicht, Richard Dronskowski, Thomas Müller, Armin Reller, and Anke Weidenkaff. Perovskite-related oxynitrides—recent developments in synthesis, characterisation and investigations of physical properties. *Progress in Solid State Chemistry*, 37(2-3):173–205, 2009.
- [146] H Muthurajan, HH Kumar, V Samuel, UN Gupta, and V Ravi. Novel hydroxide precursors to prepare nanbo_3 and knbo_3 . *Ceramics International*, 34(3):671–673, 2008.
- [147] Anne Michelle Garrido Pedrosa Souza, Grace Rafaela Oliveira Silva, José Carlos dos Santos, Danielle MH Martinelli, Marcelo José Barros de Souza, and Dulce Maria Araújo Melo. Synthesis and characterization of $\text{lanixco}_{1-x}\text{o}_3$ perovskites via complex precursor methods. *Materials Sciences and Applications*, 1(3):102–110, 2010.
- [148] Zhaoqiang Li, Ming Meng, Qian Li, Yaning Xie, Tiandou Hu, and Jing Zhang. Fe-substituted nanometric $\text{la}_{0.9}\text{ko}_{1-x}\text{fexo}_{3-\delta}$ perovskite catalysts used for soot combustion, nox storage and simultaneous catalytic removal of soot and nox. *Chemical Engineering Journal*, 164(1):98–105, 2010.
- [149] Nunzio Russo, Pietro Palmisano, and Debora Fino. Pd substitution effects on perovskite catalyst activity for methane emission control. *Chemical Engineering Journal*, 154(1-3):137–141, 2009.
- [150] Masatsugu Oishi, Keiji Yashiro, Kazuhisa Sato, Junichiro Mizusaki, and Tatsuya Kawada. Oxygen nonstoichiometry and defect structure analysis of b-site mixed perovskite-type oxide $(\text{la}, \text{sr})(\text{cr}, \text{m})\text{o}_{3-\delta}$ ($\text{m} = \text{ti}, \text{mn}$ and fe). *Journal of Solid State Chemistry*, 181(11):3177–3184, 2008.
- [151] Guang Zhu and Likun Pan. *Perovskite Materials-Synthesis, Characterisation, Properties, and Applications*. InTechOpen, 2016.
- [152] Joonghoe Dho and NH Hur. Magnetic and transport properties of lanthanum perovskites with b-site half doping. *Solid state communications*, 138(3):152–156, 2006.
- [153] Paula Kayser, María Jesús Martínez-Lope, and Jose Antonio Alonso. Crystal structure, phase transitions, and magnetic properties of iridium per-

- ovskites $\text{Sr}_{2-x}\text{M}_{x-2}\text{NiO}_6$ ($\text{M} = \text{Ni}, \text{Zn}$). *Inorganic Chemistry*, 52(19):11013–11022, 2013.
- [154] Tim Ferreira, Stuart Calder, David S Parker, Mary H Upton, Athena Safa Sefat, and H-C zur Loye. Relationship between a-site cation and magnetic structure in 3d-5d-f double perovskite iridates Ln_2NiO_6 ($\text{Ln} = \text{La}, \text{Pr}, \text{Nd}$). *Physical Review Materials*, 5(6):064408, 2021.
- [155] JRL Mardegan, LSI Veiga, T Pohlmann, SS Dhesi, S Francoual, JR Jesus, C Macchiutti, EM Bittar, and L Bufaical. 3d and 5d electronic structures and orbital hybridization in Ba- and Ca-doped $\text{La}_2\text{CoIrO}_6$ double perovskites. *Physical Review B*, 107(21):214427, 2023.
- [156] Avijit Kumar Paul, Manfred Reehuis, Vadim Ksenofontov, Binghai Yan, Andreas Hoser, Daniel M Többens, Paula M Abdala, Peter Adler, Martin Jansen, and Claudia Felser. Lattice instability and competing spin structures in the double perovskite insulator $\text{Sr}_2\text{FeOsO}_6$. *Physical review letters*, 111(16):167205, 2013.
- [157] Somnath Pal, Somnath Jana, Sharada Govinda, Banabir Pal, Sumanta Mukherjee, Samara Keshavarz, Danny Thonig, Yaroslav Kvashnin, Manuel Pereiro, Roland Mathieu, et al. Peculiar magnetic states in the double perovskite $\text{Nd}_2\text{NiMnO}_6$. *Physical Review B*, 100(4):045122, 2019.
- [158] Chenyang Shi, Yongmei Hao, and Zhongbo Hu. Local valence and physical properties of double perovskite $\text{Nd}_2\text{NiMnO}_6$. *Journal of Physics D: Applied Physics*, 44(24):245405, 2011.
- [159] Ruchika Yadav and Suja Elizabeth. Magnetic frustration and dielectric relaxation in insulating $\text{Nd}_2\text{NiMnO}_6$ double perovskites. *Journal of Applied Physics*, 117(5), 2015.
- [160] D. Choudhury, P. Mandal, R. Mathieu, A. Hazarika, S. Rajan, A. Sundaresan, U. V. Waghmare, R. Knut, O. Karis, P. Nordblad, and D. D. Sarma. Near-room-temperature colossal magnetodielectricity and multiglass properties in partially disordered $\text{La}_2\text{NiMnO}_6$. *Physical Review Letters*, 108(12):127201, March 2012. doi: 10.1103/PhysRevLett.108.127201. Epub 2012 Mar 19.

- [161] Felicia Gheorghiu, Lavinia Curecheriu, Isabelle Lisiecki, Patricia Beaunier, Simona Feraru, Mircea N Palamaru, Valentina Musteata, Nicoleta Lupu, and Liliana Mitoseriu. Functional properties of sm2nimno6 multiferroic ceramics prepared by spark plasma sintering. *Journal of Alloys and Compounds*, 649:151–158, 2015.
- [162] KB Zhou, HD Chen, Qun Tian, BW Zhu, DX Shen, and XB Xu. Synergistic effect of palladium and oxygen vacancies in the pd/perovskite catalysts synthesized by the spc method. *Journal of Environmental Sciences (China)*, 17(1):19–24, 2005.
- [163] Priti V Gosavi and Rajesh B Biniwale. Pure phase lafeo3 perovskite with improved surface area synthesized using different routes and its characterization. *Materials Chemistry and Physics*, 119(1-2):324–329, 2010.
- [164] Bernard Dennis Cullity and RJPT Smoluchowski. Elements of x-ray diffraction. *Physics Today*, 10(3):50–50, 1957.
- [165] William Henry Bragg and William Lawrence Bragg. The reflection of x-rays by crystals. *Proceedings of the Royal Society of London. Series A, Containing Papers of a Mathematical and Physical Character*, 88(605):428–438, 1913.
- [166] Soorya N Kabekkodu, Anja Dosen, and Thomas N Blanton. 5+: A comprehensive powder diffraction fileTM for materials characterization. *Powder Diffraction*, 39(2):47–59, 2024.
- [167] WB Dress, PD Miller, JM Pendlebury, Paul Perrin, and Norman F Ramsey. Search for an electric dipole moment of the neutron. *Physical Review D*, 15(1):9, 1977.
- [168] Helmut Schober. An introduction to the theory of nuclear neutron scattering in condensed matter. *Journal of Neutron Research*, 17(3-4):109–357, 2014. doi: 10.3233/JNR-140016.
- [169] E Ressouche. Reminder: Magnetic structures description and determination by neutron diffraction. *École thématique de la Société Française de la Neutronique*, 13:02001, 2014.

- [170] Laurent C Chapon, Pascal Manuel, Paolo G Radaelli, Chris Benson, Leigh Perrott, Stuart Ansell, Nigel J Rhodes, Davide Raspino, D Duxbury, E Spill, et al. Wish: The new powder and single crystal magnetic diffractometer on the second target station. *Neutron News*, 22(2):22–25, 2011.
- [171] Dylan Behr. *On the Phenomenology of Competing Instabilities in Selected Transition Metal Oxides*. Ph.d. thesis, University College London, London, UK, September 2024. Submitted in partial fulfilment of the requirements for the award of the degree of Doctor of Philosophy.
- [172] Ricardo D dos Reis, Ulisses F Kaneko, Barbara A Francisco, Jairo Fonseca Jr, Marcos AS Eleoterio, and Narcizo M Souza-Neto. Preliminary overview of the extreme condition beamline (ema) at the new brazilian synchrotron source (sirius). In *Journal of Physics: Conference Series*, volume 1609, page 012015. IOP Publishing, 2020.
- [173] Renan Ramalho Geraldes, Sergio Augusto Lordano Luiz, João Leandro de Brito Neto, Telles René Silva Soares, Ricardo Donizeth Dos Reis, Guilherme A Calligaris, Gert Witvoet, and JPMB Vermeulen. Fly-scan-oriented motion analyses and upgraded beamline integration architecture for the high-dynamic double-crystal monochromator at sirius/lnls. *Synchrotron Radiation*, 30(1):90–110, 2023.
- [174] Bernard Dennis Cullity and Chad D Graham. *Introduction to magnetic materials*. John Wiley & Sons, 2011.
- [175] Richard L McCreery. *Raman spectroscopy for chemical analysis*. John Wiley & Sons, 2005.
- [176] Hugo M Rietveld. A profile refinement method for nuclear and magnetic structures. *Applied Crystallography*, 2(2):65–71, 1969.
- [177] Juan Rodríguez-Carvajal. Recent advances in magnetic structure determination by neutron powder diffraction. *Physica B: Condensed Matter*, 192(1-2):55–69, 1993.
- [178] Juan Rodriguez-Carvajal. Fullprof. *CEA/Saclay, France*, 1045:132–146, 2001.

- [179] Alexei A Belik. Rise of a-site columnar-ordered $a_2a'a''b_4o_{12}$ quadruple perovskites with intrinsic triple order. *Dalton Transactions*, 47(10):3209–3217, 2018.
- [180] Amitava Ghosh, Roumita Roy, RC Sahoo, Sachindra Nath Sarangi, Mithun Ghosh, Dipak Mazumdar, D Samal, PS Anil Kumar, Zakir Hossain, Sudipta Kanungo, et al. Magnetic anisotropy and magnetocaloric effect in gd_2nimno_6 thin films. *Physical Review B*, 108(21):214423, 2023.
- [181] RI Dass, J-Q Yan, and JB Goodenough. Oxygen stoichiometry, ferromagnetism, and transport properties of $la_{2-x}nimno_{6+\delta}$. *Physical Review B*, 68(6):064415, 2003.
- [182] Amit Kumar Singh, Samta Chauhan, Saurabh Kumar Srivastava, and Ramesh Chandra. Influence of antisite disorders on the magnetic properties of double perovskite ind_2nimno_6 . *Solid State Communications*, 242:74–78, 2016.
- [183] Ranjan Das, Premakumar Yanda, A Sundaresan, and DD Sarma. Ground-state ferrimagnetism and magneto-caloric effects in ind_2nimno_6 . *Materials Research Express*, 6(11):116122, 2019.
- [184] Masahito Mochizuki, Nobuo Furukawa, and Naoto Nagaosa. Spin model of magnetostrictions in multiferroic mn perovskites. *Phys. Rev. Lett.*, 105(3):037205, 2010. doi: 10.1103/PhysRevLett.105.037205.
- [185] Anzar Ali, G Sharma, Abhinay Vardhan, Kanika Pasrija, S Rajput, Tulika Maitra, Sanjeev Kumar, and Yogesh Singh. Magnetocaloric effects from an interplay of magnetic sublattices in ind_2nimno_6 . *Journal of Physics: Condensed Matter*, 31(30):305803, 2019.
- [186] Hena Das, Umesh V Waghmare, T Saha-Dasgupta, and DD Sarma. Electronic structure, phonons, and dielectric anomaly in ferromagnetic insulating double perovskite la_2nimno_6 . *Physical review letters*, 100(18):186402, 2008.
- [187] RJ Booth, R Fillman, H Whitaker, Abanti Nag, RM Tiwari, KV Ramanujachary, J Gopalakrishnan, and SE Lofland. An investigation of structural, magnetic and dielectric properties of r_2nimno_6 (r = rare earth, y). *Materials Research Bulletin*, 44(7):1559–1564, 2009.

- [188] Chenyang Shi, Yongmei Hao, and Zhongbo Hu. Local valence and physical properties of double perovskite $\text{Nd}_2\text{NiMnO}_6$. *Journal of Physics D: Applied Physics*, 44(24):245405, jun 2011. doi: 10.1088/0022-3727/44/24/245405. URL <https://dx.doi.org/10.1088/0022-3727/44/24/245405>.
- [189] J Sánchez-Benítez, MJ Martínez-Lope, JA Alonso, and JL García-Muñoz. Magnetic and structural features of the $\text{NdNi}_1-x\text{Mn}_x\text{O}_3$ perovskite series investigated by neutron diffraction. *Journal of Physics: Condensed Matter*, 23(22):226001, 2011.
- [190] L. C. Chapon, P. Manuel, P. G. Radaelli, C. Benson, L. Perrott, S. Ansell, N. J. Rhodes, D. Raspino, D. Duxbury, E. Spill, and J. Norris. Wish: The new powder and single crystal magnetic diffractometer on the second target station. *Neutron News*, 22(2):22–25, 2011. doi: 10.1080/10448632.2011.569650. URL <https://doi.org/10.1080/10448632.2011.569650>.
- [191] J. Rodríguez-Carvajal. Recent advances in magnetic structure determination by neutron powder diffraction, 1993. FULLPROF software.
- [192] B. J. Campbell, H. T. Stokes, D. E. Tanner, and D. M. Hatch. Isodistort: A tool for exploring structural distortions. *Journal of Applied Crystallography*, 39(4):607–614, 2006. doi: 10.1107/S0021889806014075.
- [193] Anzar Ali, Gyaneshwar Sharma, and Yogesh Singh. Critical behavior near the ferromagnetic phase transition in double perovskite $\text{Nd}_2\text{NiMnO}_6$. In *AIP Conference Proceedings*, volume 1953. AIP Publishing, 2018.
- [194] Yusheng Zhao, Donald J Weidner, John B Parise, and David E Cox. Thermal expansion and structural distortion of perovskite—data for NaMgF_3 perovskite. part i. *Physics of the Earth and Planetary Interiors*, 76(1-2): 1–16, 1993.
- [195] Dipak Mazumdar and I Das. Structural, magnetic, and magnetocaloric properties of the multiferroic host double perovskite compound Pr_2FeO_6 . *Physical Chemistry Chemical Physics*, 23(9):5596–5606, 2021.
- [196] P Neenu Lekshmi, GR Raji, M Vasundhara, Manoj Raama Varma, S Savitha Pillai, and M Valant. Re-entrant spin glass behaviour and magneto-dielectric effect in insulating $\text{Sm}_2\text{NiMnO}_6$ double perovskite. *Journal of Materials Chemistry C*, 1(40):6565–6574, 2013.

- [197] Elbio Dagotto, Takashi Hotta, and Adriana Moreo. Colossal magnetoresistant materials: the key role of phase separation. *Physics reports*, 344(1-3): 1–153, 2001.
- [198] RS Silva Jr, C Santos, MT Escote, BFO Costa, NO Moreno, SPA Paz, RS Angélica, and NS Ferreira. Griffiths-like phase, large magnetocaloric effect, and unconventional critical behavior in the NdSrCoFeO_{6-x} disordered double perovskite. *Physical Review B*, 106(13):134439, 2022.
- [199] Dexin Yang, Giulio I Lampronti, CR Sebastian Haines, and Michael A Carpenter. Magnetoelastic coupling behavior at the ferromagnetic transition in the partially disordered double perovskite $\text{La}_{1-x}\text{Ca}_x\text{MnO}_6$. *Physical Review B*, 100(1):014304, 2019.
- [200] Rinku Kumar, Padmanabhan Balasubramanian, M Anas, Ankita Singh, Ramesh Chandra, and VK Malik. Griffiths phase, re-entrant spin-glass behaviour and schottky anomaly in anti-site disordered double perovskite $\text{Pr}_{2-x}\text{Mn}_{1+x}\text{NiO}_6$. *Physica Scripta*, 98(10):105931, 2023.
- [201] K Jonason, J Mattsson, and P Nordblad. Dynamic susceptibility of a re-entrant ferromagnet. *Physical Review B*, 53(10):6507, 1996.
- [202] John M Attah-Baah, Dmitry D Khalyavin, Pascal Manuel, Nilson S Ferreira, Alexei A Belik, and Roger D Johnson. Spin reorientation and the interplay of magnetic sublattices in $\text{Er}_2\text{CuMnMn}_4\text{O}_{12}$. *Structural Science*, 80(6), 2024.
- [203] Wasim Akram, Manisha Bansal, Reshma Peremadathil Pradeep, Aswathi Kaipamangalath, Samir Kumar Giri, and Tuhin Maity. Evolution of the inverse magnetocaloric effect for random-field to spin-glass crossover in SmCaCoMnO_6 - SmMnO_3 nanocomposite. *Physical Review B*, 107(22):224403, 2023.
- [204] Gyaneshwar Sharma, TS Tripathi, J Saha, and S Patnaik. Magnetic entropy change and critical exponents in double perovskite Y_2NiMnO_6 . *Journal of magnetism and magnetic materials*, 368:318–323, 2014.
- [205] Aleksandr M Tishin and Youry I Spichkin. *The magnetocaloric effect and its applications*. CRC Press, 2016.

- [206] Tirthankar Chakraborty, Hariharan Nhalil, Ruchika Yadav, Aditya A Wagh, and Suja Elizabeth. Magnetocaloric properties of r2nimno6 ($\text{r} = \text{pr, nd, tb, ho and y}$) double perovskite family. *Journal of Magnetism and Magnetic Materials*, 428:59–63, 2017.
- [207] RC Sahoo, Sananda Das, and TK Nath. Role of gd spin ordering on magnetocaloric effect and ferromagnetism in sr substituted gd2comno6 double perovskite. *Journal of Applied Physics*, 124(10), 2018.
- [208] V Franco and A Conde. Scaling laws for the magnetocaloric effect in second order phase transitions: From physics to applications for the characterization of materials. *international journal of refrigeration*, 33(3):465–473, 2010.
- [209] Carlos Romero-Muniz, Ryo Tamura, Shu Tanaka, and Victorino Franco. Applicability of scaling behavior and power laws in the analysis of the magnetocaloric effect in second-order phase transition materials. *Physical Review B*, 94(13):134401, 2016.
- [210] Yikun Zhang, Yun Tian, Zhenqian Zhang, Youshun Jia, Bin Zhang, Minqiang Jiang, Jiang Wang, and Zhongming Ren. Magnetic properties and giant cryogenic magnetocaloric effect in b-site ordered antiferromagnetic gd2mgtio6 double perovskite oxide. *Acta Materialia*, 226:117669, 2022.
- [211] Yujia Liu, Weiqi Liu, Yue Li, Shuangjiu Feng, Zhitao Zhang, Xucai Kan, and Xiansong Liu. Investigation of griffiths phase, spin reorientation and magnetism in double perovskite gd2femno6 . *Ceramics International*, 49(10):15536–15543, 2023.
- [212] GV Brown. Magnetic heat pumping near room temperature. *Journal of Applied Physics*, 47(8):3673–3680, 1976.
- [213] O Tegus, E Brück, KHJ Buschow, and FR De Boer. Transition-metal-based magnetic refrigerants for room-temperature applications. *Nature*, 415(6868):150–152, 2002.
- [214] John M Attah-Baah, Romualdo S Silva Jr, Cledson Santos, Maria H Carvalho, and Nilson S Ferreira. Magnetocaloric effect and critical behavior across the second-order ferromagnetic–paramagnetic phase transition of a NdSmNiMnO_6 double perovskite. *ACS omega*, 2025.

- [215] James S Kouvel and Michael E Fisher. Detailed magnetic behavior of nickel near its curie point. *Physical Review*, 136(6A):A1626, 1964.
- [216] Michael E Fisher. The theory of equilibrium critical phenomena. *Reports on progress in physics*, 30(2):615, 1967.
- [217] Anthony Arrott and John E Noakes. Approximate equation of state for nickel near its critical temperature. *Physical Review Letters*, 19(14):786, 1967.
- [218] H Eugene Stanley. *Phase transitions and critical phenomena*, volume 7. Clarendon Press, Oxford, 1971.
- [219] Yu Liu and C Petrovic. Three-dimensional magnetic critical behavior in CrI_3 . *Physical Review B*, 97(1):014420, 2018.
- [220] Harikrishnan S Nair, Diptikanta Swain, Shilpa Adiga, Chandrabhas Narayana, Suja Elizabeth, et al. Griffiths phase-like behavior and spin-phonon coupling in double perovskite $\text{Nb}_2\text{NiMnO}_6$. *Journal of applied physics*, 110(12), 2011.
- [221] Anasua Khan, Debdatta Banerjee, Divya Rawat, TK Nath, Ajay Soni, Swastika Chatterjee, and A Taraphder. Emergence of spin-phonon coupling in Gd -doped $\text{Y}_{1-x}\text{Ca}_x\text{CoMnO}_6$ double perovskite oxide: a combined experimental and ab-initio study. *arXiv preprint arXiv:2407.02407*, 2024.
- [222] CL Bull, D Gleeson, and KS Knight. Determination of b-site ordering and structural transformations in the mixed transition metal perovskites $\text{La}_{2-x}\text{Ca}_x\text{MnO}_6$ and $\text{La}_{2-x}\text{NiMnO}_6$. *Journal of Physics: Condensed Matter*, 15(29):4927, 2003.
- [223] MN Iliev, MM Gospodinov, MP Singh, J Meen, KD Truong, P Fournier, and S Jandl. Growth, magnetic properties, and raman scattering of $\text{La}_2\text{NiMnO}_6$ single crystals. *Journal of Applied Physics*, 106(2), 2009.
- [224] MN Iliev, H-G Lee, VN Popov, MV Abrashev, A Hamed, RL Meng, and CW Chu. Raman-and infrared-active phonons in hexagonal YMnO_3 : experiment and lattice-dynamical calculations. *Physical Review B*, 56(5):2488, 1997.

- [225] M. N. Iliev, H. Guo, and A. Gupta. Raman spectroscopy evidence of strong spin-phonon coupling in epitaxial thin films of the double perovskite $\text{La}_2\text{NiMnO}_6$. *Applied Physics Letters*, 90(15):151914, 04 2007. ISSN 0003-6951. doi: 10.1063/1.2721142. URL <https://doi.org/10.1063/1.2721142>.
- [226] Shiming Zhou, Lei Shi, Haipeng Yang, and Jiyin Zhao. Evidence of short-range magnetic ordering above T_c in the double perovskite $\text{La}_2\text{NiMnO}_6$. *Applied Physics Letters*, 91(17), 2007.
- [227] M Viswanathan, PS Anil Kumar, Venkata Srinu Bhadrani, Chandrabhas Narayana, AK Bera, and SM Yusuf. Influence of lattice distortion on the curie temperature and spin-phonon coupling in $\text{LaMnO}_{0.5}\text{Co}_{0.5}\text{O}_3$. *Journal of Physics: Condensed Matter*, 22(34):346006, 2010.
- [228] MN Iliev, VN Popov, AP Litvinchuk, MV Abrashev, Joakim Bäckström, YY Sun, RL Meng, and CW Chu. Comparative raman studies of Sr_2RuO_4 , $\text{Sr}_3\text{Ru}_2\text{O}_7$ and $\text{Sr}_4\text{Ru}_3\text{O}_{10}$. *Physica B: Condensed Matter*, 358(1-4):138–152, 2005.
- [229] M Balkanski, RF Wallis, and E Haro. Anharmonic effects in light scattering due to optical phonons in silicon. *Physical Review B*, 28(4):1928, 1983.
- [230] PG Klemens. Anharmonic decay of optical phonons. *Physical Review*, 148(2):845, 1966.
- [231] Raimundo Bezerra Macedo Filho, Alejandro Pedro Ayala, and Carlos William de Araujo Paschoal. Spin-phonon coupling in Y_2NiMnO_6 double perovskite probed by raman spectroscopy. *Applied Physics Letters*, 102(19), 2013.
- [232] Christoph Meyer, Philipp Ksoll, Vladimir Roddatis, and Vasily Moshnyaga. Spin-phonon coupling in A_2BmNO_6 ($\text{A} = \text{La, Pr, Nd, Sm, Gd}$; $\text{B} = \text{Co, Ni}$) double-perovskite thin films: impact of the a-site cation radius. *Crystals*, 11(7):747, 2021.
- [233] Arkadeb Pal, Surajit Ghosh, Amish G Joshi, Shiv Kumar, Swapnil Patil, Prince K Gupta, Prajyoti Singh, VK Gangwar, P Prakash, Ranjan K Singh, et al. Investigation of multi-mode spin-phonon coupling and local b-site disorder in $\text{Pr}_2\text{CoFeO}_6$ by raman spectroscopy and correlation with its electronic

- structure by xps and xas studies. *Journal of Physics: Condensed Matter*, 31(27):275802, 2019.
- [234] D Choudhury, P Mandal, Roland Mathieu, A Hazarika, S Rajan, A Sundaresan, UV Waghmare, Ronny Knut, Olof Karis, Per Nordblad, et al. Near-room-temperature colossal magnetodielectricity and multiglass properties in partially disordered $\text{La}_{2-x}\text{NiMnO}_6$. *Physical review letters*, 108(12):127201, 2012.
- [235] E Granado, A García, JA Sanjurjo, C Rettori, I Torriani, F Prado, RD Sánchez, A Caneiro, and SB Oseroff. Magnetic ordering effects in the raman spectra of $\text{La}_{1-x}\text{Mn}_{1-x}\text{O}_3$. *Physical Review B*, 60(17):11879, 1999.
- [236] J Laverdière, S Jandl, AA Mukhin, V Yu Ivanov, VG Ivanov, and MN Iliev. Spin-phonon coupling in orthorhombic R_2MnO_3 ($\text{R} = \text{Pr, Nd, Sm, Eu, Gd, Tb, Dy, Ho, Y}$): A raman study. *Physical Review B—Condensed Matter and Materials Physics*, 73(21):214301, 2006.
- [237] JOHN MICHAEL DAVID Coey, P Stamenov, RD Gunning, M Venkatesan, and K Paul. Ferromagnetism in defect-ridden oxides and related materials. *New Journal of Physics*, 12(5):053025, 2010.
- [238] AS Erickson, Sumohan Misra, Gordon J Miller, RR Gupta, Z Schlesinger, WA Harrison, JM Kim, and IR Fisher. Ferromagnetism in the mott insulator Ba_2NiO_3 . *Physical Review Letters*, 99(1):016404, 2007.
- [239] Manh-Huong Phan and Seong-Cho Yu. Review of the magnetocaloric effect in manganite materials. *Journal of Magnetism and Magnetic Materials*, 308(2):325–340, 2007.
- [240] Warren E Pickett. Electronic structure of the high-temperature oxide superconductors. *Reviews of Modern Physics*, 61(2):433, 1989.
- [241] Maria Retuerto, Stella Skiadopoulou, Man-Rong Li, Artem M. Abakumov, Mark Croft, Alexander Ignatov, Tapati Sarkar, Brian M. Abbett, Jan Pokorný, Maxim Savinov, et al. $\text{Pb}_{2-x}\text{MnTeO}_6$ double perovskite: An antipolar antiferromagnet. *Inorganic Chemistry*, 55(9):4320–4329, 2016.

- [242] BJ Kim, Hosub Jin, SJ Moon, J-Y Kim, B-G Park, CS Leem, Jaejun Yu, TW Noh, C Kim, S-J Oh, et al. Novel j eff= 1/2 mott state induced by relativistic spin-orbit coupling in Sr_2IrO_4 . *Physical review letters*, 101(7):076402, 2008.
- [243] Gang Cao and Pedro Schlottmann. The challenge of spin-orbit-tuned ground states in iridates: a key issues review. *Reports on Progress in Physics*, 81(4):042502, 2018.
- [244] A Kolchinskaya, P Komissinskiy, M Baghaie Yazdi, M Vafaei, D Mikhailova, N Narayanan, H Ehrenberg, F Wilhelm, A Rogalev, and L Alff. Magnetism and spin-orbit coupling in ir-based double perovskites $\text{La}_2\text{SrIrO}_6$. *Physical Review B—Condensed Matter and Materials Physics*, 85(22):224422, 2012.
- [245] T Dey, A Maljuk, DV Efremov, O Kataeva, S Gass, CGF Blum, F Steckel, D Gruner, T Ritschel, AUB Wolter, et al. Ba_2YrO_6 : a cubic double perovskite material with ir 5+ ions. *Physical Review B*, 93(1):014434, 2016.
- [246] Gyaneswar Sharma, Kanika Pasrija, Anzar Ali, Sanjeev Kumar, and Yogesh Singh. Large magnetocaloric effect and magnetic phase transitions in $\text{Nd}_2\text{NiMnO}_6$. *arXiv preprint arXiv:1610.07742*, 2016.
- [247] Shohaib Abass, Fauqia Bilal, Khalid Sultan, Mudassir Rashid Rather, and Mohd Ikram. Understanding the impact of Ca doping on structural, morphological and low temperature transport properties of $\text{Nd}_2\text{NiMnO}_6$. *Ceramics International*, 50(7):10216–10224, 2024.
- [248] C Ritter, S Sharma, and DT Adroja. Magnetic structures of the iridium-based double perovskites $\text{Pr}_2\text{NiIrO}_6$ and $\text{Nd}_2\text{NiIrO}_6$ reinvestigated using neutron diffraction. *Physical Review Materials*, 6(8):084405, 2022.
- [249] H Guo, C Ritter, Y Su, AC Komarek, and JS Gardner. Distinct magnetic ground states of R_2ZnIrO_6 ($\text{R} = \text{La}, \text{Nd}$) determined by neutron powder diffraction. *Physical Review B*, 103(6):L060402, 2021.
- [250] M. M. Attah-Baah and et al. Structural and magnetic transitions in $\text{Nd}_2\text{NiMnO}_6$. Manuscript in preparation, 2024.

- [251] RC Currie, JF Vente, E Frikkee, and DJW Ijdo. The structure and magnetic properties of La_2MnO_6 with $\text{M} = \text{Mg, Co, Ni, and Zn}$. *Journal of Solid State Chemistry*, 116(1):199–204, 1995.
- [252] Xiaxin Ding, Bin Gao, Elizabeth Krenkel, Charles Dawson, James C Eckert, Sang-Wook Cheong, and Vivien Zapf. Magnetic properties of double perovskite $\text{Ln}_2\text{CoIrO}_6$ ($\text{Ln} = \text{Eu, Tb, Ho}$): Hetero-tri-spin 3d-5d-4f systems. *Physical Review B*, 99(1):014438, 2019.
- [253] A Meisel and G Leonhardt. Die kristallstruktur von β -iridium (iii)-chlorid. *Zeitschrift für anorganische und allgemeine Chemie*, 339(1-2):57–66, 1965.
- [254] Catherine E Housecroft and Alan G Sharpe. *Chimie inorganique*. De Boeck Supérieur, 2010.
- [255] John E Greedan. Geometrically frustrated magnetic materials. *Functional Oxides*, 11:41–117, 2010.
- [256] AP Ramirez. Strongly geometrically frustrated magnets. *Annual Review of Materials Science*, 24(1):453–480, 1994.
- [257] P Kayser, Angel Munoz, Jose Luis Martinez, F Fauth, Maria Teresa Fernández-Díaz, and Jose Antonio Alonso. Enhancing the néel temperature in $3\text{d}/5\text{d}$ R_2NiIrO_6 ($\text{R} = \text{La, Pr and Nd}$) double perovskites by reducing the R^{3+} ionic radii. *Acta Materialia*, 207:116684, 2021.
- [258] Yoshinori Tokura and Naoto Nagaosa. Orbital physics in transition-metal oxides. *science*, 288(5465):462–468, 2000.
- [259] K-I Kobayashi, T Kimura, Y Tomioka, H Sawada, K Terakura, and YJPRB Tokura. Intergrain tunneling magnetoresistance in polycrystals of the ordered double perovskite $\text{Sr}_2\text{FeReO}_6$. *Physical Review B*, 59(17):11159, 1999.
- [260] Leon Balents. Spin liquids in frustrated magnets. *nature*, 464(7286):199–208, 2010.
- [261] Kurt Binder and A Peter Young. Spin glasses: Experimental facts, theoretical concepts, and open questions. *Reviews of Modern physics*, 58(4):801, 1986.

- [262] David Sherrington and Scott Kirkpatrick. Infinite-ranged models of spin-glasses. *Phys. Rev. B*, 17(11):4384–4403, 1978.
- [263] JG Cheng, Y Sui, ZN Qian, ZG Liu, JP Miao, XQ Huang, Z Lu, Y Li, XJ Wang, and WH Su. Schottky-like anomaly in the low-temperature specific heat of single-crystal NdMnO_3 . *Solid state communications*, 134(6):381–384, 2005.
- [264] JG Cheng, Y Sui, XJ Wang, ZG Liu, JP Miao, XQ Huang, Z Lü, ZN Qian, and WH Su. Specific heat of single-crystal PrMnO_3 . *Journal of Physics: Condensed Matter*, 17(37):5869, 2005.
- [265] S Harikrishnan, CM Naveen Kumar, HL Bhat, Suja Elizabeth, UK Röbller, K Dörr, S Röbller, and S Wirth. Investigations on the spin-glass state in $\text{La}_{1-x}\text{Sr}_x\text{MnO}_3$ single crystals through structural, magnetic and thermal properties. *Journal of Physics: Condensed Matter*, 20(27):275234, 2008.
- [266] Brian F Woodfield, Michael L Wilson, and Jeff M Byers. Low-temperature specific heat of $\text{La}_{1-x}\text{Sr}_x\text{MnO}_{3+\delta}$. *Physical review letters*, 78(16):3201, 1997.
- [267] Anatoly Beznosov, Elena Fertman, Vladimir Desnenko, Marcela Kajňáková, and Alexander Feher. The Nd-Mn exchange interaction, low temperature specific heat and magnetism of $\text{Nd}_{2/3}\text{Ca}_{1/3}\text{MnO}_3$. *Journal of magnetism and magnetic materials*, 323(18-19):2380–2385, 2011.
- [268] Birender Singh, M Vogl, S Wurmehl, S Aswartham, B Büchner, and Pradeep Kumar. Coupling of lattice, spin, and intraconfigurational excitations of Eu^{3+} in Eu_2ZrO_6 . *Physical Review Research*, 2(4):043179, 2020.
- [269] Khyati Anand, Arkadeb Pal, Mohd Alam, Sambhab Dan, Shiv Kumar, Surajit Ghosh, Seema Kumari, A Das, Masahiro Sawada, Anita Mohan, et al. Emergence of metamagnetic transition, re-entrant cluster glass and spin phonon coupling in $\text{ Tb}_2\text{CoMnO}_6$. *Journal of Physics: Condensed Matter*, 33(27):275802, 2021.
- [270] MN Iliev, AP Litvinchuk, H-G Lee, CL Chen, ML Dezaneti, CW Chu, VG Ivanov, MV Abrashev, and VN Popov. Raman spectroscopy of SrRuO_3

- near the paramagnetic-to-ferromagnetic phase transition. *Physical Review B*, 59(1):364, 1999.
- [271] MN Iliev, P Padhan, and AJPRB Gupta. Temperature-dependent raman study of multiferroic $\text{Bi}_2\text{NiMnO}_6$ thin films. *Physical Review B—Condensed Matter and Materials Physics*, 77(17):172303, 2008.
- [272] Hlynur Gretarsson, JP Clancy, X Liu, JP Hill, Emil Bozin, Yogesh Singh, S Manni, Philipp Gegenwart, Jungho Kim, AH Said, et al. Crystal-field splitting and correlation effect on the electronic structure of a La_2NiO_3 . *Physical review letters*, 110(7):076402, 2013.
- [273] Venkata Srinu Bhadram, B Rajeswaran, A Sundaresan, and Chandrabhas Narayana. Spin-phonon coupling in multiferroic RCoO_3 (R = Y, Lu, Gd, Eu, Sm): a raman study. *Europhysics Letters*, 101(1):17008, 2013.
- [274] MN Iliev, MV Abrashev, H-G Lee, VN Popov, YY Sun, Ch Thomsen, RL Meng, and CW Chu. Raman spectroscopy of orthorhombic perovskite-like YMnO_3 and LaMnO_3 . *Physical Review B*, 57(5):2872, 1998.
- [275] KD Truong, MP Singh, S Jandl, and P Fournier. Influence of Ni/Mn cation order on the spin-phonon coupling in multifunctional $\text{La}_2\text{NiMnO}_6$ epitaxial films by polarized raman spectroscopy. *Physical Review B—Condensed Matter and Materials Physics*, 80(13):134424, 2009.
- [276] Jasminka Terzic, Hao Zheng, Feng Ye, Pedro Schlottmann, Hengdi Zhao, Shujuan Yuan, and Gang Cao. Breakdown of the spin-orbit imposed $J_{\text{eff}} = 0$ singlet state in double-perovskite iridates with $\text{Ir}^{5+}(5d^4)$ ions. In *APS March Meeting Abstracts*, volume 2017, pages K43–010, 2017.
- [277] Dharendra Kumar, Satish Kumar, and Vasant G Sathe. Spin-phonon coupling in ordered double perovskites A_2CoMnO_6 (A = La, Pr, Nd) probed by micro-Raman spectroscopy. *Solid state communications*, 194:59–64, 2014.
- [278] AB Sushkov, O Tchernyshyov, W Ratcliff II, SW Cheong, and HD Drew. Probing spin correlations with phonons in the strongly frustrated magnet ZnCr_2O_4 . *Physical review letters*, 94(13):137202, 2005.
- [279] Pankaj K Pandey, RJ Choudhary, Dileep K Mishra, VG Sathe, and DM Phase. Signature of spin-phonon coupling in Sr_2CoO_4 thin film: a Raman spectroscopic study. *Applied Physics Letters*, 102(14), 2013.

- [280] Stuart Calder, JH Lee, MB Stone, MD Lumsden, JC Lang, M Feygenson, Z Zhao, J-Q Yan, YG Shi, YS Sun, et al. Enhanced spin-phonon-electronic coupling in a 5 d oxide. *Nature Communications*, 6(1):8916, 2015.
- [281] Harish Kumar, VG Sathe, and AK Pramanik. Spin-phonon coupling in hole-doped pyrochlore iridates $\text{Y}_2\text{Ir}_2\text{O}_7$: A raman scattering study. *Journal of Magnetism and Magnetic Materials*, 478:148–154, 2019.
- [282] Xiaoyun Chen, Jun Xu, Yueshan Xu, Feng Luo, and Yaping Du. Rare earth double perovskites: a fertile soil in the field of perovskite oxides. *Inorganic Chemistry Frontiers*, 6(9):2226–2238, 2019.
- [283] LT Corredor, G Aslan-Cansever, M Sturza, Kaustuv Manna, A Maljuk, S Gass, T Dey, AUB Wolter, Olga Kataeva, A Zimmermann, et al. Iridium double perovskite Sr_2IrO_6 : A combined structural and specific heat study. *Physical Review B*, 95(6):064418, 2017.
- [284] Junping Yuan, Yan Zhang, Jiayue Xu, Tian Tian, Kuankuan Luo, and Liwu Huang. Novel Cr^{3+} -doped double-perovskite Ca_2MnBO_6 ($\text{M} = \text{Ga}, \text{Al}$) phosphor: Synthesis, crystal structure, photoluminescence and thermoluminescence properties. *Journal of Alloys and Compounds*, 815:152656, 2020.
- [285] Marin Cernea, F Vasiliu, C Plapcianu, Cristina Barthä, I Mercioniu, I Pasuk, R Lowndes, R Trusca, GV Aldica, and L Pintilie. Preparation by sol-gel and solid state reaction methods and properties investigation of double perovskite $\text{Sr}_2\text{FeMoO}_6$. *Journal of the European Ceramic Society*, 33(13-14):2483–2490, 2013.
- [286] Mohd Alam and Sandip Chatterjee. B-site order/disorder in $\text{A}_2\text{BB}'\text{O}_6$ and its correlation with their magnetic property. *Journal of Physics: Condensed Matter*, 35(22):223001, 2023.
- [287] Harold T Stokes, Erich H Kisi, Dorian M Hatch, and Christopher J Howard. Group-theoretical analysis of octahedral tilting in ferroelectric perovskites. *Structural Science*, 58(6):934–938, 2002.
- [288] Romualdo S Silva Jr, Javier Gainza, Cledson dos Santos, João Elias FS Rodrigues, Catherine Dejoie, Yves Huttel, Nevenko Biskup, Norbert M Nemes, José Luis Martínez, Nilson S Ferreira, et al. Magnetoelastic coupling

- and cryogenic magnetocaloric effect in two-site disordered GdSrCoFeO_6 double perovskite. *Chemistry of Materials*, 35(6):2439–2455, 2023.
- [289] J Krishna Murthy and A Venimadhav. Reentrant cluster glass behavior in $\text{La}_2\text{CoMnO}_6$ nanoparticles. *Journal of Applied Physics*, 113(16), 2013.
- [290] Qiuhan Li, Lei Xing, and Mingxiang Xu. Magnetic properties, resistivity and magnetoresistance effects of double perovskite $\text{La}_2\text{Co}_{1-x}\text{Fe}_x\text{MnO}_6$. *Journal of Alloys and Compounds*, 710:771–777, 2017.
- [291] Rosivaldo X Silva, Alan S de Menezes, Rafael M Almeida, Roberto L Moreira, R Paniago, Xavi Marti, Helena Reichlova, Miroslav Maryško, Marcos Vinicius dos S Rezende, and Carlos William A Paschoal. Structural order, magnetic and intrinsic dielectric properties of magnetoelectric $\text{La}_2\text{CoMnO}_6$. *Journal of Alloys and Compounds*, 661:541–552, 2016.
- [292] John B Goodenough, A Wold, RJ Arnett, and NJPR Menyuk. Relationship between crystal symmetry and magnetic properties of ionic compounds containing Mn^{3+} . *Physical Review*, 124(2):373, 1961.
- [293] G Blasse. Ferromagnetic interactions in non-metallic perovskites. *Journal of physics and Chemistry of Solids*, 26(12):1969–1971, 1965.
- [294] VL Joseph Joly, PA Joy, SK Date, and CS Gopinath. Two ferromagnetic phases with different spin states of Mn and Ni in $\text{La}_{0.5}\text{Ni}_{0.5}\text{O}_3$. *Physical Review B*, 65(18):184416, 2002.
- [295] Haizhong Guo, Arunava Gupta, Maria Varela, Stephen Pennycook, and Jiandi Zhang. Local valence and magnetic characteristics of $\text{La}_2\text{NiMnO}_6$. *Physical Review B—Condensed Matter and Materials Physics*, 79(17):172402, 2009.
- [296] MP Singh, KD Truong, S Jandl, and P Fournier. Long-range Ni/Mn structural order in epitaxial double perovskite $\text{La}_2\text{NiMnO}_6$ thin films. *Physical Review B—Condensed Matter and Materials Physics*, 79(22):224421, 2009.
- [297] MC Sánchez, J García, J Blasco, G Subías, and J Perez-Cacho. Local electronic and geometrical structure of $\text{La}_{1-x}\text{Mn}_x\text{O}_{3+\delta}$ perovskites determined by x-ray-absorption spectroscopy. *Physical Review B*, 65(14):144409, 2002.

- [298] AN Vasiliev, OS Volkova, LS Lobanovskii, IO Troyanchuk, Z Hu, LH Tjeng, DI Khomskii, H-J Lin, CT Chen, N Tristan, et al. Valence states and metamagnetic phase transition in partially b-site-disordered perovskite $\text{Eu}_{0.5}\text{Co}_{0.5}\text{O}_3$. *Physical Review B—Condensed Matter and Materials Physics*, 77(10):104442, 2008.
- [299] Supriyo Majumder, Malvika Tripathi, R Raghunathan, P Rajput, SN Jha, DO De Souza, L Olivi, S Chowdhury, RJ Choudhary, and DM Phase. Mapping the magnetic state as a function of antisite disorder in $\text{Sm}_{0.2}\text{Ni}_{0.8}\text{MnO}_6$ double perovskite thin films. *Physical Review B*, 105(2):024408, 2022.
- [300] K.D. Truong, M.P. Singh, S. Jandl, and P. Fournier. Investigation of phonon behavior in $\text{Pr}_2\text{NiMnO}_6$ by micro-Raman spectroscopy. *Journal of Physics: Condensed Matter*, 23:052202, 2011. doi: 10.1088/0953-8984/23/5/052202.
- [301] R.B.M.E. Filho, A.P. Ayala, and C.W. De Araujo Paschoal. Spin-phonon coupling in Y_2NiMnO_6 double perovskite probed by Raman spectroscopy. *Applied Physics Letters*, 102:182904, 2013. doi: 10.1063/1.4804988.
- [302] Rui Vilarinho, Mads C Weber, Maël Guennou, AC Miranda, Catarina Dias, P Tavares, Jens Kreisel, Abilio Almeida, and J Agostinho Moreira. Magnetostructural coupling in RFeO_3 ($\text{R} = \text{Nd, Tb, Eu and Gd}$). *Scientific reports*, 12(1):9697, 2022.
- [303] Anjali Panchwatee, V Raghavendra Reddy, Ajay Gupta, and VG Sathe. Study of spin-phonon coupling and magnetic field induced spin reorientation in polycrystalline multiferroic GdFeO_3 . *Materials Chemistry and Physics*, 196:205–212, 2017.
- [304] H.S. Nair, T. Chatterji, and A.M. Strydom. Antisite disorder-induced exchange bias effect in multiferroic Y_2CoMnO_6 . *Applied Physics Letters*, 106, 2015. doi: 10.1063/1.4906204.
- [305] R.X. Silva, M.C. Castro Júnior, S. Yáñez-Vilar, M.S. Andújar, J. Mira, M.A. Señarís-Rodríguez, and C.W.A. Paschoal. Spin-phonon coupling in multiferroic Y_2CoMnO_6 . *Journal of Alloys and Compounds*, 690:909–915, 2017. doi: 10.1016/j.jallcom.2016.07.010.
- [306] E. Granado, N.O. Moreno, A. García, J.A. Sanjurjo, C. Rettori, I. Torriani, S.B. Oseroff, J.J. Neumeier, K.J. McClellan, S.-W. Cheong, and Y. Tokura.

- Phonon raman scattering in $r_{1-x}a_x\text{mno}_3$ ($r = \text{la, pr}$; $a = \text{ca, sr}$). Unpublished.
- [307] A. Nonato, B.S. Araujo, A.P. Ayala, A.P. Maciel, S. Yáñez-Vilar, M. Sánchez-Andújar, M.A. Señarís-Rodríguez, and C.W.A. Paschoal. Spin-phonon and magnetostriction phenomena in $\text{camn}_7\text{o}_{12}$ helimagnet probed by raman spectroscopy. *Applied Physics Letters*, 105:1–5, 2014. doi: 10.1063/1.4902234.
- [308] P.W. Anderson and H. Hasegawa. Considerations on double exchange. *Physical Review*, 100:675–681, 1955. doi: 10.1103/PhysRev.100.675.
- [309] S.H. Battle and P.D. Kim. Structural and electronic properties of the mixed co/ru perovskites aa'coruo_6 ($a, a' = \text{sr, ba, la}$). *Journal of Solid State Chemistry*, 114:174–183, 1994. doi: 10.1006/jssc.1994.1174.
- [310] A.J. Barón-González, C. Frontera, J.L. García-Muñoz, B. Rivas-Murias, and J. Blasco. Effect of cation disorder on structural, magnetic and dielectric properties of $\text{la}_2\text{mncoo}_6$ double perovskite. *Journal of Physics: Condensed Matter*, 23:496003, 2011. doi: 10.1088/0953-8984/23/49/496003.
- [311] I. Dass, J.Q. Yan, and J.B. Goodenough. Oxygen stoichiometry, ferromagnetism, and transport properties of $\text{la}_{2-x}\text{nimno}_{6+\delta}$. *Physical Review B*, 68:064415, 2003. doi: 10.1103/PhysRevB.68.064415.
- [312] J.M. De Teresa, M.R. Ibarra, P.A. Algarabel, C. Ritter, J. Blasco, J. García, A. del Moral, and Z. Arnold. Evidence for magnetic polarons in the magnetoresistive perovskites. *Nature*, 386:256–259, 1997. doi: 10.1038/386256a0.
- [313] J. Rodríguez-Carvajal. An introduction to the program (version july 2001). Technical report, Laboratoire Léon Brillouin (CEA-CNRS), 2002. Available at <https://www.ill.eu/sites/fullprof/>.
- [314] P. Thompson, D. E. Cox, and J. B. Hastings. Rietveld refinement of debye-scherrer synchrotron x-ray data from Al_2O_3 . *Journal of Applied Crystallography*, 20:79–83, 1987.
- [315] G.S. Pawley. Unit-cell refinement from powder diffraction scans. *Journal of Applied Crystallography*, 14:357–361, 1981. doi: 10.1107/S0021889881009618.

- [316] R.D. Dos Reis, U.F. Kaneko, B.A. Francisco, J. Fonseca, M.A.S. Eleotério, and N.M. Souza-Neto. Preliminary overview of the extreme condition beamline (ema) at the new brazilian synchrotron source (sirius). In *Journal of Physics: Conference Series*, volume 1609, page 012015, 2020. doi: 10.1088/1742-6596/1609/1/012015.
- [317] P. Hohenberg and W. Kohn. Inhomogeneous electron gas. *Physical Review*, 136:B864–B871, 1964. doi: 10.1103/PhysRev.136.B864.
- [318] W. Kohn and L.J. Sham. Self-consistent equations including exchange and correlation effects. *Physical Review*, 140:A1133–A1138, 1965. doi: 10.1103/PhysRev.140.A1133.
- [319] P. Blaha, K. Schwarz, G.K.H. Madsen, D. Kvasnicka, and J. Luitz. *WIEN2k: An Augmented Plane Wave + Local Orbitals Program for Calculating Crystal Properties*. Technische Universität Wien, Austria, 2001. URL <https://www.researchgate.net/publication/237132866>.
- [320] O. Krogh Andersen. Linear methods in band theory. *Physical Review B*, 12:3060–3083, 1975. doi: 10.1103/PhysRevB.12.3060.
- [321] V.I. Anisimov, A.I. Poteryaev, M.A. Korotin, A.O. Anokhin, and G. Kotliar. First-principles calculations of the electronic structure and spectra of strongly correlated systems: Dynamical mean-field theory. *Journal of Physics: Condensed Matter*, 9:7359–7367, 1997. doi: 10.1088/0953-8984/9/35/010.
- [322] J.P. Perdew, A. Ruzsinszky, G.I. Csonka, O.A. Vydrov, G.E. Scuseria, L.A. Constantin, X. Zhou, and K. Burke. Generalized gradient approximation for solids and their surfaces. *Physical Review Letters*, 100:136406, 2008. doi: 10.1103/PhysRevLett.100.136406.
- [323] A.M. Glazer. Perovskites modern and ancient. by roger h. mitchell. thunder bay, ontario: Almaz press, 2002. price usd 70.00. isbn 0-9689411-0-9. *Acta Crystallographica Section B: Structural Science*, 58:1075, 2002. doi: 10.1107/S0108768102020220.
- [324] K. Momma and F. Izumi. Vesta: A three-dimensional visualization system for electronic and structural analysis. *Journal of Applied Crystallography*, 41:653–658, 2008. doi: 10.1107/S0021889808012016.

- [325] Hong Jian Zhao, Xiao Qiang Liu, Xiang Ming Chen, and L Bellaiche. Effects of chemical and hydrostatic pressures on structural, magnetic, and electronic properties of $r\text{NiMnO}_6$ (r = rare-earth ion) double perovskites. *Physical Review B*, 90(19):195147, 2014.
- [326] Jonathan Spring, Gabriele De Luca, Simon Jöhr, Javier Herrero-Martín, Charles Guillemard, Cinthia Piamonteze, Carlos MM Rosário, Hans Hilgenkamp, and Marta Gibert. Paramagnetic nd sublattice and thickness-dependent ferromagnetism in $\text{Nd}_2\text{NiMnO}_6$ double perovskite thin films. *Physical Review Materials*, 7(10):104407, 2023.
- [327] Mohd Nasir, Mahmud Khan, Sunil Kumar, Subhash Bhatt, Nirmalendu Patra, Dibyendu Bhattacharya, Shambhu Nath Jha, Sajal Biring, and Somaditya Sen. The effect of high temperature annealing on the antisite defects in ferromagnetic $\text{La}_2\text{NiMnO}_6$ double perovskite. *Journal of Magnetism and Magnetic Materials*, 483:114–123, 2019.
- [328] Mohd Nasir, Sunil Kumar, Nirmalendu Patra, Dibyendu Bhattacharya, Shambhu Nath Jha, Dharma R Basaula, Subhash Bhatt, Mahmud Khan, Shun-Wei Liu, Sajal Biring, et al. Role of antisite disorder, rare-earth size, and superexchange angle on band gap, curie temperature, and magnetization of r_2NiMnO_6 double perovskites. *ACS Applied Electronic Materials*, 1(1):141–153, 2019.
- [329] Vera Cuartero, Sara Lafuerza, Mauro Rovezzi, Joaquín García, Javier Blasco, G Subías, and Erika Jiménez. X-ray absorption and emission spectroscopy study of mn and co valence and spin states in $\text{TbMn}_{1-x}\text{Co}_x\text{O}_3$. *Physical Review B*, 94(15):155117, 2016.
- [330] F Bridges, CH Booth, M Anderson, GH Kwei, JJ Neumeier, J Snyder, J Mitchell, JS Gardner, and E Brosha. Mn k-edge xanes studies of $\text{La}_{1-x}\text{A}_x\text{MnO}_3$ systems ($\text{A} = \text{Ca}, \text{Ba}, \text{Pb}$). *Physical Review B*, 63(21):214405, 2001.
- [331] Yuqiao Guo, Lei Shi, Shiming Zhou, Jiyin Zhao, Cailin Wang, Wenjie Liu, and Shiqiang Wei. Tunable exchange bias effect in sr-doped double perovskite $\text{La}_2\text{NiMnO}_6$. *Journal of Physics D: Applied Physics*, 46(17):175302, 2013.

- [332] Y. Li, Q. Lv, S. Feng, K.M. Ur Rehman, X. Kan, and X. Liu. A comparative investigation of b-site ordering and structure, magnetic, magnetocaloric effect, critical behavior in double perovskite Nd_2BmNO_6 ($\text{b} = \text{Co}$ and Ni). *Ceramics International*, 47:32599–32609, 2021. doi: 10.1016/j.ceramint.2021.08.155.
- [333] R.P. Madhogaria, E.M. Clements, V. Kalappattil, M.H. Phan, H. Srikanth, R. Das, N.T. Dang, D.P. Kozlenko, and N.S. Bingham. Metamagnetism and kinetic arrest in a long-range ferromagnetically ordered multicaloric double perovskite Y_2CoMnO_6 . *Journal of Magnetism and Magnetic Materials*, 507:166821, 2020. doi: 10.1016/j.jmmm.2020.166821.
- [334] G. Zhang, H. Chen, Z. Gu, P. Zhang, T. Zeng, and F. Huang. Facile synthesis, magnetic and electric characterization of mixed valence $\text{La}_{0.75}\text{K}_{0.25}\text{AmNiTiO}_6$ ($\text{a} = \text{Sr}$ and Ba) perovskites. *Inorganic Chemistry*, 56:10404–10411, 2017. doi: 10.1021/acs.inorgchem.7b01337.
- [335] T. Moriya and Y. Takahashi. Spin fluctuations in itinerant electron magnetism. In *Journal de Physique Colloques*, volume 39, 1978. doi: 10.1051/jphyscol:19786588.
- [336] Y. Tokura and Y. Tomioka. Colossal magnetoresistive manganites. *Journal of Magnetism and Magnetic Materials*, 200:1–23, 1999. doi: 10.1016/S0304-8853(99)00375-6.
- [337] S. Phokha, J. Klinkaewnarong, S. Hunpratub, K. Boonserm, E. Swatsitang, and S. Maensiri. Ferromagnetism in Fe-doped MnO nanoparticles. *Journal of Materials Science: Materials in Electronics*, 27:33–39, 2016. doi: 10.1007/s10854-015-3713-9.
- [338] R.R. Das, P.N. Lekshmi, S.C. Das, and P.N. Santhosh. Competing short-range magnetic correlations, metamagnetic behavior and spin-phonon coupling in $\text{Nd}_2\text{CoMnO}_6$ double perovskite. *Journal of Alloys and Compounds*, 773:770–777, 2019. doi: 10.1016/j.jallcom.2018.09.171.
- [339] I. Dzyaloshinsky. A thermodynamic theory of gadolinium molybdate. *Physica Status Solidi (B)*, 46:763–772, 1971. doi: 10.1002/pssb.2220460236.

- [340] S. Kumar, G. Giovannetti, J. van den Brink, and S. Picozzi. Theoretical prediction of multiferroicity in double perovskite Y_2NiMnO_6 . *Physical Review B*, 82:134429, 2010. doi: 10.1103/PhysRevB.82.134429.
- [341] Arkadeb Pal, Khyati Anand, Neha Patel, Amitabh Das, Surajit Ghosh, Peter Tsung-Wen Yen, Shin-Ming Huang, RK Singh, HD Yang, AK Ghosh, et al. Interplay of spin, phonon, and lattice degrees in a hole-doped double perovskite: Observation of spin-phonon coupling and magnetostriction effect. *Journal of Applied Physics*, 132(22), 2022.
- [342] M.R. Ibarra, P.A. Algarabel, C. Marquina, J. Blasco, and J. García. Large magnetovolume effect in yttrium doped la-ca-mn-o perovskite. *Physical Review Letters*, 75:3541–3544, 1995. doi: 10.1103/PhysRevLett.75.3541.
- [343] H.S. Nair, D. Swain, N. Hariharan, S. Adiga, C. Narayana, and S. Elizabeth. Griffiths phase-like behavior and spin-phonon coupling in double perovskite $\text{ Tb}_2\text{NiMnO}_6$. *Journal of Applied Physics*, 110:123919, 2011. doi: 10.1063/1.3671674.
- [344] KD Truong, MP Singh, S Jandl, and P Fournier. Investigation of phonon behavior in $\text{Pr}_2\text{NiMnO}_6$ by micro-Raman spectroscopy. *Journal of Physics: Condensed Matter*, 23(5):052202, 2011.
- [345] H.Z. Guo, J. Burgess, E. Ada, S. Street, A. Gupta, M.N. Iliev, A.J. Kellock, C. Magen, M. Varela, and S.J. Pennycook. Influence of defects on structural and magnetic properties of multifunctional $\text{La}_2\text{NiMnO}_6$ thin films. *Physical Review B*, 77:174423, 2008. doi: 10.1103/PhysRevB.77.174423.
- [346] M.O. Ramirez, M. Krishnamurthi, S. Denev, A. Kumar, S.Y. Yang, Y.H. Chu, E. Saiz, J. Seidel, A.P. Pyatakov, A. Bush, D. Viehland, J. Orenstein, R. Ramesh, and V. Gopalan. Two-phonon coupling to the antiferromagnetic phase transition in multiferroic BiFeO_3 . *Applied Physics Letters*, 92:022901, 2008. doi: 10.1063/1.2829681.
- [347] M.O. Ramirez, A. Kumar, S.A. Denev, Y.H. Chu, J. Seidel, L.W. Martin, S.Y. Yang, R.C. Rai, X.S. Xue, J.F. Ihlefeld, N.J. Podraza, E. Saiz, S. Lee, J. Klug, S.W. Cheong, M.J. Bedzyk, O. Auciello, D.G. Schlom, J. Orenstein, R. Ramesh, J.L. Musfeldt, A.P. Litvinchuk, and V. Gopalan. Spin-charge-

- lattice coupling through resonant multimagnon excitations in multiferroic bifeo₃. *Applied Physics Letters*, 94:161905, 2009. doi: 10.1063/1.3118576.
- [348] S. Kamba, V. Goian, V. Skoromets, J. Hejtmánek, V. Bovtun, M. Kempa, F. Borodavka, P. Vaněk, A.A. Belik, J.H. Lee, O. Pacheroová, and K.M. Rabe. Strong spin-phonon coupling in infrared and raman spectra of srmno₃. *Physical Review B*, 89:064308, 2014. doi: 10.1103/PhysRevB.89.064308.
- [349] W.S. Li, Z.X. Shen, Z.C. Feng, and S.J. Chua. Temperature dependence of raman scattering in hexagonal gallium nitride films. *Journal of Applied Physics*, 87:3332–3337, 2000. doi: 10.1063/1.372344.
- [350] H. Tang and I.P. Herman. Raman microprobe scattering of solid silicon and germanium at the melting temperature. *Physical Review B*, 43:2299–2304, 1991. doi: 10.1103/PhysRevB.43.2299.
- [351] M. Balkanski, R.F. Wallis, and E. Haro. Anharmonic effects in light scattering due to optical phonons in silicon. *Physical Review B*, 28:1928–1934, 1983. doi: 10.1103/PhysRevB.28.1928.
- [352] P.G. Klemens. Anharmonic decay of optical phonon in diamond. *Physical Review B*, 11:3206–3207, 1975. doi: 10.1103/PhysRevB.11.3206.
- [353] S. Sarkar, I. Maity, H.L. Pradeepa, G. Nayak, L. Marty, J. Renard, J. Coraux, N. Bendiab, V. Bouchiat, S. Das, K. Majumdar, M. Jain, and A. Bid. Anharmonicity in raman-active phonon modes in atomically thin mos₂. *Physical Review B*, 101:205302, 2020. doi: 10.1103/PhysRevB.101.205302.
- [354] A. Pal, C.H. Huang, T.W. Yen, P.H. Lee, Y.H. Chang, C.H. Yeh, T.W. Kuo, A. Tiwari, D.C. Kakarla, S.M. Huang, M.C. Chou, H.S. Kunwar, S. Rana, V.G. Sathe, B.H. Chen, Y.C. Chuang, and H.D. Yang. Spin-induced strongly correlated magnetodielectricity, magnetostriction effect, and spin-phonon coupling in helical magnet fe₃(po₄)o₃. *Physical Review B*, 106:094404, 2022. doi: 10.1103/PhysRevB.106.094404.
- [355] L. Du, J. Tang, Y. Zhao, X. Li, R. Yang, X. Hu, X. Bai, X. Wang, K. Watanabe, T. Taniguchi, D. Shi, G. Yu, X. Bai, T. Hasan, G. Zhang, and Z. Sun.

- Lattice dynamics, phonon chirality, and spin-phonon coupling in 2d itinerant ferromagnet Fe_3GeTe_2 . *Advanced Functional Materials*, 29:1904734, 2019. doi: 10.1002/adfm.201904734.
- [356] A. Pal, S. Ghosh, A.G. Joshi, S. Kumar, S. Patil, P.K. Gupta, P. Singh, V.K. Gangwar, P. Prakash, R.K. Singh, E.F. Schwier, M. Sawada, K. Shimada, A.K. Ghosh, A. Das, and S. Chatterjee. Investigation of multi-mode spin-phonon coupling and local b-site disorder in $\text{Pr}_2\text{CoFeO}_6$ by raman spectroscopy and correlation with its electronic structure by xps and xas studies. *Journal of Physics: Condensed Matter*, 31, 2019. doi: 10.1088/1361-648X/ab144f.
- [357] K. Anand, A. Pal, A.G. Joshi, P. Pal, and R. Singh. Giant exchange bias in antiferromagnetic $\text{Pr}_2\text{CoFe}_{0.5}\text{Mn}_{0.5}\text{O}_6$. n.d.
- [358] K.X. Xu, J.M. Lai, Y.F. Gao, F. Song, Y.J. Sun, P.H. Tan, and J. Zhang. High-order raman scattering mediated by self-trapped exciton in halide double perovskite. *Physical Review B*, 106:085205, 2022. doi: 10.1103/PhysRevB.106.085205.
- [359] J. Kusz, S. Juszczyk, and J. Warczewski. An x-ray diffraction study of magnetostriction in $\text{Zn}_x\text{Cu}_{1-x}\text{Cr}_2\text{Se}_4$ ($0.2 \leq x \leq 1.0$), 1988.
- [360] G. Kotnana, V.G. Sathe, and S. Narayana Jammalamadaka. Spin-phonon coupling in $\text{HoCr}_{1-x}\text{Fe}_x\text{O}_3$ ($x = 0$ and 0.5) compounds. *Journal of Raman Spectroscopy*, 49:764–770, 2018. doi: 10.1002/jrs.5332.
- [361] A. Ghosh, M. Palit, S. Maity, V. Dwij, S. Rana, and S. Datta. Spin-phonon coupling and magnon scattering in few-layer antiferromagnetic FePS_3 . *Physical Review B*, 103:064431, 2021. doi: 10.1103/PhysRevB.103.064431.
- [362] C. Meyer, V. Roddatis, P. Ksoll, B. Damaschke, and V. Moshnyaga. Structure, magnetism, and spin-phonon coupling in heteroepitaxial $\text{La}_2\text{CoMnO}_6/\text{Al}_2\text{O}_3(0001)$ films. *Physical Review B*, 98:134433, 2018. doi: 10.1103/PhysRevB.98.134433.
- [363] B. Poojitha, A. Rathore, A. Kumar, and S. Saha. Signatures of magnetostriction and spin-phonon coupling in magnetoelectric hexagonal 15r-baMnO_3 . *Physical Review B*, 102:134436, 2020. doi: 10.1103/PhysRevB.102.134436.

- [364] D. Haskel, G. Fabbri, N.M. Souza-Neto, M. Van Veenendaal, G. Shen, A.E. Smith, and M.A. Subramanian. Stability of the ferromagnetic ground state of $\text{La}_2\text{MnNiO}_6$ against large compressive stress. *Physical Review B*, 84:100403, 2011. doi: 10.1103/PhysRevB.84.100403.
- [365] P. Granger and V. I. Parvulescu. *Perovskites and Related Mixed Oxides*. Wiley, 2016. doi: 10.1002/9783527686605.
- [366] M. W. Lufaso, P. W. Barnes, and P. M. Woodward. Structure prediction of ordered and disordered multiple octahedral cation perovskites using spuds. *Acta Crystallographica Section B: Structural Science*, 62:397–410, 2006.
- [367] M. W. Lufaso and P. M. Woodward. Jahn-teller distortions, cation ordering and octahedral tilting in perovskites. *Acta Crystallographica Section B: Structural Science*, 60:10–20, 2004.
- [368] L. Li, P. Xu, S. Ye, et al. Magnetic properties and excellent cryogenic magnetocaloric performances in b-site ordered $\text{Re}_2\text{ZnMnO}_6$ ($\text{Re} = \text{Gd}, \text{Dy}$ and Ho) perovskites. *Acta Materialia*, 194:354–365, 2020.
- [369] J. Krishna Murthy, K. Devi Chandrasekhar, S. Mahana, D. Topwal, and A. Venimadhav. Giant magnetocaloric effect in $\text{Gd}_2\text{NiMnO}_6$ and $\text{Gd}_2\text{CoMnO}_6$ ferromagnetic insulators. *Journal of Physics D: Applied Physics*, 48:355001, 2015.
- [370] K. G. Sandeman. Magnetocaloric materials: The search for new systems. *Scripta Materialia*, 67:566–571, 2012.
- [371] V. Franco, J. S. Blázquez, B. Ingale, and A. Conde. The magnetocaloric effect and magnetic refrigeration near room temperature: Materials and models. *Annual Review of Materials Research*, 42:305–342, 2012.
- [372] C. Santos, J. M. Attah-Baah, R. S. S. Junior, et al. Insights into the Fe^{3+} doping effects on the structure and electron distribution of Cr_2O_3 nanoparticles. *Nanomaterials*, 13:980, 2023.
- [373] P. R. Mandal, A. Khan, and T. K. Nath. Antisite disorder driven magnetodielectric and magnetocaloric effect in double perovskite $\text{La}_{2-x}\text{Sr}_x\text{CoMnO}_6$ ($x = 0.0, 0.5, 1.0$). *Journal of Applied Physics*, 128:024104, 2020.

- [374] A. Fujita, S. Fujieda, Y. Hasegawa, and K. Fukamichi. Itinerant-electron metamagnetic transition and large magnetocaloric effects in $\text{La}(\text{Fe}_{1-x}\text{Si}_x)_2$ compounds and their hydrides. *Physical Review B*, 67:104416, 2003.
- [375] I. N. Bhatti, R. N. Mahato, and M. A. H. Ahsan. Magnetic behavior, griffiths phase and magneto-transport study in 3d based nano-crystalline double perovskite $\text{Pr}_2\text{CoMnO}_6$. *Physics Letters A*, 383:2326–2332, 2019.
- [376] Sam Mugiraneza and Alannah M Hallas. Tutorial: a beginner’s guide to interpreting magnetic susceptibility data with the curie-weiss law. *Communications Physics*, 5(1):95, 2022.
- [377] J. Y. Law, V. Franco, L. M. Moreno-Ramírez, et al. A quantitative criterion for determining the order of magnetic phase transitions using the magnetocaloric effect. *Nature Communications*, 9:2680, 2018.
- [378] M. Jeddi, H. Gharsallah, M. Bejar, et al. Magnetocaloric study, critical behavior and spontaneous magnetization estimation in $\text{La}_{0.6}\text{Ca}_{0.3}\text{Sr}_{0.1}\text{MnO}_3$ perovskite. *RSC Advances*, 8:9430–9439, 2018.
- [379] S. Tarhouni, R. M’nassri, A. Mleiki, et al. Analysis based on scaling relations of critical behaviour at pm-fm phase transition and universal curve of magnetocaloric effect in selected ag-doped manganites. *RSC Advances*, 8:18294–18307, 2018.
- [380] P. Z. Z. Nehan, O. Vitayaya, D. R. Munazat, et al. The magnetocaloric effect properties for potential applications of magnetic refrigerator technology: a review. *Physical Chemistry Chemical Physics*, 26:14476–14504, 2024.
- [381] Z. Zheng, F. Zhang, H. Shentu, et al. Magnetic properties and magnetocaloric effect of chromium-based high-entropy perovskite oxides. *Journal of Alloys and Compounds*, 1010:177632, 2025.
- [382] S. Huang, J. Lin, Y. Shu, and Y. Zhang. Magnetic properties and magnetocaloric effect in $\text{ Tb}_2\text{FeCoO}_6$ double perovskite oxide. *Journal of Electronic Materials*, 53:2302–2308, 2024.
- [383] R. Masrour. Effect of magnetic field on the magnetocaloric and magnetic properties of perovskite orthoferrites. In *Magnetoelectronic, Optical, and*

- Thermoelectric Properties of Perovskite Materials*, pages 109–118. Springer Nature Switzerland, Cham, 2024.
- [384] F. x. Hu, B. Shen, J. Sun, Z. Cheng, and X. Zhang. Magnetic entropy change in $\text{La}(\text{Fe}_{0.98}\text{Co}_{0.02})_{11.7}\text{Al}_{1.3}$. *Journal of Physics: Condensed Matter*, 12:L691, 2000.
- [385] Z. M. Wang, G. Ni, Q. Y. Xu, H. Sang, and Y. W. Du. Magnetocaloric effect in perovskite manganites $\text{La}_{0.7-x}\text{Nd}_x\text{Ca}_{0.3}\text{MnO}_3$ and $\text{La}_{0.7}\text{Ca}_{0.3}\text{MnO}_3$. *Journal of Applied Physics*, 90:5689–5691, 2001.
- [386] V. K. Pecharsky and K. A. Gschneidner. Giant magnetocaloric effect in $\text{Gd}_5(\text{Si}_2\text{Ge}_2)$. *Physical Review Letters*, 78:4494, 1997.
- [387] M. H. Phan, H. X. Peng, and S. C. Yu. Large magnetocaloric effect in single crystal $\text{Pr}_{0.63}\text{Sr}_{0.37}\text{MnO}_3$. *Journal of Applied Physics*, 97:10M306, 2005.
- [388] K. Das, T. Paramanik, and I. Das. Large magnetocaloric effect in $\text{Ln}_{0.5}\text{Ca}_{0.5}\text{MnO}_3$ ($\text{Ln} = \text{Gd}, \text{Dy}$) compounds: Consequence of magnetic precursor effect of rare earth ions. *Journal of Magnetism and Magnetic Materials*, 374:707–710, 2015.
- [389] Q. Li, L. Xing, and M. Xu. Magnetic properties, resistivity and magnetoresistance effects of double perovskite $\text{La}_2\text{Co}_{1-x}\text{Fe}_x\text{MnO}_6$. *Journal of Alloys and Compounds*, 710:771–777, 2017.
- [390] H. E. Stanley and G. Ahlers. Introduction to phase transitions and critical phenomena. *Physics Today*, 26:71–72, 1973.
- [391] K. Ghosh, C. J. Lobb, R. L. Greene, et al. Critical phenomena in the double-exchange ferromagnet $\text{La}_{0.7}\text{Sr}_{0.3}\text{MnO}_3$. *Physical Review Letters*, 81:4740–4743, 1998.
- [392] A. K. Pramanik and A. Banerjee. Critical behavior at paramagnetic to ferromagnetic phase transition in $\text{Pr}_{0.5}\text{Sr}_{0.5}\text{MnO}_3$: A bulk magnetization study. *Phys. Rev. B*, 79, 2009. doi: 10.1103/PhysRevB.79.214426.
- [393] B. K. Banerjee. On a generalised approach to first and second order magnetic transitions. *Physics Letters*, 12:16–17, 1964.

- [394] L. Zhang, T. Shi, J. Cao, et al. Critical behavior and magnetocaloric effect in the multiferroic double perovskite $\text{Lu}_2\text{NiMnO}_6$. *Journal of Alloys and Compounds*, 763:613–621, 2018.
- [395] B. Widom. Equation of state in the neighborhood of the critical point. *Journal of Chemical Physics*, 43:3898–3905, 1965.
- [396] M. E. Fisher Baker and I. Aboratory. The renormalization group in the theory of critical behavior. *Rev. Mod. Phys.*, 46:597, 1974.
- [397] S. F. Fischer, S. N. Kaul, and H. Kronmüller. Critical magnetic properties of disordered polycrystalline $\text{Cr}_{75}\text{Fe}_{25}$ and $\text{Cr}_{70}\text{Fe}_{30}$ alloys. *Phys. Rev. B*, 65: 644431, 2002.
- [398] M. Campostrini, M. Hasenbusch, A. Pelissetto, P. Rossi, and E. Vicari. Critical exponents and equation of state of the three-dimensional heisenberg universality class. *Phys. Rev. B*, 65(144520), 2002.
- [399] M. B. Salamon and M. Jaime. The physics of manganites: Structure and transport. *Rev. Mod. Phys.*, 73:583, 2001.
- [400] J. Deisenhofer, D. Braak, H. A. Krug von Nidda, et al. Observation of a griffiths phase in paramagnetic $\text{La}_{1-x}\text{Sr}_x\text{MnO}_3$. *Phys. Rev. Lett.*, 95(257202), 2005.
- [401] A. J. Bray. Theory of phase-ordering kinetics. *Adv. Phys.*, 51:481–587, 2002.
- [402] K. G. Wilson. The renormalization group: Critical phenomena and the kondo problem. *Rev. Mod. Phys.*, 47:773, 1975.
- [403] T. Kimura et al. Magnetic control of ferroelectric polarization. *Nature*, 426: 55–58, 2003.
- [404] H. Serrano-González et al. Structural and magnetic characterization of the frustrated triangular-lattice antiferromagnets $\text{CsFe}(\text{SO}_4)_2$ and $\text{RbFe}(\text{SO}_4)_2$. *Phys. Rev. B*, 59(14451), 1999.
- [405] J. Blasco, G. Subías, J. L. García-Muñoz, F. Fauth, and J. García. Determination of the crystal structures in the a-site-ordered YbMn_2O_6 perovskite. *J. Phys. Chem. C*, 125:19467–19480, 2021.

- [406] J. Blasco, J. L. García-Muñoz, J. García, et al. Magnetic order and magnetoelectric properties of $r_2\text{comno}_6$ perovskites ($r = \text{ho, tm, yb, and lu}$). *Phys. Rev. B*, 96(024409), 2017.
- [407] H. Horner and C. M. Varma. Nature of spin-reorientation transitions. *Phys. Rev. Lett.*, 20:845–846, 1968. doi: 10.1103/PhysRevLett.20.845. URL <https://link.aps.org/doi/10.1103/PhysRevLett.20.845>.
- [408] S. A. J. Kimber, A. H. Hill, Y-Z. Zhang, H. O. Jeschke, R. Valentí, C. Ritter, I. Schellenberg, W. Hermes, R. Pöttgen, and D. N. Argyriou. Local moments and symmetry breaking in metallic PrMnSbO . *Phys. Rev. B*, 82:100412, 2010. doi: 10.1103/PhysRevB.82.100412. URL <https://link.aps.org/doi/10.1103/PhysRevB.82.100412>.
- [409] A. Marcinkova, T. C. Hansen, C. Curfs, S. Margadonna, and J. W. G. Bos. Nd-induced Mn spin-reorientation transition in NdMnAsO . *Phys. Rev. B*, 82:174438, 2010. doi: 10.1103/PhysRevB.82.174438. URL <https://link.aps.org/doi/10.1103/PhysRevB.82.174438>.
- [410] Q. Zhang, W. Tian, S. G. Peterson, K. W. Dennis, and D. Vaknin. Spin reorientation and Ce-Mn coupling in antiferromagnetic oxypnictide CeMnAsO . *Phys. Rev. B*, 91:064418, 2015. doi: 10.1103/PhysRevB.91.064418. URL <https://link.aps.org/doi/10.1103/PhysRevB.91.064418>.
- [411] A. J. Corkett, D. G. Free, and S. J. Clarke. Spin-reorientation transition in CeMnAsO . *Inorganic Chemistry*, 54(3):1178–1184, 2015. doi: 10.1021/ic5026608. URL <https://doi.org/10.1021/ic5026608>.
- [412] R. L. White. Review of Recent Work on the Magnetic and Spectroscopic Properties of the Rare-Earth Orthoferrites. *Journal of Applied Physics*, 40(3):1061–1069, 1969. ISSN 0021-8979. doi: 10.1063/1.1657530. URL <https://doi.org/10.1063/1.1657530>.
- [413] J. P. Bolletta, F. Pomiro, R. D. Sánchez, V. Pomjakushin, G. Aurelio, A. Maignan, C. Martin, and R. E. Carbonio. Spin reorientation and metamagnetic transitions in $R\text{Fe}_{0.5}\text{Cr}_{0.5}\text{O}_3$ perovskites ($R = \text{Tb, Dy, Ho, Er}$). *Phys. Rev. B*, 98:134417, 2018. doi: 10.1103/PhysRevB.98.134417. URL <https://link.aps.org/doi/10.1103/PhysRevB.98.134417>.

- [414] Z. Tie-son, J. Han-min, G. Guang-hua, H. Xiu-feng, and C. Hong. Magnetic properties of R ions in $R\text{Co}_5$ compounds ($R = \text{Pr}, \text{Nd}, \text{Sm}, \text{Gd}, \text{Tb}, \text{Dy}, \text{Ho}, \text{and Er}$). *Phys. Rev. B*, 43:8593–8598, 1991. doi: 10.1103/PhysRevB.43.8593. URL <https://link.aps.org/doi/10.1103/PhysRevB.43.8593>.
- [415] A. M. Vibhakar, D. D. Khalyavin, P. Manuel, L. Zhang, K. Yamaura, P. G. Radaelli, A. A. Belik, and R. D. Johnson. Magnetic structure and spin-flop transition in the a -site columnar-ordered quadruple perovskite TmMn_3O_6 . *Phys. Rev. B*, 99:104424, 2019. doi: 10.1103/PhysRevB.99.104424. URL <https://link.aps.org/doi/10.1103/PhysRevB.99.104424>.
- [416] N. Locatelli, V. Cros, and J. Grollier. Spin-torque building blocks. *Nature Materials*, 13:11–20, 2014. doi: 10.1038/nmat3823. URL <https://doi.org/10.1038/nmat3823>.
- [417] Y. Yang, R.B. Wilson, J. Gorchon, C.-H. Lambert, S. Salahuddin, and J. Bokor. Ultrafast magnetization reversal by picosecond electrical pulses. *Nature Materials*, 3:e1603117, 2017. doi: 10.1126/sciadv.1603117. URL <https://doi.org/10.1126/sciadv.1603117>.
- [418] F. Mezzadri, G. Calestani, M. Calicchio, E. Gilioli, F. Bolzoni, R. Cabassi, M. Marezio, and A. Migliori. Synthesis and characterization of multiferroic $\text{BiMn}_7\text{O}_{12}$. *Phys. Rev. B*, 79:100106, 2009. doi: 10.1103/PhysRevB.79.100106. URL <https://link.aps.org/doi/10.1103/PhysRevB.79.100106>.
- [419] R. D. Johnson, L. C. Chapon, D. D. Khalyavin, P. Manuel, P. G. Radaelli, and C. Martin. Giant improper ferroelectricity in the ferroaxial magnet $\text{CaMn}_7\text{O}_{12}$. *Phys. Rev. Lett.*, 108:067201, 2012. doi: 10.1103/PhysRevLett.108.067201. URL <https://link.aps.org/doi/10.1103/PhysRevLett.108.067201>.
- [420] D. Behr, A. A. Belik, D. D. Khalyavin, and R. D. Johnson. $\text{BiMn}_7\text{O}_{12}$: Polar antiferromagnetism by inverse exchange striction. *Phys. Rev. B*, 107:L140402, 2023. doi: 10.1103/PhysRevB.107.L140402. URL <https://link.aps.org/doi/10.1103/PhysRevB.107.L140402>.
- [421] Z. Zeng, M. Greenblatt, M. A. Subramanian, and M. Croft. Large low-field magnetoresistance in perovskite-type $\text{CaCu}_3\text{Mn}_4\text{O}_{12}$ without double exchange. *Phys. Rev. Lett.*, 82:3164–3167, 1999. doi: 10.1103/PhysRevLett.82.3164. URL <https://link.aps.org/doi/10.1103/PhysRevLett.82.3164>.

- [422] R. D. Johnson, D. D. Khalyavin, P. Manuel, A. Bombardi, C. Martin, L. C. Chapon, and P. G. Radaelli. Modulated spin helicity stabilized by incommensurate orbital density waves in a quadruple perovskite manganite. *Phys. Rev. B*, 93:180403, 2016. doi: 10.1103/PhysRevB.93.180403. URL <https://link.aps.org/doi/10.1103/PhysRevB.93.180403>.
- [423] G. King and P. M. Woodward. Cation ordering in perovskites. *J. Mater. Chem.*, 20:5785–5796, 2010. doi: 10.1039/B926757C. URL <http://dx.doi.org/10.1039/B926757C>.
- [424] A. A. Belik. Rise of A-site columnar-ordered $A_2A'B_4O_{12}$ quadruple perovskites with intrinsic triple order. *Dalton Trans.*, 47:3209–3217, 2018. doi: 10.1039/C7DT04490A. URL <http://dx.doi.org/10.1039/C7DT04490A>.
- [425] A. M. Glazer. The classification of tilted octahedra in perovskites. *Acta Crystallographica Section B*, 28(11):3384–3392, 1972. doi: 10.1107/S0567740872007976. URL <https://doi.org/10.1107/S0567740872007976>.
- [426] A. A. Belik, D. D. Khalyavin, L. Zhang, Y. Matsushita, Y. Katsuya, M. Tanaka, R. D. Johnson, and K. Yamaura. Intrinsic triple order in A-site columnar-ordered quadruple perovskites: Proof of concept. *ChemPhysChem*, 19(19):2449–2452, 2018. doi: <https://doi.org/10.1002/cphc.201800593>. URL <https://chemistry-europe.onlinelibrary.wiley.com/doi/abs/10.1002/cphc.201800593>.
- [427] J. Rodríguez-Carvajal. Recent advances in magnetic structure determination by neutron powder diffraction. *Physica B: Condensed Matter*, 192(1): 55–69, 1993. ISSN 0921-4526. doi: [https://doi.org/10.1016/0921-4526\(93\)90108-I](https://doi.org/10.1016/0921-4526(93)90108-I). URL <https://www.sciencedirect.com/science/article/pii/092145269390108I>.
- [428] M. Hutchings. *Solid State Physics*, 16:227, 1964.
- [429] A.J. Freeman and J.P. Desclaux. Dirac-Fock studies of some electronic properties of rare-earth ions. *Journal of Magnetism and Magnetic Materials*, 12(1):11–21, 1979. ISSN 0304-8853. doi: [https://doi.org/10.1016/0304-8853\(79\)90328-7](https://doi.org/10.1016/0304-8853(79)90328-7). URL <https://www.sciencedirect.com/science/article/pii/0304885379903287>.
- [430] F. K. K. Kirschner, R. D. Johnson, F. Lang, D. D. Khalyavin, P. Manuel, T. Lancaster, D. Prabhakaran, and S. J. Blundell. Spin jahn-teller antifer-

romagnetism in CoTi_2O_5 . *Phys. Rev. B*, 99:064403, 2019. doi: 10.1103/PhysRevB.99.064403. URL <https://link.aps.org/doi/10.1103/PhysRevB.99.064403>.